WOODHEAD PUBLISHING SERIES IN ELECTRONIC AND OPTICAL MATERIALS

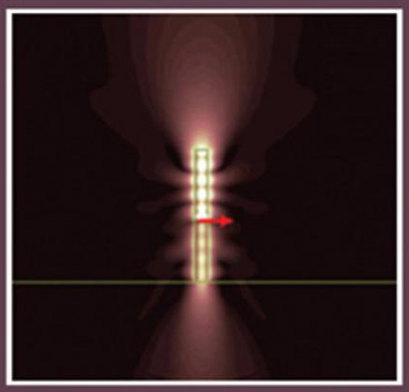

Quantum Information Processing with Diamond

Principles and Applications

Edited by Steven Prawer and Igor Aharonovich

WP
WOODHEAD PUBLISHING

Quantum Information Processing with Diamond

Related titles:

Quantum optics with semiconductor nanostructures
(ISBN 978-0-85709-232-8)

Optical switches: Materials and design
(ISBN 978-1-84569-579-8)

Semiconductor lasers: Fundamentals and applications
(ISBN 978-0-85709-121-5)

Woodhead Publishing Series in Electronic and Optical Materials:
Number 63

Quantum Information Processing with Diamond

Principles and Applications

Edited by
Steven Prawer and Igor Aharonovich

AMSTERDAM • BOSTON • CAMBRIDGE • HEIDELBERG • LONDON
NEW YORK • OXFORD • PARIS • SAN DIEGO
SAN FRANCISCO • SINGAPORE • SYDNEY • TOKYO
Woodhead Publishing is an imprint of Elsevier

Woodhead Publishing is an imprint of Elsevier
80 High Street, Sawston, Cambridge, CB22 3HJ, UK
225 Wyman Street, Waltham, MA 02451, USA
Langford Lane, Kidlington, OX5 1GB, UK

Copyright © 2014 Elsevier Ltd. All rights reserved

No part of this publication may be reproduced, stored in a retrieval system or transmitted in any form or by any means electronic, mechanical, photocopying, recording or otherwise without the prior written permission of the publisher.
Permissions may be sought directly from Elsevier's Science & Technology Rights Department in Oxford, UK: phone (+44) (0) 1865 843830; fax (+44) (0) 1865 853333; email: permissions@elsevier.com. Alternatively, you can submit your request online by visiting the Elsevier website at http://elsevier.com/locate/permissions, and selecting Obtaining permission to use Elsevier material.

Notice
No responsibility is assumed by the publisher for any injury and/or damage to persons or property as a matter of products liability, negligence or otherwise, or from any use or operation of any methods, products, instructions or ideas contained in the material herein. Because of rapid advances in the medical sciences, in particular, independent verification of diagnoses and drug dosages should be made.

British Library Cataloguing-in-Publication Data
A catalogue record for this book is available from the British Library.

Library of Congress Control Number: 2014934012

ISBN 978-0-85709-656-2 (print)
ISBN 978-0-85709-668-5 (online)

For information on all Woodhead Publishing publications visit our website at http://store.elsevier.com/

Typeset by RefineCatch Limited, Bungay, Suffolk

Printed and bound in the United Kingdom

Contents

Contributor contact details *xi*
Woodhead Publishing Series in Electronic and Optical Materials *xv*
Foreword *xxi*

Part I Principles and fabrication techniques 1

1 Principles of quantum information processing (QIP) using diamond 3
P. E. Barclay, University of Calgary, Canada

1.1 Introduction 3
1.2 The role of diamond impurities in quantum information processing (QIP) 3
1.3 Types of diamond color center 4
1.4 Key properties of nitrogen–vacancy (NV) centers 6
1.5 Techniques for creating NV centers 8
1.6 QIP with NV centers: diamond photonic networks 10
1.7 Conclusion 17
1.8 References 18

2 Principles of quantum cryptography/quantum key distribution (QKD) using attenuated light pulses 21
H. Weinfurter, LMU Munich, Germany

2.1 Introduction 21
2.2 Principles of quantum key distribution (QKD): the BB84 protocol 22
2.3 Protocol extensions and alterations 24
2.4 Implementing QKD 26
2.5 Fiber-based QKD 27
2.6 Free-space QKD 29
2.7 Future trends 32

2.8 Conclusion 33
2.9 References 33

3 Ion implantation in diamond for quantum information processing (QIP): doping and damaging 36
R. KALISH, Technion, Israel Institute of Technology, Israel

3.1 Introduction 36
3.2 Doping diamond 38
3.3 Doping diamond by ion implantation 41
3.4 Controlled formation of implant–defect centers 50
3.5 Applications of graphitization of diamond by highly damaging implantations 54
3.6 Computer simulations of damage in diamond 57
3.7 Conclusion 64
3.8 Acknowledgments 65
3.9 References 65

4 Characterisation of single defects in diamond in the development of quantum devices 68
J. M. SMITH, University of Oxford, UK

4.1 Introduction 68
4.2 Experimental methods for fluorescence microscopy of single colour centres in diamond 70
4.3 Optical spectroscopy of single defects 81
4.4 Photon statistics 86
4.5 Spin resonance 90
4.6 Conclusions and future trends 95
4.7 References 95

5 Nanofabrication of photonic devices from single-crystal diamond for quantum information processing (QIP) 98
J. T. CHOY, B. J. M. HAUSMANN, M. J. BUREK, T. M. BABINEC and M. LONČAR, Harvard University, USA

5.1 Introduction 98
5.2 Fabrication approaches for single-crystal diamond nanostructures 101
5.3 Single-photon sources in nanostructured diamond: diamond nanowires and diamond–silver hybrid resonators 106
5.4 Single-photon sources in nanostructured diamond: integrated ring resonators and photonic-crystal cavities 113
5.5 Conclusions and future trends 116
5.6 Acknowledgments 119
5.7 References 119

Part II Experimental demonstrations and emerging applications of quantum information processing (QIP) using diamond 125

6 Diamond-based single-photon sources and their application in quantum key distribution 127
E. Neu, Universität des Saarlandes, Germany and University of Basel, Switzerland and C. Becher, Universität des Saarlandes, Germany

6.1 Introduction 127
6.2 Characterization and key parameters of a single-photon source 130
6.3 Suitability of colour centres in diamond as single-photon sources 135
6.4 Colour centres in diamond as single-photon sources: types of colour centres investigated as single emitters 137
6.5 Colour centres in diamond as single-photon sources: specific properties 142
6.6 Quantum key distribution with nitrogen–vacancy (NV) and silicon–vacancy (SiV) centres 150
6.7 Future trends 153
6.8 References 154

7 Using defect centres in diamonds to build photonic and quantum optical devices 160
A. W. Schell, J. Wolters, T. Schröder and O. Benson, Humboldt-Universität zu Berlin, Germany

7.1 Introduction 160
7.2 Architectures for single-photon collection and single-photon interaction 161
7.3 Properties of defect centres in nanodiamonds 164
7.4 A method for controlled assembly of fundamental photonic elements using a scanning probe technique 168
7.5 Fundamental photonic and plasmonic elements assembled from nanodiamonds by a scanning probe technique 171
7.6 Photonic elements made from nanodiamonds in laser-written structures 177
7.7 Applications of engineered single-photon sources based on nanodiamonds 180
7.8 Future trends 187
7.9 Acknowledgements 189
7.10 References 189

8 Spin–photon entanglement in diamond for quantum optical networks 195
G. Dutt and M. U. Momeen, University of Pittsburgh, USA

8.1 Introduction 195
8.2 How measurements of single photons result in entanglement 196
8.3 Optical properties of nitrogen–vacancy (NV) center for spin–photon entanglement generation 200
8.4 Generation of spin–photon entanglement 202
8.5 Hong–Ou–Mandel interference between identical photons from NV centers 210
8.6 Single-shot projective readout of NV centers 213
8.7 Future trends 213
8.8 Sources of further information and advice 216
8.9 Acknowledgements 216
8.10 References 216

9 Quantum microscopy using nanodiamonds 219
L. P. McGuinness, University of Ulm, Germany

9.1 Introduction 219
9.2 Properties of nanodiamonds for bioimaging 220
9.3 Conventional microscopy with nanodiamonds 224
9.4 Quantum microscopy with nanodiamonds I: magnetometry 226
9.5 Quantum microscopy with nanodiamonds II: rotational tracking, electrometry and thermometry 230
9.6 Future trends 232
9.7 Sources of further information and advice 233
9.8 References 233

10 Diamond magnetic sensors 240
P. Maletinsky, University of Basel, Switzerland and V. Jacques, Université Paris Sud and ENS Cachan, France

10.1 Introduction 240
10.2 Magnetometry with nitrogen–vacancy (NV) centers 241
10.3 Scanning NV magnetometry 251
10.4 Conclusion and future trends 257
10.5 References 259

11 Hybridization of quantum systems: coupling nitrogen–vacancy (NV) centers in diamond to superconducting circuits 264
R. Amsüss, Technische Universität Wien, Austria and S. Saito and W. J. Munro, NTT Corporation, Japan

11.1 Introduction 264
11.2 Spin ensembles 266

11.3 Superconducting circuits 271
11.4 Collective coupling in the hybrid system 276
11.5 Towards quantum memory operations 284
11.6 Conclusions and future trends 286
11.7 References 287

12 Neural circuits and *in vivo* monitoring using diamond 291
K. Fox and S. Prawer, University of Melbourne, Australia
12.1 Introduction 291
12.2 The diamond–cell interface 292
12.3 Diamond biosensors 294
12.4 Neural networks using diamond 295
12.5 Neural stimulation and recording using diamond 297
12.6 Future trends 300
12.7 References 300

Part III The future 305

13 Promising directions in diamond technologies for quantum information processing (QIP) and sensing 307
I. Aharonovich, University of Technology Sydney, Australia and S. Prawer, University of Melbourne, Australia
13.1 Introduction 307
13.2 Nanodiamonds for high-resolution sensors 307
13.3 Exploiting fundamental properties: optomechanics and other areas of advanced research 309
13.4 Challenges in diamond materials science 311
13.5 Conclusion 314
13.6 References 315

Index *318*

This page intentionally left blank

Contributor contact details

(* = main contact)

Editors

S. Prawer
Melbourne Materials Institute
School of Physics
University of Melbourne
Room 159
Parkville, VIC 3010, Australia

E-mail: s.prawer@unimelb.edu.au

I. Aharonovich
School of Physics and Advanced Materials
University of Technology Sydney
Ultimo, NSW 2007, Australia

E-mail: igor.aharonovich@uts.edu.au

Chapter 1

P. E. Barclay
Institute for Quantum Information Science
University of Calgary
Calgary, AB T2N 1N3, Canada

E-mail: pbarclay@ucalgary.ca

Chapter 2

H. Weinfurter
Faculty of Physics
LMU Munich
Schellingstr. 4
D-80799 Munich, Germany

E-mail: h.w@lmu.de

Chapter 3

R. Kalish
Physics Department and Solid State Institute
Technion, Israel Institute of Technology
Technion City
Haifa 32000, Israel

E-mail: kalish@technion.ac.il

Chapter 4

J. M. Smith
Department of Materials
University of Oxford
Parks Road
Oxford OX1 3PH, UK

E-mail: jason.smith@materials.ox.ac.uk

Chapter 5

J. T. Choy, B. J. M. Hausmann, M. J. Burek, T. M. Babinec and M. Lončar*
Harvard University
Maxwell Dworkin 127
33 Oxford Street
Cambridge, MA 02138, USA

E-mail: loncar@seas.harvard.edu

Chapter 6

E. Neu
Universität des Saarlandes
Fachrichtung 7.2 Experimentalphysik
Campus E2.6
66123 Saarbrücken, Germany

and

Department of Physics
University of Basel
Klingelbergstrasse 82
CH-4056 Basel, Switzerland

E-mail: elke.neu@unibas.ch

C. Becher*
Universität des Saarlandes
Fachrichtung 7.2 Experimentalphysik
Campus E2.6
66123 Saarbrücken, Germany

E-mail: christoph.becher@physik.uni-saarland.de

Chapter 7

A. W. Schell, J. Wolters, T. Schröder and O. Benson*
AG Nanooptik
Institut für Physik
Humboldt-Universität zu Berlin
Newtonstr. 15
12489 Berlin, Germany

E-mail: oliver.benson@physik.hu-berlin.de

Chapter 8

G. Dutt* and M. U. Momeen
Department of Physics and Astronomy
University of Pittsburgh
100 Allen Hall
3941 O'Hara Street
Pittsburgh, PA 15260, USA

E-mail: gdutt@pitt.edu

Chapter 9

L. P. McGuinness
Institute for Quantum Optics
Albert-Einstein-Allee 11
University of Ulm
89081 Ulm, Germany

E-mail: liam.mcguinness@uni-ulm.de

Chapter 10

P. Maletinsky*
Department of Physics
University of Basel
Klingelbergstrasse 82
CH-4056 Basel, Switzerland

E-mail: patrick.maletinsky@unibas.ch

V. Jacques
Laboratoire Aim′e Cotton, CNRS
Universit′e Paris Sud and ENS Cachan
91405 Orsay, France

E-mail: vincent.jacques@ens-cachan.fr

Chapter 11

R. Amsüss
Vienna Center for Quantum Science and Technology
Atominstitut
Technische Universität Wien
Stadionallee 2
1020 Vienna, Austria

S. Saito and W. J. Munro*
NTT Basic Research Laboratories
NTT Corporation
3-1 Morinosato-Wakamiya
Atsugi
Kanagawa 243-0198, Japan

E-mail: bilmun@qis1.ex.nii.ac.jp

Chapter 12

K. Fox and S. Prawer*
Melbourne Materials Institute
School of Physics
University of Melbourne
Room 159
Parkville, VIC 3010, Australia

E-mail: kfox@unimelb.edu.au;
s.prawer@unimelb.edu.au

Chapter 13

I. Aharonovich
School of Physics and Advanced Materials
University of Technology Sydney
Ultimo, NSW 2007, Australia

E-mail: igor.aharonovich@uts.edu.au

S. Prawer
Melbourne Materials Institute
School of Physics
University of Melbourne
Room 159
Parkville, VIC 3010, Australia

E-mail: s.prawer@unimelb.edu.au

This page intentionally left blank

Woodhead Publishing Series in Electronic and Optical Materials

1 **Circuit analysis**
J. E. Whitehouse

2 **Signal processing in electronic communications: For engineers and mathematicians**
M. J. Chapman, D. P. Goodall and N. C. Steele

3 **Pattern recognition and image processing**
D. Luo

4 **Digital filters and signal processing in electronic engineering: Theory, applications, architecture, code**
S. M. Bozic and R. J. Chance

5 **Cable engineering for local area networks**
B. J. Elliott

6 **Designing a structured cabling system to ISO 11801: Cross-referenced to European CENELEC and American Standards**
Second edition
B. J. Elliott

7 **Microscopy techniques for materials science**
A. Clarke and C. Eberhardt

8 **Materials for energy conversion devices**
Edited by C. C. Sorrell, J. Nowotny and S. Sugihara

9 **Digital image processing: Mathematical and computational methods**
Second edition
J. M. Blackledge

10 **Nanolithography and patterning techniques in microelectronics**
Edited by D. Bucknall

11 **Digital signal processing: Mathematical and computational methods, software development and applications**
Second edition
J. M. Blackledge

12 **Handbook of advanced dielectric, piezoelectric and ferroelectric materials: Synthesis, properties and applications**
Edited by Z.-G. Ye

13 **Materials for fuel cells**
Edited by M. Gasik

14 **Solid-state hydrogen storage: Materials and chemistry**
Edited by G. Walker

15 **Laser cooling of solids**
S. V. Petrushkin and V. V. Samartsev

16 **Polymer electrolytes: Fundamentals and applications**
Edited by C. A. C. Sequeira and D. A. F. Santos

17 **Advanced piezoelectric materials: Science and technology**
Edited by K. Uchino

18 **Optical switches: Materials and design**
Edited by S. J. Chua and B. Li

19 **Advanced adhesives in electronics: Materials, properties and applications**
Edited by M. O. Alam and C. Bailey

20 **Thin film growth: Physics, materials science and applications**
Edited by Z. Cao

21 **Electromigration in thin films and electronic devices: Materials and reliability**
Edited by C.-U. Kim

22 ***In situ* characterization of thin film growth**
Edited by G. Koster and G. Rijnders

23 **Silicon-germanium (SiGe) nanostructures: Production, properties and applications in electronics**
Edited by Y. Shiraki and N. Usami

24 **High-temperature superconductors**
Edited by X. G. Qiu

25 **Introduction to the physics of nanoelectronics**
S. G. Tan and M. B. A. Jalil

26 **Printed films: Materials science and applications in sensors, electronics and photonics**
Edited by M. Prudenziati and J. Hormadaly

27 **Laser growth and processing of photonic devices**
Edited by N. A. Vainos

28 **Quantum optics with semiconductor nanostructures**
Edited by F. Jahnke

29 **Ultrasonic transducers: Materials and design for sensors, actuators and medical applications**
Edited by K. Nakamura

30 **Waste electrical and electronic equipment (WEEE) handbook**
Edited by V. Goodship and A. Stevels

31 **Applications of ATILA FEM software to smart materials: Case studies in designing devices**
Edited by K. Uchino and J.-C. Debus

32 **MEMS for automotive and aerospace applications**
Edited by M. Kraft and N. M. White

33 **Semiconductor lasers: Fundamentals and applications**
Edited by A. Baranov and E. Tournie

34 **Handbook of terahertz technology for imaging, sensing and communications**
Edited by D. Saeedkia

35 **Handbook of solid-state lasers: Materials, systems and applications**
Edited by B. Denker and E. Shklovsky

36 **Organic light-emitting diodes (OLEDs): Materials, devices and applications**
Edited by A. Buckley

37 **Lasers for medical applications: Diagnostics, therapy and surgery**
Edited by H. Jelínková

38 **Semiconductor gas sensors**
Edited by R. Jaaniso and O. K. Tan

39 **Handbook of organic materials for optical and (opto)electronic devices: Properties and applications**
Edited by O. Ostroverkhova

40 **Metallic films for electronic, optical and magnetic applications: Structure, processing and properties**
Edited by K. Barmak and K. Coffey

41 **Handbook of laser welding technologies**
Edited by S. Katayama

42 **Nanolithography: The art of fabricating nanoelectronic and nanophotonic devices and systems**
Edited by M. Feldman

43 **Laser spectroscopy for sensing: Fundamentals, techniques and applications**
Edited by M. Baudelet

44 **Chalcogenide glasses: Preparation, properties and applications**
Edited by J.-L. Adam and X. Zhang

45 **Handbook of MEMS for wireless and mobile applications**
Edited by D. Uttamchandani

46 **Subsea optics and imaging**
Edited by J. Watson and O. Zielinski

47 **Carbon nanotubes and graphene for photonic applications**
Edited by S. Yamashita, Y. Saito and J. H. Choi

48 **Optical biomimetics: Materials and applications**
Edited by M. Large

49 **Optical thin films and coatings**
Edited by A. Piegari and F. Flory

50 **Computer design of diffractive optics**
Edited by V. A. Soifer

51 **Smart sensors and MEMS: Intelligent devices and microsystems for industrial applications**
Edited by S. Nihtianov and A. Luque

52 **Fundamentals of femtosecond optics**
S. A. Kozlov and V. V. Samartsev

53 **Nanostructured semiconductor oxides for the next generation of electronics and functional devices: Properties and applications**
S. Zhuiykov

54 **Nitride semiconductor light-emitting diodes (LEDs): Materials, technolgies and applications**
Edited by J. J. Huang, H. C. Kuo and S. C. Shen

55 **Sensor technologies for civil infrastructures**
Volume 1: Sensing hardware and data collection methods for performance assessment
Edited by M. Wang, J. Lynch and H. Sohn

56 **Sensor technologies for civil infrastructures**
Volume 2: Applications in structural health monitoring
Edited by M. Wang, J. Lynch and H. Sohn

57 **Graphene: Properties, preparation, characterisation and devices**
Edited by V. Skákalová and A. B. Kaiser

58 **Handbook of silicon-on-insulator (SOI) technology**
Edited by O. Kononchuk and B.-Y. Nguyen

59 **Biological identification: DNA amplification and sequencing, optical sensing, lab-on-chip and portable systems**
Edited by P. Schaudies

60 **High performance silicon imaging: Fundamentals and applications of CMOS and CCD sensors**
Edited by D. Durini

61 **Nanosensors for chemical and biological applications: Sensing with nanotubes, nanowires and nanoparticles**
Edited by K. C. Honeychurch

62 **Composite magnetoelectrics: Materials, structures, and applications**
G. Srinivasan, S. Priya and N. Sun

63 **Quantum information processing with diamond: Principles and applications**
Edited by S. Prawer and I. Aharonovich

64 **Advances in non-volatile memory and storage technology**
Edited by Y. Nishi

65 **Laser surface engineering: Processes and applications**
Edited by J. Lawrence, C. Dowding, D. Waugh and J. Griffiths

66 **Power ultrasonics: A handbook of materials, design and applications of high power ultrasound transducers**
Edited by J. A. Gallego-Juárez

67 **Advances in delay-tolerant networks (DTNs): Architecture and enhanced performance**
Edited by J. Rodrigues

68 **Handbook of flexible organic electronics: Materials, manufacturing and applications**
Edited by S. Logothetidis

69 **Machine-to-machine (M2M) communications: Architecture, performance and applications**
Edited by C. Anton-Haro and M. Dohler

70 **Ecological design of smart home networks: Technologies, social impact and sustainability**
Edited by N. Saito and D. Menga

71 **Industrial tomography: Systems and applications**
Edited by M. Wang

72 **Vehicular communications and networks: Architectures, protocols, operation and deployment**
Edited by W. Chen

73 **Modeling, characterization, and production of nanomaterials: Electronics, photonics and energy applications**
Edited by V. Tewary and Y. Zhang

74 **Reliability characterisation of electrical and electronic systems**
Edited by J. Swingler

75 **Handbook of industrial wireless sensor networks: Monitoring, control and automation**
Edited by R. Budampati S. Kolavennu

76 **Epitaxial growth of complex metal oxides: Techniques, properties and applications**
Edited by G. Koster and G. Rijnders

77 **Semiconductor nanowires: Materials, synthesis, characterization and applications**
Edited by J. Arbiol and Q. Xiong

This page intentionally left blank

Foreword

Diamond exhibits several unique physical properties: a wide band gap, high thermal conductivity, hardness and inertness. These unique characteristics mean that diamond plays a unique role in many technologies. During the last decade, a new field of application of diamond related to quantum engineering has emerged. This book reports the fascinating progress that has been achieved in this rapidly developing interdisciplinary field of research.

A number of leading scientists have reported how the unique properties of diamond and methods for controlling those properties have created the potential for using 'quantum diamond' in a wide range of new technologies. There are three major applications of diamond in the context of the control of single defects. The first is related to the generation of scalable quantum registers for quantum information-processing protocols. The second field relates to the generation of single-photon emitters using color centers as a light source. This application is crucial for linear-optics quantum computing and the rapidly growing field of quantum communications. The third area is the application of diamond defects for novel imaging and sensing technologies.

The book is organized into a number of parts. The first part covers the background to novel diamond technologies and includes an overview of single-photon sources for quantum cryptography, quantum information processing with defects and the basic principles of nanoengineering of diamond. The ability to engineer color centers on demand and with high spatial accuracy is crucial for many quantum-based technologies. This is why the field of ion implantation is reviewed in depth in the book. The second part of the book covers different application areas associated with single color centers in diamond. Some of the applications are already at a very advanced stage. As an example, diamond-based single-photon sources are now commercially available. Part II also contains an overview of diamond sensor technology, such as novel diamond-based microscopy techniques and neuroimaging, that will potentially come to the market in the near future. Applications related to quantum information processing include scalable quantum networks, integrated diamond photonics and quantum memories based on ensembles of diamond spins. Finally, the interdisciplinary field of quantum

applications in biological systems is also highlighted, paving the way to one of the most fascinating applications of diamond – direct sensing in living cells.

The field of quantum applications of diamond is at quite an early stage of development. This book summarizes the successes in this field during the last decade and shows potential avenues for the future. Written in an accessible style by world-leading experts in the field, the book will be of interest to a broad community of scientists working in the fields of solid-state quantum physics, magnetic resonance, quantum optics and biophysics, as well as to graduate students and those starting out on research in this important field.

Professor Fedor Jelezko
Ulm University, Germany

Part I

Principles and fabrication techniques

This page intentionally left blank

1

Principles of quantum information processing (QIP) using diamond

P. E. BARCLAY, University of Calgary, Canada

DOI: 10.1533/9780857096685.1.3

Abstract: Impurities in diamond are promising candidate qubits for applications in quantum information processing. Electron and nuclear spins associated with these impurities combine long coherence times with optical addressability, and have been used to demonstrate several important elements of proposed quantum information processing systems. Here we review recent experimental progress in the optical manipulation of impurities in diamond, and efforts to build more complex quantum systems involving coupled qubits.

Key words: diamond, quantum, nuclear spins, nitrogen-vacancy, impurities, qubits, colour centre, electronic, photonic networks.

1.1 Introduction

Since the first experimental demonstration in 1997 by Gruber *et al.* of optically detected magnetic resonance of single nitrogen–vacancy (NV) color centers in diamond,[1] researchers have made rapid progress towards utilizing impurities in diamond for applications in quantum information science. Today, impurities in diamond, and NV centers in particular, are leading candidates for solid-state implementations of quantum information processing (QIP) devices.[2–4] This progress has been driven by improvements in the properties of the available material, and by increasingly sophisticated experimental techniques for probing and manipulating the electronic and nuclear spin degrees of freedom of atom-like impurities in diamond.

In the subsequent sections, we review experimental progress towards performing photonic-network-based quantum information processing with diamond. We begin by discussing the properties of diamond impurities which make them suitable for qubits, and introduce approaches to creating diamond impurities suitable for QIP. We then discuss how these impurities can be used for photonic-network-based QIP, in which NV centers separated by microns or meters are entangled using quantum optical interference and measurement.

1.2 The role of diamond impurities in quantum information processing (QIP)

The study of impurities in crystalline materials has long been a topic of interest to solid-state and optical physicists. Impurities play a crucial role in determining the

© 2014 Elsevier Ltd

electronic properties of semiconductors,[5] and are responsible for the color of nominally transparent crystals such as diamond. These latter types of optically active impurities are referred to as color centers. Color centers are candidate qubits when they possess appropriate electronic properties and symmetry within the crystal lattice for optical transitions to be used to manipulate and read out their electronic spin states. In practice, it is also desirable for these spin states to have sufficiently long lifetimes and coherence properties to enable implementation of the operations needed for the proposed quantum information processing.[6]

Beginning in 1974, Davies and colleagues performed many of the first studies of the optical and electronic properties of the spectral lines associated with diamond color center emission,[7–10] laying the groundwork for much of the research described below. By observing the effect of external fields on the photoluminescence properties of diamond color centers, in concert with group-theoretic and other first-principles arguments, researchers have been able to identify spectral features with specific diamond impurities. Since then, over 100 color centers have been identified in diamond.[11] Most of these diamond color centers have been studied in bulk, owing to relatively weak optical transitions, which make it experimentally challenging to observe emission from a single impurity. Although ensembles of color centers may be used as elements in quantum information processing – see for example the progress towards creating quantum memories in diamond,[12, 13] silicon[14] and rare-earth-doped crystals and glasses[15] – it is the unprecedented ability of researchers to manipulate single color centers which makes diamond an attractive platform for quantum information processing.

In recent years, experimentalists have demonstrated manipulation of single color centers with exquisite sensitivity. The quantum state of single electron spins associated with diamond color centers can be manipulated using combinations of optical, microwave and RF fields.[16, 17] These spins have sufficiently long coherence times to enable observation of their coherent coupling to nearby nuclear spins, enabling the first ever demonstration of the measurement of a single nuclear spin.[18, 19] Using related techniques, quantum information can be reversibly mapped from electronic to nuclear spins,[20, 21] where it can be stored for record lengths of times with high fidelity.[22]

Below, we discuss these properties in more detail, and highlight material science issues which must be considered for implementation of practical quantum information processing devices.

1.3 Types of diamond color center

Color centers in diamond consist of a combination of defects in the diamond crystal lattice, which include common impurities such as nitrogen and configurations of missing carbon atoms, referred to as vacancies. A given color center may be found in several possible charge states, depending on the possibility

of accepting or donating charge from or to other carbon atoms or defects in the diamond lattice. If the localized electronic states of a defect support optical transitions between excited and ground states such that the defect is optically active, it may be referred to as a color center. These optical transitions may be accompanied by the generation of phonons through coupling between the change in the electronic wave function during an optical transition and the surrounding elastic crystal lattice.

For the purposes of quantum information processing, the desirable properties of color centers include the potential for their quantum state to be initialized, manipulated and read out. These operations are critical elements of the DiVincenzo criteria for a physical system to be useful for quantum computing.[23] The QIP scheme considered in Section 1.6 requires execution of these operations at the single-color-center level using optical fields, and at a sufficiently high rate to overcome decoherence of the spin states. Linear-optics QIP schemes[24] relying on the generation, interference and detection of single photons do not require the ability to manipulate spin degrees of freedom, but benefit from generation of single photons at a high rate with a high level of indistinguishably. This requires optical transitions with short radiative lifetimes, high radiative efficiency and, ideally, transform-limited linewidths.

With the benefit of experimental evidence, we can understand how the intrinsic physical properties of diamond allow color centers in diamond to be excellent candidate qubits. The theoretical basis for this was studied by Weber *et al.*,[25] in the context of understanding the desirable coherence properties that have been observed in studies of NV centers. Among crystalline materials, diamond has one of the largest electronic band gaps, of 5.5 eV. This allows localized electronic excited and ground states of impurities to be isolated from the valence and conduction bands of the surrounding diamond lattice, even for energies at optical wavelengths. If the diamond lattice consists of the isotopically abundant ^{12}C, which possesses zero nuclear spin, the ground state of the color center spins will not be subjected to magnetic-field fluctuations from the nuclear spins of the surrounding atoms. Finally, the large Young's modulus of diamond results in a high Debye temperature, and a relatively low room temperature phonon population compared with other crystals, decreasing the effect of thermal excitation of crystal lattice phonons on the spin coherence properties.

Of the many color centers identified in diamond, only a small number have been observed at the single-impurity level. The first single color center to be measured was the NV color center,[1] which consists of a nitrogen impurity adjacent to a vacancy in an otherwise perfect diamond carbon lattice. Since then, optical emission from single nickel-related defects,[26] silicon–vacancy defects[27, 28] and chromium[29] impurities has been observed. These impurities all possess optical transitions with relatively large dipole moments characterized by short spontaneous-emission lifetimes. In practice, these transitions allow photoluminescence measurements in which 10^4–10^6 photons per second can be

collected from a single color center using a standard confocal microscope equipped with a high-numerical-aperture (NA = 0.4–0.9) objective.[30] This emission can be efficiently measured using single-photon counters. (Owing to the relatively high detector dark count rates of non-Si-based single-photon counters, this is more challenging for emitters in the near-IR band. Progress in the development of superconducting photon counters[31] promises to alleviate this difficulty.) Depending on the interaction between the emitter and phonons in the crystal lattice, the emission may be spread over a wide bandwidth owing to phonon-assisted emission. (Isolating color center emission from background emission or dark counts becomes more challenging as the transition linewidth broadens.)

1.4 Key properties of nitrogen–vacancy (NV) centers

Of the observed color centers in diamond, negatively charged NV centers have proven to date to be the most promising for QIP applications. The negatively charged NV center, NV^-, has so far been the focus of research attention, and will be considered exclusively in the remainder of this chapter. The electronic structure of a negatively charged NV center, shown in Fig. 1.1, consists of a $^3A_2$ spin triplet ground state connected to a manifold of ^3E excited states by optical transitions with a zero-phonon-line (ZPL) wavelength of 637 nm. In many experiments, NV centers are excited incoherently using a green source at 532 nm. This source excites the NV centers to high-energy states not shown in Fig. 1.1, which decay nonradiatively to the excited states discussed here, before decaying to the ground state and emitting a photon. In addition to this zero-phonon process, phonon sidebands at longer and shorter wavelengths can be generated during emission and absorption via these transitions.

The ground states of the NV^- electronic spin triplet are labeled by $m_s = 0, \pm 1$. The $m_s = \pm 1$ and $m_s = 0$ states are split in energy by 2.87 GHz by the crystal field. The Zeeman effect can be used to tune this splitting with an external magnetic field. In some experiments, the $m_s = -1$ and $m_s = 0$ states have been tuned close to

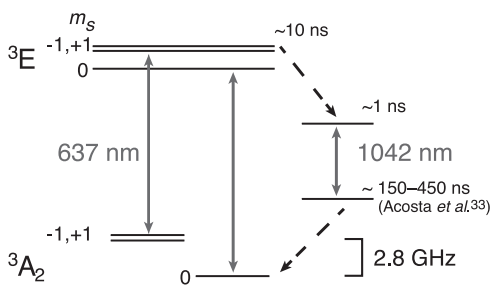

1.1 Electronic structure of NV center.

resonance using a 1000 G magnetic field, where they undergo spin mixing.[32] The ^{3}E excited state is also a spin triplet; however, its fine structure is extremely sensitive to temperature and stress.[33]

A remarkable property of incoherent excitation of NV^- is that this method can be used to initialize and read out the spin ground state. Under 532 nm excitation, the NV^- normally decays via spontaneous emission back to its initial ground state. This is the result of the spin-preserving nature of the incoherent optical excitation and subsequent phononic decay to the ^{3}E states. However, with a small probability, an intersystem crossing may occur, in which population is transferred from the $m_s = \pm 1$ to the $m_s = 0$ ground states. This is mediated by a combination of nonradiative decay and an optical transition at 1042 nm between a pair of singlet states of the NV^-, and has been the topic of significant study in recent years.[34] As a result, after a sufficiently long period of continuous excitation (approximately 1–10 μs), the NV population will be shelved in the $m_s = 0$ ground state. Because of the relatively long lifetime (approximately 100 ns) of the 1042 nm transition, the brightness of the emission from an NV center initialized in the $m_s = 0$ state will be higher than for one in the $m_s = \pm 1$ state. This difference in brightness is the mechanism by which the NV spin state is read out optically. This behavior is exhibited at both room and cryogenic temperature, and is critical to all experiments involving optical measurement and control of NV centers.

Using the incoherent optical initialization and readout techniques described above, in combination with microwave fields, the coherence times of the electronic spin ground states of single NV centers can be measured. By increasing the purity of the diamond carbon lattice – reducing nitrogen impurities to below the ppb level, and ensuring a ^{12}C isotope content of 99.7% – coherence times exceeding a millisecond can be observed at room temperature. Achieving these purities is now possible in diamond samples grown synthetically using chemical vapor deposition (CVD).[35] When the background magnetic-field fluctuations associated with impurities are sufficiently small to enable long electronic spin coherence times, the electronic spin can be used as a sensitive probe of the state of the small number of nuclear spins that have not been removed. Recent experiments have demonstrated coherent coupling between single NV electronic spins and nuclear spins associated with ^{13}C impurities near the NV center. Coherence times exceeding 1 s have been demonstrated for the nuclear spins, making them attractive candidates for storage of quantum information.[22]

At low temperature, the ZPL linewidth narrows, as the effect of thermally excited crystal phonons is reduced. At temperatures below 10 K, the ZPL can have a linewidth as narrow as 13 MHz,[36] limited by the spontaneous-emission lifetime of the excited state. Emission into the zero-phonon line accounts for approximately $\eta_{zpl} \sim 3.5\%$ of the NV emission. Phonon sideband emission accounts for the remainder, and is the result of Franck–Condon coupling between changes in the electronic waveguide during the optical transition which couple to the surrounding crystal lattice. From an the point of view of experimental measurement, phonon

sideband emission both poses challenges and provides opportunities. It decreases the spectral brightness of the NV emission, making it more challenging to distinguish photons emitted by an NV center from background light or detector noise. Coupling NV centers to resonant optical structures such as cavities also becomes challenging, since cavity linewidths are typically much narrower than the sideband bandwidth. As a result, optical cavities only enhance a fraction of the NV emission. In the case of a cavity resonant with the zero-phonon line, the cavity–dipole coupling rate is essentially reduced by a factor of $\sqrt{\eta_{\mathrm{zpl}}}$ relative to the case where all of the emission is into the zero-phonon line, as is the case with atomic quantum emitters and certain quantum dot emitters. Conversely, phonon sideband emission can aid in measurements involving resonant excitation to measure the properties of NV centers. Using spectral filters to separate scattered excitation photons from emitted phonon sideband photons, the population dynamics of the NV centers can be studied as a function of wavelength and other parameters of the resonant excitation field.

Optical transitions between ground states and specific excited states are governed by selection rules dependent on the initial and final spin states and on the polarization of the excitation field. The allowed transitions also depend on the local strain applied to the diamond crystal lattice. In the absence of strain, the excited states consist of a manifold of six excited states split in energy owing to spin–orbit and spin–spin interactions.[37] Stress mixes these states, and creates two branches of excited state with well-defined linear momentum. In many diamond samples, this splitting exceeds the spontaneous-emission linewidth, and can easily be identified by low-resolution (>1 GHz) spectroscopic measurements at cryogenic temperatures. At intermediate stress levels, the states become mixed.[38] Careful control of this mixing is essential for implementing the Λ optical transitions necessary for the measurement-based entanglement schemes presented in the following section. By controlling the polarization of the excitation field, as well its wavelength, it is possible to resonantly excite specific optical transitions of the NV center.[16, 39] This capability is essential for many recent impressive quantum optics experiments involving NV centers, including EIT, spin–photon entanglement and single-shot readout.

1.5 Techniques for creating NV centers

Many of the experimental studies described above were done using ‘naturally occurring’ NV centers. These centers are incorporated into high-purity diamond samples during the CVD growth process, or are found in natural diamond without any special processing. Many proposed QIP applications of NV centers require or would benefit from the ability to locate them deterministically in the crystal lattice. In particular, the QIP schemes discussed in Section 1.3 require an ability to position NV centers relative to optical cavities or other NV centers, with which they can interact directly. An ability to control the density of NV centers is also desirable in

applications in which ensembles of NV centers are needed, for example electromagnetically induced transparency, magnetometry and quantum memory.[12, 13]

There are several methods for postprocessing diamond samples to create NV centers. Generally, the goal of these techniques is to create NV centers whose properties, for example optical linewidth and spin coherence time, are as close to ideal as possible, and to control the location and density of the NV centers created. In practice, it is necessary to balance these sometimes competing requirements. It can be challenging to introduce the elements needed to create an NV center – a vacancy and a nitrogen impurity – without introducing more imperfections than necessary and without degrading the spin coherence and optical transition properties. Similarly, neighboring NV centers will begin to interact as their density is increased, also modifying and/or degrading their optical and spin properties.

Three commonly used techniques for creating NV centers are ion implantation, electron or positron irradiation, and selective nitrogen doping during the CVD growth of diamond. These techniques are typically combined with high-temperature annealing (at $T > 650\,^{\circ}\mathrm{C}$), which causes vacancies to migrate throughout the diamond crystal. It is energetically favorable for vacancies to combine with nitrogen impurities to form NV centers, and if there is a sufficient number of electron donors in the crystal lattice, the NV centers will be preferentially in the desired negatively charged state.

1.5.1 Ion implantation

Ion implantation allows impurities such as N, Ga and He to be implanted into the diamond lattice. The implantation process also damages the diamond lattice, creating vacancies. Ideally, when the sample is annealed, the vacancies will either be removed or combine with nitrogen impurities to create NV centers. Implantation depth profiles vary depending on the implantation element, but can be controlled by adjusting the energy of the ion beam (usually in the keV range). Typically, implantation depths between a few nanometers and 100 nm are used. The profiles can be modeled using widely available software.[40]

A powerful aspect of ion implantation is the spatial control of the implanted ions that it provides. Ions can be implanted with a spatial resolution of less than 50 nm either by using a focused source, for example a He ion microscope[41] or a scanning tip,[42] or by patterning a protective mask on the diamond surface with ~30 nm diameter holes.[43] Thanks to the high spatial resolution of ion implantation, it is an attractive technique for QIP applications requiring the coupling of NV centers to nanophotonic devices such as waveguides and cavities in an on-chip photonic network, as discussed in Section 1.6.

The challenges associated with this approach include minimizing the number of implanted ions needed to create a single NV center, and the relatively high uncertainty in the number of NV centers created per implantation site when one is attempting to create single NV centers. Implantation statistics are Poissonian,

and the likelihood of creating zero or two NV centers when the target is a single NV center per site is high. It may also be difficult to remove excess vacancies that do not create NV centers, as they may combine with other impurities to form other non-NV complexes in the diamond lattice. Excess damage or residual impurities created during ion implantation degrade the properties of the resulting NV centers. Optically, this is manifested in spectral shifts and broadening of the NV ZPL, which is most easily observed at low temperatures. It can also create charge traps which prevent the NV centers from being preferentially observed in the NV^- state.[44] The spin coherence time may also be degraded. Gaining a better understanding of these effects is complicated by the proximity of the implanted NV centers to the diamond surface, which also has an effect on their properties.[45]

1.5.2 Irradiation

Irradiation with an MeV-energy electron or positron flux is a technique commonly used for creating vacancies in diamond samples. As with ion-implanted samples, annealing is used to encourage the vacancies to migrate towards N impurities and form NV centers. The characteristic length scale of the damage profile produced by this technique is much longer than that for ion implantation, and the irradiation usually creates vacancies with a uniform density throughout the diamond sample (with a typical thickness of 250 μm or larger). This technique has been used to create diamond samples with relatively high NV densities whose inhomogeneous linewidths are relatively low compared with ensembles created using ion implantation.[46] It can be applied to both bulk and nanocrystalline diamond samples.

1.5.3 Diamond heterostructures

Incorporation of thin layers of NV centers into otherwise high-purity diamond during the CVD growth process is a recently demonstrated alternative to the implantation techniques described above. This technique allows sheets of NV centers to be embedded near the surface of the diamond sample without introducing unnecessary damage or impurities into the crystal lattice. As has been demonstrated,[47–49] NV centers within 100 nm of the diamond surface with narrow optical linewidths (140 MHz–1.2 GHz) and long coherence times ($T_2 > 600\,\mu s$) have been created in this way. It has been demonstrated[50] that the orientation of these centers within the crystal lattice can also be controlled. These NV centers can be coupled to microwave circuits[51] or nanophotonic structures patterned on the diamond surface.[52, 53]

1.6 QIP with NV centers: diamond photonic networks

As discussed above, the high precision with which the quantum state of NV centers can be controlled makes them attractive candidates for performing QIP.

Their relatively efficient coupling to photons further strengthens their suitability for these applications. Diamond-based QIP has become a major experimental and theoretical research activity, with groups around the world attempting to harness the desirable properties of NV centers to implement the resources needed for QIP. These efforts to utilize NV centers for QIP can be roughly divided into three categories:

- QIP based on NV center single-photon sources;
- QIP based on entanglement and coherent interactions between neighboring NV centers;
- QIP based on long-range entanglement between NV centers within a quantum optical network.

Below, we review progress towards realizing the latter approach.

Optical-network-based QIP involves creating entanglement between multiple quantum systems, or nodes, without a direct interaction between the individual nodes. This scheme, illustrated in cartoon form in Fig. 1.2, relies on being able to coherently map the quantum state of a stationary 'storage qubit' onto a physical system that can be transmitted, called a 'flying qubit', and reversibly mapped back onto a new storage qubit. Photons are excellent flying qubits, thanks to their noninteracting nature and to the existence of nanoscale, microscale, fiber and free-space optical technology optimized for routing and manipulating light. Atomic and solid-state quantum emitters are natural systems for implementing stationary qubits, owing to their optical transitions, which, through judicious experimental design, can be used to manipulate and transmit information describing their internal electronic or nuclear spin quantum state.

Early work on developing the theory underlying this QIP approach was jump-started by a proposal in 1997 from Cirac *et al.*[54] for distributing entanglement

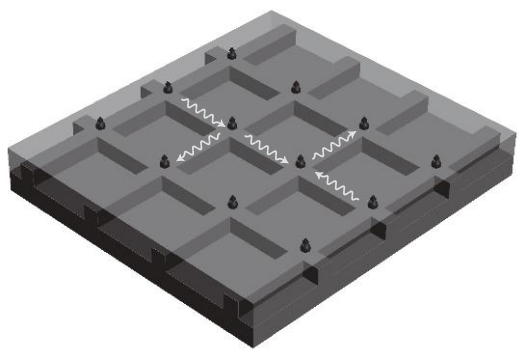

1.2 Cartoon of a photonic-network QIP device in which stationary storage qubits are coherently connected through on-chip photonic channels.

between two nodes of a quantum network. In this proposal, illustrated in Fig. 1.3, two ground states of a three-level atom are assumed to function as a stationary storage qubit. Each of the ground states, labeled $|\uparrow\rangle$ and $|\downarrow\rangle$, is connected to a shared excited state through optical transitions, creating a so-called Λ system. One of these transitions is coupled to a classical 'control field', while the other is coupled to a mode of an optical cavity. As discussed in more detail below, the cavity is an important part of this proposal, as it serves the dual purpose of enhancing the vacuum coupling rate between the excited state and the second ground state ($|\downarrow\rangle$) and of allowing the light emitted by the transition to be efficiently collected. When the classical field is used to drive the transition between the first ground state ($|\uparrow\rangle$) and the excited state, the cavity-coupled optical transition quickly causes the excitation to coherently emit a 'cavity photon' and transition to the second ground state ($|\downarrow\rangle$). This is effectively a Raman, or Λ, coupling between $|\uparrow\rangle$ and $|\downarrow\rangle$, and we refer to this type of system as an 'optically coupled spin' below. For a suitably designed system, when the classical drive is applied, the spin coherence between the two ground states is transferred onto the state of the photon emitted into the cavity mode. Assuming the initial spin state is a superposition $\alpha|\uparrow\rangle+\beta|\downarrow\rangle$ of the ground states and there are initially no cavity photons, the state of the system before and after the classical drive can be expressed as

$$\left|0\right\rangle\left(\alpha\left|\uparrow\right\rangle+\beta\left|\downarrow\right\rangle\right)\rightarrow\left(\alpha\left|0\right\rangle+\beta\left|1\right\rangle\right)\left|\downarrow\right\rangle \qquad [1.1]$$

where $|0\rangle$ and $|1\rangle$ refer to cavity photon populations equal to 0 and 1, respectively. This cavity photon state can be outcoupled, transmitted through a low-loss optical channel and reversibly reabsorbed by an identical atomic spin system in a cavity at a spatially distant location. In this way, quantum states can be transferred between distant qubits, and a quantum network can be created in which nodes are coupled via an optical quantum bus.[55]

In a related proposal in 1999, Cabrillo *et al.*[56] introduced a scheme for entangling two optically coupled spins by building an experiment in which the detection of a photon created after simultaneous excitation of two spins cannot be uniquely correlated with one of the two spins. This proposal has evolved into a canonical

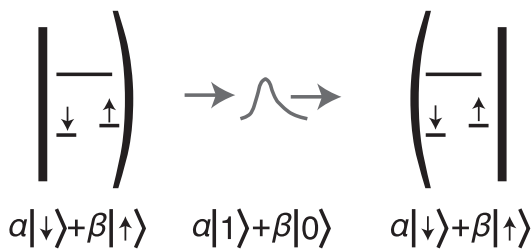

1.3 Illustration of transfer of a quantum state between two distant qubits via a photonic channel.

implementation in which the emission from each system is interfered in a beam splitter whose outputs are monitored by photon counters. This concept is referred to as measurement-based entanglement, and was extended in 2001 by Duan, Lukin, Cirac and Zoller,[57] who described how measurement-based entanglement can be used to implement a set of gates sufficient to build a quantum computer – this is often referred to as the DLCZ scheme for quantum computing, and is illustrated in Fig. 1.4. The measurement-based entanglement central to these proposals relies on simultaneously exciting two optically coupled spins using weak classical control fields, such that each spin has a low probability of making the Λ transition and generating a cavity photon. If the output from each cavity is interfered in a 50:50 beam splitter or waveguide coupler, and if the cavity photons generated by each system are indistinguishable, then upon detection of a photon at one of the output ports of the interference device, it is impossible to determine from which spin it originated. Under these conditions, it can be shown that the two spin systems, labeled *A* and *B*, are entangled. In the simplest ideal implementation considered here, the system has initial and final states

$$|\uparrow\rangle_A |\uparrow\rangle_B \rightarrow \frac{1}{\sqrt{2}}\left[|\uparrow\rangle_A |\downarrow\rangle_B \pm e^{i\phi} |\downarrow\rangle_A |\uparrow\rangle_B \right] \qquad [1.2]$$

where ϕ is a phase shift associated with differences in the optical path lengths of the arms of the interference device, and the choice of + or − in '±' is determined by which detector measures a photon. If a sufficiently large number of spins can be entangled in this way, a rich class of applications may become possible. Of particular interest are quantum computing and simulation schemes involving cluster states, which can introduce the fault tolerance necessary for building realistic QIP hardware.[58, 59]

At the time of the initial proposals described above, trapped ions or neutral atoms were assumed to be the medium of choice for realizing the cavity–spin system. Indeed, in recent years, formidable progress has been made in trapping

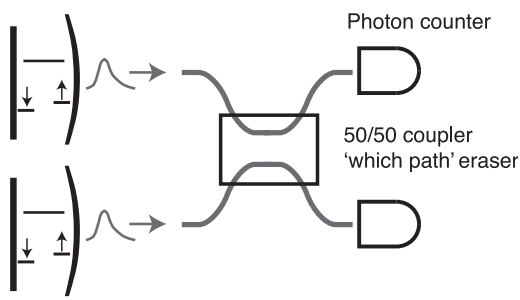

1.4 Illustration of scheme for measurement-based entanglement between two spin qubits interacting indirectly through photon interference.

atoms within cavities, and in creating measurement-based entanglement between atomic and optical systems.[60–70] However, a challenge for performing practical QIP with a large number of atomic systems is scaling the technical overhead related to trapping atoms within cavities. For this reason, researchers have sought out solid-state implementations of atom–cavity systems, which use 'artificial atoms' such as quantum dots and NV centers to eliminate the complexities of optical trapping, at the cost of introducing new challenges related to the influence of a solid-state environment on the quantum state of an artificial atom. These systems also provide the dual challenge and opportunity associated with creating nanoscale solid-state cavities and photonic hardware, within which artificial atoms can be embedded and connected in a manner analogous to the sketch in Fig. 1.2. In order to successfully realize this vision, several technical requirements related to the NV centers and the cavity properties must be met, and in some cases new photonic technology must be developed.

1.6.1 Requirements

The key element of the measurement-based entanglement protocols introduced above is a stationary qubit whose state can be coherently transferred to a photon. Here, we assume that the storage qubit is an electron spin associated with the ground state of an NV center. As discussed above, heralded entanglement between two spins can be generated by weakly exciting each spin such there is a small probability of emitting a photon on which the spin state is encoded, and then interfering the emitted fields from each spin on the input ports of a beam splitter and measuring the output ports of the beam splitter. Several conditions must be satisfied for entanglement to be generated upon detection of a photon at the beam splitter output.

First, it must be possible to coherently transfer the spin state onto the degrees of freedom of an outgoing photon. In the simplest scheme, illustrated in Figs. 1.3 and 1.5, this is achieved using a Λ transition between two spin states. In the example illustrated in Fig. 1.3, if the spin is in the up or the down state, a single photon or a vacuum state, respectively, is emitted into the cavity. Polarization or other optical degrees of freedom may also be used in place of the photon for an appropriately designed system. Realizing Λ systems in atomic media is relatively straightforward owing to their well-defined optical transitions and selection rules. Solid-state systems such as NV centers are more challenging to work with in this regard, and not all spin systems can be optically coupled via a Λ transition.

A second requirement is that the photons emitted from each artificial atom be indistinguishable.[71] This ensures that the beam splitter erases 'which path' information, so that upon detection of a photon it is not possible to determine from which spin it was emitted. In practice, this requires that the optical transitions for each spin emit photons of the same wavelength, polarization and temporal wave function. As discussed below, finding two identical artificial atoms which emit

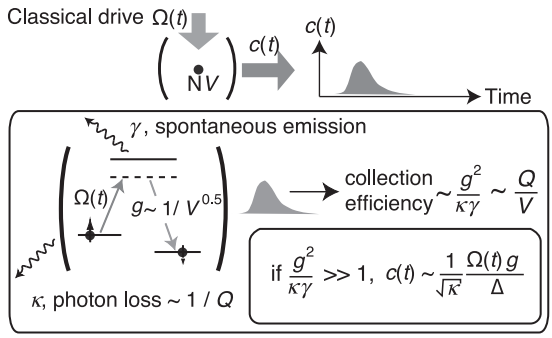

1.5 Cavity-enhanced photon generation from a spin qubit with a Λ optical transition. g is the single-photon coupling rate between the cavity mode and the optical transition. κ and γ are the decay rate of the cavity photon and the spontaneous emission rate of the NV excited state, respectively. Q and V are the quality factor of the cavity and the mode volume, respectively. $c(t)$ is the temporal wave function of the photon amplitude, and $\Omega(t)$ is the temporal wave function of the classical drive.

photons at the same wavelength can be challenging. Generating photons with indistinguishable temporal wave functions can be achieved by carefully designing the classical driving field used to excite the Λ system. The key parameters for this process are illustrated in Fig. 1.5. If the classical drive is turned on and off slowly compared with the optical transition rates g and Ω, and if the vacuum coupling rate between the cavity and the optical transition of the spin is sufficiently high compared with the spontaneous emission rate γ of the atom and the decay rate κ of the cavity photon, the temporal wave function of the outgoing flying qubit will follow the classical drive wave function. This process is often referred to as stimulated Raman adiabatic passage (STIRAP), and is sensitive to the properties of the cavity, such as the mode volume V and the quality factor Q, which determine the coupling and decay rates of the cavity photon. For the proposed schemes to work efficiently, it is necessary for $g^2/\kappa\gamma > 1$, corresponding to the coupled cavity–atom system operating in a Purcell enhanced regime, where emission from the atom into the cavity dominates over spontaneous emission processes.[37]

Finally, it is desirable to collect, transmit and detect the emitted photons with sufficiently high efficiency for the scheme to be capable of generating entanglement at a rate faster than the decoherence rate of the spins.

Among solid-state quantum emitters, diamond NV centers are a promising system for realizing this entanglement scheme. Their electron spin ground states have long coherence times, and can be coherently coupled through well-defined optical transitions, which form a Λ system under suitable strain conditions.[39, 72] In principle, all NV centers have identical electronic and optical properties, although in practice these properties are affected by the local environment of the NV center.

For example, local variations in strain and in the charge environment can significantly shift the energies of the excited states of the centers and of the photons emitted during the spin–photon state transfer process. This can destroy the indistinguishability of the photons, preventing the generation of measurement-based entanglement.

Another challenge posed by NV centers is that the majority of their emission is into phonon sidebands whose wavelengths span a range greater than 100 nm; only 3.5% of NV emission at low temperature is into the spectrally narrow ZPL. Optical micro- and nano-cavities can address this limitation by resonantly enhancing the ZPL via the Purcell effect. In principle, cavities with a sufficiently high optical Q and small optical mode volume V may enhance the rate of spontaneous emission into the ZPL by several orders of magnitude, such that it becomes the dominant emission wavelength of the NV center.[72] This has the additional benefit of coupling the NV emission into a well-defined cavity mode, from which it can be efficiently collected using an on-chip or fiber-based waveguide.[74] From a practical point of view, enhanced collection efficiency of the NV emission is necessary for so-called 'single-shot' readout of the NV spin state, in which the NV photoluminescence is sufficiently bright that the spin state can be measured in a time short compared with its lifetime.

Creating a quantum network connecting multiple NV centers on-chip is also challenging. A major difficulty is in creating multiple identical cavities, each of which is coupled to an NV center and part of a large on-chip photonic network. This difficulty is in part related to the relative infancy of diamond-based photonics research, and in part a more general challenge associated with creating complex photonic devices and circuits. As discussed below, progress in diamond photonics has been promising in recent years, and researchers' abilities to create functional photonic circuits are constantly advancing with efforts to develop on-chip optical interconnects for classical computing applications.

1.6.2 Experimental progress and challenges

In recent years, major experimental milestones in the realization of optical-network- and measurement-based QIP with NV centers have been demonstrated. In addition to the experiments described in Section 1.2 demonstrating the spin coherence and manipulation properties of NV centers, researchers have made significant progress with all-optical coherent manipulation and readout of NV center spins.

Santori *et al.*[39, 72] used optical fields to create coherent superpositions of NV spin states, an initial step towards coherently transferring the spin state to an outgoing photon. Faraday rotation of an optical field by a single NV center was demonstrated by Buckley *et al.*[75] In 2010, Togan *et al.*[76] demonstrated entanglement between a single NV center spin and an emitted photon. This experiment required a detailed understanding of the properties of the selection rules describing the

optical transitions of NV centers, careful management of the stress environment of the NV center in order to implement a Λ transition between two NV spin states, and precise timing to separate excitation photons from emitted photons.

In 2011, a further breakthrough was made in Delft by Robledo *et al.*,[77] who demonstrated single-shot readout of an NV spin. This experiment utilized a solid immersion lens, which was fabricated on a diamond chip using focused ion beam milling, around an NV center of interest. This immersion lens was essential for boosting the collection efficiency of photons from the NV center, allowing the electron spin state to be read out more quickly than in previous experiments. Unlike optical cavities, a solid immersion lens enhances the collection efficiency for the ZPL as well as for the phonon sidebands. This work was followed by a demonstration of photon indistinguishability using emission from two unique NV centers on the same chip,[78] employing a DC electric field provided by on-chip electrodes to Stark-shift the NV ZPL emissions to the same wavelength. Most recently, measurement-based entanglement between two NV centers separated by a macroscopic distance (3 m)[79] has been demonstrated. This is the first experiment demonstrating measurement-based entanglement of two solid-state systems, and major step towards implementing QIP using NV centers.

In order to scale these experiments sufficiently to enable QIP, it is necessary that hardware enabling efficient routing of photons between NV centers, beam splitters and detectors be developed. Several groups have recently succeeded in integrating NV centers into nanophotonic devices. Researchers at HP Laboratories have used an optical cavity to enhance the NV ZPL emission,[52, 74, 80] while researchers at Harvard have developed on-chip circuitry for collecting and manipulating light coupled into the cavity field.[81] A limiting factor in the use of these devices for QIP is the relatively poor quality of the optical transitions of the NV centers embedded in the nanostructures used for these tasks. Compared with the NV centers found in bulk, unpatterned material, these centers suffer from larger nonradiative dephasing and spectral diffusion. Overcoming these limitations is critical for these devices to play a key role in future measurement-based QIP on chip using NV centers.

1.7 Conclusion

During the last decade, NV centers in diamond have enabled researchers to conduct quantum optics and spin manipulation experiments with a precision previously restricted to atomic systems. At the single-NV-center level, some important initial solid-state demonstrations of a host of quantum information storage and manipulation experiments suggest that NV centers have a promising future for implementing QIP protocols. The development of the integrated photonic technology necessary to efficiently use NV centers as a QIP resource is under way, and future work will likely tackle the challenge of coherently connecting a growing number of NV centers, with the ultimate goal of creating on-chip quantum networks.

1.8 References

1. A. Gruber, A. Dräbenstedt, C. Tietz, L. Fleury, J. Wrachtrup, and C. von Borczyskowski, *Science* **276**, 2012 (1997).
2. J. Wrachtrup and F. Jelezko, *J. Phys.: Condens. Matter* **18**, S807 (2006).
3. S. C. Benjamin, B. W. Lovett and J. M. Smith, *Laser Photon. Rev.* **3**, 556 (2009).
4. D. D. Awschalom, L. C. Bassett, A. S. Dzurak, E. L. Hu and J. R. Petta, *Science* **339**, 1174 (2013).
5. K. Seeger, *Semiconductor Physics: An Introduction* (Springer, 2004).
6. M. A. Nielsen and I. L. Chuang, *Quantum Computation and Quantum Information* (Cambridge University Press, Cambridge, 2000).
7. G. Davies, *J. Phys. C: Solid State Phys.* **7**, 3797 (1974).
8. G. Davies and M. F. Hamer, *Proc. R. Soc. Lond. A* **348**, 285 (1976).
9. A. Collins, M. Thomaz and M. I. B. Jorge, *J. Phys. C: Solid State Phys.* **16**, 2177 (1983).
10. G. Davies, S. C. Lawson, A. T. Collins, A. Mainwood and S. J. Sharp, *Phys. Rev. B* **46**, 13157 (1992).
11. A. Zaitsev, *Optical Properties of Diamond* (Springer, 2001).
12. V. M. Acosta, K. Jensen, C. Santori, D. Budker and R. G. Beausoleil, *Phys. Rev. Lett.* **110**, 213605 (2013), URL http://link.aps.org/doi/10.1103/PhysRevLett.110.213605.
13. K. Heshami, C. Healey, B. Khanaliloo, V. Acosta, C. Santori, *et al.*, in preparation (2013).
14. M. Steger, K. Saeedi, M. Thewalt, J. Morton, H. Riemann, *et al.*, *Science* **336**, 1280 (2012).
15. C. Simon, M. Afzelius, J. Appel, A. B. de La Giroday, S. Dewhurst, *et al.*, *Eur. Phys. J. D* **58**, 1 (2010).
16. F. Jelezko, I. Popa, A. Gruber, C. Tietz, J. Wrachtrup, *et al.*, *Appl. Phys. Lett.* **81**, 2160 (2002).
17. F. Jelezko, T. Gaebel, I. Popa, A. Gruber and J. Wrachtrup, *Phys. Rev. Lett.* **92**, 076401 (2004).
18. F. Jelezko, T. Gaebel, I. Popa, M. Domhan, A. Gruber and J. Wrachtrup, *Phys. Rev. Lett.* **93**, 130501 (2004).
19. L. Childress, M. V. Gurudev Dutt, J. M. Taylor, A. S. Zibrov, F. Jelezko, *et al.*, *Science* **314**, 281 (2006).
20. M. V. Gurudev Dutt, L. Childress, L. Jiang, E. Togan, J. Maze, *et al.*, *Science* **316**, 1312 (2007).
21. P. Neumann, J. Beck, M. Steiner, F. Rempp, H. Fedder, *et al.*, *Science* **329**, 542 (2010).
22. P. C. Maurer, G. Kucsko, C. Latta, L. Jiang, N. Y. Yao, *et al.*, *Science* **336**, 1283 (2012).
23. D. P. DiVincenzo, *Fortschr. Phys.* **48**, 771 (2000).
24. E. Knill, R. Laamme and G. J. Millburn, *Nature* **409**, 46 (2001).
25. J. Weber, W. Koehl, J. Varley, A. Janotti, B. Buckley, *et al.*, *Proc. Natl. Acad. Sci.* **107**, 8513 (2010).
26. T. Gaebel, I. Popa, A. Gruber, M. Domhan, F. Jelezko and J. Wrachtrup, *New J. Phys.* **6**, 98 (2004).
27. C. Wang, C. Kurtsiefer, H. Weinfurter and B. Burchard, *J. Phys. B: At., Mol. Opt. Phys.* **39**, 37 (2006).
28. E. Neu, D. Steinmetz, J. Riedrich-Möller, S. Gsell, M. Fischer, *et al.*, *New J. Phys.* **13**, 025012 (2011).
29. I. Aharonovich, S. Castelletto, B. C. Johnson, J. C. McCallum, D. A. Simpson, *et al.*, *Phys. Rev. B* **81**, 121201 (2010).

30. I. Aharonovich, S. Castelletto, D. Simpson, C. Su, A. Greentree and S. Prawer, *Rep. Prog. Phys.* **74**, 076501 (2011).
31. R. H. Hadfield, *Nature Photon.* **3**, 696 (2009).
32. P. R. Hemmer, A. V. Turukhin, S. M. Shahriar and J. A. Musser, *Opt. Lett.* **26**, 361 (2001).
33. M. Doherty, F. Dolde, H. Fedder, F. Jelezko, J. Wrachtrup, *et al.*, *Phys. Rev. B* **85**, 205203 (2012).
34. V. Acosta, A. Jarmola, E. Bauch and D. Budker, *Phys. Rev. B* **82**, 201202 (2010).
35. G. Balasubramanian, P. Neumann, D. Twitchen, M. Markham, R. Kolesov, *et al.*, *Nature Mater.* **8**, 383 (2009).
36. K.-M. C. Fu, C. Santori, P. E. Barclay, L. J. Rogers, N. B. Manson and R. G. Beausoleil, *Phys. Rev. Lett.* **103**, 256404 (2009).
37. C. Santori, D. Fattal and Y. Yamamoto, *Single-Photon Devices and Applications* (Wiley, 2010).
38. P. Tamarat, N. Manson, J. Harrison, R. McMurtrie, A. Nizovtsev, *et al.*, *New J. Phys.* **10**, 045004 (2008).
39. C. Santori, P. Tamarat, P. Neumann, J. Wrachtrup, D. Fattal, *et al.*, *Phys. Rev. Lett.* **97**, 247401 (2006).
40. J. Ziegler, *The Stopping Range of Ions in Matter*, software package srim-2008 (2008).
41. Z. Huang, W.-D. Li, C. M. Santori, V. M. Acosta, A. Faraon, *et al., Appl. Phys. Lett.* **103**, 081906 (2013) doi: 10.1063/1.4819339.
42. C. Weis, A. Schuh, A. Batra, A. Persaud, I. Rangelow, *et al., JVSTB* **26**, 2596 (2008) doi: 10.1116/1.2968614.
43. D. M. Toyli, C. D. Weis, G. D. Fuchs, T. Schenkel and D. D. Awschalom, *Nano Lett.* **10**, 3168 (2010).
44. C. Santori, P. E. Barclay, K.-M. C. Fu and R. G. Beausoleil, *Phys. Rev. B* **79**, 125313 (2009).
45. K. Fu, C. Santori, P. Barclay and R. Beausoleil, *Appl. Phys. Lett.* **96**, 121907 (2010).
46. V. Acosta, E. Bauch, M. Ledbetter, C. Santori, K.-M. Fu, *et al.*, *Phys. Rev. B* **80**, 115202 (2009).
47. T. Ishikawa, K.-M. C. Fu, C. Santori, V. M. Acosta, R. G. Beausoleil, *et al.*, *Nano Lett.* **12**, 2083 (2012).
48. A. Stacey, D. A. Simpson, T. J. Karle, B. C. Gibson, V. M. Acosta, *et al.*, *Adv. Mater.* **24**, 3333 (2012).
49. K. Ohno, F. J. Heremans, L. C. Bassett, B. A. Myers, D. M. Toyli, *et al.*, *Appl. Phys. Lett.* **101**, 082413 (2012).
50. A. Edmonds, U. D. Haenens-Johansson, R. Cruddace, M. Newton, K.-M. Fu, *et al.*, *Phys. Rev. B* **86**, 035201 (2012).
51. G. Fuchs, V. Dobrovitski, D. Toyli, F. Heremans and D. Awschalom, *Science* **326**, 1520 (2009).
52. P. E. Barclay, K. M. C. Fu, C. Santori, A. Faraon and R. G. Beausoleil, *Phys. Rev. X* **1**, 011007 (2011).
53. K.-M. C. Fu, C. Santori, P. E. Barclay, I. Aharonovich, S. Prawer, *et al.*, *Appl. Phys. Lett.* **93**, 234107 (2008).
54. J. I. Cirac, P. Zoller, H. J. Kimble and H. Mabuchi, *Phys. Rev. Lett.* **78**, 3221 (1997).
55. H. Kimble, *Nature* **453**, 1023 (2008).
56. C. Cabrillo, J. I. Cirac, P. García-Fernández and P. Zoller, *Phys. Rev. A* **59**, 1025 (1999).
57. L.-M. Duan, M. D. Lukin, J. I. Cirac and P. Zoller, *Nature* **414**, 413 (2001).

58. R. Raussendorf and J. Harrington, *Phys. Rev. Lett.* **98**, 190504 (2007).
59. H. J. Briegel, D. E. Browne, W. Dur, R. Raussendorf and M. Van den Nest, *Nature Phys.* **5**, 19 (2009), URL http://dx.doi.org/10.1038/nphys1157.
60. H. Mabuchi, Q. A. Tuchette, M. S. Chapman and H. J. Kimble, *Opt. Lett.* **21**, 1393 (1996).
61. P. W. H. Pinkse, T. Fischer, P. Maunz and G. Rempe, *Nature* **404**, 365 (2000).
62. B. Julsgaard, A. Kozhekin and E. S. Polzik, *Nature* **413**, 400 (2001).
63. A. Mundt, A. Kreuter, C. Becher, D. Leibfried, J. Eschner, *et al.*, *Phys. Rev. Lett.* **89**, 103001 (2002).
64. B. Blinov, D. Moehring, L.-M. Duan and C. Monroe, *Nature* **428**, 153 (2004).
65. J. McKeever, A. Boca, A. D. Boozer, R. Miller, J. R. Buck, *et al.*, *Science* **303**, 1992 (2004).
66. C. W. Chou, H. de Riedmatten, D. Felinto, S. V. Plyakov, S. J. V. Enk and H. J. Kimble, *Nature* **438**, 828 (2005).
67. J. F. Sherson, H. Krauter, R. K. Olsson, B. Julsgaard, I. C. K. Hammerer and E. S. Polzik, *Nature* **443**, 557 (2006).
68. A. D. Boozer, A. Boca, R. Miller, T. E. Northup and H. J. Kimble, *Phys. Rev. Lett.* **98**, 193601 (2007).
69. M. Hijlkema, B. Weber, H. P. Specht, S. C. Webster, A. Kuhn and G. Rempe, *Nature Phys.* **3**, 253 (2007).
70. A. Stute, B. Casabone, P. Schindler, T. Monz, P. Schmidt, *et al.*, *Nature* **485**, 482 (2012).
71. L. Mandel and E. Wolf, *Optical Coherence and Quantum Optics* (Cambridge University Press, 1995).
72. C. Santori, D. Fattal, S. Spillane, M. Fiorentino, R. Beausoleil, *et al.*, *Opt. Express* **14**, 7986 (2006).
73. C. Santori, P. Barclay, K. Fu, R. Beausoleil, S. Spillane and M. Fisch, *Nanotechnology* **21**, 274008 (2010).
74. K.-M. C. Fu, P. E. Barclay, C. Santori, A. Faraon and R. G. Beausoleil, *New J. Phys.* **13**, 055023 (2011).
75. B. Buckley, G. Fuchs, L. Bassett and D. Awschalom, *Science* **330**, 1212 (2010).
76. E. Togan, Y. Chu, A. Trifonov, L. Jiang, J. Maze, *et al.*, *Nature* **466**, 730 (2010).
77. L. Robledo, L. Childress, H. Bernien, B. Hensen, P. F. Alkemade and R. Hanson, *Nature* **477**, 574 (2011).
78. H. Bernien, L. Childress, L. Robledo, M. Markham, D. Twitchen and R. Hanson, *Phys. Rev. Lett.* **108**, 043604 (2012).
79. H. Bernien, B. Hensen, W. Pfaff, G. Koolstra, M. Blok, *et al.*, *Nature* **497**, 86 (2013).
80. A. Faraon, P. E. Barclay, C. Santori, K.-M. C. Fu and R. G. Beausoleil, *Nature Photon.* **5**, 301 (2011).
81. B. J. Hausmann, I. B. Bulu, P. B. Deotare, M. McCutcheon, V. Venkataraman, *et al.*, *Nano Lett.* **13**, 1898 (2013).

2

Principles of quantum cryptography/ quantum key distribution (QKD) using attenuated light pulses

H. WEINFURTER, LMU Munich, Germany

DOI: 10.1533/9780857096685.1.21

Abstract: Based on the very foundations of quantum physics, quantum information methods can enhance conventional communication methods and enable completely new types of information processing. Quantum cryptography or, more precisely, quantum key distribution is the first application that enables communications to be made secure against eavesdropping attacks. This chapter gives an overview of the principle of the method and of how to implement this method based on attenuated laser pulses.

Key words: quantum information, quantum communication, quantum cryptography, secure communication, free space.

2.1 Introduction

Communication is ubiquitous in our daily life, and the need for protection of data is paramount. Cryptography provides numerous methods to ensure that communications are secure against eavesdropping attacks; however, all of them rely on certain assumptions about the capabilities of the eavesdropper. For example, the security of public-key cryptosystems and of the frequently employed advanced data encryption standards AES for point-to-point communication is based on the assumption that the mere computational complexity of deciphering the encrypted message prevents an attack. But how can we make sure that the eavesdropper does not have algorithms or machines which are way beyond what is the publicly available state of the art? After all, we know that a quantum computer can easily break into current public-key systems – *we* just do not have a working machine, yet.

The one-time pad is the unique exception to all these issues. There, the sender encodes every bit of the message with a new bit from a perfectly random key. If the message and key are of equal length, the randomness of the key results in perfect randomness of the cipher, the bit sequence which is sent to the receiver. If the cipher is fully random, it could in fact mean any message with equal probability. An eavesdropper knowing this cipher still cannot do any better than guessing the initial message – in fact, for this, the eavesdropper would not even have needed to tamper with the communication. This sounds great, but the sender and receiver

© 2014 Elsevier Ltd

now have to first share the secret key. As mentioned above, it is of equal length to the message, and thus the one-time pad is often referred to as 'the perfect method to communicate securely, provided one can communicate securely'. The conventional method used to distribute keys securely for most of the last century has been the 'trusted courier', carrying a long random key from one location to the other. Here again assumptions have to be made, for example that we really can trust the courier. However, there is a little twist to the story: the key can be any random bit sequence, not a specific message anymore.

This is where quantum cryptography or, better, quantum key distribution (QKD) enters the stage (Bennett and Brassard, 1984; for a review, see Gisin *et al.*, 2002). Based on the laws of physics, it guarantees the security of key distribution. Even better, it gives an upper bound on the information an eavesdropper can have about the key. For the first time in the field of cryptography we can quantify and specify the security of the communication, a feat completely impossible in conventional cryptography. The technology required for employing quantum cryptography is largely identical to that for standard optical communication methods, and thus the first commercial providers are already offering turnkey-ready systems. Here, we give an overview of the underlying principle and introduce the state of the art of QKD based on attenuated light pulses.

2.2 Principles of quantum key distribution (QKD): the BB84 protocol

As mentioned above, the one-time pad requires a perfectly random bit sequence as a key, which is known only to the legitimate users. QKD achieves this by employing basic principles of quantum physics, especially the Heisenberg uncertainty relationship. The quantum properties of light are used to encode the key for transmission, as any unauthorized measurement results in irreversible changes in the quantum system, thereby revealing the attack.

QKD was introduced in 1984 by Bennett and Brassard based on some initial ideas of Wiesner (1983). In Bennett and Brassard's scheme, single quantum systems are prepared in well-defined, randomly chosen states by the sender (Alice) and sent over a quantum channel to the receiver (Bob), who observes a particular property of the quantum system. Given some additional negotiations over a public communication channel, they can distill a key whose secrecy can be determined.

Several different properties of light can be utilized for encoding; let us use the general notation of a qubit, i.e., a two-state quantum system. In analogy to its classical counterpart, which can have the value '0' or '1', a qubit can be in the two uniquely distinguishable states $|0\rangle$ or $|1\rangle$. In a way that is unimaginable for classical systems, Alice and Bob can now also prepare and observe so-called superposition states, in particular the (distinguishable) states $|\bar{0}\rangle = \left(|0\rangle + |1\rangle\right)\Big/\sqrt{2}$ and $|\bar{1}\rangle = \left(|0\rangle - |1\rangle\right)\Big/\sqrt{2}$. In an experiment, these states might correspond, for example, to horizontal and vertical linear polarizations of photons, single quanta

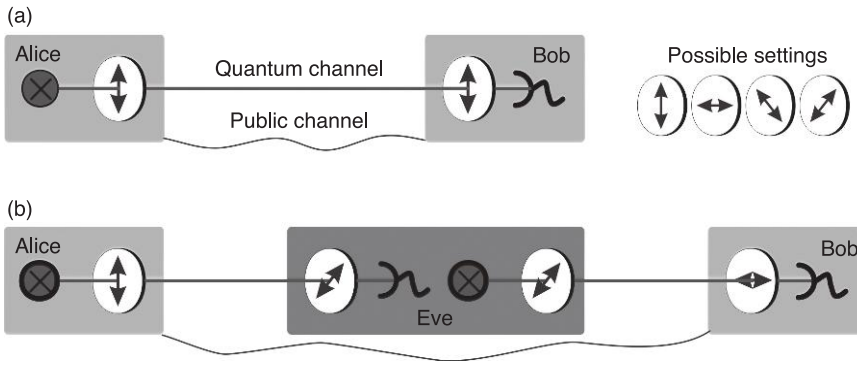

2.1 Principle of BB84 quantum key distribution. (a) A single photon prepared by Alice randomly in one of four polarization directions is sent over the quantum channel to Bob. Bob analyzes the photon either along the vertical and horizontal polarizations or along the ±45° linear polarizations. Provided he detects the photon, he sends information about the measurement basis to Alice via the public channel. (b) If an eavesdropper (Eve) intercepts the line, there are instances where Eve will choose the other basis relative to Alice, and thus Bob can detect the photon in a polarization orthogonal to the one sent by Alice. This results in errors in the key bits, revealing the attack.

of light, or ±45° linear polarizations respectively (Fig. 2.1). Alice and Bob agree to associate the states $|0\rangle$ and $|\bar{0}\rangle$ with the bit value '0' and the states $|1\rangle$ and $|\bar{1}\rangle$ with the bit value '1'.

For key distribution, Alice prepares a stream of photons, each randomly prepared in one of the four states, and sends them over to Bob, who now performs measurements randomly for every photon either for the set (basis) $B_0 = \{|0\rangle, |1\rangle\}$ or for the set $B_1 = \{|0\rangle, |1\rangle\}$. Note that the operators associated in quantum mechanics with these two bases do not commute, and Heisenberg's uncertainty relation comes into effect. Observing the state $|0\rangle$, say, in the basis B_0 will give the unique result '0'. However, when the state $|0\rangle$ obtains in the basis B_1, the result is maximally unsharp and random, and Bob observes '0' and '1' with equal probability. Moreover, quantum mechanics tells us that for two such operators which cannot be measured simultaneously in theory, there simply does not exist an apparatus in the real world which could do the job. For the polarization encoding mentioned above, this means that Bob can orient his analyzer either to measure along the horizontal and vertical directions *or* to measure along the ±45° directions. He cannot do both at the same time.

After the measurements, communication over the public channel starts. For each instance, Bob informs Alice (a) whether he observed the photon, i.e., that the photon was not lost during transmission or measurement, and (b) which of the two bases he used. Alice replies to say whether she used the same basis. She and Bob

erase all instances where they used different bases, as in those cases Bob's result is not at all correlated with Alice's preparation. The remaining results make up the so-called 'sifted key'. Ideally, thanks to the perfect correlations that occur when the same basis is used, these strings of preparations by Alice and of measurement results obtained by Bob are identical and thus can be used as a key for communication.

But is this key secure? What happens if an eavesdropper (Eve) tries to interfere? For example, she could cut the quantum channel and perform the same measurements as Bob does. Eve then uses these results to encode a new set of photons and now sends them to Bob. If Alice and Bob were to use only a single basis, i.e., only two perfectly distinguishable states, Eve could gather all information about the key. Alice and Bob would not see any difference whether Eve attacked or not. But in that case, they did not actually use quantum physics at all. They only encoded classical states in a quantum system. However, as Alice and Bob use the four states from mutually conjugate bases randomly, they force the eavesdropper to behave similarly. There is then a probability of 1:2 that if Alice and Bob use the same basis, Eve will measure (and reprepare) in the other basis. In this case Eve's state will be uncorrelated with Alice's state and, finally, Bob's result will be uncorrelated with both Eve's *and* Alice's preparation. Thus, with a probability of 25%, Bob's bit in the sifted key will differ from Alice's bit – the eavesdropper has introduced a significant amount of noise. There are better strategies, but even the best one, acting on all sent photons simultaneously, will cause about 11% of errors (Gisin *et al.*, 2002). This noise is not just a technical issue, like the 'click' that eavesdroppers caused some tens of years ago in (ancient) telephone links; it is of fundamental character and directly linked to the uncertainty principle. According to the laws of quantum physics, eavesdropping will unavoidably cause noise in the sifted key.

Alice and Bob can thus evaluate the noise in the sifted key by determining the quantum bit error ratio (QBER) given by the fraction of wrong bits in the sifted key. From this, they can deduce the amount of information the eavesdropper has. This information can now be shrunk to a negligible level by 'privacy amplification', essentially by shrinking the key according to the QBER. Thereby, finally, Alice and Bob obtain a perfectly random bit sequence whose security is quantifiable thanks to the laws of quantum physics.

2.3 Protocol extensions and alterations

This original protocol was later supplemented by various extensions and alternative strategies. For example, Bennett proposed the B92 protocol, which used only two nonorthogonal states for encoding, together with a check that forced the eavesdropper to really resend some photons even in cases where the results were not unique (Bennett, 1992). Six-state protocols for qubits and protocols for higher-dimensional quantum systems have been designed to increase

the complexity of the protocol and thereby increase the noise that eavesdropping attacks cause (Bruss, 1998). Higher-dimensional systems also enable one to simultaneously confirm the security of the transmission and obtain a bit from every sent photon (Beige *et al.*, 2002). Similarly, by unbalancing the frequency of use of B_0 and B_1, the sifted key can be made almost as long as the number of detected photons (Lo *et al.*, 2005a).

The initial protocol, as in the description above, relies on the indivisibility of single quanta. This is evidently fulfilled when single photons are used for the encoding. Attenuated pulses of light may contain, with a certain probability, more than only a single photon. This gives an eavesdropper a chance to split the pulse and use the additional photon for an attack. Alice can then use only very feeble pulses, whose attenuation also depends on the losses along the quantum channel (Lütkenhaus, 2000). This would shorten the maximum link length dramatically. However, a simple twist in the original protocol, namely encoding '0' with states from B_0 and '1' with states from B_1, renders the eavesdropper unable to obtain information from two-photon pulses; only very rare pulses with an even higher number of photons can then be used by her (Scarani *et al.*, 2004).

The so-called decoy protocols completely remove the photon number problem (Hwang, 2003; Lo *et al.*, 2005b). Essentially, Alice and Bob use the basic principle of QKD, i.e., detection of eavesdropping is enabled by using nonorthogonal states, to also shield the photon number degree of freedom against attacks. Again, any information which might have leaked to an adversary can be quantified and removed by privacy amplification. Based on this protocol, the secret-key rate for attenuated-pulse QKD exhibits the same scaling as the ideal case of sending single photons. The probability of obtaining a key bit from a sent pulse (for BB84) is lower by a factor of about two or three and suffers mainly in extreme cases where there is very low transmission or there is detector saturation.

Different quantum properties of light are used in two further groups of protocols. On the one hand, entanglement between a pair of photons distributed to Alice and Bob results in correlated measurement results between the two distant observers. Thus, without preparation, but with only measurements in a symmetric configuration, a key can be generated (Ekert, 1991). Its security can be tested by evaluating the entanglement, again with measurements in nonorthogonal directions. On the other hand, the quantum nature of the electric-field states can be utilized to encode and protect the key (Grosshans and Grangier, 2002). Electric-field variables again cannot be measured simultaneously with arbitrary precision, and thus offer similar opportunities for QKD to qubits.

In conclusion, for key distribution QKD utilizes the perfect correlation between the preparation and the measurement result when the same basis is used, and it utilizes the randomness of the results when the measurement is done in a conjugate basis to secure the distribution against eavesdroppers.

2.4 Implementing QKD

After learning about the first quantum communication protocol, the BB84 protocol, which enables secure key exchange, one might think that it would be straightforward to set up an experiment. Yet it took quite a few years, and in particular also the initiative of the inventors Bennett and Brassard, who, together with Besette, Savail and Smolin, started experiments on QKD. The first secure quantum key between Alice and Bob was established back in 1991 in the laboratories of the IBM Research Center in Yorktown Heights (Bennett *et al.*, 1992). In this setup, called 'Aunt Martha', attenuated light pulses were transmitted over 32 cm between the sender and the receiver unit (Fig. 2.2). Based on the BB84 protocol, Bennett *et al.* demonstrated how Alice and Bob could indeed verify whether an eavesdropper had disturbed the transmission or whether it was possible to extract a secure key. The first experiment used a light-emitting diode as the light source and fast Pockels cells to choose the polarization direction. A key rate of a few hundred bits per second was achieved, and a number of eavesdropping attacks were simulated. It was even demonstrated how to correct residual bit errors and how to guarantee full security in the presence of (experimental) noise. This shining example became the model for numerous quantum cryptography systems developed worldwide. In the following sections, an overview of the current status of developments is given, which have led to the first commercial systems.

The most important criteria for QKD systems are a high key rate and a long distance. Usually one cannot optimize both at the same time, and some compromises have to be made. No compromise, however, is acceptable when it comes to reliability and user-friendliness. To make QKD a real application, it is thus necessary to develop new optics, quite different from the standard quantum optics setups. These latter setups allow high flexibility, but they are quite expensive

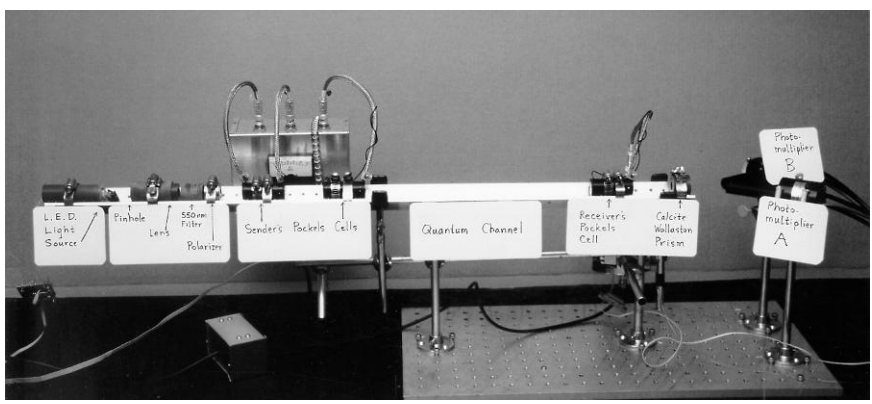

2.2 Setup for the first quantum cryptography demonstration (Bennett *et al.*, 1992b) (© C. Bennett).

and, owing to the many alignment options, are usually not stable enough for continuous operation.

The distance between Alice and Bob is limited mainly by losses in the quantum channel and by the efficiency and noise of single-photon detectors. Losses or low efficiency reduce the number of detected photons and thus the number of bits in the raw key. Noise (dark counts) in Bob's detectors results in a noise floor of bit errors, which are indistinguishable from those caused by eavesdropping attacks. It can be corrected for, but only at the cost of raw key material. In the case of low efficiency or high loss, this noise floor can easily reach the 11% level, at which no secure key can be distilled anymore. Any attempts to amplify the single-photon signal have to fail as well, since, according to the no-cloning theorem, any amplifier or repeater as used in a conventional optical communication scheme introduces the same noise as an eavesdropper would do. This would therefore ruin the remarkable advantages of quantum key distribution. Only a quantum repeater with intermediate quantum error correction and memory stages along the quantum channel could enable truly long-distance communication. Its basic components are being developed now. As it will take some time before we are able to use it, we have to rely on conventional means to transmit light.

Two options for quantum channels are available, which determine the wavelength and consequently distinguish the complete system. Photons can be distributed either using glass fiber connecting Alice and Bob or using telescopes aligned mutually for optimal coupling. In the following, the two systems are compared, in the form in which they have been implemented in prototypes or commercial systems. Most of the systems under development rely on attenuated light pulses, as this is less expensive and enables high-rate systems.

Before going into detail, we shall say a word about hacking QKD systems. In several demonstrations, it has been shown that key generation can be eavesdropped without being detected by Alice and Bob (Zhao *et al.*, 2008; Gerhardt *et al.*, 2011; Weier *et al.*, 2011). This was possible because the systems concerned had one or other hardware feature which enabled the attack. Typically, particular features of the detector, for example timing issues or dead time, allowed manipulation of the quantum channel that was not revealed by the standard QBER analysis. It is evident that a QKD system requires very careful design to avoid any possible side channels and to stop any intrusion of an eavesdropper into the sender and receiver modules along the quantum channel. Moreover, it is crucial to continuously control the functioning of the system components, above all the detector. However, all quantum hacking can only utilize hardware features of the system; it is never the principle of QKD which can be threatened.

2.5 Fiber-based QKD

Glass fiber systems make the best use of standard telecommunication fibers. These fibers are already available between the main communication centers or

could be installed with reasonable effort. The standard telecommunication wavelengths are 1300 and 1550 nm, where dispersion and loss, respectively, reach a minimum. State preparation, manipulation and analysis can be achieved with standard telecommunication components.

So far, the disadvantage of this wavelength regime is the high noise and relatively low efficiency of current single-photon detectors (germanium and InGaAs avalanche diodes). Optimization of these detectors has enabled us to steadily increase the distance over the last few years up to a limit of about 200 km. The superconducting detectors under development at the moment are effectively noise-free owing to their very high time resolution and are achieving increasingly higher efficiencies. Distances of 500 km seem feasible with these new developments.

Glass fiber is slightly birefringent. Over long distances, this effect adds up. Care has to be taken because this birefringence may vary, depending on the stress in or the temperature of the fiber. As a result, a well-defined initial polarization fluctuates strongly at the receiver and one has to compensate for the birefringence based on reference measurements. However, it is more advisable to define a new encoding for the qubit. The two-state system in this case is defined by two possible times at which the photon can be detected ('time-bin coding'). A (variable) beam splitter determines the relative size of the amplitudes, and a phase shifter in one of the arms behind the beam splitter enables one to set any desired state. The two arms are recombined at a second beam splitter. If the lengths of the two arms differ by more than the coherence time of the light, no interference occurs at the second beam splitter, and the light exits in two time slots from this unbalanced interferometer. Only one output is chosen, but this does not matter at all for attenuated light pulses as this reduction still happens within Alice's sender module. At Bob, an equivalent unbalanced interferometer is used to split and recombine the incoming amplitudes again, and, after application of Bob's phase, it allows us to observe interference depending on Alice and Bob's phases (with 50% efficiency). Accepting this reduction, one is thus able to observe interference over very large distances, almost independent of possible fluctuations along the quantum channel.

A very reliable and stable system was developed at the University of Geneva. The group led by Nicolas Gisin and Hugo Zbinden found a clever extension of the basic principle which significantly increased the stability and quality of the system (Ribordy *et al.*, 2000). In addition to using time-bin coding to reduce the influence of the fiber, they made the receiver, Bob, the source of the light pulses. He first generates bright, coherent pulses at two different times with a polarizing, unbalanced interferometer and sends them to Alice. She can now use the bright pulses to easily synchronize her actions, consisting of the application of one of four possible phase shifts, back reflection at a Faraday mirror and attenuation to the single-photon level. On the way back to Bob, all rotations of the light are undone, and only then does Bob apply his phase shift. Under the assumption that

all fluctuations occur on a much slower time scale than the time it takes the light to travel from Bob to Alice and back again, all disturbances cancel. Only the phase difference between Alice and Bob's modulations remains and determines the result of the measurement. By using a polarizing interferometer together with a Faraday mirror (which rotates the polarization of the reflected light by 90°), this system does not suffer from the usual 50% reduction of time-bin-coding systems. From the measurement results, Alice and Bob can infer the mutual phase settings and obtain the key bits, which are now more or less immune to any disturbance.

With such a so-called 'plug & play' system, QKD was demonstrated between the cities of Geneva and Lausanne over a distance of 67 km at a rate of about 150 bit/s. Even more remarkably, the glass fiber connecting Alice and Bob was a standard fiber used by Swisscom. The sender and receiver modules were integrated into 19 inch racks and placed in buildings belonging to Swisscom, which were far from being the air-conditioned laboratories of standard quantum optics experiments. This very reliable system was the basis for the development of the first commercial QKD system by the spin-off company ID Quantique. Today, Vectis offers secure point-to-point connection, easily integrable into standard communication networks. Similarly, SeQureNet is offering a newly developed system based on continuous-variable QKD.

The development of dedicated electronics for operating single-photon detectors at very high rates enabled the team of Andrew Shields at Toshiba, UK, to develop the currently most capable system (Dixon *et al.*, 2010). By implementing the concept of the decoy-based BB84 protocol, key rates of more than 1 Mbit/s were achieved over a distance of 50 km. It will be exciting to see what improvements beyond the current state of the art can be achieved, possibly with superconducting detectors or novel encoding schemes.

2.6 Free-space QKD

If a direct line of sight is available, coupling the sender and receiver with telescopes becomes possible. High transmission through air can be achieved for wavelengths in the range from 780 to 850 nm. Highly efficient, low-noise silicon avalanche photodiodes are available for this range. Free-space links are very flexible and can be used in a number of different possible scenarios, for example over short-range links of a few meters (e.g., to ATMs for authentication and key upload) or over medium-distance links of several kilometers directly connecting buildings in urban areas. Over such distances, near-IR wavelengths guarantee higher key rates thanks to the higher detector efficiency. But free-space links also offer new possibilities at very long distances. Provided there are trusted satellites, global key exchange becomes possible (Nordholt *et al.*, 2002)). From a height of about 500–1000 km, a sender on a satellite tracks a ground station and sends polarized light pulses, which in turn are collected by a large telescope on earth to exchange

a secret key. If the satellite then flies over another ground station, a second secret key can be exchanged. Combining the two keys in the satellite gives a secure key between the ground stations and enables worldwide communication within a trusted network.

For free-space QKD, all of the required components, in particular the laser diodes, are low-price, standard products. Instead of costly polarization modulators, it is thus more economic to use four differently oriented laser diodes. By activating only one of the four laser diodes at any time, the required polarized attenuated light pulses can be generated. The main problem that free-space links suffer from is air turbulence, which reduces the effective aperture of the telescopes significantly. Thus, to collect the maximum number of attenuated pulses, large receiver telescopes are required.

Figure 2.3 shows a schematic illustration of a pair of sender and receiver modules developed for free-space QKD. In the sender, eight laser diodes are mounted on a ring around a gold-plated cone such that the light reflected from the cone into the quantum channel is already oriented along four different directions at two different brightness levels for decoy state encoding. The design guarantees high stability under harsh conditions.

The power of such modules and their suitability for future applications has been demonstrated in various experiments, starting with a distance of 23.4 km in the Alps (Kurtsiefer *et al.*, 2002) in quite tough atmospheric conditions, such as temperatures down to −20 °C and strong winds. The ultimate distance for links between stations on earth is offered by a test range between the Canary Islands of Tenerife and La Palma (Fig. 2.3). There, over a distance of 144 km, QKD could be evaluated under conditions perfectly representative of links to satellites (Schmitt-Manderbach *et al.*, 2007). In this experiment, the sender was implemented as a simple telescope with an output lens 15 cm in diameter. The receiver was at the optical ground station of the European Space Agency, where a 1 m mirror telescope collected the strongly scattered light, followed by standard polarization analysis. In a static scenario, the polarization is a very reliable and stable degree of freedom for encoding quantum states. No reduction in the degree of polarization due to air scattering was observed. Owing to the long link, the effective aperture was reduced to about 3 cm, reducing the overall link efficiency by more than 30 dB. Yet, despite this, the results can be compared favorably with links to satellites in low earth orbits about 1000 km in height but with significantly less disturbing atmosphere along the path.

While the above long-distance QKD scheme could operate only during the night, the groups of Richard Hughes at Los Alamos (Hughes *et al.*, 2002) and Christian Kurtsiefer at the University of Singapore (Peloso *et al.*, 2009) have also demonstrated the feasibility of daylight key exchange. Narrow filtering in the frequency and spatial domains and precise selection of the detection time are necessary for this.

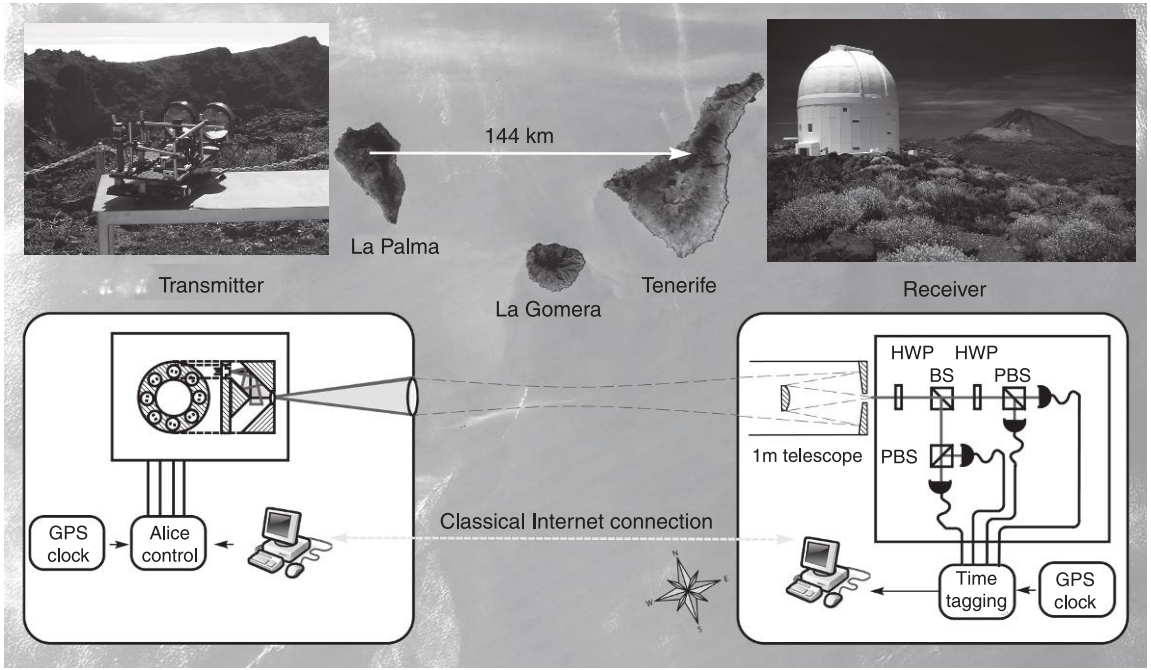

2.3 Schematic illustration of free-space quantum key distribution over a distance of 144 km between the Canary Islands of La Palma and Tenerife. The insets schematically show details of the sender and receiver modules. Based on GPS timing signals, the Alice control unit fires one of eight laser diodes with one out of four polarizations and three different light intensities to enable security analysis based on the decoy protocol. In the receiver, the light is detected behind one of four polarization analyzer outputs and time-tagged for further communication. In spite of more than 32 dB loss, a key rate of 12.8 bit/s was achieved.

2.7 Future trends

So, where can we use quantum cryptography today? What is possible, and where should future research be directed? Evidently, only point-to-point key distribution is possible with the scheme presented here. An entanglement-based scheme, which would be somewhat more involved, might enable the construction of networks based on multipartite entanglement; however, this is surely too far-fetched. Nevertheless, it will be necessary to develop network structures in order to best support current types of communication.

Designed as a point-to-point communication link, a bridge (network layer 2) connecting two communication partners would surely best utilize the power of quantum key distribution. Standard encryptors may, for example, use the Advanced Encryption Standard (AES) for such connections to provide communication rates of up to 10 Gbps, which is of course way beyond the capability of QKD. However, such conventional, widespread systems also have to provide some cipher key management, which is often done once per session only, using RSA-type or Diffie–Hellman codes (which, in turn, could be attacked by a future quantum computer). Key exchange using QKD now enables one, for the first time, to securely provide new keys for AES at a high rate of more than 1000 times per second. This enhances the security of the system dramatically. At a lower rate, encryptors could be configured to use one-time-pad encryption over the bridge and thus provide ultimate security against eavesdroppers.

The first publicly known regular use of QKD-enhanced communication has been during elections in Geneva, Switzerland, since 2007. Encryptor systems as described above, made by ID Quantique, secured the connection between the ballot data entry center and the government repository where the votes were stored. The additional benefit of such a system is not so much protection from outside attempts to eavesdrop as the ability to verify that the data have not been corrupted in transit between entry and storage. Since then, a number of links have been installed (see http://www.idquantique.com/news-and-events/press-releases.html), for example to secure low-latency links from bank headquarters to branches or disaster recovery centers, and between data centers of network providers.

Besides these point-to-point applications, several network structures have been demonstrated. The basic elements here are ‘trusted nodes’, which are interconnected by QKD links and provide high-level key management and rerouting for all nodes. After the first three-node Darpa Quantum Network in Boston (Elliot, 2006), the SECOQC demonstration network in the Vienna area combined six nodes with eight links (Peev *et al.*, 2009). The nodes consisted of a combination of node modules responsible for all classical communication and QKD modules which could be integrated and exchanged in a highly flexible manner, depending on the particular environment and requirements, such as long distance or high rate. The next development step was taken with the Tokyo

Network in 2010, where even one-time-pad-encoded video conferences have proven to be feasible over 50 km links (Sasaki *et al.*, 2011). As an additional result, a standardization effort was initiated to define the structures of future QKD links and network modules.

QKD links to satellites have been proposed for secure global communication. Developments towards this challenging goal have brought impressive results, with free-space link distances increasing successively from 20 to 144 km, and with the development of daylight key distribution, enabled by precise filtering in all degrees of freedom to enable the registration of signals at the single-photon level in bright sunshine. It has been shown that today's optical communication links can be enhanced by quantum communication methods. Additional improvements are necessary, as the link efficiencies have to be better by a few orders of magnitude relative to conventional optical links. Finally, a very recent experiment has shown that it is feasible to link an aircraft and an optical ground station (Nauerth *et al.*, 2013). The goal of metropolitan networks consisting of fiber or short free-space-based QKD links, connected via satellite links to provide worldwide secure key exchange, is coming within reach.

2.8 Conclusion

Quantum cryptography has become the first commercial application of the principles of quantum information. A novel level of security has been made possible by using the very basic principles of quantum physics. Any eavesdropper, allowed to perform any possible attack, will be revealed. Even better, QKD allows one to quantify the maximum amount of information which might have leaked to the eavesdropper. The systems which are operative at the moment use either a fiber channel or a connection through free space to transmit feeble light signals. Attenuated laser pulses can be used, supported by additional protocol features, and allow the design of robust, cost-effective systems. High-speed point-to-point connections, very long connections over more than 100 m and networks in metropolitan areas have been developed and will be connected by satellite links, enabling global secure communication in the future.

2.9 References

Beige, A., Englert, B.-G., Kurtsiefer, C. and Weinfurter, H. (2002) Secure communication with a publicly known key, *Acta Phys. Pol. A* 101, 357–366.

Bennett, C. H. (1992) Quantum cryptography using any two nonorthogonal states, *Phys. Rev. Lett.* 68, 3121–3124.

Bennett, C. H. and Brassard, G. (1984) Quantum cryptography: public-key distribution and coin tossing, *Proceedings of IEEE International Conference on Computers, Systems and Signal Processing*, 175–179.

Bennett, C. H., Bessette F., Brassard, G., Salvail, L. and Smolin, J. (1992) Experimental quantum cryptography, *J. Cryptol.* 5, 3–28.

Bruss, D. (1998) Optimal eavesdropping in quantum cryptography with six states, *Phys. Rev. Lett.* 81, 3018–3021.

Dixon, A.R., Yuan, Z.L., Dynes, J.F., Sharpe, A.W. and Shields, A.J. (2010) Continuous operation of high bit rate quantum key distribution, *Appl. Phys. Lett.* 96, 161102.

Ekert, A. K. (1991) Quantum cryptography based on Bell's theorem, *Phys. Rev. Lett.* 67, 661–663.

Elliot, C. (2006) The Darpa quantum network, in *Quantum Communications and Cryptography*, ed. A. V. Sergienko, CRC Press, pp. 83–102.

Gerhardt, I., Liu, Q., Lamas-Linares, A., Skaar, J., Kurtsiefer, C. and Makarov, V. (2011) Full-field implementation of a perfect eavesdropper on a quantum cryptography system, *Nature Commun.* 2, 349.

Gisin, N., Ribordy, G., Tittel, W. and Zbinden, H. (2002) Quantum cryptography, *Rev. Mod. Phys.* 74, 145–195.

Grosshans, F. and Grangier, P. (2002) Continuous variable quantum cryptography using coherent states, *Phys. Rev. Lett.* 88, 057902.

Hughes, R. J., Nordholt, J. E., Derkacs, D. and Peterson, C. G. (2002) Practical free-space quantum key distribution over 10 km in daylight and at night, *New J. Phys.* 4, 43.

Hwang, W.-Y. (2003) Quantum key distribution with high loss: toward global secure communication, *Phys. Rev. Lett.* 91, 057901.

Kurtsiefer, C., Zarda, P., Halder, M., Weinfurter, H., Gorman, P. M., *et al.* (2002) A step towards global key distribution, *Nature* 419, 450.

Lo, H.-K., Chau, H. F. and Ardehali, M. (2005a) Efficient quantum key distribution scheme and proof of its security, *J. Cryptol.* 18, 133–165.

Lo, H.-K., Ma, X. and Chen, K. (2005b) Decoy state quantum key distribution, *Phys. Rev. Lett.* 94, 230504.

Lütkenhaus, N. (2000) Security against individual attacks for realistic quantum key distribution, *Phys. Rev. A* 61, 052304.

Nauerth, S., Moll, F., Rau, M., Fuchs, C., Horwath, J., *et al.* (2013) Air to ground quantum communication, *Nature Photon.* 7, 382–386.

Nordholt, J., Hughes, R., Morgan, G., Peterson, C. and Wipf, C. (2002) Present and future free-space quantum key distribution, *Proc. SPIE* 4635, Free-Space Laser Communication Technologies XIV, 116–126.

Peev, M., Pacher, C., Alléaume, R., Barreiro, C., Bouda, J., *et al.* (2009) The SECOQC quantum key distribution network in Vienna, *New J. Phys.* 11, 075001.

Peloso, M. P., Gerhardt, I., Ho, C., Lamas-Linares, A. and Kurtsiefer, C. (2009) Daylight operation of a free space, entanglement-based quantum key distribution system, *New J. Phys.* 11, 045007.

Ribordy, G., Gautier, J.-D., Gisin, N., Guinnard, O. and Zbinden, H. (2000), Fast and user-friendly quantum key distribution, *J. Mod. Opt.* 47, 517–531.

Sasaki, M., Fujiwara, M., Ishizuka, H., Klaus, W., Wakui, K., *et al.* (2011) Field test of quantum key distribution in the Tokyo QKD network, *Opt. Express* 19, 10387–10409.

Scarani, V., Acín, A., Ribordy, G. and Gisin, N. (2004) Quantum cryptography protocols robust against photon number splitting attacks for weak laser pulses implementations, *Phys. Rev. Lett.* 92, 057901.

Schmitt-Manderbach, T., Weier, H., Fürst, M., Ursin, R., Tiefenbacher, F., *et al.* (2007) Experimental demonstration of free-space decoy-state quantum key distribution over 144 km, *Phys. Rev. Lett.* 98, 010504.

Weier, H., Krauss, H., Rau, M., Fürst, M., Nauerth, S. and Weinfurter, H. (2011) Quantum eavesdropping without interception: an attack exploiting the dead time of single-photon detectors, *New J. Phys.* 13, 073024.

Wiesner, S. (1983) Conjugate coding, *SIGACT News* 15, 78–88.

Zhao, Y., Fung, C.-H. F., Qi, B., Chen, C. and Lo, H.-K. (2008) Quantum hacking: Experimental demonstration of time-shift attack against practical quantum key distribution systems, *Phys. Rev. A* 78, 042333.

3

Ion implantation in diamond for quantum information processing (QIP): doping and damaging

R. KALISH, Technion, Israel Institute of Technology, Israel

DOI: 10.1533/9780857096685.1.36

Abstract: The creation of specific luminescent centers in semiconductors, in particular the controlled creation of nitrogen–vacancy (NV) centers in diamond, relies heavily on ion implantation. Furthermore, the formation of vacancies and the creation of various photonic devices for the manipulation and transportation of the photons emitted by these centers rely on the bond breakage that accompanies ion implantation. In this chapter, we review the physics related to the slowing down of ions in diamond, stressing its implications for implantation doping, the controlled introduction of vacancies and the creation of sacrificial graphitic regions in diamond.

Key words: ion implantation in diamond, NV center in diamond, ion-induced graphitization of diamond, photonic crystals in diamond.

3.1 Introduction

For many applications, solid materials need to be modified by the introduction of foreign atoms. This can be done during growth of the material, by postgrowth in-diffusion of the desired impurities or by ion implantation. Ion implantation, being a violent process in which atoms are shot into the target at energies which exceed the binding energies of the atoms in the target, is always accompanied by displacement of host atoms, i.e., damage to the implanted target material. This damage is undesirable in most doping applications, and it has to be avoided. This is usually achieved by the choice of specific implantation schemes or by postimplantation annealing.

Ion implantation into semiconductors has many advantages in cases in which control of the concentration and depth profile of impurities is required. The dopant atoms are shot into the semiconductor under specific implantation conditions (i.e., with a specific implantation energy and implantation fluence), thus enabling accurate design of the dopant profile. Ion implantation, when done at high fluences, is also used to create composite materials by loading the target with the required foreign atoms at high concentrations. However, it also has drawbacks, mainly due to the damage inflicted on the implanted material by the ions during their slowing down in the solid. This damage can, however, be beneficial for some applications, as will be described below.

© 2014 Elsevier Ltd

The general topic of ion implantation for material modification, which is mainly done for the doping of semiconductors, is well studied and well documented. Ion implantation into diamond has also been extensively studied, in the search for ways to achieve electronic doping of diamond, into which foreign atoms cannot be readily introduced by diffusion. Furthermore, the unique dual bonding configuration of carbon, which is sp^3 bonded in diamond and sp^2 bonded in graphite, has triggered much research into the physics involved in the conversion of sp^3 to sp^2 bonding of carbon.[1, 2]

Renewed interest has recently awakened in the ion implantation of diamond, mainly driven by the discovery that specific luminescent centers in diamond, based on impurity–vacancy complexes, can serve as qubits. This new application of ion implantation to create luminescent centers imposes very strict requirements on the implantation process. For many applications it is desirable to have *single, well-isolated* emission centers, located at *well-defined positions* in the diamond. Hence an entire new field of ion implantation has emerged. It includes single-ion implantations at predetermined locations, and often at low ion energies. The recent developments in this technology will be discussed below, but with reference to only a limited number of key publications in the field. Furthermore, the photons emitted by the luminescent centers in the diamond need to be efficiently propagated and manipulated in photonic structures, preferably constructed in the same diamond in which the photoluminescent centers reside. Hence a new discipline of creating photonic crystals in diamond has emerged. Much of it also hinges on ion implantation of diamond.[3]

The damage inflicted on the implanted material can be beneficial in cases in which modification of the crystallinity or the bonding configuration of the target atoms is required. This applies to the case of diamond, amongst other materials, because it is highly insulating, extremely hard and chemically inert owing to the short, strong sp^3 bonds between the carbon atoms of which it is composed. Diamond can be drastically modified by breaking sp^3 bonds, turning it into electrically conducting, chemically etchable, sp^2-bonded graphite. This finds application, amongst other things, in the creation of a sacrificial graphitic layer in diamond that can be chemically removed, enabling the production of thin diamond membranes and other submicron-sized structures. Damage-related graphitization can also be used to create fine, well-defined, electrically conductive graphitic regions in diamond. Also, the fact that ions slowing down in matter displace atoms can be used to introduce point defects (vacancies) in a controlled manner. This is of importance, for example, when vacancy-containing complexes (i.e., NV centers) need to be created in diamond for quantum applications. All these specific propertied of ion-damaged diamond will be discussed in detail below.

It should be noted that the requirements for efficient doping of diamond by ion implantation, i.e., the removal of implantation-related defects from the vicinity of the implanted impurities, and the requirements for the formation of

impurity–vacancy complexes are orthogonal. In the first case, the vacancies formed by the implantation must be removed from the implanted ions, whereas in the second case, the vacancies must be manipulated so as to be located at specific positions in the diamond; for the formation of NV centers, their presence near the implant is essential.

In the following, we briefly describe the general concepts of importance for an understanding of the results of ion implantation as far as the damage and the final implant location are concerned. We then focus on implantation-related damage in the particular case of ion implantation of diamond for doping purposes. We summarize the current situation regarding doping of diamond as achieved by ion implantation for p- and n-type doping. The controlled introduction of damage that accompanies ion implantation in diamond finds application, amongst other things, in the creation of particular impurity–defect-related luminescent centers, as well as in the production of nanosized structures in diamond. These and various implantation/annealing schemes designed for the efficient exploitation of the various ion-induced modifications of diamond will be reviewed below.

3.2 Doping diamond

3.2.1 Doping during high-pressure high-temperature (HPHT) growth

The phase diagram of carbon shows that under conditions of normal temperature and pressure (NTP), the thermodynamically stable form of bonding in carbon is sp^2, i.e., graphitic. This is in contrast to diamond, which is composed of sp^3-bonded carbon atoms. The latter can be formed only at high pressures and high temperatures. Nevertheless, stable diamond exists in nature under NTP conditions owing to the high potential barrier between the sp^2 and sp^3 configurations, which in practice prevents a spontaneous transition from sp^3-bonded carbon atoms (diamond) to sp^2-bonded atoms (graphite). Diamond can thus be formed in nature only under high-pressure high-temperature (HPHT) conditions, such as exist deep in the earth, in very large HPHT laboratory devices and during explosions.

During the above thermodynamic processes, impurities present in the growth environment can be introduced into the diamond. The most common impurities (‘dopant atoms’) that are introduced into diamond during these ‘natural’ processes are nitrogen, boron and some transition metals. These impurities are, apart from boron, which is a p-type dopant with a reasonably shallow level, useless as electronic dopants at practical temperatures owing to the deep levels they form in the diamond band gap. The status of the doping of diamond by application of ‘thermodynamic’ conditions has been thoroughly studied for several decades, and many reviews on this have been published. Hence this topic will not be dealt with further here.

3.2.2 Doping diamond during chemical vapor deposition (CVD) growth

The discovery that diamond can be grown under 'nonequilibrium' low-temperature, low-pressure conditions by chemical vapor deposition (CVD) has renewed the search for ways of achieving p- and n-type-doped diamond.

Boron-doped p-type diamonds exist in nature (type IIb diamonds). They can also be readily grown in the laboratory by CVD methods by adding B to the growth gas mixture, as described in detail elsewhere. When grown on single-crystal diamond (preferably ⟨100⟩ oriented), single-crystal B-doped diamond layers can be grown. The growth of thin B-containing homoepitaxial 'delta-doped' diamond layers with exceptional electrical properties has recently been reported. These layers, which were obtained by careful, very slow homoepitaxial CVD growth, exhibit high doping efficiencies and very high hole mobilities owing to the extremely low concentration of defects in them.

Much effort has been devoted to achieving n-type doping of diamond to enable the realization of bipolar devices based on p–n junctions. Natural n-type diamonds with a low enough activation energy to allow electronic applications at room temperature do not exist. Computations have shown that the introduction of foreign atoms into diamond to make it n-type is likely to be difficult. The possibility of growing diamond by CVD methods has opened up many possibilities to introduce foreign atoms into diamond during growth, including atoms which are expected to act as shallow donors.[3] Several different molecular species which contain the required impurity atoms (mainly from Groups V and I) have been introduced into the plasma during CVD growth, in the expectation that these will be incorporated into the growing diamond as effective donors, thus inducing n-type conductivity. It has turned out that, to date, despite many attempts, the only useful donor that can be introduced into diamond by CVD methods (apart from nitrogen) is phosphorus – a rather deep donor, with an activation energy of 0.56 eV.[4] Unfortunately, the epitaxial growth of P-containing diamond is optimal when it is grown on the ⟨111⟩ face of the crystal, in contrast to the preferred epitaxial growth of B-containing diamond, which grows best on the ⟨100⟩ face. Hence the creation of p–n junctions in epitaxially grown B- and P-doped layers of diamond is still problematic. Nevertheless, luminescence from an interface between B-doped and P-doped structures has recently been reported. This topic of the search for donors in diamond has been thoroughly reviewed in the literature, and will thus not be addressed further here.

Other 'promising' donors in diamond grown by CVD, such as Li and As, have been studied, but with no proven success.

An interesting approach to obtaining thin layers of diamond which contain the desired impurities by CVD has recently been demonstrated by Aharonovich *et al.*[5] Impurity atoms were introduced at large concentrations into the near-surface area of a diamond, which served as a substrate for epitaxial overgrowth. It was found

that impurities from the heavily doped substrate were incorporated in small quantities into the overgrown layer, thus building a thin diamond layer which contained the desired impurity. This novel approach, which, in principle, should enable the introduction of many desired impurities into the near-surface region of single-crystal diamond, has not yet yielded doped diamond layers for practical applications, however. More work on this topic is needed.

3.2.3 Electrically active defect complexes in diamond

Electrically active species need not necessarily be pure, single atomic dopants. Defect complexes can also have energy levels in the gap of a semiconductor, thus serving as 'dopant centers'. This holds also for the case of diamond; hence the search for shallow donor states in diamond has been extended to investigating the option of having effective 'donor complexes' in diamond, as it seems that no single impurity atom can serve as a useful donor in diamond. The idea is to search for defect complexes in diamond which can donate a lone electron to the conduction band, thus giving rise to n-type conductivity. Several theoretical predictions of possible donor-like defect complexes in diamond have been published, but with no experimental verification.

A promising finding that substitutional boron in diamond, when bonded to two hydrogen atoms, gives rise to n-type conduction with a low activation energy and reasonable electron mobilities was reported in 2003. It was shown[6] that the introduction of hydrogen into a p-type B-doped diamond layer may bond hydrogen to B atoms and thus passivate the acceptors by the formation of B–H complexes. Further introduction of hydrogen may form a BH_2 complex, which has an extra electron that can, in principle, contribute to n-type conduction. Indeed, H–B–H complexes have been created in diamond by exposure of a B-doped layer to a hydrogen plasma (in fact, a deuterium plasma, for experimental reasons). It was found that, as expected, when B–H complexes were formed, the p-type conduction of the original sample vanished (i.e., the formation of this complex had passivated the acceptor activity). Further exposure to an H (or, rather, D) plasma resulted in the observation of n-type conduction with a rather shallow donor level and reasonable electron mobilities. This finding has triggered much theoretical and experimental work; some studies have verified the claim of the existence of n-type conduction due to B–2H complexes and others not. It seems as if different growth sectors of the single-crystal diamond used as a substrate for the epitaxial growth of the B-containing layer react differently to further hydrogenation.[7] Furthermore, the way in which H (deuterium) is introduced to passivate the B acceptors by forming B–H complexes and the subsequent introduction of more H to form H–B–H complexes is problematic, as it seems to affect the results of electrical measurements. Making electrically contacting regions in B-doped, H-plasma-treated diamond is also problematic.[7] Hence, to date, no reliable, useful n-type-doped diamond has been achieved by this method.

3.3 Doping diamond by ion implantation

3.3.1 Ion implantation: general considerations

Ion implantation is always accompanied by radiation damage. It is an inherent part of the stopping process of an energetic ion slowing down in matter. The entire stopping process is of a statistical nature: every stopping ion undergoes a sequence of collisions with the atoms and electrons of the stopping material, resulting in a cascade of secondary recoiling target atoms. Hence the stopping of any single ion results in a 'collision cascade' containing many atoms set in motion during the slowing-down process. This cascade lasts for as long as the recoiling atoms and the entire surrounding lattice are in motion. This is termed a 'thermal spike' and lasts for about 1 ps. As long as this spike is present, extremely high local temperatures, well above the thermodynamic melting temperature of the bulk, are expected.

The implantation process can be simulated by Monte Carlo computer programs such as the SRIM code.[8] In this program, the desired atoms are shot, one at a time, into a solid target, assumed to be amorphous. The program simulates the entire collision process, i.e., the trajectories and collision histories of the primary ion and of the secondary recoiling ions. It follows the slowing down of the moving ions until they all come to rest. The hot spot generated by each implanted ion eventually cools down, leaving the surroundings of the trajectory of the primary implanted ion disordered. The state of the material following the implantation depends on the ability of the remaining defects to anneal out or to agglomerate into stable structures, i.e., on the properties of the material, the implantation temperature and any postimplantation thermal treatment. However, SRIM, even though it is widely used to simulate the results of ion implantation and gives, amongst other things, the final depth profiles of the implanted ions and the resulting defects (vacancies and interstitials), suffers from several drawbacks:

- SRIM assumes the sample temperature to be 0 K, i.e., the damage is 'frozen in' and no diffusion or bond rearrangements are considered;
- it assumes an amorphous target;
- all ions are shot, one at a time, into the target material at the same spot.

The output of the program gives statistics for the entire collision history of the slowing ions (the number of vacancies they have created, their final stopping location, and the ion and the damage profiles, to list just the major statistics). SRIM requires, as an input, various parameters related to the stopping material (i.e., composition, density and displacement energy), and not all of them are well known. This holds in particular for the case of diamond, as will be discussed below. Figure 3.1 depicts the damage cascades predicted by SRIM for a single C and a single Xe ion shot into diamond at 100 keV and 320 keV, respectively. Once many ions have been shot into the diamond, SRIM offers a statistical distribution

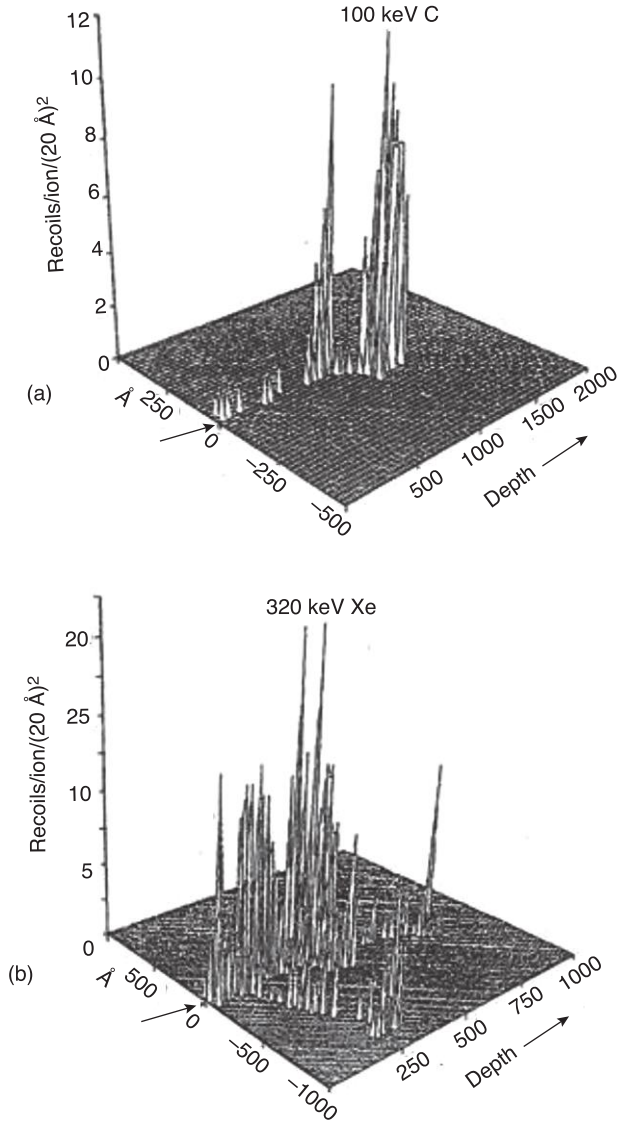

3.1 Collision cascades following penetration into diamond of (a) a single 100 keV C ion and (b) a single 320 keV Xe ion, as predicted by SRIM.

of both vacancies and implanted ions, as shown in Fig. 3.2. The nonoverlap of the vacancy and implant distributions should be noted, as it is of importance for the points discussed below. More sophisticated computations, based on molecular dynamics, which simulate the damage in the vicinity of the stopping site of the implanted ion, have been published. These are obviously more accurate, once

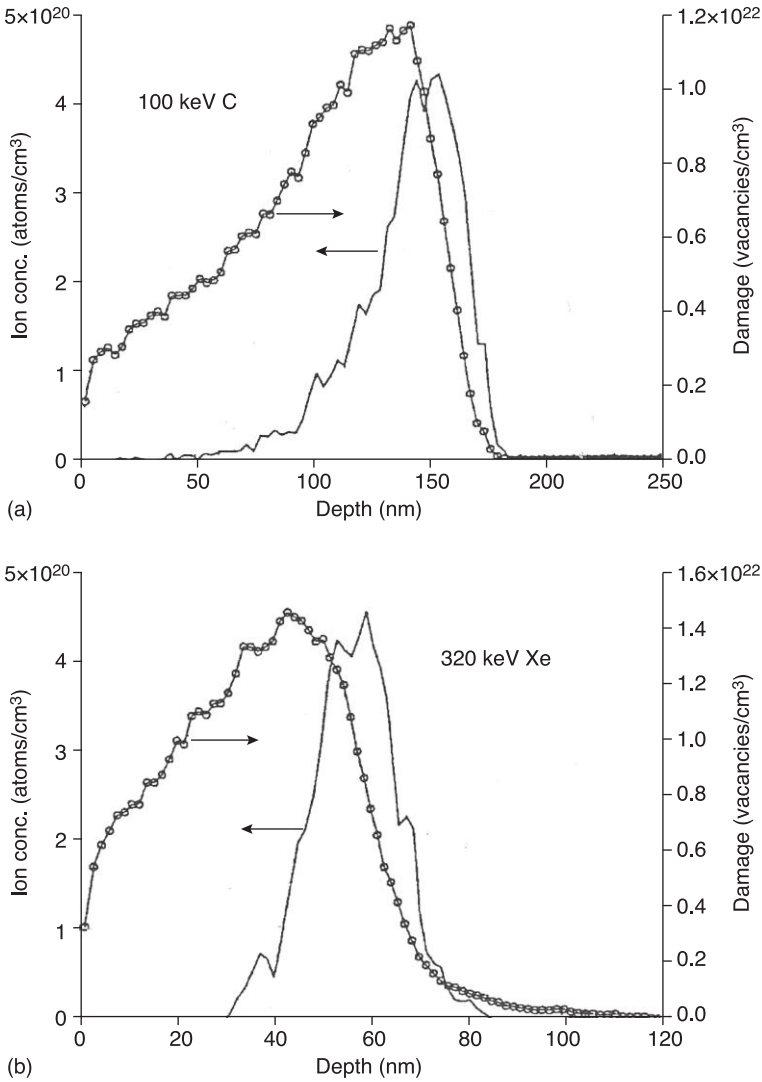

3.2 SRIM damage and ion profiles for (a) 100 keV C and (b) 320 keV Xe ions implanted into diamond (taking E_d = 52 eV) to a fluence of 1×10^{15} /cm^2.

the interatomic potentials are known, but they are limited, owing to computational limitations, to small samples containing only a few atoms. The results of these computations are, however, very helpful in understanding the local transformations that diamond undergoes as a result of implantation. This topic will be discussed below in more detail.

3.3.2 Ion-implantation-related damage in diamond

The question of the nature and properties of implantation-induced damage in diamond has recently received renewed interest, because it is the major means of formation of thin diamond membranes for the formation of conductive regions in diamond, and of formation of specific optically active impurity–vacancy complexes. These all require tailoring of the ion-induced damage and its postimplantation behavior.

As mentioned above, diamond is a unique material owing to its thermodynamic instability. Hence broken diamond bonds may rearrange into more stable sp^2 (graphitic) bonds. This fact is of great importance for all ion implantation processes in diamond. It has been extensively studied, both theoretically and experimentally. The mechanism of the amorphization of diamond by ions has recently been summarized by Fairchild *et al.*[9] The main fundamental questions regarding the formation of permanent damage in ion-implanted diamond are:

- What is the minimum momentum, or the minimum energy (the so-called displacement energy, E_d), that needs to be imparted to a C atom in the diamond matrix to dislodge it far enough from the vacancy that it leaves behind so that it does not fall back into the vacancy?
- What is the minimum density of broken C bonds (D_c) required to cause the damaged diamond to grow into graphite following thermal treatment, rather than anneal back to diamond?
- What are the physical and chemical properties of 'partially graphitized' diamond?

Displacement energy (E_d) in diamond

The displacement energy E_d is defined as the minimum energy (or momentum) that needs to be imparted to an atom in a solid so that it will be removed from its native site in the lattice far enough not to fall back into the vacancy that it has left behind. This number is of fundamental importance in the understanding and analysis of all damage events in a solid, including ion implantation. It is difficult to measure this number directly, and hence computer simulations, described in more detail in Section 3.6.2, are employed to obtain it. The value of E_d deduced from simulations for a random collision direction with respect to the crystallographic axes of diamond is 52 eV[10] (see Section 3.6.2). This value is close to that already obtained by Wu and Fahy by molecular dynamics simulations in 1994.[11]

Critical damage density (D_c) for graphitization of diamond

During the slowing-down process, an ion undergoes nuclear collisions that displace atoms from their regular sites. The number of these depends on E_d. Once

a certain volume density of sp^3-bonded carbon atoms have been broken, the 'heavily damaged' diamond volume so formed will not anneal back to diamond but will, rather, regrow to the more stable sp^2 form of C bonding, resulting in the graphitization of the entire volume damaged to a level higher than D_c. The question of what this 'critical damage density' D_c is of great importance both for the possibility of recovering the diamond structure after ion implantation by annealing, as required for efficient doping, and for intentional graphitization, as needed for the creation of free-standing diamond membranes by methods based on implantation, graphitization, chemical removal of graphite and liftoff, as well as for various applications of selected graphitic (electrically conductive) regions in diamond.

The breakage of sp^3 bonds and the resulting graphitization of diamond have been studied experimentally for the last 30 years, mainly by measuring the change in resistivity[12] of a pure diamond sample as function of implantation-induced damage, as shown in Fig. 3.3. Analysis of the measured changes in the electrical conductivity of ion-damaged diamond as a function of ion species, ion energy and implantation temperature based on percolation between conductive regions formed around the position of each implanted stopping-ion position[13] has shown that once a certain implantation-related defect density around each ion track is reached, the electrical conductivity rises sharply. This was explained[13] by fitting the resistivity vs. dose data with a 2D percolation model in which connectivity between the conducting damaged 'graphitic' islands sets in once they percolate. This was the first time that an estimate of the size of the conductive region around a single ion track (as shown in Fig. 3.1) had been obtained experimentally. Much experimental and theoretical work on the evolution of damage in diamond has followed, relying mainly on electrical-conductivity measurements. The major finding of these studies is the discovery that a 'critical damage density' D_c exists, beyond which the disrupted sp^3-bonded diamond structure collapses to mostly sp^2-bonded amorphous carbon, which, following further annealing, crystallizes as chemically etchable graphite.

The graphitization limit has been determined directly by measuring (by secondary ion mass spectrometry) changes in the depth profile of a buried marker layer, deeply implanted with Li ions, yielding the thickness of the removed layer. When a damage density (as given by SRIM using $E_d = 52$ eV) of about 1×10^{22} vac/cm^3 is reached, the diamond structure is damaged to such an extent that it cannot be recovered by annealing anymore[14] (Fig. 3.4). There are some indications that the critical damage density depends on the depth of the damaged buried layer in the diamond. This is most likely caused by the internal pressure that a diamond cap layer induces in a heavily damaged buried layer, thus retarding graphitization.

Comprehensive work on the effect of radiation damage in diamond, as measured by Raman spectroscopy,[15] has been published. In that work, the evolution of different peaks in the Raman spectrum as a function of depth in diamond subjected to different implanted ions, fluences and annealing temperatures was studied. The

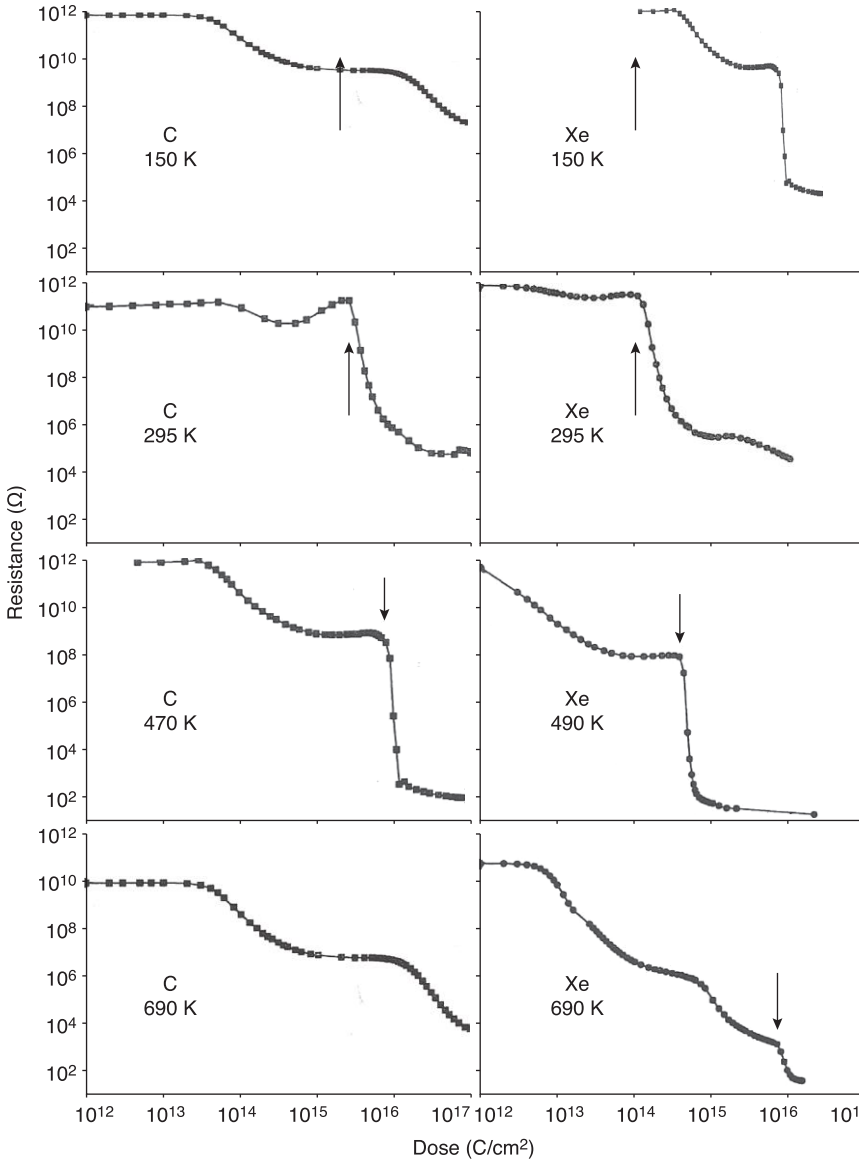

3.3 Resistance of damaged diamond as a function of fluence for 100 keV C and 320 keV Xe ion implantations at different implantation temperatures.[12]

data obtained as a function of depth along the ion damage profile confirmed the existence of the critical damage density deduced from other experimental methods. Several very detailed investigations of these damage/annealing-related changes of diamond to sp^2-rich amorphous 'graphitic' regions have followed, employing

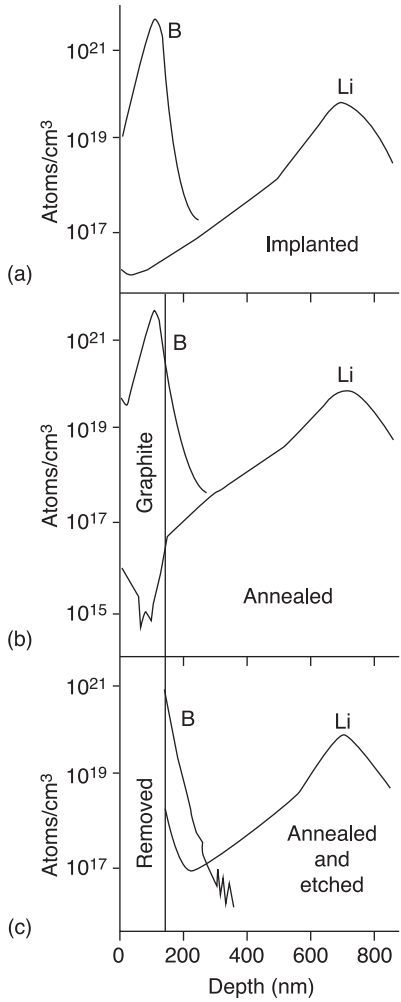

3.4 SIMS depth profiles of boron-and lithium-implanted diamond (a) as implanted; (b) implanted and annealed; (c) implanted, annealed and etched (graphite removed).[14]

different experimental methods, all consistently yielding rather similar values for the critical damage density for graphitization.

The kinetics of the conversion of diamond bonds broken by ion impact to form graphitic bonds, and their response to annealing have been investigated by analyzing experimental results on changes in the electrical and vibrational (Raman) properties of damaged diamond.[16]

Electrical effects of native defects in diamond

Prins[17] has reached the conclusion, based on the results of electrical and optical measurements of B-implanted diamonds, that nonannealed implantation-induced damage forms a compensating donor level located about 1.2 eV above the top of the valence band. This is in accord with a finding that C implantations into type IIa diamond, to a dose below the graphitization limit, caused electrical conduction characterized by an activation energy of 1.2 eV.[18] However, earlier data on the temperature dependence of ion-induced charge transport has been interpreted as being due to variable-range (Mott) hopping between localized states around the Fermi level. This does not seem to agree with the above findings.

The effect that implantation-induced point defects have on the electrical properties of doped (both n- and p-type) diamonds has been studied by Reznik *et al.*[19] Hydrogen ion irradiations *through* B- and P-doped homoepitaxial layers were used to introduce well-known amounts of point defects into the doped layers. The changes in resistivity, mobility and carrier concentration were measured as a function of increasing H damaging fluence. It was found that for B-doped layers, the introduction of point defects increased the resistivity of the implanted diamond up to that of pristine diamond without changing the activation energy of the p-type carriers (0.37 eV). It did, however, increase the compensation ratio N_d/N_a linearly with increasing defect density and it considerably reduced the mobility of the p-type carriers. The temperature dependence of the mobility also changed from the dependence expected for a doped semiconductor to only a weak dependence governed by defect scattering. It was also found that the defect density at which loss of conductivity set in for H-irradiated n-type, P-doped homoepitaxial layers occurred at a dose three orders of magnitude higher than that needed for the p-doped samples.

These finding clearly support the hypothesis that ion-implantation-induced defects are responsible for the presence of a deep donor level in the diamond band gap. For p-type doped diamond, these defects compensate the acceptors (B) and reduce the hole mobility. In n-doped layers, these defects may form neutral defects, thus reducing strongly the mobility of the n-carriers, as observed in P-doped diamond.

Properties of partially damaged (below D_c) diamond

The effects that broken sp^3 bonds have on the electrical properties of diamond are due to the fact that they create energy levels within the band gap of the diamond and hence induce electrical conductivity. The resistivity vs. damaging-ion fluence curves $\rho(D)$ exhibit three distinct regions,[12] regardless of the implanted ion: for fluences lower than the critical damage density D_c, ρ remains almost constant; for $D \approx D_c$, a sharp drop in ρ occurs; and for $D >> D_c$, ρ saturates at a value comparable to that for polycrystalline graphite (see Fig. 3.3). The conduction in the transition region is described by variable-range hopping conductivity ($\rho(T) \propto T^{1/4}$),

presumably with carriers hopping between highly conductive small regions. The very high conductivity observed in the saturation regime is that of graphite (i.e., metallic, $\rho(T)$ = constant) and occurs when the graphitic islands percolate.

Regarding the nature of the conductivity induced by the implantation damage, detailed studies of the electrical resistivity as a function of temperature for a variety of implants have shown[18] that at low temperature, heavy-ion implantation yields p-type conductivity with poor mobilities (~10 cm^2/V s), whereas implantation at higher temperatures or postimplantation annealing of the damage was found to yield n-type conductivity. As doping by ion implantation always requires annealing, one can expect the residual damage following incomplete annealing to act as donor centers in the diamond. These will either give rise to n-type conduction or compensate acceptor states.

3.3.3 Damage-annealing schemes for efficient ion implantation doping

To ensure that real chemical doping, with *electrical effects not related to broken C bonds*, is achieved by ion implantation, control experiments are essential. In these experiments, nondopant ions have to be implanted into identical diamond samples under conditions which create damage profiles similar to those due to the implanted dopants. These samples must be subjected to annealing protocols identical to those applied to the dopant-implanted samples, and the electrical outcomes must be compared. Only if the nondopant-implanted sample returns to its pristine high resistivity following annealing, whereas the chemically doped sample shows electrical effects, can these effects be attributed to the presence of the implanted dopant and its doping effect. Not all published data reporting 'successful doping' by implantation of ions do include such important control experiments. That is, some 'successful' n-type doping of diamond by various ion implantations (Li, Na, P and S) may be uncertain.[20, 21]

It is thus clear that for real chemical doping by the implantation of potential donor or acceptor impurities, the damage resulting from the implantation process must be removed. This requires devising implantation/annealing schemes which will either prevent the formation of defects in the first place, or lead to their annihilation during implantation or following the implantation by postimplantation annealing.

Prins[22] has theoretically analyzed the kinetics of the motion of vacancies and interstitials in diamond. Based on the conclusions of this analysis, Prins came up with an implantation/annealing scheme expected to yield higher doping efficiencies and higher carrier mobilities. According to Prins, in order to achieve successful substitutional doping of implanted potential donor or acceptor ions, it is important to devise implantation/annealing schemes that result in the desired final configuration of the crystal and the impurities. Namely, it is important to allow annihilation of vacancy–interstitial pairs, hence avoiding the formation of

native defect complexes (divacancies or sp^2-bonded clusters) and, at the same time, to drive the implanted atoms into sites in the lattice where they can be expected to act as the desired dopants in an undisturbed diamond lattice. One obvious approach to achieving this is to perform the implantation into heated diamond, hence leading to instantaneous annihilation of the point defects or preventing their formation in the first place.

An alternative approach to obtaining effective activation of implanted dopants is another implantation/annealing scheme proposed by Prins, which he has termed CIRA ('cold implantation, rapid annealing').[18] This is based on performing the impurity implantation into cold diamond (close to liquid nitrogen temperature) followed by rapidly heating the sample *in situ* to a high temperature (around 1000 °C). The idea behind CIRA is that when the implantation is performed 'cold', all defects formed during the slowing-down process are immobile, i.e., they are frozen in, and the formation of complexes that include native defects is inhibited. Rapid heating of the sample with its 'as frozen in' vacancies and interstitials will allow, according to Prins, quick short-range diffusion of the defects, enhancing the recovery of the disrupted crystal structure around the implanted impurity atoms, resulting in substitutional doping. Indeed, Prins has published a series of papers in which successful doping of several different implants in diamond has been reported. Phosphorus-related donor (n-type) electrical behavior, with an activation energy of ~0.7 eV, and nitrogen with a donor activation of 0.29 eV have been measured by applying CIRA. These early results have not, however, all been confirmed by further careful experiments which included nondopant implants as controls.[23] CIRA has been more successful when applied to the well-known acceptor dopant in diamond, i.e., boron. Several reports from different laboratories have all shown that good p-type activity could be obtained by B implantation using the CIRA scheme. The importance of the two stages in CIRA, i.e., the cold implantation followed by the immediate heating of the sample, has been investigated. Whereas the results of these studies do indicate that cold implantation has some advantages over room temperature or 'hot' implantation, the 'rapid' heating stage immediately following the implantation could not be shown to improve the p-type nature of B-implanted diamond.

3.4 Controlled formation of implant–defect centers

Not only is ion implantation used for the purpose of doping or damaging, but it also finds application in the controlled formation of selected defect–impurity defect centers in diamond such as the nitrogen–vacancy (NV) complex mentioned above. This requires the possibility of controlling the behavior of native defects (vacancies and interstitials) in diamond, not only to remove them, as is required for elemental doping, but also to manipulate them to form defect–impurity complexes, as required for the formation of specific optically active centers. Hence it is important to understand the diffusion of point defects (i.e., vacancies)

in damaged diamond, to know the nature of their bonding to specific impurities and to other defects in the diamond, and to know how to control their mobility.

It should be stressed once more that the requirements of control of the motion of native defects in implantation-damaged diamond to *achieve chemical doping* (as described above) and to *form selected impurity–defect complexes* (such as the NV center) are in a sense orthogonal to each other. In the first case the defects must be annihilated, whereas in the second they must be manipulated to form some particular defect complex with the impurity.

3.4.1 Formation of nitrogen–vacancy (NV) complexes in diamond by ion implantation

The most studied impurity–defect complex in diamond, to date, is the NV center, with its unique luminescence properties (discussed elsewhere in this book). The accepted model for the formation of this defect center is the trapping of a vacancy by a substitutional nitrogen atom during postimplantation annealing.[24] The vacancies are usually introduced into a diamond that already contains the N impurity either from a previous N ion implantation or because it was introduced during growth. The vacancies are formed by a damaging ion implantation or by some other defect formation mechanism (e.g., electron irradiation). Thermal treatment is expected to induce diffusion so as to form the desired NV defects. This process needs to be well under control, and its yield should be as high as possible. Furthermore, the NV centers should have a long relaxation time, which requires them to reside in a 'perturbation-free' environment.

A requirement on the NV centers for many applications is that they should be *negatively charged*, i.e., NV^- centers, and that they should be *isolated centers* in the diamond, located at *predetermined, well-known locations*. These conditions impose very stringent requirements on the ways in which the NV centers are introduced and formed.

The nitrogen impurities in the diamond can either be present in the 'as received' natural (type Ib) or CVD-grown diamonds or be introduced by N ion implantation. Sometimes implantation of the isotope ^{15}N is performed into ultrapure diamond, which contains very few unintentional ^{14}N atoms. This is done in order to be able to experimentally follow the luminescence from the implantation-induced ^{15}NV centers and avoid disturbance from the unavoidable ^{14}NV centers.[25]

In order to have control over the exact number and location of the nitrogen atoms in the sample, single N ion implantations using well-focused N ion beams and implantations through masks or another constriction (i.e., a nanohole in an scanning tunneling microscope (STM) tip) have been performed, with some success, as reviewed recently.[26] A schematic picture of the setup required to achieve this is shown in Fig. 3.5.[27] However, the state of this field is complicated, and much work is still needed to make such techniques a practical way of producing well-localized, single NV centers in diamond.

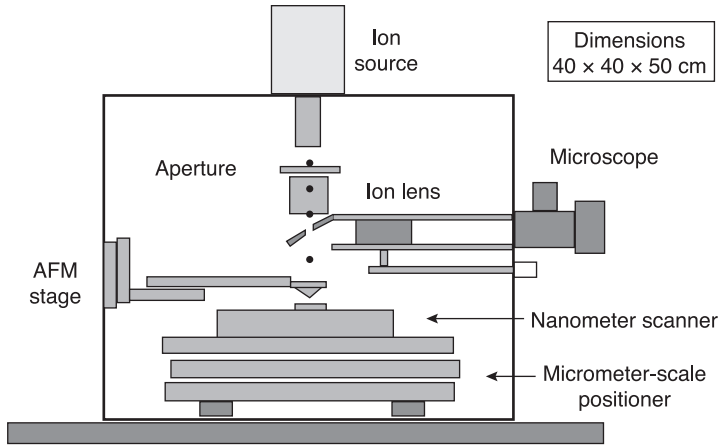

3.5 Experimental setup for single-ion implantation. Top to bottom, an ion gun; a micro-ion lens with apertures; an optical microscope with a pierced mirror; and a movable table with subnanometer resolution. The pierced atomic force microscope (AFM) tip can be moved precisely in all directions using micromotors. The diamond target is placed on a piezo table with 0.1 nm resolution.[27]

Once the N ion has been introduced into the diamond matrix, it must capture a vacancy to form an NV center, preferably without losing its predetermined location. This requires the presence of vacancies in the vicinity of the N atom. The vacancies formed by the implantation of a single N ion, created during its slowing-down process, can seldom serve as a source of vacancies for the formation of an NV center from that particular implanted N ion, the reason being that no vacancies originating from nuclear collisions at the end of track of a single ion are likely to form in the vicinity of the final site, as at this stage the energy of the moving ion is below the displacement energy E_d. Many vacancies originating from other implantations or from electron or neutron irradiation must be formed in the vicinity of the N atom to serve as a source for capture by that N impurity. These must be driven to combine, with high efficiency, with the substitutional nitrogen by thermal annealing, but without losing the original predetermined location of the N. This poses severe experimental problems, which are still under intensive study.

Several different approaches to achieving efficient formation of NV centers to meet the above requirements have been published, including well-defined single N ion implantations and well-defined damage implantations. Different implantation/annealing schemes have also been applied to increase the NV formation efficiency.[28] Most of these have been summarized in a recent review. In Fig. 3.6, some results from a comprehensive study[27] of the NV center formation yield following different N and damaging co-implantations are shown. A damaging ion implantation of carbon into heated N-containing diamond seems to be the most effective scheme.

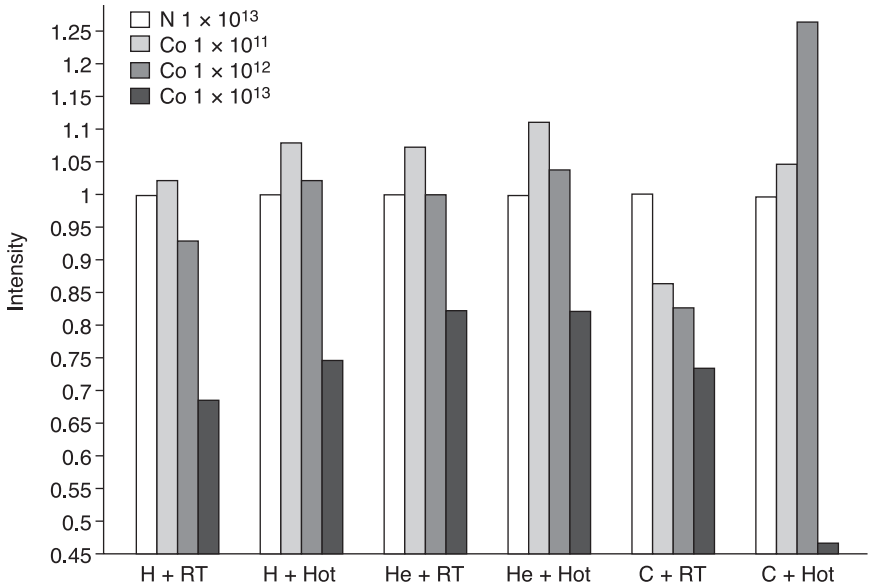

3.6 Histogram summarizing the evolution of the NV photoluminescence intensity when hydrogen, helium and carbon ions are co-implanted (all at 7.7 keV) into diamond samples held at room temperature (RT) or heated to 780 °C.[27]

Very recently, work describing the local controlled introduction of vacancies into well-known locations in N-containing diamond by irradiation with well-focused electrons from an STM has been reported.[29] Following moderate thermal annealing (800 °C) after such implantations, an increase in the NV center formation probability by a factor of 1.8 was observed. Prolonging the coherence time has also been achieved recently by controlling the implantation and annealing temperatures, thus minimizing the perturbing effects caused by defects in the vicinity of the NV centers.[30]

3.4.2 Formation of other optically active complexes in diamond by ion implantation

There are numerous defect- or impurity-related optically active centers in diamond which can, in principle, serve as qubits. Their luminescence was studied intensively in the last century, mainly in order to understand and control the color of diamond gemstones. However, the requirements that the luminescence from these centers must meet for quantum applications either are not met or have not yet been studied in detail. Some of the defects which are currently under study are complex defects in diamond related to Si, Ni, Cr and Xe. These must be introduced into the diamond under the same restrictions that apply to the formation of the NV centers

discussed above. Hence ion implantation seems to be the method of choice for the creation of these defects, and many of the points mentioned here will be relevant also to the formation of these centers.

The Si–V complex in nanodiamonds, introduced by CVD methods, has recently been studied and exhibits promising luminescence properties for use as qubits.[31] The Ni–nitrogen (NE8) complex in diamond is a well-known photoluminescence center that was studied long ago. Recently, single NE8 centers formed in diamond by CVD have been observed, and their luminescence properties relevant to various quantum applications have been studied.[32]

Chromium-related optical centers have also been studied. These have been introduced into diamond by ion implantation in experiments exploring the efficiency of the formation of this center following various co-implantations and annealing procedures, including Cr + Si, Cr + O, Cr + S and Cr + B co-implantations. Following 1000 °C annealing, some luminescent centers were detected; however, their formation efficiency is still extremely low.[33]

3.5 Applications of graphitization of diamond by highly damaging implantations

As already discussed in Section 3.3, solid carbon is unique in that it can support different hybridization states, depending on external conditions such as temperature and pressure. The thermodynamically most stable bonding configuration of carbon is graphitic bonding, i.e., sp^2; however, when ions slow down in diamond, sp^3 bonds may break, as shown in SRIM simulations (their number depends on the value of E_d used!). Once a certain 'critical' fraction of the sp^3 diamond bonds have been disrupted, annealing will transform the damaged diamond into graphite. The fact that graphite has extremely different physical and chemical properties can be beneficial for the controlled formation of graphitized sections in diamond, and for their application. Of particular relevance are the facts that graphite can be chemically etched, that graphite is highly electrically conductive and that the adsorption of various chemical and biological species is very sensitive to the bonding configuration of the surface C atoms. Since graphitized regions in diamond can be accurately controlled by an ion implantation process using either focused ion beams or implantation through constrictions, this allows the conversion of selected regions in a diamond to graphite, thus inducing local modifications of the properties of the diamond.

3.5.1 Formation of free-standing diamond membranes

Quantum computing relies on the ability to read, manipulate, initialize and store information encoded into states of a single quantum bit (qubit). The most promising candidate for this, at the moment, is the negatively charged nitrogen–vacancy color center (NV^-) in diamond. The photons emitted by this center must

be propagated and manipulated to enable their application. For this, the emitting NV center needs to be located in or in close contact with optical components such as waveguides and photonic crystals. The basic idea is that each qubit (i.e., NV^-) is coupled to a high-Q cavity, and the cavities are optically interconnected via waveguides. The obvious material for the realization of such a device is diamond itself, as it has excellent optical transparency and the NV centers can be created at predetermined locations in the device itself.[34]

Major progress has been made in diamond photonics and processing in recent years, including the design of ultrahigh-Q cavities and the development of new patterning and material-processing schemes for diamond. Many of these are based on structures created in thin diamond membranes. However, the production of such membranes with high optical quality, as required for the fabrication of photonic crystal structures, is still a major challenge.

3.5.2 Realization of photonic crystals in diamond by ion beams

The fact that highly damaged diamond transforms to chemically etchable graphite has been used to fabricate free-standing diamond membranes. Several slightly different approaches have been employed. The first relies on deep implantation of damaging ions, typically 2.0 MeV He ions to fluences of the order of 5×10^{16} ions/cm^2. This results in a defect density which exceeds the critical dose for graphitization in a layer located some 200 nm below the surface. Annealing at about 1000 °C graphitizes this layer. Drilling holes from the surface to the graphitic buried layer by use of a Ga focused ion beam (FIB) allows acids to reach the layer and etch the graphite, leaving a free diamond membrane, the thickness of which is determined by the damage profile. This membrane can be lifted out from the diamond substrate, as shown in Fig. 3.7. One surface of the membrane thus formed is that of the starting diamond, and the other is that of the lifted-off membrane. The optical properties of these are not identical, with the lifted-off surface requiring some treatment (H plasma) for smoothing, cleaning and removal of residual graphite.[35] A variation of this method employs two damaging implantations at different energies, resulting in two buried damage layers. Hence the entire membrane is buried in the diamond, and its thickness can be controlled by the difference in energy of the two implantations.[36]

Once the membrane is free-standing, it can be characterized further and be used for the creation of various forms of photonic crystals (by use of FIB pattening[33]), and for the formation of NV centers at required locations within the photonic device by well-positioned N or V implantations as described above. It should be stressed that the optical quality of the membrane surfaces is of major importance, as it determines the reflectivity and absorbance for the photons to be propagated in the membrane.

Recently, several different structures for photonic crystals in diamond have been considered. Amongst these is a micron-sized triangular diamond beam into

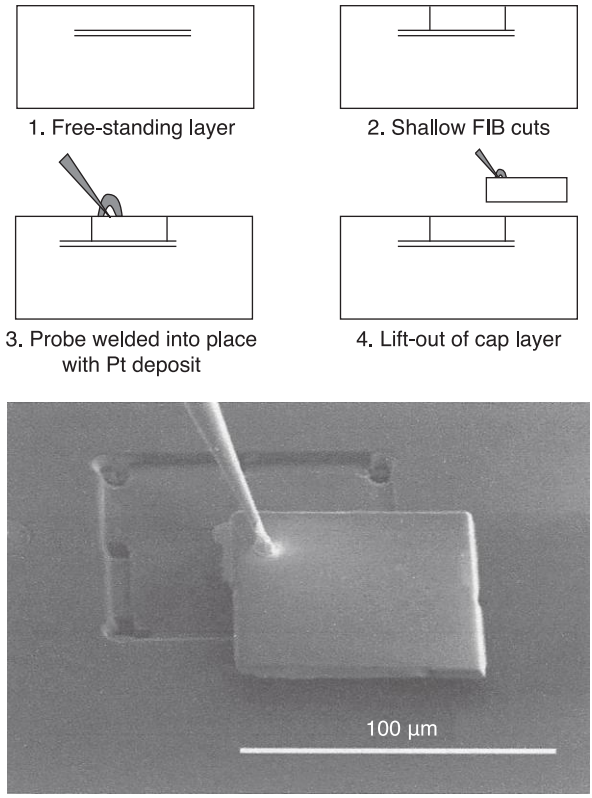

3.7 Schematic illustration of the fabrication of a thin diamond membrane by the graphitization–etching–liftoff procedure.[33]

which photonic crystal structures are carved by use of Ga FIB milling.[37] It should be mentioned that the FIB milling leaves behind a damaged surface (and some diamond debris and shallowly implanted Ga ions) very similar to the residual damage following the ion implantation/graphitization/liftoff procedure that is used for membrane formation. Hence further surface treatment is required to ensure good optical quality of the surfaces thus formed.[38]

3.5.3 Ion-beam-induced graphitization for the realization of nanosized features in diamond

The fact that damaged diamond, even when the damage concentration is below the critical density of broken bonds and even without annealing, exhibits increased electrical conductivity relative to that of pristine diamond finds application in the creation of conductive pathways in diamond by damaging implantations. The graphitization of damaged diamond at selected locations has been extensively

used in the last few years to make electrical contacts to diamond in order to enable electrical-conductivity and Hall measurements. The technique is particularly useful when fine conductive features in diamond are required, as these can be created by the use of damaging focused ion beams. The depth flexibility offered by controlling the location underneath the surface at which the damage is concentrated allows the formation of three-dimensional conductive nanochannels in diamond.

These properties have been used by the Turin/Melbourne group[39] both to study the nature of the electrical conduction in diamond damaged by focused MeV He ions to different degrees before and after annealing, and to demonstrate how highly conductive pathways can be created at a depth of several microns in pristine diamond. The conductive regions were implanted through masks with smoothly sloping edges; hence the positions of the damage in the diamond could be tailored to reach the surface for electrical-conduction measurements at selected locations. MeV ion implantation across such edges forms a highly damaged layer at a modulated depth, thus allowing connection of the endpoint of the buried layer to the sample surface. The results obtained by this group have been summarized in an extensive recent publication.[39]

3.6 Computer simulations of damage in diamond

3.6.1 Computer simulations of solids: general considerations

Computer simulation of the structure of solids is a common way of understanding and predicting the modifications that solids subjected to different physical conditions undergo. The SRIM code discussed above is a computer simulation which follows the *global response* of solids as a result of ion implantation. It does *not* include information at the individual-atom level.

Most computer simulations of solids at the atomic level suffer from inherent problems related to computational limitations set by today's computational power and by uncertainty in the 'input parameters'. Computational capabilities limit the simulations to small samples. This limitation is commonly circumvented by applying periodic boundary conditions mimicking an infinitely large sample, a situation which does not always represent the actual physical situation, as it includes the repetition of irregularities in the 'mother' sample (i.e., defects deliberately introduced will be repeated indefinitely). The restricted number of computational cycles that is feasible for realistic computations imposes another limitation, namely that the computation can follow the evolution of solid structures for a rather limited number of steps, i.e., for a relatively short time. On the other hand, any desired external conditions, either physical or nonphysical, can be simulated – for example, exposing the sample to extremely high (perhaps even unrealistic) temperatures or pressures. However, as mentioned above, this can be done for only short times (of the order of a few tens of picoseconds at most).

Obviously, the computations require input parameters, such as potentials between the atoms in the sample, which are not always well known. Furthermore, several different computational approaches and hence different codes have been employed; some are less accurate but allow complex computations, while others, which address atomistic properties of the sample, are more demanding and are restricted to only a small number of atoms. The *ab initio* approach, which follows the interactions between individual atoms in the sample, is the one that simulates the most 'real' physical processes, and hence yields reliable information regarding atomic arrangements in solids following ion impact. It suffers, however, from the computational limitations mentioned above. Nevertheless, important information has been obtained from computer simulations of solids, involving, amongst other things, various kinds of carbon-related materials. Much work on these materials has been published by the Technion computational group, and can be found on the website http://comphy.technion.ac.il.

3.6.2 Computer simulations of diamond/graphite

Numerous publications simulating C-related structures have been published over the years, and hence it is impossible to review them all. In the following, we mention only some selected publications which are of particular relevance to the present topic of ion implantation in diamond, the resulting damage and its annealing.

A rough discrimination between sp^3- and sp^2-bonded carbon atoms in a sample can be obtained from computations which yield information about the structure of the sample by taking advantage of the large difference in the C–C bond length and bond angle between sp^2 (graphitic) and sp^3 (diamond) bonding. The sp^2 bond length in pure graphite is 0.146 nm, and the bond angle is 120°. This is to be compared with the sp^3 bond length in pure diamond, which is 0.154 nm, and the bond angle, which is 109.5°. Hence, based on just examining the bond length (or bond angle) distribution, as obtained by analyzing the radial distribution function (RDF) of a sample composed of a mixture of sp^2- and sp^3-bonded C atoms, the graphitic/diamond structure of the sample can be obtained and visualized (for pictures and movies, see the Technion computational group's website at http://comphy.technion.ac.il).

Computations applying both molecular dynamics approaches (using the Tersoff potential) and *ab initio* tight-binding approaches have been employed to study the formation of sp^2-bonded C in diamond due to diamond bond breakage, as a function of the momentum imparted by an impact to sp^3-bonded atoms in an ideal diamond sample.[10, 40, 41] The outcome of these studies has yielded, amongst other things, an estimate of the duration of the 'thermal spike', i.e., the time during which the atoms in the vicinity of the implanted atom are in motion (found to be of the order of 1 ps or less); the structure and extent of the volume of disrupted diamond caused by single-ion impacts; and the annealing of this volume.

Three major questions of direct relevance to the topic of ion-implantation-induced damage in diamond discussed here have been treated by computer simulations. These are:

- What is the displacement energy?
- What is the critical vacancy concentration above which heavily damaged diamond will not anneal back to diamond?
- What is the structure of the boundary region between well-annealed diamond and completely graphitized damaged diamond?

Computation of displacement energy (E_d)

A knowledge of the value of the minimum energy (the displacement energy E_d) required to dislodge a C atom from its perfect sp^3-bonded location in the pure diamond matrix is of fundamental importance to all issues related to the conversion of damaged diamond to graphite. The displacement energy is also, as mentioned above, a most important input parameter for SRIM simulations. Hence, whenever information on defect formation and concentrations in implanted diamond is extracted from SRIM, the results depend directly on the value of E_d fed into SRIM. It is thus most important, when quoting SRIM results, to mention the value of E_d used in the simulation; the use of different values of E_d may result in very different results for the damage, in particular for the density of point defects which marks the boundary between annealing diamond back to its pristine structure and it collapsing to graphite.

Questions regarding the energetics involved in the formation of vacancies and interstitials in diamond and the relaxation of the crystal lattice around irradiation-induced defects yield, amongst other things, the value of D_c. These questions have been addressed by Saada *et al.*[10] by performing molecular dynamics and classical Monte Carlo calculations at 0 K using the Tersoff potential. The outcome of these calculations showed that the stable defect around a dislodged carbon atom in diamond is the (100) split interstitial, confirming the results of other calculations.

By investigating the spatial extent of C atoms which have only three neighbors (coordination number 3), the average size of the 'graphitic islands' proposed by Kalish *et al.*[13] to be responsible for the measured electrical conductivity in ion-implantation-damaged diamond was determined.

In order to obtain E_d, C atoms located on lattice sites in a diamond sample were subjected to different momentum impulses, pointing in different directions in the crystal, and their resulting motion was followed in the computer. It was found that once the C atom was dislodged, in a random direction, from its lattice site with an energy that exceeded 52 eV it would not fall back into its original lattice site. Hence it was concluded that E_d was 52 eV. A slight variation of this value was observed for different directions of the momentum imparted to the C atom with respect to the various crystallographic directions of the diamond sample. The value of E_d found in that work agrees well with other published results;[11] it gives

an estimate of the minimum energy required for the formation of a nonrecombining vacancy–interstitial pair in diamond. This number is, amongst other things, an important parameter for the formation of NV centers by N or other damaging ion implantations of diamond. The computations also yielded information about the size of the disrupted region of the diamond lattice around the final resting site of the slowing-down C atom, which was of the order of a few nanometers. It should be noted that the simulation was carried out at 0 K on an 'infinitely large' diamond sample, as periodic boundary conditions were applied. The experimental values of E_d and, based on them, the extracted critical density of point defects (as obtained from SRIM) for the ion fluence leading to the critical density D_c for graphitization seem to depend on the depth in the diamond at which the event occurs. For damage caused by low-energy ions, which come to rest close to the surface, E_d seems to be somewhat smaller than that for high-energy ions, where the damage is buried below many diamond layers and pressure is exerted by those layers on the ion displacement site.

Simulations of critical defect density for diamond-to-graphite conversion

A topic of major importance for the understanding and exploitation of the effects of damage in diamond is the question of how ion-damaged diamond containing different densities of displaced C atoms behaves following different annealing procedures; will it turn graphitic or anneal back to diamond? This information is of great importance for annealing damaged diamond back to its pristine structure following impurity ion implantations, as required for doping purposes (see Section 3.3.3). It is also of major importance for the production of free-standing submicron-sized structures in diamond (membranes), and of electrically conducting regions by the formation of selected regions of heavy damage (which are graphitic, and hence electrically conductive and chemically etchable) by ion implantation (see Section 3.3.2).

The structural modifications that highly damaged regions in diamond undergo following thermal annealing have been studied by molecular dynamics simulations using the Tersoff potential.[41] A deeply buried damaged region was obtained by imparting high momenta to host C atoms (corresponding to a kinetic energy of 416 eV, i.e., $8E_d$) to lattice atoms aimed toward the same point in the crystal. This resulted in the partial 'amorphization' of a volume with a radius of about 14 nm. The sp^2 and sp^3 bonding configurations in the damaged sphere and in its vicinity were evaluated and visualized. The 'damaged' sample was subjected to virtual 'annealing' at temperatures up to 3000 K, for up to 25 ps. It was found that atoms in the heavily damaged core diffused upon annealing by several lattice sites and vacancy–interstitial recombination took place, forming sp^3 bonds, leading to the formation of a diamond-like region. Atoms in the periphery of this region tended to form threefold-coordinated C bonds preferentially oriented along the $\langle 111 \rangle$ directions, as shown in Fig. 3.8.

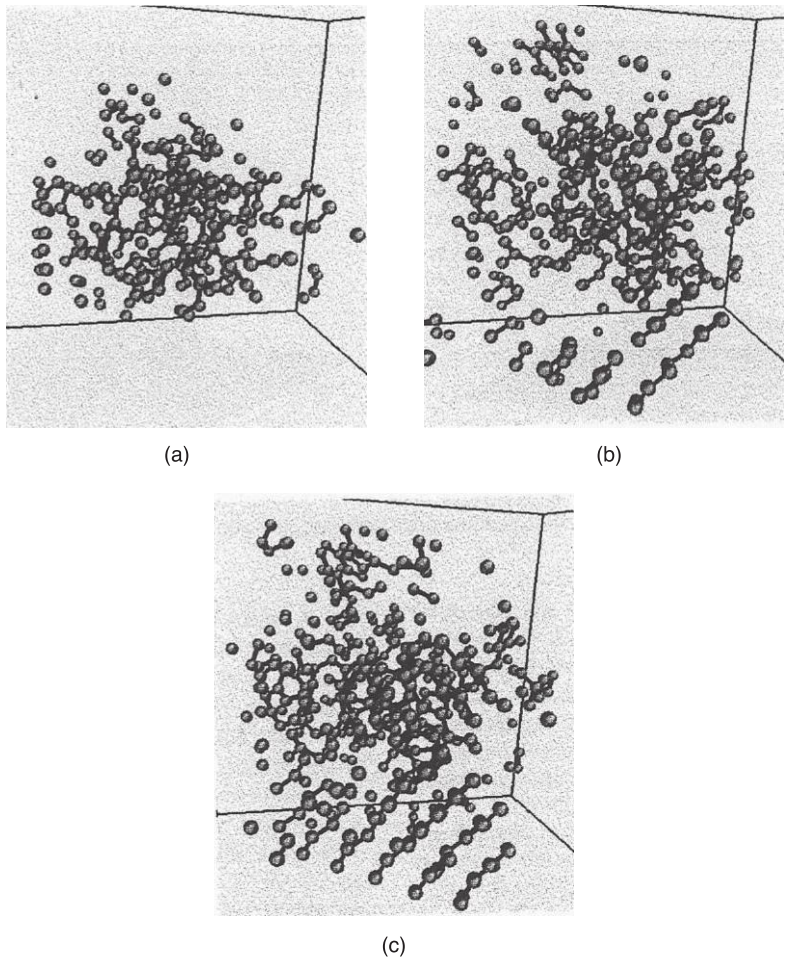

3.8 Results of computer simulations of the evolution of the structure of a heavily damaged region in diamond following annealing at 3000 K for different times: (a) the damaged region before annealing; (b) after annealing at 3000 K for 16.25 ps; (c) after annealing at 3000 K for 20 ps. Only threefold-coordinated C atoms and their nearest neighbors (if threefold) are displayed. Note the gradual formation of ordered graphitic planes.[40]

3.6.3 Simulation of the diamond–graphite interface

The fabrication of diamond membranes in which photonic crystals and other nanosized optical devices could be produced (discussed in Sections 3.3.2 and 3.5.2) is of great importance for some applications of qubits in diamond. One approach to fabricating such membranes begins with creating a heavily damaged buried layer (rich in broken bonds) in a diamond by ion implantation. Following

annealing, this layer converts to graphite, which can be chemically removed, leaving a free-standing diamond membrane. Unfortunately, the optical properties of the exposed diamond membrane surface following this process have been found not to be high enough for photonic devices.

In order to understand the bonding properties of the heavily damaged 'sacrificial' layer and of the less damaged diamond and to provide guidelines for the optimal implantation and annealing procedures to yield the sharpest graphite/diamond interface, molecular dynamics studies of the atomic structure of the etchable-graphite/diamond interface have recently been performed.[42] Several different implantation and annealing conditions were simulated using methods similar to those applied by Saada *et al.*[41] A buried layer in a perfect diamond crystal was 'damaged' in the computer to a density that exceeded D_c by repeated 'implantations' of C atoms aimed toward different positions but all delivering their damage in the same layer (i.e., at the same 'depth'). Different damage layers were obtained by employing different implantation temperatures. The samples thus formed were subjected to different simulated annealing procedures. The sharpness of the boundary layer between the heavily 'graphitized' layer and the regrown perfect diamond was studied. The results showed that cold implantation followed by high-temperature annealing (>1500 °C) led to the sharpest diamond–etchable-graphite interface. Figure 3.9 shows atomic images of several differently damaged and annealed samples. The sharpest diamond/etchable-graphite interface is depicted in Fig. 3.9(b) (cold implantation followed by a 2000 °C anneal). This finding should provide experimentalists with an implantation/annealing scheme that yields optimal optical properties of the lifted-off film as required for application of diamond membranes for optical (photonic crystal) purposes.

Simulations of NV complex formation

As mentioned above, the nitrogen–vacancy complex in diamond offers many attractive properties for serving as qubits in future quantum computers, and for many other applications. Much effort has recently been devoted to finding ways of efficiently forming this complex, preferably in well-defined positions as described above. The use of ion implantation both for the controlled introduction of N into diamond and for the formation of vacancies to combine with the N has recently been attempted. In some very recent work, the Technion group has performed computations in which the energetics and kinetics of the formation of the NV center have been studied (A. Silverman, J. Adler and R. Kalish, in preparation). The computations, using tight binding, concentrated on evaluating the energetically preferred sites of N residing in various locations in the diamond crystal, as well as the energetics of diamond with N in it together with vacancies located in different positions with respect to the N. When the sample was heated in the computer to experimentally available temperatures (up to 1200 °C), the motions of the vacancies and the N atom could be followed.

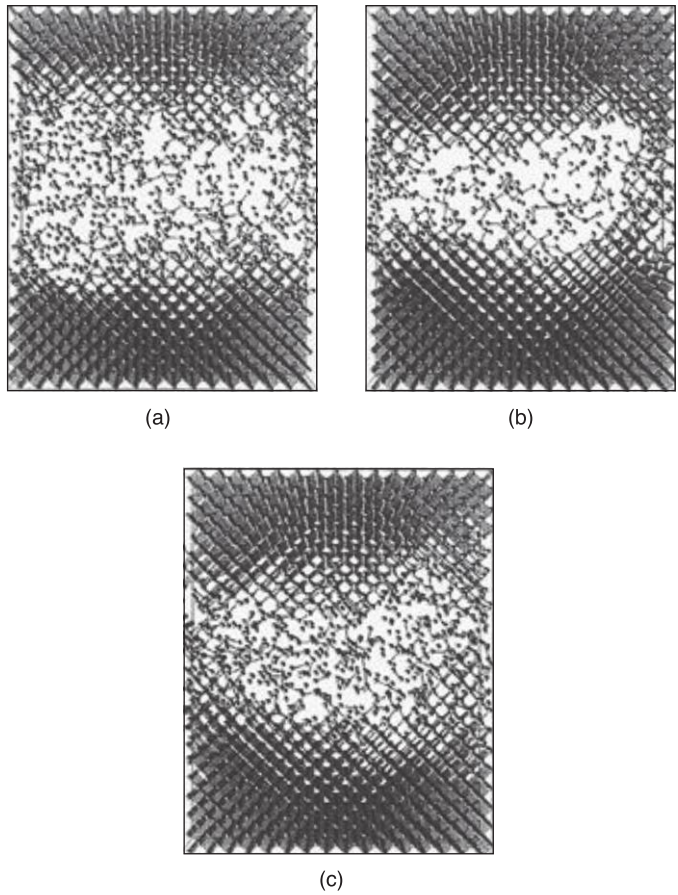

3.9 Results of computer simulations of a heavily damaged region in diamond (in the center, above D_c), following different implantation damage/annealing schemes: (a) sample as prepared (at 0 K); (b) sample prepared at 0 K and annealed at 2000 °C; (c) sample implanted at 2000 °C. Only fourfold-coordinated C atoms are displayed. The increased sharpness of the diamond/graphite interface should be noted. (The graphite appears blank because the bonds are not shown). Cold implantation followed by high-temperature (>2000 °C) annealing is predicted to yield the sharpest diamond membrane following 'liftoff'.[42]

The major findings of this study, providing guidelines to experimentalists on how to produce NV centers in diamond most efficiently, were:

- The preferred location for N in a diamond crystal is a substitutional site when the diamond is grown in the presence of N. When the N is introduced by ion implantation, i.e., is 'forced' into the lattice, the preferred site is a split interstitial.

- Once the N is residing on an interstitial site, no vacancy can be attracted to it to form an NV center at any reasonable temperature.
- When N occupies a split interstitial site, it can attract a vacancy and form an NV center only when two vacancies reside in second-neighbor sites. Under these conditions, NV centers form at temperatures as low as 600 K.

These findings are supported by the experimentally well-documented fact that orders of magnitude more vacancies need to be present in the vicinity of the N impurity to lead to the formation of an NV center.

3.7 Conclusion

The entire field of ion implantation of diamond, which has not been too active in the last decade (after the field of ion implantation doping had matured), has received a tremendous boost with the recent discovery that particular defect-related centers in diamond have luminescence properties that may find many applications. In this chapter, we have summarized the current status of the topic, emphasizing the physics related to the slowing down of ions in matter and the resulting creation of vacancies, as well as the nature of the damage inflicted on diamond by implantation and the applications of ion implantation of diamond.

Since the topic is very large, it was impossible to cover it fully, so we have presented here only the major points and given some references to older publications, and have concentrated on more recent results of relevance to the creation of nitrogen–vacancy defects in diamond, which have already found application in the realization of qubits. The fabrication of photonic structures in diamond to assist the propagation and manipulation of photons in diamond-based photonic crystals and other devices also relies on implantation. Here, the formation of graphitic sacrificial layers for the fabrication of thin membranes in which the required structures can be formed is based on implantation-induced damage.

It is important to mention here, once more, that the requirements for removing the damage accompanying the implantation process, which is essential for the purpose of elemental electronic doping, are in a sense orthogonal to the requirements for the exploitation of implantation-induced damage in diamond. The latter is needed for the creation of vacancy-related specific defects and for the formation of conductive regions in diamond in which the diamond sp^3 bonding is converted to the graphitic sp^3 bonding, with their extremely different chemical and physical properties.

It is clear that in light of the many existing luminescent centers in diamond, much work on their creation and on studying their suitability to serve as single qubits is still to come. The advantages that ion implantation offers for the controlled introduction of impurities and defects as described here are obvious; however, the various difficulties and pitfalls accompanying the implantation

process require much work on the sample preparation side, not to mention the study of the resulting luminescence and its practical implementation.

3.8 Acknowledgments

This work was partly supported by the GIF contract #1-1026-9.14/2009. The help of Drs C. Saguy and A. Bolker is appreciated.

3.9 References

1. Dresselhaus, S. and Kalish, R. *Ion Implantation in Diamond, Graphite, and Related Materials* (Springer, 1992).
2. Kalish, R. *Thin-Film Diamond I*, Semiconductors and Semimetals Series, pp. 145–179 (Elsevier Academic, 2003).
3. Kalish, R. The search for donors in diamond. *Diamond and Related Materials* **10**, 1749–1755, doi:10.1016/s0925-9635(01)00426-5 (2001).
4. Koizumi, S., Kamo, M., Sato, Y., Ozaki, H. and Inuzuka, T. Growth and characterization of phosphorous doped {111} homoepitaxial diamond thin films. *Applied Physics Letters* **71**, 1065–1067 (1997).
5. Aharonovich, I., Zhou, C., Stacey, A., Treussart, F., Roch, J.-F. and Prawer, S. Formation of color centers in nanodiamonds by plasma assisted diffusion of impurities from the growth substrate. *Applied Physics Letters* **93**, 243112–243113 (2008).
6. Teukam, Z., Chevallier, J., Saguy, C., Kalish, R., Ballutaud, D., *et al.* Shallow donors with high n-type electrical conductivity in homoepitaxial deuterated boron-doped diamond layers. *Nature Materials* **2**, 482–486 (2003).
7. Yom-Tov, N., Saguy, C., Bolker, A., Kalish, R. and Yaish, Y. E. Accurate carrier-type determination of nonhomogenously doped diamond. *Journal of Applied Physics* **108**, 043711–043715 (2010).
8. Ziegler, J. F., Ziegler, M. D. and Biersack, J. P. SRIM – The stopping and range of ions in matter (2010). *Nuclear Instruments and Methods in Physics Research B: Beam Interactions with Materials and Atoms* **268**, 1818–1823, doi:10.1016/j.nimb.2010.02.091 (2010).
9. Fairchild, B. A., Rubanov, S., Lau, D. W. M., Robinson, M., Suarez-Martinez, I., *et al.* Mechanism for the amorphisation of diamond. *Advanced Materials* **24**, 2024–2029, doi:10.1002/adma.201104511 (2012).
10. Saada, D., Adler, J. and Kalish, R. Transformation of diamond (sp^3) to graphite (sp^2) bonds by ion-impact. *International Journal of Modern Physics C* **09**, 61–69, doi:10.1142/S0129183198000066 (1998).
11. Wu, W. and Fahy, S. Molecular-dynamics study of single-atom radiation damage in diamond. *Physical Review B* **49**, 3030–3035 (1994).
12. Prawer, S. and Kalish, R. Ion-beam-induced transformation of diamond. *Physical Review B* **51**, 15711–15722 (1995).
13. Kalish, R., Bernstein, T., Shapiro, B. and Talmi, A. Percolation theory approach to the implantation induced diamond to amorphous-carbon transition. *Radiation Effects* **52**, 153–168 (1980).
14. Uzan-Saguy, C., Cytermann, C., Brener, R., Richter, V., Shaanan, M. and Kalish, R. Damage threshold for ion-beam induced graphitization of diamond. *Applied Physics Letters* **67**, 1194–1196 (1995).

15. Orwa, J. O., Nugent, K. W., Jamieson, D. N. and Prawer, S. Raman investigation of damage caused by deep ion implantation in diamond. *Physical Review B* **62**, 5461–5472 (2000).
16. Reznik, A., Richter, V. and Kalish, R. Kinetics of the conversion of broken diamond (sp^3) bonds to graphitic (sp^2) bonds. *Physical Review B* **56**, 7930–7934 (1997).
17. Prins, J. F. C^+-damaged diamond: electrical measurements after rapid thermal annealing to 500 °C. *Diamond and Related Materials* **10**, 463–468, doi:10.1016/s0925-9635(00)00538-0 (2001).
18. Prins, J. F. Activation of boron-dopant atoms in ion-implanted diamonds. *Physical Review B* **38**, 5576–5584 (1988).
19. Reznik, A., Uzan-Saguy, C. and Kalish, R. Effects of point defects on the electrical properties of doped diamond. *Diamond and Related Materials* **9**, 1051–1056, doi:10.1016/s0925-9635(00)00225-9 (2000).
20. Prawer, S., Uzan-Saguy, C., Braunstein, G. and Kalish, R. Can n-type doping of diamond be achieved by Li or Na ion implantation? *Applied Physics Letters* **63**, 2502–2504 (1993).
21. Kalish, R., Uzan-Saguy, C., Philosoph, B., Richter, V. and Prawer, S. Loss of electrical conductivity in boron-doped diamond due to ion-induced damage. *Applied Physics Letters* **70**, 999–1001 (1997).
22. Prins, J. F. Fermi–Dirac statistics and the nature of the compensating donors in boron-doped diamond layers. *Physical Review B* **39**, 3764–3770 (1989).
23. Prins, J. F. Ion-implanted n-type diamond: electrical evidence. *Diamond and Related Materials* **4**, 580–585, doi:10.1016/0925-9635(94)05261-1 (1995).
24. Mainwood, A. Nitrogen and nitrogen–vacancy complexes and their formation in diamond. *Physical Review B* **49**, 7934–7940 (1994).
25. Rabeau, J. R., Reichart, P., Tamanyan, G., Jamieson, D. N., Prawer, S., *et al.* Implantation of labelled single nitrogen vacancy centers in diamond using ^{15}N. *Applied Physics Letters* **88**, 023113 (2006).
26. Pezzagna, S., Naydenov, B., Jelezko, F., Wrachtrup, J. and Meijer, J. Creation efficiency of nitrogen–vacancy centres in diamond. *New Journal of Physics* **12**, 065017 (2010).
27. Meijer, J., Pezzagna, S., Vogel, T., Burchard, B., Bukow, H. H., *et al.* Towards the implanting of ions and positioning of nanoparticles with nm spatial resolution. *Applied Physics A* **91**, 567–571, doi:10.1007/s00339-008-4515-1 (2008).
28. Naydenov, B., Richter, V., Beck, J., Steiner, M., Neumann, P., *et al.* Enhanced generation of single optically active spins in diamond by ion implantation. *Applied Physics Letters* **96**, 163108 (2010).
29. Schwartz, J., Michaelides, P., Weis, C. D. and Schenkel, T. In situ optimization of co-implantation and substrate temperature conditions for nitrogen–vacancy center formation in single-crystal diamonds. *New Journal of Physics* **13**, 035022 (2011).
30. Naydenov, B., Reinhard, F., Lammle, A., Richter, V., Kalish, R., *et al.* Increasing the coherence time of single electron spins in diamond by high temperature annealing. *Applied Physics Letters* **97**, 242511 (2010).
31. Neu, E., Steinmetz, D., Riedrich-Möller, J., Gsell, S., Fischer, M., *et al.* Single photon emission from silicon–vacancy colour centres in chemical vapour deposition nano-diamonds on iridium. *New Journal of Physics* **13**, 025012 (2011).
32. Rabeau, J. R., Chin, Y. L., Prawer, S., Jelezko, F., Gaebel, T. and Wrachtrup, J. Fabrication of single nickel–nitrogen defects in diamond by chemical vapor deposition. *Applied Physics Letters* **86**, 131926 (2005).

33. Aharonovich, I., Castelletto, S., Johnson, B. C., McCallum, J. C., Simpson, D. A., *et al.* Chromium single-photon emitters in diamond fabricated by ion implantation. *Physical Review B* **81**, 121201 (2010).
34. Bayn, I., Meyler, B., Lahav, A., Salzman, J., Kalish, R., *et al.* Processing of photonic crystal nanocavity for quantum information in diamond. *Diamond and Related Materials* **20**, 937–943, doi:10.1016/j.diamond.2011.05.002 (2011).
35. Drumm, V. S., Meyler, B., Lahav, A., Salzman, J., Kalish, R., *et al.* Surface damage on diamond membranes fabricated by ion implantation and lift-off. *Applied Physics Letters* **98**, 231904 (2011).
36. Fairchild, B. A., Olivero, P., Rubanov, S., Greentree, A. D., Waldermann, F., *et al.* Fabrication of ultrathin single-crystal diamond membranes. *Advanced Materials* **20**, 4793–4798, doi:10.1002/adma.200801460 (2008).
37. Bayn, B. M. I., Salzma, J. and Kalish, R. Triangular nanobeam photonic cavities in single-crystal diamond. *New Journal of Physics* **13**, 025018 (2011).
38. Bayn, A. B. I., Cytermann, C., Meyler, B., Richter, V., Salzman, J. and Kalish, R. Diamond processing by focused ion beam – surface damage and recovery. *Applied Physics Letters* **99**, 183109 (2011).
39. Picollo, D. G. M. F., Olivero, P., Fairchild, B. A., Rubanov, S., Prawer, S. and Vittone, E. Fabrication and electrical characterization of three-dimensional graphitic microchannels in single crystal diamond. *New Journal of Physics* **14**, 053011 (2012).
40. Marks, N. A., Cooper, N. C., McKenzie, D. R., McCulloch, D. G., Bath, P. and Russo, S. P. Comparison of density-functional, tight-binding, and empirical methods for the simulation of amorphous carbon. *Physical Review B* **65**, doi:10.1103/PhysRevB.65.075411 (2002).
41. Saada, D., Adler, J. and Kalish, R. Computer simulation of damage in diamond due to ion impact and its annealing. *Physical Review B* **59**, 6650–6660 (1999).
42. Silverman, A., Adler, J. and Kalish, R. Diamond membrane surface after ion-implantation-induced graphitization for graphite removal: Molecular dynamics simulation. *Physical Review B* **83**, 224206 (2011).

4

Characterisation of single defects in diamond in the development of quantum devices

J. M. SMITH, University of Oxford, UK

DOI: 10.1533/9780857096685.1.68

Abstract: This chapter describes the characterisation of single defects in diamond using fluorescence-based techniques and how it can be used to determine the properties both of the defects themselves and of their local environment. Emphasis is placed on methodologies and aspects of the science that can be applied to a range of fluorescent defects, and which illustrate the essential role of characterisation at the single-defect level in the development of quantum devices.

Key words: single colour centres, microscopy, photoluminescence, PLE, photon statistics, photon antibunching, optically detected magnetic resonance, inhomogeneous broadening.

4.1 Introduction

Characterisation at the single-defect level in diamond is currently carried out exclusively using fluorescence measurements of colour centres and, more specifically, photoluminescence measurements: that is, optical excitation of a colour centre into an electronic excited state via an electric-dipole allowed transition, and detection of the subsequently emitted photons as the system relaxes back to its electronic ground state. This seemingly simple process has a number of variants which give access to a large amount of information about the electronic states of the system and the transitions that take place between them. We can use it to help identify the physical structure of colour centres and understand their internal workings, and to probe the local strain, electronic and magnetic environments. In the most recent experiments it has been possible to obtain information about single 'dark' defects via their interactions with nearby colour centres, thereby extending single-defect studies to systems which cannot be measured by direct means. Such capabilities not only are useful from a characterisation perspective, but also feed in to sophisticated schemes for quantum processing which require colour centres for optical initialisation and readout of quantum states, and in which those centres communicate with other defects in the lattice for information storage and manipulation. Such schemes are discussed in more detail elsewhere in this book.

© 2014 Elsevier Ltd

Study of defects at the single-dopant level is a fairly recent development. The first such experiments were on nitrogen–vacancy (NV) single defects in diamond (Kurtsiefer *et al.*, 2000), demonstrating their attractive qualities as robust quantum light sources. A few years later, Jelezko *et al.* (2004) found that NV centres in the negatively charged state showed attractive spin properties, the study of which is documented in detail in other chapters of this book. Since then, a large amount of work has been carried out on single NV^- defects, but only a handful of other defects have been studied in this way. Experiments have been reported on single silicon–vacancy centres (Wang *et al.*, 2006; Neu *et al.*, 2011), nickel complexes (Gaebel *et al.*, 2004; Castelletto *et al.*, 2012), defects attributed to chromium impurities (Aharonovich *et al.*, 2010) and a few others as yet unidentified (Aharonovich *et al.*, 2009; Simpson *et al.*, 2009; Smith *et al.*, 2011). These comprise but a small fraction of the fluorescence lines observed in diamond (Zaitsev, 2001), so it is likely that the reports to date constitute only the tip of the iceberg in terms of what is possible. In time, such studies may extend beyond fluorescence measurements, but for now at least it is this technique that monopolises single-defect studies, and as such will be the sole focus of this chapter.

The chapter is intended to provide an overview of the basics of single-defect fluorescence, covering both experimental techniques and some elementary theoretical considerations. The chapter is laid out as follows. Section 4.2 contains an overview of the experimental apparatus and sample requirements for the study of single-defect fluorescence. As well as descriptions of the basic techniques, it provides tips on sample preparation, effective light collection strategies, low-temperature studies and super-resolution microscopy. Section 4.3 then focuses on single-defect fluorescence spectroscopy as a characterisation tool, and the information that it can reveal about defects and their environment. Section 4.4 turns our attention to time-resolved spectroscopy using photon counting, in particular the measurement and analysis of photon correlation statistics to provide unambiguous identification of fluorescence from single defects and to reveal information about electronic transition rates and dephasing effects. Finally, in Section 4.5, we introduce optically detected spin resonance experiments, and the use of them to study the local spin environment and establish the functionality of single colour centres as solid-state spin qubits.

Throughout the chapter, I have tried to maintain focus on issues particular to the study of *single* defects. As a result, many experimental details are left out on the basis that they apply equally well to measurements of large ensembles of defects. In addition, to keep the discussion general and in the interests of space, the descriptions provided of the physics of the defects themselves are also very minimalist. For more detailed and comprehensive accounts of the physics of the defects, which of course are often necessary to appreciate the full beauty of the experiments, the reader is encouraged to explore some of the references to the increasingly wide body of work in the published literature.

4.2 Experimental methods for fluorescence microscopy of single colour centres in diamond

4.2.1 Basic equipment

The methodology for fluorescence microscopy of single defects in diamond is similar to that widely used for studies of the fluorescence of single atoms, molecules or semiconductor quantum dots, namely a combination of laser excitation, high-sensitivity photodetection and high-performance optical microscopy. Whilst high-end fluorescence imaging systems capable of single-defect fluorescence studies are available commercially, the flexibility afforded by a custom-built system is often a great advantage. Here I present some of the basic elements.

The choice of laser to be used for optical excitation depends on the defect being studied. For general-purpose photoluminescence experiments, the laser wavelength must be within the absorption band of the defect, corresponding to excitation from the electronic and vibrational ground state to both electronic and vibrational excited states (Fig. 4.1). The absorption band typically spans a range from the resonant electronic-transition energy to about 0.5 eV higher in energy, depending on the vibronic nature of the defect. For example, the absorption band of the NV^- defect for its strongest fluorescent transition at 1.945 eV (637 nm) extends up to an energy of about 2.6 eV (480 nm). In general, if the fluorescence spectrum of a defect is known, a good indication of the absorption band can often be obtained by 'reflecting' the phonon sideband of the emission in the zero-phonon line (see Fig. 4.1(a)). This is a direct consequence of the Franck–Condon principle, which predicts similar phonon coupling for both absorption and emission provided the vibrational potential is similar in the ground and excited states of the electronic system. The laser power required depends very much on the experiment to be carried out and the excitation spot size of the microscope. However, an excitation power of a few milliwatts at the sample should be enough for most purposes.

Since the fluorescence signal intensity from single defects is very low, a single-photon detector is a necessary component of the characterisation apparatus. Indeed, the ready availability of silicon avalanche photodiodes with a single-photon detection efficiency of 70% or higher combined with dark count rates of less than $100\,s^{-1}$ has been a significant factor in the widespread study of single colour centres in the past decade. New single-photon detectors such as those made from superconducting wires offer reasonable efficiencies at longer wavelengths, and may permit the study of colour centres with emission wavelengths beyond 1 μm. As well as high detection efficiency and low noise, the timing resolution of a single-photon detector is an important consideration in many characterisation techniques – this will be discussed in more detail in Section 4.4.

To observe fluorescence from single defects with good signal-to-background ratios, confocal microscopy is generally essential. The confocal microscope, in

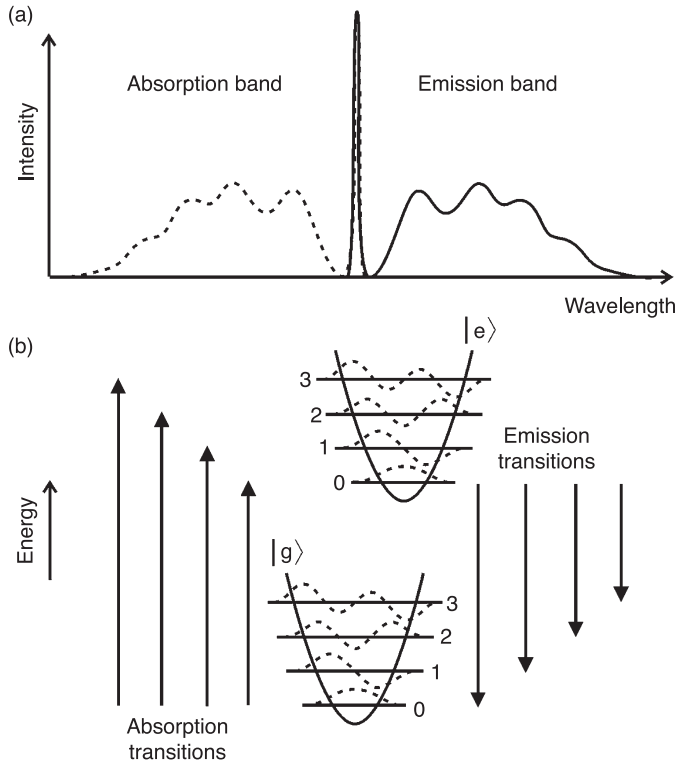

4.1 Photoluminescence of vibronic defects. (a) Schematic illustration of an emission spectrum (solid line) and an absorption spectrum (dashed line). (b) Optical transitions between the electronic ground state |g⟩ and excited state |e⟩, with vibrational sublevels numbered 0–3.

which both the laser excitation and the detected fluorescence are selective of a small focal spot on (or in) the sample, serves to minimise contributions to the detected signal that originate from outside of the intended focal plane. In this way, light reflected from the diamond surface and Raman scattering from the surrounding bulk material do not overwhelm the fluorescence from the colour centre itself. The use of a high-numerical-aperture objective lens provides three advantages: high spatial resolution for identifying single defects; optimal focusing of the excitation laser beam for maximum excitation intensity per milliwatt of laser power (this is important for many experiments, in which extraneous excitation of the surrounding material should be minimised); and a large solid angle for the efficient collection of fluorescence. Light collection efficiency is a major issue in single-defect fluorescence studies, and is the subject of Section 4.2.3.

To achieve confocal operation, the signal is spatially filtered at an image plane using an aperture that is well matched in size to the image of the focused excitation

spot on the sample. The aperture can be formed either using a free-space element or by coupling light into an optical fibre of known mode diameter. This aperture requires careful spatial alignment so that the fluorescence generated at the excitation focal spot of the sample is transmitted efficiently to the detector.

Finally, a good set of optical filters is required so that the desired fluorescence can reach the detector unimpeded, but unwanted scattered laser light, autofluorescence and Raman scattering from the sample and apparatus are blocked. Typically this involves a minimum of three filters: a laser clean-up filter in the excitation arm of the confocal microscope, a dichroic beam splitter to reflect the excitation light towards the sample but transmit the counter-propagating fluorescence, and a high-extinction (>OD4) notch filter in the collection arm to block any remaining laser light. A further bandpass filter matched to the fluorescence signal, situated in the collection arm, can often be useful to minimise any other background signals and 'pick out' the desired fluorescence.

4.2.2 Sample requirements

The first experiments on single colour centres were carried out on NV defects in naturally occurring type IIa diamonds with a nitrogen content in the 1 ppm range. Such bulk crystals allow individual NV centres to be observed, typically after irradiating with a high-energy electron beam to generate vacancies and then annealing at greater than 800 °C to mobilise the vacancies and form the stable NV complexes. The advent of ultrahigh-purity synthetic material grown by plasma-assisted chemical vapour deposition (CVD) has enabled a new degree of control to be exercised over the distribution and properties of NV centres, and of defects in general. In particular, material can now be produced with such low nitrogen densities (<1 ppb) that single NV centres are sparsely distributed in the as-grown material, providing opportunities for implantation of nitrogen by ion bombardment so that single defects can be positioned at selected locations in the lattice. More generally, the availability of ultrapure material provides a 'blank slate' for defect engineering, by implanting exotic ions to form defects not found in natural material.

Observation of fluorescence from single defects requires low background signals, and so the removal or photobleaching of organic fluorophores on the diamond surface is highly desirable. Aggressive cleaning with a hot mixture of nitric, sulphuric, and hydrochloric or perchloric acid is a common route, although great care should be taken in carrying out these 'acid boils' as they present substantial safety risks. Such chemical cleaning is often combined with a photobleaching stage before fluorescence imaging, in which the sample area of interest is irradiated with the highest laser power available for as long as possible to bleach any remaining surface contaminants. Since the colour centres themselves are stable emitters which do not (in general) photobleach, the presence of surface contamination can be inferred from transients in the fluorescence signal.

Nanodiamond provides an alternative to single-crystal material that can be attractive for single-defect studies. Since individual diamond nanocrystals can be isolated relatively easily for study, they offer a means to characterise single defects without such stringent requirements on sample purity. Moreover, fluorescence characterisation of single colour centres in nanodiamond is greatly assisted by the fact that the emitted photons are not trapped in the diamond material (see Section 4.2.3), leading to substantially higher photon counts being recorded by the detector. The drawbacks of nanodiamond are that it tends to incorporate substantial lattice strain, and that the surfaces provide a source of noise in many of the most sensitive measurements. In particular, the electronic and spin coherence of defects in nanodiamond is likely to be too short for use in quantum-information-processing applications. Nanodiamond is, however, highly attractive for applications such as single-photon generation and nanomagnetometry, where electronic coherence is less important and the nanosized particles can be of direct benefit by allowing close proximity of the defect to external objects.

Nanodiamond is produced by several different methods, including CVD and explosive detonation, and is commercially available from a number of sources. For single-defect fluorescence studies, it is usually necessary first to clean the nanodiamond thoroughly to de-aggregate the crystals and to reduce the fluorescence from graphitic material surrounding the diamond crystals. The methods employed include oxygen plasma or air annealing to etch away graphitic material – this method can also be used to reduce the size of the nanodiamond itself where necessary (Gaebel *et al.*, 2012). Hydrogen annealing of nanodiamond powder can be used to allow the formation of stable aqueous solutions with the aid of a high-powered ultrasound bath (Williams *et al.*, 2010).

4.2.3 Light collection issues and strategies

The brightest colour centres recorded to date provide a maximum of a few million photons per second at the detector (Aharonovich *et al.*, 2009), so it is important that as many of the emitted photons as possible are collected and directed to the detector. In this section, we consider issues of light collection based on the assumption that the emission is approximately isotropic. This is true in most general microscopy applications where the colour centre is located in bulk diamond, and in nanodiamond with dimensions much smaller than the emission wavelength. More advanced strategies for efficient light collection by modifying the local density of optical states using waveguides and cavities are discussed in later chapters.

Our starting point for evaluating a fluorescence collection efficiency is that the fraction of photons emitted into a solid angle Ω is given by $\Omega/4\pi$. In terms of the maximum angle to the optical axis at which emitted photons will be collected, labelled θ, the fraction F is given by

$$F = \frac{1}{2}(1 - \cos\theta) \qquad [4.1]$$

If the photons are to be collected into a lens with numerical aperture *NA*, the maximum collection angle is determined by sin $\theta = NA/n$, where n is the refractive index of the medium surrounding the emitter, so that

$$F = \frac{1}{2}\left(1 - \cos\left(\sin^{-1}\frac{NA}{n}\right)\right) \qquad [4.2]$$

This function, with $n = 1$ and with $n = 2.4$, is plotted as solid and dashed lines, respectively, in Fig. 4.2. The case $n = 1$ applies to microscopy of colour centres in nanodiamond where the refractive index surrounding the sample is that of air, while $n = 2.4$ applies to microscopy of colour centres in bulk diamond beneath a planar surface. From the graph, it is clear that a high-*NA* objective lens is desirable, if not essential, for maximising the optical signal. This is particularly important for observing colour centres in bulk diamond, where refraction at the diamond surface substantially reduces the solid angle over which fluorescence photons can be emitted if they are to couple into the objective lens. In this case numerical apertures greater than 1 are highly desirable, thereby bringing in the use of an oil immersion or solid immersion lens.

This requirement for high-*NA* optics is probably the single most important consideration in designing an optical microscope for single-colour-centre fluorescence measurements. However, high-*NA* objective lenses tend to have short working distances, and clearly the use of oil immersion lenses places substantial constraints on the apparatus design.

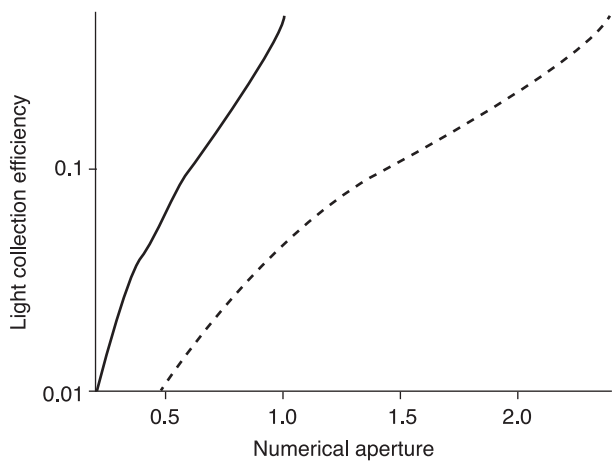

4.2 Fluorescence collection efficiency as a function of numerical aperture of the collection lens for a defect surrounded by air (solid line) and surrounded by diamond (dashed line). The curves are plots of Eq. 4.2 with $n = 1$ and $n = 2.4$, respectively.

A related consideration in situations where colour centres are located deep beneath the surface in bulk diamond is that of optical aberrations. Objective lenses are typically designed to focus light at a fixed focal length through a homogeneous medium (air or immersion oil), or in some cases through a glass cover slip or window with $n = 1.5$, but when focusing into diamond through a planar interface, substantial spherical aberrations occur. For an uncorrected lens, the point spread function (PSF) of the microscope is effectively stretched along the optical axis to a length given by

$$\Delta d = d_{\min}\left(1 - \frac{n_1}{n_2}\sqrt{\frac{n_2^2 - NA^2}{n_1^2 - NA^2}}\right) \qquad [4.3]$$

The term in parentheses is plotted in Fig. 4.3 for the cases where $n_1 = 1$ (air objective) and 1.5 (oil immersion objective). For example, using an uncorrected $NA = 0.8$ air objective to observe a colour centre at a depth of 10 μm will result in a PSF of approximately 6 μm, some five times larger than the depth of field in an aberration-free system. This elongation of the PSF results in a substantial further reduction in the emission collection efficiency of light beyond that shown in Fig. 4.3. The use of air objectives which provide aberration-corrected focusing through glass cover slips or cryostat windows up to 1.5 mm thick can provide some improvement, but it is important to note that the aberration correction required depends on the depth of the colour centre in the diamond sample. Custom aberration correction systems can be built that approach the theoretical optimum, and adaptive optical techniques can be used to offer flexibility and active optimisation (Simmonds *et al.*, 2011), but these are non-trivial to implement and are not (at the time of writing) available on commercial microscopes.

4.2.4 Scanning confocal imaging

To locate single colour centres in a sample, it is necessary to scan the focal spot of the confocal microscope and construct an image. Two different scanning methods are employed – scanning the sample or scanning the optical beam, shown in Fig. 4.4(a) and (b), respectively. In sample scanning, the optics can all be set up on-axis for the optical elements, thereby achieving optimal performance and aberration-free imaging. In addition, the area that can be imaged is limited only by the range of the scanner on which the sample is mounted. In beam scanning, the sample is fixed relative to the objective, and the image is formed by scanning a mirror which steers both the excitation beam and the counter-propagating fluorescence. The angle of the mirror is mapped directly onto the angle of transmission through the objective lens by two telecentric lenses in a 4-*f* configuration. This optical set-up keeps aberrations to a minimum (it is advisable to use achromatic lenses in the telecentric positions as their chromatic aberrations

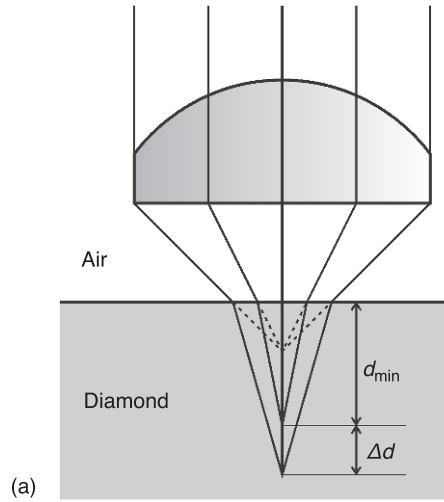

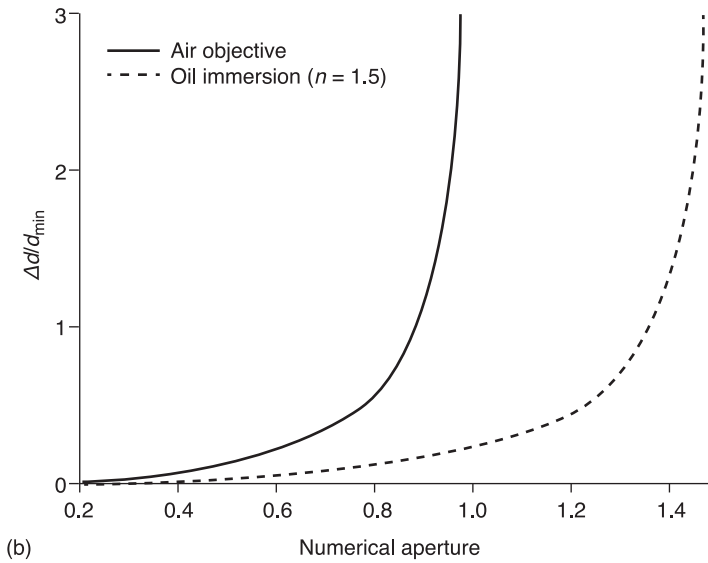

4.3 Spherical aberrations resulting from focusing through a planar diamond surface. (a) Schematic ray diagram illustrating how the large-angle rays focus deeper into the diamond sample than do the near-axial rays as a result of refraction at the surface. (b) Plot of the elongation Δd of the point spread function as a multiple of the depth of focus of the near-axial rays d_{min}, as a function of the numerical aperture of the lens. Plots are shown for both an air objective and an oil immersion lens with an oil of refractive index 1.5.

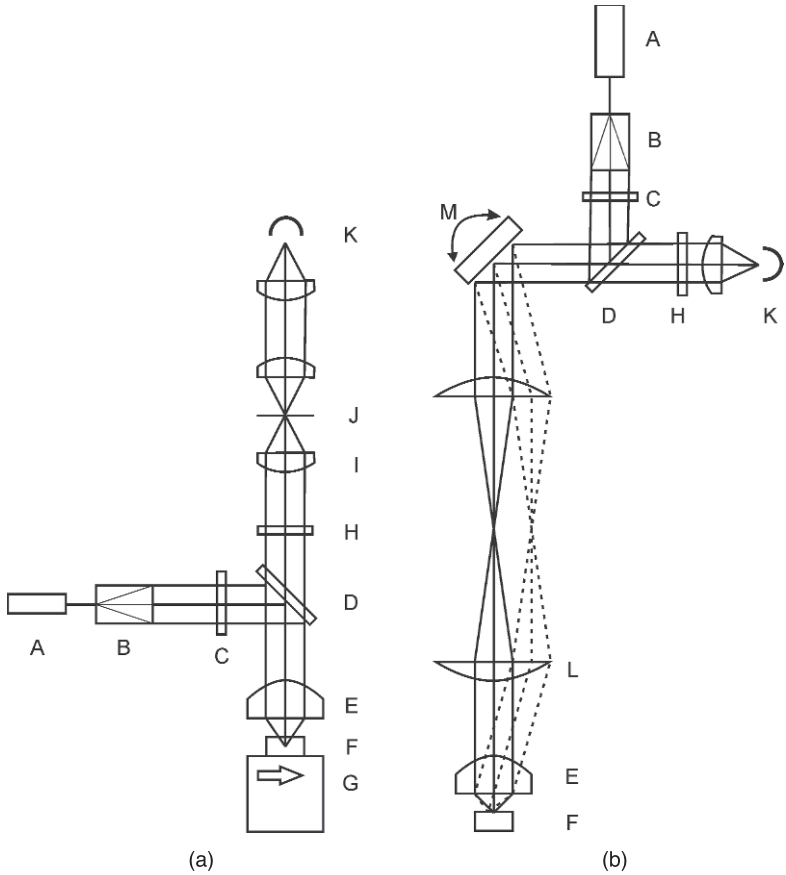

4.4 Schematic optical set-up for scanning confocal microscopy with (a) sample scanning and (b) beam scanning. The labelled components are A, excitation laser; B, beam expander; C, laser clean-up filter; D, dichroic beam splitter; E, high-*NA* objective lens; F, diamond sample; G, *XY* or *XYZ* scanning positioner; H, laser-blocking notch filter; I, focusing lens; J, pinhole; K, single-photon-counting detector; L, telecentric lens; M, beam-steering mirror.

are additive) and is very robust to small misalignments. The area of sample that can be imaged is then determined by the maximum angle of incidence achievable – limited either by the scanning mirror or by the diameter of the telecentric lenses – and by the focal length of the objective lens. For example, a 25 mm diameter, $f = 250$ mm telecentric lens subtends an angle of 50 mrad on an objective, so with an objective of focal length 3 mm (~60×) it will provide a circular field of view of radius $0.05 \times 3000 = 150\,\mu$m.

4.2.5 Low-temperature systems

If the sample is to be cooled to cryogenic temperatures, then the ability to place it on a scanner is severely impeded. At the time of writing, low-temperature scanners have a range limited to a few tens of micrometres, so it is more common for these experiments to use beam scanning. Maximising light collection in cryogenic systems poses additional challenges. Oil immersion lenses cannot be used, and either the objective lens must be capable of imaging through a cryostat window, therefore requiring a working distance of greater than 1 mm and adjustable aberration correction for transmission through at least 0.5 mm of glass, or it must be cooled along with the sample. Cooling the objective lens can be an attractive approach in that it removes the need for a window and so allows very high-*NA* air objectives to be used. This does, however, raise problems in instruments where an achromatic objective is required, as the epoxy used in doublets and compound lenses tends to fracture easily upon cooling. A further advantage of 'cold lens' systems is that they can offer far superior mechanical stability, by virtue of the fact that the mechanical distance between the sample and the objective lens is much shorter. Microscopes have been built in which alignment with a single colour centre can be maintained for days at a time without active control (Grazioso *et al.*, 2013). Cold-lens microscopes have historically required the use of cheap, 'disposable' objectives, however, which do not tend to offer high-efficiency light collection. For long-time-duration experiments with the objective lens outside the cryostat, high-quality optics can be used, but it is generally necessary to employ an active feedback system to maintain alignment.

Figure 4.5(a) shows a cold-lens scanning confocal microscope built in Oxford, which uses the scanning beam configuration of Fig. 4.4(b). The sample stage, objective and telecentric lenses are all mounted on a 30 mm cage system and suspended in a thin-walled stainless steel vacuum tube. The tube is evacuated and refilled with ~50 mbar of dry helium gas (to act as a heat exchange medium) before being inserted into the liquid-helium-bath dewar, and the remaining optics are then mounted on the top of the tube. An example image showing about 100 NV centres in a $60 \times 60\,\mu$m region of single-crystal diamond held at a temperature of 4.2 K is displayed in Fig. 4.5(b).

4.2.6 Super-resolution imaging

In some cases it is desirable to image single defects with a spatial resolution beyond that achievable with far-field diffraction-limited optics, for example if two or more colour centres nearby in the lattice need to be distinguished. In recent years techniques for super-resolution imaging have been developed that provide an impressive solution to this problem. The technique most widely applied to diamond is that of stimulated emission depletion (STED) microscopy, in which a pulsed excitation of the system is followed immediately by a strong second pulse

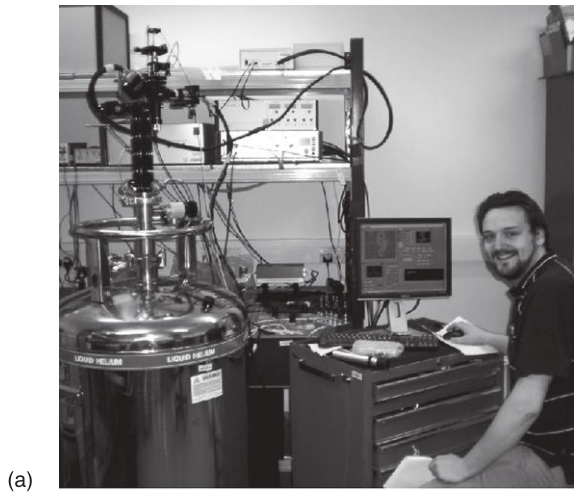

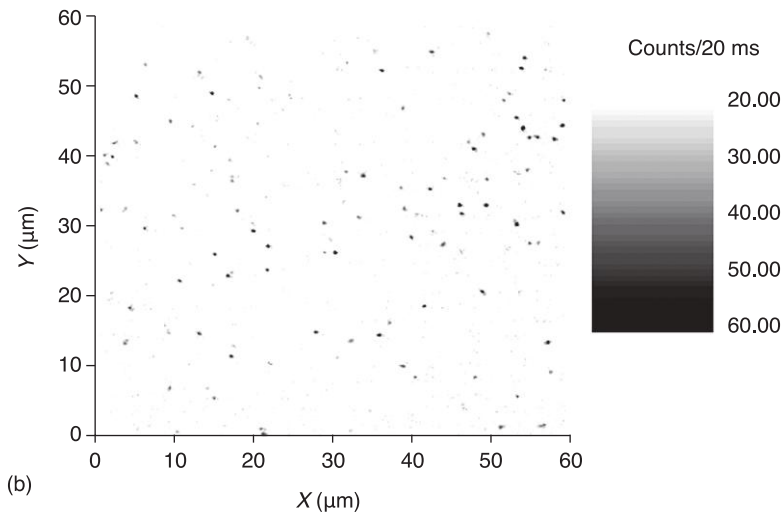

4.5 Scanning confocal microscopy of single colour centres. (a) The cold-lens scanning confocal microscope built in Oxford, being operated by Dr Brian Patton. (b) A fluorescence image of ~100 NV centres in single-crystal diamond at a temperature of 4.2 K.

of light at a wavelength redshifted from the electronic resonance and corresponding to a phonon sideband. This is known as the STED pulse, whose role is to deplete the excited state of previously photoexcited colour centres by stimulated emission, without further optical absorption. The STED pulse is constructed in such a way that the intensity distribution contains a well-defined zero, usually at the centre,

thereby forming a 'doughnut' shape (Fig. 4.6). Efficient depletion of the optically excited state occurs for intensities above a certain threshold, shown as a dotted line in the figure. Fluorescence is then recorded from the region that remains excited after the depletion pulse, indicated by the narrow vertical band. Since very robust zeros of field intensity can be generated by optical phase plates, the resolution of STED is ultimately dependent on the intensity of the depletion pulse, a higher intensity resulting in a smaller sub-threshold region.

Colour centres in diamond are ideal for STED microscopy since they are extremely robust to the intense STED pulse (they do not photobleach), and the technique has been applied to NV centres with impressive results. Rittweger *et al.* (2009) demonstrated a spatial resolution of around 7 nm using an oil immersion lens focusing into a planar single-crystal sample. Most recently, Wildanger *et al.* (2012) showed that a spatial resolution of 2.4 nm in the image plane could be achieved when imaging NV centres under a solid immersion lens. In this work, the localisation of the colour centre in the lattice was achieved to better than 1 Å, equivalent to identifying the precise lattice site at which the defect resides (at least in the image plane). If only in-plane resolution is required, STED microscopy can be implemented using a standard scanning confocal microscope as described above. However, the zero of the STED pulse in the doughnut-shaped beam is

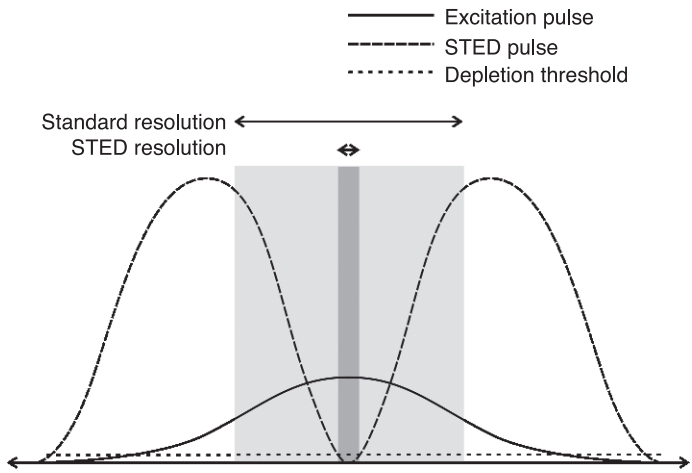

4.6 Schematic illustration of the principle of spatial-resolution enhancement using stimulated emission depletion microscopy. The width of the initial excitation pulse distribution (solid line) is limited by far-field diffraction, but when a depletion pulse with an intensity distribution indicated by the dashed line is applied, only defects located in a small central region below the depletion threshold (dotted line) will subsequently remain excited and their fluorescence be detected.

continuous along the optical axis, so no improvement in depth resolution is achieved compared with standard fluorescence microscopy. It is, with further effort, possible to achieve high resolution in all three dimensions using additional STED beams with orthogonal propagation axes (Han *et al.*, 2009).

With a spatial resolution much better than 10 nm, one can imagine interrogating arrays of colour centres that are sufficiently dense to allow their spins to be coupled and conditional gating to be performed. Besides quantum information applications, STED and other super-resolution techniques are becoming popular for use in biomedical imaging, and it appears likely that nanodiamond fluorescent probes may well play a role as inert biolabels for live cell imaging (Fu *et al.*, 2007).

4.3 Optical spectroscopy of single defects

Photoluminescence (PL) spectroscopy of single defects is an important tool for characterising the electronic states and transition rates that determine the functionality of those defects for use in quantum information processing. When individual colour centres are measured, the signal inhomogeneity resulting from different orientations or local environments is removed, thereby providing significantly more detail than can be observed using ensemble measurements.

The principal sources of inhomogeneity in diamond colour centres are the local lattice strain and the surrounding defect environment. Strain affects the electronic energy structure of colour centres and their spin properties through the spin–orbit interaction. Electronic excited states tend to be affected to a greater degree than are electronic ground states, as being closer to the band edge their orbitals are spatially larger, and so they are more perturbed by the displacement of atomic nuclei from their unstrained positions. The local defect environment can affect the optical properties through strain, and by providing sources and traps for electrons it can influence the charge state of the defect in question and can generate substantial local electric fields, which perturb its electronic structure and properties.

Inhomogeneous broadening is particularly noticeable when measurements are carried out at low temperature and homogeneous line widths are narrow, or where the diamond in question contains a high degree of strain such as in nanocrystalline material. It also affects some colour centres more than others, since the degree to which a local field perturbs the transition energy depends on the polarisability of the electron orbital, which is related to the transition dipole moment. A correlation therefore exists between the emission strength of a colour centre and the degree of inhomogeneity in its PL emission. For example, the bright nickel- and chromium-related colour centres with emission between 740 and 850 nm display inhomogeneity of the order of hundreds of meV, such that the emission spectra of individual centres are clearly distinguishable even at room temperature (Aharonovich *et al.*, 2009; Castelletto *et al.*, 2012). The transition energies of

these centres can be tuned to a similar degree by application of external electric fields (Mueller *et al.*, 2011).

4.3.1 Photoluminescence (PL) spectroscopy

In standard PL spectroscopy, the fluorescence signal is dispersed using a grating monochromator and the spectrum imaged onto a CCD camera. Such apparatus can typically provide a spectral resolution of order 100 GHz (0.1 meV) in the visible spectrum, along with the ability to collect fluorescence over several minutes or even hours with minimal background noise, to provide highly detailed spectra.

As well as removing inhomogeneity between individual defects, measuring PL from single defects can also allow the fluorescence signal from the defect to be isolated from that from other sources, allowing detailed analysis of its vibronic spectrum. By recording an image in which fluorescence from an isolated single defect stands out against a background, it is straightforward to identify the spectroscopic features resulting from the defect by simple background subtraction. Davies and Hamer (1976) showed that an effective method for analysing the vibronic spectrum is to apply the Franck–Condon principle, whereby the emission spectrum as a function of energy E is given by

$$I(E) = E^3 \sum_{n=1}^{\infty} \frac{S^n}{n!} I_n(E_V) \qquad [4.4]$$

where E_v is the phonon energy, S is the Huang–Rhys factor and $I_n(E_v)$ is the spectrum of the nth phonon sideband, determined by iterative convolution of the single-phonon spectrum according to the expression

$$I_n(E_V) = \int_{x=0}^{E_{max}} I_1(x) I_{n-1}(E_V - x)\, dx \qquad [4.5]$$

A good example of this is provided in a study of an unknown defect (Smith *et al.*, 2011), in which the method allows exact simulation of the recorded spectrum, allowing identification of coupling to both the broadband bulk phonon dispersion and two sharp localised modes. Without single-defect analysis, the latter would likely otherwise have been mistaken for a second zero-phonon line.

4.3.2 Photoluminescence excitation (PLE) spectroscopy

Photoluminescence excitation (PLE) is a variation of PL spectroscopy in which the total intensity of emission over a fixed wavelength range is monitored while the excitation wavelength is swept through resonance with absorbing transitions of the colour centre. This technique is commonly used to characterise transitions which absorb photons but which relax non-radiatively to 'feed' lower-energy fluorescence transitions. A further advantage of the technique is that it allows one

to achieve much higher spectral resolution than standard PL, limited by the source line width and one's ability to tune the source wavelength rather than the ability to disperse a weak fluorescence signal. Lasers provide excellent narrow-line-width sources, offering resolution of MHz or less, some five orders of magnitude better than is achieved in the PL spectroscopy described above.

For example, PLE on single NV^- centres is a powerful tool for measuring the fine structure of the zero-phonon line, and allows one to resolve the six different transitions between the $^3A_2$ ground state and the optically excited ^3E state. It has been used to characterise the roles of the spin–orbit and spin–spin interactions (Batalov *et al.*, 2009) and the dynamic Jahn–Teller effect (Fu *et al.*, 2009), and to map in detail the dependence of these energy levels on local electric and strain fields.

The main additional apparatus requirement for PLE of zero-phonon-line fine structure is a narrow-line-width tunable laser source. The most commonly used design is the external-cavity semiconductor diode laser, in which the wavelength of the laser resonator can be adjusted with MHz accuracy using a piezoelectric actuator. The laser must operate in a single mode and be tuned without mode-hopping, placing limitations on the spectral range that can be recorded. A high-resolution wavemeter and/or Fabry–Pérot etalon are often also employed to measure and monitor the mode structure and wavelength of the excitation laser with a high degree of accuracy.

Example PLE spectra from three individual NV^- defects under different local strains are shown in Fig. 4.7, reproduced from Batalov *et al.* (2009). Each spectrum reveals up to six lines, corresponding to the multiple electric-dipole allowed transitions from the electronic ground state of the colour centre. Each PLE line is a few tens of megahertz in width, not much broader than the lifetime-limited line width of 14 MHz for these transitions (Tamarat *et al.*, 2006), providing exquisite detail and allowing detailed analysis of the defect to be performed.

One difficulty with PLE spectroscopy is that if the colour centre is somehow driven off resonance with the narrow excitation laser, the signal will disappear. In NV^- defects this occurs in two ways – firstly as a result of spin pumping, and secondly as a result of a change in charge state. These two problems are dealt with in different ways. Spin pumping can be reduced by applying some external field that reduces the spin relaxation time, usually a microwave or optical modulation tuned into resonance with an appropriate spin transition. Changes in charge state can be addressed by optical pumping of the system. The restoration of a charge state by optical pumping is, in general, a random process which involves promoting carriers into conduction or valence band states so that they have a chance to move between trap sites. However, in some circumstances it is also possible to repump deterministically by exciting only the existing charge state of the defect (Beha *et al.*, 2012). Even with an effective pumping process in place, however, most samples reveal some fluctuation in the measured transition energy as a result of charge redistribution in the vicinity of the defect being studied. Minimising these

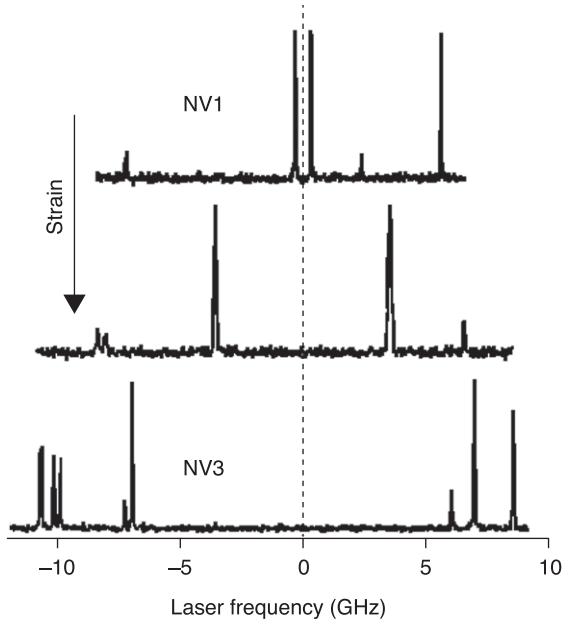

4.7 Photoluminescence excitation (PLE) data from three different single NV^- defects. The laser is tuned through resonance with the zero-phonon transitions while the intensity of emission is monitored by measuring the phonon sideband. Spectral resolution of order 10 MHz is achievable using this method. The differences between the three spectra shown result from strain inhomogeneity in the single-crystal lattice. Reprinted figure with permission from A. Batalov *et al.*, *Phys. Rev. Lett.* 102, 195506 (2009), http://link.aps.org/doi/10.1103/PhysRevLett.102.195506. Copyright (2009) by the American Physical Society.

fluctuations is likely to be crucial if robust quantum optical devices are to be constructed from diamond colour centres.

PLE can in principle be carried out on any colour centre that has some vibronic character in its fluorescence such that a phonon-assisted fluorescence channel can be monitored while the electronic resonances are excited. At the time of writing, it has only been applied to NV^-, although there is clear potential for investigation of other defects using this technique.

4.3.3 Local strain effects

Strain in the diamond lattice imposes small changes on the positions of the atomic nuclei in and around defects, and therefore perturbs the electronic orbitals in ways that affect their energies, symmetry and spin properties. Strain built into the

diamond material is therefore an important consideration in determining defect properties, while the deliberate introduction of strain – via an applied stress – is both an important spectroscopic tool and of potential value in the development of controllable functionality. Through the development of group theory as a powerful tool in identifying the symmetry of defects, applied uniaxial stress has been widely used in identifying colour centres since pioneering work in the 1970s.

Conversely, once the effect of strain on a particular defect is well understood, the measurement of transition energies and transition dipole orientations in the spectroscopy of single colour centres can be used to characterise the local strain in the diamond lattice. Since strain is a second-rank tensor with up to six independent components at a given point in space, this is no simple task.

The effect of strain on the electronic structure of NV^- defects is now well documented (Doherty *et al.*, 2011). The NV^- centre lies along one of the four {111} directions in the diamond lattice and therefore possesses threefold rotational symmetry plus three mirror planes (point group C_{3v}). Components of the strain field can be grouped into terms that preserve the rotational symmetry, and those that break rotational symmetry by acting in the plane perpendicular to the NV axis. The former components merely shift the energy of the transition, and the latter components lead to splitting of the zero-phonon line into a linearly polarised doublet. It has been noted that the effect of strain on the NV electronic structure is indistinguishable from that of an electric field, since the grouping of strain terms as described above is equivalent to the resolving of a vector into components along and in the plane perpendicular to the NV axis.

Ab initio calculation of the electronic perturbation that results from local strain is computationally challenging; however, the empirical relationship between applied stress and observed perturbations has been extensively studied. Davies and Hamer (1976) measured energy shifts and splittings due to stresses applied along the ⟨100⟩ and ⟨111⟩ axes, providing sufficient information to establish the perturbations to the zero-phonon line transitions resulting from an arbitrary strain field.

In turn, by measuring the zero-phonon line positions from single NV^- centres one can reconstruct the local stress tensor. A single NV centre can only provide three independent pieces of information, corresponding to the global shift, the splitting and the orientation of the transition dipoles, insufficient to establish the six independent strain components. However, if three or more colour centres of different orientations share the same stress field, the information extracted forms a set of overdetermined simultaneous equations that can be solved to derive all six stress components (Grazioso *et al.*, 2013). In a diamond crystal, there are likely to be both long-range stress fields from extended defects and external forces on the crystal faces, and short-range stress fields resulting from point defects. An enticing prospect is that by measuring stress-induced perturbations of colour centres it might be possible to identify the presence and locations of other, ‘dark’ defects such as lattice vacancies or substitutional impurities.

Other single defects display energy splittings and inhomogeneity in their fluorescence that appear to be attributable to lattice strain, but few detailed studies have been carried out. Application of uniaxial stress to these colour centres has much to offer in establishing the symmetry – and thereby the structure – of these defects, and in identifying their electronic structure via the symmetries of the various electronic states of the system.

4.4 Photon statistics

By measuring the timing statistics of emitted photons, it is possible to obtain information about the electronic energy levels and interlevel transition rates of a single defect. The simplest example of this occurs in measuring the fluorescence decay time using time-correlated single-photon counting, in which the distribution of photon arrival times on a detector subsequent to an excitation event provides a measure of the population relaxation in the excited state. Whilst single defects are not required for such measurements *per se*, in some situations they can allow more precise measurements by ensuring that the excited state is well defined and homogeneous, so that (provided the system is Markovian) the fluorescence decay is monoexponential.

The vast majority of measurements of photon timing statistics require single-photon detectors with a timing resolution (jitter) faster than the radiative lifetime of the colour centre. The most widely used single-photon detectors are avalanche photodiodes, offering timing down to about 100 ps, which is sufficient for all colour centres measured to date. Several different models are available commercially, offering different options that focus on optimising either high timing resolution or high photon detection efficiency (the two are somewhat competing parameters).

4.4.1 Hanbury Brown and Twiss (HBT) measurements

The most commonly used method for identifying whether a fluorescence signal originates from a single colour centre is by measuring the second-order (intensity) autocorrelation function in the time domain, defined by

$$g^{(2)}(\tau) = \frac{\left\langle I(t)I(t+\tau)\right\rangle}{\left\langle I(t)\right\rangle^2} \qquad [4.6]$$

In essence, the signature of a single emitter is that $g^{(2)}(\tau)$ dips to zero close to $\tau = 0$, because a single quantum system that has just emitted a photon requires on average a spontaneous emission lifetime before a further photon emission takes place, so there is no possibility of two photons being emitted simultaneously. This situation contrasts starkly with that of coherent light, for which $g^{(2)}(\tau) = 1$ independent of τ, and thermal light sources, for which $g^{(2)}(\tau) > 1$ for small τ. The

photon emission statistics for a single quantum emitter are therefore said to be 'sub-Poissonian', or 'antibunched'.

The correlation function is measured by simply splitting the fluorescence signal with a 50:50 beam splitter and directing the two halves of the signal onto two single-photon detectors. A timing circuit measures the time delay between successive photon detection events on the two detectors, and a histogram of these delay times is compiled to produce the $g^{(2)}(\tau)$ correlation function. High signal intensities are required, as the rate of acquisition of the histogram scales as the square of the single-photon detection efficiency – in practice, it is difficult to measure $g^{(2)}(\tau)$ for a photon count rate much below 10^4 s^{-1}.

The observation of an antibunching dip in an HBT measurement with $g^{(2)}(0) < 0.5$ is widely recognised as the definitive test of a single emitter. In any practical experiment there will of course be some background signal, whether from thermal counts on the detector, other sources of fluorescence or stray light reaching the detector, and it is often necessary to correct for these before making the assessment. Separating the intensity function into a signal and an uncorrelated background in Eq. 4.6 reveals that the background of the correlation function is at least twice that of the signal intensity.

4.4.2 Rate equation analysis

Analysis of $g^{(2)}(\tau)$ datasets is generally carried out using a set of rate equations derived from the proposed electronic structure of the system. The dependence of the function on the excitation power is particularly important, as it can reveal the presence of a metastable excited state of the system via the appearance of a bunching effect in addition to the observed $\tau = 0$ antibunching. In such cases, the electronic structure of the colour centre is modelled as a three-level system as illustrated in Fig. 4.8. The coupled rate equations for the three-level system can be solved analytically, providing the functional form for the autocorrelation function,

$$g^{(2)}(\tau) = 1 - ce^{-|\tau|/\tau_1} + (c-1)e^{-|\tau|/\tau_2} \qquad [4.7]$$

where

$$\tau_{1,2} = \frac{2}{A \pm \sqrt{A^2 - 4B}} \qquad [4.8]$$

$$A = k_{12} + k_{21} + k_{23} + k_{31} \qquad [4.9]$$

$$B = k_{12}k_{23} + k_{12}k_{31} + k_{21}k_{31} + k_{23}k_{31} \qquad [4.10]$$

$$c = \frac{1 - \tau_1 k_{31}}{k_{23}(\tau_2 - \tau_1)} \qquad [4.11]$$

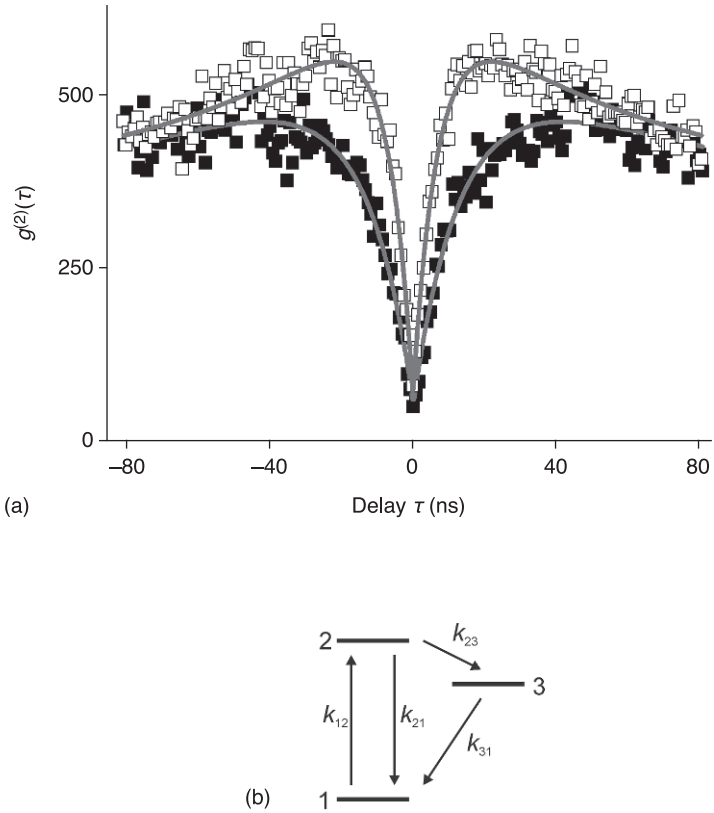

4.8 Photon statistics for the second-order autocorrelation function $g^{(2)}(\tau)$ measured using the Hanbury Brown and Twiss method. At low excitation intensity (■), the characteristic 'antibunching dip' below 0.5 indicates that the emission is from a single defect. At higher excitation intensities (□), 'bunching' is also observed, indicative of a metastable state populated from the optically excited state. The solid grey lines indicate fits achieved using a three-level rate equation model described in the text. (b) The three-level diagram with corresponding rate constants used in Eqs 4.9–4.15.

In these equations, k_{ij} is the transition rate between level i and level j, and k_{12} is therefore proportional to the excitation intensity. In the limit of high excitation intensity,

$$k_{12} >> k_{12s} = \frac{k_{31}(k_{21} + k_{23})}{k_{31} + k_{23}} \qquad [4.12]$$

the population of level 2 saturates, and the total photon emission rate is

$$I_{\text{sat}} = \frac{k_{31}k_{21\text{r}}}{k_{31} + k_{23}} \quad [4.13]$$

where $k_{21\text{r}}$ is the radiative component of k_{21}, accounting for the fact that many defects also exhibit non-radiative relaxation (sub-unity fluorescence quantum yield). The dependence of the emission intensity on the excitation intensity is given by

$$I = \frac{I_{\text{sat}}P}{P + P_s} \quad [4.14]$$

where P is the incident optical excitation power, related to the excitation rate by the coupling efficiency η and the photon energy:

$$k_{12} = \frac{\eta}{h\nu}P \quad [4.15]$$

The saturation excitation intensity P_s is established by measuring the power dependence of the fluorescence intensity and fitting this to Eq. 4.14.

With the NV^- defect, a strong bunching effect is observed as a result of the presence of an intermediate spin singlet state or states that act as long-lived shelving states aside from the main optical transition (Kurtsiefer *et al.*, 2000), and this bunching effect is therefore directly linked to the spin polarisation and readout properties of the defect. Rate equation analysis can be extended to multiple levels using numerical simulations, but as yet no examples exist of $g^{(2)}(\tau)$ data that require more than three levels to accurately reproduce the observations.

Some colour centres have been found that display no bunching effect even under high-intensity laser excitation, indicating that they have no metastable excited state that is accessible from the optically excited state (Aharonovich *et al.*, 2009). The suggestion is that these may be spin-½ systems with no intersystem crossing, offering attractive properties for single-photon sources, but these are likely to be less straightforward to use as spin qubits, as there will be no comparable spin-pumping or readout mechanism.

As well as energy level structure and transition rates, HBT measurements can also be used to study coherent effects in single colour centres. By recording the $g^{(2)}(\tau)$ function for a colour centre that is strongly driven with a resonant excitation, Rabi oscillations in the population of the optically excited state can be observed (Batalov *et al.*, 2008), and the decoherence time measured. Selected NV centres held at cryogenic temperature have been shown to display excited-state electronic dephasing limited by the spontaneous emission rate of the system.

The study of photon statistics can reach beyond the straightforward second-order autocorrelation function described above. One example of this has been the use of the cross-correlation function, whereby the correlation between photon arrival events in two different signals is studied. Such measurements can reveal

whether two different fluorescence lines emanate from the same defect, or whether there is a causal relationship between the ability of two defects to emit, for example if an electron is required to hop between them. Since such processes are usually directional, they produce asymmetry in the $g^{(2)}(\tau)$ function between positive and negative τ.

4.5 Spin resonance

Characterisation of single colour centres offers significant advantages over ensemble measurements when one is investigating the spin properties. Inhomogeneity in the local spin environment, in terms of the local distribution of ^{13}C nuclear spins plus electron spins on substitutional nitrogen within a few nanometres, leads to broadening of the spin resonance signal for ensembles. The spin resonance spectra of single defects measured using fluorescence methods, in turn, provide information about this local environment, and are a vital tool in identifying which defects can offer the functionality required for quantum devices.

4.5.1 Optically detected magnetic resonance (ODMR) of NV centres

The NV^- centre is, at the time of writing, the only colour centre in diamond for which a spin resonance signature has been observed in fluorescence, and thus the only colour centre for which spin characterisation and control have been achieved at the single-defect level. The spin resonance signature comes about as a result of the difference in coupling between the sublevels of the optically 'bright' spin triplet excited state and the optically 'dim' spin singlet levels. The strongest fluorescence signal occurs where the defect can remain in a pure $S=1$, $m_s=0$ state, also known as spin 'z', whereupon the triplet–singlet intersystem crossing is weak and so the singlet is very rarely populated. Any perturbation that mixes the spin character of the sublevels or reduces the spin relaxation lifetime results in an optically excited state that is more likely to relax to the singlet, where it remains for hundreds of nanoseconds, and this brings about a consequent reduction in the fluorescence intensity.

At the most basic level, then, ODMR spectroscopy of single NV centres is carried out by applying some perturbation that mixes the spin states in a resonant fashion, so as to measurably reduce the fluorescence intensity when the resonant condition is met. This can be achieved in three ways:

- by applying an alternating magnetic field at a frequency tuned to one of the magnetic dipole transitions involving the spin z state;
- by driving a Raman transition between spin sublevels via an excited state of mixed spin character;
- by applying a DC bias field that mixes the spin states owing to an avoided crossing or to breaking of symmetry.

The most common method for ODMR of NV centres has been to apply a microwave-frequency magnetic field that is near-resonant with the 2.87 GHz splitting of the $m_s = \pm 1$ levels from the $m_s = 0$ level in the $^3A_2$ ground state. This magnetic dipole transition can be driven with readily available microwave sources, the field being generated by a simple inductive wire or strip-line resonator. The alternating field is aligned perpendicular to the axis of symmetry that defines the spin eigenstates. It is often also desirable to apply a DC magnetic field aligned parallel to the axis of symmetry, to perturb the energies of the spin eigenstates via the Zeeman effect. In the case of NV^-, such a DC field is used to lift the degeneracy of the $m_s = \pm 1$ levels, causing the ODMR signal to split into two $\Delta m_s = \pm 1$ transitions. It is important to align this bias field parallel to the axis of the NV^- defect in order to preserve the spin character of the eigenstates and therefore the contrast of the ODMR signal. The magnetic resonance in NV^- is indicated by a reduction of up to 30% in the fluorescence intensity, corresponding to an increased transition rate k_{23} between the $m_s = \pm 1$ optically excited states and the metastable singlet (see Eq. 4.13).

Further detail in the ODMR spectrum is generated by spin–spin coupling with nearby unpaired electrons, for example on a paramagnetic substitutional nitrogen defect, and by the hyperfine coupling with local nuclear spins. In NV^-, the magnetic dipole interaction between an electron on an NV centre and an electron on a nearby substitutional nitrogen can lead to a splitting of tens of megahertz (Gaebel *et al.*, 2006). Hyperfine interaction with the $I = 1$ spin of the ^{14}N nucleus is observed as a triplet with a splitting of 2.2 MHz, whilst the splitting due to an $I = ½$ spin of a ^{13}C nucleus on one of the lattice sites adjoining the vacancy is 130 MHz, and the next nearest neighbours result in splittings of order 13 MHz (He, 1993; Jelezko, 2004). Example ODMR spectra illustrating various hyperfine interactions are shown in Fig. 4.9 (Jelezko and Wrachtrup, 2006).

ODMR experiments can be carried out using either continuous-wave (CW) or pulsed microwave signals. CW measurements have the advantage of simplicity, requiring no timing electronics; the spectrum is achieved by sweeping either the microwave frequency or the DC magnetic field intensity through the resonances. However, pulsed measurements offer several significant advantages and are crucial for demonstrating the quantum coherent properties.

In the simplest pulsed ODMR experiment, the spin is first polarised, and then driven coherently using a microwave pulse of variable 'area' (essentially the product of the pulse amplitude and duration), before being read out. The read-out signal as a function of microwave pulse area then reflects the Rabi nutations of the spin in the presence of the driving microwave field. The Fourier transform of this time domain signal provides frequency domain information comparable to that obtained by CW measurements.

Dephasing rates are generally measured by one of two techniques, namely Ramsey interference and Hahn echo. These techniques involve creating a superposition spin state, allowing it to evolve ('dephase') for a defined time

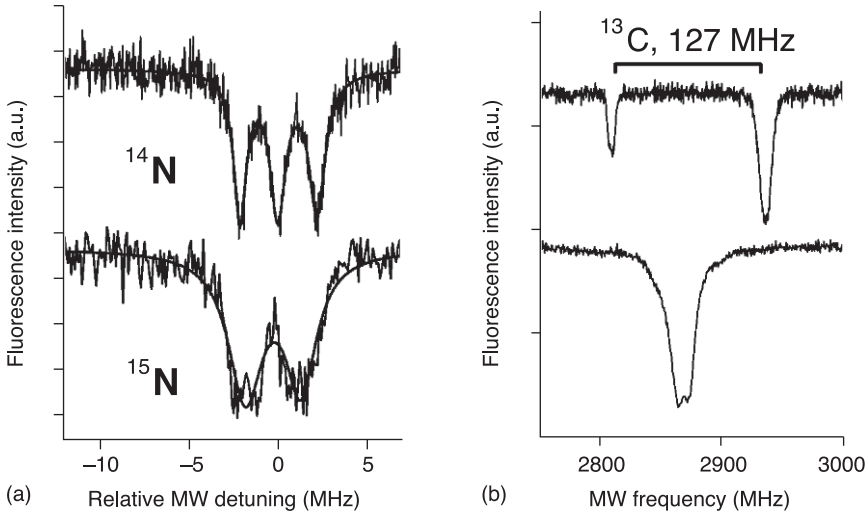

4.9 Optically detected magnetic resonance spectra recorded from single NV^- defects, showing hyperfine splitting due to coupling between the NV^- electron spin and the nuclear spin on (a) the N atom of the defect, and (b) a nearby ^{13}C atom. The most abundant N isotope ^{14}N has a nuclear spin $I=1$, leading to a triplet, while ^{15}N has $I=1/2$, leading to a doublet. Hyperfine coupling to ^{13}C depends strongly on the location of the carbon nucleus in question. Reprinted figure with permission from F. Jelezko and J. Wrachtrup, *Physica Status Solidi (a)* 203, 3207–3225 (2006). Copyright © 2006 Wiley-VCH Verlag GmbH & Co. KGaA, Weinheim.

period, and then measuring the altered superposition by first performing a spin rotation to convert the phase of the superposition into a population and then measuring the ODMR signal. The pulse sequences for the basic Rabi flopping experiment and for Ramsey interference and Hahn echo are shown in Fig. 4.10. For all of these techniques, the spin state must first be polarised. For NV^-, this is carried out using green laser illumination of duration greater than 1 μs to place the spin in the $m_s=0$ sublevel. For Ramsey interference and Hahn echo, a superposition spin state is then created by applying a $\pi/2$ microwave pulse tuned to either the $\Delta m=+1$ or the $\Delta m=-1$ transition. In Ramsey interferometry, a second $\pi/2$ microwave pulse is applied after a delay Δt to translate the accumulated phase into a population, which is then measured. In Hahn echo, a delay Δt is followed by a π microwave pulse and a further delay Δt, before a $\pi/2$ microwave pulse is applied and the spin population is measured. The Hahn echo technique is useful because it eliminates the dephasing effect of any fields that are static on the timescale of the pulse sequence, such as those caused by fluctuations in the local magnetic field due to the random flipping of nearby electron or nuclear spins, and allows the measurement of longer 'intrinsic' dephasing times.

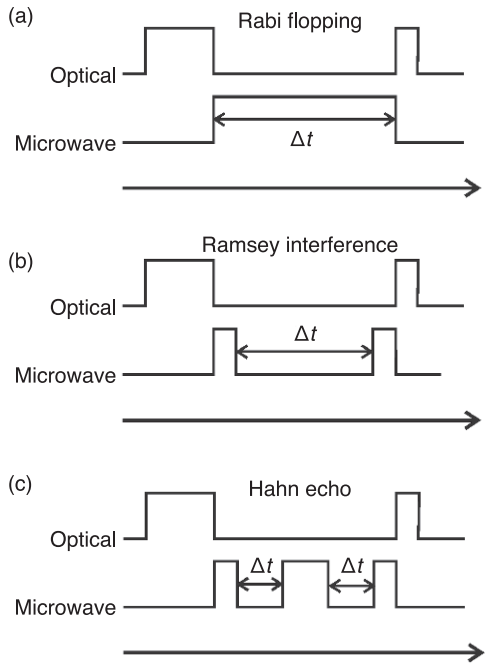

4.10 Optical and microwave pulse sequences for pulsed spin resonance measurements. (a) Rabi flopping, in which the duration of a microwave pulse is varied and the resulting spin rotation measured; (b) Ramsey interference, in which dephasing is measured by creating a superposition spin state and allowing it to evolve freely for a time Δt before the population is reconstituted and measured; and (c) Hahn echo, in which the spin phase is refocused using an additional pulse to remove the effect of slowly varying fields.

Other sophisticated variants of these techniques have been developed to provide improved control over the spin dynamics of electrons and nuclei in NV^- and other single-spin systems.

4.5.2 Quantum control via local spin interactions

The ability to execute fine control over the electron spin state of a single nitrogen–vacancy defect using optical pumping and microwave driving, combined with the ability to identify coupling with adjacent 'dark' spin systems, facilitates full control over the dark spins also. This can be used to significant advantage for quantum information processing in four main ways: firstly, to provide a local resource for computation using few-qubit systems; secondly, to provide access to the longer coherence times of nuclear spins; thirdly, to allow 'brokering' schemes

that protect qubits from the damaging effects of measurement; and fourthly, to offer a route to 'wiring' of qubits together using spin chains. In this section, we will touch on each of these four topics in turn.

Traditional 'circuit-based' schemes for quantum computing involve deterministic entanglement between qubits, usually via some local interaction, which can be controlled using external gates. Much of the difficulty in realising quantum computers stems from the need to scale this capability up to large systems. More recent 'measurement-based' schemes (Benjamin *et al.*, 2009) dispense with scalable deterministic entanglement as a requirement, but it is nevertheless beneficial if some deterministic entanglement can be present, even if only between a small number of qubits.

Several examples of local entanglement between spins have been demonstrated with NV centres. Entanglement between an NV electron spin and a single neighbouring electronic or nuclear spin is a straightforward extension of the measurement of hyperfine coupling, since the resolved hyperfine transitions permit conditional state transfer with a resonant microwave field. The largest entangled states to have been created in this way to date are the tripartite Greenberg–Horne–Zeilinger (GHZ) and 'W' states, using the NV electron spin and two ^{13}C nuclear spins (Neumann *et al.*, 2008).

These same processes allow the storage of a computational qubit onto a nuclear spin, for later retrieval. Nuclear spins offer much longer dephasing times than do electron spins as a result of the smaller nuclear magnetic moment: using spin echo techniques in isotopically purified ^{12}C diamond, qubits have been stored on a ^{13}C nuclear spin for in excess of a second at room temperature (Maurer *et al.*, 2012).

This transfer of a qubit from an NV electron spin onto a nearby nuclear spin also then renders the electron spin available for further manipulation without disturbing the stored qubit. This is the idea behind 'brokering' schemes, in which measurement-based entanglement is first created between remote broker qubits (NV electron spins) and then transferred to the neighbouring client qubits (nuclear spins), so that further entanglement operations can be carried out and a large-scale 'cluster' or 'graph' of entangled qubits created (Benjamin *et al.*, 2006). Because entanglement operations are generally inefficient (Barrett and Kok, 2005) and failed attempts are potentially damaging to existing entanglement, the broker–client relationship is an important feature in the efficient building of large-scale entangled states as a universal resource for quantum computing.

The potential to use surrounding spins as a means to communicate spin information between two NV centres has also been suggested. For example, a linear chain of paramagnetic spins on substitutional nitrogen impurities could couple via exchange interactions such that spin information could propagate along the chain (Yao *et al.*, 2011). With an NV centre at either end, the spin chain thereby acts as 'wiring' between two physical qubits, enabling coupling that could potentially lead to an all-solid-state quantum processor. Whether such an architecture is feasible is still very much an open question, however, and the

potential robustness of spin chains as a means to communicate quantum information is the subject of current theoretical research (Ping *et al.*, 2013).

4.6 Conclusions and future trends

Characterisation of defects in diamond at the single-dopant level using fluorescence techniques is now well established, providing a wealth of information about the electronic structure and quantum properties. Detailed understanding of the behaviour of these defects, in turn, allows them to be used as probes of the local crystal environment, revealing the presence and even the location of nearby impurities via the electric, magnetic and strain fields that they generate. Whilst most work has been carried out on the NV^- defect owing to its great attraction as a quantum spin register, the techniques described in this chapter are equally applicable to other colour centres. There is considerable scope for further exploration of the diversity of fluorescence signatures in diamond, the origins of which have yet to be identified, as well as the creation of novel defects using ion implantation and the synthesis of doped materials.

Single-defect characterisation that extends beyond the fluorescence-based techniques described here may ultimately be developed. Arguably, the greatest need is for methods of direct physical characterisation, so that the structure of as-yet-unidentified colour centres can be determined. Modern electron microscopy techniques, including scanning transmission electron microscopy and high-end aberration-corrected transmission electron microscopy, offer a combination of sub-angstrom spatial resolution and compatibility with species-selective analysis techniques such as electron energy loss spectroscopy and annular dark field imaging, which in principle can allow single point defects to be characterised in suitably prepared samples.

For quantum information schemes that involve optical interactions with single colour centres, fluorescence-based characterisation is clearly an essential element of the toolbox. It will allow the identification of individual colour centres with the properties required for the device functionality that could be of direct benefit to schemes for distributed quantum computing. Super-resolution optical microscopy can offer a means for characterisation of arrays of colour centres separated by distances short enough for useful interactions between spins, thereby opening up possibilities for scalable on-chip devices in circuit-based or hybrid schemes.

4.7 References

Aharonovich, I., Castelletto, S., Simpson, D. A., Greentree, A. D. and Prawer, S. (2009) 'Two-level ultrabright single photon emission from diamond nanocrystals', *Nano Lett.*, 9, 3191–3195.

Aharonovich, I., Castelletto, S., Johnson, B. C., McCallum, J. C., Simpson, D. A., *et al.* (2010) 'Chromium single photon emitters in diamond fabricated by ion implantation', *Phys. Rev. B* 81, 121201(R).

Barrett, S. D. and Kok, P. (2005) 'Efficient high-fidelity quantum computation using matter qubits and linear optics', *Phys. Rev. A* 71, 060310.

Batalov, A., Zierl, C., Gaebel, T., Neumann, P., Chan, I. -Y., *et al.* (2008) 'Temporal coherence of photons emitted by single nitrogen–vacancy defect centers in diamond using optical Rabi-oscillations', *Phys. Rev. Lett.* 100, 077401.

Batalov, A., Jaques, V., Kaiser, F., Siyushev, P., Neumann, P., *et al.* (2009) 'Low temperature studies of the excited state structure of negatively charged nitrogen–vacancy color centers in diamond', *Phys. Rev. Lett.* 102, 195506.

Beha, K., Batalov, A., Manson, N. B., Bratschitsch, R. and Leitenstorfer, A. (2012) 'Optimum photoluminescence excitation and recharging cycle of single nitrogen–vacancy centers in ultrapure diamond', *Phys. Rev. Lett.* 109, 097404.

Benjamin, S. C., Browne, D. E., Fitzsimons, J. and Morton, J. J. L. (2006) 'Brokered graph state quantum computation', *New J. Phys.* 8, 141.

Benjamin, S. C., Lovett, B. W. and Smith, J. M. (2009) 'Prospects for measurement-based quantum computing with solid state spins', *Laser Photon. Rev.* 3, 556–574.

Castelletto, S., Edmonds, A., Gaebel, T. and Rabeau, J. (2012) 'Production of multiple diamond-based single photon sources', *IEEE J. Sel. Top. Quantum Electron.* 18, 1792–1798.

Davies, G. and Hamer, M. F. (1976) 'Optical studies of the 1.945 eV vibronic band in diamond', *Proc. R. Soc. Lond. A* 348, 285–298.

Doherty, M. W., Manson, N. B., Delaney, P. and Hollenberg, L. C. L. (2011) 'The negatively charged nitrogen–vacancy center in diamond: the electronic solution', *New J. Phys.* 13, 025019.

Fu, C.-C., Lee, H.-Y., Chen, K., Lim, T.-S., Wu, H.-Y., *et al.* (2007) 'Characterization and application of single fluorescent nanodiamonds as cellular biomarkers', *Proc. Natl. Acad. Sci. USA* 104, 727–732.

Fu, K.-M. C., Santori, C., Barclay, P. E., Rogers, L. J., Manson, N. B. and Beausoleil, R. G. (2009) 'Observation of the dynamic Jahn–Teller effect in the excited states of nitrogen–vacancy centers in diamond', *Phys. Rev. Lett.* 103, 256404.

Gaebel, T., Popa, I., Gruber, A., Domhan, M., Jelezko, F. and Wrachtrup, J. (2004) 'Stable single photon source in the near infrared', *New J. Phys.* 6, 1–7.

Gaebel, T., Domhan, M., Popa, I., Wittmann, C., Neumann, P., *et al.* (2006) 'Room temperature coherent coupling of single spins in diamond', *Nature Phys.* 2, 408–413.

Gaebel, T., Bradac, C., Chen, J., Say, J. M., Brown, L., *et al.* (2012) 'Size-reduction of nanodiamonds via air oxidation', *Diamond Relat. Mater.* 21, 28–32.

Grazioso, F., Patton, B. R., Delaney, P., Markham, M. L. Twitchen, D. J. and Smith, J. M. (2013) 'Measurement of the full stress tensor in a crystal using photoluminescence from point defects: The example of nitrogen vacancy centers in diamond', *Appl. Phys. Lett.* 103, 101905 (2013).

Han, K. Y., Willig, K. I., Rittweger, E., Jelezko, F., Eggeling, C. and Hell, S. W. (2009) 'Three-dimensional stimulated emission depletion microscopy of nitrogen–vacancy centers in diamond using continuous-wave light', *Nano Lett.* 9, 3323–3329.

He, X-F. (1993) 'Paramagnetic resonance of photoexcited N-V defects in diamond. II. Hyperfine interaction with the ^{14}N nucleus', *Phys. Rev. B* 47, 8816–8822.

Jelezko, F. (2004) 'Observation of coherent oscillation of a single nuclear spin and realization of a two qubit conditional quantum gate', *Phys. Rev. Lett.* 93, 130501.

Jelezko, F. and Wrachtrup, J. (2006) 'Single defect centres in diamond: a review', *Phys. Stat. Solidi (a)* 203, 3207–3225.

Jelezko, F., Gaebel, T., Popa, I., Gruber, A. and Wrachtrup, J. (2004) 'Observation of coherent oscillations in a single electron spin', *Phys. Rev. Lett.* 92, 076401.

Kurtsiefer, C., Mayer, S., Zarda, P. and Weinfurter, H. (2000) 'Stable solid state source of single photons', *Phys. Rev. Lett.* 85, 290–293.

Maurer, P. C., Kucsko, G., Latta, C., Jiang, L., Yao, N. Y., *et al.* (2012) 'Room temperature quantum bit memory exceeding one second', *Science* 336, 1283–1286.

Mueller, T., Aharonovich, I., Lombez, L., Alaverdyan, Y., Vamivakas, A. N., *et al.* (2011) 'Wide-range electrical tunability of single-photon emission from chromium-based colour centres in diamond', *New J. Phys.* 13, 075001.

Neu, E., Steinmetz, D., Riedrich-Möller, J., Gsell, S., Fischer, M., *et al.* (2011) 'Single photon emission from silicon–vacancy colour centres in chemical vapour deposition nano-diamonds on iridium', *New J. Phys.* 13, 125012.

Neumann, P., Mizuochi, N., Rempp, F., Hemmer, P., Watanabe, H., *et al.* (2008) 'Multipartite entanglement among single spins in diamond', *Science* 320, 1326–1329.

Ping, Y. T., Lovett, B. W., Benjamin, S. C. and Gauger, E. M. (2013) 'Practicality of spin chain wiring in diamond quantum technologies', *Phys. Rev. Lett.* 110, 100503.

Rittweger, E., Han, K. Y., Irvine, S. E., Eggeling, C. and Hell, S. W. (2009) 'STED microscopy reveals crystal colour centres with nanometric resolution', *Nature Photon.* 3, 144–147.

Simmonds, R. D., Salter, P. S., Jesacher, A. and Booth, M. J. (2011) 'Three dimensional laser microfabrication in diamond using a dual adaptive optics system', *Opt. Express* 19, 24122–24128.

Simpson, D. A., Ampem-Lassen, E., Gibson, B. C., Trpkovski, S., Hossain, F. M., *et al.* (2009) 'A highly efficient two level diamond based single photon source', *Appl. Phys. Lett.* 94, 203107.

Smith, J. M., Grazioso, F., Patton, B. R., Dolan, P. R., Markham, M. J. and Twitchen, D. J. (2011) 'Optical properties of a single colour centre in diamond with a green zero phonon line', *New J. Phys.* 13, 045005.

Tamarat, P., Gaebel, T., Rabeau, J. R., Khan, M., Greentree, A. D., *et al.* (2006) 'Stark shift control of single optical centers in diamond', *Phys. Rev. Lett.* 97, 083002.

Wang, C., Kurtsiefer, C., Weinfurter, H. and Burchard, B. (2006) 'Single photon emission from SiV centres in diamond produced by ion implantation', *J. Phys. B* 39, 37–41.

Wildanger, D., Patton, B. R., Schill, H., Marseglia, L., Hadden, J. P., *et al.* (2012) 'Solid immersion facilitates fluorescence microscopy with nanometer resolution and sub-Ångström emitter localization', *Adv. Mater.* 24, OP309–313.

Williams, O. A., Hees, J., Dieker, C., Jaeger, W., Kirste, L. and Nebel, C. E. (2010) 'Size dependent reactivity of diamond nanoparticles', *ACS Nano* 4, 4824–4830.

Yao, N. Y., Jiang, L., Gorshkov, A. V., Gong, Z.-X., Zhai, A., *et al.* (2011) 'Robust quantum state transfer in random unpolarized spin chains', *Phys. Rev. Lett.* 106, 040505.

Zaitsev, A. M. (2001) *Optical properties of diamond: A data handbook*, Springer.

5

Nanofabrication of photonic devices from single-crystal diamond for quantum information processing (QIP)

J. T. CHOY, B. J. M. HAUSMANN, M. J. BUREK, T. M. BABINEC and M. LONČAR, Harvard University, USA

DOI: 10.1533/9780857096685.1.98

Abstract: We describe top-down nanofabrication approaches to photonic devices in single-crystal diamond and analyze their performance by optical characterization. The devices presented include nanowires, angle-etched nanobeams, plasmonic resonators and integrated planar resonators, which have been used to engineer the collection efficiency and spontaneous emission rate for nitrogen–vacancy (NV) centers.

Key words: nanofabrication, photonics, waveguide, resonator, Purcell effect.

5.1 Introduction

Nanophotonics has recently emerged as a powerful platform capable of interfacing macroscopic optical elements (e.g., optical fibers and lenses) with atomic-scale solid-state quantum emitters (e.g., luminescent color centers in diamond). Specifically, progress in the field of diamond nanophotonics has already enabled efficient generation, storage and manipulation of quantum information,[1–6] and in the near future will likely result in the realization of integrated chip-scale systems for quantum communication and information processing (e.g., quantum repeaters[7]). At the heart of these applications are diamond's luminescent crystalline defects – color centers – and the negatively charged nitrogen–vacancy (NV) color center in particular. Quantum information can be stored in the electron spin of an NV center or the nuclear spin of nearby atoms, with very long coherence times even at room temperature.[8, 9] Quantum logic can be achieved via the application of microwave and RF fields to drive transitions between electron and nuclear spin sublevels.[1, 10] Finally, spin quantum information can be communicated via spin-dependent fluorescence intensity, resulting in a source of spin–photon entangled pairs.[11] In addition to their optical properties, a factor that makes diamond color centers greatly appealing is that they are atom-like systems housed in a solid-state bulk crystal, and thus provide a natural avenue for integrated quantum photonics. Indeed, visions of quantum networks in which single color centers play the central role (either acting as single-photon sources, or, in the case of the NV center, also as an interface between photons and spin qubits) have largely motivated the

© 2014 Elsevier Ltd

efforts that have been made to generate optical elements, such as waveguides and resonators, in single-crystal diamond.

Beyond applications in quantum science and technology, NV center spins can also act as nanoscale magnetometers[12–14] and temperature probes.[15] Moreover, diamond nanophotonics holds promise for the realization of advanced devices and systems that can leverage many of diamond's outstanding material properties. For example, diamond's transparency over a wide wavelength range, moderate third-order nonlinearity and excellent thermal properties are of great interest for the construction of frequency combs and integrated Raman lasers.[16] Owing to diamond's excellent mechanical properties, advances in diamond optomechanics[17] will lead to better force, mass and displacement sensors, as well as robust and reliable RF MEMS. Diamond is also an inert material that makes it well suited for biological applications and for devices that must operate in harsh environments.

In this chapter, we describe diamond devices that are designed to control the emission properties of color centers, specifically the NV center, to make them more suitable for quantum information processing and communication. However, many of the techniques and devices described here are of great interest for applications that extend beyond quantum applications. We focus mainly on bulk and planar devices fabricated directly in single-crystal diamond with embedded NV centers, which might be advantageous in practical applications owing to their potential scalability and relative ease of integration. Alternative approaches that rely on diamond nanocrystals[18] coupled to photonic devices fabricated in other materials[19–21] are not discussed here.

The emerging applications of NV centers in quantum cryptography protocols,[22] quantum registers[1, 4, 23] and ultrasensitive magnetometers[12–14] rely critically on efficient generation and collection of photons. Therefore, there is a need to engineer the emission of the NV center towards:

- *Improved in- and out-coupling efficiency between emitted photons and collection optics*. Efficient single-photon extraction from NV centers in the bulk diamond crystal is limited by total internal reflection (TIR) at the diamond–air interface, owing to the relatively large refractive index of diamond ($n = 2.4$). In fact, TIR allows light emission within a solid angle of less than 25° to escape from the diamond crystal, so that the overall collection efficiency is only about 3–5% for a microscope objective of moderate to high numerical aperture (NA). Approaches to overcoming this issue have included the fabrication of nanowires[24] (discussed in detail in Section 5.3.1), and of solid immersion lenses (SILs)[25–28] in bulk diamond crystals, through which the collected single-photon count rates are increased by roughly an order of magnitude. The increase in photon count rate has improved the sensitivity of field imaging in the case of a nanowire-based scanning magnetometer,[14] and with SILs it has enabled single-shot readout[3] and entanglement between distant NV centers.[5, 6]
- *Improved photon production efficiency*. The NV center in homogeneous diamond medium has a relatively long radiative lifetime of 13 ns. Moreover, its

emission spectrum is characterized by a zero-phonon line (ZPL) at 637 nm and a broad phonon sideband that extends to around 800 nm. At low temperature, the ZPL, which represents the purely electronic transition between the ground and excited states, narrows but still only constitutes around 3% of the total emission.[29] Since only the ZPL transition is of interest in applications that require indistinguishable photons (e.g., entanglement schemes), there is a need to use optical cavities to enhance the radiative rate and emission into the ZPL.

In the weak-coupling limit, the enhancement of the spontaneous emission rate for a dipole optimally positioned in the field maximum and well aligned (both spectrally and in polarization) with the electric field is described by the Purcell factor, P_F, which depends on the quality factor Q and mode volume V as follows:[30]

$$P_F = \frac{3}{4\pi^2}\left(\frac{\lambda}{n}\right)^3 \frac{Q}{V}$$

where λ is the emission wavelength of the dipole, n is the mode index and V is defined by

$$V = \frac{\int\int\int \varepsilon(\vec{r})\left|E\left(\vec{r}\right)\right|^2 d^3\vec{r}}{\varepsilon\left(\vec{r}_{\max}\right)\left|E\left(\vec{r}_{\max}\right)\right|^2}$$

where $\varepsilon(r)$ is the dielectric constant, $E(r)$ is the electric field and r_{max} represents the location of the field maximum. Q, which describes the photon storage time of the cavity, can be defined in terms of the rate at which the electric field decays in the cavity, κ, and the cavity resonant frequency ω_c, as

$$Q = \frac{\omega_c}{2\kappa}.$$

Therefore, a high Q and/or a small V, corresponding to a longer interaction time between the emitted photons and a stronger electric field around the emitter, are desired. We provide two examples of structures that can enable Purcell enhancement of NV centers: diamond–metallic nanocavities (Section 5.3.2) that provide broadband enhancement of the NV emission (both ZPL and the phonon sideband), and fluorescence enhancement of the NV center's ZPL only (Sections 5.4.1 and 5.4.2). The former are of interest for applications such as sensitive magnetometry that require control of the overall NV emission, whereas the latter are of interest for quantum-optics applications that rely on a large number of indistinguishable photons.

- *Low multiphoton probability of collected photons*. An important metric for single-emitter devices is a high signal-to-background ratio. This can be quantified by the second-order autocorrelation function,

$$g^{(2)}(\tau) = \frac{\left\langle I(t)I(t+\tau)\right\rangle}{\left\langle I(t)\right\rangle^2}$$

where I is the intensity and $\langle\ \rangle$ is the expectation value. $g^{(2)}(\tau)$ describes the probability of detecting a photon at time $t+\tau$ given a photon arrival at time t. An ideal nonclassical source is characterized by $g^{(2)}(0)=0$, which is known as antibunching, and comes from the finite time between consecutive single-photon arrivals. In experiments, background from the sample, detector dark counts and stray light can increase $g^{(2)}(0)$, so by convention photon emission with $g^{(2)}<1/2$ is attributed to a single emitter. A low multiphoton probability can be engineered by a choice of material and defect implantation conditions, as discussed in Section 5.3.1.

In Section 5.2, we summarize the fabrication techniques used for generating nanostructures in single-crystal diamond. Sections 5.3 and 5.4 describe the modeling, fabrication and characterization of single-photon sources based on diamond nanowires (Section 5.3.1), diamond–silver apertures (Section 5.3.2), and integrated devices such as ring resonators (Section 5.4.1) and photonic-crystal cavities (Section 5.4.2). A summary of the accomplishments in this field, a discussion of the remaining challenges and the ongoing efforts to address them, and a summary of the outlook for diamond nanophotonics in general are provided in Section 5.5.

5.2 Fabrication approaches for single-crystal diamond nanostructures

The fabrication of monolithic devices in single-crystal diamond encounters a set of material challenges, namely the difficulty of growing thin single-crystal diamond membranes on sacrificial or low-index substrates, and the physical and chemical resilience of the material. Various techniques to fabricate devices in bulk diamond have been investigated, including ion slicing, focused ion beam (FIB) milling and reactive-ion etching (RIE).

Ion slicing[31] has been used to fabricate thin diamond slabs, but the damage introduced into the diamond during the process has prevented applications in quantum science. However, recent techniques based on the regrowth of single-crystal material on sliced membranes[32, 33] are promising.

FIB machining sputters away material by causing a beam of gallium ions to impinge on the surface and provides a means of sculpting a wide variety of nanophotonic structures in bulk diamond.[25, 27, 34, 35] Despite the versatility of the method, the resulting devices are one of a kind and, for NV centers close to the surface, prone to damage and implantation by gallium ions. Nonetheless, functional photon devices are possible in cases where the emitter is located far away from the processed surface, such as in solid immersion lenses[25] or when postprocessing techniques are used.[36, 37]

Advances in top-down fabrication in single-crystal diamond allow three-dimensional and planar nanoscale diamond structures to be made with scalability and high yield. This technique involves the patterning of an etch mask using

electron beam lithography (EBL) and subsequent reactive-ion etching of diamond material in an oxygen-based environment.[38]

The schematic in Fig. 5.1(a) shows the basic fabrication process that we used to make diamond nanowires in single-crystal diamond substrates.[24] The fabrication sequence started with cleaning the bulk diamond substrate in a boiling mixture of sulfuric, nitric and perchloric acids. Next, a negative electron beam resist (flowable oxide) was spun onto the sample and electron-beam lithography was performed to define the etch mask. Etching of samples was performed in an inductively coupled plasma (ICP) reactor at a chamber pressure of 10 mT, with an oxygen flow rate of 30 sccm, a typical ICP power of 700 W and a bias power of 100 W. This provided a combination of physical and chemical etching of the sample and resulted in smoothly etched surfaces. To counter irregularities in the etch profile for high-aspect-ratio structures (e.g., diamond nanowires), etching could be done in several steps with varying ICP power, to modify the degree of chemical and/or physical etching. Thousands of devices can be made in parallel this way (Fig. 5.1(b)–(d)),

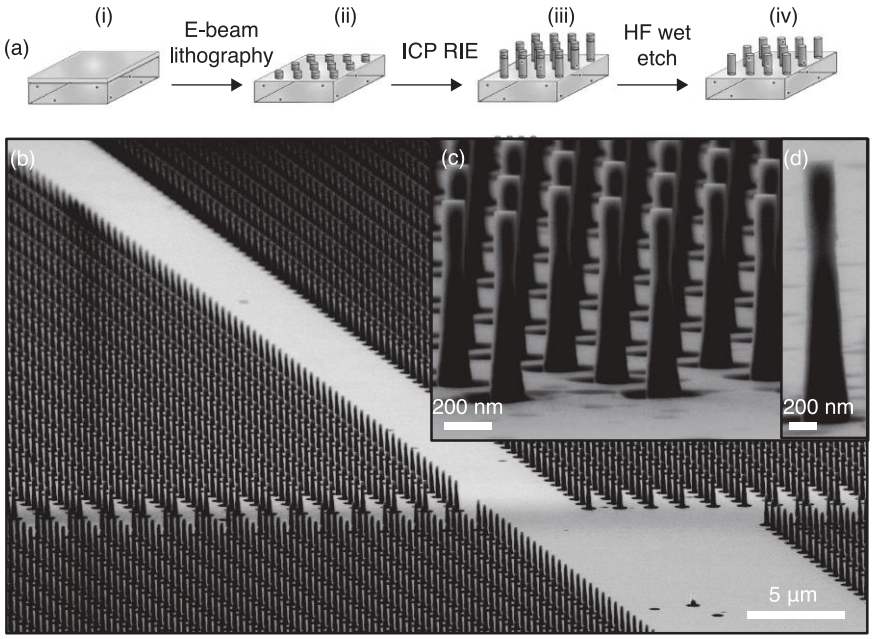

5.1 (a) The fabrication sequence for diamond nanowires on a bulk diamond crystal involves (i) spinning of an XR/Fox resist, (ii) e-beam lithography to define arrays of circularly shaped masks, (iii) reactive ion etching in an oxygen plasma to transfer the mask into the crystal, and (iv) removal of the resist in an HF etch.[40] (b)–(d) SEM images of arrays of 2 μm tall nanowires.[39] Reprinted (adapted) with permission from Hausmann *et al.*[40] Copyright 2011 IOP Publishing and Deutsche Physikalische Gesellschaft. CC BY-NC-SA.

which suggests that the technique might eventually enable the construction of chip-scale quantum networks. Additionally, the top-down approach can be used in conjunction with ion implantation to provide deterministic positioning of color centers in nanophotonic devices;[39] the implantation and annealing conditions are given in later sections.

For the fabrication of more complex, three-dimensional structures, such as suspended photonic-crystal nanobeam cavities and waveguides, two alternative approaches can be used. The first involves a combination of top-down etching, where ions in the RIE chamber impinge vertically onto the diamond surface, with subsequent angled etching,[41] where ions are directed at an angle onto the etched features. In the later etch step, the sample is inserted into a Faraday cage, whose geometry defines the angle of incidence of the ions on the etched substrate. Faraday cages work by shielding the sample from the electromagnetic field inside the chamber, instead allowing a field gradient to build up over the cage surface, and directing the ions onto the sample along a path that is perpendicular to the cage surface.[42, 43] Examples of triangular and conical Faraday cages are shown in Fig. 5.2(a) and (c), respectively. In these cases, plasma ions are directed at angles that are determined by the inclination angle of the prism and in all directions, respectively (illustrated in Fig. 5.2(b) and (d)).

The fabrication procedure for angle-etched nanobeams is shown in Fig. 5.2(e). While suspended triangular-cross-section nanobeams have been proposed and demonstrated in single-crystal diamond via FIB milling,[35] the use of the angled-etching technique avoids gallium implantation, crystal damage and material redeposition, and can generate structures much faster and with higher throughput. Single-crystal diamond substrates were first cleaned and an ~200 nm thick titanium etch mask was defined on the prepared diamond substrate using electron beam evaporation and EBL techniques. Oxygen-based plasma etching was then carried out in a two-part process. First, a conventional top-down anisotropic plasma etch was used to transfer the etch mask pattern into the bulk diamond to a depth near 600 nm. Subsequently, a second anisotropic etch step was performed with the sample placed inside a triangular-prism Faraday cage to release the nanostructures and yield the final suspended nanobeams shown in Fig. 5.3. These beams are suspended above the diamond substrate with a significant clearance (~2 μm) and have a span up to 85 μm long, with widths ranging from 75 nm to over a micron wide. They can be used as nanomechanical resonators and optical waveguides.

Using similar approaches, all-diamond photonic-crystal nanobeam cavities (Fig. 5.3(d) and (e)), microdisks, ring resonators, curved segments and cantilevers (Fig. 5.4) can be fabricated with high yield.

Planar photonic structures can also be fabricated by thinning down a single-crystal diamond substrate to the device thickness, using RIE deep etching.[44] The fabrication procedure is shown in Fig. 5.5. The single-crystal diamond substrate is first commercially laser-sliced and polished to result in ~20 μm thick diamond

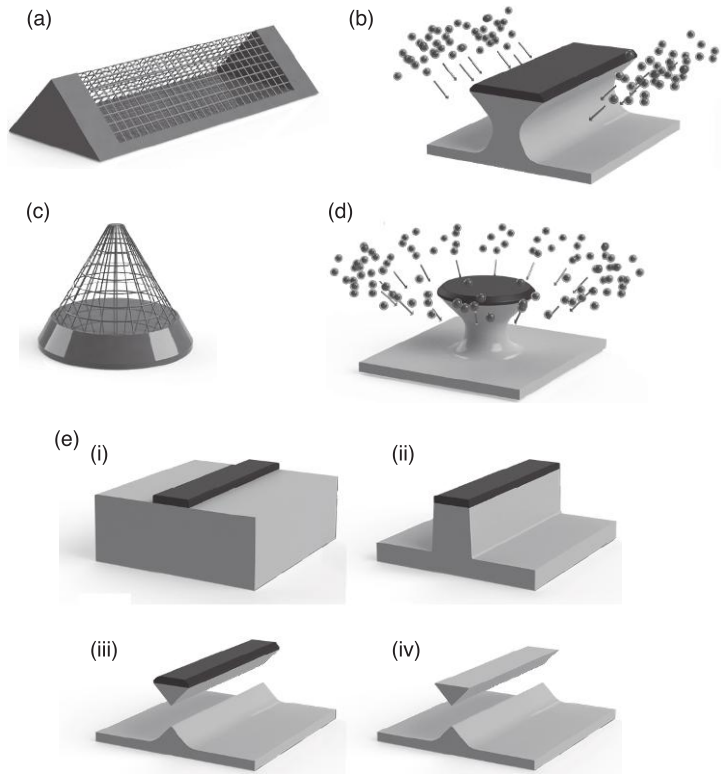

5.2 (a) Schematic illustration of a triangular-prism Faraday cage design. (b) The directions of the ions after passing through the Faraday cage. (c) Schematic illustration of a conical Faraday cage design. (d) Illustration showing that the ions impinge on the sample from all directions after passing through the cage. (e) Fabrication procedure for a diamond nanobeam: (i) EBL defines an etch mask; (ii) the structure is etched top-down; (iii) the sample is placed in a triangular-prism Faraday cage and etched; (iv) the etch mask is removed.[41] Reprinted (adapted) with permission from Childress *et al*.[7] Copyright 2012 American Chemical Society.

plates. Owing to the nature of this process, diamond plates are often wedge-shaped, with a thickness variation of ~200 nm over the chip size. This needs to be taken into account when designing and fabricating nanophotonic devices. Next, the diamond sample is placed on either a sacrificial or a low-index substrate (silicon or silicon dioxide on silicon, for example) and etched in an oxygen plasma until the desired thickness (generally around hundreds of nanometers) is reached. The thinning is done by RIE using alternating cycles of O_2 and Ar/Cl_2 etching environments and Ar purging for cooling. The sample can then be used to generate

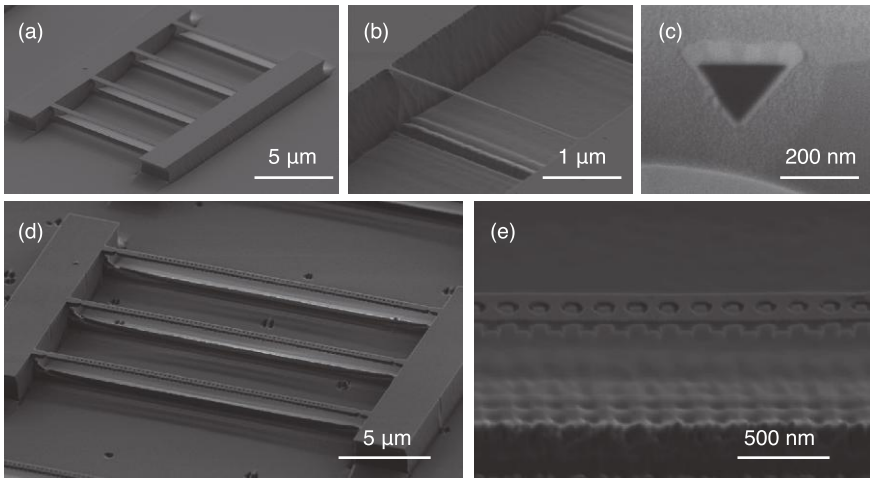

5.3 SEM images (taken at a 60° stage tilt) of (a) an array of diamond nanobeams, (b) a 75 nm wide nanobeam, and (c) a cross section of a 250 nm wide beam as sectioned by FIB. SEM images of (d) an array of diamond nanobeam cavities and (e) the cavity region.[41] Reprinted (adapted) with permission from Childress *et al*.[7] Copyright 2012 American Chemical Society.

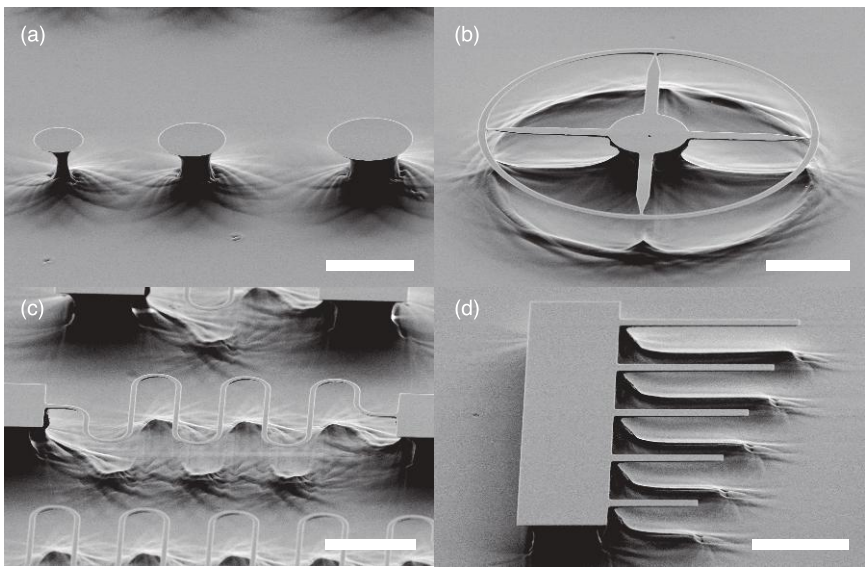

5.4 SEM images (taken at a 60° stage tilt) of (a) microdisks, (b) a nanoring, (c) meandering nanobeams and (d) cantilevers made by angled etching. The scale bars are 5 μm.[41] Reprinted (adapted) with permission from Childress *et al*.[7] Copyright 2012 American Chemical Society.

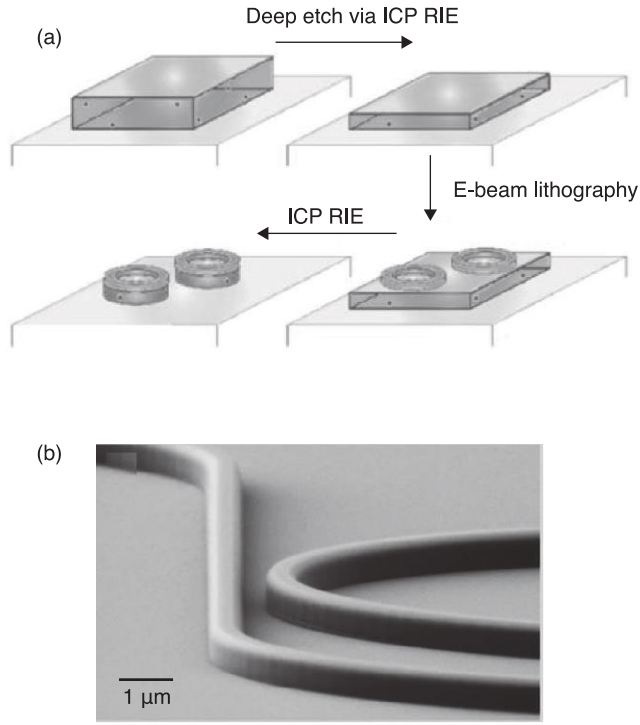

5.5 (a) To define planar devices on a low-index substrate, the fabrication involves the thinning of an 20 μm thick single-crystal diamond membrane by a deep etch down to the device thickness, and e-beam lithography to define mask patterns that are transferred to the diamond layer by RIE.[44] Reprinted with permission from Hausmann *et al.*[44] Copyright 2012 American Chemical Society. (b) Waveguide-coupled ring resonator fabricated in a thinned diamond film on a silica-on-silicon substrate.[45] Reprinted with permission from Hausmann *et al.*[45] Copyright 2013 American Chemical Society.

any planar structures required, such as waveguides, rings and racetrack resonators (Fig. 5.5(b)), and on-substrate and suspended photonic-crystal nanocavities.

5.3 Single-photon sources in nanostructured diamond: diamond nanowires and diamond–silver hybrid resonators

5.3.1 Diamond nanowires

As mentioned previously, a diamond nanowire provides efficient excitation and collection channels for single-photon emission by coupling a color center to the nanowire's waveguide mode. Three-dimensional finite-difference time-domain (FDTD) simulations of the far-field emission of NV centers in the bulk and optimally

placed in a diamond nanowire show that there is an order of magnitude increase in photon collection efficiency, with a similar degree of enhancement in pump efficiency (Plate I(a)) (see colour section between pages 218 and 219). The spectrally and polarization-averaged collection efficiency is ~30% for a microscope objective with a numerical aperture of 0.95 and the optimal nanowire dimensions (a diameter of ~200 nm and a height of ~2 μm). Nanowire devices were fabricated in both type Ib high-pressure high-temperature (HPHT)[24, 38] and ultrapure electronic-grade chemical-vapor-deposited (CVD)[39] diamond using the top-down nanofabrication procedure described in Section 5.2, which results in a high yield of working devices. Whereas type Ib diamond crystals are nitrogen-rich and contain random distributions of NV centers, the nitrogen concentration of CVD-grown diamond can be controlled during growth and be made very low. Then, NV incorporation can be done via ion implantation and annealing after the growth process. The density and depth of the defects can be controlled by selecting a suitable dose and energy of the nitrogen ions. With this latter approach, we can deterministically place single NV centers in an optimal longitudinal position along a diamond nanowire.

The first-generation diamond nanowires were fabricated in type Ib diamond and characterized in a 0.95 NA confocal microscope.[24] A confocal scan of an array of nanowire devices showed that many of the nanowires contained NV fluorescence (Plate I(b)). $g^{(2)}$ measurements were taken on the devices with a Hanbury Brown–Twiss (HBT) setup to identify single-NV-containing nanowires.[24] To evaluate the efficiency of a single-photon source, the photon count rate of a nanowire can be plotted as a function of pump power. This is done by subtracting the linear background signal from the overall count rate to extract the NV signal as a function of pump power, which is then fitted to the saturation model for the power-dependent intensity $I(P)$, $I(P)=I_{sat}/(1+P_{sat}/P)$, where I_{sat} and P_{sat} are the saturation intensity and power, respectively. A representative saturation curve is shown in Plate I(c). For the device shown, the background-subtracted intensity saturated at 168 000 counts per second and the pump power needed to saturate the NV center was 0.058 mW, corresponding to a tenfold improvement in both photon flux and pump power compared with the bulk. Such a comparison is shown for many single NV centers in the bulk and in nanowires in Plate I(d), and the results match well with FDTD modeling.

Diamond nanowires have also been fabricated in ultrapure, electronic-grade diamonds.[39] NV centers were introduced by ion implantation of ^{15}N (at an energy of 1.7 MeV, which corresponds to an implantation depth of around 1 μm) at a dose of ~10^9 cm^{-2} and annealing (at ~800 °C in high vacuum) either before or after the fabrication process. The high photon collection efficiency provided by the nanowire, along with the low background fluorescence of the starting material, allowed us to observe photon antibunching even at pump powers well above saturation. For instance, a $g^{(2)}(0)$ of around 0.1 was measured in the saturated regime without any background subtraction (Fig. 5.6(a)), which represents a more than a fivefold reduction compared with nanowire devices demonstrated in type Ib material (Fig. 5.6(b)).

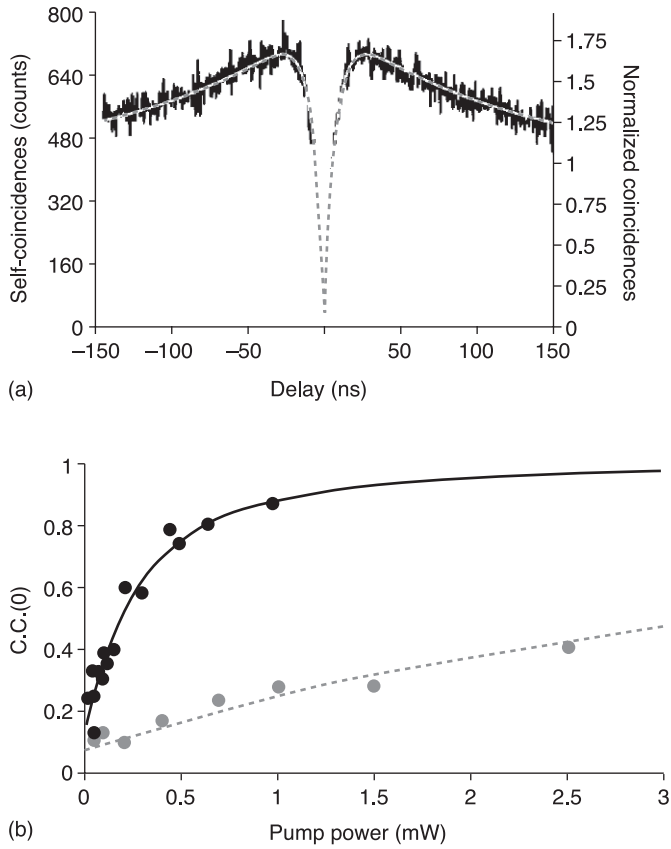

5.6 (a) $g^{(2)}$ of nanowire fluorescence, taken below saturation, showing that the device contains a single NV center.[39] Reprinted (adapted) with permission from Hausmann *et al.*[40] Copyright 2011 IOP Publishing and Deutsche Physikalische Gesellschaft. CC BY-NC-SA. (b) Normalized coincidence counts at zero time delay, $g^{(2)}(0)$, as a function of pump power for a single NV center in type Ib and electronic-grade diamond nanowires. The solid lines represent the expected coincidence counts, $1-\rho^2$, based on measured saturation data, where $\rho = S/(S+B)$, and S is the number of signal counts of the NV center and B is the number of background fluorescence counts. The analysis follows that of Beveratos *et al.*[18]

Moreover, the combination of the directionality of the emission (with the far-field emission mostly concentrated within a 30° angle for a dipole polarized perpendicular to the nanowire axis[38]) along with low background fluorescence in the diamond nanowire suggests that such a nanowire is suitable for photon collection in low-NA and nonconfocal systems. Indeed, we observed similar count rates ($I_{\text{sat}} \sim 10^5$) and antibunching behavior in a confocal microscope with a reduced

NA of 0.6. Finally, because of the purity of the material, it became possible to remove the pinhole filtering in the confocal system (previously achieved by focusing the collimated light into a single-mode fiber) and collect photons using a multimode fiber. This collection method provided us with another threefold increase in the collected single-photon emission, with a total photon count of $\sim 3.8 \times 10^5$ cps (from an initial I_{sat} of $\sim 1.3 \times 10^5$ cps) and $g^{(2)}(0)$ values of ~0.14.

5.3.2 Diamond–silver hybrid resonators

The nanowire geometry operates by coupling the NV center emission to a broadband waveguide mode. The intrinsic emission properties (such as the radiative decay rate) remain mostly unchanged. Indeed, the measured lifetime of an NV center in a diamond nanowire was ~13 ns, which is similar to that in the bulk and corresponds to a P_F of 1. Engineering the emission rate as well as the spectral profile of an NV center would require placing the emitter in an optical cavity. Broadband control of the NV center emission might be desirable in cases that require a high overall yield of single photons and a high repetition rate of the process, such as in optical readout of the electronic spin state of an NV center. For applications that require a large number of ZPL photons, narrowband resonators such as ring resonators and photonic-crystal cavities might be more suitable (Section 5.4.1).

A subwavelength diamond waveguide with silver (Ag) cladding supports guided modes that become tighter with decreasing radius. If the ends of the diamond–Ag waveguide are truncated, reflections between the facets of the aperture form broad resonances that can be tailored by changing the radius and height of the post that forms the waveguide.[46] Ag was chosen since it provides the lowest optical loss in the visible among all metals. However, it is also prone to oxidation under ambient conditions. To mitigate this problem, we chose a nanocavity design (Fig. 5.7(a)) consisting of cylindrical diamond nanoposts (with radius $r \sim 50$ nm and height $h \sim 180$ nm) embedded in a thick Ag film, which places the device layer away from the silver–air interface. Excitation and collection of the NV fluorescence were done through the bulk diamond crystal. Such structures support modes with mode volumes as small as $0.07(\lambda/n)^3$ and have resonances that are redshifted with increasing post radius. According to 3D FDTD simulations, spontaneous-emission-rate enhancements on the order of ~30 can be expected for a radially polarized NV center placed at the maximum field intensity in an optimized structure (Fig. 5.7(b)).

The hybrid diamond–metal device was fabricated[47] using the blanket ion implantation and top-down nanofabrication techniques described in Section 5.2. Two ultrapure bulk diamond crystals were used for this experiment. The samples were implanted with nitrogen ions (at an energy of 14 keV and a dose of 1.25×10^{12}/cm^2 for a 20 nm implant, and at 75 keV and 1.5×10^{11}/cm^2 for a 90 nm implant) and subsequently annealed under high vacuum to generate a dense layer of NV centers.

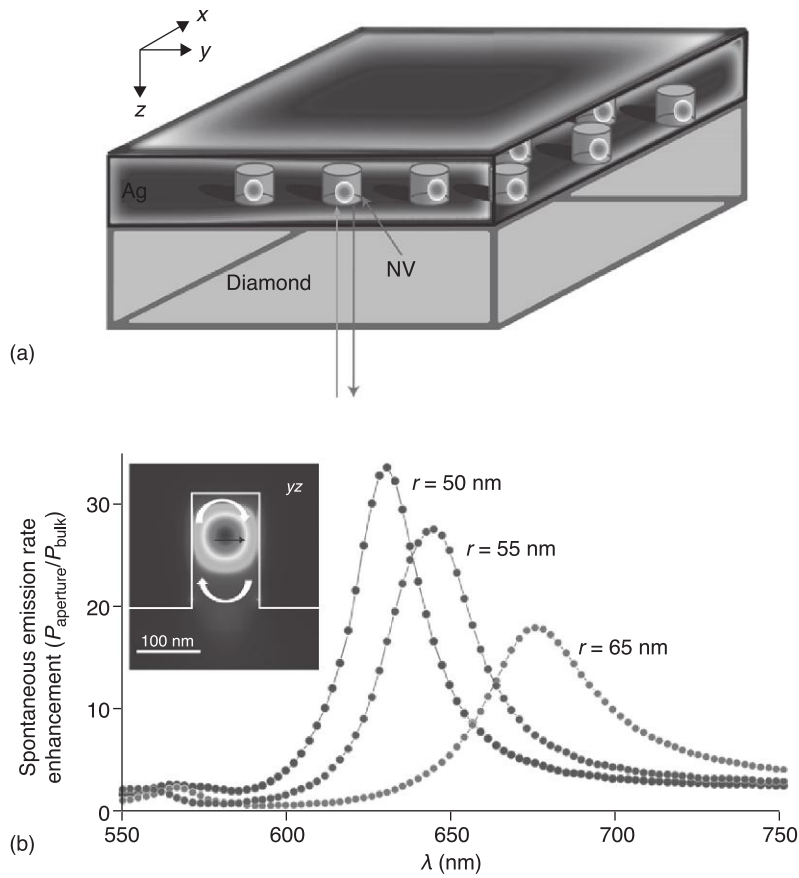

5.7 (a) Schematic illustration of a diamond–plasmonic system. The idealized structure for coupling to the NV emission consists of a diamond nanopost (with height ~180 nm and diameter ~100 nm) embedded in a 500 nm thick layer of silver (Ag). NV fluorescence is excited and collected through the bulk part of the diamond sample. (b) Simulated spontaneous-emission enhancement as a function of wavelength for nanoposts with different radii, calculated when the dipole was placed at the field maximum. Inset: cross-sectional view of the structure in the *YZ* plane, along with the longitudinal mode profile. The dipole is shown to be radially polarized and positioned in the field maximum.[47]

Arrays of diamond nanoposts of radii from 50 to 70 nm and height ~180 nm were then fabricated using EBL followed by a 1 minute oxygen dry etch. An SEM image of an array of nanoposts taken before silver deposition is shown in Fig. 5.8(a). Optical characterization indicated that many of the nanoposts within an array emitted NV fluorescence under excitation (Fig. 5.8(b)), with some (>10%) showing antibunching below $g^{(2)}=0.5$.

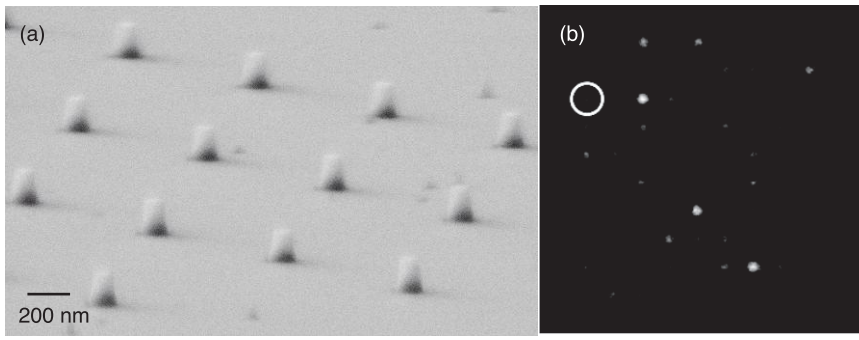

5.8 (a) Scanning electron microscope image of a representative array of diamond posts. (b) Confocal microscope scan of an array of $r \sim 65$ nm posts before Ag deposition. The spacing between adjacent posts is 2 μm. The circled post was confirmed to contain a single NV center. $g^{(2)}$ curves taken on posts of similar intensity also showed antibunching.[47]

A 500 nm thick Ag film could then be deposited on the nanoposts by electron beam evaporation. $g^{(2)}$ measurements were performed on devices that had previously been characterized before the metal deposition, and only single-photon-emitting devices were considered. A comparison of fluorescence decays measured for a representative device before and after Ag deposition is shown in Fig. 5.9(a). The fitted NV lifetimes are 37.17 ns for the bare post, 5.65 ns after it was embedded in Ag and 16.7 ns in the bulk. For the 90 nm implant sample, lifetimes as short as 2.4 ns were measured, corresponding to roughly a sixfold decrease over the bulk lifetimes and over tenfold in comparison with the bare nanopost lifetimes, which were prolonged by the reduced optical density of states in the structure. Photoluminescence spectra of single NV centers in the Ag–diamond apertures showed broad resonances ($Q \sim 10$) with peak wavelengths between 670 and 720 nm (Fig. 5.9(b)), which overlap with the phonon sideband of the NV center emission.

To illustrate the overall performance improvement, the saturation intensity was plotted against the lifetime for a number of devices in the bare and Ag-capped cases for the two implantation depths. Figure 5.10(a) shows that the lifetime reduction was accompanied by a comparable increase in the photon count rate, so that the observed plasmonic enhancement can be attributed to radiative processes.

The deviations of the observed Purcell enhancements from the predicted values (up to 30) can be attributed to geometric effects, a suboptimal implantation depth and straggling, and the emitter spectrum, as well as ambiguity in the polarization angle of the dipole moment due to the [100] orientation of the crystal. In particular, the peak emission enhancement was calculated to be reduced by about 40% from the straight-sidewall case for an 85° sidewall angle, which matches well with the

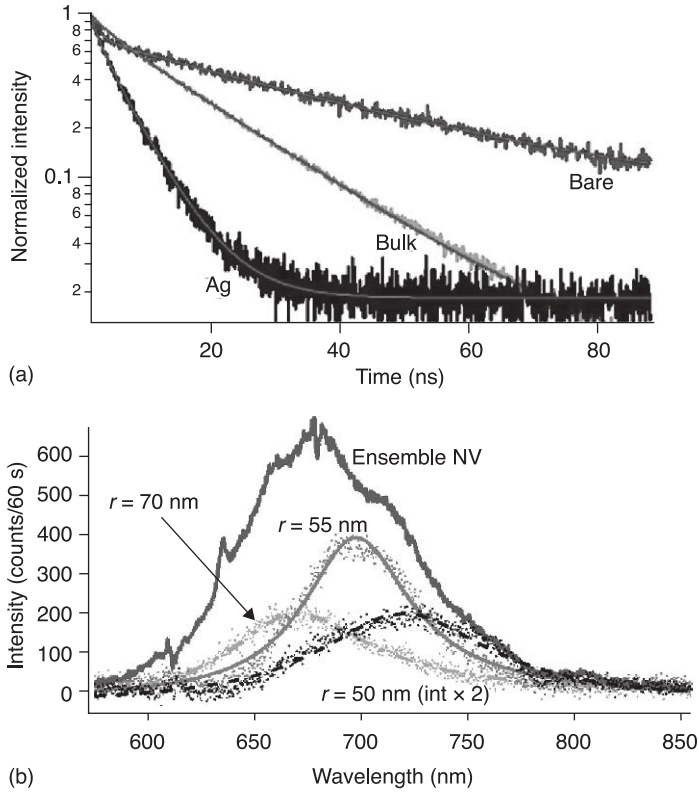

5.9 (a) Normalized fluorescence decays for the same nanopost, containing a single NV center, before and after Ag deposition and for an ensemble population of NV centers in the bulk region, along with fits to an exponential model (smooth lines). (b) Background-subtracted photoluminescence spectra of Ag-coated nanoposts (with different radii *r* from 50 to 70 nm) in the 90 nm implant sample, along with a reference NV center spectrum taken from an ensemble of NV centers in an Ag-covered, unstructured region of the sample. Dotted lines represent the fits to the raw data (dots). The *r*=50 nm device was integrated for twice as long.[47]

experimentally obtained values. The photon yield wan our system is modest (with count rates between the high 10^4 and low 10^5 cps ranges). In addition to TIR at the bottom diamond–air interface, the photon losses in the system could be attributed to coupling of emitted photons to surface plasmons, which propagated laterally on the diamond–silver surface and could not be collected. This suggests that further structure optimization, such as the addition of gratings (Fig. 5.10(b)),[48] might be necessary to increase the number of collected photons.

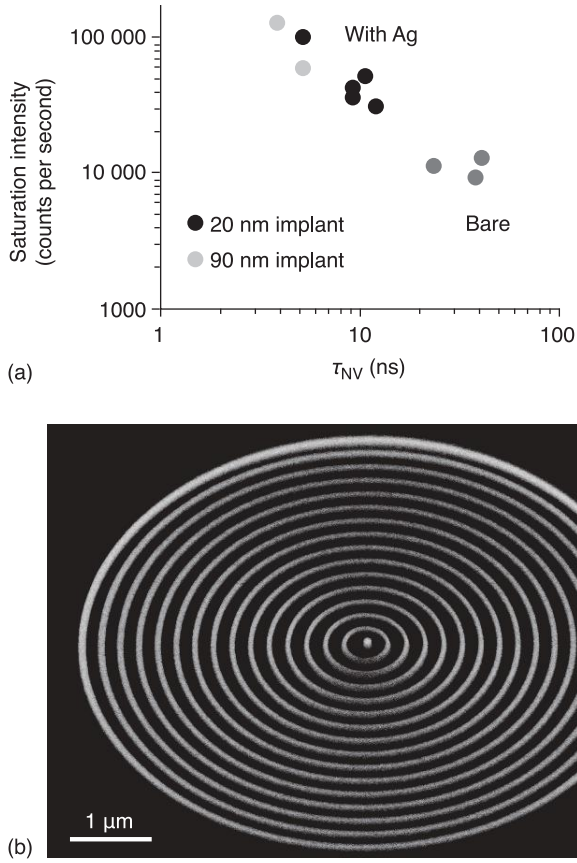

5.10 (a) Performance plot of saturation intensity as a function of fluorescence lifetime for the bare and Ag-capped devices that we tested in this study, showing that the plasmonic enhancement provided by the geometry led to shorter lifetimes and correspondingly higher count rates.[47] (b) SEM image of a diamond nanopost surrounded by SiO_2 rings that can be used to form plasmonic gratings by molding the silver film deposited on top.

5.4 Single-photon sources in nanostructured diamond: integrated ring resonators and photonic-crystal cavities

5.4.1 Integrated ring resonators

Both nanowire and nanoaperture cavity platforms are tailored to applications requiring free-space out-coupling of photons. However, for the realization of scalable systems for quantum information processing, it is of interest to keep the information carriers (photons) on-chip and take advantage of chip-scale integrated

nanophotonics for information routing. Furthermore, for these applications it is important to enhance the percentage of photons emitted into the NV center's ZPL. To address this, we have recently developed a single-crystal thin-diamond-film technology – diamond on insulator (DOI) – and used it to demonstrate single-photon routing in a ring resonator coupled to a low-loss waveguide with gratings at its ends (Fig. 5.11(a)).[44] The waveguide contained a second-order grating at each end to facilitate free-space coupling of photons. The structures were characterized by coupling light from a broadband white light source into one grating and collecting transmitted light from the other grating. The transmission spectrum shows regularly spaced dips corresponding to the different (longitudinal) resonant modes of the 5 μm ring resonator (Fig. 5.11(b)), which have quality (Q) factors up to 3200. For a larger ring with a diameter of 20 μm, Q factors as high as

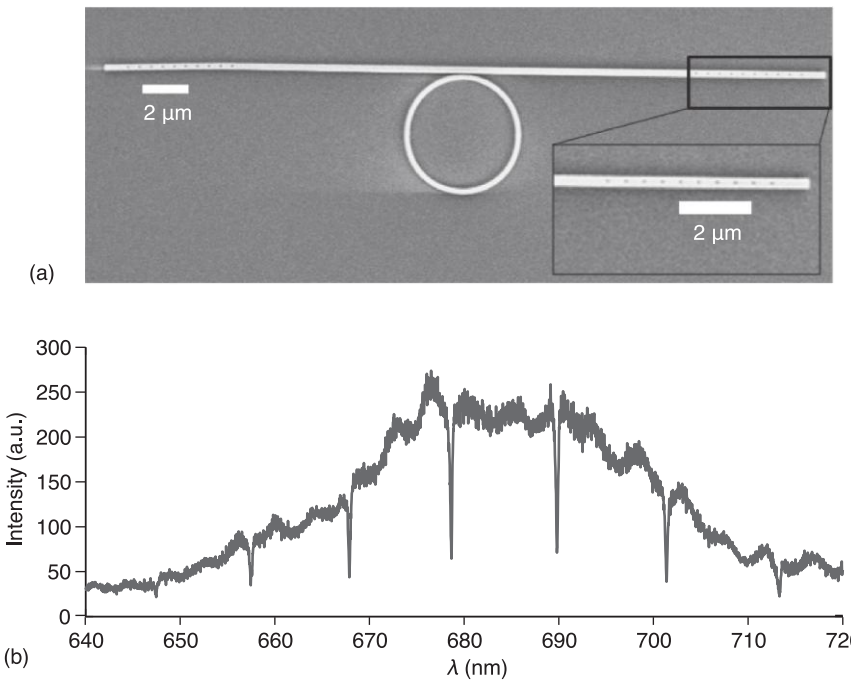

5.11 (a) SEM image of a waveguide-coupled diamond ring resonator on a silica/Si substrate. To efficiently couple light in and out of the device, grating couplers are implemented at the ends of the waveguide (see inset). (b) Transmission spectrum obtained by exciting the structure with white light (from a super-continuum source) using the grating at one end, and measuring the transmitted signal using the grating at the other end. The dips in transmission correspond to the ring resonator modes, which have Q factors up to 3200.[44] Reprinted (adapted) with permission from Hausmann *et al.*[44]. Copyright 2012 American Chemical Society.

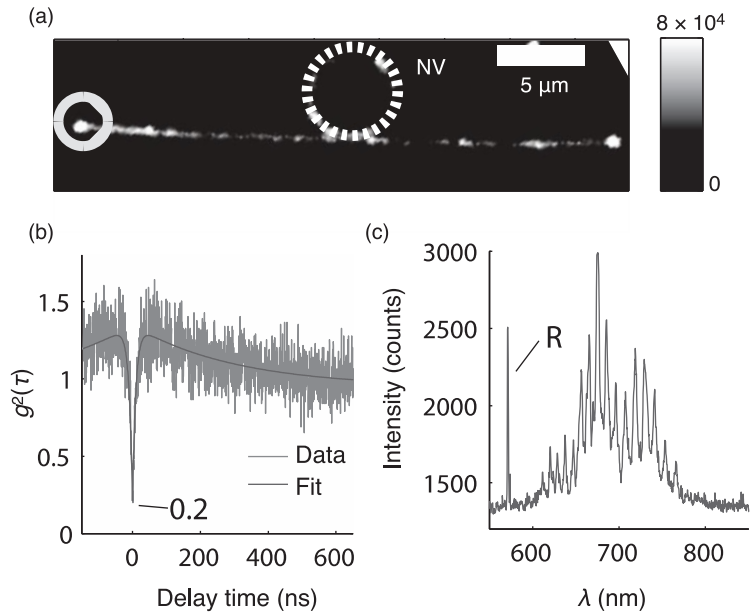

5.12 (a) Confocal image of a ring resonator, and (b) second-order cross-correlation $g^{(2)}(\tau)$ between photons collected directly above an NV center inside the ring resonator (circled with dashed line) and the routed single-photon stream at the end of the waveguide (circled with solid line). A strong antibunching dip ($g^{(2)}(0)<0.5$), characteristic of single-photon statistics, can be seen. (c) The spectrum collected at the gratings shows periodic modes superimposed on the NV center's emission. 'R' represents the Raman signal.[44] Reprinted (adapted) with permission from Hausmann *et al*.[44] Copyright 2012 American Chemical Society.

12 000 were extracted, which is consistent with the scaling of Q with the resonator length. Single-photon emission from a single NV center embedded inside a ring (circled with a dashed line in Fig. 5.12(a)) and on-chip waveguiding of single photons were also confirmed by cross-correlation measurements (Fig. 5.12(b)) between the photon streams above the NV center and at the end of the waveguide.

5.4.2 Photonic-crystal cavities

We used similar techniques to make small-mode-volume suspended photonic-crystal cavities in nanobeams that were capable of enhancing the spontaneous photon emission in the ZPL of single NV centers.[49] The devices were fabricated in type IIa CVD diamond with naturally occurring NV centers that had relatively good spectral properties, with ZPLs down to 4 GHz.[50] The fabricated devices are depicted in Fig. 5.13. The diamond nanobeams were fabricated on a silicon

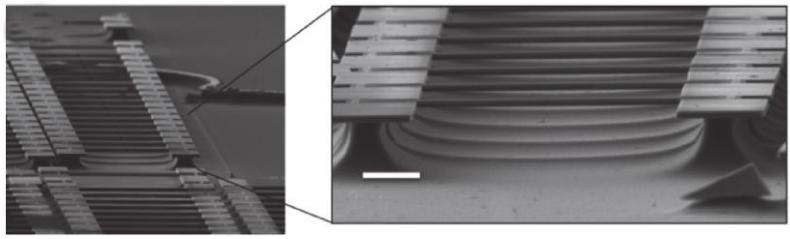

5.13 SEM images of arrays of 1D diamond suspended photonic-crystal nanobeams, fabricated on a thinned diamond film on a silicon substrate. The beams were undercut using isotropic RIE for silicon; the pads at the ends of the beams are used for support.[49]

substrate, and the devices were released from the substrate using an isotropic RIE recipe for silicon. The cavities had Q factors up to 6000, as verified in transmission measurements with white-light excitation, and mode volumes in the range of $2–3.5(\lambda/n)^3$.

Imperfections in fabrication and film thickness variations can lead to initially red-detuned modes with respect to the ZPL. To overcome this, we developed postfabrication tuning techniques based on etching of diamond material. Tuning was done in one of two ways: etching in an RF plasma reactor under an oxygen flow rate of 20 sccm, or oxidation by rapid thermal annealing at 465 °C in an oxygen environment. The etch time was varied for both methods, and the resulting blue-shifting of the cavity mode was measured for several cavities after each etch step. Representative results for a cavity with a modest Q factor of ~1100 are shown in Plate II. By varying the duration of the etch, the resonances could be tuned in steps ranging from 0.2 to 5.3 nm. Overall, the plasma-etching approach provided more reproducible etch rates than does oxidation. In total, the cavity mode could be shifted over a range of 23 nm without deterioration of the Q factor. When the mode was shifted to the blue and close to the ZPL, we could reversibly red-tune it over the ZPL, using injection of Xe gas in a cryogenic chamber,[49, 50] to infer the fluorescence enhancement in the ZPL emission. With this technique, a ZPL fluorescence enhancement of 7 could be achieved (data not shown).

5.5 Conclusions and future trends

The diamond photonic devices discussed in this chapter are aimed at improving the photon collection and/or production efficiency. The diamond nanowire geometry provides an order-of-magnitude improvement in both the pump and the single-photon collection efficiency for single NV centers in comparison with centers in the bulk, with count rates greater than 3×10^5 cps. Single-NV-center-containing nanowires can be fabricated by top-down nanofabrication on both nitrogen-rich

type Ib diamond and, combined with ion implantation techniques, on ultrapure electronic-grade diamond. The top-down approach has provided a very high yield of working devices per fabrication run. We have also shown that the devices are compatible with low-NA and nonconfocal systems, owing to the fact that a nanowire emits into a small angular cone, so the device can potentially be integrated directly with a fiber without the need for bulky optics. The nanowire geometry has already found an application in the construction of a sensitive scanning near-field and magnetic-field sensor.[5] It has also been used in the discovery of a second NV-like emitter in diamond, showing optical initialization and readout of a single spin at room temperature at the level of a single color center.[51]

To modify the spontaneous emission rate of the NV center, the emitter can be made to interact with a cavity in the weak-coupling regime. Owing to the small fraction of emission into the ZPL, for applications that require a large number of photons in the ZPL, a narrowband cavity such as a ring resonator or a photonic-crystal cavity would be suitable. Despite material and fabrication challenges, these devices can be made with high quality in single-crystal diamond that has been thinned down to optical thickness using reactive-ion etching, suggesting the feasibility of this approach for developing chip-scale diamond quantum photonic networks. Diamond planar resonators are also promising for reaching the strong-coupling limit. Similarly, the angled-etching technique can be used to make three-dimensional structures, including planar devices that include the resonators described above. Together, these fabrication procedures have enabled a host of devices that can expand the potential applications of diamond photonics to nanomechanics,[17] sensing[14, 15] and nonlinear optics.[16]

For example, to leverage diamond's wide transparency window and demonstrate that an integrated photonics system can be coupled to optical fibers on- and off-chip, we constructed a fully integrated network consisting of diamond waveguide-coupled ring (and racetrack) resonators that operated in the telecommunication wavelength range, with Q factors as high as 250 000.[45] In addition to designing and fabricating integrated resonators according to the technique described earlier, polymer in- and out-coupling pads consisting of SU-8 were defined in a second e-beam lithography step to extend the adiabatically tapered diamond waveguides to both ends of the sample. Two lensed fibers were then used to couple light into and out of the cleaved and polished facets of the device. An outline of the experimental setup and the butt-coupling technique are depicted in Fig. 5.14(a); they are described in more detail elsewhere.[52] Figure 5.14(b) shows an SEM image of some racetrack resonators before the pads were defined. A transmission spectrum of such a complete integrated device is shown in Fig. 5.14(c), which reveals periodic resonator modes.

We have designed and implemented diamond–silver apertures to enhance the spontaneous emission of single NV centers. This geometry is intended to provide a broadband alternative to narrowband cavities with a higher tolerance for wavelength mismatch between the cavity and the NV emission, so that no tuning

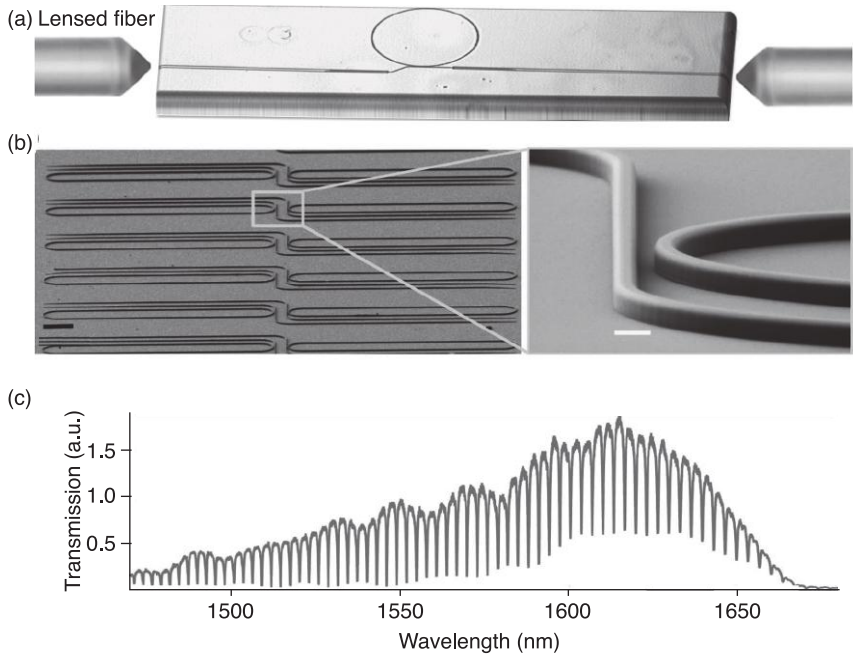

5.14 (a) Schematic illustration of the transmission measurement setup. An optical image of a diamond ring resonator next to a diamond waveguide is shown, along with SU-8 pads extending the diamond waveguides to the end of the chip. Lensed fibers are used for coupling light in and out of the device. (b) SEM micrograph of an array of diamond racetrack resonators (330 μm long) coupled to diamond waveguides. The coupling polymer pads are not shown here. Inset: close-up of the waveguide–resonator coupling region. The height, width and gap size of the devices are in the range of 600–700 nm, 550–650 nm and 450–500 nm, respectively. (c) Transmission spectrum obtained from a 314 μm long racetrack resonator. *Q* factors of up to 250 000 (not shown in this spectrum) were achieved.[45] Reprinted (adapted) with permission from Hausmann *et al.*[45] Copyright 2013 American Chemical Society.

mechanism is necessary. While the devices demonstrated so far enhance mostly the phonon sideband of the NV center, smaller apertures may be used for enhancement of the ZPL. Another potential application of this platform is to provide improved, faster optical readout for NV-center-based magnetometry. Here, a long spin coherence time is needed, which remains to be measured experimentally.

Despite the large photon count rates (10^5–10^6 cps) and the ability to make multiple devices in parallel, identical photons are needed for some entanglement schemes between distant NV centers, such that the emission into the ZPL needs

to be stable and sufficiently narrow (lifetime-limited). Meanwhile, the NV centers used in our devices were implanted and the emitters are in close proximity to the diamond surface, suggesting that they might be more susceptible to surface effects that could contribute to spectral diffusion at low temperature. Towards this end, various approaches are currently being investigated to mitigate spectral diffusion in nanostructures, including optimization of the etch recipe and control of surface termination. Furthermore, techniques such as repumping by a yellow laser[53] and external feedback control[54] can be implemented. Finally, while the work presented here has focused on the NV center, the structures can be scaled to interact with other promising color centers closer to the near infrared region.[55–57]

5.6 Acknowledgments

We would like to thank all contributors to the work summarized here: Y. Zhang, M. Khan, M. McCutcheon, Q. Quan, I. Bulu, K. Martinick, K. Smith, J. Maze, A. Kubanek, B. Shields, Y. Chu, N. de Leon, R. Evans, A. Zibrov, P. Hemmer, S. Hong, P. Maletinsky, H. Park, A. Yacoby and M. Lukin. We thank D. Twitchen and M. Markham from Element Six for their support and for providing samples. We also thank F. Huber, E. Togan, F. Jelezko, M. Grinolds, C. L. Yu, O. Bakr, K.P. Chen, V. Shalaev, P. Deotare and H. Atikian for their help. Devices were fabricated in the Center for Nanoscale Systems (CNS) at Harvard. J.T.C. acknowledges support from the National Science Foundation (NSF) graduate student fellowship. B.J.M.H. gratefully acknowledges support from the Harvard Quantum Optics Center (HQOC). M.J.B. is supported in part by the Natural Science and Engineering Council (NSERC) of Canada. T.M.B. acknowledges support from NSF and National Defense Science and Engineering Graduate (NDSEG) student fellowships. M. Lončar acknowledges support from the Sloan Foundation. This work was supported in part by the Defense Advanced Research Projects Agency (QuEST, QuASAR and QuINESS programs), Harvard University's Nanoscale Science and Engineering Center (NSEC), an NSF Nanotechnology and Interdisciplinary Research Team grant (ECCS-0708905), the King Abdullah University of Science and Technology Faculty Initiated Collaboration Award (FIC/2010/02), and AFOSR MURI (grant FA9550-12-1-0025).

5.7 References

1. Dutt, M. V. G., Childress, L., Jiang, L., Togan, E., Maze, J. *et al.* Quantum register based on individual electronic and nuclear spin qubits in diamond. *Science* **316**, 1312 (2007).
2. Neumann, P., Beck, J., Steiner, M, Rempp, F., Fedder, H. *et al.* Single-shot readout of a single nuclear spin. *Science* **329**, 542 (2010).
3. Robledo, L., Childress, L., Bernien, H., Hensen, B., Alkemade, P. F. A. *et al.* High-fidelity projective read-out of a solid-state spin quantum register. *Nature* **477**,

574–578, http://www.nature.com/nature/journal/v477/n7366/abs/nature10401.html, supplementary information (2011).
4. Maurer, P. C., Kucsko, G., Latta, C., Jiang, L., Yao, N. Y. *et al.* Room-temperature quantum bit memory exceeding one second. *Science* **336**, 1283 (2012).
5. Bernien, H., Childress, L., Robledo, L., Markham, M., Twitchen, D. *et al.* Two-photon quantum interference from separate nitrogen vacancy centers in diamond. *Phys. Rev. Lett.* **108**, 043604 (2012).
6. Bernien, H., Hensen, B., Pfaff, W., Koolstra, G., Blok, M. S. *et al.* Heralded entanglement between solid-state qubits separated by three metres. *Nature* **497**, 86–90, doi:10.1038/nature12016, http://www.nature.com/nature/journal/v497/n7447/abs/nature12016.html, supplementary information (2013).
7. Childress, L., Taylor, J. M., Sorensen, A. S. and Lukin, M. D. Fault-tolerant quantum repeaters with minimal physical resources and implementations based on single-photon emitters. *Phys. Rev. A* **72**, 052330 (2005).
8. Balasubramanian, G., Neumann, P., Twitchen, D., Markham, M., Kolesov, R. *et al.* Ultralong spin coherence time in isotopically engineered diamond. *Nature Mater.* **8**, 383–387 (2009).
9. Gaebel, T., Domhan, M., Popa, I., Wittman, C., Neumann, P. *et al.* Room-temperature coherent coupling of single spins in diamond. *Nature Phys.* **2**, 408–413 (2006).
10. Jiang, L., Hodges, J. S., Maze, J. R., Maurer, P., Taylor, J. M. *et al.* Repetitive readout of a single electronic spin via quantum logic with nuclear spin ancillae. *Science* **326**, 267–272 (2009).
11. Togan, E., Chu Y., Trifonov, A. S., Jiang, L., Maze, J. *et al.* Quantum entanglement between an optical photon and a solid-state spin qubit. *Nature* **466**, 730–734 (2010).
12. Maze, J. R., Stanwix, P. L., Hodges, J. S., Hong, S., Taylor, J. M. *et al.* Nanoscale magnetic sensing with an individual electronic spin in diamond. *Nature* **455**, 644–648 (2008).
13. Balasubramanian, G., Chan, I. Y., Kolesov, R., Al-Hmoud, M., Tisler, J. *et al.* Nanoscale imaging magnetometry with diamond spins under ambient conditions. *Nature* **455**, 648–651 (2008).
14. Maletinsky, P., Hong, S., Grinolds, M. S., Hausmann, B., Lukin, M. D. *et al.* A robust scanning diamond sensor for nanoscale imaging with single nitrogen–vacancy centres. *Nature Nanotechnol.* **7**, 320–324 (2012).
15. Kucsko, G., Maurer, P. C., Yao, N. Y., Kubo, M., Noh, H. J. *et al.* Nanometer scale quantum thermometry in a living cell. *Nature* **500**, 54–58 (2013).
16. Mildren, R. P., Butler, J. E. and Rabeau, J. R. CVD-diamond external cavity Raman laser at 573 nm. *Opt. Express* **16**(23), 18950 (2008).
17. Ovartchaiyapong, P., Pascal, L., Myers, B., Lauria, P. and Jayich, A. B. High quality factor single-crystal diamond mechanical resonators. *Appl. Phys. Lett.* **101**, 163505 (2012).
18. Beveratos, A., Brouri, R., Gacoin, T., Poizat, J.-P. and Grangier, P. Nonclassical radiation from diamond nanocrystals. *Phys. Rev. A* **64**, 061802(R) (2001).
19. Englund, D., Shields, B., Rivoire, K., Hatami, F., Vuckovic, J. *et al.* Deterministic coupling of a single nitrogen vacancy center to a photonic crystal cavity. *Nano Lett.* **10**, 3922–3926 (2010).
20. van der Sar, T, Hagemeier, J., Pfaff, W., Heeres, E. C., Thon, S. M. *et al.* Deterministic nano-assembly of a coupled quantum emitter–photonic crystal cavity system. *Appl. Phys. Lett.* **98**, 193103 (2011).
21. Schietinger, S., Barth, M., Aichele, T. and Benson, O. Plasmon enhanced single photon emission from a nanoassembled metal–diamond hybrid structure at room temperature.

Nano Lett. **9**(4), 1694–1698 (2009).
22. Beveratos, A., Brouri, R., Gacoin, T., Villing, A., Poizat, J.-P. *et al.* Single photon quantum cryptography. *Phys. Rev. Lett.* **89**, 187901 (2002).
23. Childress, L., Gurudev Dutt, M. V., Zibrov, A. S., Jelezko, F., Wrachtrup, J. *et al.* Coherent dynamics of coupled electron and nuclear spin qubits in diamond. *Science* **314**, 281–285 (2006).
24. Babinec, T., Hausmann, B. J. M., Khan, M., Zhang, Y., Maze, J. R. *et al.* A diamond nanowire single photon source. *Nature Nanotechnol.* **5**, 195–199 (2010).
25. Hadden, J. P., Harrison, J. P., Stanley-Clarke, A. C., Marseglia, Ho, Y.-L. D. *et al.* Strongly enhanced photon collection from diamond defect centres under microfabricated integrated solid immersion lenses. *Appl. Phys. Lett.* **97**, 241901 (2010).
26. Siyushev, P., Kaiser, F., Jacques, V., Gerhardt, I., Bischof, S. *et al.* Monolithic diamond optics for single photon detection. *Appl. Phys. Lett.* **97**, 241902 (2010).
27. Schröder, T., Gädeke, F., Banholzer, M. J. and Benson, O. Ultrabright and efficient single-photon generation based on nitrogen–vacancy centres in nanodiamonds on a solid immersion lens. *New J. Phys.* **13**, 055017 (2011).
28. Babinec, T. M., Hausmann, B. J. M., Choy, J. T., Khan, M., Hemmer, P. R. *et al.* Quantum photonics with diamond. *IEEE Photon. Soc. Newsl.* **25**, 13–18 (2011).
29. Santori, C., Barclay, P. E., Fu, K.-M. C., Beausoleil, R. G., Spillane, S. *et al.* Nanophotonics for quantum optics using nitrogen–vacancy centers in diamond. *Nanotechnology* **21**, 274008 (2010).
30. Vuckovic, J., Sanori, C., Fattal, D., Pelton, M., Solomon, G. *et al.* Cavity-enhanced single photons from a quantum dot, in *Optical Microcavities* (ed. K. Vahala) (World Scientific, 2004).
31. Olivero, P. *et al.* Ion-beam-assisted lift-off technique for three-dimensional micromachining of freestanding single-crystal diamond. *Adv. Mater.* **17**, 2427–2430 (2005).
32. Aharonovich, I., Lee, J. C., Magyar, A. P., Buckley, B. B., Yale, C. G. *et al.* Homoepitaxial growth of single crystal diamond membranes for quantum information processing. *Adv. Mater.* **24**, OP54–OP59 (2012).
33. Magyar, A. P., Lee, J. C., Limarga, A. M., Aharonovich, I., Rol, F. *et al.* Fabrication of thin, luminescent, single-crystal diamond membranes. *Appl. Phys. Lett.* **99**, 081913 (2011).
34. Babinec, T., Choy, J. T., Smith, K., Khan, M. and Loncar, M. Design and focused ion beam fabrication of single crystal diamond nanobeam cavities. *J. Vac. Sci. Technol. B* **29**, 010601 (2011).
35. Bayn, I., Meyler, B., Salzman, J. and Kalish, R. Triangular nanobeam photonic cavities in single-crystal diamond. *New J. Phys.* **13**, 025018 (2011).
36. Bayn, I., Bolker, A., Cytermann, C., Meyler, B., Richter, V. *et al.* Diamond processing by focused ion beam – surface damage and recovery. *Appl. Phys. Lett.* **99**, 183109 (2011).
37. Riedrich-Möller, J., Kipfstuhl, L., Hepp, C., Neu, E., Pauly, C. *et al.* One-and two-dimensional photonic crystal microcavities in single crystal diamond. *Nature Nanotechnol.* **7**, 69–74 (2011).
38. Hausmann, B. J. M., Khan, M., Babinec, T. M., Zhang, Y., Martinick, K. *et al.* Fabrication of diamond nanowires for quantum information processing applications. *Diamond Relat. Mater.* **19**, 621 (2010).

39. Hausmann, B. J. M., Babinec, T. M., Choy, J. T., Hodges, J. S., Hong, S. *et al.* Single color centers implanted in diamond nanostructures. *New J. Phys.* **13**, 045004 (2011).
40. Hausmann, B. J. M., Choy, J. T., Babinec, T. M., Shields, B. J., Bulu, I. *et al.* Diamond nanophotonics and applications in quantum science and technology. *Phys. Status Solidi A* **209**, 1619–1630 (2012).
41. Burek, M. J., de Leon, N. P., Shields, B. J., Hausmann, B. J. M., Chu, Y. *et al.* Free-standing mechanical and photonic nanostructures in single-crystal diamond. *Nano Lett.* **12**, 6084–6089 (2012).
42. Boyd, G., Coldren, L. and Storz, F. Directional reactive ion etching at oblique angles. *Appl. Phys. Lett.* **36**, 583–585 (1980).
43. Lee, J.-K., Lee S.-H., Min, J.-H., Jang, I.-Y., Kim, C.-K. *et al.* Oblique-directional plasma etching of Si using a Faraday cage. *J. Electrochem. Soc.* **156**, D222–D225 (2009).
44. Hausmann, B. M., Shields, B., Quan, Q., Maletinsky, P., McCutcheon, M. *et al.* Integrated diamond networks for quantum nanophotonics. *Nano Lett.* **12**, 1578 (2012).
45. Hausmann, B. J., Bulu, I., Deotare, P. B., McCutcheon, M. W., Venkataraman, V. *et al.* Integrated high quality factor optical resonators in diamond. *Nano Lett.* **13**, 1898–1902 (2013).
46. Bulu, I., Babinec, T., Hausmann, B., Choy, J. T. and Loncar, M. Plasmonic resonators for enhanced diamond NV^- center single photon sources. *Opt. Express* **19**, 5268–5276 (2011).
47. Choy, J. T., Hausmann, B. J. M., Babinec, T. M., Bulu, I., Khan, M. *et al.* Enhanced single photon emission from a diamond–silver aperture. *Nature Photon.* **5**, 738–743 (2011).
48. Choy, J. T., Bulu, I., Hausmann B. J. M., Janitz E., Huang, I., and Loncar, M. Spontaneous emission and collection efficiency enhancement of single emitters in diamond via plasmonic cavities and gratings. *Appl. Phys. Lett.* **103**, 161101 (2013).
49. Hausmann, B. J. M., Shields, B. J., Quan, Q., Chu, Y., de Leon, N. P. *et al.* Coupling of NV centers to photonic crystal nanobeams in diamond. *Nano Lett.*, **13**, 5791–5796 (2013).
50. Faraon, A., Santori, C., Huang, Z., Acosta, V. M. and Beausoleil, R. G. Coupling of nitrogen–vacancy centers to photonic crystal cavities in monocrystalline diamond. *Phys. Rev. Lett.* **109**, 033604 (2012).
51. Lee, S.-Y., Widmann, M., Rendler, T., Doherty, M., Babinec, T. M. *et al.* Readout and control of a single nuclear spin with a meta-stable electron spin ancilla. *Nature Nanotechnol.* **8**, 487 (2013).
52. Deotare, P. B., Bulu, I., Frank, I. W., Quan, Q., Zhang, Y. *et al.* All optical reconfiguration of optomechanical filters. *Nature Commun.* **3**, 846 (2012).
53. Siyushev, P., Pinto, H., Gali, A., Jelezko, F. and Wrachtrup, J. Low temperature studies of charge dynamics of nitrogen–vacancy defect in diamond. *Phys. Rev. Lett.* **110**, 167402 (2013).
54. Acosta, V., Santori, C., Faraon, A., Huang, Z., Fu K.-M. C. *et al.* Dynamic stabilization of the optical resonances of single nitrogen–vacancy centers in diamond. *Phys. Rev. Lett.* **108**, 206401 (2012).
55. Neu, E., Steinmetz, D., Riedrich-Möller, J., Gsell, S., Fischer, M. *et al.* Single photon emission from silicon–vacancy colour centres in chemical vapour deposition nano-diamonds on iridium. *New J. Phys.* **13**, 025012 (2011).

56. Aharonovich, I., Castelletto, S., Simpson, D. A., Stacey, A., McCallum, J. *et al.* Two-level ultrabright single photon emission from diamond nanocrystals. *Nano Lett.* **9**(9), 3191 (2009).
57. Gaebel, T., Popa, I., Gruber, M., Domhan, M., Jelezko, F. *et al.* Stable single-photon source in the near infrared. *New J. Phys.* **6**, 98 (2004).

This page intentionally left blank

Part II

Experimental demonstrations and emerging applications of quantum information processing (QIP) using diamond

This page intentionally left blank

6

Diamond-based single-photon sources and their application in quantum key distribution

E. NEU, Universität des Saarlandes, Germany and University of Basel, Switzerland and C. BECHER, Universität des Saarlandes, Germany

DOI: 10.1533/9780857096685.2.127

Abstract: This chapter introduces solid-state single-photon sources based on single colour centres in diamond. Following an introduction to the applications of single-photon sources, we discuss the basic principles of their operation. We summarize the key parameters for characterizing a single-photon source and comment on diamond as a host material for single emitters. The main part of the chapter contains an extensive discussion of the various colour centres in diamond that have been investigated as single-photon sources, followed by a look at future prospects. In the final part of the chapter, we summarize the implementations of quantum key distribution with diamond-based single-photon sources and discuss the results.

Key words: colour centre, diamond, single-photon source, photon correlation, population dynamics, quantum key distribution.

6.1 Introduction

A single-photon source is a light source which, ideally, upon a trigger signal, emits a light field described by a photon number state or Fock state with a single excitation, i.e. a single photon. Real single-photon sources often deviate from this ideal situation in various respects: the probability of collecting and detecting a photon from the source is often much smaller than 1; the source emits light into a superposition of spectral and spatial modes instead of into a well-defined single spatio-temporal mode; within the temporal detection window, the source might emit more than one photon owing to re-excitation processes or less than one photon owing to finite internal quantum efficiencies; and there are many more deviations from the ideal situation. During recent years there has been much effort to realize single-photon sources as close to the ideal as possible, and many physical systems have been investigated for their suitability as single-photon sources, for example single molecules, single semiconductor quantum dots, single trapped atoms and ions, and single colour centres in diamond, just to name the most important. An extensive overview of the field has been given in several recent reviews (Lounis and Orrit, 2005; Oxborrow and Sinclair, 2005; Scheel, 2009; Santori *et al.*, 2010; Buller and Collins, 2010; Eisaman *et al.*, 2011;

© 2014 Elsevier Ltd

Aharonovich *et al.*, 2011b). In the following sections, we present some of the key principles and parameters of single-photon sources and give an overview of the current state of the art for diamond-based single-photon sources.

6.1.1 Applications of single-photon sources

Research in the field is driven by a multitude of applications for single-photon sources. Here, the most common application is in the field of quantum information technologies (see e.g. Zoller *et al.*, 2005), i.e. systems and processes that will allow the implementation of quantum information protocols (Nielsen and Chuang, 2000). In this context, photons serve as fast carriers of quantum information, offering the possibility of being transmitted through long-distance optical communication channels (Sangouard and Zbinden, 2012). This property is especially exploited in quantum cryptography, where a secret key is encoded and transmitted using single photons, allowing secure exchange of information (see also Section 6.6; extensive reviews have been given by Gisin *et al.* (2002) and Gisin and Thew (2007)). There exist a large number of protocols for employing single photons for quantum communication; most of them utilize the polarization degree of freedom for encoding information (e.g. Bennett and Brassard, 1984) or the phase of a single photon. In essence, the application of single-photon sources in the field of quantum communication places requirements on those sources, requiring emission into well-defined spectral, spatial and polarization modes.

On the other hand, single photons may be employed as quantum bits in all-optical quantum computers (Knill *et al.*, 2001). In stark contrast to a classical bit, a quantum bit can be prepared in any superposition state of its internal states. Quantum computers potentially offer to solve several important computational tasks faster than classical computers (for a general review, see e.g. Ladd *et al.*, 2010). For the employment of single photons in all-optical quantum computers, however, the requirements are even stronger: in addition to well-defined spectral, spatial and polarization modes, the photons have to be indistinguishable to enable two-particle interference. In a more general sense, in integrating the two applications discussed above, single photons may act as flying quantum bits in a quantum network (Kimble, 2008), where they can be used to exchange quantum information between distant stationary qubits and quantum memories. Similarly, single photons can serve as a ‘quantum bus’ in schemes for the distribution of entanglement over large distances (Sangouard and Zbinden, 2012), i.e. in quantum repeaters (Briegel *et al.*, 1998), where they might interconnect several system components of the repeater.

The development of single-photon sources with precisely measurable parameters would also advance the field of metrology in the area of measurement of low light levels: here, recent research activities aim at a redefinition of the candela, the unit of optical illumination strength, using single photons (the ‘quantum candela’: see e.g. Cheung *et al.*, 2007). Furthermore, single-photon

sources with an adjustable photon rate would establish a link to existing classical radiometry, i.e. single-photon detectors may be linked to classical analogue detectors, traced to a primary standard (Zwinkels *et al.*, 2010).

Eventually, a single-photon source might be used as a nanoscopic light source and thus potentially enable high-resolution optical near-field microscopy with single photons (Michaelis *et al.*, 2000).

6.1.2 Principles of single-photon emission

The light emitted from a single quantum system inherently consists of single photons owing to the fact that the excitation–emission cycle of a single quantum system can never take place twice simultaneously. Thus, under continuous excitation, a stream of single photons with stochastic emission times evolves: it never contains two photons at the same time; adjacent photons retain a certain time distance determined by the quantum emitters' internal dynamics. If a pulsed excitation is applied to a single emitter, single photons can be created within certain time windows following the excitation pulse.

For practical single-photon sources, one has to raise the question whether there is a convenient excitation mechanism. Often, optical excitation using laser light is employed. However, excitation using an electrical current to drive a single-photon source allows the fabrication of more compact and practically applicable devices and is thus highly desirable. For electrical excitation, the source has to be embedded into a suitable structure, for example a light-emitting diode. In the following, we focus on the more common optical pumping of colour centres in diamond; for electrical excitation, see Section 6.7.

For optical excitation, a simple excitation scheme is depicted in Fig. 6.1. Here, a non-resonant pump laser excites the colour centre to an intermediate state. The relaxation from this state is supposed to be fast so that the intermediate state does

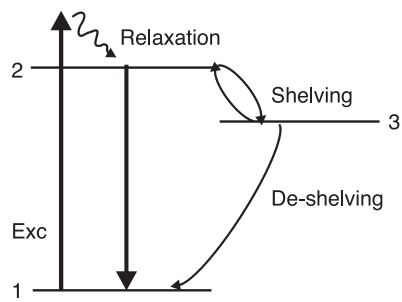

6.1 Schematic illustration of a single-photon source using non-resonant optical excitation. The existence of a shelving state (state 3) is disadvantageous for the development of a single-photon source.

not accumulate population. As a consequence, if a sufficiently strong pumping pulse is applied, it is possible to excite the colour centre with a probability close to unity. The length of the pumping pulse has to be sufficiently short 1 µm, and this depends on the lifetime of the emitter (Brouri *et al.*, 2000b). If the relaxation is not fast enough, stimulated emission of the pumping transition hinders a full population inversion. More sophisticated excitation schemes include the use of Rabi oscillations, i.e. coherent oscillations of the population between the ground and excited states to drive the source. In multilevel systems, more complex coherent population transfer techniques such as the STIRAP technique can also be employed (for more details, see e.g. Oxborrow and Sinclair, 2005).

In addition to the existence of a feasible excitation mechanism, the source has to provide a suitable emission process: the single photons should be emitted with a high quantum efficiency and, preferably, with a narrow bandwidth (see the next section for further discussion). Moreover, the transition that leads to the desired emission should take place with a high probability. However, in many cases the emitter's internal dynamics includes additional, often long-lived states, called shelving states, that are detrimental to single-photon emission as the emitter can be 'trapped' in these states for comparatively long times without emitting photons (see Fig. 6.1).

6.2 Characterization and key parameters of a single-photon source

This section summarizes the key parameters of a single-photon source and the respective measurements. For more details of the characterization of colour centres at the single-emitter level, see Chapter 4.

6.2.1 Emission lifetime and repetition rate

The creation of single photons in defined time windows relies mostly on pulsed excitation of the source and subsequent spontaneous emission of a photon. For a two-level system with an off-resonant excitation capability (Fig. 6.1, levels 1 and 2 and the intermediate pumping level), a suitable repetition rate of the pulsed excitation is given by the inverse of the emission lifetime of the excited state of the single-photon source: only after the system has decayed with high probability does applying the next excitation pulse make sense. For illustration, even after one has waited for three times the lifetime of the system, a probability of approximately 5% remains that the system still resides in the excited state and is thus not available for re-excitation. To obtain trigger rates in the several 100 MHz regime, a lifetime of the order of 1 ns or slightly lower is required; for example, if one waits for three times the lifetime, the maximum trigger rate for a source with an emission lifetime of 1 ns is 333 MHz. Moreover, a short lifetime leads to the emission of single photons mostly within narrow time intervals (low emission

jitter; see e.g. Oxborrow and Sinclair, 2005) and thus allows efficient gating of single-photon detectors. This, in turn, is advantageous for suppressing noise or background from detectors (dark counts) and the environment (stray light). The latter is especially crucial when one is developing sources to demonstrate quantum key distribution (QKD) systems that are supposed to operate in free space under daylight conditions (see e.g. Duligall *et al.*, 2006). Note that the participation of additional, long-lived states, called shelving states (state 3 in Fig. 6.1), can also reduce the most suitable repetition rate as the colour centre may reside in these states for longer time intervals, not being available for re-excitation. In addition to the repetition rate, the lifetime of the emitter also sets an upper limit on the optimal length of the excitation pulse; for details, see for example Brouri *et al.* (2000b).

6.2.2 Single-photon purity and statistics

The light emitted from a single quantum system under continuous excitation consists of a stream of single photons with stochastic emission times: it never contains two photons at the same time, and adjacent photons retain a minimum time distance between them. This observation is termed photon antibunching and can be investigated by measuring the intensity autocorrelation function $g^{(2)}$, which is classically defined for a source with constant intensity as

$$g^{(2)}(\tau) = \langle I(t)I(t+\tau)\rangle / (\langle I(t)\rangle)^2 \qquad [6.1]$$

(see e.g. Lounis and Orrit, 2005; Fox, 2006). Here, $I(t)$ is the intensity at time t, $I(t+\tau)$ is the intensity at time $t+\tau$ and $\langle\,\rangle$ denotes temporal averaging. To represent $g^{(2)}$ for light emitted by a single emitter, Eq. 6.1 has to be rewritten using the number of photons or photon detection events n, a quantity proportional to the classical intensity (Fox, 2006):

$$g^{(2)}(\tau) = \langle n(t)n(t+\tau)\rangle / (\langle n(t)\rangle)^2 \qquad [6.2]$$

The explicit form of the $g^{(2)}$ function for a continuously driven two-level system (levels 1 and 2 in Fig. 6.1) can be derived quantum mechanically by considering the interaction of a quantized light field with a two-level atom (see e.g. Loudon, 2000). Here, however, we follow a more intuitive approach to obtain the $g^{(2)}$ function (see also Kurtsiefer *et al.*, 2000; Kitson *et al.*, 1998)): if a first detection event has occurred at time $t=0$, $g^{(2)}(\tau)$ gives the conditional probability of detecting a subsequent photon at time =. The detection of a photon at time + = 0 ensures that the system has been projected to the ground state at $t=0$. To emit a consecutive photon, the system has to undergo an additional cycle of excitation and relaxation. The probability of detecting a subsequent photon at time τ is now directly proportional to the excited-state population at time τ. Thus, the $g^{(2)}$ function can be derived by calculating the excited-state population at time τ assuming that the system starts in the ground state at time $t=0$. To obtain the normalized $g^{(2)}$ function, the excited-state population at time τ has to be divided by the excited-state

population at an infinite delay time τ (the steady-state population). To derive the excited-state population, rate equations can be used. For a two-level system with off-resonant pumping, the rate equations read

$$dN_1/d\tau = -k_{12}N_1 + k_{21}N_2$$

$$dN_2/d\tau = k_{12}N_1 - k_{21}N_2$$

Here, N_1 and N_2 are the populations of the ground and excited states (with $N_1 + N_2 = 1$), $d/d\tau$ denotes the time derivative, and k_{12} and k_{21} are the transition rate coefficients. Note that the pumping rate coefficient k_{12} depends on the excitation laser intensity. The steady-state population can be inferred via setting all time derivatives to zero: $N_2^{steady} = k_{12}/k_{12} + k_{21}$. Solving the rate equations gives

$$N_2(\tau) = [k_{12}/(k_{12} + k_{21})] - [k_{12} \exp(-(k_{12} + k_{21})\tau)/(k_{12} + k_{21})]$$

and thus, after normalization to the steady-state population,

$$g^{(2)}(\tau) = 1 - \exp(-|\tau| / \tau_0) \quad [6.3]$$

with $\tau_0 = 1/(k_{12} + k_{21})$. As introduced above, $g^{(2)}(\tau)$ represents the probability of detecting two photons separated by a time interval τ. Thus, for an ideal single-photon source, $g^{(2)}(\tau)$ vanishes at $\tau = 0$, indicating that the fluorescence light never contains simultaneously emitted photons. For N independent single emitters with equal emission intensities, the contrast of the $g^{(2)}$ function scales as $g^{(2)}(0) = 1 - 1/N$. Correspondingly, a minimum of $g^{(2)}(0) < 0.5$ indicates the presence of a single emitter.

For a three-level system (states 1–3 in Fig. 6.1), the function is extended to read

$$g^{(2)}(\tau) = 1 - (1 + \alpha) \exp(-|\tau| / \tau_1) + \alpha \exp(-1\,\tau|/\tau_2) \quad [6.4]$$

(for details of the constants, see e.g. Kurtsiefer *et al.*, 2000; Neu *et al.*, 2011a). For such a system, both a minimum (antibunching) and a maximum (bunching) can be observed in the $g^{(2)}$ function. Thus, it is clear that via measuring the $g^{(2)}$ function, the population dynamics of a single emitter can be investigated. The antibunching time constant τ_1 at low excitation power indicates the excited-state lifetime of the source, whereas τ_2 and α indicate the dynamics associated with the third level, the shelving state. For more details, see Section 6.5.2. Photon correlation measurements can also be performed using pulsed excitation. In this form, they can serve to analyse fluorescence intermittence dynamics as, for example, in the work of Wu *et al.* (2008), and to prove pulsed single-photon emission (single photons on demand) from a system.

The $g^{(2)}$ function can, in principle, be measured using one single-photon-sensitive detector, as recently demonstrated by Steudle *et al.* (2012). However, the frequently employed single-photon avalanche diode detectors suffer from a dead time on the order of 100 ns after each photon detection event (for details, see e.g. Eisaman *et al.*, 2011). Thus, time delays τ shorter than this time period are not accessible using a single detector but are nevertheless significant, as the lifetime

of the single-photon source is desired to be on the order of nanoseconds. Thus, the $g^{(2)}$ function is usually measured using a Hanbury Brown–Twiss (HBT) interferometer, first introduced by Hanbury Brown and Twiss (1956). The general principle of this intensity interferometer is to distribute the light under investigation equally onto two (single-photon-sensitive) detectors. Consequently, two closely spaced photons can be dispensed onto the two detectors and thus individually detected. The $g^{(2)}$ function can be obtained from a normalized histogram of the delay times τ between detection events on the two detectors (Kitson *et al.*, 1998).

Several factors can diminish the antibunching effect. First, background emission can lower the single-photon purity of the source. In the case of colour centres in diamond, the background emission mostly originates from the diamond host material. This fluorescence, which is often broadband, is expected to be uncorrelated with the fluorescence of the colour centre (Brouri *et al.*, 2000a) and thus leads to stochastic multiphoton events. If the brightness of the background fluorescence is known, for example from measurements of the fluorescence of the diamond in the close spatial vicinity of the colour centre, the $g^{(2)}$ function can be corrected for the influence of the background (Brouri *et al.*, 2000a). Moreover, timing uncertainties in the measurement set-up often induce a reduced antibunching: typical single-photon detectors, such as avalanche photodiodes, exhibit a timing jitter in the output signal due to the varying time that elapses during the process of detection of a single photon (for details, see e.g. Eisaman *et al.*, 2011). This jitter is mostly in the order of 100 ps. As a consequence, photons with time delays in this range might be accidentally registered as simultaneous photons, reducing the degree of antibunching. It has to be kept in mind that this reduction of the antibunching does not indicate a loss of single-photon purity but represents a measurement imperfection. If the time response of the HBT set-up has been measured independently, it can be taken into account when interpreting the $g^{(2)}$ function, and the effect of the timing jitter can be distinguished from a reduced single-photon purity (see e.g. Neu *et al.*, 2012a; Wu *et al.*, 2006).

The value $g^{(2)}(0)$ can serve as a measure of the ratio of the probabilities of multi-photon versus single-photon emission, i.e. $g^{(2)}(0) = 2p_2/p_1^2$, where p_1 and p_2 are the one- and two-photon probabilities, respectively, and it is usually compared to the value for a classical light source with Poissonian statistics. Beyond this simple analysis, the full photon number statistics of the source can be analysed, by determining the decomposition of the measured light field into a photon number (Fock state) basis. Such a measurement can be performed, for example, by using photon-number-resolving detectors and pulsed excitation of the source. Using this technique, the photon number statistics of a single colour centre (a nitrogen–vacancy (NV) centre) have been analysed by Schmunk *et al.* (2012). These authors discovered that the probability of finding a number state with zero photons (the vacuum state) was 99.9×10^{-2}, whereas the probability of finding a single-photon state was 2.2×10^{-4} and the probability of finding two or more photons vanished. Thus, considering the photon number statistics, a very pure but low-efficiency

single-photon source has been observed. The possible causes of low source efficiency are described in the following paragraphs.

6.2.3 Collection efficiency

For an ideal single-photon source, one would expect perfectly directional emission into a single spatial mode so that each emitted photon could be collected and become usable. However, real single-photon sources do not enable a collection efficiency of unity. A radiating colour centre can be described by one or more radiating dipoles (for a discussion of the NV centre, see e.g. Alegre *et al.*, 2007). Depending on the orientation of these dipoles, often only a small fraction of the emitted light can be collected into the aperture angle of typical collection optics (e.g. a microscope objective). Additionally, only a fraction of the light can be extracted from the high-index diamond host material (refractive index 2.4) owing to total internal reflection at the diamond–air interface. The collection efficiencies that have been obtained for colour centres in diamond are discussed below and in Section 6.5.1. There are several different approaches to obtaining high collection efficiencies for single-photon sources based on colour centres in diamond. In an initial step, the collection efficiency can be enhanced using nanodiamonds of sub-wavelength size to drastically reduce the influence of total internal reflection in the host material, thus modifying the radiation pattern as well as the out-coupling efficiency for the fluorescence. A more controlled enhancement can be achieved using nanostructures and microstructures (see Section 6.5.1).

6.2.4 Quantum efficiency

In general, the quantum efficiency is the probability that an optical photon is emitted per excitation cycle (Oxborrow and Sinclair, 2005). It can be reduced by non-radiative processes or processes that do not lead to photon creation in the detected wavelength range. For example, the colour centre under investigation might undergo a transition not directly from the excited to the ground state (2 to 1 in Fig. 6.1) as desired, but from the excited state (2) to an intermediate shelving state (3). From there, it might relax non-radiatively or emit a ‘non-usable’ photon that is not detected. Furthermore, the transition from 2 to 1 might occur non-radiatively, for example via emission of phonons. The fluorescence rate and thus the quantum efficiency might also vary temporally. The effect of temporary loss (intermittence) of fluorescence is known as blinking, and permanent loss of fluorescence is known as bleaching. An ideal single-photon source should have a quantum efficiency of unity without any fluorescence intermittence.

6.2.5 Spectral properties and polarization

Spectral filtering aids in discriminating between background photons and the desired single photons. It is unavoidable if, for example, the single-photon source

is intended for the implementation of free-space communication and, in particular, daylight quantum key distribution, where detection events due to background photons lead to significantly enhanced error rates (see e.g. Duligall *et al.*, 2006). Thus, the emission bandwidth of a single-photon source should be as narrow as possible to enable narrow-band, efficient filtering. The desired emission wavelength of the source depends on the application. If the photons are intended to be transmitted through free space, visible wavelengths are suitable. In contrast, for fibre communication, infrared wavelengths are needed (see e.g. Gisin *et al.*, 2002). A second crucial property of the photons is the polarization, where the ideal case is emission into a stable, reproducible and well-defined polarization state. First, the polarization degree of freedom of the photons can be used to encode information, as described in the BB84 protocol (Bennett and Brassard, 1984). Second, only photons with a defined polarization can be indistinguishable, as discussed below.

6.2.6 Indistinguishable photons

In most proposals in quantum information and also in advanced approaches to QKD (see e.g. Sangouard and Zbinden, 2012), the spectral, temporal and polarization properties have to fulfil rigid requirements: often, indistinguishable photons are required. Experimentally, photon indistinguishability can be tested via two-photon interference experiments: if two indistinguishable photons simultaneously impinge on a beam splitter, they always exit the beam splitter at the same output port, as first discovered by Hong *et al.* (1987). For solid-state systems, in contrast to atomic systems, the creation of indistinguishable photons is challenging owing to the inhomogeneous spread of the emission frequency of the colour centre and the need for perfect spectral overlap. Thus, it requires mostly the tuning of emitter resonances, and low temperatures to control the spectral bandwidth. Very recently, the creation of single indistinguishable photons from NV centres in diamond has been demonstrated by two groups (Bernien *et al.*, 2012; Sipahigil *et al.*, 2012); see also Section 6.7.

6.3 Suitability of colour centres in diamond as single-photon sources

Colour centres in diamond feature a number of unique properties which make them an ideal system for the implementation of solid-state single-photon sources, as discussed in the following paragraphs.

6.3.1 Emission range and band gap

Pure, single-crystal diamonds are optically transparent in the visible and even in the ultraviolet spectral range for wavelengths exceeding 230 nm (Mildren *et al.*,

2008), as a result of the large band gap energy of diamond: diamond shows an indirect band gap of 5.5 eV, and the direct band gap is even higher, at 7.3 eV. Owing to this large band gap, a large energy range is accessible for the formation of discrete, impurity-induced energy levels inside the band gap. Absorption by large ensembles of optically active impurities or impurity and defect complexes leads to the coloration of natural diamonds, and the impurities are thus termed colour centres. Nearly 500 of these centres have been reported (Zaitsev, 2001), thus offering many potential candidates for single-photon sources as well as the coverage of almost any emission wavelength in the visible or near infrared spectral range.

6.3.2 Phonons

Diamond is the hardest of all solids and therefore supports high energy phonons, with energies from 70 meV up to 168 meV (see e.g. Zaitsev, 2000). The low-energy contributions of the phonon density of states significantly influence the linewidths of electronic transitions in a solid (Davies, 1981). Therefore, the high phonon energies in diamond induce comparatively low room temperature linewidths of the purely electronic transitions (zero-phonon). If, in addition, a low phonon coupling of the defect is present, preventing emission into generally broad sidebands, colour centres in diamond offer the unique possibility of low-bandwidth single-photon emission at room temperature. A generally low phonon coupling for colour centres involving heavy impurities, for example silicon, nickel and chromium, has been reported, rendering them especially interesting as single-photon sources (Zaitsev, 2000). Note that also local modes, i.e. modes due to the vibration of the colour centre and its nearest-neighbour carbon atoms, can occur and may have relatively low energies (typically 20–40 meV) for heavy impurities (Zaitsev, 2000). The (linear) electron–phonon coupling is measured by either the Debye–Waller factor or the Huang–Rhys factor. The Debye–Waller factor DW is defined as the integrated luminescence intensity of the zero-phonon line (ZPL), I_{ZPL}, divided by the integrated luminescence intensity of the colour centre, I_{tot} (Gaebel *et al.*, 2004). The Huang–Rhys factor S is defined by $I_{ZPL}/I_{tot} = \exp(-S)$ (Walker, 1979).

On the other hand, the high phonon energies may pose a challenge. Especially for transitions with a high phonon coupling, multiphonon quenching of optical transitions may dominate over radiative decays even for comparatively high transition energies. The question ‘How far into the infrared can a colour centre in diamond emit?’ was discussed in detail by Rogers (2010), who pointed out that there are few emission lines in diamond with wavelengths exceeding 1000 nm, as transitions with such energies instead take place non-radiatively because fewer than seven phonons are needed to bridge the transition energy. Thus it is questionable if it will be possible to extend single-photon emission in diamond to the telecommunication windows of optical fibres at around 1300 and 1500 nm. However, such an extension of the wavelength range might be achieved using nonlinear frequency conversion of single photons (Zaske *et al.*, 2012).

6.3.3 Refractive index

The refractive index of diamond is equal to 2.4 in the near infrared spectral region around 740 nm (Zaitsev, 2001). The high refractive index of diamond is detrimental for the application of single colour centres in bulk diamond as single-photon sources: the critical angle for total internal reflection at a diamond–air interface is 24.6°. Thus, depending on the radiation pattern, the major fraction of the colour centre's fluorescence is internally reflected and cannot be extracted from the diamond to be collected by optics in air. Even for light impinging perpendicularly onto the surface, a fraction of 17% of the light intensity is reflected and lost back into the diamond material (Fresnel reflection). On the other hand, the high refractive index of diamond enables the implementation of photonic microstructures and nanostructures, for example nanowires (Babinec *et al.*, 2010), microring resonators (Faraon *et al.*, 2011) and photonic crystals (Riedrich-Möller *et al.*, 2012), which generally rely on a high-refractive-index material. These photonic elements potentially offer improved single-photon sources by cavity-enhanced emission, including improved directivity, bandwidth and repetition rate. For more details and additional methods for obtaining enhanced collection efficiency in diamond, see Section 6.2.3.

6.4 Colour centres in diamond as single-photon sources: types of colour centres investigated as single emitters

The following section discusses the types of colour centres investigated as single emitters to date. The most important parameters are summarized in Table 6.1. A comparison of the spectra of three different types of colour centres is given in Fig. 6.2.

6.4.1 Nitrogen-based colour centres

In 1997, single nitrogen–vacancy centres were observed for the first time (Gruber *et al.*, 1997). Subsequently, single-photon emission from NV centres was demonstrated in 2000 by two groups (Kurtsiefer *et al.*, 2000; Brouri *et al.*, 2000a). The first experiments were carried out on NV centres in type Ib high-pressure high-temperature (HPHT) diamond and were extended to NV centres formed *in situ* in chemical vapour deposition (CVD) diamond (Rabeau *et al.*, 2007). For details of CVD of diamond, see for example Koizumi *et al.* (2008) and Balmer *et al.* (2009). If a diamond sample does not contain NV centres as grown, NV centres can be created by ion implantation of nitrogen and subsequent annealing. The formation of these centres may have a high yield of up to 50% for MeV implantation energies (Pezzagna *et al.*, 2010). For details of ion implantation in diamond, see Chapter 3.

Table 6.1 Summary of colour centres demonstrated as single-photon emitters

Colour centre	Reference	ZPL wavelength (nm)	Emission bandwidth (nm)	HR (DW)	Emission rate (kcps)	Lifetime (ns) (QE%)
TR12	Naydenov *et al.* (2009)	470.5	~60	2.3 (0.1)		3.6
H3 (N_2V)	Hsu *et al.* (2011)	503	~100			24 ± 15
532	Smith *et al.* (2011)	532	~70	2.48 (0.08)	60	3.
NV-	Beveratos *et al.* (2001); Bernien *et al.* (2012)	637	~100	3.2 (0.04)	50	11.6–25
734	Simpson *et al.* (2009)	734	4.1	0.2 (0.81)	1800	13.6
SiV	Neu *et al.* (2011a); Neu *et al.* (2011b); Neu *et al.* (2012b); Wang *et al.* (2006)	730–750	~0.7–5	0.1–0.6 (0.9–0.5)	Up to 6000	~1 (0.3–9%)
Cr related	Aharonovich *et al.* (2010a) Castelletto and Boretti (2011)	740–770	1.5–11		3200	1–14 (1–100%)
Ni-Si related	Aharonovich *et al.* (2009a)	768	7	0.11 (0.9)	200	2 (100%)
	Steinmetz *et al.* (2011)	767–775	1.4–2.7		78	1.3
NE8	Wu *et al.* (2006)	782	2	0.36 (0.7)	40	2 (52 ± 20%)
	Rabeau *et al.* (2005)	797.7	1.5	0.35 (0.7)	40	
	Gaebel *et al.* (2004)	802	1.2	0.36 (0.7)	75	11.5 (70%)

Notes:

HR, Huang–Rhys factor; DW, Debye–Waller factor; QE, quantum efficiency.

The emission bandwidth gives the approximate spectral range covered by the ZPL and the strong sideband emission. Note that for the TR12 centre, all values given refer to measurements at 2 K. For the 532 nm centre, the Huang–Rhys factor and the bandwidth were measured at 77 K. All other values refer to room temperature experiments. Simpson *et al.* (2009) erroneously confused the Huang–Rhys and Debye–Waller factors, which we have corrected in accordance with other authors (Smith *et al.*, 2011). The column 'emission rate' lists the measured emission rate in the given reference under continuous-wave (CW) excitation. We chose the CW emission rate for comparison, as most references did not investigate maximum emission rates under pulsed excitation. Note that no emission rates that are enhanced by coupling to nanophotonic devices have been included in this summary. The estimation of the quantum efficiency always involves estimating the efficiency of the experimental set-up. We note that the estimated efficiencies of the set-ups employed differ by more than an order of magnitude, which hinders direct comparison.

For single-photon experiments, so far mostly the negatively charged NV centre with a ZPL at 637 nm has been employed. Single NV centres have been shown to switch temporarily to the neutral charge state with a ZPL at 575 nm under green laser excitation (photochromism) (Gaebel *et al.*, 2006). Owing to a comparatively

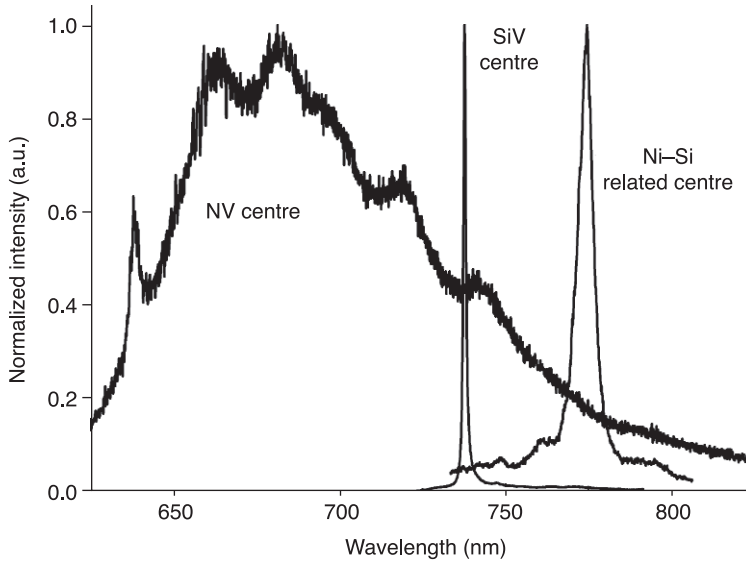

6.2 Comparison of photoluminescence spectra of three different types of single colour centre, namely the NV and SiV centres and a near-infrared-emitting centre (nickel–silicon-related). All spectra have been normalized to the emission maximum. The SiV and near-infrared centres were excited using 671 nm laser light, and the NV centre with 532 nm laser light.

strong electron–phonon coupling, the emission band spans about 100 nm and only 4% of the emission is found in the ZPL even at low temperature (10 K) (Bernien *et al.*, 2012). The photoluminescence spectrum of a single NV centre at room temperature is displayed in Fig. 6.2. The large bandwidth of the NV emission has to be considered as a disadvantage in the context of single-photon sources. The lifetime of the centre in bulk diamond is 11.6 ns and is approximately doubled in nanodiamonds owing to the modified local density of states (Beveratos *et al.*, 2001). Very recently, neutral NV centres have been employed for single-photon emission using direct excitation by an electrical current (Lohrmann *et al.*, 2011; Mizuochi *et al.*, 2012). The centre is best described using two transition dipoles orthogonal to its high-symmetry axis (Alegre *et al.*, 2007) and emits only partially linearly polarized light (Alleaume *et al.*, 2004).

Besides the prominent NV centre, H3 centres, consisting of two nitrogen atoms and a vacancy, have been investigated as single-photon emitters. H3 centres are formed in natural type Ia diamond upon thermal annealing by trapping of a vacancy at an A-aggregate (N–N). These centres have a comparatively long lifetime of around 20 ns and a ZPL at 503 nm, and display a room temperature emission bandwidth of about 100 nm (Hsu *et al.*, 2011). Single H3 centres in 50 nm-sized natural type Ia nanodiamond have shown stable room temperature

single-photon emission under pulsed excitation. In the studies of Hsu *et al.* (2011), the centres exhibited a large quantum yield of 0.95; however, the emission rate of single centres was not reported.

6.4.2 Silicon centres

Like nitrogen atoms, silicon atoms form an optically active complex with a lattice vacancy. The silicon–vacancy (SiV) centre is commonly found in CVD diamond owing to *in situ* doping resulting from the etching of the quartz reactor wall or the silicon substrate (e.g. Bergman *et al.*,1993), but can be also fabricated via ion implantation (e.g. Wang *et al.*, 2006). The negatively charged SiV centre emits at around 740 nm, while the neutral charge state displays a much weaker emission at 946 nm (D'Haenens-Johanson *et al.*, 2011). Single SiV^- centres created *in situ* in 200 nm CVD nanodiamonds have shown emission rates of up to 6 Mcps (Neu *et al.*, 2012b), whereas SiV^- centres created by ion implantation in natural bulk diamond have shown emission rates of around 1000 cps (Wang *et al.*, 2006). Owing to a low phonon coupling, the SiV^- fluorescence is mostly (> 70%) concentrated in a narrow ZPL with a width down to 0.7 nm (Neu *et al.*, 2011a), as shown in Fig. 6.2. However, the phonon coupling of individual centres varies considerably (see Table 6.1), and mechanical stress inside nanodiamonds leads to an inhomogeneous distribution of ZPL wavelengths between 730 and 750 nm (Neu *et al.*, 2011b). The emitted light is fully linearly polarized (Neu *et al.*, 2011b). The emission dynamics varies strongly between individual emitters, including changes in the shelving behaviour and in the quantum efficiency (Neu *et al.*, 2012b). At low temperature, the ZPL splits into four fine-structure transitions owing to split excited and ground states (Clark *et al.*, 1995). For single centres, evidence for an additional ZPL in the spectral region around 820 nm has been presented (Neu *et al.*, 2012a).

6.4.3 Nickel-related centres

Nickel in diamond has a tendency to form a multitude of nickel–nitrogen complexes. These complexes occur especially in HPHT diamond grown using nickel as a catalyst but are also found in natural diamonds. Nadolinny *et al.* (1999) described the NE8 centre, which involves a nickel atom, two vacancies and four nitrogen atoms, and exhibits a ZPL at 793.6 nm. Three publications refer to the NE8 centre as a single-photon source. Gaebel *et al.* (2004) reported single-photon emission from a colour centre in natural, untreated type IIa diamond with a ZPL at 802 nm (1.2 nm width). A low phonon coupling ($DW = 0.7$) and a high quantum efficiency (70%) render the results promising. Also using natural type IIa diamond, Wu *et al.* (2006) presented an emitter with similar phonon coupling and a ZPL at 782 nm (width 2 nm); however, it had a shorter lifetime, 2 ns, compared with the results of Gaebel *et al.* (2004), where the lifetime was 11.5 ns (quantum efficiency

52 ± 20%). Rabeau *et al.* (2005) and Wu *et al.* (2007) demonstrated the fabrication of NE8 centres in CVD diamond films and nanodiamonds grown in the presence of nickel powder. The observed centres emitted at 797.6 and 793.7 nm with a low phonon coupling (a Huang–Rhys factor of 0.35) (Rabeau *et al.*, 2005). Furthermore, the more recent publication (Wu *et al.*, 2007) demonstrated pulsed single-photon emission. The NE8 centre is best described using a single emitting dipole; full linear polarization of the emitted fluorescence has been inferred from the measured polarization (Wu *et al.*, 2006).

Despite these promising results, it should be pointed out that, to date, the controlled fabrication of NE8 centres via ion implantation and HPHT annealing (at 2000 °C) has failed. Orwa *et al.* (2010) observed purely nickel-related centres (885 nm centre), confirming the incorporation of nickel into diamond; however, no NE8 centres were found. Also, recent experiments on the incorporation of nickel and nitrogen during the CVD process did not lead to the observation of single NE8 centres; however, ensembles of NE8 centres were observed in cathodoluminescence (Wolfer *et al.*, 2010). As a concluding remark, we should mention that Pezzagna *et al.* (2010) re-evaluated the vibronic sideband structure of the NE8 centre and assigned a much higher phonon coupling, with a Debye–Waller factor of 0.01 (Huang–Rhys factor 4.6).

Aharonovich *et al.* (2008) showed that CVD nanodiamonds grown on nickel-implanted silica substrates were able to host single nickel-related centres with narrow-band emission at 806, 820 and 860 nm and a short lifetime (3 ns). The atomic composition of these centres remains unclear. A centre related to a nickel–silicon complex has been fabricated via ion implantation of nickel into silicon-containing CVD nanodiamonds (Aharonovich *et al.*, 2009a). Its bright emission (200 kcps) is situated at 768 nm with a lifetime of 2 ns. The fabrication of this complex in bulk diamond has been demonstrated (Steinmetz *et al.*, 2011), but with low efficiency (10^{-6}). The centres created via ion implantation show preferential absorption of linearly polarized light, and emission mostly between 767 and 775 nm and a short lifetime (1.3 ns) (Steinmetz *et al.*, 2011). An example of such a narrow-bandwidth near-infrared-emitting centre found in a CVD nanodiamond is shown in Fig. 6.2.

Very recently, Castelletto *et al.* (2012) reported a multitude of narrow-bandwidth colour centres emitting in the near infrared (700–900 nm) in a CVD diamond film grown in the presence of nickel powder during the CVD process. Thus nickel is potentially responsible for the formation of many infrared-emitting complexes; however, their exact composition and structure remain unclear, as well as how to form these complexes via ion implantation.

6.4.4 Chromium-related centres

Chromium-related centres were first observed in nanodiamonds grown on synthetic sapphire, which is known to contain chromium. The observed centres

have a narrow emission (11 nm) between 740 and 770 nm, and a very recent publication also mentions chromium centres emitting at 790 nm (Müller *et al.*, 2012). For centres emitting at 756 nm, absorption of linearly polarized light and high-brightness (3200 kcps) emission have been demonstrated (Aharonovich *et al.*, 2009b). More recent studies have demonstrated strong variations in the shelving behaviour of the centres, including two- and three-level behaviour (Aharonovich *et al.*, 2010a). Aharonovich *et al.* (2010b) reported the formation of chromium-related centres after ion implantation of oxygen and chromium into type IIa CVD diamond. However, according to more recent results, the generation of chromium-related centres succeeds only in conventional type IIa CVD diamond with [N] < 1 ppm and [B] < 0.05 ppm. Despite tests of different implantations, including nitrogen co-implantation, formation of these centres has been established neither in CVD diamond with higher purity nor in HPHT diamond, leaving open questions concerning the reliable formation of chromium-related centres via ion implantation (Aharonovich *et al.*, 2011a). The quantum efficiency of the centres varies significantly between individual emitters, from several per cent to nearly unity (Castelletto and Boretti, 2011).

6.4.5 Other colour centres

The above-mentioned colour centres involve without exception an extrinsic, non-carbon impurity. However, single-photon emission using an intrinsic defect in diamond, namely the TR12 centre, related to carbon interstitials, has also been demonstrated. The TR12 centre was created via high-energy ion implantation (6 MeV) of carbon ions and moderate annealing (650 °C) and has a ZPL at 470.5 nm with a comparatively high phonon coupling ($S = 2.3$) (Naydenov *et al.*, 2009).

Furthermore, single-photon emission using an unidentified colour centre in high-purity CVD diamond fluorescing in the green spectral range (ZPL 532 nm, width 0.8 nm) has been demonstrated. This centre is probably related to a nitrogen or boron complex. It has a lifetime of 3.3 ns (at 300 K), and displays fully linearly polarized emission and a Huang–Rhys factor of 2.48 (Smith *et al.*, 2011). A further unidentified colour centre, emitting at 734, nm has been reported in CVD nanodiamonds grown on fused silica. This centre exhibited bright emission (1.8 Mcps) mostly (81%) into a narrow ZPL with a width of 4.1 nm. Despite the promising properties, however, only a single centre was observed (Simpson *et al.*, 2009).

6.5 Colour centres in diamond as single-photon sources: specific properties

6.5.1 Collection efficiency

Owing to the high refractive index of diamond ($n = 2.4$), extracting light from diamond is challenging: light impinging onto the diamond–air interface at angles

exceeding 24.6° is totally internally reflected and cannot leave the diamond. Thus, depending on the radiation pattern, i.e. the angles at which the fluorescence is emitted, and on the numerical aperture of the collection optics, only a small fraction of the fluorescence of a colour centre can be collected. The radiation pattern of the colour centre is described by a radiation pattern of emitting dipoles: the negatively charged NV centre's emission is best described using two orthogonal emission dipoles (Alegre *et al.*, 2007). In contrast, for example, the negatively charged SiV centre has been found to be best described by a single emission dipole (Brown and Rand, 1995; Neu *et al.*, 2011b). The orientation and number of the transition dipoles are given by the type of the electronic transition of the colour centre and its symmetry (Kaplyanskii, 1963). The orientation of the radiating dipole is crucial for the collection efficiency: assuming a single dipole radiating in air and a typical numerical aperture of 0.8 (corresponding to a maximum collection angle of 53.1°), the collection efficiency for a dipole oriented perpendicular to the optical axis of the collecting optics is 2.4 times higher than for a dipole parallel to the axis (Plakhotnik *et al.*, 1995).

To calculate the more realistic case of a single dipole in diamond, the emitted field can be expanded into plane waves, for which the reflection at the interface can be calculated using Fresnel coefficients (for details of the calculation, see Neu *et al.* (2012b)). Figure 6.3 displays the collection efficiency for differently oriented single dipoles with a near infrared emission wavelength of 770 nm. The figure summarizes the collection efficiency for a dipole in diamond and for a dipole in air above an iridium metal layer. The second case is an approximation to a colour centre in a nanodiamond on iridium as, for example, in Neu *et al.* (2011a). As is discernible from Fig. 6.3, for a colour centre in bulk diamond, represented by a single dipole, a maximum collection efficiency of approximately 4% can be achieved. In contrast, the same dipole in air above an iridium layer leads to a collection efficiency of up to nearly 80%. However, the collection efficiency now depends more significantly on the distance of the dipole from the interface. Thus, nanodiamonds on a suitable substrate can be hosts for single-photon sources with a high collection efficiency. Furthermore, nanodiamonds offer the possibility to be incorporated into dielectric multilayer structures, called dielectric antennas, that have demonstrated 99% collection efficiency for single-molecule fluorescence (Lee *et al.*, 2011). However, it should be noted that a nanodiamond, in contrast to the simple approximation of a colour centre radiating in air, also modifies the radiation pattern owing to resonant modes (Mie resonances) and thus the collection efficiency can also vary strongly with the size of the nanodiamond (Greffet *et al.*, 2011). Castelletto and Boretti (2011) found a collection efficiency oscillating between approximately 10 and 20% for nanodiamonds with sizes between 100 and 400 nm.

The collection efficiency has been enhanced in a more controlled way by nanostructuring of bulk diamond. Using cylindrical nanowires etched out of bulk diamond, Babinec *et al.* (2010) demonstrated an order-of-magnitude increase in

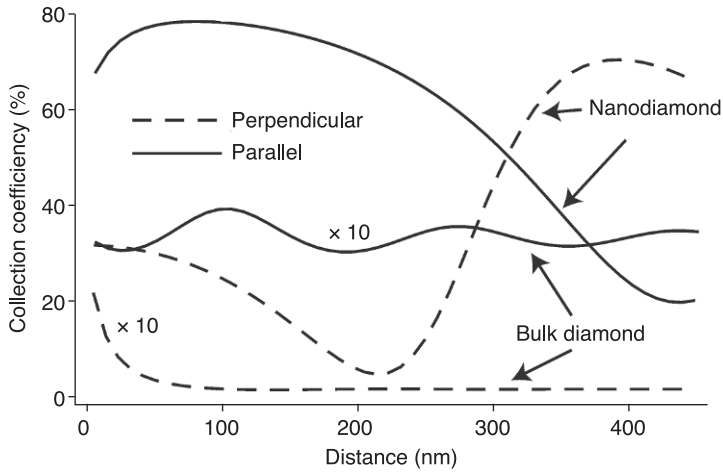

6.3 Collection efficiency for a single dipole radiating at 770 nm using collection optics (microscope objective) with numerical aperture 0.8. The curves labelled 'nanodiamond' correspond to the situation of a dipole radiating in air above an iridium metal layer. The curves labelled 'bulk diamond' refer to a colour centre in diamond with collection optics in air (the refractive index of diamond was taken as 2.4, and that of iridium as 2.68 + i 5.06). The calculation was performed by Dr Mario Agio (INO-CNR and LENS, Sesto Fiorentino, Italy) and the figure is printed with permission.

the photon out-coupling for single NV centres due to fluorescence waveguiding in the nanowires. Hemispherical solid immersion lenses (SILs) geometrically avoid any refraction at the diamond–air interface. SILs can be fabricated directly in bulk diamond (e.g. Siyushev *et al.*, 2010; Marseglia *et al.*, 2011), or nanodiamonds can be placed onto SILs made out of a high-refractive-index material. For SILs in diamond, a collection efficiency of 30% for an NA of 0.9 can be reached (Siyushev *et al.*, 2010). Schröder *et al.* (2011a) obtained a record brightness of 2.4 Mcps with a single NV centre using nanodiamond placement on a SIL. A further way to obtain enhanced collection efficiency and to obtain single-photon emission directly into light-guiding fibres is to couple nanodiamonds to tapered fibres or photonic-crystal fibres (Schröder *et al.*, 2011b, 2012). To summarize, high collection efficiencies have been obtained in diamond, despite its high refractive index, using nanodiamonds and photonic nanostructures. For more details of the nanostructuring of diamond and of possible nanostructure designs, see Chapters 5 and 7.

6.5.2 Quantum efficiency and shelving states

Most colour centres in diamond represent multilevel systems that include long-lived shelving states. Only for an unidentified single colour centre emitting at

734 nm (Simpson *et al.*, 2009) and for some chromium-related centres (Aharonovich *et al.*, 2009b) has two-level or close to two-level emission dynamics been observed. A schematic level scheme and the processes that have to be taken into account are depicted in Fig. 6.4. For the NV centre, singlet states play the role of shelving states, whereas the single-photon generation (via the ZPL and phonon sidebands) is due to transitions between the triplet states of the system (for details, see e.g. Acosta *et al.*, 2010). For all other centres, the nature of the shelving states remains subject to discussion. With respect to single-photon generation, the existence of a shelving state is disadvantageous. First, each time the colour centre undergoes a transition to the shelving state after a successful (pulsed) excitation, no single photon at the desired wavelength is emitted, thus reducing the quantum efficiency of the system. Second, if the colour centre is trapped in the shelving state, it might not be excited by following laser pulses, thus significantly reducing the possible repetition rate of the excitation or triggering of a single-photon source (see e.g. Wu *et al.*, 2008). Third, if the colour centre can undergo thermally driven transitions from the shelving state to the excited state, as for example in the case

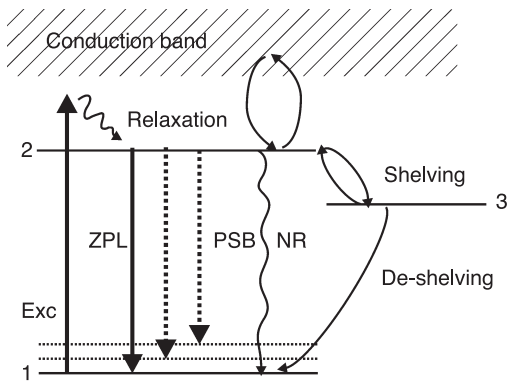

6.4 Excitation and de-excitation processes for a single colour centre in diamond. Non-resonant optical excitation (labelled 'Exc') brings the colour centre to an intermediate excited state, from which it relaxes to a purely electronic excited state (labelled '2'). From state 2, the colour centre can relax via photon emission into the ZPL or into redshifted phonon sidebands (PSB) that end on vibrationally excited states (dashed lines), and it ends up in the ground state (state 1). However, the same relaxation process might also occur non-radiatively (NR). Alternatively, the colour centre may undergo a transition from the excited state to the shelving state (state 3) and relax from there (de-shelving), or it may be re-excited thermally to the excited state. The de-shelving process can also be induced by a laser-assisted transition (Neu *et al.*, 2012b). Additionally, the colour centre can be (photo)-ionized: it loses an electron. The reverse process, recharging of a centre, also occurs.

of the NV centre (Kurtsiefer *et al.*, 2000), this process might also induce photon emission not closely following the excitation laser pulse.

A further reduction of the quantum efficiency of a single-photon source occurs if the colour centre is temporarily ionized: the emission of the new charge state will most probably not coincide with the selected detection window for the single photons, effectively reducing the emission rate. For details, see the discussion below.

In addition to the multilevel dynamics, the ZPL transition itself can occur non-radiatively, thus reducing the quantum efficiency. One indicator of thermally activated non-radiative processes is a temperature-dependent luminescence lifetime. This has been observed, for example, for a single green-emitting colour centre (Smith *et al.*, 2011). Quantum efficiencies far below unity for the transitions from the excited to the ground state (see Fig. 6.4) have also been reported for chromium centres (Castelletto and Boretti, 2011) and SiV centres (Neu *et al.*, 2012b). For chromium centres, an increase of the quantum efficiency to values close to one at liquid helium temperature has been found, corresponding to increased luminescence intensity for a single centre (Müller *et al.*, 2012), whereas for SiV centres, similar results could not be verified (Neu *et al.*, 2013). The origin of the quenching processes is still subject to discussion; possible origins include thermally activated quenching and defect-assisted quenching (due to radiation damage) (Castelletto and Boretti, 2011). To use colour centres in diamond as efficient single-photon sources, it is crucial to ensure a mostly radiative ZPL transition, as well as low coupling to shelving states.

To determine the quantum efficiency and the population dynamics, $g^{(2)}$ measurements under pulsed and continuous excitation can be used. Figure 6.5(b) depicts a correlation measurement for the fluorescence from a single SiV centre under continuous excitation, which displays the well-known antibunching feature around zero delay time τ. The dip does not decrease fully to zero, which might in other cases be an indication of impure single-photon emission due to background emission or the presence of several emitters. However, here this observation is entirely due to the timing jitter of the measurement set-up washing out the $g^{(2)}$ function of the SiV centre. The effect is especially pronounced because of the short lifetime of the centre; including the timing jitter in the fitting function leads to the solid curve in Fig. 6.5(b).

In addition to the antibunching dip, witnessing single-photon emission from the colour centre, the $g^{(2)}$ function displays a second feature: it increases for intermediate delay times and decays to one for longer delay times. This bunching indicates the presence of a third, long-lived state besides the excited and ground states of the ZPL transition. Changes in the bunching with changing excitation power give information about the shelving and de-shelving dynamics of a colour centre and indicate, for example, if the colour centre can be re-excited from the shelving state by the excitation laser (see e.g. Neu *et al.*, 2012b). For SiV, as well as for chromium-related centres, it has been found that the coupling to the shelving

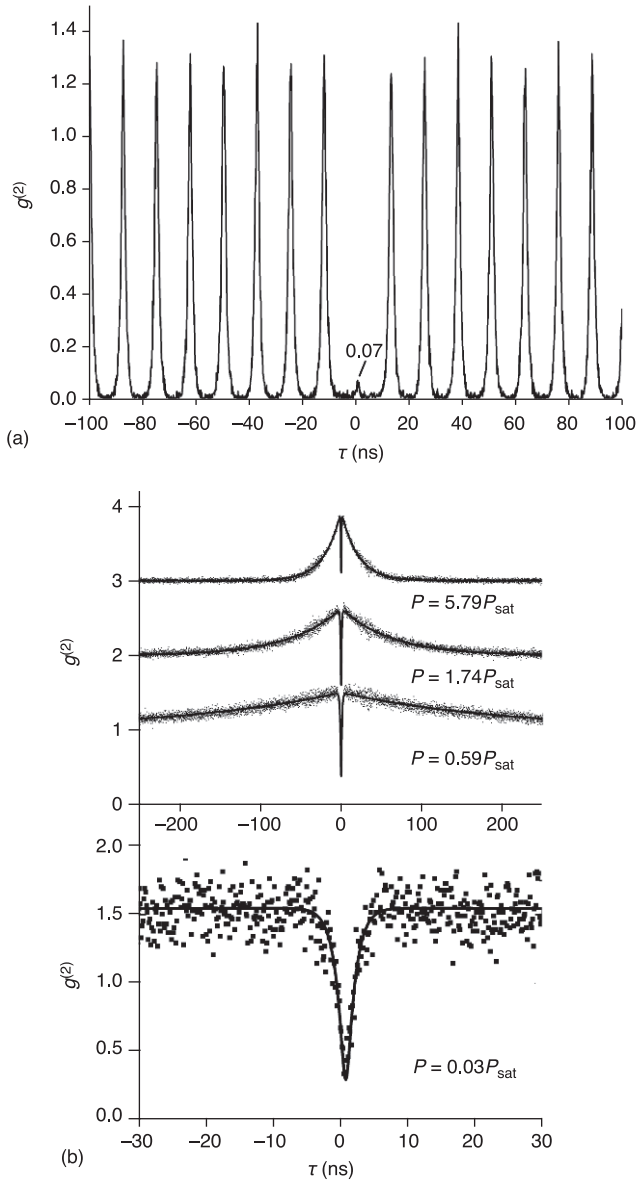

6.5 (a) Pulsed photon correlation measurements of a single SiV centre in a nanodiamond on iridium. The pulsed excitation was performed using a mode-locked Ti:sapphire laser with an average power of 50 μW (repetition rate 80 MHz) and a centre wavelength of 700 nm. The vanishing dip at zero delay clearly confirms the single-photon emission of the centre. (b) Continuous-excitation $g^{(2)}$ measurements for a single SiV centre in a nanodiamond on iridium using 671 nm laser excitation. The excitation power is given in units of the saturation power, which was equal to 105 μW.

state varies strongly between individual centres. Thus, it might be possible to identify single centres with a very low influence of the shelving state, suitable as highly efficient single-photon sources.

The emission and excitation dynamics, as well as the collection efficiency and the repetition rate of the excitation, determine the maximum single-photon rate that can be obtained under pulsed excitation. It should be noted that most of the work summarized in Section 6.4 does not present data on the pulsed excitation of colour centres, and especially not on the maximum single-photon rate obtained under pulsed excitation. Figure 6.5(a) displays a $g^{(2)}$ function measured for an individual SiV centre under pulsed excitation. The curve illustrates the population dynamics: the well-separated peaks in the pulsed measurements indicate that even at an excitation repetition rate of 80 MHz, corresponding to a laser pulse separation of 12.5 ns, the short lifetime of about 0.8 ns leads to well-separated single-photon emission events. In contrast, for an NV centre with a lifetime exceeding 10 ns, excitation with such a repetition rate no longer leads to well-separated single-photon pulses. The maximum single-photon rates from SiV centres in nanodiamonds on iridium that have been obtained using 80 MHz excitation and 0.8 NA collection optics are about $1–2 \times 10^5$ cps, which, as discussed above, indicate a quantum efficiency far below unity, in the range of several per cent. For NV centres, a rate of about 9×10^4 cps (NA 0.95, for NV nanocrystals on a dielectric mirror) has been measured under 5.3 MHz excitation (Alleaume *et al.*, 2004). Here, enhancing the rate using a higher excitation rate is not suitable, owing to the long lifetime of the NV centre. For the NE8 centre, a maximum pulsed single-photon emission rate of 3.5×10^4 cps using 20 MHz excitation has been shown (Wu *et al.*, 2007).

To summarize, the repetition rate of diamond-based single-photon sources is still comparatively low; however, as discussed in Section 6.6, even these low-repetition-rate true single photons can be useful for quantum information.

6.5.3 Photostability and charge state stability

In principle, colour centres in diamond can be fully photostable, enabling long observation times and reliable single-photon generation. However, especially in nanodiamonds, fluorescence intermittence (blinking) has been reported: NV^- centres may blink on a timescale of milliseconds in 5 nm-sized nanodiamonds (Bradac *et al.*, 2010), and SiV centres may blink on a timescale of seconds (Neu *et al.*, 2012b). In addition to fluorescence intermittence, the fluorescence may undergo spectral jumps of up to several nanometers (Siyushev *et al.*, 2009). The blinking of NV^- centres has been associated with charges trapped on the surface of nanodiamonds; surface modifications may inhibit the blinking (Bradac *et al.*, 2010). It is known, furthermore, that colour centres in diamond may change their charge state under optical illumination, an effect known as photochromism (Gaebel *et al.*, 2006). By choosing suitable excitation wavelengths, the effect of

photochromism can be minimized, as has been shown for the NV centre. For more details, see the discussion in Section 6.7.

In contrast to temporary changes in the charge state based on photochromism, surface charges can permanently alter the charge state of a colour centre in diamond: for NV centres, it has been demonstrated that surface charge traps due to amorphous carbon can convert the centres to the neutral form (e.g. Rondin *et al.*, 2010). In contrast, oxidizing the surface leads to negatively charged centres, and hydrogen termination converts the centres back to the neutral form (Petrakova *et al.*, 2012). The influence of the surface increases with decreasing nanodiamond size. As the use of nanodiamonds is highly desirable for single-photon applications owing to the high fluorescence extraction efficiency, controlling the charge state of a colour centre of interest close to the surface is crucial. However, so far only single NV centres have been investigated in detail with respect to their charge state stability close to surfaces.

6.5.4 Polarization of the emitted photons

For application in quantum cryptography, especially if the polarization degree of freedom is used to encode information, it is desirable to generate single photons with a defined, preferably linear polarization. In principle, if the colour centre is described by a single emission dipole, fully linearly polarized emission can be achieved. However, it should be noted that the degree of linear polarization depends not only on the emitter but also on the imaging and collection, which is done through high-numerical-aperture optics. Fourkas (2001) discussed the polarization anisotropy introduced by imaging through a high-numerical-aperture objective. If light from a dipole oriented perpendicular to the optical axis of the collection optics is collected, the polarization is spatially constant over the collimated fluorescence beam; linear polarization with an orientation parallel to the dipole axis is observed. For a dipole parallel to the optical axis of the collection optics, no net polarization is observed, as the polarization varies spatially in the collimated beam (polarization anisotropy). For other orientations, only partial polarization is observed.

Nevertheless, polarized emission has been identified for several colour centres in diamond: for an unidentified colour centre with a ZPL at 532 nm (Smith *et al.*, 2011), for NE8 centres (Wu *et al.*, 2006) and for SiV centres (Neu *et al.*, 2011b). Figure 6.6 depicts the polarized emission of a single SiV centre in a nanocrystal on iridium. The curve was recorded by rotating a linear polarization analyser and recording the transmitted fluorescence. The decrease to zero indicates a linear polarization; the angle of the maximum indicates the orientation of the dipole. In contrast, for NV centres, population transfer between different excited states leads to a temperature-dependent polarization, where the degree of polarization increases with decreasing temperature (Fu *et al.*, 2009). At room temperature, only partial (46 %) polarization is obtained (Beveratos *et al.*, 2002). To summarize,

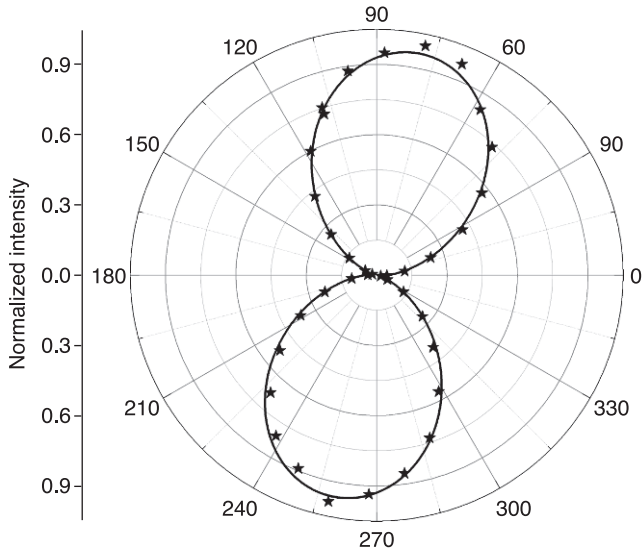

6.6 Polarized emission of a single SiV centre recorded using a linear polarization analyser.

regarding polarization, colour centres in diamond have proven very promising as single-photon sources for quantum cryptography.

6.6 Quantum key distribution with nitrogen–vacancy (NV) and silicon–vacancy (SiV) centres

Single photons from NV centres in diamond have been used successfully to demonstrate quantum key distribution based on the BB84 protocol, which uses the polarization of single photons to encode the information (Bennett and Brassard, 1984). Alleaume *et al.* (2004) and Beveratos *et al.* (2002) have used single photons from an NV centre in a nanodiamond on a mirror to perform QKD over a distance of 30 m in the open air (between two buildings at night) and over 50 m in free space with careful shielding from ambient light. Schröder (2012) and Leifgen *et al.* (2014) reported QKD over a short distance in the laboratory using a compact single-photon source, built by using an NV centre in a nanodiamond placed on an SIL made of zirconia. It is also noteworthy that the first commercially available single-photon source was constructed using an NV centre in diamond (see http://qcvictoria.com).

However, apart from these proof-of-principle experiments, QKD has mostly been implemented using attenuated laser pulses (weak coherent pulses, WCPs) as quasi-single-photon sources. With this technique, the probability of pulses containing multiple photons is directly connected to the mean intensity of the laser pulse owing to the Poissonian light statistics of these pulses. As a result of

the security leak opened up by multiphoton pulses, WCPs have to be attenuated more and more to guarantee security as the transmission loss in QKD becomes larger. Thus, either the transmission rate approaches zero for long distances or secure transfer is not guaranteed. For details of quantum cryptography protocols and the associated security hazards, see Chapter 2 in this book, and for comprehensive reviews, see for example Gisin *et al.* (2002), Mauerer *et al.* (2008) and Lütkenhaus and Shields (2009).

As mentioned above, the use of a true single-photon source is advantageous in the case of a lossy channel as it permits a potentially higher secure transmission rate. Using single photons created by pulsed excitation (with an excitation repetition rate of 5.3 MHz) of a single NV centre corresponding to a mean number $\mu = 0.0235$ of polarized single photons per pulse sent on the quantum channel, a single-photon source performed better than WCPs if the channel loss exceeded 9 dB (Alleaume *et al.*, 2004). This fact is illustrated in Fig. 6.7 using numerical simulations and experimental data. The secure bit transfer rate obtained with the NV centre in the absence of attenuation was 16 kbit/s.

The single-photon sources realized so far using NV centres suffer from three drawbacks. First, the light from the NV centre is not fully polarized at room

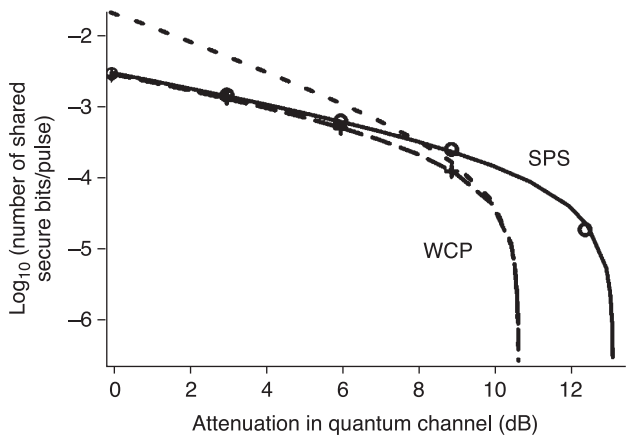

6.7 Simulation and experimental data for the number of exchanged secure bits per time slot versus attenuation in the quantum channel, reprinted with permission from R. Alleaume *et al.* (2004), *New Journal of Physics* 6, 92, Experimental open-air quantum key distribution with a single-photon source, IOP Publishing, doi:10.1088/1367-2630/6/1/092. The solid and long-dashed lines correspond to numerical simulations assuming a mean photon number $\mu = 0.0235$. The short-dashed line was obtained by optimizing the number of secure bits per pulse with respect to μ and corresponds to the limit of the WCP performance under the experimental conditions of Alleaume *et al.* (2004).

temperature, reducing the efficiency of the source. Second, the broad emission spectrum of the NV centre renders spectral filtering of the single photons and background light very challenging. Third, the long lifetime of the NV centre limits the efficiency of temporal gating to reduce detection noise (60 ns gates were used by Alleaume *et al.* (2004)).

Two different routes to enhanced single-photon sources are available. First, NV centres can be coupled to a cavity to narrow the emission and shorten the lifetime. This approach was investigated theoretically by Su *et al.* (2008), whose simulation revealed the possibility of a near-unity single-photon emission probability from an NV centre in a high-finesse cavity (Q factor 10^5) with a lifetime of only 70 ps and an emission bandwidth of only 0.01 nm. However, it should be noted that efficiently coupling an NV centre to such a cavity is technically challenging and is currently under experimental investigation.

A second route to enhanced single-photon sources is to use alternative colour centres. The first demonstration of the BB84 protocol using single photons from an SiV centre in a nanodiamond on iridium has recently been accomplished (Schröder, 2012; Leifgen *et al.*, 2014). Despite the high degree of polarization of the photons from SiV defect centres and the short lifetime, however, the secure key rates achieved so far have not outperformed NV-centre-based systems. This observation is partly due to experimental limitations (a low cycle frequency) but also due to the low quantum efficiency of the SiV defect. Here, enhanced performance will depend on the identification of brighter, more suitable SiV defects, as a large spread of photophysical properties has been found for the SiV centre (Neu *et al.*, 2012b). The technique of cavity coupling is also promising for the enhancement of the performance of single photon sources for QKD based other colour centres. Detailed calculations for the NE8 and SiV centres have been performed by Su *et al.* (2009).

Here it should be noted that, owing to their emission wavelengths in the visible or near infrared, colour centres are suitable for open-air QKD but not very suitable for fibre-based communication, as silica-based fibres display excessively high losses in the emission range of colour centres in diamond. To illustrate this issue, at 800 nm, the fibre attenuation is about 2 dB/km (i.e. half the photons are lost after 1.5 km), whereas the attenuation is only around 0.35 and 0.20 dB/km at 1300 and 1550 nm (the telecommunication windows), respectively (corresponding to 50% photon loss after about 9 and 15 km, respectively) (Gisin *et al.*, 2002). This disadvantage might, however, be overcome by nonlinear single-photon frequency downconversion: via a nonlinear process in which the single photons are mixed with a strong laser field, the frequency of the photons can be converted with high efficiency into the telecommunication band, as has been demonstrated for photons from single semiconductor quantum dots recently (Zaske *et al.*, 2012). For a scheme suitable for the conversion of SiV centre emission, see Zaske *et al.* (2011).

6.7 Future trends

A multitude of colour centres have been investigated as single-photon sources. However, so far only the NV and SiV centres have been reliably and reproducibly fabricated, by various methods in various diamond materials. Deterministic production of the promising chromium- and nickel-related centres in any chosen diamond material still remains a challenge. Furthermore, the emission wavelengths of these centres show large variations and overlap with each other. Thus, the ideal colour centre for single-photon emission potentially still remains to be identified, as most of the systems investigated suffer from a three-level emission dynamics and a low quantum efficiency. In contrast, the drawback of low collection efficiency from a high-index material has been overcome in several ways.

There has been a recent development that is capable of significantly reducing the experimental effort of using diamond single-photon sources. Lohrmann *et al.* (2011) and Mizuochi *et al.* (2012) have demonstrated single-photon emission from neutral NV centres embedded in a p–i–n diode in diamond. The p–i–n structures were fabricated either by ion implantation doping of diamond or by p- and n-type doping of diamond during CVD. Electrical excitation opens the way to single-photon light-emitting diodes, reducing the amount of optics needed to establish single-photon emission. It should be noted that other colour centres, for example xenon colour centres, have also demonstrated electroluminescence, thus promoting the development of narrow-bandwidth single-photon LEDs in the near infrared (794 and 813 nm) based on diamond (Zaitsev *et al.*, 2006; Pezzagna *et al.*, 2011).

One important goal when single-photon sources for quantum information are being considered is the generation of indistinguishable photons that will enable, for example, long-distance distribution of entanglement for long-range quantum communication. Recently, photon indistinguishability has been demonstrated using polarization-filtered photons from the ZPL of negatively charged NV centres (Bernien *et al.*, 2012; Sipahigil *et al.*, 2012). In support of further experiments on the creation of indistinguishable photons, important technical progress has been achieved recently. First, the charge state of the colour centre has to be preserved during the excitation and emission cycles to allow efficient generation of single photons. Beha *et al.* (2012) found that emission from negatively charged NV centres was most efficiently excited using yellow laser light at 575 nm, corresponding to the ZPL of the neutral charge state. On the other hand, for the most commonly used excitation at 532 nm, the NV centre spends about 20–30% of its time in the neutral charge state (Beha *et al.*, 2012; Aslam *et al.*, 2013). Second, using Stark shift tuning of the ZPL frequency of the NV centre, the resonance frequency of single NV centres has been temporally stabilized sufficient time to counteract spectral jumps as a result of spectral diffusion (Acosta *et al.*, 2012).

6.8 References

Acosta, V., Jarmola, A., Bauch, E. and Budker, D. (2010) 'Optical properties of the nitrogen–vacancy singlet levels in diamond', *Phys Rev B*, 82, 201202(R), DOI 10.1103/PhysRevB.82.201202.

Acosta, V., Santori, C., Faraon, A., Huang, Z., Fu, K., *et al.* (2012) 'Dynamic stabilization of the optical resonances of single nitrogen vacancy centers in diamond', *Phys Rev Lett*, 108, 206401, DOI 10.1103/PhysRevLett.108.206401.

Aharonovich, I., Zhou, C., Stacey, A., Treussart, F., Roch, J.-F. and Prawer, S. (2008) 'Formation of color centers in nanodiamonds by plasma assisted diffusion of impurities from the growth substrate', *Appl Phys Lett*, 93, 243112, DOI 10.1063/1.3049606.

Aharonovich, I., Zhou, C., Stacey, A., Orwa, J., Castelletto, S., *et al.* (2009a) 'Enhanced single photon emission in the near infrared from a diamond color center', *Phys Rev B*, 79, 235316, DOI 10.1103/PhysRevB.79.235316.

Aharonovich, I., Castelletto, S., Simpson, D., Stacey, A., McCallum, J., *et al.* (2009b) 'Two-level ultrabright single photon emission from diamond nanocrystals', *Nano Lett*, 9, 3191–3195, DOI 10.1021/nl9014167.

Aharonovich, I., Castelletto, S., Simpson, D., Greentree, A. and Prawer, S. (2010a) 'Photophysics of chromium related diamond single photon emitters', *Phys Rev A*, 81, 043813, DOI 10.1103/PhysRevA.81.043813.

Aharonovich, I., Castelletto, S., Johnson, B., McCallum, J., Simpson, D., *et al.* (2010b) 'Chromium single-photon emitters in diamond fabricated by ion implantation', *Phys Rev B*, 81, 121201(R), DOI 10.1103/PhysRevB.81.121201.

Aharonovich, I., Castelletto, S., Johnson, B., McCallum, J. and Prawer, S. (2011a) 'Engineering chromium-related single photon emitters in diamond', *New J Phys*, 13, 045015, doi:10.1088/1367–2630/13/4/045015.

Aharonovich, I., Castelletto, S., Simpson, D., Su, C., Greentree, A. and Prawer, S. (2011b) 'Diamond based single photon emitters', *Rep Prog Phys*, 74, 076501, doi:10.1088/0034-4885/74/7/076501.

Alegre, T., Santori, C., Medeiros-Ribeiro, G. and Beausoleil, R. (2007) 'Polarization-selective excitation of nitrogen vacancy centers in diamond', *Phys Rev B*, 76, 165205, DOI 10.1103/PhysRevB.76.165205.

Alleaume, R., Treussart, F., Messin, G., Dumeige, Y., Roch, J.F., *et al.* (2004) 'Experimental open-air quantum key distribution with a single-photon source', *New J Phys*, 6, 92, DOI 10.1088/1367-2630/6/1/092.

Aslam, N., Waldherr, G., Neumann, P., Jelezko, F. and Wrachtrup, J. (2012) 'Photo induced ionization dynamics of the nitrogen vacancy defect in diamond investigated by single shot charge state detection', *New J Phy* 15, 013064, DOI 10.1088/1367-2630/15/1/01364.

Babinec, T., Hausmann, B., Khan, M., Zhang, Y., Maze, J., *et al.* (2010) 'A diamond nanowire single photon source', *Nature Nanotechnol*, 5, 195–199, DOI 10.1038/NNANO.2010.6.

Balmer, R. S., Brandon, J. R., Clewes, S. L., Dhillon, H. K., Dodson, J. M., *et al.* (2009) 'Chemical vapour deposition synthetic diamond: materials, technology and applications', *J Phys: Condens Matter*, 21, 364221, DOI 10.1088/0953-8984/21/36/364221.

Beha, K., Batalov, A., Manson, N., Bratschitsch, R. and Leitensdorfer, A. (2012) 'Optimum photoluminescence and recharging cycle of single nitrogen vacancy centers in ultrapure diamond', *Phys Rev Lett*, 109, 097404, DOI 10.1103/PhysRevLett.109.097404.

Bennett, C. H. and Brassard, G. (1984) 'Quantum cryptography: Public key distribution and coin tossing', *Proceedings of IEEE International Conference on Computers, Systems and Signal Processing*, Bangalore, India, p. 175.

Bergman, L., Stoner, B., Turner, K., Glass, J. and Nemanich, R. (1993) 'Microphotoluminescence and Raman-scattering study of defect formation in diamond films', *J Appl Phys*, 73, 3951–3957.

Bernien, H., Childress, L., Robledo, L., Markham, M., Twitchen, D. and Hanson, R. (2012) 'Two-photon quantum interference from separate nitrogen vacancy centers in diamond', *Phys Rev Lett*, 108, 043604, DOI 10.1103/PhysRevLett.108.043604.

Beveratos, A., Brouri, R., Gacoin, T., Poizat, J.-F. and Grangier, P. (2001) 'Nonclassical radiation from diamond nanocrystals', *Phys Rev A*, 64, 061802(R), DOI 10.1103/PhysRevA.64.061802.

Beveratos, A., Brouri, R., Gacoin, T., Villing, A., Poizat, J. and Grangier, P. (2002) 'Single photon quantum cryptography', *Phys Rev Lett*, 89, 187901, DOI 10.1103/PhysRevLett.89.187901.

Bradac, C., Gaebel, T., Naidoo, N., Sellars, M., Twamley, J., *et al.* (2010) 'Observation and control of blinking nitrogen vacancy centre in discrete nanodiamonds', *Nature Nanotechnol*, 5, 345–349, DOI 10.1038/NNANO.2010.56.

Briegel, H.-J., Dürr, W., Cirac, J. I. and Zoller, P. (1998) 'Quantum repeaters: The role of imperfect local operations in quantum communication', *Phys Rev Lett*, 81, 5932–5935, DOI 10.1103/PhysRevLett.81.5932.

Brouri, R., Beveratos, A., Poizat, J.-P. and Grangier, P. (2000a) 'Photon antibunching in the fluorescence of individual color centers in diamond', *Opt Lett*, 25, 1294–1296.

Brouri, R., Beveratos, A., Poizat, J. and Grangier, P. (2000b) 'Single-photon generation by pulsed excitation of a single dipole', *Phys Rev A*, 62, 063817, DOI 10.1103/PhysRevA.62.063817.

Brown, S. and Rand, S. (1995) 'Site symmetry analysis of the 738 nm defect in diamond', *J Appl Phys*, 78, 4096–4075.

Buller, G. and Collins, R. (2010) 'Single-photon generation and detection', *Meas Sci Technol*, 21, 012002, DOI 10.1088/0957-0233/21/1/012002.

Castelletto, S. and Boretti, A. (2011) 'Radiative and nonradiative decay rates in chromium related centers in nanodiamonds', *Opt Lett*, 36, 4224–4226.

Castelletto, S., Edmonds, A., Gaebel, T. and Rabeau, J. (2012) 'Production of multiple diamond-based single photon sources', *IEEE J Sel Top Quantum Electron*, 18, 1792–1798.

Cheung, J. Y., Chunnilall, C. J., Woolliams, E. R., Fox, N. P., Mountford, J. R., *et al.* (2007) 'The quantum candela: a re-definition of the standard units for optical radiation', *J Mod Opt*, 54, 373.

Clark, C. D., Kanda, H., Kiflawi, I. and Sittas, G. (1995) 'Silicon defects in diamond', *Phys Rev B*, 51, 16681–16688, DOI 10.1103/PhysRevB.51.16681.

Davies, G. (1981) 'The Jahn–Teller effect and vibronic coupling at deep levels in diamond', *Rep Prog Phys*, 44, 787–830.

D'Haenens-Johanson, U., Edmonds, A., Green, B., Newton, M., Davies, G., *et al.* (2011) 'Optical properties of the neutral silicon split vacancy center in diamond', *Phys Rev B*, 84, 245208, DOI 10.1103/PhysRevB.84.245208.

Duligall, J., Godfrey, M., Harrison, K., Munro, W. and Rarity, J. (2006) 'Low cost and compact quantum key distribution', *New J Phys*, 8, 249, DOI 10.1088/1367-2630/8/10/249.

Eisaman, M., Fan, J., Migdall, A. and Polyakov, S. (2011) 'Invited review article: Single-photon sources and detectors', *Rev Sci Instrum*, 82, 071101, DOI 10.1063/1.3610677.

Faraon, A., Barclay, P., Santori, C., Fu, K. and Beausoleil, R. (2011) 'Resonant enhancement of the zero-phonon emission from a colour centre in a diamond cavity', *Nature Photon*, 5, 301–305, DOI 10.1038/NPHOTON.2011.52.

Fourkas, J. (2001) 'Rapid determination of the three-dimensional orientation of single molecules', *Opt Lett*, 26, 211–213.

Fox, M. (2006) *Quantum Optics: An Introduction*, Oxford University Press.

Fu, K., Santori, C., Barclay, P., Rogers, L., Manson, N. and Beausoleil, R. (2009) 'Observation of the dynamic Jahn–Teller effect in the excited states of nitrogen–vacancy centers in diamond', *Phys Rev Lett*, 103, 256404, DOI 10.1103/PhysRevLett.103.256404.

Gaebel, T., Popa, I., Gruber, A., Domham, M., Jelezko, F. and Wrachtrup, J. (2004) 'Stable single photon source in the near infrared', *New J Phys*, 6, 98, DOI 10.1088/1367-2630/6/1/098.

Gaebel, T., Domham, M., Wittmann, C., Popa, I., Jelezko, F., *et al.* (2006) 'Photochromism in single nitrogen vacancy defect in diamond', *Appl Phys B*, 82, 243–246, DOI 10.1007/s00340-005-2056-2.

Gisin, N., Ribordy, G., Tittel, W. and Zbinden, H. (2002) 'Quantum cryptography', *Rev Mod Phys*, 74, 145–190.

Gisin, N. and Thew, R. (2007) 'Quantum communication', *Nature Photon*, 1, 165.

Greffet, J.-J., Hugonin, J., Besbes, M., Lai, N., Treussart, J. and Roch, J.-F. (2011) 'Diamond nanoparticles as nanoantennas for nitrogen vacancy color centers', arXiv preprint 1107.0502.

Gruber, A., Dräbenstedt, A., Tietz, C., Fleury, L., Wrachtrup, J. and von Borcyskowski, C. (1997) 'Scanning confocal optical microscopy and magnetic resonance on single defect centers', *Science*, 276, 2012–2014.

Hanbury Brown, R. and Twiss, R. (1956) 'Correlation between photons in 2 coherent beams of light', *Nature*, 177, 27–29.

Hong, C. K., Ou, Z. Y. and Mandel, L. (1987) 'Measurement of subpicosecond time intervals between two photons by interference', *Phys Rev Lett*, 59, 2044–2046, DOI 10.1103/PhysRevLett.59.2044.

Hsu, J., Su, W., Yang, K., Tzeng, Y. and Chang, H. (2011) 'Nonblinking green emission from single H3 color centers in nanodiamonds', *Appl Phys Lett*, 98, 193116, DOI 10.1063/1.3591156.

Kaplyanskii, A. (1963) 'Noncubic centers in cubic crystals and their piezospectroscopic investigation', *Opt Spectrosc*, 16, 329–337.

Kimble, H. (2008) 'The quantum internet', *Nature*, 453, 1023–1030, DOI 10.1038/nature07127.

Kitson, S., Jonsson, P., Rarity, J. and Tapster, P. (1998) 'Intensity fluctuation spectroscopy of small numbers of dye molecules in a microcavity', *Phys Rev A*, 58, 620–627.

Knill, E., Laflamme, R. and Milburn, G. (2001) 'A scheme for efficient quantum computation with linear optics', *Nature*, 409, 46–52, DOI 10.1038/35051009.

Koizumi, S., Nebel, C. E. and Nesladek, M. (eds) *Physics and Applications of CVD Diamond*, Wiley-VCH, DOI 10.1002/9783527623174.

Kurtsiefer, C., Mayer, S., Zarda, P. and Weinfurter, H. (2000) 'Stable solid state source of single photons', *Phys Rev Lett*, 85, 290–293, DOI 10.1103/PhysRevLett.85.290.

Ladd, T., Jelezko, F., Laflamme, R., Nakamura, Y., Monroe, C. and O'Brien, J. (2010) 'Quantum computers', *Nature*, 464, 45–53, DOI 10.1038/nature08812.

Lee, K., Chen, X., Eghlidi, H., Kukura, P., Lettow, R., *et al.* (2011) 'A planar dielectric antenna for directional single-photon emission and near-unity collection efficiency', *Nature Photon*, 5, 166–169.

Leifgen, M., Schröde, T., Gädebe, F., Riewam, R., Metillam, V., *et al.* (2014) *New J Phy*, 16, 023021, DOI 10.1088/1367-26301/612/023021.

Lohrmann, A., Pezzagna, S., Dobrinets, I., Spinicelli, P., Jacques, V., *et al.* (2011) 'Diamond bases light-emitting diode for visible single-photon emission at room temperature', *Appl Phys Lett*, 99, 251106, DOI 10.1063/1.3670332.

Loudon, R. (2000) *The Quantum Theory of Light*, Oxford University Press.

Lounis, B. and Orrit, M., (2005) 'Single photon sources', *Rep Prog Phys*, 68, 1129–1179, DOI 10.1088/0034-4885/68/5/R04.

Lütkenhaus, N. and Shields, A. J. (2009) 'Focus on quantum cryptography: Theory and practice', *New J Phys*, 11, 045005, DOI 10.1088/1367-2630/11/4/045005.

Marseglia, L., Hadden, J., Stanley-Clarke, A., Harrison, J., Patton, B., *et al.* (2011) 'Nanofabricated solid immersion lenses registered to single emitters in diamond', *Appl Phys Lett*, 98, 133107, DOI 10.1063/1.3573870.

Mauerer, W., Helwig, W. and Silberhorn, C. (2008) 'Recent developments in quantum key distribution: theory and practice', *Ann Phys (Leipzig)*, 17, 158–175.

Michaelis, J., Hettich, C., Mlynek, J. and Sandoghdar, V. (2000) 'Optical microscopy using a single-molecule light source', *Nature*, 405, 325–328, DOI 10.1038/35012545.

Mildren, R., Butler, J. and Rabeau, J. (2008) 'CVD-diamond external cavity Raman laser at 573 nm', *Opt Express*, 16, 18950–18955.

Mizuochi, N., Makino, T., Kato, H., Takeuchi, D., Ogura, M., *et al.* (2012) 'Electrically driven single-photon source at room temperature in diamond', *Nature Photon*, 6, 299–303, DOI 10.1038/NPHOTON.2012.75.

Müller, T., Aharonovich, I., Wang, Z., Yuan, X., Castelletto, S., *et al.* (2012) 'Phonon-induced dephasing of chromium color centers in diamond', *Phys Rev B* 89, 195–210.

Nadolinny, V., Yelisseyev, A., Baker, J., Newton, M., Twitchen, D., *et al.* (1999) 'A study of ^{13}C hyperfine structure in the EPR of nickel–nitrogen-containing centres in diamond and correlation with their optical properties', *J Phys: Condens Matter*, 11, 7357–7376.

Naydenov, B., Kolesov, R., Batalov, A., Meijer, J., Pezzagna, S., *et al.* (2009) 'Engineering single photon emitters by ion implantation in diamond', *Appl Phys Lett*, 95, 181109, DOI 10.1063/1.3257976.

Neu, E., Steinmetz, D., Riedrich-Möller, J., Gsell, S., Fischer, M., *et al.* (2011a) 'Single photon emission from silicon vacancy colour centres in chemical vapour deposition nano-diamonds on iridum', *New J Phys*, 13, 025012, DOI 10.1088/1367-2630/13/2/025012.

Neu, E., Fischer, M., Gsell, S., Schreck, M. and Becher, C. (2011b) 'Fluorescence and polarization spectroscopy of single silicon vacancy centers in heteroepitaxial nanodiamonds on iridum', *Phys Rev B*, 84, 205211, DOI 10.1103/PhysRevB.84.205211.

Neu, E., Albrecht, R., Fischer, M., Gsell, S., Schreck, M. and Becher, C. (2012a) 'Electronic transitions of single silicon vacancy centers in the near infrared spectral region', *Phys Rev B*, 85, 245207, DOI 10.1103/PhysRevB.85.245207.

Neu, E., Agio, M. and Becher, C. (2012b) 'Photophysics of single silicon vacancy centers in diamond: implications for single photon emission', *Opt Express*, 29, 19956–19971.

Neu, E., Hepp, C., Hauschild, M., Snell, G., Fischer, M., *et al. New J Phys*, 15, 043005, DOI 10.1088/1367-2630/15/4/043005.

Nielsen, M. A. and Chuang, I. L. (2000) *Quantum Computation and Quantum Information*, Cambridge: Cambridge University Press.

Orwa, J., Aharonovich, A., Jelezko, F., Balasubramanian, G., Balog, P., *et al.* (2010) 'Nickel related optical centres in diamond created by ion implantation', *J Appl Phys*, 107, 093512, DOI 10.1063/1.3357374.

Oxborrow, M. and Sinclair, A. (2005) 'Single photon sources', *Contemp Phys*, 107, 093512, DOI 10.1080.00107510512331337936.

Petrakova, V., Taylor, A., Kratochvilova, I., Fendrych, F., Vacik, J., *et al.* (2012) 'Luminescence of nanodiamond driven by atomic functionalization: Towards novel detection principles', *Adv Funct Mater*, 22, 812–819, DOI 10.1002/adfm.201101936.

Pezzagna, S., Naydenov, B., Jelezko, F., Wrachtrup, J. and Meijer, J. (2010) 'Creation efficiency of nitrogen–vacancy centres in diamond', *New J Phys*, 12, 065017, DOI 10.1088/1367-2630/12/6/065017.

Pezzagna, S., Rogalla, D., Wildanger, D., Meijer, J. and Zaitsev, A. (2011) 'Creation and nature of optical centres in diamond for single photon emission – overview and critical remarks', *New J Phys*, 13, 035024, DOI 10.1088/1367-2630/13/3/035024.

Plakhotnik, T., Moerner, W., Palm, V. and Wild, U. (1995) 'Single molecule spectroscopy: maximum emission rate and saturation intensity', *Opt Commun*, 114, 83–88.

Rabeau, J., Chin, Y., Prawer, S., Jelezko, F., Gaebel, T. and Wrachtrup, J. (2005) 'Fabrication of single nickel–nitrogen defects in diamond by chemical vapor deposition', *Appl Phys Lett*, 86, 131926, DOI 10.1063/1.1896088.

Rabeau, J., Stacey, A., Rabeau, A., Prawer, S., Jelezko, F., *et al.* (2007) 'Single nitrogen vacancy centers in chemical vapour deposition nanocrystals', *Nano Lett*, 7, 3433–3437, DOI 10.1021/nl0719271.

Riedrich-Möller, J., Kipfstuhl, L., Hepp, C., Neu, E., Pauly, C., *et al.* (2012) 'One- and two-dimensional photonic crystal microcavities in single crystal diamond', *Nature Nanotechnol*, 7, 69–74, DOI 10.1038/NNANO.2011.190.

Rogers, L. (2010) 'How far into the infrared can a colour centre in diamond emit?', *Phys Procedia*, 3, 1557–1561, DOI 10.1016/j.phpro.2010.01.221.

Rondin, L., Dantelle, G., Slablab, A., Grosshans, F., Treussart, F., *et al.* (2010) 'Surface-induced charge state conversion of nitrogen–vacancy defects in nanodiamonds', *Phys Rev B*, 82, 115449, DOI 10.1103/PhysRevB.82.115449.

Sangouard, N. and Zbinden, H. (2012) 'What are single photons good for?', *J Mod Opt*, 59, 1458.

Santori, C., Fattal, D. and Yamamoto, Y. (2010) *Single-Photon Devices and Applications*, Weinheim: Wiley-VCH.

Scheel, S. (2009) 'Single-photon sources – an introduction', *J Mod Opt*, 56, 141–160, DOI 10.1080/09500340802331849.

Schmunk, W., Gramegna, M., Brida, G., Degiovanni, I., Genovese, M., *et al.* (2012) 'Photon number statistics of NV centre emission', *Metrologica*, 49, S156–S160, DOI 10.1088/0026-1394/49/2/S156.

Schröder, T. (2012) 'Integrated photonic systems for single photon generation and quantum applications: Assembly of fluorescent diamond nanocrystals by novel nano-manipulation techniques', Dissertation, Humboldt University Berlin.

Schröder T., Gädeke, F., Banholzer, M. and Benson, O. (2011a) 'Ultrabright and efficient single-photon generation based on nitrogen–vacancy centres in nanodiamonds on a solid immersion lens', *New J Phys*, 13, 055017.

Schröder, T., Schell, A., Kewes, G., Aichele, T. and Benson, O. (2011b) 'Fiber-integrated diamond-based single photon sources', *Nano Lett*, 11, 198–202.

Schröder, T., Fujiwara, M., Noda, T., Zhao, H., Benson, O. and Takeuchi, S., (2012) 'A nanodiamond-tapered fiber system with high single-mode coupling efficiency', *Opt Express*, 20, 10490.

Simpson, D., Ampen-Lassen, E., Gibson, B., Trpkovski, S., Hossain, F., *et al.* (2009) 'A highly efficient two level diamond based single photon source', *Appl Phys Lett*, 94, 203107, DOI 10.1063/1.3141450.

Sipahigil, A., Goldman, M., Togan, E., Chu, Y., Twitchen, D., *et al.* (2012) 'Quantum interference of single photons from remote nitrogen–vacancy centers in diamond', *Phys Rev Lett*, 108, 143601, DOI 10.1103/PhysRevLett.108.143601.

Siyushev, P., Jacques, V., Aharonovich, I., Kaiser, F., Müller, T., *et al.* (2009) 'Low temperature optical characterization of a near-infrared single-photon emitter in nanodiamonds', *New J Phys*, 11, 113029, DOI 10.1088/1367-2630/11/11/113029.

Siyushev, P., Kaiser, F., Jacques, V., Gerhardt, I., Bischof, S., *et al.* (2010) 'Monolithic diamond optics for single photon detection', *Appl Phys Lett*, 97, 241902, DOI 10.1063/1.3519849.

Smith, J., Grazioso, F., Patton, B., Dolan, P., Markham, M. and Twitchen, D. (2011) 'Optical properties of a single colour centre in diamond with a green zero-phonon line', *New J Phys*, 13, 045005, DOI 10.1088/1367-2630/13/4/045005.

Steinmetz, D., Neu, E., Meijer, J., Bolse, W. and Becher, C. (2011) 'Single photon emitters based on Ni/Si related defects in single crystalline diamond', *Appl Phys B*, 102, 451–458, DOI 10.1007/s00340-011-4402-x.

Steudle, G., Schietinger, S., Höckel, D., Dorenbos, S., Zadeh, I., *et al.* (2012) 'Measuring the quantum nature of light with a single source and a single detector', *Phys Rev A*, 86, 053814, DOI 10.1103/PhysRevA.86.053814.

Su, C., Greentree, A. and Hollenberg, L. (2008) 'Towards a picosecond transform-limited nitrogen–vacancy based single photon source', *Opt Express*, 16, 6240–6250.

Su, C., Greentree, A. and Hollenberg, L. (2009) 'High-performance diamond-based single-photon sources for quantum communication', *Phys Rev A*, 80, 052308, DOI 10.1103/PhysRevA.80.052308.

Wang, C., Kurtsiefer, C., Weinfurter, H. and Burchard, B. (2006) 'Single photon emission from SiV centres in diamond produced by ion implantation', *J Phys B*, 39, 37–41, DOI 10.1088/0953-4075/39/1/005.

Walker, J. (1979) 'Optical Absorption and Luminescence in diamond' *Rep Prog Phys,* 42, 1605

Wolfer, M., Obloh, H., Williams, O., Leancu, C.-C., Kirste, L., *et al.* (2010) 'Doping of single crystalline diamond with nickel', *Phys Status Solidi A*, 207, 2054–2057, DOI 10.1002/pssa.201000364.

Wu, E., Jacques, V., Zeng, H., Grangier, P., Treussart, F. and Roch, J.-F. (2006) 'Narrow-band single-photon emission in the near infrared for quantum key distribution', *Opt Express*, 14, 1296–1303.

Wu, E., Rabeau, J., Roger, G., Treussart, F., Zeng, H., *et al.* (2007) 'Room temperature triggered single-photon source in the near infrared', *New J Phys*, 9, 434, DOI :10.1088/1367-2630/9/12/434.

Wu, E., Rabeau, J. R., Treussart, F., Zeng, H., Grangier, P., *et al.* (2008) 'Nonclassical photon statistics in a single nickel–nitrogen diamond color center photoluminescence at room temperature', *J Mod Opt*, 55, 2893–2901, DOI 10.1080/09500340802267118.

Zaitsev, A. (2000) 'Vibronic spectra of impurity-related optical centers in diamond', *Phys Rev B*, 61, 12909, DOI 10.1103/PhysRevB.61.12909.

Zaitsev, A. (2001) *Optical Properties of Diamond: A Data Handbook*, Springer.

Zaitsev, A., Bergman, A., Gorokhovsky, A. and Huang, M. (2006) 'Diamond light emitting diode activated with Xe optical centers', *Phys Stat Solidi A*, 3, 638–642, DOI 10.1002/pssa.200521125.

Zaske, S., Lenhard, A. and Becher, C. (2011) 'Efficient frequency downconversion at the single photon level from the red spectral range to the telecommunications C-band', *Opt Express*, 19, 12825–12836.

Zaske, S., Lenhard, A., Keßler, C. A., Kettler, J., Hepp, C., *et al.* (2012) 'Visible-to telecom quantum frequency conversion of light from a single quantum emitter', *Phys Rev Lett*, 109, 147404, DOI 10.1103/PhysRevLett.109.147404.

Zoller, P., Beth, T., Binosi, D., Blatt, R., Briegel, H., *et al.* (2005) 'Quantum information processing and communication', *Eur Phys J D*, 36, 203–228, DOI: 10.1140/epjd/e2005-00251-1.

Zwinkels, J. C., Ikonen, E., Fox, N. P., Ulm, G. and Rastello, M. L. (2010) 'Photometry, radiometry and "the candela": evolution in the classical and quantum world', *Metrologia* 47, R15.

7

Using defect centres in diamonds to build photonic and quantum optical devices

A. W. SCHELL, J. WOLTERS, T. SCHRÖDER and O. BENSON, Humboldt-Universität zu Berlin, Germany

DOI: 10.1533/9780857096685.2.160

Abstract: In this chapter, we introduce defect centres in diamond nanocrystals as building blocks of fundamental photonic and quantum optical devices. We first present the motivation for these devices and introduce the optical properties of nanodiamond. We then describe some approaches to establishing enhanced light–matter interaction on the nanoscale and introduce a method for controlled assembly. Integrated nanophotonic and nanoplasmonic elements are the topic of the next section, and we then present two applications of a fundamental light source based on nanodiamonds. We conclude the chapter with the future prospects for nanodiamond research.

Key words: nanodiamond, single-photon source, photonic crystal, surface plasmon, nitrogen–vacancy defect centre.

7.1 Introduction

A fundamental photonic device, involving single elementary excitations such as photons and spins, consists of various coupled and/or integrated entities, such as single emitters, optical microcavities, optical waveguides, and photon-to-electron or photon-to-spin interfaces (Benson, 2011). An immediate advantage of such a device is its potentially small size. Fundamental entities can be integrated on the scale of a micrometre, possibly down to a few nanometres. However, there are more advantages of a fundamental photonic device over a macroscopic object:

- its state can be controlled, initialised and read out with precision at the fundamental quantum mechanical limit;
- its operational fidelity – often based on the interconversion of single excitations – can approach 100%;
- its functionality may be based on coherent rather than incoherent dynamics, allowing devices that maintain quantum coherence, which is a crucial requirement for applications in quantum information processing.

Thus, a fundamental device could outperform traditional devices in terms of operation speed, integrability and energy efficiency.

On the other hand, fundamental photonic systems can also be regarded as ideal model systems to study the interaction of small quantum systems with each other

© 2014 Elsevier Ltd

or with a (local) structured environment. The rich physics of these systems, such as quantum mechanical decoherence, energy transfer processes and non-Markovian back-action, has not been fully understood yet.

In this chapter, we first describe strategies to 'harvest' light from a fundamental light-emitting entity, i.e. a single quantum emitter (Section 7.2). Approaches to enhancing light–matter interaction at the fundamentally lowest intensity of light – a single photon at a time – will be discussed as well. Then, in Section 7.3, we introduce our main workhorse, i.e. nanodiamonds containing single defect or colour centres, serving as robust quantum emitters. Sections 7.4 and 7.6 show two techniques which allow controlled integration of these emitters into various photonic structures. Examples where some basic functionalities of a fundamental photonic device, i.e. the generation and guiding of elementary excitations, were realised are described in Sections 7.5 and 7.6. Finally, Section 7.7 presents two experiments where we show applications of fundamental light sources. We conclude this chapter with a discussion of prospects and future directions.

7.2 Architectures for single-photon collection and single-photon interaction

The most fundamental light emitter is a single quantum system that decays spontaneously. With the ability to isolate quantum systems and to detect extremely small optical signals, it has become possible to realise such single-photon sources in a number of different systems. Single atoms, molecules and quantum dots, as well as defect centres, have been studied successfully (Grangier *et al.*, 2004).

The quality of single-photon sources and a proof of single-photon emission from them is routinely derived from a measurement of the second-order coherence function $g^{(2)}(\tau)$ given by (Loudon, 2000)

$$g^{(2)}(\tau) = \langle :I(t)I(t+\tau): \rangle / \langle I(t) \rangle^2$$

where $I = E^{\dagger}E$ is the field intensity operator and $::$ denotes normal ordering. For uncorrelated light, for example laser light, with a Poissonian photon number distribution, $g^{(2)}(\tau) = 1$ for all τ. However, for a number state $|;n\rangle$, this function drops at $\tau = 0$ to $g^{(2)}(0) = 1 - 1/n < 1$ (Loudon, 2000). The function $g^{(2)}(\tau)$ is typically measured in a Hanbury Brown and Twiss (HBT) set-up (Hanbury Brown and Twiss, 1956) utilizing a 50/50 beam splitter, two single-photon detectors, and coincidence electronics. Figure 7.1 shows a schematic illustration of such an HBT set-up and a measurement of $g^{(2)}(\tau)$ for fluorescence from a single quantum emitter (in this case a single nitrogen–vacancy centre in diamond, as introduced in the next section). A clear so-called antibunching at $\tau = 0$ can be observed.

A useful single-photon source should emit photons at a high rate into a single mode. However, the maximum rate of spontaneous emission is limited by the excited-state lifetime of the emitter, and photons are typically emitted in a dipole

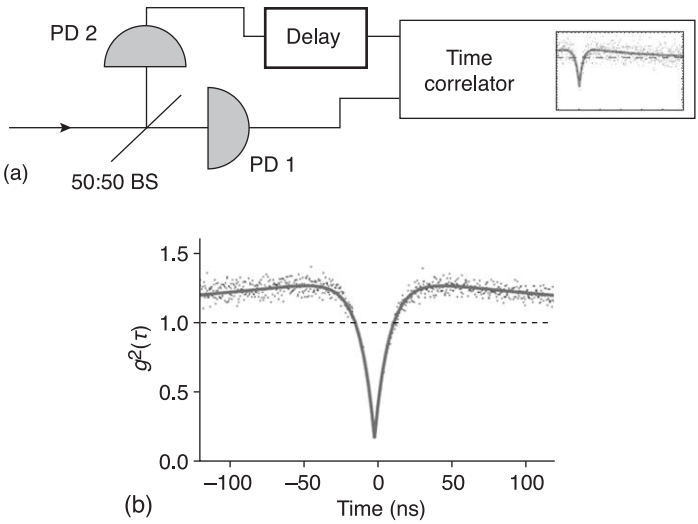

7.1 (a) Schematic illustration of a Hanbury Brown and Twiss set-up to measure the second-order coherence function. (b) Measurement of the normalised second-order coherence function $g^{(2)}(\tau)$ from a single nitrogen–vacancy defect centre in a nanodiamond, showing a pronounced antibunching under continuous-wave excitation.

emission pattern over almost the full solid angle of 4π. Figure 7.2 shows three approaches to increasing single-photon emission into specific modes.

- The first approach, shown in Fig. 7.2(a), utilises dielectric structures surrounding the single-photon emitter. Enhanced emission of the emitter into a medium with a higher index of refraction and light-guiding into a specific direction are exploited. Typical architectures are thin dielectric wires or pillars (Claudon *et al.*, 2010; Babinec *et al.*, 2010) and solid immersion lenses (Hadden *et al.*, 2010; Siyushev *et al.*, 2010; Schröder *et al.*, 2011b). The spontaneous-emission rate is not or only weakly enhanced in these configurations.
- The second approach utilises resonant or Purcell enhancement (Purcell, 1946) of the spontaneous emission into a specific mode. It relies on the modification of the density of states by an optical cavity with a high quality factor Q and a small mode volume V_{eff}. The enhancement factor F can be derived from Fermi's golden rule as

$$F = \frac{3}{4\pi^2}\left(\frac{\lambda_c}{n}\right)^3 \frac{Q}{V_{\text{eff}}}$$

It is assumed that the emitter (emission wavelength λ_c in a medium with refractive index n) is aligned with respect to the cavity mode and in resonance with the cavity. An example of a quantum dot embedded in a tiny Fabry–Pérot cavity formed by two Bragg mirrors is shown in Fig. 7.2(b) (Heindel *et al.*, 2010).

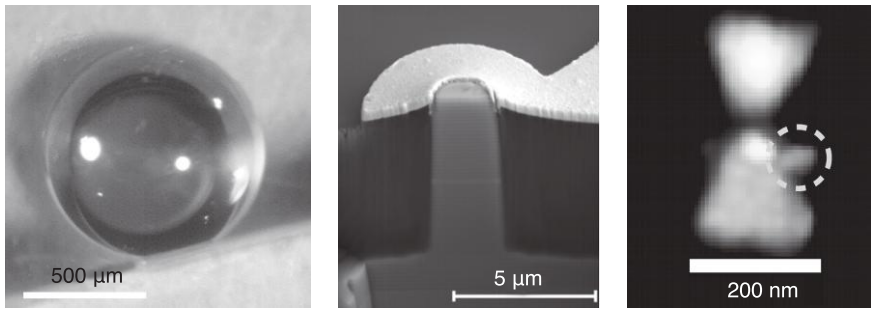

7.2 Different approaches to increasing the single-photon emission into specific modes. (a) Passive collection via a solid immersion lens (SIL), here by means of diamond defect centres in a diamond SIL (Siyushev *et al.*, 2010; Schröder *et al.*, 2011b), (b) Resonant Purcell enhancement, here by means of a single quantum dot in a micropillar cavity formed from two Bragg stacks (Heindel *et al*, 2010) (© 2010, AIP). (c) Plasmonic enhancement, here by means of a single nanodiamond on a plasmonic bowtie antenna (Schell *et al.*, 2011a) (© 2011, OSA).

- The density of states cannot only be modified by a resonant dielectric structure. Another approach exploits the large field enhancement close to a metal–dielectric interface. There, surface plasmon polaritons (SPPs) (Maier, 2007; Bozhevolnyi and García-Vidal, 2008), which arise from the coupling of electromagnetic fields to oscillations of the electron plasma, are supported. The spontaneous emission of a quantum emitter placed in an SPP mode can be enhanced by orders of magnitude (Kinkhabwala *et al.*, 2009; Russell *et al.*, 2012). Figure 7.2(c) shows an example where a diamond defect centre in a nanodiamond is coupled to a plasmonic structure, i.e. a bowtie antenna, in order to enhance the spontaneous-emission rate (Schell *et al.*, 2011a). In addition to the field enhancement obtainable, SPPs offer another advantage: they can be efficiently guided along thin metal stripes or wires, called SPP waveguides. Long-range propagation over distances of a few millimetres is possible at telecommunication wavelengths. By comparison with their purely optical counterparts, the narrow spatial confinement to fractions of a free-space optical wavelength makes them ideal building blocks for future chip-based nanophotonic components and devices (Bozhevolnyi and García-Vidal, 2008).

Coupling of single-photon emitters to photonic, plasmonic or resonant structures is thus an ideal approach to making use of single elementary excitations of the electromagnetic field in fundamental devices. We shall come back to this issue after the introduction of our ‘workhorse’ quantum emitter in the following two sections.

7.3 Properties of defect centres in nanodiamonds

Diamond exists not only in the form of large bulk diamonds with macroscopic sizes, but also in the form of nanoscopic monocrystals with a size of only a few nanometres. Such diamond nanocrystals (referred to here as nanodiamonds) can be synthesised on an industrial scale using high pressure and high temperature (HPHT) or detonation-chamber growth. After removal of contamination and non-diamond carbon, the diamond particles feature an oriented crystal structure with parallel-running cleavage planes, similar to natural diamond. Such industrial diamonds are a popular choice for grinding, lapping and polishing purposes. High-energy ball milling to produce nanodiamonds from bulk diamonds and several other synthesis methods are frequently used as well (Boudou *et al.*, 2009; Pentecost *et al.*, 2010; Krueger, 2011).

In principle, the optical properties of defect centres in bulk diamond are identical to those of defect centres in nanodiamonds. Here, we focus on optically active defect centres (called colour centres) in nanodiamonds. Only a few centres have been investigated systematically at the single-centre level. Among them, the nitrogen–vacancy (NV) centre is the most extensively studied. It has a high abundance in nanodiamonds. We estimate that 5% of typical commercially available nanodiamonds with a size of about 30 nm contain a single centre. By spin-coating with a properly diluted and ultrasonically treated diamond solution, individual nanodiamonds can be deposited on suitable substrates such as cover slips cleaned with an oxygen plasma, acid or an alkaline liquid. Small amounts of a polymer such as polyvinyl alcohol can be added to improve the distribution and sticking of the nanodiamonds to the substrate.

Other centres, such as the silicon–vacancy (SiV) centre and nickel/chromium-related centres, can be grown by chemical vapour deposition (CVD) using commercial nanodiamonds as seeds (Fig. 7.3). Here, impurity atoms from the substrate are incorporated into the diamond nanocrystal during the growth process (Neu *et al.*, 2011, 2012a, 2012b) or can be implanted by means of ion beams (Siyushev *et al.*, 2009; Aharonovich *et al.* 2009, 2010a, 2011a, 2010b). This results in an increased abundance of impurity atoms and the corresponding defect centres. Table 7.1 lists some optical properties of defect centres in nanodiamonds.

Optically active defect centres in nanodiamonds are stable solid-state quantum systems. As single-photon sources, they provide the advantage of efficient photon collection. In bulk diamond, with a relatively large index of refraction of 2.4, the photon extraction efficiency is limited by total internal reflection at the diamond surface. This is not the case for sub-wavelength-sized nanodiamonds, which resemble point-like sources and thus allow all emitted photons to be collected, in principle. Therefore, it is not surprising that defect centres in nanodiamonds are among the brightest stable solid-state single-photon sources. For example, for SiV centres in nanodiamond on a 150 nm iridium layer, single-photon count rates of up

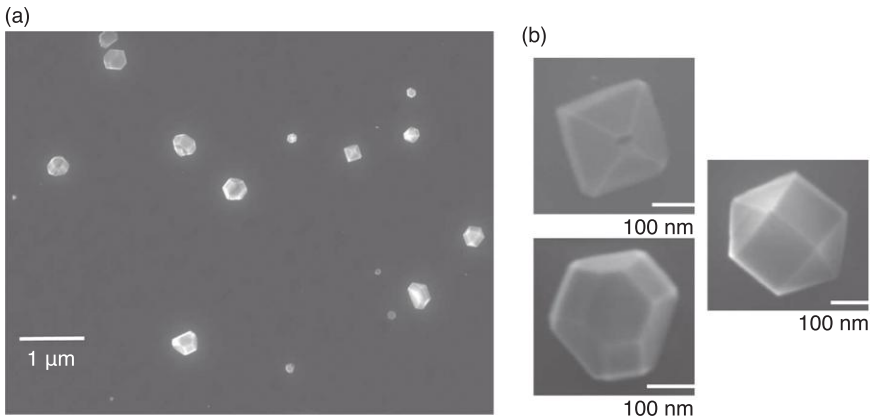

7.3 (a) Scanning electron microscope image of CVD diamond nanocrystals on an iridium surface. (b) Magnified images of individual well-faceted nanodiamonds. From Neu *et al.* (2012b), © IOP Publishing and Deutsche Physikalische Gesellschaft. CC BY-NC-SA.

Table 7.1 Summary of optical properties of different defect centres in nanodiamonds studied at the single-centre level

Defect centre	Negatively charged nitrogen–vacancy (Collins *et al.*, 1983; Jelezko and Wrachtrup, 2006; Schröder *et al.*, 2011b; Shen *et al.*, 2008)	Silicon–vacancy (Neu *et al.*, 2011; Neu *et al.*, 2012a; Neu *et al.*, 2012b)	Chromium-related (Aharonovich *et al.* 2010a; Aharonovich *et al.* 2009)
ZPL wavelength	638 nm	740 nm	740–770 nm
Lifetime	~12 ns (bulk)	1.2 ns	1–14 nm
Quantum efficiency	0.9 (bulk)	0.1	0.9
Debye–Waller factor	0.05	0.9	>0.9
Maximum count rate	1 Mcount/s	5 Mcount/s	2–3 Mcount/s
Minimum linewidth	16 MHz	25 GHz	~4 nm

to 4.8 million counts per second could be observed (Neu *et al.*, 2011, 2012b). In contrast, for SiV centres in bulk diamond, count rates as low as 1000 counts/s have been reported (Wang *et al.*, 2006). Although the influence of the iridium layer on the experiment is unclear, this demonstrates strikingly how effectively nanodiamonds can serve as single-photon sources. This also holds for NV centres,

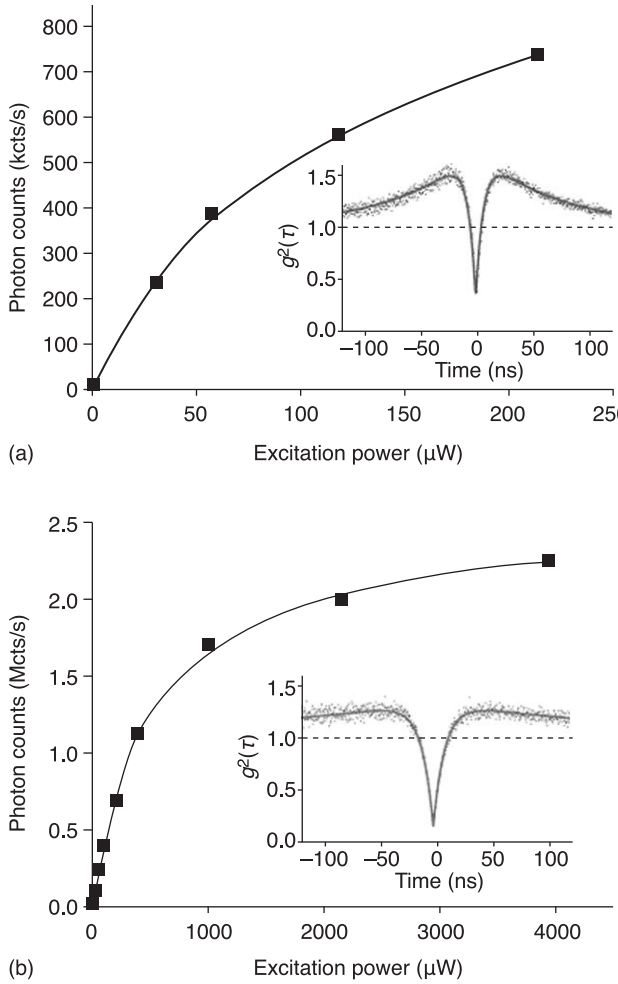

7.4 Saturation measurements of a stable, bright NV^- centre (a) and a brighter, but blinking NV centre (b). The insets show the normalised autocorrelation function $g^{(2)}(\tau)$. From Schröder *et al.* (2011b), © IOP Publishing and Deutsche Physikalische Gesellschaft. CC BY-NC-SA.

where up to one million counts/s can be achieved with solid or oil immersion microscopy (Schröder *et al.*, 2011b), as shown in Fig. 7.4.

Although defect centres in nanodiamonds are, in general, stable quantum emitters even at room temperature, blinking, photobleaching and spectral diffusion have been observed. These phenomena are also well known in single molecules and colloidal semiconductor quantum dots. For example, blinking has been reported for NV centres in very small detonation nanodiamonds

with a size of approximately 5 nm (Bradac *et al.*, 2010). About 25% of these diamonds show an on/off behaviour with an average on/off time in the order of a few tens of milliseconds. As the on/off time is measured to be dependent on the excitation power, it is assumed that the additional electron of the negatively charged NV centre is trapped in surface charge traps during the excitation cycle (Bradac *et al.*, 2010). A similar blinking of NV centres was also reported by Schröder *et al.* (2011b) (see Fig. 7.4). A few individual SiV centres have shown photobleaching on timescales of about one hour (Neu *et al.*, 2011). Here the underlying process is unclear, but surface-related effects are suspected.

A major challenge for the use of nanodiamonds in quantum technology is the high abundance of impurities and defects. Additionally, surface effects can have significant influence on the optical coherence properties. Even at liquid helium temperatures and below, stable Fourier-limited optical transitions have not been observed so far, not even for the zero-phonon line (ZPL). In experiments, off-resonant and on-resonant excitation have to be distinguished. Under resonant excitation, a linewidth of 4 GHz has been observed in Ni-related defects emitting at around 770 nm using photoluminescence excitation spectroscopy (Siyushev *et al.*, 2009). This is 50 times broader than the homogeneous lifetime-limited linewidth of about 80 MHz. For NV centres in nanodiamonds, almost Fourier-limited lines with a width of only 16 MHz (Shen *et al.*, 2008) were observed in type Ib nanodiamonds at a temperature of about 10 K. Unfortunately, here the absorption line jumped on a timescale of a few seconds, resulting in a much broader line on longer timescales.

Under off-resonant excitation, the observed linewidths are usually much broader. For SiV centres, linewidths down to 25 GHz were observed at temperatures around 5 K (Neu *et al.*, 2012b), which is close to the lifetime limit. In contrast, NV centres in milled type Ib nanodiamonds show linewidths on the order of 300 GHz. Recent systematic studies by photon correlation interferometry have revealed that this broadening is due to fast spectral diffusion, i.e. sudden jumps of a narrow emission line (Wolters *et al.*, 2013) (see Fig. 7.5). These jumps occur on microsecond timescales and are linearly dependent on the excitation power, which gives evidence that the excitation laser is the main cause of spectral diffusion. The laser ionises charge traps, resulting in a change of the local electrostatic environment and, consequently, a fluctuating Stark shift of the optical transition.

As a concluding remark for this section, we note that spectral diffusion is a major drawback of defect centres in nanodiamonds, in particular for applications in quantum information processing where indistinguishable photons are needed. Nevertheless, defect centres in nanodiamonds are frequently used, since they are small (down to a few nanometres) and can be easily integrated into hybrid devices using bottom-up approaches, as shown in the following sections.

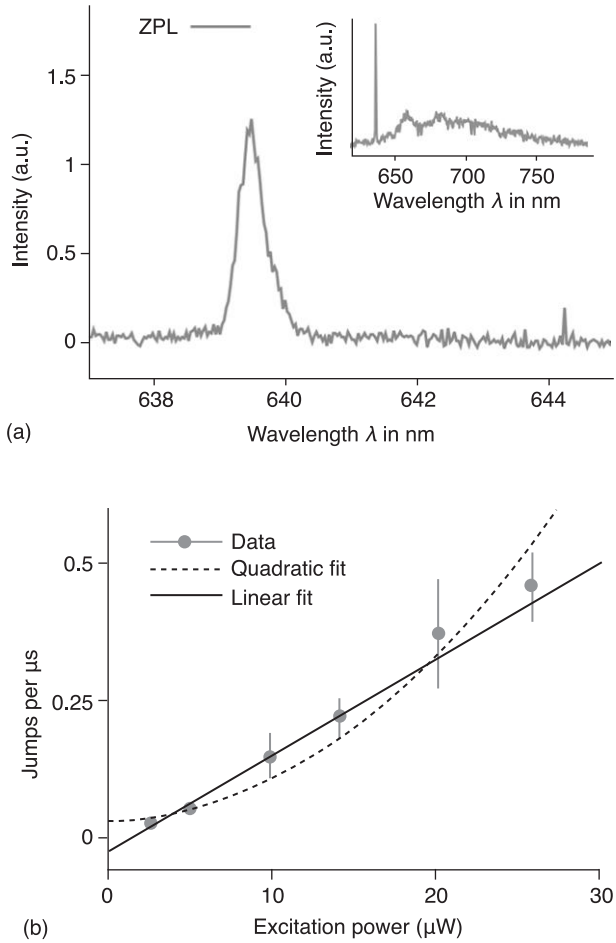

7.5 (a) Fluorescence spectrum of a single NV centre in type Ib nanodiamond around the zero-phonon line measured at 5 K. The inset shows the full spectrum. (b) Measured spectral jump rate in type Ib nanodiamonds as a function of excitation power. From Wolters *et al.* (2013), © 2013, APS.

7.4 A method for the controlled assembly of fundamental photonic elements using a scanning probe technique

In order to study or exploit fundamental interactions in photonic or plasmonic systems in a controlled way, first an advanced assembly technique is required. There are various approaches (Benson, 2011), but in general two classes can be distinguished: random techniques and deterministic ones. Random techniques, for example spin-coating and drop-casting, are fast and easy to implement. In

Section 7.7, we introduce an example where spin-coating has been utilised to produce a bright, stand-alone single-photon source. A drawback of the random approach is, however, that it deposits the nanodiamonds all over a supporting structure. This leads to huge amounts of unneeded and unwanted particles on the sample and in most cases requires post-processing by nanomanipulation (Junno *et al.*, 1995; van der Sar *et al.*, 2009). Random techniques in general require post-selection or post-processing of the nanodiamonds and structures, because the desired configuration can only be achieved by chance.

In contrast, in deterministic approaches, a nanoparticle is pre-selected and brought to a pre-selected structure, usually in a pick and place procedure (Ampem-Lassen *et al.*, 2009; Schell *et al.*, 2011b; van der Sar *et al*., 2011). Using such deterministic positioning methods, contamination of the whole sample with unwanted nanoparticles is avoided. However, the most important advantage of pick and place methods is their scalability. Positioning of a second (or third and so on) nanoparticle takes only as long as it took to position the first one. This is in sharp contrast to random methods, where one has to try until enough suitable emitters are placed in the right position by chance, which is highly unlikely.

The deterministic techniques used so far include the employment of a tapered fibre to deposit nanodiamonds (Barclay *et al.*, 2009; Gregor *et al.*, 2009), transfer with a nanomanipulator in a scanning electron microscope (SEM) (Ampem-Lassen *et al.*, 2009; van der Sar *et al.*, 2011), and using the tip of an atomic force microscope (AFM) to pick up nanodiamonds and place them in a controlled way (Schell *et al.*, 2011b). Here, we will focus on the latter technique. The pick and place technique using an AFM usually consists of the following three steps, which are illustrated in Fig. 7.6. Step one is identification and pre-characterisation (Fig. 7.6(a) and (b)); step two is picking up (Fig. 7.6(c) and (d)); and step three is placing (Fig. 7.6(e) and (f)).

An appropriate experimental set-up for the first step is an inverted confocal microscope with an AFM on top. A sample of nanodiamonds spin-coated on a glass cover slip is scanned optically (e.g. by sample scanning) in order to find a nanodiamond with the desired properties (photon correlation is used to reveal the number of emitting centres, lifetime, spectrum, etc.). Then, the confocal volume is searched for the pre-characterised nanodiamond with the AFM tip by scanning in tapping mode.

With a knowledge of the position of the nanodiamond relative to the AFM tip, the second step, the pick-up, can be performed. The AFM mode is switched to contact mode, and the tip is pressed onto the nanodiamond with a force of up to 1 μN and afterwards retracted. While the nanodiamond is being pressed down, fluorescence of the cantilever is visible in addition to the nanodiamond's fluorescence. Upon retraction, there is a sharp drop in fluorescence, either to its former level, or to the background level if the nanodiamond sticks to the tip owing to adhesion. The adhesion forces can be influenced by the choice of tip material (e.g. a Pt/Ti-coated tip) and by air humidity.

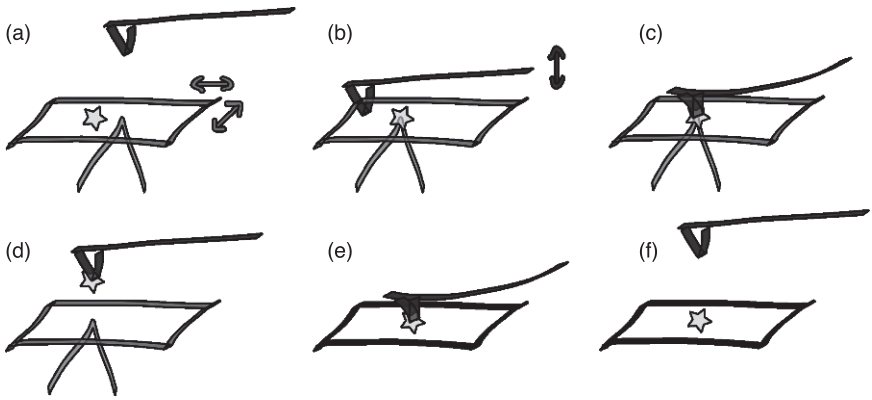

7.6 Pick and place technique. In (a), the nanodiamond is optically pre-characterised by means of scanning confocal microscopy and positioned in the confocal volume. A tapping-mode AFM scan reveals its shape and exact position, as shown in (b). (c) and (d) illustrate the pick-up process. The AFM tip is pressed onto the nanodiamond in (c). The nanodiamond can subsequently stick to the tip and exit the laser focus as shown in (d). In (e), the AFM tip is pressed onto another sample in order to release the diamond. This is repeated until successful. (f) shows a successful pick and place action (Schell *et al.*, 2011b, © 2011, AIP).

The third step is to place the nanodiamond at its assigned position. This can be on an arbitrary sample mounted on the inverted microscope. The only requirement is accessibility with the AFM tip. A small area is scanned in tapping mode to ensure that the nanodiamond will be placed at the right spot. Then, similarly to the second step, the tip is pressed onto that spot in contact mode to place the diamond. A small AFM scan or optical feedback from the microscope reveals if the nanodiamond is placed correctly. Once the nanodiamond has been deposited, its position can be adjusted using standard AFM nanomanipulation techniques. If the deposition was not successful, step three has to be repeated. Depending on the experimental conditions, the overall process yield is up to about 33%, owing to nanodiamonds sticking to the side of the tip or being lost unnoticed during the initial scan.

In addition to the three steps described above, it may be required to add some more steps in order to adjust the procedure for special experimental conditions. When, for example, the target structure has a complex topography, it may be necessary first to place the nanodiamond away from the structure by the process described above, then to identify the right place via AFM scanning without the nanodiamond on the tip and then, finally, to perform the pick and place procedure again (Wolters *et al.*, 2010; Schröder *et al.*, 2011a).

The following section describes two examples of how to assemble nanophotonic architectures using the pick and place technique.

7.5 Fundamental photonic and plasmonic elements assembled from nanodiamonds by a scanning probe technique

In this section, we show that nanodiamonds are ideal building blocks for realising fundamental photonic or plasmonic elements. These elements can be regarded as model systems for future highly integrated devices. In the first example, a dielectric resonant structure is exploited to increase the collection efficiency for single photons from a defect centre in a nanodiamond. The second example shows that defect centres can be regarded – in a more general way – as sources of single quanta of excitations such as surface plasmon polaritons.

7.5.1 Optical microcavities for single-photon harvesting

As discussed in Section 7.2, the emission properties of individual quantum emitters can be drastically changed by coupling to resonant cavities. In such structures, the vacuum fluctuations of the electromagnetic field are enhanced at resonance, while off-resonant vacuum fluctuations are suppressed. The different regimes of cavity quantum electrodynamics depend on the ratio of three rates. These are the coupling rate of the emitter to the cavity mode, g; the spontaneous-emission rate γ of the emitter to non-cavity modes; and the cavity loss rate κ (Benson, 2011; Yoshie *et al.*, 2004). With NV centres in nanodiamonds, the weak-coupling regime ($g < \kappa$) can be reached (McCutcheon and Lončar, 2008). In this regime, the radiative emission into the cavity mode is significantly increased by the Purcell factor F introduced in Section 7.2. With a large Purcell factor, more photons are emitted into a well-defined spectral and spatial mode. Enhancing the radiative rate increases the quantum efficiency of the emitter, i.e. more energy from the excited state is transferred into photons. Moreover, if a cavity mode is tuned to the zero-phonon line of an NV centre, emission to higher phonon modes is suppressed, i.e. the Debye–Waller factor is enhanced. These effects are crucial to obtaining a large number of indistinguishable photons, a key requirement for optical quantum-information-processing tasks.

One particularly interesting resonant structure is a photonic-crystal cavity. This provides the smallest mode volumes V_{eff} and large Q-factors and thus promises high Purcell factors (Vahala, 2003; Tanabe *et al.*, 2007) (see also Section 7.2). Furthermore, photonic-crystal cavities provide all of the requirements for on-chip integration of photonic circuits consisting of several emitters, cavities and waveguides (Joannopoulos *et al.*, 1997; O'Brien *et al.*, 2009; Faraon *et al.*, 2011).

Coupling of single NV centres in diamond to photonic microcavities and nanocavities has been a major challenge. Besides fabrication of all-diamond structures, where optical cavities are processed from diamond membranes right from the start (Riedrich-Möller *et al.*, 2012; Faraon *et al.*, 2012), there are hybrid approaches using diamond nanocrystals coupled to external cavities. In that case, the photonic-crystal cavity can be made from another material, for example a

semiconductor that is transparent at the emission wavelength of the defect centre. Silicon nitride (Si_3N_4) and gallium phosphide (GaP) are particularly suited for the NV centre. Nevertheless, in early experiments using Si_3N_4 photonic-crystal cavities, the intrinsic material fluorescence from the cavity was much brighter than an NV centre's single-photon emission. Thus, radiative coupling of an individual NV centre to an Si_3N_4 photonic-crystal cavity could not be proven (Barth *et al.*, 2009, 2010a). Later, using photonic-crystal cavities made from GaP, several groups (Englund *et al.*, 2010; Wolters *et al.*, 2010; van der Sar *et al.*, 2011) demonstrated enhanced single-photon emission from a single NV centre in a nanodiamond inside a photonic-crystal cavity.

It is possible to distinguish two hybrid approaches. In one approach, a photonic-crystal membrane made from GaP can be isolated and moved with a micropositioner over a thin polymer film containing nanodiamonds (Englund *et al.*, 2010). In order to extend this method to several emitters, NV centres must be placed at well-defined locations in the polymer film, which is not possible. Another disadvantage is that the polymer film disturbs the cavity mode, leading to reduced cavity *Q*-factors. In the second approach, pre-selected nanodiamonds are positioned directly on a free-standing photonic-crystal membrane. In this case, the mode is disturbed only weakly by the small nanodiamond. Deterministic production of complex devices consisting of several pre-selected emitters in several cavities is also possible (Wolters *et al.*, 2010; van der Sar *et al.*, 2011; Wolters *et al.*, 2012). Figure 7.7 shows an approach where an SEM manipulator was used to position a single nanodiamond in a so-called S1 cavity, consisting of a photonic-crystal membrane with one missing hole.

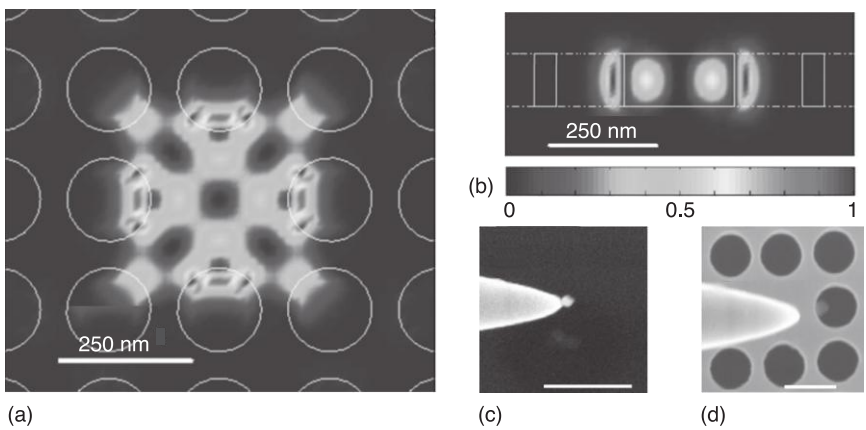

7.7 Positioning of a nanodiamond in a photonic-crystal S1 cavity using an SEM manipulator. (a) Top view of the calculated mode profile of an S1 cavity consisting of a single missing hole. (b) Cross-section of the mode profile. (c) SEM image of a diamond nanocrystal on a tip. (d) SEM image of an NV-containing nanodiamond placed in the field maximum of the photonic-crystal cavity. From van der Sar *et al.* (2011), © 2011, AIP.

Alternatively, the pick and place method using an AFM, described in Section 7.4, can be applied. Figure 7.8 shows the results of an experiment where a single pre-selected nanodiamond containing a single NV centre was placed in a photonic-crystal L3 cavity (with three missing holes) fabricated from GaP. The fundamental

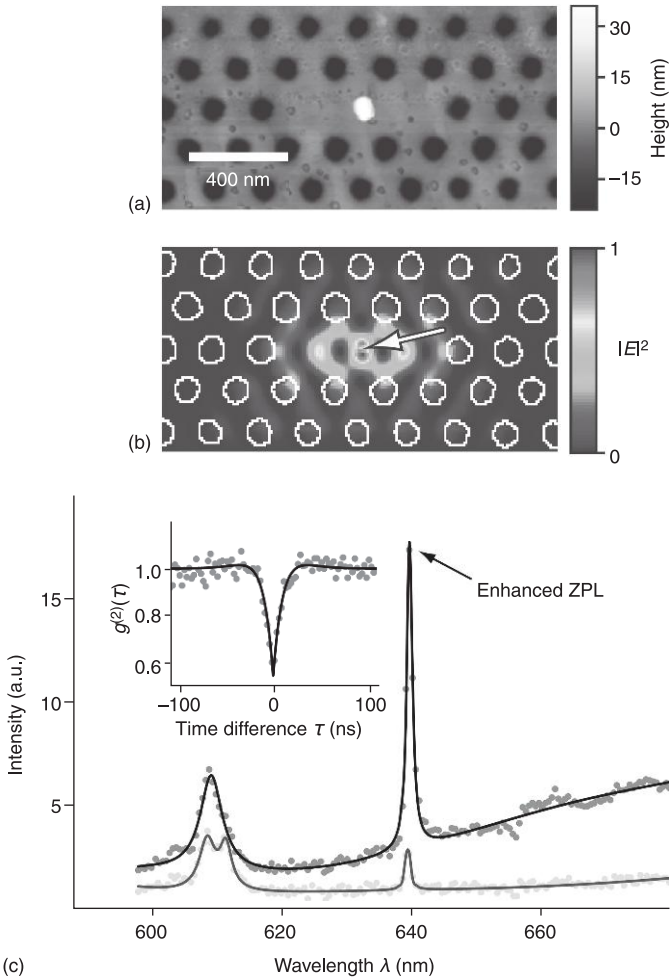

7.8 Positioning of a nanodiamond in a photonic-crystal cavity using a pick and place approach. (a) AFM image of an L3 GaP cavity with a nanodiamond of height 35 nm located close to the centre. The lattice constant is 200 nm. (b) Simulated FDTD electric-field profile of the fundamental mode of this cavity. The arrow indicates the position of the diamond. (c) Enhancement of the zero-phonon line (ZPL) of a single NV centre in the photonic-crystal cavity. The inset shows its measured $g^{(2)}$ function. The lower curve indicates the measured ZPL outside the photonic structure, and the upper curve the measured ZPL after placing the NV centre in a photonic-crystal cavity. The enhancement, by a factor of 12, is very large. From Wolters *et al.* (2010), © 2010, AIP.

mode of the cavity was tuned to overlap with the zero-phonon line of the NV centre. A resonant enhancement of the ZPL emission by a Purcell factor $F = 12$ was observed.

These experiments are a major step towards more complex quantum hybrid devices. For example, if a single NV centre is placed in a waveguide-coupled cavity, enhanced readout of the NV spin becomes possible (Young *et al.*, 2009), and several NV centres can be coupled using high-quality cavities with the ultimate goal of building quantum-information-processing devices (Yang *et al.*, 2010, 2011; Chen Q *et al.*, 2011).

7.5.2 Defect centres in nanodiamonds as single-plasmon sources

Another approach to enhancing light–matter interaction, which was described in Section 7.2, utilises surface plasmon polaritons. SSPs concentrate electromagnetic fields in very small volumes, achieving field strengths much higher than those obtainable with photons of the same energy (Barnes *et al.*, 2003). This field enhancement is accompanied by an elevated density of states, leading to a pronounced increase in an emitter's decay rate at this position. Surface plasmons can also be used to guide this concentrated electromagnetic energy along surface plasmon waveguides (Barnes *et al.*, 2003).

Much effort has been put into coupling nanodiamonds to plasmonic structures. NV centres have been coupled to metal surfaces (Lim *et al.*, 2009; Cuche *et al.*, 2010), gold nanospheres in an antenna-like configuration (Schietinger *et al.*, 2009), optical antennas (Schell *et al.*, 2011a; Dregely *et al.*, 2012; Wolters *et al.*, 2012) and silver nanowires (Kolesov *et al.*, 2009; Huck *et al.*, 2011; Schell *et al.*, 2011a). In the following, we describe the controlled coupling of a single NV centre in a nanodiamond to a silver nanowire serving as a waveguide, resembling a three-port single-plasmon beam splitter (Schell *et al.*, 2011a). Coupling was achieved by the pick and place technique described in Section 7.4 in a very controlled way. A pre-selected nanodiamond with a single NV centre was coupled to a silver nanowire approximately 80 nm in diameter, as shown in Fig. 7.9(a). When the NV centre was excited, there were four bright spots visible in the optical microscope image (right). The spot at the position of the nanodiamond (labelled '2') originated from photons emitted from the diamond and collected directly with the microscope objective. The other three spots were surface plasmons excited by the NV centre, scattered out to discontinuities in the waveguide, namely the two ends and a kink in the middle. Figure 7.9(c) shows a cross-correlation measurement between photons emitted directly from the diamond and photons scattered out at the ends of the waveguide (labelled '1' in Fig. 7.9(a)). The non-classical behaviour of the photons is demonstrated by the antibunching dip visible in the measured cross-correlation here. Since it was known from the pre-selection that only a single NV centre was involved, the reduced dip could be attributed to a background, i.e. background plasmons created by the autofluorescence of the nanowire.

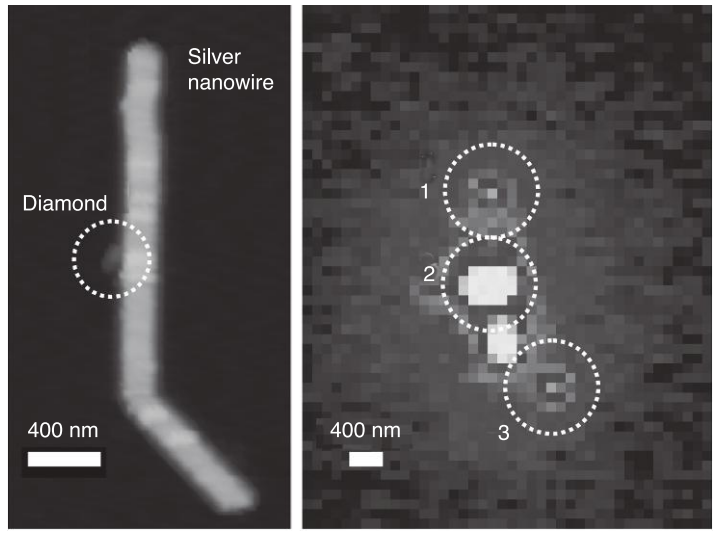

(a)

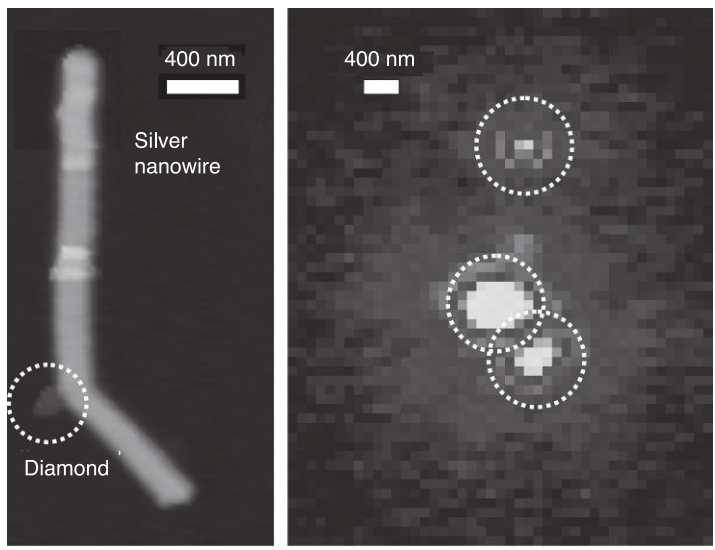

(b)

7.9 Coupling of NV centres to plasmonic structures. (a) and (b) show AFM (left) and optical (right) images of a nanodiamond coupled to a silver nanowire. The nanodiamond was excited by a laser beam and created single plasmons, which were scattered out at discontinuities in the wire. (*Continued*).

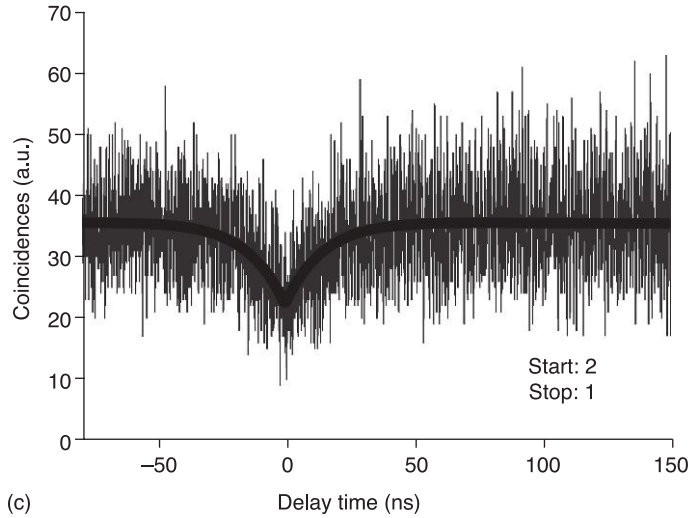

(c)

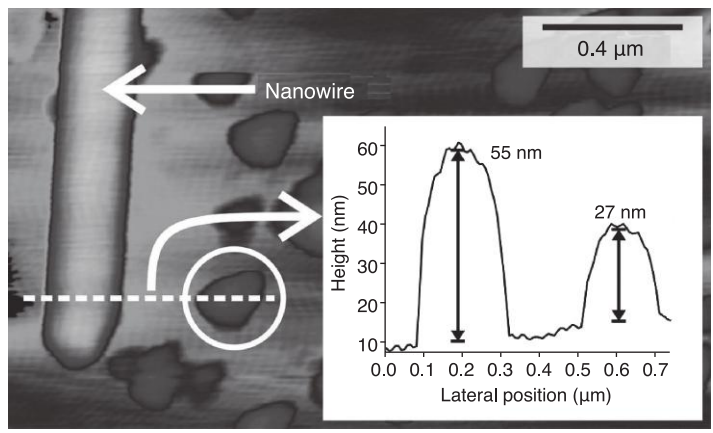

(d)

7.9 (*Continued*) (c) Cross-correlation between photons emerging from the position of the nanodiamond and the plasmons scattered out from the points '1' in (a). (d) Another example of coupling of a nanodiamond to a silver nanowire, where the sample was prepared using spin-coating. (a), (b), (c) adapted from Schell *et al.* (2011a), © 2011, OSA; (d) from Huck *et al.* (2011), © 2011, APS.

The high degree of control offered by AFM nanomanipulation in combination with the pick and place technique can be inferred from Fig. 7.9(d). The nanodiamond can be moved to different positions on the wire, and therefore the coupling can be adjusted. Furthermore, no other nanoparticles that might be nearby hinder this process. Such ultimate control is impossible when spin-coating is used to prepare the sample.

This section has shown that single nanodiamonds are versatile building blocks for highly integrated nanophotonic and nanoplasmonic elements, which can be assembled in a very controlled way with advanced nanomanipulation techniques. In the next section, another way of integrating nanodiamonds into photonic elements will be shown. Instead of using nanomanipulation, the nanodiamonds are dispersed in a photoresist, which is subsequently structured via two-photon direct laser-writing.

7.6 Photonic elements made from nanodiamonds in laser-written structures

In two-photon direct laser-writing (Kawata *et al.*, 2001; Deubel *et al.*, 2004), tightly focused femtosecond laser pulses are used to define structures through polymerisation of a photoresist. This allows for three-dimensional structures of nearly arbitrary shape. For example, it is easily possible to build microresonators (Liu *et al.*, 2010; Grossmann *et al.*, 2011) and waveguides (Lee *et al.*, 2012). By adding active ingredients, such as fluorescent dyes (Sun *et al.*, 2001) or quantum dots (Li *et al.*, 2006), to the photoresist, it is possible to build structures from an active hybrid material. These nanodiamond-based hybrid materials may consist of nanodiamonds in a soft glass (Henderson *et al.*, 2011) or nanodiamonds in a photoresist polymerised via two-photon direct laser-writing (Schell *et al.*, 2013). In the following, the latter approach and its application are described.

The photoresist which formed the basis of the hybrid material consisted of pentaerythritol tetraacrylate (PETTA) as a monomer and 350 ppm monomethyl ether hydroquinone as an inhibitor, together with 0.25 wt% of 7-diethylamino-3-thenoylcoumarin serving as a photoinitiator (cf. Fischer and Wegener, 2011). To this photoresist, 2 wt% of nanodiamonds in an ethanol suspension were added, bringing quantum optics functionality to the material. Polymerisation was achieved using a Ti:sapphire laser with an average power of 6 mW, 100 fs pulses and a central wavelength of 810 nm. After polymerisation, isopropyl alcohol and acetone were used to develop the samples. Figure 7.10(a) shows a sketch of the writing process. The femtosecond laser beam is tightly focused into the photoresist using a high-numerical-aperture oil-immersion objective. Polymerisation of the photoresist happens via a two-photon process in the focal region only. By scanning the sample and exposing different regions, three-dimensional structures can be defined.

With this fabrication process, all basic photonic elements – resonant structures, waveguides and emitters – can easily be produced and combined. Some assemblies of resonators and waveguides that have been produced are shown in Fig. 7.10(b) and (c). As a first example, disc resonators have been built and their single-photon functionality shown. These disc resonators consisted of a disc 20 μm in diameter sitting on a 10 μm diameter stem. Measurements with a tunable laser and a tapered fibre revealed modes with quality factors of up to 10^4. To avoid the need for

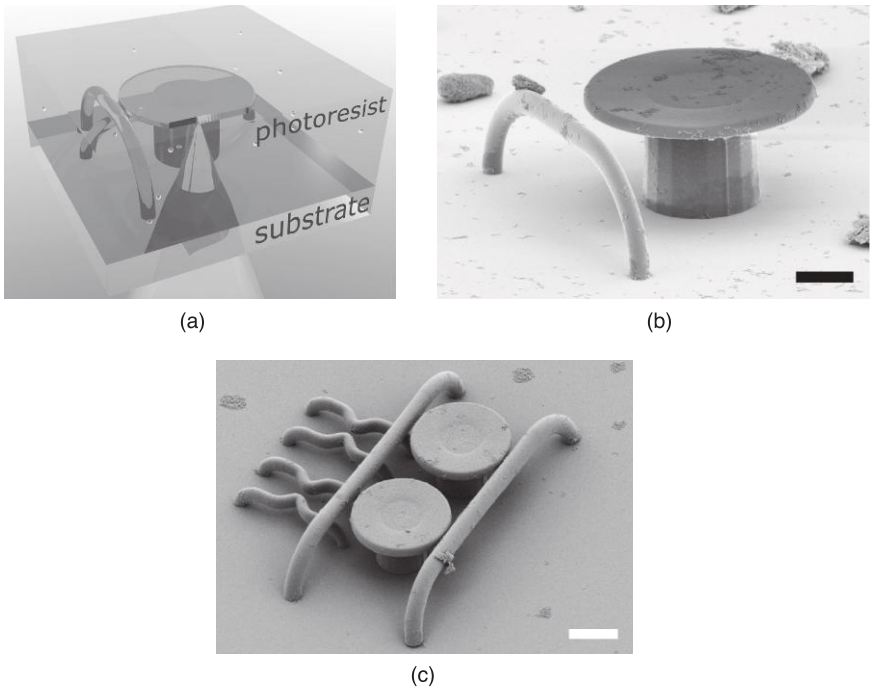

7.10 Two-photon direct laser-writing in diamond photoresist. (a) Sketch of the fabrication process. A photoresist which contains nanodiamonds is polymerized via a two-photon process by scanning the position of a laser beam. (b) Scanning electron micrograph of a structure similar to the one depicted in (a). In (c), a more complicated structure consisting of two resonators and multiple waveguides is shown. The scale bars are 5 μm. Adapted from Schell *et al.* (2013), © 2013, Nature Publishing Group.

coupling a tapered fibre to the resonators in subsequent work, the resonators were interfaced with directly integrated waveguides. A scanning electron micrograph of the coupled system is shown in Fig. 7.10(b).

The capability of the combined system to emit single photons coupled to a resonant structure and subsequently route the photons via a waveguide is demonstrated in Fig. 7.11. The focus of a green excitation laser was scanned over the resonator disc with a second objective while the photons coming from the output ports of the waveguides were monitored. In this way, only photons coupling to the waveguide were detected. It is clearly visible in Fig. 7.11(b) that when the excitation laser hit the waveguide directly, many photons were detected. When the excitation spot hit the rim of the resonator – where the whispering gallery modes are located – the count rate also rose, a clear indication of coupling from the modes to the waveguide. Furthermore, when an NV centre which coupled to

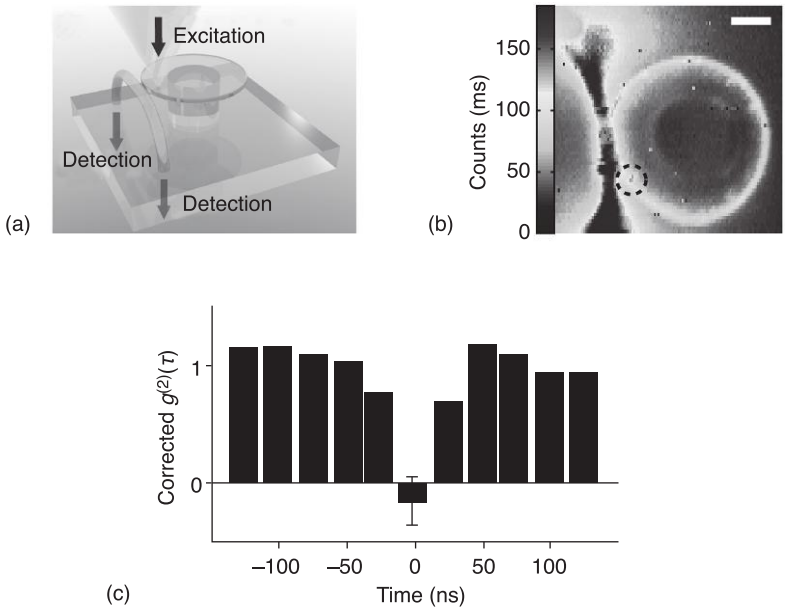

7.11 Integrated microoptical assembly. (a) Schematic illustration of the measurement. A laser is used to excite a diffraction-limited spot on the resonator disc and the light at both outputs of the waveguide is collected and analysed. (b) Intensity at the output ports when the excitation laser is scanned over the structure. The shape of the structure is clearly visible. The dashed circle indicates the position of an NV centre coupling to the resonator's modes. The scale bar is 5 μm. (c) Background-corrected autocorrelation function for the NV center. A $g^{(2)}(0)$ value of -0.18 ± 0.21 clearly indicates single-photon emission. Figure from Schell *et al.* (2013), © 2013, Nature Publishing Group.

the modes was excited, this was visible as a bright spot in the scan. Such diamonds could emit single photons coupled to the mode (Fig. 7.11(c)), which were subsequently transferred to the waveguide.

The approach of building a microphotonic system from a hybrid material by two-photon direct laser-writing makes it possible to build complex integrated structures with functionalities at the single-photon level. With future developments in the on-demand localisation of the diamonds prior to writing the structures, this will become a scalable technique to build integrated quantum photonic elements that interface many emitters in a controlled way.

The next section concentrates on a less integrated approach, where single NV centres in nanodiamonds form the basis of fundamental sources of light quanta.

7.7 Applications of engineered single-photon sources based on nanodiamonds

In principle, a single NV centre in a nanodiamond already represents a source of single light quanta. However, the application of such a source requires a robust and stand-alone implementation as a true device. Some important features of such a device are a high photon rate, coupling into well-defined fibre or free-space modes, and room temperature operation. Figure 7.12 shows an example of such a single-photon source. The device is basically a confocal optical microscope. Efficient collection of photons is achieved by spin-coating a solution of nanodiamonds onto the back surface of a solid immersion lens. In this way, count rates of up to a few million photons per second from a single NV centre can be achieved. Sources like this were used in the experiments by Steudle *et al.* (2012) and Jiang *et al.* (2012) reviewed in the following subsections.

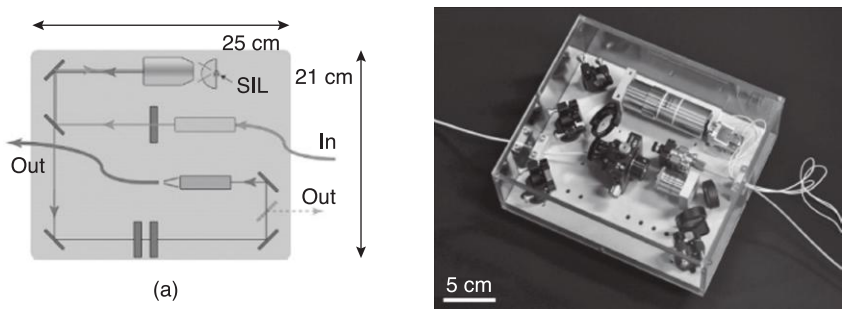

7.12 Schematic illustration (a) and photograph (b) of a single-photon source. The source is a confocal microscope which collects photons from single NV centres in individual nanodiamonds. The nanodiamonds are spin-coated onto a ZrO_2 solid immersion lens (SIL). Excitation occurs via a fibre-coupled laser. After spectral filtering, single photons can be extracted via a fibre or via a free-space output port.

7.7.1 A fundamental experiment to measure the quantum nature of light

General concept

The quantum nature of light manifests itself in the discrete number of excitations per mode. Such states of light are called Fock states. Fock states and other non-classical states can be discriminated from classical states by photon counting, for example in an HBT set-up as introduced in Section 7.2 (see also Fig. 7.13(a)). 'Non-classical' means that a measurement performed on the state cannot be

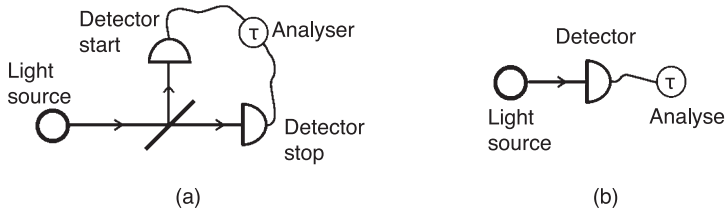

7.13 (a) Schematic illustration of a standard Hanbury Brown and Twiss correlator with a 50/50 beam splitter and two photodetectors. (b) The simplest configuration for a photon correlation measurement, consisting of only a single detector and an analyser. From Steudle *et al.* (2012), © 2012, APS.

explained by a classical theory of electromagnetism, i.e. Maxwell's equations. With an HBT set-up, the second-order coherence function $g^{(2)}(\tau)$ or intensity autocorrelation function, as defined in Section 7.2, can easily be measured. As mentioned, it is found that Fock states violate the inequality for classical states $g^{(2)}(\tau=0)\geq 1$. In particular, $g^{(2)}(\tau=0)=0$ for a single-photon Fock state as produced by a single-photon source. The anticorrelation, or *antibunching*, observed for a single-photon Fock state can be interpreted as a result of the indivisibility of photons. In an HBT set-up, light is split by a beam splitter and sent to two detectors. Now, one might say that photons are indivisible and cannot be split. Thus, they have to choose one path after the beam splitter and will never be detected at both detectors at once. This is, however, an oversimplified interpretation and evokes the false impression that a beam splitter is necessary to prove indivisibility of photons.

Indeed, the only reason to use a beam splitter and two detectors in a standard HBT set-up is a technical one: using two detectors circumvents the dead time of the individual detectors, which often prevents the detection of photon coincidence events within the coherence time of typical single-photon sources, which is on the order of a few nanoseconds. However, it was pointed out by Loudon (2000) that a much simpler experiment, in which the light is arranged to fall on a single phototube, would in principle be sufficient (Fig. 7.13(b)). In the following, we introduce such an experiment, which can also be regarded as the simplest experiment to show the quantum nature of light.

Experimental implementation

In our experiment (see the set-up in Fig. 7.14(b)), we used a fibre-coupled superconducting single-photon detector (SSPD) (Gol'tsman *et al.*, 2001), which consisted of a thin NbN meandering nanowire (see the schematic illustration in Fig. 7.14(a)). The detector chip was cooled to liquid helium temperature (4.2 K) and biased close to its critical current. Details can be found in Steudle *et al.*

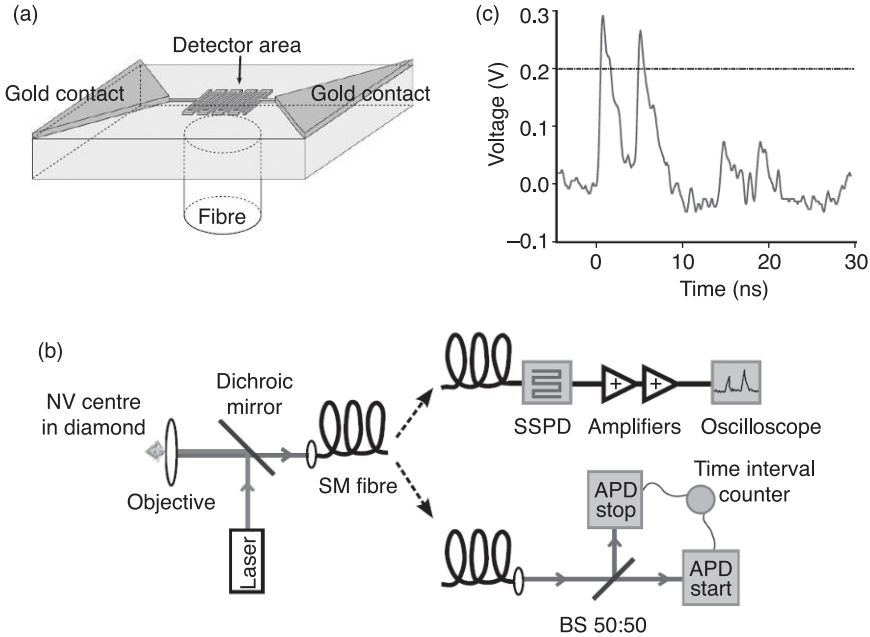

7.14 Experimental tools. (a) Schematic illustration of a fibre-coupled superconducting single-photon detector (SSPD). (b) Experimental set-up for measuring the $g^{(2)}$ function. The fluorescence was coupled into a single-mode fibre, and detection was done in two configurations. Configuration 1 was a single-detector set-up, i.e. the light was sent via an optical fibre directly to the SSPD. In configuration 2, the HBT set-up, light was coupled for comparison into a standard free-space HBT set-up consisting of a beam splitter and two avalanche photodiodes (APDs). In configuration 1, the amplified electrical pulses from the SSPD were fed to an oscilloscope of 1 GHz bandwidth. The oscilloscope was programmed to save a pulse trace whenever a trigger level of 200 mV was exceeded twice with a time difference between 5 and 200 ns (c). In configuration 2, the time intervals between the signals from the two APDs, with a dead time of 30 ns, were recorded with a time interval counter. From Steudle *et al.* (2012), © 2012, APS.

(2012). The dark count rate of the detector was less than $50\,s^{-1}$ and its overall efficiency at 630 nm (close to the zero-phonon line of the NV centre) was around 10%. Its dead time was limited by its kinetic inductance (Kerman *et al.*, 2006) and was shorter than 5 ns.

In order to generate single photons, we exploited a single-photon source based on nanodiamonds similar to the one introduced above. The coherence time of its photons corresponded to the lifetime of the excited state and was around 30 ns, which was much longer than the detector dead time. We measured the $g^{(2)}$ function

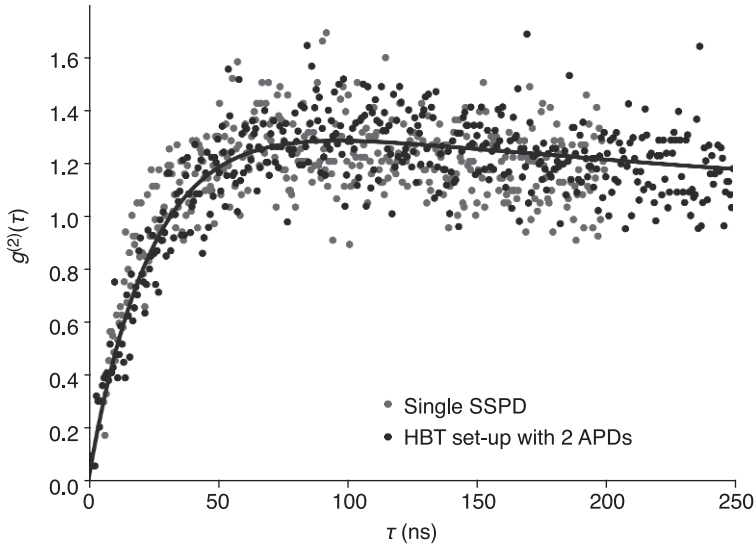

7.15 Measurements of the $g^{(2)}$ function in the single-detector configuration 1 of Fig. 7. 14 (grey dots) and the standard HBT configuration, configuration 2 of Fig. 7.14 (black dots). The black line is a fit to a three-level rate equation model. Additional bunching is observed owing to occasional population of a metastable singlet state of the NV centre. From Steudle *et al.* (2012), © 2012, APS.

as defined in Section 7.2 in two different configurations, as shown in Fig. 7.14(b), namely a single-detector set-up with an SSPD (configuration 1) and a standard HBT set-up with two commercial avalanche photodiodes (configuration 2). The experimental results are shown in Fig. 7.15. The grey dots correspond to the $g^{(2)}$ function measured with the single SSPD. This has a pronounced antibunching dip which fits well to a three-level rate equation model (solid black line). The black dots correspond to the standard HBT measurement. Obviously, both measurements reveal the quantum nature of the photon stream in the same manner, proving that a statistical analysis of a stream of single photons can be performed very well with a only single detector.

Interpretation

Our results highlight the fact that the non-classicality of light can appear even in a very elementary experiment, without the need to introduce additional optical elements such as a beam splitter that divides photons or a second detector. A single fast detector with a short dead time can provide the same statistical information as a standard HBT set-up with two detectors.

7.7.2 Incoherent single-photon conversion

General concept

A closer look at the generation of on-demand photons using spontaneous emission reveals that the key requirement is to generate a *single excitation* in an optically active system. A single quantum system fulfils this requirement automatically, since it can only absorb a single quantum of light (Fig. 7.16(a)). A complementary approach is to utilise an arbitrary ensemble of emitters, but to excite it with only a single quantum of light (Fig. 7.16(b)). In both cases single photons are emitted. In the following, we present the use of such an approach to realise a stable, non-blinking, room temperature infrared single-photon source. The key idea is to use efficient absorption of single photons in the visible and subsequent Stokes-shifted emission at a longer wavelength.

There are two key requirements for this idea: (1) a bright single-photon source and (2) an efficient absorber with an appropriate Stokes-shifted emission spectrum in the target optical spectrum. For the bright single-photon source, we used a source similar to the one described at the beginning of this section. A suitable absorber was provided by an ensemble of colloidal CdHgTe quantum dots (QDs) (Harris *et al.*, 2011) in toluene solution, since they provided a large absorption cross-section, a quantum efficiency of nearly 10% and a peaked emission spectrum

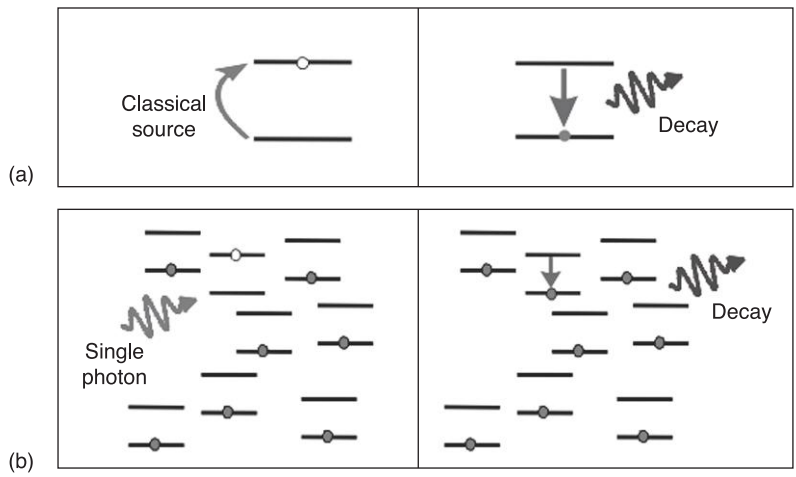

7.16 Two complementary approaches to on-demand single-photon generation. (a) Excitation of a single quantum system with a classical source and subsequent spontaneous emission of a single photon. (b) Excitation of an arbitrary ensemble with a single photon. In this case also, only a single excitation is present, and hence decay of the ensemble also leads to emission of only a single photon. From Jiang *et al.* (2012), © 2012, OSA.

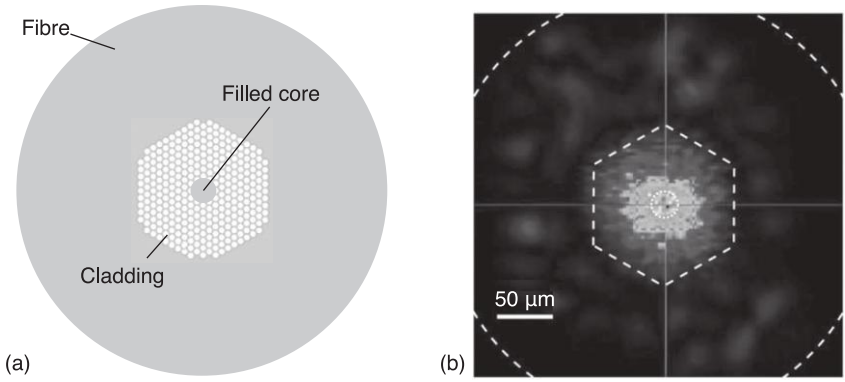

7.17 (a) Schematic illustration of an HCPCF. The fibre has a diameter of 135 μm, and the core a diameter of 9.5 μm. The cladding consists of a hexagonal glass structure with a pitch of 2.3 μm and an air fraction of 0.9. (b) CCD fluorescence image of the photoluminescence from a CdHgTe QD solution in the HCPCF collected at the end of the fibre. The white dashed lines indicate the fibre and the cladding region, and the dotted line shows the core. From Jiang *et al.* (2012), © 2012, OSA.

centred at around 870 nm. In order to achieve both a large single-photon absorption probability and a very high re-collection efficiency for Stokes-shifted fluorescence, we utilised a hollow-core photonic-crystal fibre (HCPCF) (Fig. 7.17(a)) with a selectively filled central core (Barth *et al.*, 2010b) containing a solution of QDs. The HCPCF allows tight light confinement and guiding over macroscopic distances. By adapting the concentration of QDs and the fibre length, the absorption of single photons could be up to unity and, at the same time, a large fraction of the fluorescence could be collected and guided.

Experimental implementation

Similarly to the previous experiment, single photons were generated by an efficient source using single NV centres in nanodiamonds. From a photon correlation measurement, a value of 0.2 was derived for the normalised autocorrelation function $g^{(2)}(0)$, proving the single-photon character.

Using a microscope objective, 86% of these photons could be transmitted through the HCPCF filled with a pure polymer toluene solution. This value is limited by scattering out of the core mode induced by tiny bubbles in the solution. Moreover, the coupling efficiency from free space to the filled fibre is reduced by partial scattering from the polymer around the core region when the fibre is cleaved.

In order to investigate the optical properties of an active HCPCF selectively filled with a solution of colloidal CdHgTe QDs, the single-photon source was replaced by a much brighter diode laser emitting at a wavelength of 640 nm. This

was coupled into the filled fibre, where it excited the QDs. As can be seen from the fluorescence image in Fig. 7.17(b), most of the emission from the CdHgTe QDs at around 850 nm was confined inside the filled core region. However, a significant fraction of the fluorescence was lost into the cladding region. The onset of re-absorption limited the maximum concentration of QDs, which unfortunately also resulted in a conversion efficiency of visible (640 nm) to infrared (850 nm) light much lower than unity.

To measure the absolute conversion efficiency, we again utilised a red diode laser as a classical photon source, which we coupled into the HCPCF. We compared the intensity, i.e. the photon generation rate, of the diode laser with the photon counts of near infrared photons collected at the end of the fibre. The ratio is the total conversion efficiency η_{tot}, which we found to be equal to 0.1%. From the independently measured coupling efficiency of laser light from free space to the fibre (see Jiang *et al.* (2012) for details), the transmission of the fluorescence light inside the fibre and the collection efficiency of the photoluminescence from the QDs at the end of the fibre, we derived the probability η_{convert} for a single visible photon at 640 nm to be absorbed by a QD in the HCPCF and re-emitted as an infrared photon at 850 nm as 3%. This number is large compared with what can be achieved by simply focusing on and collecting from a QD solution with a high-NA objective (Smolka *et al.*, 2007).

With these numbers, we can estimate the number of single infrared photons that we can expect when we replace the attenuated red laser with the single-photon source. When the maximum generated stream of 280 kcts/s of visible single photons is launched into the fibre, we expect a photon rate of converted near infrared single photons of about 280 cts/s. Unfortunately, this is similar to the dark count rate of our detectors, and not sufficient for further spectral analysis and autocorrelation measurements. However, improving the conversion efficiency is straightforward, for example by using QDs with a larger Stokes shift, shorter lifetime and higher quantum efficiency or by reducing the losses of the filled HCPCF. Figure 7.18 compares the state of the art of stable single-photon sources in the visible with the source used in our experiment.

Although the total conversion efficiency of 0.1% obtained in the experiment was still too small to verify conversion of single photons from a true single-photon source based on nitrogen–vacancy defect centres in diamond, the approach is still promising. With improvements by two orders of magnitude, which are experimentally feasible, as well as visible photon sources approaching 10 Mcts/s, the generation rate of single photons in the infrared could be as high as several hundreds of kilocounts per second, which is better than existing true single-photon sources in the infrared (Intallura *et al.*, 2007). With the method introduced above, single-photon generation in the near infrared, for example in the telecommunication band at around 1550 nm, is accessible without the need to have quantum emitters in that wavelength regime. In this respect, our experiments show that ultrabright single-photon sources even of poor optical quality may be very useful as pump sources to generate single quanta of excitation.

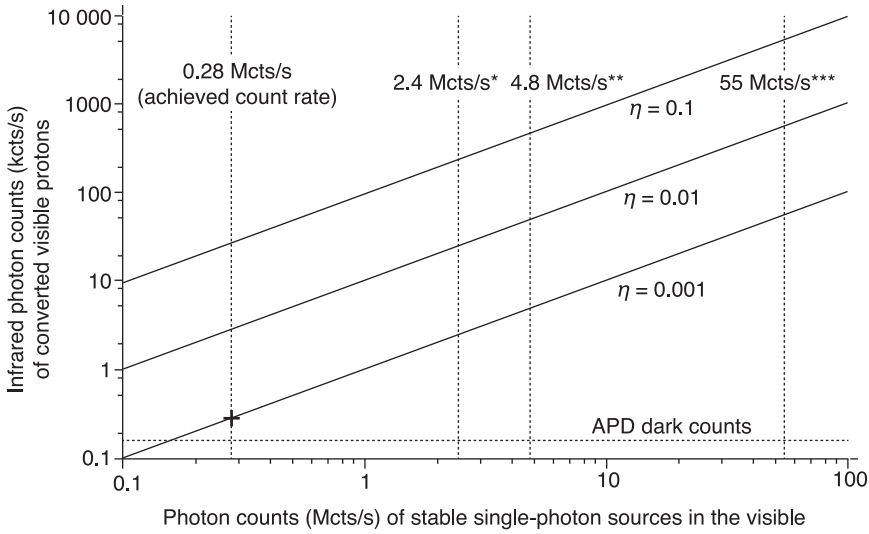

7.18 Overview of single-photon sources realised so far, and expected single-photon count rates from incoherent photon conversion to the near infrared using an HCPCF system. The cross marks the achieved conversion rate of 0.1% and the resulting single-photon count of 280 cts/s for the conversion of NV centres in diamond to CdHgTe QDs emitting at 850 nm. The solid lines show the expected infrared single-photon counts for conversion rates of 1% and 10%. The vertical dotted lines represent the single-photon source employed, and other sources in the visible that have been realised (Neu *et al.*, 2011; Schröder *et al.*, 2011b), indicated by asterisks. The rightmost vertical dotted line gives our expectation for a possible implementation of NV centres in a dielectric layer system with a collection efficiency of 99%, as has been achieved with single molecules (Chen X W *et al.*, 2011). From Jiang *et al.* (2012), © 2012, OSA.

7.8 Future trends

Diamond nanocrystals containing single defect centres are so far the only room temperature quantum emitters with unlimited optical stability. This makes them unique building blocks for fundamental nanophotonic devices. As sources for single quanta, they offer quantum features which are the basis for a number of concepts for improved functionality. A prominent example is quantum information processing. Yet, like almost any quantum emitter in the solid state, they cannot be compared with single atoms well isolated in a vacuum. The influence of the surrounding solid-state matrix has to be taken into account. With respect to defect centres in nanodiamonds, this concerns impurities, strain and the close proximity to an uncontrolled surface, which deteriorate the quality of the emitted single photons (Bradac *et al.*, 2010; Rondin *et al.*, 2010). For example, so far it has not

been possible to provide indistinguishable photons, i.e. photons with exactly defined spectral, spatial and temporal modes, not even from one and the same defect centre.

There are many prospects for nanophotonics with nanodiamonds (Aharonovich *et al.*, 2011b; Krueger, 2011). Here, at the end of this chapter, we list only a few of them:

- In order to improve the quality of single photons from defect centres in nanodiamonds, future studies are required to reveal the physical origin of, for example, spectral diffusion. It is not surprising that the optical quality of emitters in commercially available nanodiamonds is inferior to that of defect centres in ultrapure material. Detailed studies investigating defect centres in nanoparticles ground from ultrapure bulk diamond would be very interesting (Wolters *et al.*, 2013). There, any remaining deterioration should result from the surface. The electronic states on the surface and their possible control via surface chemistry could, on the one hand, open the way to further improvement of the optical quality of the emission from nanodiamonds. On the other hand, studying the physics and chemistry of such states in nanoparticles is a rewarding research topic in itself and of high relevance not only to nanodiamonds. Beyond electrostatic coupling, which is mainly responsible for Stark shifts of the emission line, phonon coupling has not been explored on the nanoscale. A nanodiamond is an interesting system where a single optically active quantum emitter couples to phonons which are confined within nanoscopic dimensions. Here, the unlimited stability of a single defect centre is in itself advantageous for studying the coupling of quantum-confined phonons in detail.
- The integration of single nanodiamonds into photonic and plasmonic structures was addressed in Sections 7.4–7.6. With an AFM, it is possible to transfer pre-characterised nanodiamonds to nearly any structure in a controlled way. This can be used to build hybrid structures (Benson, 2011), for example to integrate nanodiamonds into photonic-crystal cavities in order to enhance the NV centre's zero-phonon line (Wolters *et al.*, 2010) or to couple NV centres to plasmonic waveguides in a controlled way (Schell *et al.*, 2011a; Huck *et al.*, 2011), which results in the excitation of single plasmons. Another way of integrating nanodiamonds is to engineer a new material (Henderson *et al.*, 2011; Schell *et al.*, 2013) from which photonic elements can be built. A future technique to identify emitters and build structures at these sites would enable a scalable way of integrating nanodiamonds into photonic structures.
- In Section 7.7, we addressed another role of a single defect, going beyond a mere single-photon source. Photons are elementary excitations of the electromagnetic field. We showed that they can be converted into excitations of other modes such as single collective excitations of ensembles of emitters (Jiang *et al.*, 2012). Owing to their stability and small size, nanodiamonds are convenient generators of quantum excitations in a more general context. As

discussed in Section 7.7, the limits in terms of optical quality of direct single-photon emission from nanodiamonds do not necessarily apply to the quality of the converted elementary excitations.

- Finally, the long-term stability of defect centres and the possibility of hosting them in diamond nanocrystals only a few nanometres in diameter have introduced the possibility of using them as local quantum probes (Taylor *et al.*, 2008; Balasubramanian *et al.*, 2008). Attached to a scanning probe, a nanodiamond provides a well-localised electronic system with a single electron spin that can be initialised and read out optically. Locality together with good sensitivity and stability is a unique feature of defect centres in nanodiamond. Measuring local electric fields (Dolde *et al.*, 2011) and local magnetic fields (Hall *et al.*, 2012) even down to single spins (Pham *et al.*, 2012) has been demonstrated. Furthermore, diamond nanocrystals are small and non-toxic and can be introduced into cells (McGuinness *et al.*, 2011), which is a key requirement in studies of biophysical systems. We have not addressed the issue of nanosensing by exploiting nanodiamonds in this chapter. However, it may be that this will be the field with the most significant impact.

7.9 Acknowledgements

This work was supported by the DFG (FOR 1493 Quantum Optics in Diamond) and BMBF (KEPHOSI). J.W. acknowledges funding by the state of Berlin (Elsa-Neumann Scholarship).

7.10 References

Aharonovich I, Castelletto S, Simpson D A, Stacey A, McCallum J, *et al.* (2009), 'Two-level ultrabright single photon emission from diamond nanocrystals', *Nano Lett.*, 9, 3191–3195.

Aharonovich I, Castelletto S, Simpson D A, Greentree A D and Prawer S (2010a), 'Photophysics of chromium-related diamond single-photon emitters', *Phys. Rev. A*, 81, 1–7.

Aharonovich I, Castelletto S, Johnson B C, McCallum J C, Simpson D A, *et al.* (2010b), 'Chromium single-photon emitters in diamond fabricated by ion implantation', *Phys. Rev. B*, 81, 1–4.

Aharonovich I, Castelletto S, Johnson B C, McCallum J C and Prawer S (2011a), 'Engineering chromium-related single photon emitters in single crystal diamonds', *New J. Phys.*, 13, 045015.

Aharonovich I, Greentree A D and Prawer S (2011b), 'Diamond photonics', *Nature Photon.*, 5, 397–405.

Ampem-Lassen E, Simpson D A, Gibson B C, Trpkovski S, Hossain F M, *et al.* (2009), 'Nano-manipulation of diamond-based single photon sources', *Opt. Express*, 17, 11287–11293.

Babinec T M, Hausmann B J M, Khan M, Zhang Y, Maze J R, *et al.* (2010), 'A diamond nanowire single-photon source', *Nature Nanotechnol.*, 5, 195–199.

Balasubramanian G, Chan I Y, Kolesov R, Al-Hmoud M, Tisler J, *et al.* (2008), 'Nanoscale imaging magnetometry with diamond spins under ambient conditions', *Nature*, 455, 648–651.

Barclay P E, Santori C, Fu K-M, Beausoleil R G and Painter O (2009), 'Coherent interference effects in a nano-assembled diamond NV center cavity-QED system', *Opt. Express*, 17, 8081–8097.

Barnes W L, Dereux A and Ebbesen T W (2003), 'Surface plasmon subwavelength optics', *Nature*, 424, 824–830.

Barth M, Nüsse N, Löchel B and Benson O (2009), 'Controlled coupling of a single-diamond nanocrystal to a photonic crystal cavity', *Opt. Lett.*, 34, 1108–1110.

Barth M, Schietinger S, Schröder T, Nüsse N, Löchel B, *et al.* (2010a), 'Controlled coupling of NV defect centers to plasmonic and photonic nanostructures', *J. Lumin.*, 130, 1628–1634.

Barth M, Bartelt H and Benson O (2010b), 'Fluid-filled optical fibers', in Hawkins A R and Schmidt H (eds), *Handbook of Optofluidics*, Boca Raton, FL: CRC Press, pp. 15-1–15-34.

Benson O (2011), 'Assembly of hybrid photonic architectures from nanophotonic constituents', *Nature*, 480, 193–199.

Boudou J P, Curmi P A, Jelezko F, Wrachtrup J, Aubert P, *et al.* (2009), 'High yield fabrication of fluorescent nanodiamonds', *Nanotechnology*, 20, 235602.

Bozhevolnyi S and García-Vidal F (2008), 'Focus on plasmonics', *New J. Phys.*, 10, 105001.

Bradac C, Gaebel T, Naidoo N, Sellars M J, Twamley J, *et al.* (2010), 'Observation and control of blinking nitrogen–vacancy centres in discrete nanodiamonds', *Nature Nanotechnol.*, 5, 345–349.

Chen Q, Yang W, Feng M and Du J (2011), 'Entangling separate nitrogen–vacancy centers in a scalable fashion via coupling to microtoroidal resonators', *Phys. Rev. A*, 83, 054305.

Chen X W, Götzinger S and Sandoghdar V (2011), '99% efficiency in collecting photons from a single emitter', *Opt. Lett.*, 36, 3545–3547.

Claudon J, Bleuse J, Malik N S, Bazin M, Jaffrennou P, *et al.* (2010), 'A highly efficient single-photon source based on a quantum dot in a photonic nanowire', *Nature Photon.*, 4, 174–177.

Collins A T, Thomaz M F and Jorge M I B (1983), 'Luminescence decay time of the 1.945 eV centre in type Ib diamond', *J. Phys. C*, 16, 2177.

Cuche A, Mollet O, Drezet A and Huant S (2010), ' "Deterministic" quantum plasmonics', *Nano Lett.*, 10, 4566–4570.

Deubel M, Freymann G, Wegener M, Pereira S, Busch K and Soukoulis C M (2004), 'Direct laser writing of three-dimensional photonic crystal templates for telecommunications', *Nature Mater.*, 3, 444.

Dolde F, Fedder H, Doherty M W, Nöbauer T, Rempp F, *et al.* (2011), 'Electric-field sensing using single diamond spins', *Nature Phys.*, 7, 459–463.

Dregely D, Lindfors K, Dorfmüller J, Hentschel M, Becker M, *et al.* (2012), 'Plasmonic antennas, positioning, and coupling of individual quantum systems', *Phys. Stat. Solidi B*, 249, 666–677.

Englund D, Shields B, Rivoire K, Hatami F, Vucković J, *et al.* (2010), 'Deterministic coupling of a single nitrogen vacancy center to a photonic crystal cavity', *Nano Lett.*, 10, 3922–3926.

Faraon A, Majumdar A, Englund D, Kim E, Bajcsy M and Vuckovic J (2011), 'Integrated quantum optical networks based on quantum dots and photonic crystals', *New J. Phys.*, 13, 055025.

Faraon A, Santori C, Huang Z, Acosta V M and Beausoleil R G (2012), 'Coupling of nitrogen–vacancy centers to photonic crystal cavities in monocrystalline diamond', *Phys. Rev. Lett.*, 109, 033604.

Fischer, J and Wegener, M (2011), 'Three-dimensional direct laser writing inspired by stimulated-emission-depletion microscopy', *Opt. Mater. Express*, 1, 614–624.

Gol'tsman G N, Okunev O, Chulkova G, Lipatov A, Semenov A, *et al.* (2001), 'Picosecond superconducting single-photon optical detector', *Appl. Phys. Lett.*, 79, 705.

Gregor M, Henze R, Schröder T and Benson O (2009), 'On-demand positioning of a preselected quantum emitter on a fiber-coupled toroidal microresonator', *Appl. Phys. Lett.*, 95, 153110.

Grangier P, Sanders B and Vuckovic J (2004), 'Focus on single photons on demand', Focus Issue, *New J. Phys.*, vol. 6.

Grossmann T, Schleede S, Hauser M, Beck T, Thiel M, *et al.* (2011), 'Direct laser writing for active and passive high-*q* polymer microdisks on silicon', *Opt. Express* 19, 11451–11456.

Hadden J P, Harrison J P, Stanley-Clarke A C, Marseglia L, Ho Y D, *et al.* (2010), 'Strongly enhanced photon collection from diamond defect centers under microfabricated integrated solid immersion lenses', *Appl. Phys. Lett.*, 97, 241901.

Hall L T, Beart G C, Thomas E A, Simpson D A, McGuinness L P, *et al.* (2012), 'High spatial and temporal resolution wide-field imaging of neuron activity using quantum NV-diamond', *Sci. Rep.*, 2, 401.

Hanbury Brown R and Twiss R Q (1956), 'Correlation between photons in two coherent beams of light', *Nature*, 177, 27–29.

Harris D K, Allen P M, Han H S, Walker B J, Lee J and Bawendi M G (2011), 'Synthesis of cadmium arsenide quantum dots luminescent in the infrared', *J. Am. Chem. Soc.*, 133, 4676–4679.

Heindel T, Schneider C, Lermer M, Kwon S H, Braun T, *et al.* (2010), 'Electrically driven quantum dot–micropillar single photon source with 34% overall efficiency', *Appl. Phys. Lett.*, 96, 011107.

Henderson M R, Gibson B C, Ebendorff-Heidepriem H, Kuan K, Afshar S V, *et al.* (2011), 'Hybrid materials: Diamond in tellurite glass: a new medium for quantum information', *Adv. Mater.*, 23, 2772.

Huck A, Kumar S, Shakoor A and Andersen U L (2011), 'Controlled coupling of a single nitrogen–vacancy center to a silver nanowire', *Phys Rev. Lett.*, 106, 096801.

Intallura P M, Ward M B, Karimov O Z, Yuan Z L, See P, *et al.* (2007), 'Quantum key distribution using a triggered quantum dot source emitting near 1.3 μm', *Appl. Phys. Lett.*, 91, 161103.

Jiang P, Schroeder T, Barth M, Lesnyak V, Gaponik N, *et al.* (2012), 'Incoherent photon conversion in selectively infiltrated hollow-core photonic crystal fibers for single photon generation in the near infrared', *Opt. Express*, 20, 11536–11547.

Joannopoulos J D, Villeneuve P R and Fan S H (1997), 'Photonic crystals: Putting a new twist on light', *Nature*, 386, 143–149.

Jelezko F and Wrachtrup J (2006), 'Single defect centres in diamond: A review', *Phys. Stat. Solidi A*, 203, 3207–3225.

Junno T, Deppert K, Montelius L and Samuelson L (1995), 'Controlled manipulation of nanoparticles with an atomic force microscope', *Appl. Phys. Lett.*, 66, 3627–3629.

Kawata S, Sun H-B, Tanaka T and Takada K (2001), 'Finer features for functional microdevices', *Nature*, 412, 697–698.

Kerman A J, Dauler E A, Keicher W E, Yang J K W, *et al.* (2006), 'Kinetic-inductance-limited reset time of superconducting nanowire photon counters', *Appl. Phys. Lett.*, 88, 111116.

Kinkhabwala A, Yu Z, Fan S, Avlasevich Y, Müllen K and Moerner W E (2009), 'Large single-molecule fluorescence enhancements produced by a bowtie nanoantenna', *Nature Photon.*, 3, 654–657.

Kolesov R, Grotz B, Balasubramanian G, Stoehr R J, Nicolet A A L, *et al.* (2009), 'Wave–particle duality of single surface plasmon polaritons', *Nature Phys.*, 5, 470–474.

Krueger A (2011), 'Beyond the shine: recent progress in applications of nanodiamond', *J. Mater. Chem.*, 21, 12571–12578.

Lee C-W, Pagliara S, Keyser U and Baumberg J J (2012), 'Perpendicular coupling to in-plane photonics using arc waveguides fabricated via two-photon polymerization', *Appl. Phys. Lett.*, 100, 171102.

Li J, Jia B, Zhou G and Gu M (2006), 'Fabrication of three-dimensional woodpile photonic crystals in a PbSe quantum dot composite material', *Opt. Express*, 14, 10740–10745.

Lim T S, Fu C C, Lee K C, Lee H Y, Chen K, *et al.* (2009), 'Fluorescence enhancement and lifetime modification of single nanodiamonds near a nanocrystalline silver surface', *Phys. Chem. Chem. Phys.*, 11, 1508–1514.

Liu Z P, Li Y, Xiao Y-F, Li B-B, Jiang J-F, *et al.* (2010), 'Direct laser writing of whispering gallery microcavities by two-photon polymerization', *Appl. Phys. Lett.*, 97, 211105.

Loudon R (2000), *The Quantum Theory of Light*, New York: Oxford University Press.

Maier S A (2007), *Plasmonics: Fundamentals and Applications*, New York: Springer.

McCutcheon M W and Lončar M (2008), 'Design of a silicon nitride photonic crystal nanocavity with a Quality factor of one million for coupling to a diamond nanocrystal', *Opt. Express*, 16, 19136.

McGuinness L P, Yan Y, Stacey A, Simpson D A, Hall L T, *et al.* (2011), 'Quantum measurement and orientation tracking of fluorescent nanodiamonds inside living cells', *Nature Nanotechnol.*, 6, 358–363.

Neu E, Steinmetz D, Riedrich-Möller J, Gsell S, Fischer M, *et al.* (2011), 'Single photon emission from silicon–vacancy colour centres in chemical vapour deposition nanodiamonds on iridium', *New J. Phys.*, 13, 025012.

Neu E, Agio M and Becher C (2012a), 'Photophysics of single silicon vacancy centers in diamond: implications for single photon emission', *Opt. Express*, 20, 19956–19971.

Neu E, Hepp C, Hauschild M, Gsell S, Fischer M, *et al.* (2012b), 'Low temperature investigations of single silicon vacancy colour centres in diamond', arXiv 1210.3201.

O'Brien J L, Furusawa A and Vuckovic J (2009), 'Photonic quantum technologies', *Nature Photon.*, 3, 687–695.

Pentecost A, Gour S, Mochalin V, Knoke I and Gogotsi Y (2010), 'Deaggregation of nanodiamond powders using salt- and sugar-assisted milling', *ACS Appl. Mater. Interfaces*, 2, 3289–3294.

Pham L, Bar-Gill N, Belthangady C, Le Sage D, Cappellaro P, *et al.* (2012), 'Enhanced solid-state multispin metrology using dynamical decoupling', *Phys. Rev. B*, 86, 045214.

Purcell E M (1946), 'Spontaneous emission probabilities at radio frequencies', *Phys. Rev.*, 69, 681.

Riedrich-Möller J, Kipfstuhl L, Hepp C, Neu E, Pauly C, *et al.* (2012), 'One- and two-dimensional photonic crystal microcavities in single crystal diamond', *Nature Nanotechnol.*, 7, 69–74.

Rondin L, Dantelle G, Slablab A, Grosshans F, Treussart F, *et al.* (2010), 'Surface-induced charge state conversion of nitrogen–vacancy defects in nanodiamonds', *Phys. Rev. B*, 82, 115449.

Russell K J, Liu T-S, Cui S and Hu E L (2012), 'Large spontaneous emission enhancement in plasmonic nanocavities', *Nature Photon.*, 6, 459–462.

Schell A W, Kewes G, Hanke T, Leitenstorfer A, Bratschitsch R, *et al.* (2011a), 'Single defect centers in diamond nanocrystals as quantum probes for plasmonic nanostructures', *Opt. Express*, 19, 7914–7920.

Schell A W, Kewes G, Schröder T, Wolters J, Aichele T and Benson O (2011b), 'A scanning probe-based pick-and-place procedure for assembly of integrated quantum optical hybrid devices', *Rev. Sci. Instrum.*, 82, 073709.

Schell A W, Kaschke J, Fischer J, Henze R, Wolters J, *et al.* (2013), 'Three-dimensional quantum photonic elements based on single nitrogen vacancy-centres in laser-written microstructures', *Sci. Rep.*, 3, 1577.

Schietinger S, Barth M, Aichele T and Benson O (2009), 'Plasmon-enhanced single photon emission from a nanoassembled metal–diamond hybrid structure at room temperature', *Nano Lett.*, 9, 1694–1698.

Schröder T, Schell A W, Kewes G, Aichele T and Benson O (2011a), 'Fiber-integrated diamond-based single photon source', *Nano Lett.*, 11, 198–202.

Schröder T, Gädeke F, Banholzer M J and Benson O (2011b), 'Ultrabright and efficient single-photon generation based on nitrogen–vacancy centres in nanodiamonds on a solid immersion lens', *New J. Phys.*, 13, 055017.

Shen Y, Sweeney T M and Wang H (2008), 'Zero-phonon linewidth of single nitrogen vacancy centers in diamond nanocrystals', *Phys. Rev. B*, 77, 033201.

Siyushev P, Jacques V, Aharonovich I, Kaiser F, Müller T, *et al.* (2009), 'Low-temperature optical characterization of a near-infrared single-photon emitter in nanodiamonds', *New J. Phys.*, 11, 113029.

Siyushev P, Kaiser F, Jacques V, Gerhardt I, Bischof S, *et al.* (2010), 'Monolithic diamond optics for single photon detection', *Appl. Phys. Lett.*, 97, 241902.

Smolka S, Barth M and Benson O (2007), 'Highly efficient fluorescence sensing with hollow core photonic crystal fibers', *Opt. Express*, 15, 12783–12791.

Steudle G A, Schietinger S, Höckel D, Dorenbos S N, Zadeh I E, *et al.* (2012), 'Measuring the quantum nature of light with a single source and a single detector', *Phys. Rev. A*, 86, 053814.

Sun H, Tanaka T, Takada K and Kawata S (2001) 'Two-photon photopolymerization and diagnosis of three-dimensional microstructures containing fluorescent dyes', *Appl. Phys. Lett.*, 79, 1411.

Tanabe T, Notomi M, Kuramochi E, Shinya A and Taniyama H (2007), 'Trapping and delaying photons for one nanosecond in an ultrasmall high-Q photonic-crystal nanocavity', *Nature Photon.*, 1, 49–52.

Taylor J M, Cappellaro P, Childress L, Jiang L, Budker D, *et al.* (2008), 'High-sensitivity diamond magnetometer with nanoscale resolution', *Nature Phys.*, 4, 810–816.

Vahala K J (2003), 'Optical microcavities', *Nature*, 464, 839–846.

van der Sar T, Heeres E C, Dmochowski G M, de Lange G, Robledo L, *et al.* (2009), 'Nanopositioning of a diamond nanocrystal containing a single nitrogen–vacancy defect center', *Appl. Phys. Lett.*, 94, 173104.

van der Sar T, Hagemeier J, Pfaff W, Heeres E C, Thon S M, *et al.* (2011), 'Deterministic nanoassembly of a coupled quantum emitter–photonic crystal cavity system', *Appl. Phys. Lett.*, 98, 193103.

Wang C L, Kurtsiefer C, Weinfurter H and Burchard B (2006), 'Single photon emission from SiV centres in diamond produced by ion implantation', *J. Phys. B: At., Mol. Opt. Phys.*, 39, 37.

Wolters J, Schell A W, Kewes G, Nüsse N, Schoengen M, *et al.* (2010), 'Enhancement of the zero phonon line emission from a single nitrogen vacancy center in a nanodiamond via coupling to a photonic crystal cavity', *Appl. Phys. Lett.*, 97, 141108.

Wolters J, Kewes G, Schell AW, Nüsse N, Schoengen M, *et al.* (2012), 'Coupling of single nitrogen–vacancy defect centers in diamond nanocrystals to optical antennas and photonic crystal cavities', *Phys. Stat. Solidi B*, 249, 918–924.

Wolters J, Sadzak N, Schell A W, Schröder T and Benson O (2013), 'Measurement of the ultrafast spectral diffusion of the optical transition of nitrogen vacancy centers in nano-size diamond using correlation interferometry', *Phys. Rev. Lett.*, 110, 027401.

Yang W L, Yin Z Q, Xu Z Y, Feng M and Du J F (2010), 'One-step implementation of multiqubit conditional phase gating with nitrogen–vacancy centers coupled to a high-Q silica microsphere cavity', *Appl. Phys. Lett.*, 96, 241113.

Yang W L, Yin Z Q, Xu Z Y, Feng M and Oh C H (2011), 'Quantum dynamics and quantum state transfer between separated nitrogen–vacancy centers embedded in photonic crystal cavities', *Phys. Rev. A*, 84, 043849.

Yoshie T, Scherer A, Hendrickson J, Khitrova G, Gibbs H M, *et al.* (2004), 'Vacuum Rabi splitting with a single quantum dot in a photonic crystal nanocavity', *Nature* 432, 200–203.

Young A, Hu C Y, Marseglia I, Harrison J P, O'Brien J L and Rarity J G (2009), 'Cavity enhanced spin measurement of the ground state spin of an NV center in diamond', *New J. Phys.*, 11, 013007.

8

Spin–photon entanglement in diamond for quantum optical networks

G. DUTT and M. U. MOMEEN, University of Pittsburgh, USA

DOI: 10.1533/9780857096685.2.195

Abstract: This chapter describes progress towards the realization of quantum networks through optical interconnections between isolated solid-state spin quantum bits (qubits) in diamond. Measurement-induced nonlinearity between photons emitted by two such qubits, and the resulting heralded entangled state, represents a key starting primitive in many theoretical protocols for quantum networks. This chapter first reviews the theory behind heralded entanglement generation, and then discusses the key requirements and some recent experiments that demonstrate all the ingredients necessary to achieve remote entanglement between spin qubits in diamond.

Key words: quantum information, quantum entanglement, quantum networks, quantum repeaters, nitrogen–vacancy (NV) center.

8.1 Introduction

A central challenge in current scientific research is to coherently manipulate individual quantum mechanical systems (qubits) and to realize scalable quantum information systems. Isolated atoms, ions and photons have quantum states that are extremely stable and whose interactions with the environment (typically the electromagnetic vacuum field) are well understood. These states can be manipulated using optical or microwave transitions, and the long coherence times, combined with control of the motional states of the atoms and ions, have allowed elegant experiments exploring the foundations of quantum information science to be done. These significant advances in the manipulation of individual quantum systems, carried out by the groups led by Haroche and Wineland in the early 1990s, were recognized with the award of the Nobel Prize in Physics in 2012.

Because atoms interact so weakly with each other, sophisticated and difficult schemes are required to realize large-scale quantum information systems. Another means of controlling these interactions is to use single-photon wave packets as an intermediary (Cirac *et al.*, 1997; Boyanovsky, 2013; van Enk *et al.*, 1998). This approach allows interaction over very long distances, but requires us to make each atom interact strongly with a single photon. Alternatively, another approach uses only probabilistic interaction, using spontaneous emission to entangle atoms with photons, and then applying measurement-induced nonlinearity of the photons to couple two spontaneously emitting atoms (Cabrillo *et al.*, 1999; Duan *et al.*,

© 2014 Elsevier Ltd

2001). The abandonment of deterministic interaction to couple two atoms, in favor of probabilistic photon emission, may at first glance seem to be a step backwards in our goal of realizing larger quantum information systems. However, it has now been shown in theoretical proposals that by adding a few more reasonable ingredients, such as auxiliary qubits for error correction and universal quantum logic operations at each node, several useful and interesting applications such as quantum repeaters for long-distance quantum communication and optically connected quantum networks can be realized (Briegel *et al.*, 1998; Dur *et al.*, 1999; Duan *et al.*, 2001; Jiang *et al.*, 2007). Furthermore, an entirely new model of quantum computation based purely on entanglement creation and local measurements, known as cluster-state or graph-state quantum computation (Raussendorf and Briegel, 2001; Hein *et al.*, 2006; Duan and Raussendorf, 2005), is ideally suited for such probabilistic schemes of entanglement generation, and offers an exciting new fundamental challenge for scientists to explore in this area.

Solid-state devices offer advantages over atomic systems in both fundamental and practical ways. Strong interactions can be obtained between solid-state systems in close proximity to each other, the motion of solid-state systems is much easier to control, and the availability of modern nanofabrication techniques could permit us to engineer systems and tune the parameters of the Hamiltonian and control fields. While many solid-state systems have been investigated, the nitrogen–vacancy (NV) center in diamond is of particular interest owing to its extraordinary optical and spin properties (Jelezko and Wrachtrup, 2004). The NV center can be viewed as an 'atomic' solid-state system because its optical transitions allow preparation and measurement of its spin triplet ground state, which possesses long spin polarization and coherence times (Takahashi *et al.*, 2008; Balasubramanian *et al.*, 2009; Grinolds *et al.*, 2013). In addition, the presence of proximal nuclear spins (^{13}C and ^{14}N/^{15}N) creates an environment that can be manipulated (Childress *et al.*, 2006a; Dutt *et al.*, 2007) and used for scaling up the system, particularly through the optically mediated coupling mentioned above.

As discussed in previous chapters, the NV center consists of a substitutional nitrogen impurity adjacent to a vacancy in the diamond lattice. In this chapter, we briefly review the essential theory needed to understand how measurements of single photons can result in entanglement between remote isolated NV centers and discuss the key requirements for these experiments. We then explore the state of the art in current research, and possible future directions.

8.2 How measurements of single photons result in entanglement

Heralded entanglement generation between remote spin qubits is the key step for the optically connected quantum information protocols mentioned above. To begin with, we must distinguish two-photon schemes from single-photon schemes.

The latter usually require an interferometric setup, which may lead to phase decoherence being accumulated by the photon, and are usually more susceptible to photon loss (Barrett and Kok, 2005). The former are robust to both of these problems, although the trade-off is lower entanglement generation rates. We will discuss two-photon schemes, but it should be recognized that certain forms of error correction could be employed to make single-photon schemes more robust as well (Barrett and Kok, 2005; Childress *et al.*, 2006b).

The central idea is to first create spin–photon entangled pairs at two locations (labeled A and B in Fig. 8.1), and then to use Hong–Ou–Mandel (HOM) quantum interference between the two photons to project the spins into a Bell state. The first step, creation of entangled spin–photon states at A and B, results in the following wave function for the entire system:

$$|\Psi\rangle = (|\uparrow\rangle_A|\sigma-\rangle_A - |\downarrow\rangle_A|\sigma+\rangle_A) \otimes (|\uparrow\rangle_B|\sigma-\rangle_B - |\downarrow\rangle_B|\sigma+\rangle_B) \quad [8.1]$$

Here, the states $|\sigma+\rangle$ and $|\sigma-\rangle$ denote single-photon wave packets with opposite polarization helicity. It is important to note that the photons are assumed to be identical in every other aspect, such as frequency, momentum and transverse spatial modes. The entanglement could also have been written in one of these other photonic degrees of freedom, with the polarization remaining identical. Following this step, the photon wave packets collide on a 50/50 beam splitter. Owing to the bosonic character of photons, when the polarizations of the two photons are the same, the collision results in the two photons bunching and going to only one detector or the other. Since most single-photon-counting detectors cannot resolve the number of photons in a wave packet, we ignore those situations. When the polarizations are different, the two photons can now travel to either detector, resulting in coincidence counts, i.e., a single photon in each detector at the same time. With this simple argument, we see that when there is a coincidence count, the matter qubits are projected into the state

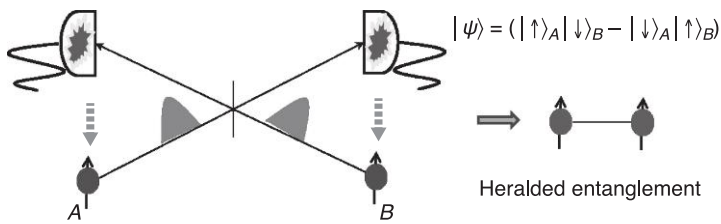

8.1 Measurement-induced remote entanglement generation between two solid-state spin qubits. The two spin qubits at A and B are first entangled with photons through laser stimulation (dashed arrows), resulting in the wave function shown in Eq. 8.1. The photons collide on the beam splitter, and coincidence counts in the detectors herald the creation of an entangled spin state at the two locations A and B.

$$|\Psi^-\rangle_{\text{spin}} = 1/\sqrt{2}\left(|\uparrow\rangle_A|\downarrow\rangle_B - |\downarrow\rangle_A|\uparrow\rangle_B\right) \quad [8.2]$$

The minus sign between the two states is a subtle issue, which is now addressed in more detail. The action of a beam splitter on the spatial degrees of freedom is that of a Hadamard gate (Yurke *et al.*, 1986), which is shown in Fig. 8.2(a). The Hadamard gate is described by

$$H|a(b)\rangle = \frac{1}{\sqrt{2}}\left(|a'\rangle \pm |b'\rangle\right) \quad [8.3]$$

Since photons are bosons, the overall wave function of the photons must remain symmetric under interchange of the particles (denoted 1 and 2 here to avoid confusion with spatial modes). The overall photonic wave function can be written as a tensor product of polarization degrees of freedom and spatial degrees of freedom,

$$|\Psi\rangle_{\text{phot}} = |\Psi\rangle_{\text{pol}} \otimes |\Psi\rangle_{\text{spatial}} \quad [8.4]$$

where

$$|\Psi\rangle_{\text{pol}} = \{|\varphi^{\pm}\rangle, |\Psi^{\pm}\rangle\}$$

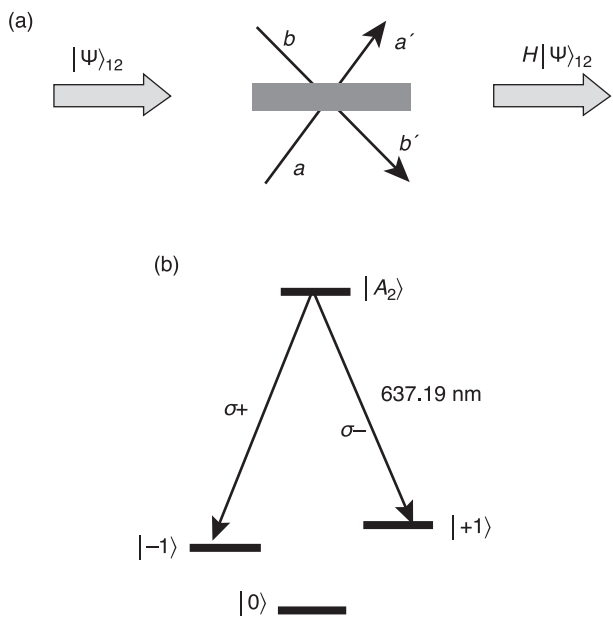

8.2 (a) Action of beam splitter on photon spatial modes. (b) Level structure for entanglement generation using the Λ-transition.

with

$$|\phi^{\pm}\rangle = 1/\sqrt{2}\left(|\sigma+\rangle_A|\sigma+\rangle_B \pm |\sigma-\rangle_A|\sigma-\rangle_B\right)$$

$$|\Psi^{\pm}\rangle = 1/\sqrt{2}\left(|\sigma+\rangle_1|\sigma-\rangle_2 \pm |\sigma-\rangle_1|\sigma+\rangle_2\right)$$

and

$$|\Psi\rangle_{\text{spatial}} = \{|\Psi\rangle^{S}_{\text{spatial}}, |\Psi\rangle^{AS}_{\text{spatial}}\}$$

with

$$|\Psi\rangle^{S}_{spatial} = 1/\sqrt{2}\left(|a\rangle_1|b\rangle_2 + |b\rangle_1|a\rangle_2\right)$$

and

$$|\Psi\rangle^{AS}_{spatial} = 1/\sqrt{2}\left(|a\rangle_1|b\rangle_2 - |b\rangle_1|a\rangle_2\right)$$

The triplet polarization states $|\varphi^{\pm}\rangle$, $|\Psi^{+}\rangle$ are symmetric under particle interchange, while the singlet polarization state $|\Psi^{-}\rangle$ is antisymmetric. Thus, the only allowable combinations are

$$|\Psi\rangle = \{|\varphi^{\pm}\rangle, |\Psi^{+}\rangle\} \otimes |\Psi\rangle^{S}_{\text{spatial}} \textbf{ or } |\Psi\rangle = |\Psi^{-}\rangle \otimes |\Psi\rangle^{AS}_{\text{spatial}} \quad [8.5]$$

Substituting the Hadamard transform into the above combinations, we find immediately that the product of the antisymmetric polarization and spatial states is the only one that results in coincidence photon counts in the two detectors placed at the output ports. This can be seen by verifying that

$$H|\Psi\rangle^{AS}_{spatial} = 1/\sqrt{2}\left(|a'\rangle_1|b'\rangle_2 - |b'\rangle_1|a'\rangle_2\right) \quad [8.6]$$

Thus, the beam splitter allows us to project the photonic wave function into the corresponding singlet polarization state by waiting for a coincidence detection event. Furthermore, the coincidence detection implies that the spin qubits are then also projected into a singlet spin state, i.e.,

$$|\Psi^{-}\rangle_{Spin} = 1/\sqrt{2}\left(|\uparrow\rangle_A|\downarrow\rangle_B - |\downarrow\rangle_A|\uparrow\rangle_B\right) \quad [8.7]$$

This can be verified by rewriting Eq. 8.1 into the following state,

$$|\Psi\rangle = |\Psi^{+}\rangle_{\text{spin}}|\Psi^{+}\rangle_{\text{phot}} - |\Psi^{-}\rangle_{\text{spin}}|\Psi^{-}\rangle_{\text{phot}} - |\Phi^{+}\rangle_{\text{spin}}|\varphi^{+}\rangle_{\text{phot}} + |\Phi^{-}\rangle_{\text{spin}}|\varphi^{-}\rangle_{\text{phot}} \quad [8.8]$$

Furthermore, we note that all the other combinations of states that start with spin–photon entangled pairs, such as

$$|\Psi\rangle = 1/2\left(|\uparrow\rangle|\sigma-\rangle + |\downarrow\rangle|\sigma+\rangle\right)_A \otimes \left(|\uparrow\rangle|\sigma-\rangle + |\downarrow\rangle|\sigma+\rangle\right)_B \quad [8.9]$$

can be written in terms of these Bell states, albeit with different signs. Thus, the beam splitter measurement will always project us into the entangled singlet spin qubit state, up to a global phase. In the process, the photons are destroyed, but we are left with an entangled matter qubit state that can become a starting point for quantum operations. Essentially, this step corresponds to entanglement swapping or entanglement teleportation between the two remote spin qubits. Thus, although postselection has been employed on the photons, the entanglement can still, ideally, be verified through local operations and classical communications between the two remote locations. This important fact may allow experimenters to finally close both the detection and the locality loopholes in measurements of Bell's inequality and other foundational quantum experiments.

The above protocol, if carried out for identical photons that have the same polarization, frequency and other degrees of freedom (i.e., they are not entangled with spin qubits), would result in bunching; path erasure occurs to ensure that both photons are routed to one detector or the other. The corresponding Hong–Ou–Mandel dip in the coincidence counts would provide a signature of the fact that the two photons were indeed identical. This can be verified by carrying out the Hadamard transform, but now on the symmetric spatial photon state

$$H\,|\Psi\rangle^{S}_{spatial} = 1/\sqrt{2}\left(|a'\rangle_1\,|a'\rangle_2 - |b'\rangle_1\,|b'\rangle_2\right) \qquad [8.10]$$

Based on the above considerations, we can thus conclude that the key requirements for realizing heralded entanglement generation are:

- the ability to generate spin–photon entangled pairs at each location;
- indistinguishable photons from the two locations;
- high-efficiency readout of single spins.

The last is only required when we are trying to verify entanglement or for further quantum operations, but is nevertheless an important step in any real system.

Following these general considerations, we now turn to a brief discussion of the optical and spin transitions of the NV center and show how these properties allow us to fulfill all of the above requirements for heralded entanglement generation.

8.3 Optical properties of the nitrogen–vacancy (NV) center for spin–photon entanglement generation

The optical transitions of the NV center are closely linked to the spin levels. The electronic and spin states of the NV center have now been intensively studied using a variety of theoretical, computational and experimental approaches (Doherty *et al.*, 2013). The NV center may be thought of as a molecule, and in most of the studies performed, the Born–Oppenheimer approximation is well

satisfied. This result in a separation of the electronic and nuclear timescales and levels, with the electronic levels governed by a hierarchy of interactions arranged roughly in decreasing order of strength as follows: Coulomb, spin–orbit, spin–spin and strain. Figure 8.3 summarizes our current understanding of the hierarchy of optical transitions for the NV center from the ground (e^2) triplet to the excited (ae) triplet states. The level structure is shown for a weakly strained NV center, such that δ is small compared with the spin–orbit or spin–spin interactions. The most important transitions for this work are shown in the boxed regions, with the $|m_s = \pm 1\rangle \rightarrow |A_2\rangle$ transition (referred to as the Λ-transition) used for entanglement generation, and the $|m_s = 0\rangle \rightarrow |E_y\rangle$ transition used for spin readout. The Λ-transition (see Fig. 8.2(b)) occurs because the excited state

$$\left(|+1\rangle|\sigma-\rangle + |-1\rangle|\sigma+\rangle\right)/\sqrt{2} \qquad [8.11]$$

decays into the two ground states $|m_s = \pm 1\rangle$, in the process creating a spin–photon entangled state

$$\left(|+1\rangle|\sigma-\rangle + |-1\rangle|\sigma+\rangle\right)/\sqrt{2} \qquad [8.12]$$

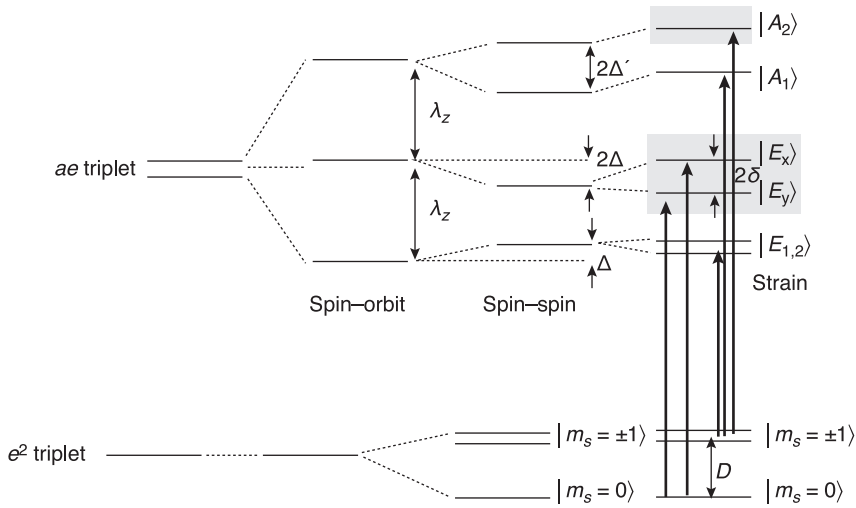

8.3 Hierarchy of interactions for the ground (e^2) and excited (ae) state triplets in a weakly strained NV center. The total of six states in the *ae* triplet are split under the ~3.3 GHz interaction. A small nonaxial strain field (δ) gives rise to six individually addressable optical transitions that are shown by the thick arrows in the figure. The ground state triplet remains unaffected by spin–orbit coupling, but a zero-field splitting (D~3.3 GHz) is induced by the spin–spin interaction. Strain plays a role in modifying the zero-field splitting.

The nuclear motion that we have ignored so far results in vibronic or phonon sidebands (PSBs) that are essentially phonon replicas of the electronic level structure; however, various complications can arise from the vibronic character owing to, for example, nuclear-wave-function overlap (Franck–Condon and Huang–Rhys effects), symmetry breaking (Jahn–Teller effects) and interaction with other phonons in the diamond lattice (Debye–Waller effects). The most important of these for our purposes is probably the Huang–Rhys factor ($S \sim 3.2$), as it governs the strength of the so-called zero-phonon line (ZPL) relative to the phonon replicas. For the NV center, this implies that only a fraction $e^{-S} \sim 0.04$ of the emission intensity is in the ZPL.

At room temperature, the vibronic sidebands are thermally populated, and, owing to broadening, it is usually impossible to address electronic transitions directly. Instead, excitation at 532 nm (the peak of the absorption in the vibronic sidebands) is typically used to drive the NV center at room temperature. This method of excitation is useful as it allows us to separate out the excitation from the emission in the ZPL and PSBs. Furthermore, several studies have shown that 532 nm excitation preserves the spin states during the excitation and emission cycle in the e^2 triplets and their vibronic partners. However, for entanglement generation, it is critical that we drive the NV center resonantly and observe only the ZPL to preserve the quantum entanglement between the spin and the photons. Since we do not observe or measure the phonons within the NV center or the diamond lattice, tracing over those degrees of freedom would result in loss of entanglement fidelity. This has also been observed through the loss of polarization fidelity in the PSBs in comparison with the ZPL. At low temperatures, the resonance lines narrow greatly, and lifetime-limited linewidths have been observed in the ZPL. A great deal of effort has now been put into understanding the characteristics of the optical transitions, and we refer the reader to Tamarat *et al.* (2008), Batalov *et al.* (2009), Acosta *et al.* (2010), Maze *et al.* (2011) and Doherty *et al.* (2013) for details.

8.4 Generation of spin–photon entanglement

In this and the following sections, we now consider the three main criteria outlined above for heralded entanglement generation, and show how each of these steps has now been realized in separate experiments. Therefore, we expect that the final step, i.e., entanglement of remote NV spin qubits via optical connections, will be very much feasible with current technology. We begin by discussing an experiment on spin–photon entanglement, and conclude with brief summaries of recent experiments on two-photon interference and on single-shot (quantum projective) readout of NV spin states at low temperature.

The experiment on spin–photon entanglement with NV centers was carried out by Togan *et al.* (2010). This paper marks the first demonstration of entanglement between a flying qubit and a solid-state qubit. The scheme they followed was

briefly outlined in the Section 8.2. Before we describe the important aspects of our experimental scheme, we also present a more complete description of the theory of the experiment on spin–photon entanglement.

8.4.1 Theoretical analysis of spin–photon entanglement scheme

A more careful analysis of the spontaneous emission in the Λ-transition can be carried out using the Wigner–Weisskopf theory. In the Λ-level scheme shown in Fig. 8.2(b), where the spin levels $|\pm 1\rangle$ are coupled to the level $|A_2\rangle$, we can write the Hamiltonian in the interaction picture and the rotating-wave approximation as follows,

$$\begin{aligned} H = \Big[& \sum_{k,s} g_{k,s}^{A2,+1}(r_0)|A2\rangle\langle +1|e^{i(\nu_k-\omega_{+1})t}\hat{\alpha}_{k,s} + \\ & \sum_{q,s'} g_{q,s'}^{A2,-1}(r_0)|A2\rangle\langle -1|e^{i(\nu_q-\omega_{-1})t}\hat{\alpha}_{q,s'} + \text{h. c.}\Big] \end{aligned} \quad [8.13]$$

where the coupling strengths are given by

$$g_{k,s}^{A2,+1}(r_0) = \sqrt{\frac{\upsilon_k}{2\varepsilon_0 V\hbar}}\left((\vec{\mu}.\varepsilon_k^s)e^{i\vec{k}.\vec{r}_0}\right)$$

$$g_{q,s'}^{A2,-1}(r_0) = \sqrt{\frac{\upsilon_q}{2\varepsilon_0 V\hbar}}\left((\vec{\mu}.\varepsilon_q^{s'})e^{i\vec{q}.\vec{r}_0}\right)$$

The Schrödinger equation can be formally integrated and the Wigner–Weisskopf approximation applied to give the wave function for the system. We now use the definition of the single-photon wave packet prior to detection, i.e.,

$$|\Psi(\sigma+;r,t_d)\rangle = \langle 0|\hat{E}^{(+)}(\sigma+;r,t_d)|\gamma_0\rangle \quad [8.14]$$

where $\hat{E}^{(+)}(\sigma+;r,t_d)$ represents the quantized electromagnetic field operator for detection of a photon at position r and time t_d with *infinitesimal time resolution*, and

$$|\gamma_0\rangle = \sum_{k,s}\sqrt{\nu_k/2\varepsilon_0 V\hbar}\,\frac{(\vec{\mu}.\varepsilon_k^s)e^{i\vec{k}.\vec{r}_0}}{(\nu_k-\omega_0)+i\Gamma/2}|1_{ks}\rangle \quad [8.15]$$

represents the single-photon state emitted by an NV center located at r_0. For a review of the Wigner–Weisskopf theory and a discussion of single-photon wave packets, see for example Scully and Zubairy (1997). We have carried out the full calculation and determined that the actual state of the spin–photon system, just prior to detection at time t_d, should be written as

$$|\Psi\rangle = \frac{\varepsilon}{\Delta r}\Theta(t_d-\Delta r/c)\,e^{-\frac{\Gamma(t_d-\Delta r/c)}{2}}\,\frac{1}{\sqrt{2}}\left[|+1\rangle|\varepsilon_{\sigma-}\rangle+|-1\rangle|\varepsilon_{\sigma+}\rangle\right] \quad [8.16]$$

where $\Theta(t)$ is the unit step function, Γ is the spontaneous-emission decay rate, ε is the single-photon electric field, the $\hat{\varepsilon}_{\sigma\pm}$ represent the polarization unit vectors of the photon and $\Delta r = |r - r_0|$ is the distance from the NV center to the detector. For a pedagogical account of spin–photon entanglement and more details of the above calculation, see Boyanovsky (2013).

The above wave function shows the expected time delay due to propagation between source and detector. A very crucial fact is also revealed by this wave function: the 'quantum eraser' effect. If we examine Fig. 8.2(b), which shows the Λ-transition for entanglement generation, more carefully, it is clear that if the states $|\boldsymbol{m_s} = \pm\mathbf{1}\rangle$ are detuned from each other, for instance by application of a magnetic field, then the photon that is emitted has two distinct frequencies, corresponding to the two legs of the Λ-transition. Measurement in an infinitesimally small time window, as assumed above, prevents knowledge of the energy difference, through the energy–time uncertainty relation. On the other hand, a long-time (slow) measurement would reveal that the photon energy was different along the two paths. Thus, the state will be projected into one or other of the two possibilities, leading to no entanglement. This statement is reflected mathematically in the above wave function, which preserves the entanglement when a perfect time-resolving detector is assumed. Perhaps the most counterintuitive part of the wave function is the fact that it makes no reference to the time at which the binning is carried out. In other words, we can collect all the photons within some (large) time window and then, after the experiment is completed, we can choose only those events that occurred in an infinitesimal time window of our choosing. From the above calculation, the wave function is still entangled, and the only difference caused by changing the arrival time t_d is the decay of the photon amplitude, which lowers the probability of detection. In the actual experiment, of course, we do not have infinitely small windows, but the quantum eraser effect will hold as long as the time resolution $\Delta t_d << 1/\delta\omega$.

The second point about this wave function is that when the photon is measured in either the $\sigma-$ or the $\sigma+$ state, the NV spin is projected into the $|+\mathbf{1}\rangle$ or $|-\mathbf{1}\rangle$ state, respectively. This demonstrates classical correlations between the spin and the photon in the computational or logical basis for the qubits. However, in accord with quantum mechanics, if we now measure the photon in either the H or the V (linearly polarized) basis state, the NV spin is also accordingly projected into a coherent superposition of the $|+\mathbf{1}\rangle$ and $|-\mathbf{1}\rangle$ states. The verification of these quantum correlations is usually considered the real signature of quantum entanglement. Since our experiments were carried out in time-resolved fashion, as required for the quantum eraser effect, it was extremely important to control the time between photon detection and the time of measurement of the spin state. Furthermore, decoherence of the spin during the protocol could also have created a problem, unless it was carefully accounted for. Our experimental design took into account all of these critical factors in order to observe spin–photon entanglement.

Finally, we also remark that the entanglement fidelity is perfect, but it is conditioned upon detection of a photon. This makes sense, since if no photon is observed, we cannot know whether this is because we failed to prepare an entangled state and thus there was no emission, or there was emission and we just failed to observe it due to imperfect detectors. This sort of postselected entanglement, conditioned upon the detection (and thereby destruction) of the photon, is acceptable for our purposes as part of the process of building up quantum optical connections, but only in so far as we do not attempt to draw more significant conclusions regarding, for instance, measurements of Bell's inequality between the spin and photon states. For instance, the 'detection loophole' argues that Bell's inequality is violated only for those spin–photon pairs which result in destruction of the photon by the detector, and that when the entire set of spin–photon pairs (including those not detected) is taken into account, the inequality is then not violated. Such foundational questions are better resolved with qubits that are not destroyed during the measurement process, such as the matter qubits obtained from the Hong–Ou–Mandel interference process. For more detailed discussion of such issues, see for instance Duan and Monroe (2010).

8.4.2 Experimental realization of spin–photon entanglement

Our experimental setup for spin–photon entanglement is shown in Fig. 8.4. Resonant excitation at two wavelengths, one for entanglement generation (tunable laser 1) and the other (tunable laser 2) for spin readout, was done using a combination of dichroic and regular beam splitters on the microscope objective. In addition, 532 nm excitation was used for preparation of the NV center, and could also be used to stabilize the charge state of the NV center in between resonant excitation cycles (Gaebel *et al.*, 2006). A small magnetic field was applied to the NV center in the cryostat to detune the $|\pm\mathbf{1}\rangle$ levels from each other and to allow resonant microwave addressing of the $|\mathbf{0}\rangle \rightarrow |+\mathbf{1}\rangle$ $(|\mathbf{0}\rangle \rightarrow |-\mathbf{1}\rangle)$ transition.

Figure 8.5 shows the photoluminescence excitation spectrum of a single NV center in the low-strain regime, demonstrating spectral lines corresponding to all the transitions shown in Fig. 8.3. The data was obtained by scanning the laser frequency slowly under continuous-wave microwave excitation (to populate the $|m_s = \pm\mathbf{1}\rangle$ states) while collecting photons in the PSB channel. The boxes indicate the important transitions for entanglement generation and spin readout. The selection rules for the entanglement transition can be verified, as shown by the data in Fig. 8.6. Here, the NV center was first initialized in the $|m_s = \mathbf{0}\rangle$ state using a 1 μs green excitation, and a microwave π-pulse was applied to transfer population to the $|m_s = \pm\mathbf{1}\rangle$ or the $|m_s = -\mathbf{1}\rangle$ state. Then a short (2 ns) resonant optical excitation pulse was tuned to the $|+\mathbf{1}\rangle \rightarrow |A_2\rangle$ $(|-\mathbf{1}\rangle \rightarrow |A_2\rangle)$ optical transition. Linearly polarized laser light passed through a quarter-wave plate (QWP), and the oscillations in the PSB channel as the angle of the QWP was rotated showed that

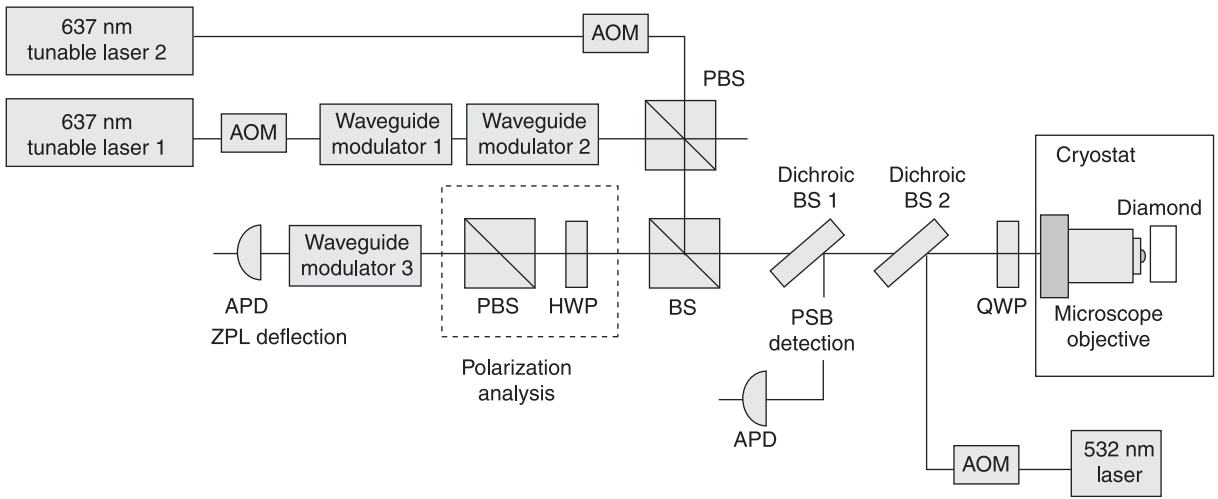

8.4 Schematic illustration of experimental setup for spin–photon entanglement generation and verification. Individual NV centers are isolated and addressed optically using a microscope objective. Two resonant lasers at 637 nm and an off-resonant laser at 532 nm address various optical transitions. Fluorescence emitted from the NV center passes through a quarter-wave plate (QWP), spectrally separated into PSB and ZPL channels, and detected with avalanche photodiodes (APDs). The latter channel contains entangled photons and is sent using a beam splitter (BS) through a polarization analysis stage consisting of a half-wave plate (HWP) and a polarizing beam splitter (PBS). Reprinted by permission from Macmillan Publishers Ltd (Togan *et al.*, 2010), http://dx.doi.org/10.1038/nature09256.

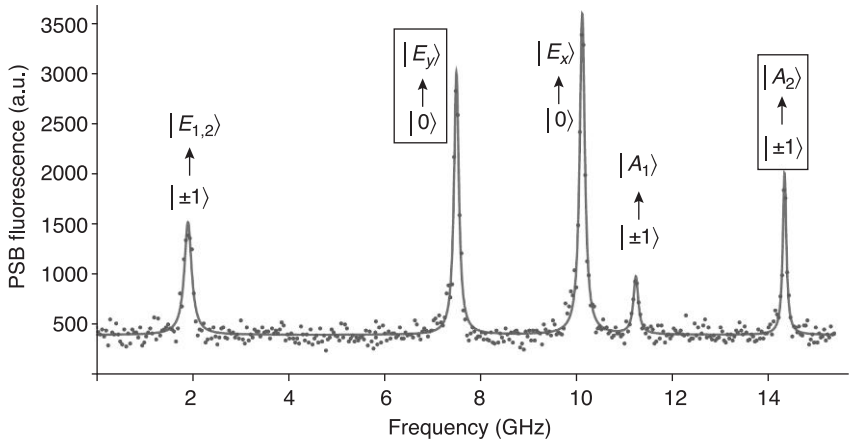

8.5 Photoluminescence excitation spectrum of a single NV center, showing the experimental observation of optical transitions described in Section 8.2 and depicted schematically in Fig. 8.3. Reprinted by permission from Macmillan Publishers Ltd (Togan *et al.*, 2010), http://dx.doi.org/10.1038/nature09256.

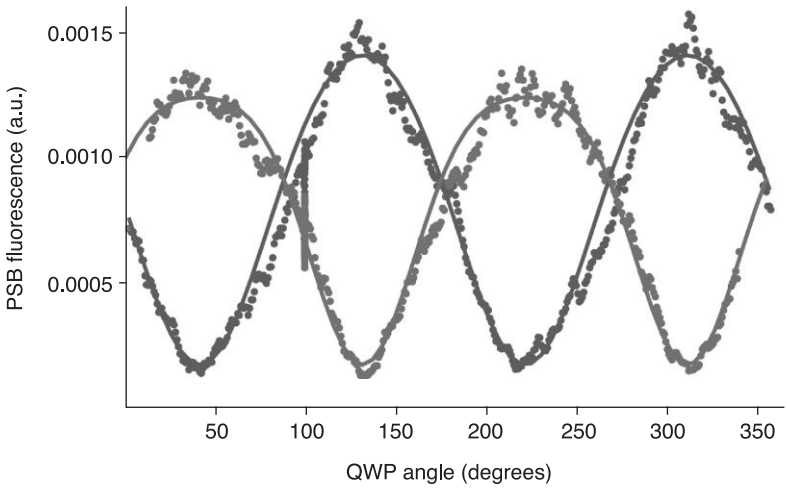

8.6 Verification of polarization selection rules for the entanglement transition. See main text for details. Reprinted by permission from Macmillan Publishers Ltd (Togan *et al.*, 2010), http://dx.doi.org/10.1038/nature09256.

the transitions $|m_s = \pm 1\rangle \rightarrow |A_2\rangle$ had mutually orthogonal circular-polarization selection rules. The QWP rotated the incident linearly polarized light into a well-defined superposition of circular polarizations, with an amplitude that was dependent sinusoidally on the angle. For more details, see Togan *et al.* (2010).

As explained above, it is the ZPL pathway that contains the information about the entanglement between the spin and photon. The PSB emission cannot be used to detect the entanglement. Isolating the weak ZPL emission presented a significant experimental challenge, owing to strong reflections of the resonant excitation pulse reaching the detector.

The ZPL path is the one that contains entangled photons, and a combination of pulsed excitation with modulators and confocal and polarization rejection was used to carefully separate the reflected laser photons from the emitted photons. The photons emitted by the NV center decay over a longer timescale (~13 ns) owing to the spontaneous-emission lifetime. By exciting the NV center with a circularly polarized 2 ns π-pulse that was shorter than the emission timescale, we could use detection timing to separate reflection from fluorescence photons. The data shows that the optics suppressed the reflections sufficiently to allow clear detection of the NV center's ZPL emission in a 20 ns region.

The experimental procedure for entanglement generation and verification is shown in Plate III (see colour section between pages 218 and 219). For photon state determination, ZPL photons in either the $|\sigma\pm\rangle$ or the

$$|H(V)\rangle = 1/\sqrt{2}\left(|\sigma+\rangle \pm |\sigma-\rangle\right)$$

basis were selected by a polarization analysis stage and detected after an optical path of ~2 m. Spin readout then occurred after a 0.5 μs spin memory interval, following photon detection by transferring population from either the $|\pm 1\rangle$ states or from an appropriately chosen superposition of them into the $|0\rangle$ state using microwave pulses $\Omega_{\pm 1.}$ The pulses selectively addressed the $|0\rangle \rightarrow |\pm 1\rangle$ transitions with resonant frequencies $\omega_{\pm}$ that differed by $\delta\omega = \omega_{+} - \omega_{-} = 122$ MHz owing to the applied magnetic field. For superpositions of $|\pm 1\rangle$ states, an echo sequence was applied before the state transfer to extend the spin coherence time (as explained below). The transfer was followed by resonant excitation of the $|m_s = 0\rangle \rightarrow |E_y\rangle$ transition and collection of the PSB fluorescence. The transferred population measured in the $|0\rangle$ state was carefully calibrated using a conditioned measurement readout procedure, detailed in Togan *et al.* (2010). However, note that owing to the low collection efficiency for the bulk diamond samples in this work, it was not possible to achieve single-shot (projective) readout of the spin state. This limitation slowed down the experiment by ~100 times, although it had no effect on entanglement fidelity and verification.

Plate IV shows the populations in the $|\pm 1\rangle$ states, measured conditionally on the detection of a single circularly polarized ZPL photon. Excellent correlations between the photon polarization and NV spin states were observed. To complete the entanglement verification, we now have to verify the quantum correlations

detected in a rotated basis. Upon detection of a linearly polarized $|H\rangle$ or $|V\rangle$ photon at time t_d, the entangled state in Eq. 8.12 is projected to

$$|\pm\rangle = 1/\sqrt{2}\left(|+1\rangle \pm |-1\rangle\right)$$

respectively. These states subsequently evolve in time (t) according to the spin Hamiltonian and give

$$|M\rangle_t = 1/\sqrt{2}\left(e^{i\omega_+(t-t_d)}|+1\rangle \pm e^{i\omega_-(t-t_d)}|-1\rangle\right) \quad [8.17]$$

This state can be verified by applying two resonant microwave fields with frequencies ω_+ and ω_- to coherently transfer the state

$$|M\rangle = 1/\sqrt{2}\left(e^{i\omega_+ t}|+1\rangle + e^{i\omega_- t}|-1\rangle\right)$$

to $|0\rangle$. Then the conditional probability of measuring the state $|M\rangle$ is

$$P_{M|H,V}(t) = (1 \pm \cos\left((\omega_+ - \omega_-)t_d\right))/2 \quad [8.18]$$

Here, we have ignored the possibility that the two microwave fields may start with some initial (constant) phase difference. The important point is that the conditional probabilities of measuring the state $|M\rangle$, given the observation of an $|H\rangle$ or $|V\rangle$ photon, oscillate out of phase with each other as a function of the detection time t_d.

The superposition state would normally experience dephasing due to the nuclear-field environment (e.g., $^{15}N/^{14}N$ static detuning or C^{13} random nuclear fields) of the NV center in each run of the experiment. This would typically restrict the time between observation of the photon and spin detection to much less than ~0.2 ms. To eliminate these effects, thereby making the experimental timing simpler, a microwave pulse sequence of the form t–2π–t was applied after detection of the $|H\rangle$ or $|V\rangle$ photon. In combination with the initial microwave π-pulse prior to the entanglement-generation optical pulse (see Plate III), this combined sequence acts as a spin-echo sequence in the so-called bright/dark basis, i.e., the basis $|M(D)\rangle = (|+1\rangle \pm |-1\rangle)/\sqrt{2}$. The conditional-probability oscillations are experimentally confirmed in Plate IV(c) and (d). The data in Plate IV can be used to estimate a lower bound on the fidelity of entanglement F, which was found to be $F \geq 0.69 \pm 0.068$, above the classical limit of 0.5, indicating the preparation of an entangled state. The entanglement fidelity was limited by several sources, such as:

- imperfection in the state $|A2\rangle$ and photon depolarization in the setup, ~12%;
- imperfection in the readout and echo microwave pulses, ~3%;
- finite signal-to-noise in the ZPL path and timing jitter, ~15%.

The resulting expected fidelity, ~70% is consistent with our experimental observations. The entanglement generation succeeds with probability $p \sim 10^{-6}$, limited by low collection and detection efficiency as well as the small (~4%) probability of ZPL emission. The experiment ran for about 24 h per measurement in each of the four basis states, accumulating a total of about 35 000 events to achieve the above error bars on the entanglement fidelity.

This low probability would greatly reduce the generation of remote entanglement of spin-qubit Bell states, as that rate depends on joint detection of two photons, making the probability $\sim p^2$. Projective readout would also contribute to a significant speedup in the overall entanglement verification and teleportation protocols. As mentioned previously, the photons must be identical in all other aspects as well, and this can only be verified using Hong–Ou–Mandel quantum interference.

8.5 Hong–Ou–Mandel interference between identical photons from NV centers

Since local strain and electric fields even within a single diamond sample cause inhomogeneous broadening of the ZPL, it is very important to be able to tune the resonance frequencies. Recently, Sipahigil *et al.* (2012) and Bernien *et al.* (2012) showed the ability to tune NV centers in different samples and within the same sample, respectively, into optical resonance with each other and demonstrated HOM interference between photons. We will discuss the work of Sipahigil *et al.* (2012) briefly here. The experimental setup used by these authors is shown in Fig. 8.7. The two key innovations in this experiment were the use of macroscopic solid immersion ('half-ball') lenses made of diamond to greatly improve the collection efficiency, and the use of electric fields applied by tuning electrodes to bring the NV centers into resonance with each other. Both resonant and off-resonant (532 nm) excitation, combined with spectral filters and polarization analysis stages, allowed Sipahigil *et al.* to separate out the ZPL emission from the $|\boldsymbol{E}_x\rangle$ and $|\boldsymbol{E}_y\rangle$ lines. These authors demonstrated DC Stark effect tuning of the resonance lines; however, for experimental convenience, they did not employ this for the actual HOM interference but instead chose two NV centers whose resonances were already close to each other. The use of ZPL lines with different linear polarizations also allowed them to use off-resonant excitation during HOM interference, which resulted in broadening of the ZPL lines. Since the resonant-excitation and ZPL paths traversed the same polarization optics, the setup allowed them to confirm which line they were observing in emission simply by using the resonant excitation to perform absorption spectroscopy.

Figure 8.8 shows the key experimental results for HOM interference. First, Sipahigil *et al.* used the PSB emission to confirm that the NV centers were single-photon emitters (Fig. 8.8(a) and (b). Next, they used NV centers that were detuned from each other (Fig. 8.8(c)) and demonstrated that the cross-correlation function did not go below 0.5. Finally, by using NV centers that were close to resonance with each other, the cross-correlation function was shown to go below 0.5. This is a signature of quantum interference between the two photons. For, if the two arms were distinguishable, then the experiment would measure autocorrelation from one emitter in the presence of uncorrelated noise from the second, thereby raising $g^{(2)}(0)$ to 0.5. For the indistinguishable case, ideally $g^{(2)}(0)$ should go to 0, but

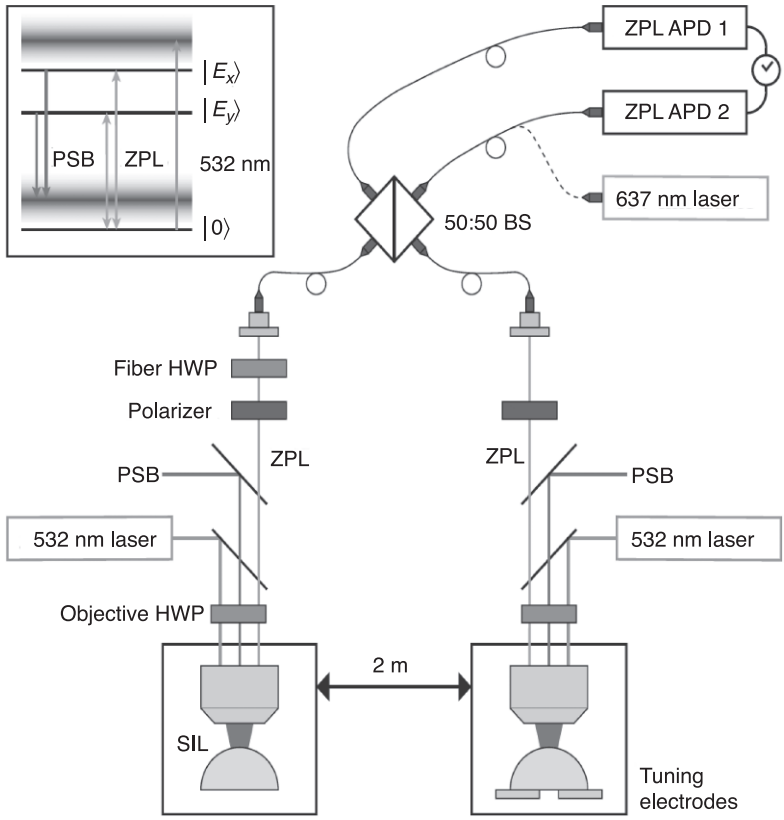

8.7 Schematic illustration of the apparatus used by Sipahigil *et al.* (2012). Two diamond SILs containing multiple NV centers are housed in continuous-helium-flow cryostats 2 m apart. Each solid immersion lens (SIL) is addressed by a separate confocal microscopy setup, which includes a path for excitation at 532 nm, a collection path for the phonon sideband (PSB), and a collection path for the zero-phonon line (ZPL). The three optical paths are superimposed using dichroic mirrors. The ZPL collection path passes through a half-wave plate (HWP) and an additional bandpass filter (633–647 nm) before being coupled into a polarization-maintaining single-mode 50:50 fiber beam splitter. The two beam splitter output arms are connected to a pair of avalanche photodiodes (APDs), completing the Hanbury Brown–Twiss detection setup. An excitation laser at 637 nm is connected in place of the ZPL APD 2 to acquire the photoluminescence excitation spectra. Electrodes for electric-field tuning are installed in one cryostat. The inset shows a simplified level structure, including resonant excitation and emission into the ZPL at 637 nm, redshifted emission into the ground state PSB, and nonresonant excitation into the excited state PSB at 532 nm. Reprinted figure with permission from Sipahigil *et al.* (2012), copyright (2013) by the American Physical Society, http://link.aps.org/doi/10.1103/PhysRevLett.108.143601.

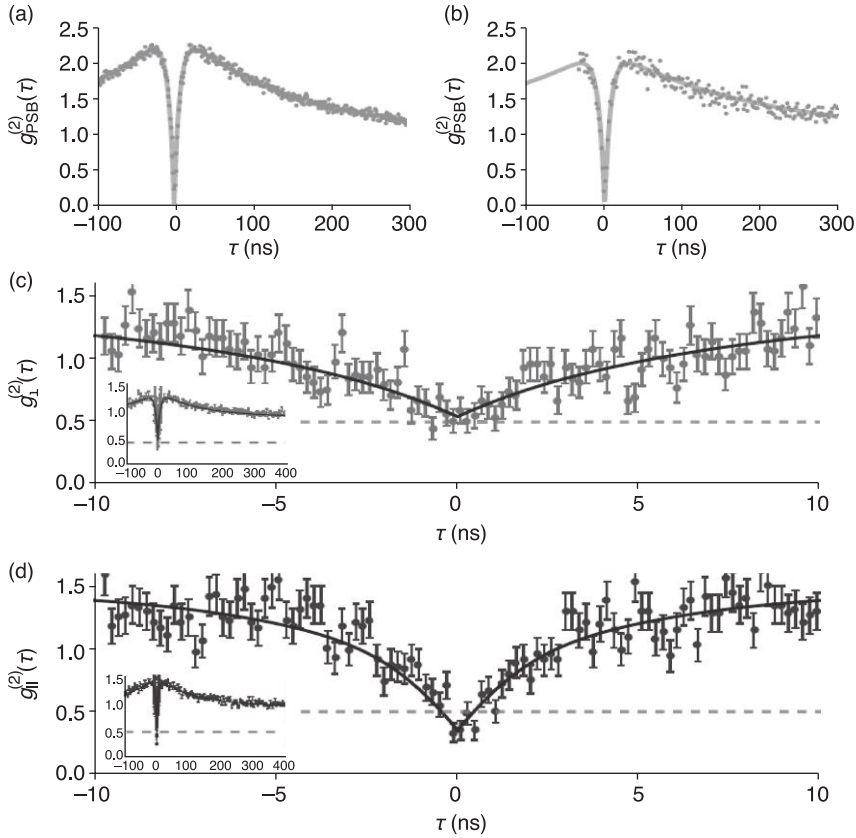

8.8 (a), (b) Single-emitter second-order autocorrelation functions $g^{(2)}{}_{PSB}(\tau)$ of the PSB emission, inferred for the two NV centers used for the HOM measurement. The FWHM of the central antibunching feature is 7.5±0.1 ns for (a) and 9.5±0.2 ns for (b). (c), (d) Demonstration of HOM interference from remote NV centers in (c) the distinguishable case and (d) the indistinguishable case. The dashed lines indicate the limit expected for independent distinguishable single-photon sources at τ=0. The solid lines are a fit to the data based on the model described in the text. For the distinguishable case (c), we find that the FWHM of the central antibunching feature is 9.2±0.4 ns and $g\perp^{(2)}(0)$=0.54±0.04. For the indistinguishable case (d), we find that the FWHM of the central antibunching feature is 5.6±0.3 ns and $g\parallel^{(2)}(0)$=0.35±0.04. The error bars are estimated based on shot noise. Reprinted figure with permission from Sipahigil *et al.* (2012), copyright (2013) by the American Physical Society, http://link.aps.org/doi/10.1103/PhysRevLett.108.143601.

imperfections due to APD dark counts, background from the sample, imperfect polarization rejection and imperfect spin polarization under green excitation raise $g^{(2)}(0)$ from this value.

8.6 Single-shot projective readout of NV centers

In the entanglement experiment, the spin state was verified using the readout transition, but because the $|E_y\rangle$ state was not perfectly cycling, the NV spin was actually optically pumped over longer timescales ($\sim 10\,\mu s$) from $|\mathbf{0}\rangle$ to the 'dark' state $|\pm\mathbf{1}\rangle$. If the number of photons collected during this window is not sufficiently high, then we are unable to distinguish the two states in one shot. However, by raising the collection efficiency, we can achieve so-called single-shot or projective readout of the NV spin state. Robledo *et al.* (2011) used a clever technique based on microfabricated solid immersion lenses that were deterministically positioned over the relevant NV center to achieve this important goal. Although such lenses had been pioneered in diamond by Hadden (2010), Robledo *et al.* were able to combine together all of the challenging elements needed: positioning of microfabricated lenses, resonant excitation and ZPL collection, and spin manipulation.

Figure 8.9 shows both an example of these diamond lenses and the improved collection efficiency obtained within the $\sim 10\,\mu s$ detection window. Figure 8.10 shows that by using this method, Robledo *et al.* achieved high ($\sim 93\%$) fidelity for the measurement. With shorter measurement windows, the readout becomes nondestructive (albeit with lowered fidelity). Through optimization, these authors were able to achieve ~84% fidelity for successive readout segments (Fig. 8.10(c)), and observe quantum jumps during continuous spin readout (Fig. 8.10(e)) owing to weak microwave driving.

8.7 Future trends

The experiments just discussed have demonstrated that all the key ingredients now exist to create remote entanglement between NV spin qubits. We expect that, through either single-photon or two-photon schemes as outlined in Section 8.2, this step will also be realized in the near future. Such a capability will allow researchers to explore many important and exciting new avenues. For instance, remote entanglement between robust, stable solid-state spin qubits will allow the verification of Bell's inequality and potentially close the detection and locality loopholes that previously existed in such experiments. Furthermore, teleportation-based quantum gates (Gottesman and Chuang, 2006) will become feasible as a building block for quantum logic operations over large distances and between arbitrarily optically connected quantum processor nodes. The key figure of merit for such optically connected quantum networks is the quantity $p^2\gamma T_M/(1+\gamma\tau)$, where T_M is the quantum memory time, γ is the spontaneous emission rate and $\tau = L/c$ is the communication time between nodes. By increasing the memory time T_M and the factor p, it should be possible to obtain a figure of merit close to one.

This has important implications for both quantum information systems and fundamental solid-state quantum optics. Through fabrication and incorporation of nanophotonic structures, not only we can expect the collection efficiency to

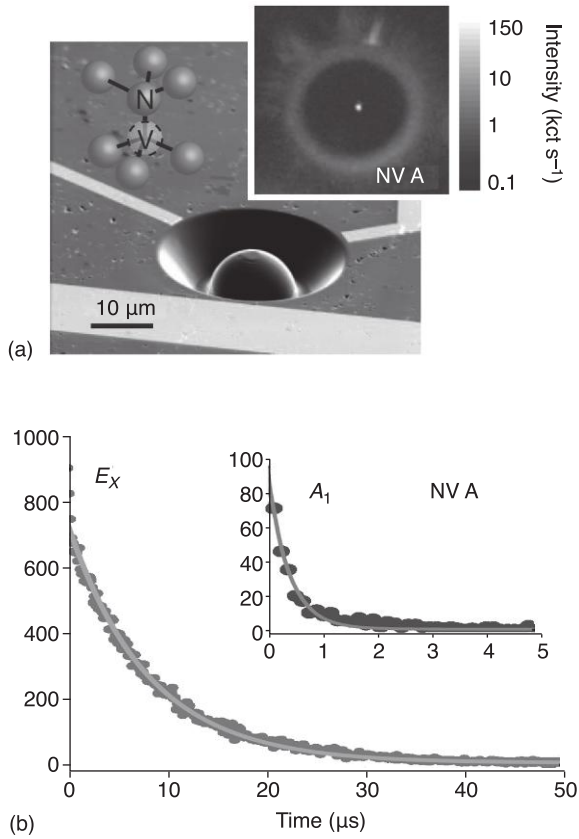

8.9 (a) Scanning electron microscope image of a solid immersion lens representative of those used in the experiments. The overlaid sketch shows the substitutional nitrogen and the adjacent vacancy that form the NV center. Inset, scanning confocal microscope image of NV A (kct, 1000 counts). (b) Fluorescence time trace of NV A, initially prepared in $m_s=0$ (E_x excitation, 4.8 nW power) and $m_s=\pm1$ (A_1 excitation, 7.4 nW power; inset), with a saturation power $P_{sat}\approx6$ nW. Spin flips in the excitation cycle lead to nearly exponential decay of the fluorescence, with fitted spin-flip times of $1/\gamma_0=8.1\pm0.1$ μs for E_x and 0.39 ± 0.01 μs for A_1, and initial respective intensities of 740 ± 5 and 95 ± 2 kct s^{-1}, giving a lower limit of $99.7\pm0.1\%$ for the $m_s=0$ preparation fidelity and of $99.2\pm0.1\%$ for the $m_s=\pm1$ preparation fidelity. The low initial intensity for A_1 is associated with a fast intersystem crossing to metastable singlet states. Reprinted by permission from Macmillan Publishers Ltd (Robledo *et al.*, 2011), http://dx.doi.org/10.1038/nature10401.

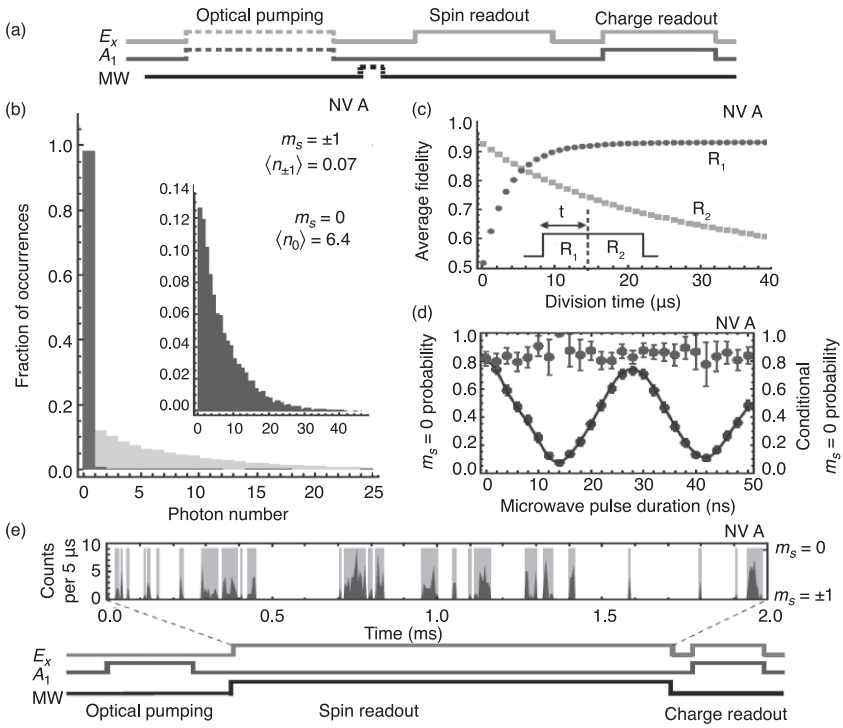

8.10 (a) Pulse sequence used for electronic-spin readout. After charge initialization (532 nm, not shown), the electron is pumped into the m_s=0 (A_1) or m_S=±1 (E_x) state, and then undergoes optional microwave spin manipulation and spin readout by a pulse resonant with E_x. Conditioning on simultaneous resonance during the final charge- and detuning-sensing stage eliminates effects of local electric-field fluctuations or ionization. (b) Statistics of photon counts detected during a t_{ro}=100 μs electronic-spin readout after initialization into the respective m_s=±1 (dark gray) and m_s=0 (superimposed light gray and inset) states, obtained from 10 000 measurement repetitions. (c) When the 100 ms readout pulse is divided into two readout segments, R1 and R2, with a variable division point, the fidelity of two consecutive segments reaches 83.4±0.5% for an optimal division time of 5.5 μs; the probability of identical sequential outcomes is 82.0±0.7%. The error bars (2 s.e., n=10 000) are smaller than the symbols. (d) Electronic-spin Rabi oscillations between m_s=0 and m_s=–1 at an axial magnetic field $B_z \approx 15$ G (lower data points): each data point comes from 1000 single-shot read-out repetitions. The fit, which includes the detailed hyperfine level structure, yields a visibility of 78±8%, where a maximum of 84% can be expected. The upper data points show the measurement outcome after projection into m_s=0 by selecting only readout events with photons detected within the first 400 ns. All errors and error bars, 2 s.e. (e) Quantum jumps in the fluorescence time trace during continuous spin readout. The durations of the dark periods depend on the microwave Rabi frequency. The dark gray data indicates the counts per 5 μs readout bin, and the deduced spin state is shown in light gray. Reprinted by permission from Macmillan Publishers Ltd (Robledo *et al.*, 2011), http://dx.doi.org/10.1038/nature10401.

increase, but also, potentially, the strong-coupling regime between single spins and photons can be realized. Such advances will enable solid-state cavity quantum electrodynamics experiments in a new regime, where remote entangled states can be prepared on demand, giving us new tools for exploring both fundamental and applied quantum mechanics on large scales.

8.8 Sources of further information and advice

During the preparation of this chapter, there were reports of the experimental realization of entanglement between two NV centers at room temperature and in a low-temperature regime. We ask the reader to refer the following papers for details: Bernien *et al.* (2013), Dolde *et al.* (2013).

8.9 Acknowledgments

The authors would like to acknowledge helpful discussions with Emre Togan, Yiwen Chu, Lilian Childress, Mikhail Lukin, Andrew Daley and Daniel Boyanovsky. This work was supported in part by the National Science Foundation (Award No. DMR-0847195 and PHY-100534) and the Alfred P. Sloan Foundation.

8.10 References

Acosta, V. M., Jarmola, A., Bauch, E. and Budker, D. (2010). Optical properties of the nitrogen–vacancy singlet levels in diamond. *Phys. Rev. B*, 82, 201202.

Balasubramanian, G., Neumann, P., Twitchen, D., Markham, M., Kolesov, R., *et al.* (2009). Ultralong spin coherence time in isotopically engineered diamond. *Nature Mater.*, 8, 383.

Barrett, S. D. and Kok, P. (2005). Efficient high-fidelity quantum computation using matter qubits and linear optics. *Phys. Rev. A*, 71, 060310.

Batalov, A., Jacques, V., Kaiser, F., Siyushev, P., Neumann, P., *et al.* (2009). Low temperature studies of the excited-state structure of negatively charged nitrogen–vacancy color centers in diamond. *Phys. Rev. Lett.*, 102, 195506.

Bernien, H., Childress, L., Robledo, L., Markham, M., Twitchen, D. and Hanson, R. (2012). Two-photon quantum interference from separate nitrogen vacancy centers in diamond. *Phys. Rev. Lett.*, 108, 043604.

Bernien, H., Hensen, B., Pfaff, W., Koolstra, G., Blok, M. S., *et al.* (2013). Heralded entanglement between solid-state qubits separated by three metres. *Nature*, 497, 86–90.

Boyanovsky, D. (2013). Coherence and decoherence in photon–spin-qubit entanglement. *Phys. Rev. A*, 87, 033815.

Briegel, H. J., Dur, W., Cirac, J. I. and Zoller, P. (1998). Quantum repeaters: The role of imperfect local operations in quantum communication. *Phys. Rev. Lett.*, 81, 5932.

Cabrillo, C., Cirac, J. I., Garcia-Fernandez, P. and Zoller, P. (1999). Creation of entangled states of distant atoms by interference. *Phys. Rev. A*, 59, 1025.

Childress, L., Dutt, M. V. G., Taylor, J. M., Zibrov, A. S., Jelezko, F., *et al.* (2006a). Coherent dynamics of coupled electron and nuclear spin qubits in diamond. *Science*, 314, 281.

Childress, L., Taylor, J. M., Sørensen, A. S. and Lukin, M. D. (2006b). Fault-tolerant quantum communication based on solid-state photon emitters. *Phys. Rev. Lett.*, 96, 070504.

Cirac, J. I., Zoller, P., Mabuchi, H. and Kimble, H. J. (1997). Quantum state transfer and entanglement distribution among distant nodes in a quantum network. *Phys. Rev. Lett.*, 78, 3221.

Doherty, M. W., Manson, N. B., Delaney, P., Jelezko, F., Wrachtrup, J. and Hollenberg, L. C. L. (2013). The nitrogen–vacancy colour centre in diamond. *Phys. Rep.*, 528, 1–45.

Dolde, F., Jakobi, I., Naydenov, B., Zhao, N., Pezzagna, S., *et al.* (2013). Room-temperature entanglement between single defect spins in diamond. *Nature Phys.*, 9, 139–143.

Duan, L. M. and Monroe, C. (2010). Colloquium: Quantum networks with trapped ions. *Rev. Mod. Phys.*, 82, 1209–1224.

Duan, L. M. and Raussendorf, R. (2005). Efficient quantum computation with probabilistic quantum gates. *Phys. Rev. Lett.*, 95, 080503.

Duan, L. M., Lukin, M. D., Cirac, J. I. and Zoller, P. (2001). Long-distance quantum communication with atomic ensembles and linear optics. *Nature*, 414, 413.

Dur, W., Briegel, H. J., Cirac, J. I. and Zoller, P. (1999). Quantum repeaters based on entanglement purification. *Phys. Rev. A.*, 59, 169.

Dutt, M. V. G., Childress, L., Jiang, L., Togan, E., Maze, J., *et al.* (2007). Quantum register based on individual electronic and nuclear spin qubits in diamond. *Science*, 316, 1312.

Gaebel, T., Domhan, M., Wittmann, C., Popa, I., Jelezko, F., *et al.* (2006). Photochromism in single nitrogen–vacancy defect in diamond. *Appl. Phys. B*, 82, 243–246.

Gottesman, D. and Chuang, I. L. (2006). Demonstrating the viability of universal quantum computation using teleportation and single-qubit operations. *Nature*, 402, 390.

Grinolds, M., Hong, S., Maletinsky, P., Luan, L., Lukin, M., *et al.* (2013). Nanoscale magnetic imaging of a single electron spin under ambient conditions.

Hadden, J. P. (2010). Strongly enhanced photon collection from diamond defect centers under microfabricated integrated solid immersion lenses. *Appl. Phys. Lett.*, 97, 241901.

Hein, M., Dür, W., Eisert, J., Raussendorf, R., Van Den Nest M. and Briegel, H.-J. (2006). Entanglement in graph states and its applications. Preprint arXiv:quant-ph/0602096. Presented at 173rd International School of Physics "Ennco Ferrni", Quantum Computers, Algorithms and Chaos, Varenna, Italy, 5–15 July, 2005.

Jelezko, F. and Wrachtrup, J. (2004). Read-out of single spins by optical spectroscopy. *J. Phys.: Condens. Matter*, 16, R1089.

Jiang, L., Taylor, J. M., Sørensen, A. S. and Lukin, M. D. (2007). Distributed quantum computation based on small quantum registers. *Phys. Rev. A*, 76, 062323.

Maze, J. R., Gali, A., Togan, E., Chu, Y., Trifonov, A., *et al.* (2011). Properties of nitrogen–vacancy centers in diamond: the group theoretic approach. *New J. Phys.*, 13, 025025.

Raussendorf, R. and Briegel, H. J. (2001). A one-way quantum computer. *Phys. Rev. Lett.*, 86, 5188.

Robledo, L., Childress, L., Bernien, H., Hensen, B., Alkemade, P. F. A. and Hanson, R. (2011). High-fidelity projective read-out of a solid-state spin quantum register. *Nature*, 477, 574–578.

Scully, M. O. and Zubairy, M. S. (1997). *Quantum Optics*, Cambridge University Press.

Sipahigil, A., Goldman, M. L., Togan, E., Chu, Y., Markham, M., *et al.* (2012). Quantum interference of single photons from remote nitrogen–vacancy centers in diamond. *Phys. Rev. Lett.*, 108, 143601.

Takahashi, S., Hanson, R., van Tol, J., Sherwin, M. S. and Awschalom, D. D. (2008). Quenching spin decoherence in diamond through spin bath polarization. *Phys. Rev. Lett.*, 101, 047601.

Tamarat, P., Manson, N. B., Harrison, J. P., Mcmurtrie, R. L., Nizovtsev, A., *et al.* (2008). Spin-flip and spin-conserving optical transitions of the nitrogen–vacancy centre in diamond. *New J. Phys.*, 10, 045004.

Togan, E., Chu, Y., Trifonov, A., Jiang, L., Maze, J., *et al.* (2010). Quantum entanglement between a single photon and a solid-state spin qubit. *Nature*, 466, 730.

van Enk, S. J., Cirac, J. I. and Zoller, P. (1998). Photonic channels for quantum communication. *Science*, 279, 205–208.

Yurke, B., McCall, S. L. and Klauder, J. R. (1986). SU(2) and SU(1,1) interferometers. *Phys. Rev. A*, 33, 4033–4054.

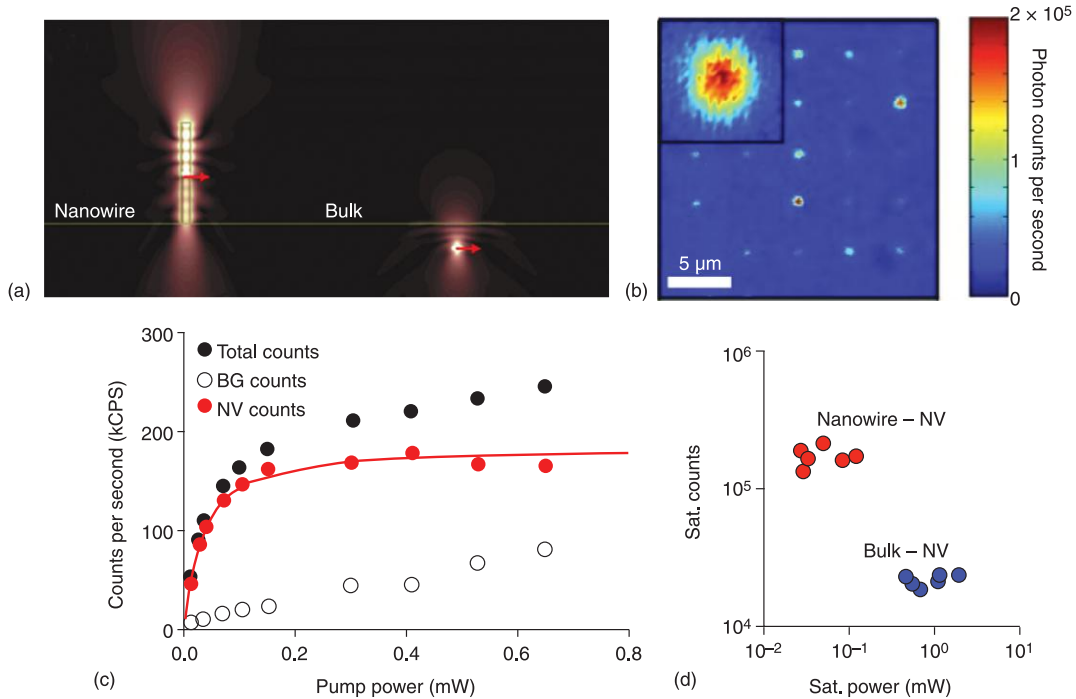

Plate I (Chapter 5) (a) Electric-field profiles of an NV center in the bulk and in a diamond nanowire.[38] (b) Confocal scan image of an array of nanowires fabricated in type Ib diamond, showing that many of them contain NV fluorescence. (c) Saturation curve for a nanowire device. The measured count rates, background and their difference are plotted in black, white and red, respectively. The fit to the saturation model is plotted with a solid line. (d) Comparison of saturation intensity and power for single-NV-containing devices in the bulk and in nanowires, showing an order of magnitude improvement in both saturation count rate and power for the diamond nanowire.[24]

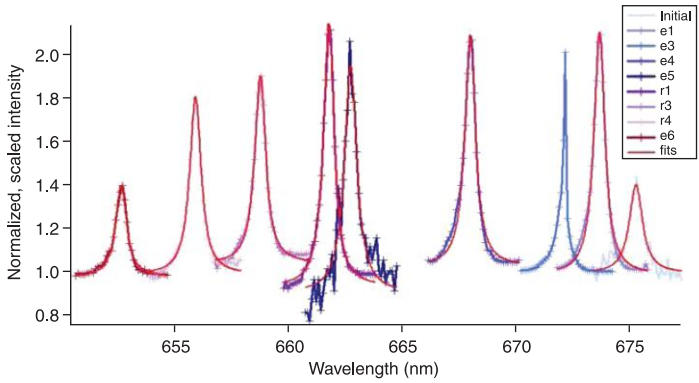

Plate II (Chapter 5) Controlled blue-tuning of a cavity mode via oxygen etching, shown over eight etching steps: 'e' refers to etching in an oxygen plasma etcher, and 'r' to etch steps performed by annealing the samples in an oxygen atmosphere in a rapid thermal processor. The etch times were of differing lengths. An overall tuning range of ~23 nm was observed in several devices.[49] Reprinted (adapted) with permission from Hausmann *et al.*[49] Copyright 2013 American Chemical Society.

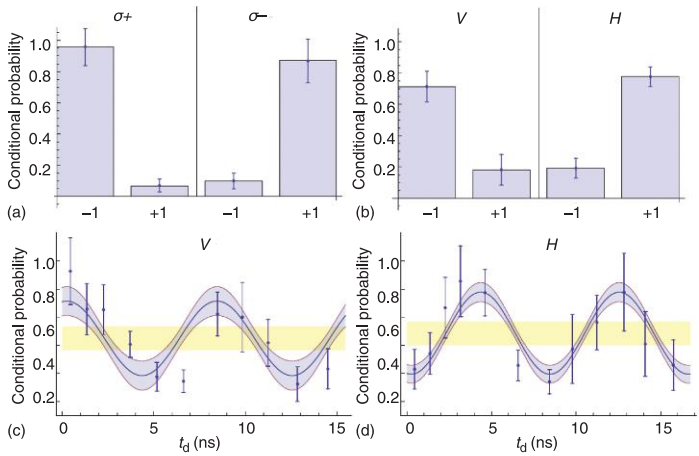

Plate III (Chapter 8) (a) Conditional probability of measuring |±1› after the detection of a σ+ or σ– photon. (b) Conditional probability of measuring |±› after the detection of an *H* or *V* photon, extracted from a fit to the data shown in (c) and (d). (c), (d) Measured conditional probability of finding the electronic spin in the state |*M*› after detection of a *V* (c) or *H* (d) photon at time t_d. The blue shaded region is the 68% confidence interval for the fit (solid line) to the time-binned data. The error bars on the data points show ±1 s.d. Combined with the data shown in (a), the oscillations with amplitude outside the yellow regions result in fidelities greater than 0.5. The visibilities of the measured oscillations are 0.59±0.18 (c) and 0.60±0.11 (d). Reprinted by permission from Macmillan Publishers Ltd (Togan *et al.*, 2010), http://dx.doi.org/10.1038/nature09256.

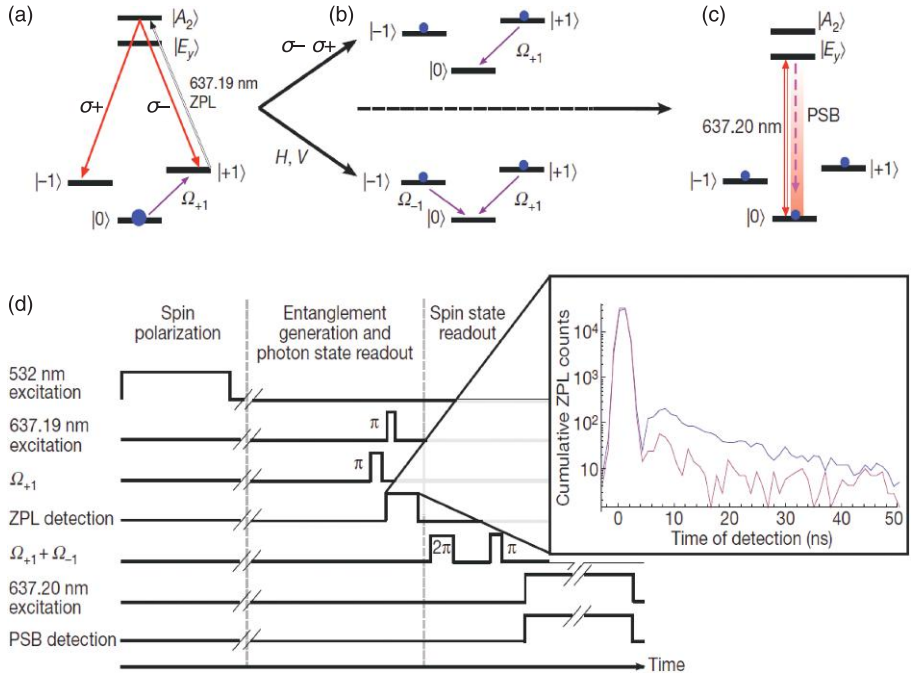

Plate IV (Chapter 8) Experimental procedure for entanglement generation. (a) After spin polarization into |0›, population is transferred to |1› by a microwave π-pulse (Ω_{+1}). The NV center is excited to $|A_2\rangle$ with a 637.19 nm π-pulse and the ZPL emission is collected. (b) If a + or – photon is detected, the population in |+1› or |–1› is transferred to |0›. If an |*H*› or |*V*› photon is detected, a τ–2π–τ echo sequence is applied with Ω_{+1} and Ω_{-1}, followed by a π-pulse which transfers the population in |*M*› to |0›. (c) The population in |0› is measured using the 637.20 nm optical-readout transition. (d) Pulse sequence for the case where an |*H*› or |*V*› ZPL photon is detected (time axis not to scale). If an s6 photon is detected instead, only a π-pulse on either Ω_{+1} or Ω_{-1} is used for spin readout. Inset, detection time for ZPL channel photons, showing reflection from diamond surface and subsequent NV emission (blue) and background counts (purple). Reprinted by permission from Macmillan Publishers Ltd (Togan *et al.*, 2010), http://dx.doi.org/10.1038/nature09256.

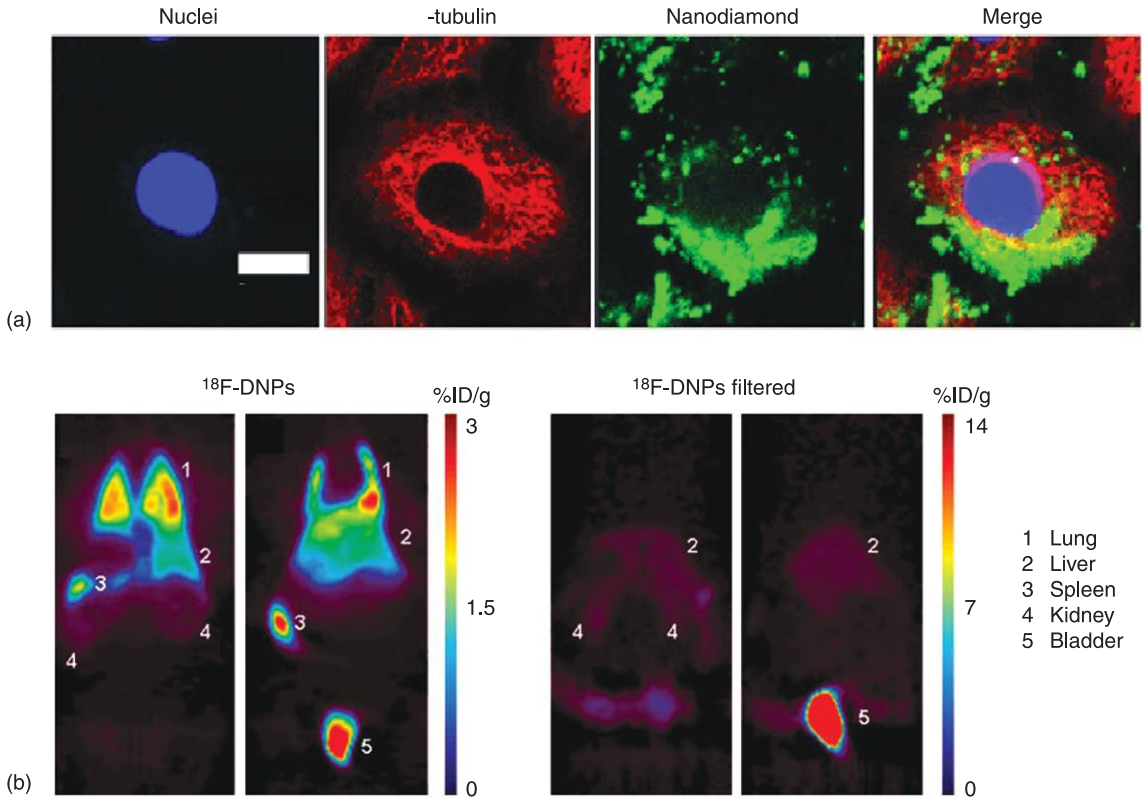

Plate V (Chapter 9) (a) Confocal microscopy of carboxylated nanodiamonds in A549 cells. The nuclei were stained with Hoechst 33258, and β-tubulin stained with Cy3-labeled anti-β-tubulin. Reproduced from Liu *et al.* (2007). (b) PET images of mice injected with ^{18}F-labeled nanodiamonds (DNPs). Reprinted with permission from Rojas *et al.* (2011). Copyright 2011, American Chemical Society.

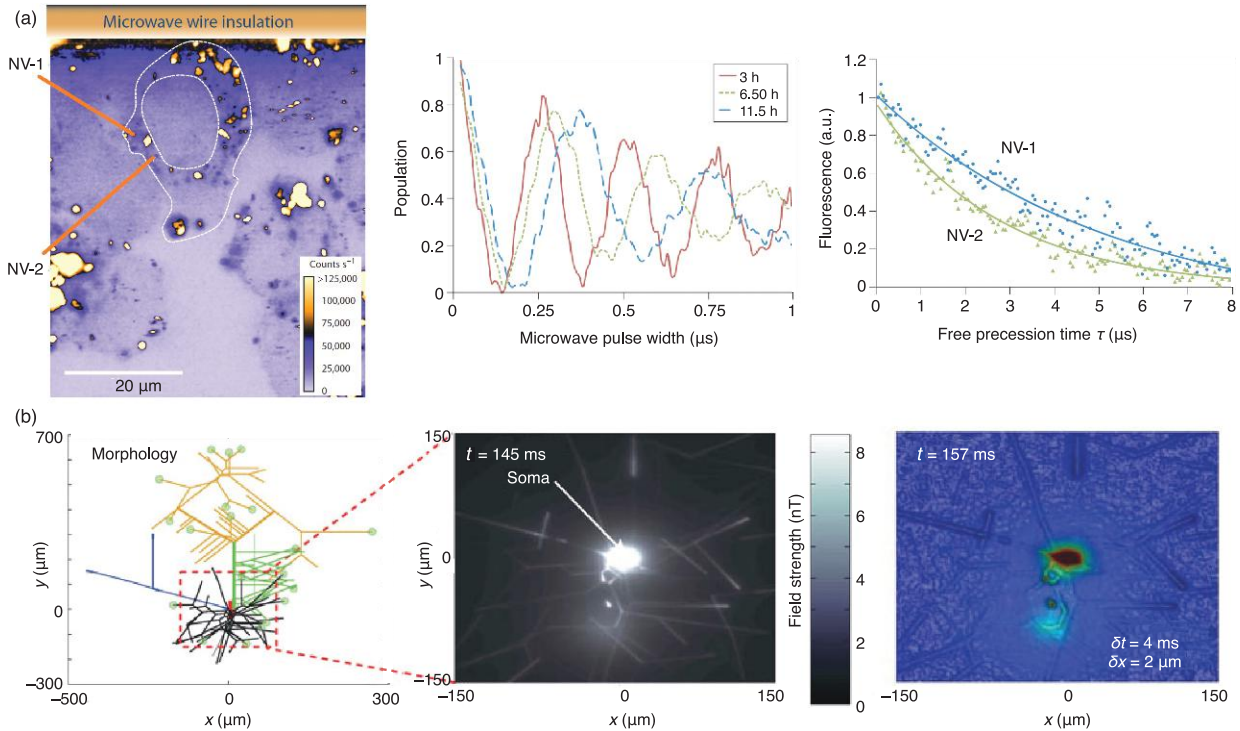

Plate VI (Chapter 9) Nanoscale biomagnetometry of living cells. (a) Quantum measurements on single spins in HeLa cells. Rabi oscillations and Hahn-echo measurements were performed on single NV centers in endocytosed nanodiamonds. Adapted by permission from Macmillan Publishers Ltd, *Nature Nanotechnology* (McGuinness *et al.*, 2011), copyright 2011. (b) Morphology of a neuron with the magnetic field at 100 nm distance from the cell membrane during action potential generation, and a simulated image of NV fluorescence captured by a CCD camera. Adapted by permission from Macmillan Publishers Ltd, *Scientific Reports* (Hall *et al.*, 2012), copyright 2012.

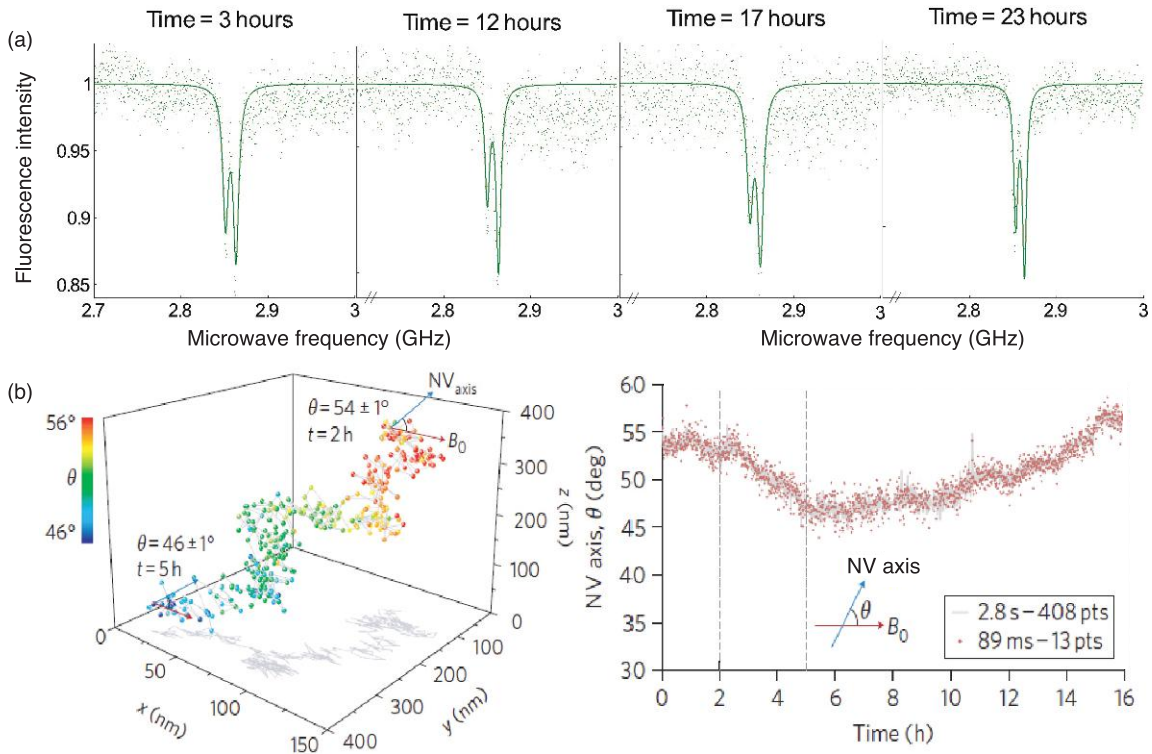

Plate VII (Chapter 9) (a) Microwave frequency identification of nanodiamonds. The ODMR spectrum from a single nanodiamond over 23 h as it is tracked inside a HeLa cell. (b) Orientation tracking of a fluorescent nanodiamond inside a HeLa cell, giving the nanodiamond position and orientation to within one-degree accuracy in under 100 ms. Reprinted by permission from Macmillan Publishers Ltd, *Nature Nanotechnology* (McGuinness *et al.*, 2011), copyright 2011.

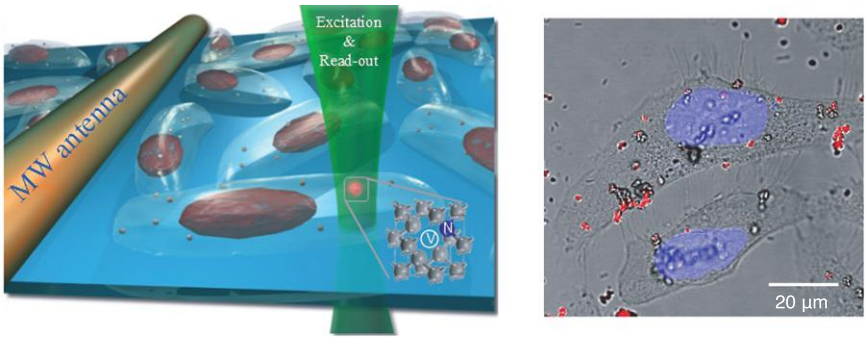

(a) (b)

Plate VIII (Chapter 9) Live-cell imaging and quantum measurements with nanodiamonds in cells. (a) Schematic of the experimental setup, with a microwave wire for spin manipulation, and confocal microscopy for imaging and spin state readout. (b) Combined bright-field and confocal image showing uptake of fluorescent nanodiamonds by HeLa cells. Adapted by permission from Macmillan Publishers Ltd, *Nature Nanotechnology* (McGuinness *et al.*, 2011), copyright 2011.

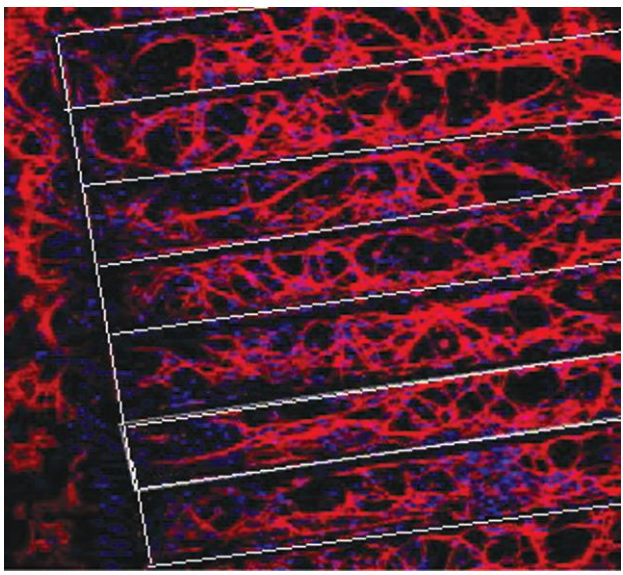

Plate IX (Chapter 12) Example of a successfully patterned neural network in diamond. A neural pattern on laser-patterned oxygen-terminated boron-doped microcrystalline diamond. The pattern was induced by laser-etching the diamond to expose the underlying silicon. The separation of channels is 100 μm. Reproduced with permission from May *et al.*[21]

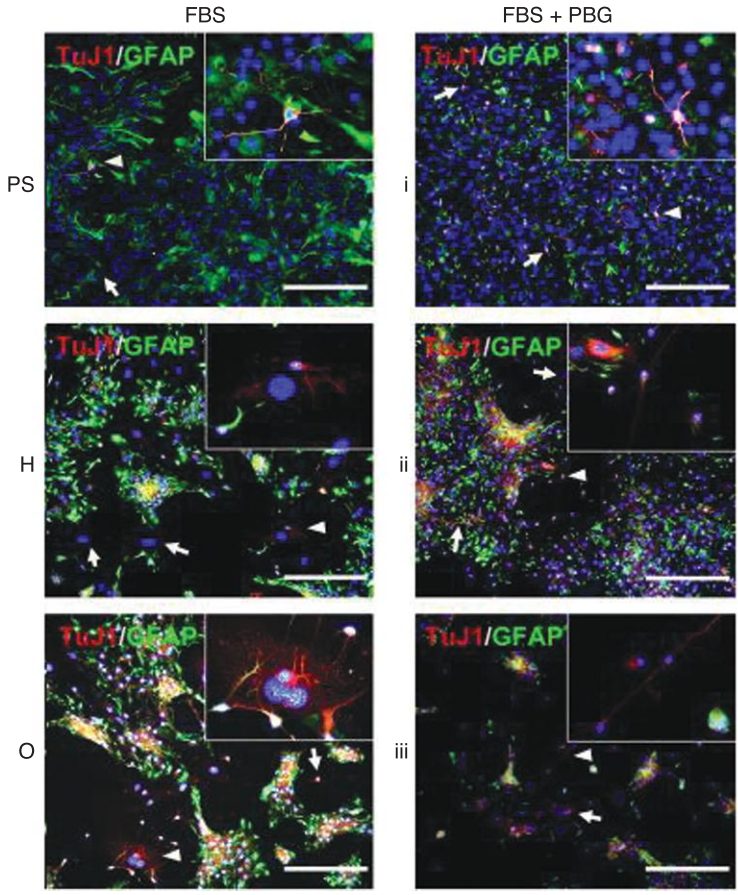

Plate X (Chapter 12) The differentiation of stem cells on diamond surfaces. Differentiation of neural stem cells (7 days) into neurons on polystyrene (PS), H-terminated ultrananocrystalline diamond (H) and O-terminated ultrananocrystalline diamond, with staining for neuron-specific βIII tubulin (TuJ1) and glial fibrillary acidic protein (GFAP) in a standard cell medium (FBS) and a cell medium supplemented with neuronal differentiating promoters (FBS and PBG), showing that both O- and H-terminated diamond provide a good substrate for neural cell activity compared with polystyrene, even in a medium without differentiation reagents. The insets are close-up images of the areas highlighted by arrows. The scale bar represents 200 μm.[12] Reproduced with permission from Chen *et al.*[12]

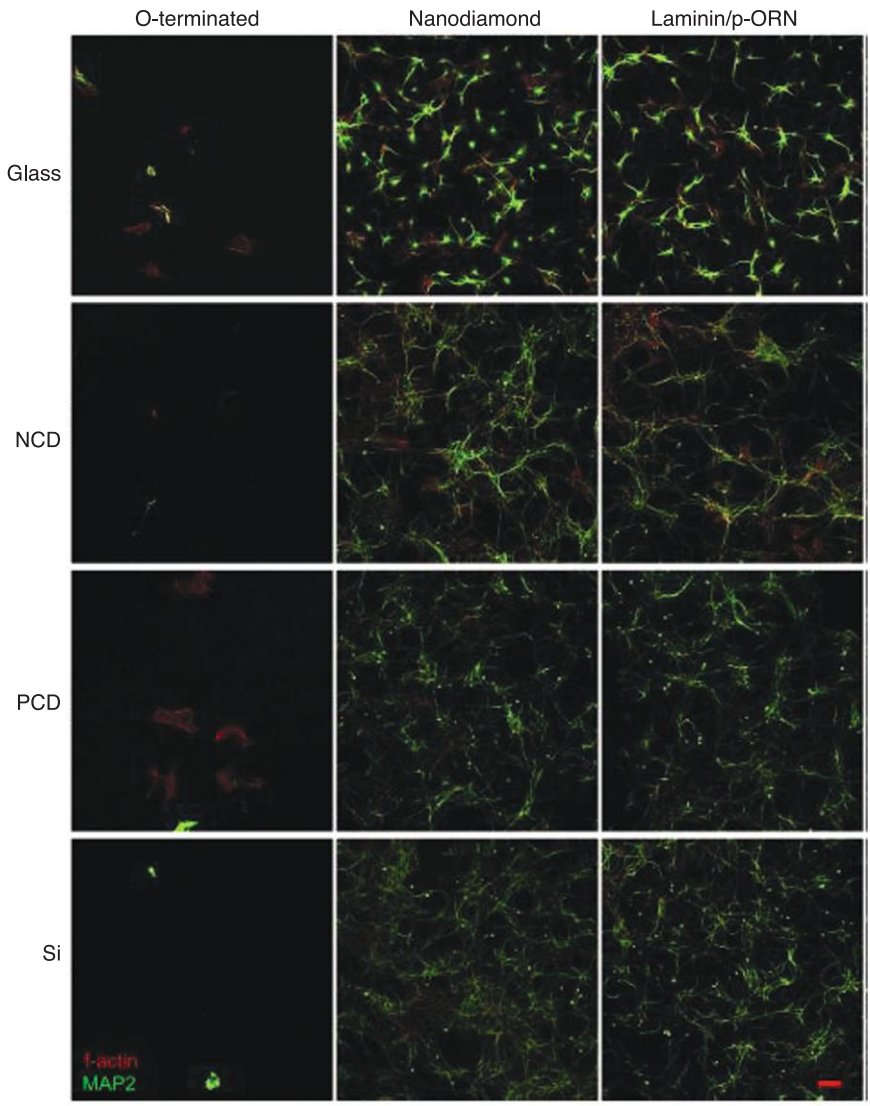

Plate XI (Chapter 12) Murine hippocampal neurons cultured on glass, nanocrystalline diamond, polycrystalline diamond and silicone substrates, before and after coating with nanodiamonds or adhesion promoters (laminin or polyornithine). It is clear that on each substrate, the nanodiamond coating promotes neuronal cell populations to an extent that is equivalent to or better than those coated with traditional neural cell adhesion molecules. The scale bar represents 50 μm. Reproduced with permission from Thalhammer *et al.*[51]

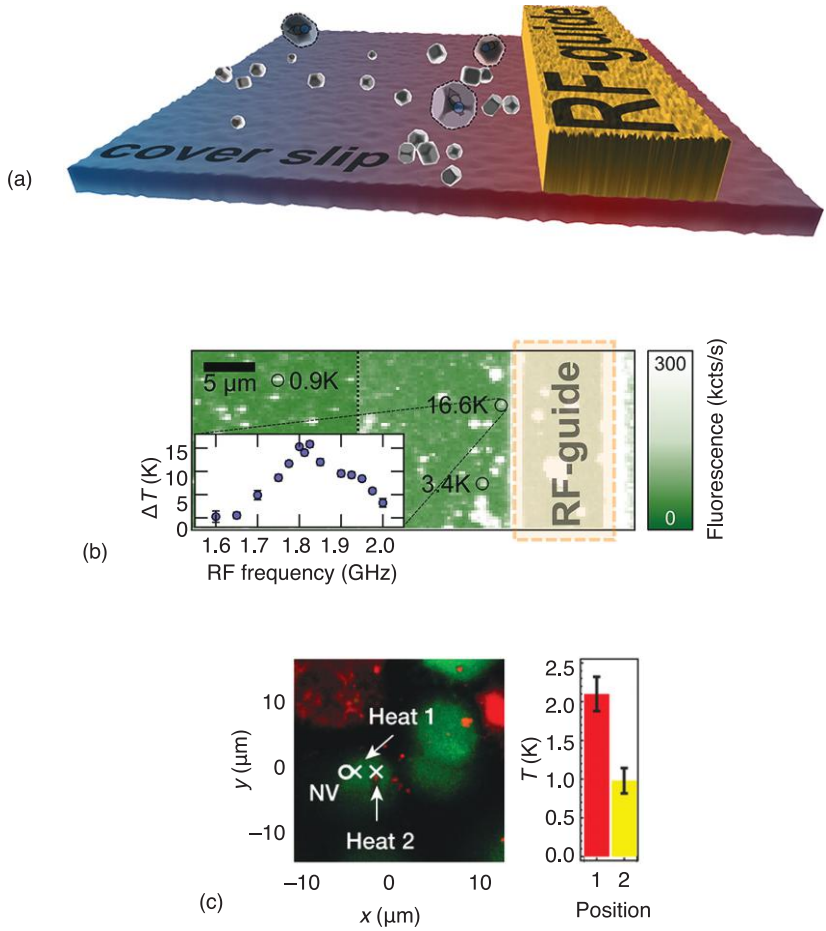

Plate XII (Chapter 13) Nanoscale temperature sensing using nanodiamonds. (a) Schematic illustration of nanodiamonds on a cover slip. (b) An actual example of temperature sensing using individual nanodiamonds induced by an RF guide. (c) Confocal fluorescence scans of individual stained cells with temperature readings. Reprinted from Neumann *et al.*[14] and Kucsko *et al.*[16]

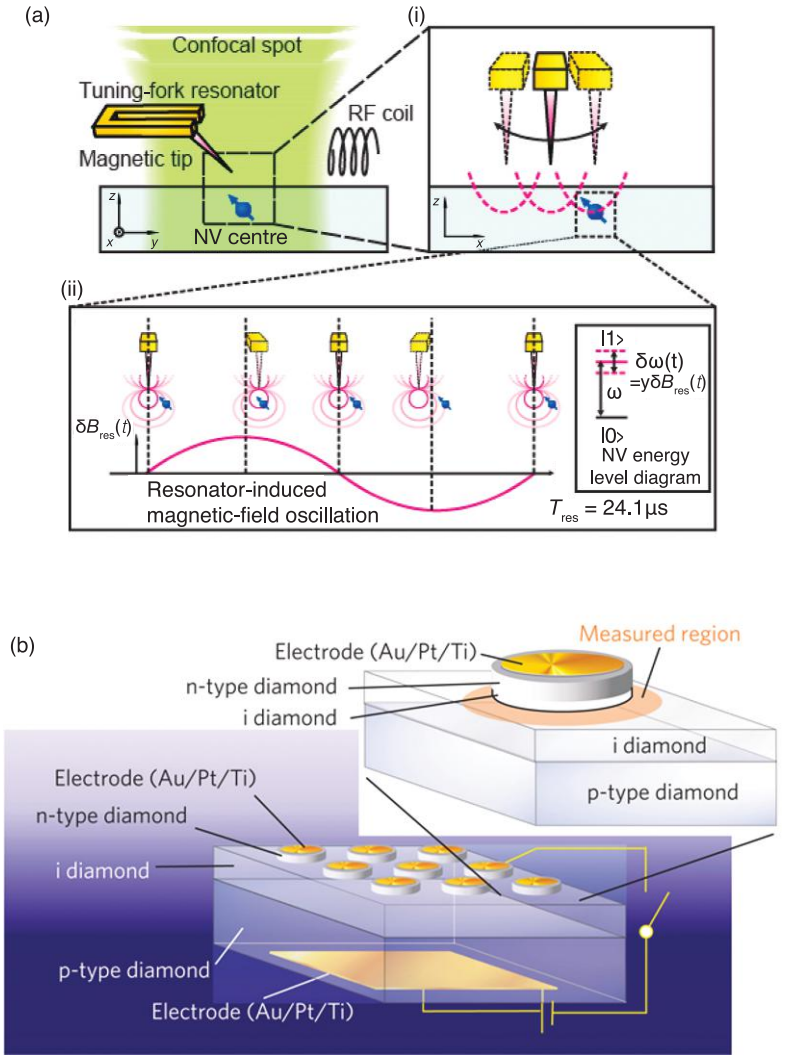

Plate XIII (Chapter 13) (a) Schematic illustration of a mechanical resonator coupled to an electron spin. A magnetic tip provides coupling between the tuning-fork resonator and the NV spin. Readout and addressing of the NV spin are provided through a confocal microscope and an RF coil. The local magnetic field at the position of the NV spin changes as a function of the resonator's motion, owing to the magnetic-field gradient around the tip.[21] (b) A pin junction used to excite an NV centre in diamond electrically. Phosphorus-doped n-type and intrinsic ('i') layers were independently grown by CVD on HPHT synthetic type IIb (001) p-type single-crystal diamond.[39]

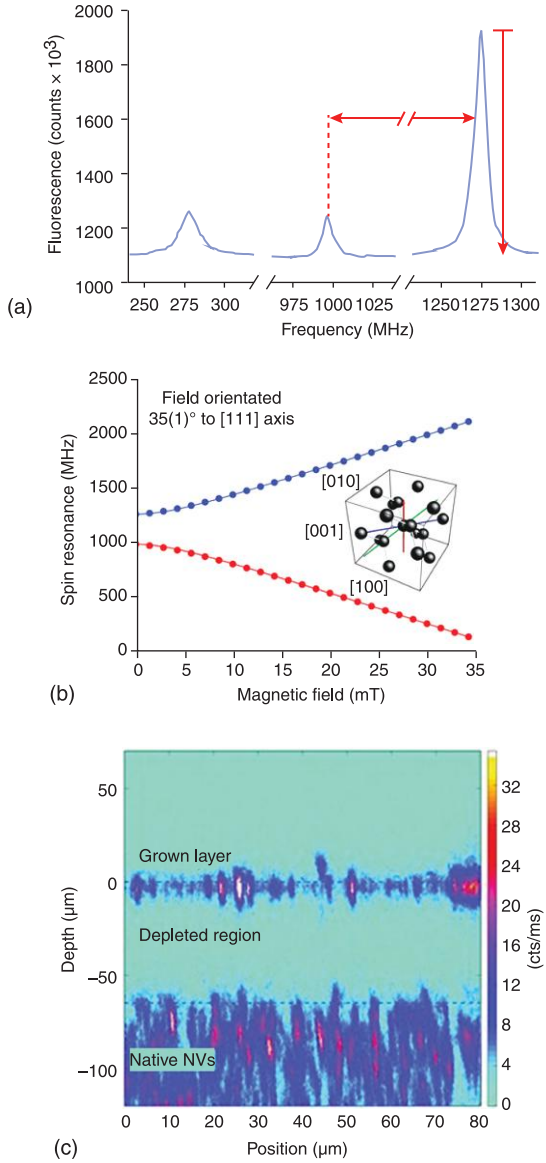

Plate XIV (Chapter 13) (a) Optically detected electron spin resonance at zero magnetic field. Resonant transitions are indicated by their splitting parameters. An exceptionally high optical spin signal contrast (~45%) of the D+E spin projection is observed. (b) Zeeman curve obtained with an aligned axial magnetic field oriented along the main symmetry axis of the defect. Inset, illustration of the crystallographic orientation of the defect. The green, blue and red arrows denote [111], [110] (the main axis of the defect) and [001] (C_{2v} symmetry axis), respectively. Reprinted from Lee *et al.*[60] (c) NV fluorescence as a function of depth showing NV centres at the surface of the grown layer, no NV centres in a depleted region due to exposure to a hydrogen plasma, and native NV centres below the depleted region in the diamond bulk.[61]

9

Quantum microscopy using nanodiamonds

L. P. McGUINNESS, University of Ulm, Germany

DOI: 10.1533/9780857096685.2.219

Abstract: The nitrogen–vacancy (NV) center offers unique capabilities for life science research, including the prospect of imaging weak magnetic fields with high spatial resolution under physiological conditions. The detection of such fields is a significant challenge in the life sciences, the solution to which would revolutionize cellular biology by allowing detection of important metabolic processes. Optical measurements of quantum coherent spins show that diamonds can be applied to magnetic imaging of cells. Additional quantum sensing technologies have also emerged, including nanothermometry, rotational tracking and enhanced identification of fluorescent nanoparticles, highlighting the role quantum sensors have to play in biology.

Key words: biophysics, quantum physics, optics, magnetometry, microscopy.

9.1 Introduction

Nanodiamonds are a highly photostable, extremely small source of fluorescence, providing many desirable applications for bioimaging. However, current microscopy techniques routinely demand that extra information be extracted from fluorophores, rather than using them simply as beacons, in particular by linking changes in fluorescence to metabolic events. This extension of fluorescence imaging to modalities other than pure spatial imaging has enabled real-time detection and monitoring of previously inaccessible but important cellular processes. For example, the dynamics of molecular motors (Forkey *et al.*, 2003), protein diffusion (Sieber, 2007) and changes in ion concentration (Miyawaki and Llopis, 1997) have all been elucidated by adding extra functionality to conventional fluorescence microscopy. Nanodiamonds have one property which sets them apart from conventional fluorophores, and that is the ability to obtain quantum information from inside living cells.

This unique property is due to the fluorescent nitrogen–vacancy (NV) defect, a common impurity in diamond. In addition to high brightness, small size and biocompatibility, which are advantageous for biological confocal microscopy, NV centers also have an unpaired electronic spin, which can be measured optically with a confocal microscope (Plate VIII) (see colour section between pages 218 and 219). This spin has observable quantum mechanical properties at room temperature, such as quantum coherence, endowing nanodiamonds with unique

© 2014 Elsevier Ltd

characteristics for live-cell imaging, and can be used for nanoscale magnetometry, possibly allowing nanometer-resolution MRI inside living cells.

Magnetic fields are important to various intracellular processes in the cell life cycle. For example, magnetic fields are associated with neural signaling (Peterka *et al.*, 2011) (action potentials), regulation of homeostasis (Hall *et al.*, 2010) (ion-channel activity) and cell death and metabolism (Riley, 1994) (free-radical production). It turns out that these fields may be detected by monitoring the effect of biological magnetic fields on the quantum coherence of an NV center. And, depending on the ultimate sensitivity, it may be possible to detect an NMR signal from a single protein or single nuclear spin. Thus it seems that at the scale of single cells or below, there are quantum signatures of life and death that may be measured by nanodiamonds. In this chapter, applications of fluorescent nanodiamonds (FNDs) for new types of quantum imaging are discussed.

9.2 Properties of nanodiamonds for bioimaging

Before considering the quantum properties of NV centers, it is worth noting that as fluorescent probes, nanodiamonds are already exceptional biomarkers. These characteristics are discussed below in terms of the following categories; size, chemistry, optical properties and quantum properties.

9.2.1 Size

Biolabel size is an important parameter when one is performing bioimaging, as bulky probes can adversely affect the function of target molecules through steric hindrance and excessive shear forces. For studies of fluorophores attached to molecules of interest, through the use of either genetically encoded fluorescent proteins or chemically specific binding, both the fluorophore size and the attachment site are critical: therefore a smaller biolabel is preferable. However, to date there are no consensus methods for labeling biomolecules with FNDs.

For intracellular studies of free nanoparticles, the capacity to reduce size is also beneficial, as smaller nanoparticles can more readily escape from membrane compartments into the cytoplasm, and the cellular response is highly size-dependent (Jiang *et al.*, 2008). In this respect, nanodiamond has an advantage over other inorganic fluorophores such as quantum dots (QDs) and metal nanoparticles, which typically have hydrodynamic diameters exceeding 10 nm. Fluorescent nanodiamonds only a few nanometers in dimensions have been manufactured (Chung *et al.*, 2007; Smith *et al.*, 2009; Tisler *et al.*, 2009; Bradac *et al.*, 2010; Vlasov *et al.*, 2009), making FNDs among the smallest biolabels currently available (Fig. 9.1(a)).

The concentration of fluorescent defects is reduced for smaller nanocrystals (Bradac *et al.*, 2009; Rabeau *et al.*, 2007), but by irradiating with high-energy electrons the fraction of defects can be increased (Tisler *et al.*, 2009; Chang *et al.*,

2008b). An additional issue associated with the use of nanodiamonds for bioimaging is their propensity to agglomerate in the cell medium, thereby increasing their effective size. Much work has been performed recently to overcome this problem, with convincing results (Tzeng *et al.*, 2011; Neugart *et al.*, 2007).

Finally, for super-resolution imaging, the resolution is ultimately limited by the fluorophore size. Nanodiamond fluorescence originates from point defects in the

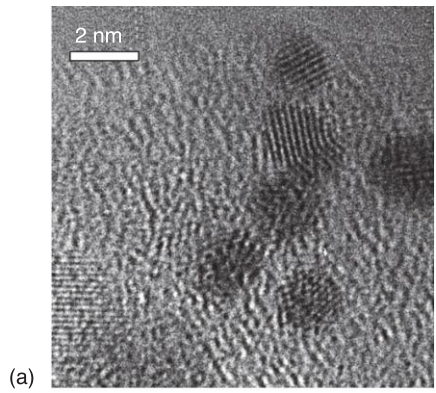

(a)

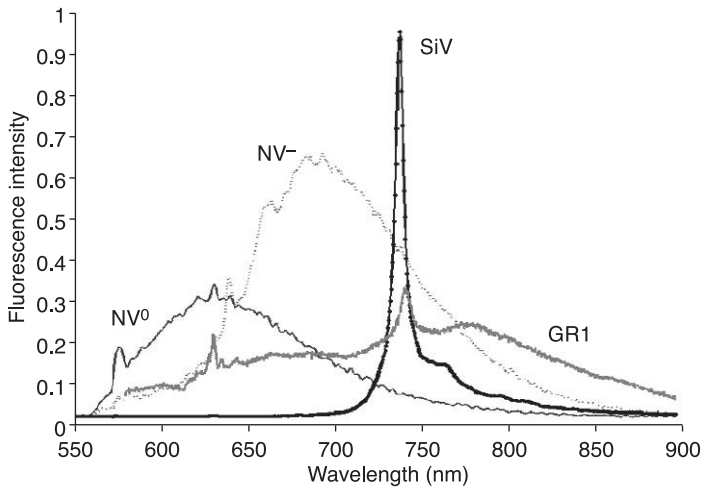

(b)

9.1 (a) Transmission electron microscope image of fluorescent ultrananocrystalline diamond film showing diamond grains of size 2–5 nm. Reprinted by permission (Vlasov *et al.*, 2009). Copyright 2009 Wiley-VCH Verlag GmbH & Co. KGaA, Weinheim. (b) Fluorescence spectra of common fluorescent diamond defects.(*Continued*)

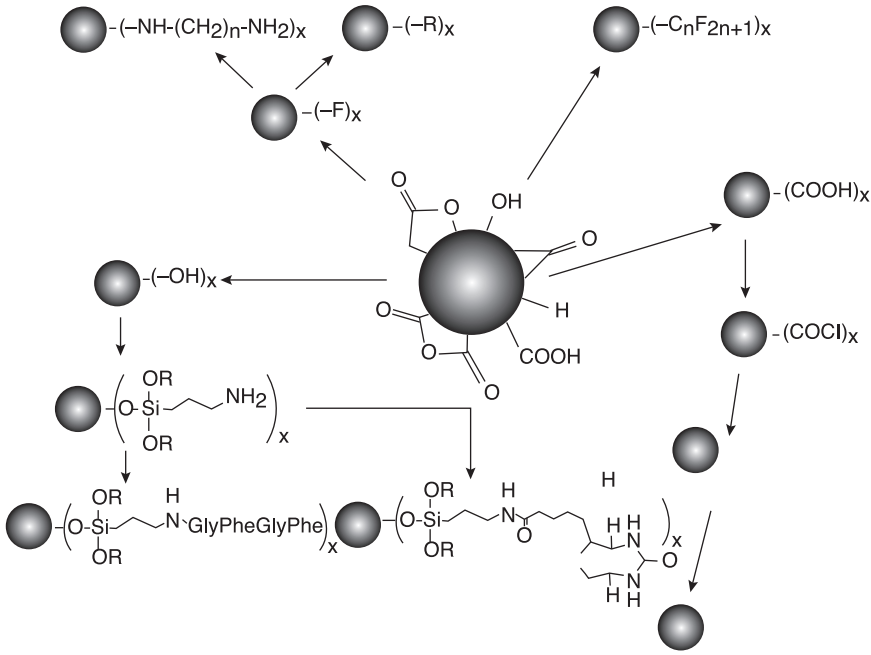

(c)

9.1 Continued (c) Biofunctionalization of nanodiamonds. Reprinted by permission (Krueger, 2008). Copyright © 2008 Wiley-VCH Verlag GmbH & Co. KGaA, Weinheim.

lattice. These atomically sized sources of light are amongst the smallest available sources of fluorescence for microscopy, leading to the best achievable resolutions to date (Han *et al.*, 2009, 2010; Maurer *et al.*, 2010; Rittweger *et al.*, 2009a,b; Tzeng *et al.*, 2011; Shin *et al.*, 2010).

9.2.2 Chemistry

The carbon chemistry present at the surface makes nanodiamond an ideal material for biological applications. Diamond is intrinsically biocompatible, and this low toxicity persists down to the nanoscale, as shown in several studies for crystals from 2 to 140 nm in size (Yu *et al.*, 2005; Chao *et al.*, 2007; Schrand *et al.*, 2007a,b; Liu *et al.*, 2007; Vaijayanthimala *et al.*, 2009). Diamond's biocompatibility compares well to metal-based QDs, which have health concerns due to the presence of heavy metals and are environmentally and biologically hazardous, making diamond nanoparticles suitable replacements for long term *in vivo* imaging studies (Kirchner *et al.*, 2005).

Added to this is diamond's chemical inertness, meaning FNDs remain stable in cells without being metabolized into substituents. After uptake, diamond

nanoparticles are typically located in cellular endosomes until cell death. 50 nm nanodiamonds have been shown to accumulate mainly in the liver and lungs of mice (Yuan *et al.*, 2009).

The nanodiamond surface can also be functionalized with specific chemical groups (Krueger, 2008) (Fig. 9.1(c)), allowing targeting to different cellular compartments (Mkandawire *et al.*, 2009) and processes (Vaijayanthimala *et al.*, 2009; Zhang *et al.*, 2009). Fluorophore-conjugated nanodiamond has been shown to travel through cellular compartments of varying pH without any effect on cell viability or loss of fluorescence over extended periods of time (Schrand *et al.*, 2011).

Nanodiamonds can be functionalized with imaging markers such as positron emission tomography labels, near-infrared-emitting dyes and other fluorescent agents by linking or adsorbing various labels (Schrand *et al.*, 2009; Mochalin and Gogotsi, 2009; Rojas *et al.*, 2011; Schrand *et al.*, 2011; Lien *et al.*, 2012), all of which provide enhanced *in vivo* imaging applications (Plate V(b)). In particular, nanodiamonds appear to be attractive carriers for drug delivery and MRI contrast agents. Covalent conjugation of Gd(III), for example, has allowed them to be used to improve the efficacy of MRI agents (Manus *et al.*, 2009; Chang *et al.*, 2008a).

9.2.3 Optical properties

The brightness of FND compares well to standard imaging dyes (Faklaris *et al.*, 2010), with the fluorescence from a single NV defect determined to be approximately a factor of 3 lower than that of commercial QDs (Faklaris *et al.*, 2009a). However, nanodiamonds have the added advantage that they may contain several defects, thus outperforming even QDs for brightness. For the smallest nanoparticles containing just a single optical center, the intensity is sufficient to perform single-molecule spectroscopy in living cells (McGuinness *et al.*, 2011) owing to the high fluorescence quantum yield of many defects. However, the excitation cross section is low compared with QDs and other dyes, so higher excitation power is required.

Another major advantage over organic fluorophores and QDs is the outstanding photostability of FND, which is due to chemical isolation of defects from their surroundings by the diamond lattice (Neugart *et al.*, 2007; Faklaris *et al.*, 2009a; Yu *et al.*, 2005). Our group has studied single defects in the laboratory for months under saturating illumination and observed no change in fluorescence rate. However, this is not universally the case, as photoblinking and irreversible bleaching of fluorescence from individual emitters has also been observed (Bradac *et al.*, 2010), and two-photon ionization can lower the fluorescence intensity (Chapman and Plakhotnik, 2012).

Fluorescence intermittency can be attributed to impurities in the diamond, which lead to spectral diffusion and photochromism – conversion of a defect to a

different charge state, resulting in a center with different fluorescence properties (Gaebel *et al.*, 2006; Waldherr *et al.*, 2011; Rondin *et al.*, 2010). Or it may be due to the surface, which provides energy traps that drastically modify fluorescence; this is particularly exacerbated as the nanodiamond size is reduced (Sun *et al.*, 2006; Cao *et al.*, 2007; Tisler *et al.*, 2009; Dréau *et al.*, 2011). The surface termination has also been shown to affect fluorescence (Hauf *et al.*, 2011; Grotz *et al.*, 2012).

Diamond defect centers span a range of wavelengths from ultraviolet to infrared (Zaitsev, 2001; Waldermann *et al.*, 2007). Among the most common are the isolated vacancy (741–742 nm), NV^0 (550–650 nm), NV^- (650–800 nm), the silicon–vacancy center (738 nm) and the H3 center (532 nm) (see Fig. 9.1(b)). The near-infrared wavelength of many optical centers is ideal for deep tissue imaging in the biological transparency window of 700–900 nm (Lim *et al.*, 2003). The long wavelength and fluorescence lifetime of many defects also allow separation from cell autofluorescence either spectrally with optical filters or temporally via lifetime imaging (Faklaris *et al.*, 2008; Weng *et al.*, 2009).

FNDs also display a nonlinear optical response (Han *et al.*, 2010; Chapman and Plakhotnik, 2012), which can be used for performing sub-diffraction-limited imaging and reducing cell autofluorescence. Although the absorption cross section is low, several studies have shown applications for two-photon microscopy (Chang *et al.*, 2008b; Hui *et al.*, 2010).

9.2.4 Quantum properties

The long-lived spin coherence of the NV center in diamond provides unique bioimaging applications. The coherence of the spin state is affected by temperature, stress, nanodiamond orientation, electric fields and magnetic fields – providing a unique *in situ* sensor of these physical parameters at the nanoscale and under physiological conditions, with unparalleled sensitivity.

The reader is referred to earlier chapters for a more in-depth background on the quantum properties of the NV center. To summarize, fluorescent nanodiamonds combine the advantages of semiconductor quantum dots (small size, high photostability and bright fluorescence) with biocompatibility, nontoxicity, rich surface chemistry and the ability to obtain quantum information in the cell environment, which means that they have the potential to revolutionize bioimaging applications.

9.3 Conventional microscopy with nanodiamonds

Amongst their numerous optical characteristics, FNDs are particularly well suited to long-term optical tracking. Therefore it is no surprise that a large number of investigations have already been performed on cell uptake and trafficking mechanisms with FNDs (Plate V(a)). The literature includes demonstrations that

FNDs are taken into cells by macropinocytosis and clathrin-mediated endocytosis (Liu *et al.*, 2009; Faklaris *et al.*, 2009b), confirmation of receptor-mediated uptake of transferrin-coated FNDs (Weng *et al.*, 2009), and colocalization studies with endosomes, indicating that FNDs are processed via the endocytic pathway and some small nanoparticles are able to escape into the cytoplasm after uptake (Faklaris *et al.*, 2008, 2009b). One particular study (Mohan *et al.*, 2010a) showed that nematodes injected with fluorescent nanodiamonds are able to produce viable progeny that inherit the nanoparticles.

Other techniques, such as Förster resonant energy transfer (FRET) and precise localization, also benefit from the good photostability of NVs, which allows virtually unlimited interrogation times. Tisler *et al.* (2011) have demonstrated FRET between single NV centers in nanodiamonds and single organic quencher molecules at the surface. Other groups have also demonstrated FRET between FNDs and IRDye with efficiencies up to 30%, in addition to FCS studies (Mohan *et al.*, 2010b; Chen *et al.*, 2011).

FND's high brightness and long fluorescence wavelength (enabling separation from cell autofluorescence) also allow single-molecule studies to be performed, giving information on intracellular dynamics. Measurements of diffusion coefficients, for example, indicate if the particle is enclosed in an endosome or freely diffusing. Numerous single-particle studies have been performed, highlighting the favorable fluorescence properties of FND for bioimaging (Fu *et al.*, 2007; Faklaris *et al.*, 2008; Neugart *et al.*, 2007; Chang *et al.*, 2008b; Faklaris *et al.*, 2010; Zhang *et al.*, 2009).

In addition to fluorescence microscopy, scattered Raman-shifted light can also be detected, allowing confocal Raman mapping of nanodiamonds in human lung epithelial cells (Cheng *et al.*, 2007). The Raman signal complements optical imaging further by giving an indication of the nanodiamond surface chemistry, allowing additional information on the intracellular environment to be obtained (Perevedentseva *et al.*, 2007). Back-scattered Rayleigh light can also be used as a detection mode owing to the high refractive index of diamond. This technique is applicable to nanoparticles greater than 30 nm in diameter (Colpin *et al.*, 2006) and has been applied to imaging nanocrystals in cells (Smith *et al.*, 2007). Cathodoluminescence provides yet another contrast mode when used in combination with electron microscopy, and has been shown to produce sub-100 nm imaging resolution (Glenn *et al.*, 2012).

Recent work demonstrating novel 'nanoscopy' techniques with optical microscopes such as stimulated emission depletion (STED) (Rittweger *et al.*, 2009a,b; Han *et al.*, 2009) and the related RESOLFT imaging (Maurer *et al.*, 2010) depend upon the good photostability of the NV defect, in particular under saturating illumination. In particular, a recent demonstration of STED in live cells highlights the potential of nanodiamonds for live-cell nanoscopy (Tzeng *et al.*, 2011).

Two-photon microscopy of FND has also been investigated by several groups. Hui *et al.* (2010) have performed two-photon fluorescence correlation spectroscopy

and shown that lipid-encapsulated nanodiamonds escape to the cytoplasm more easily and have a higher diffusion coefficient. The group of H. C. Chang have, in addition to numerous two-photon microscopy studies, demonstrated mass production of FNDs for bioimaging (Chang *et al.*, 2008b; Fu *et al.*, 2007; Wee *et al.*, 2007).

9.4 Quantum microscopy with nanodiamonds I: magnetometry

Despite the potential benefits, and although there has already been extensive work on introducing nanodiamonds into cells as fluorescent markers, *in situ* monitoring of the NV quantum properties has not been widely performed (McGuinness *et al.*, 2011; Kucsko *et al.*, 2013). The ability to monitor the quantum state of fluorescent systems provides additional information about measurable properties intrinsic to the probe or local environment and may enable new quantum sensing technologies in biology; therefore the incentives are enormous.

Many groups have already explored the magnetic sensitivity of NV centers in the 'dry' environment of the physics laboratory, but one challenge to successful biomagnetometry involves being able to determine the NV quantum state in biological environments, and doing this whilst maintaining cell viability. This problem has two interlinked components, which are seemingly at odds with each other. On the one hand, quantum measurement of the NV center (as with most single qubits) requires a carefully controlled environment, whereby extraneous noise is minimized. Living cells, on the other hand, are chaotic and noisy (affecting both quantum coherence and quantum state determination), but they are also sensitive. In the following, these issues regarding quantum measurement in cells, in addition to recent experiments, and potential applications are discussed.

9.4.1 Quantum measurement in living cells

As noted, quantum measurements in living cells present particular challenges. Measurements on single quantum systems require a method to carefully control and read out the quantum state, a sufficient signal-to-noise ratio, and manageably low decoherence rates over the observation timescales. The optical measurements needed to read out a single NV spin require single-molecule spectroscopy to be performed in living cells, and in order to obtain a manageable signal-to-noise ratio, methods to reduce background fluorescence need to be implemented. Most commercial confocal systems do not have sufficient collection efficiency to observe single NV centers, requiring construction of a dedicated single-molecule setup with a high-NA objective. To reduce background fluorescence, high-quality bandpass filters and nonfluorescent cell medium or phosphate buffered saline are also required.

The NV spin state can be read out simply by monitoring the fluorescence intensity (Gruber *et al.*, 1997), allowing noninvasive observation with minimal effect on cell function. But in order to control the NV spin state at room temperature, resonant microwaves need to be applied. Cell viability studies with microwave radiation at the levels required for spin manipulation have shown no influence on cell viability (McGuinness *et al.*, 2011).

Low decoherence of the quantum system is also required to measure quantum coherence, and it also translates directly to magnetic sensitivity. NV centers in bulk diamond have long (millisecond) coherence times at room temperature. When compared with the quantum coherence commonly observed in biological systems, such as light-harvesting molecules with coherence times less than a nanosecond, this is extraordinary. Yet, the diamond crystal protects the NV center from much of the decoherence in biological environments. In nanodiamonds, however, coherence times are typically reduced for two reasons: a higher impurity content and closer proximity to the noisy diamond surface and external environment.

The high impurity content has been shown to be circumvented in one study (Jahnke *et al.*, 2012), yet even the reduced sensitivity of 'dirty' commercial nanodiamonds does not prohibit their use as quantum sensors. The diamond surface also contains defects and unpaired surface spins, which negatively impact the NV quantum coherence. But it is precisely effects at the surface and, more particularly, the external environment on the NV coherence that need to be exploited for biomagnetometry. For other quantum imaging applications such as rotational tracking, nanodiamonds with NV centers 10 nm or more from the surface can be employed, where the effect of surface spins is negligible. In the end, if suitable care is taken, with the right choice of materials and experimental setup, quantum coherence can be preserved and measured in living cells.

Biomagnetometry with NV centers involves a delicate balance between measuring the environment and maintaining coherence. Ideally, one would like to design a situation where the NV quantum coherence is affected only by the target molecule to be detected, whilst remaining isolated from all other biological noise. In practice, this is difficult to achieve. The challenges are then of (bio)chemistry, i.e., to exclude extraneous magnetic noise in the form of unpaired spins from the environment, and of quantum metrology, i.e., to use tailored sensing protocols to enhance the signal of interest whilst reducing sensitivity to background noise. In terms of the sensitivity required, as a general rule, NV sensors closer to the diamond surface are preferable, since the magnetic field from single external spins reduces as r^{-3}, where r is the distance from the spin. So in order to measure, for example, a single proton with a sensitivity threshold of 1 μT, a separation distance from the sensor of ~1 nm is required. These sensitivities have been demonstrated with sub-second integration times for well-isolated NV sensors deep within bulk diamond, indicating that if the

above challenges are overcome, quantum nanodiamond sensors have much to offer biology.

9.4.2 Nanobiomagnetometry

In biology, particularly at the cellular level, there is great motivation to develop sensors capable of detecting electromagnetic fields. The biochemical processes involved in neuronal networks (Peterka *et al.*, 2011), ion channel activity (Hall *et al.*, 2010) and embryological development (Funk *et al.*, 2009) are all fundamentally dependent on electromagnetic fields. Detecting these fields would provide a powerful avenue to visualizing and understanding the underlying events. The detection of intracellular free radicals is perhaps the most obvious application for diamond nanobiomagnetometry. These chemical species produce a magnetic field, and are generated by mitochondria during the oxidative burst of immune cells; they are an indicator of cell stress and death (Riley, 1994).

The fields produced by these processes, however, are extremely weak, requiring small standoff distances and sophisticated pulse sequences (Zhao *et al.*, 2011; Staudacher *et al.*, 2013; London *et al.*, 2013; Belthangady *et al.*, 2013) or, when applicable, driving of target spins resonantly (Mamin *et al.*, 2013; Perunicic *et al.*, 2013). Several proof-of-principle measurements have been performed, though. The techniques required for performing sensitive biomagnetometry have been performed in living cells, although without conclusive results as to detection of cellular processes (McGuinness *et al.*, 2011) (Plate VI(a)). Recently, several works have demonstrated the detection of external target spins with impressive resolution and sensitivity under ambient conditions. Using nanodiamonds, discrimination of solutions with high and low spin concentrations has been demonstrated with a sensitivity capable of detecting a thousand electron spins in a few seconds (McGuinness *et al.*, 2013). The presence of high-spin (Mn^{2+}) solution could be observed through changes in the T_2 time of the NV centers. The fluctuating magnetic field arising from spin-5/2 manganese ions disrupted the NV coherence, leading to reduced T_2 times. This work shows that it is feasible to detect localized changes in diffusing spins which may be associated with important biochemical processes in living cells, for instance the generation of free radicals. Additionally, changes in spin dynamics at the nanodiamond surface were detected, indicating the potential for detecting chemical reactions involving species linked to the diamond surface. Direct detection of biomolecules has also been achieved: two groups have shown sensitivity to a few molecules of the iron-containing metalloprotein ferritin, using either nanodiamonds (Ermakova *et al.*, 2013) or a microfluidic channel on bulk diamond (Ziem *et al.*, 2013).

A further demonstration of the applicability of nanodiamonds to bio-magnetometry has been done with the incorporation of nanodiamonds into lipid bilayers conjugated with high-spin gadolinium species (Kaufmann *et al.*, 2013). Measurements on the relaxation rates of NV spins inside the nanodiamonds

provided information on the nanoscale dynamics of lipid molecules surrounding the nanoparticles.

Although not performed with nanodiamonds, several other significant works have been published recently. Steinert *et al.* (2013) have performed several studies, including imaging of spin concentrations over wide areas using bulk diamond with shallow implanted nitrogen as a sensor. These studies monitored the T_1 time of the NV sensor in response to gadolinium spins in solution, in close analogy to T_1-weighted MRI contrast detection. Dipolar coupling between NV spins and the diffusing gadolinium spins at the NV Larmor frequency induced relaxation of the NV spin's polarization, which could be used as the contrast mode. Using this imaging technique, Steinert *et al.* successfully detected spin concentrations as low as 80 μM in 20 seconds, and were able to magnetically image gadolinium-labeled cells with 400 nm resolution.

Optical imaging of magnetotactic bacteria has also been performed (Le Sage *et al.*, 2013), demonstrating the advantages of NV-diamond readout over conventional magnetic imaging techniques. The magnetic field of magnetite nanoparticles within bacteria could be imaged, thus providing an avenue for exploring how magnetosomes form and orient within live bacteria, and determining how magnetotactic organisms navigate.

Mamin *et al*. (2012) used shallow implanted NV centers to detect electronic spins at the diamond surface. A prepared polymer containing 5% w/w DPPH was spin-coated onto the diamond surface and, when the target spins were driven resonantly, a change in the NV coherence was observed. All of this work was preceded by that of Grotz *et al.* (2011), who first showed detection of an unknown electronic spin on the surface of nanodiamonds functionalized with the free-radical molecule TEMPO.

The detection of neuron action potentials is also an area of active research in biomedical science. Current techniques exist but are limited in their sensitivity (Perron *et al.*, 2009), signal-to-noise ratio (Baker *et al.*, 2005; Homma *et al.*, 2009), spatial resolution (Qing *et al.*, 2010) or temporal resolution (Kralj *et al.*, 2012). Therefore, this challenge in biomagnetometry is another area in which the optical and magnetic properties of NVs could have an immediate impact. Magnetic detection of neuronal activity requires a sensor with micron spatial and millisecond temporal resolution in order to fully observe the pulse dynamics along different parts of the cell. The fields produced are on the order of a few nanotesla, so high magnetic sensitivity is also required. In fact the fields are too weak to be detected by a single NV center, and therefore using a high-density two-dimensional layer, which would allow wide areas containing several neurons to be imaged, has been proposed (Hall *et al.*, 2012; Pham *et al.*, 2011) (Plate VI(b)). These substrates would allow questions concerning interconnectivity and neural networking to be addressed, and initial work shows promising results.

In summary, there is no shortage of applications for detecting weak magnetic fields in biology, and the coming years promise many exciting advances.

9.5 Quantum microscopy with nanodiamonds II: rotational tracking, electrometry and thermometry

9.5.1 Microwave-frequency nanoparticle identification

Although disparate NV centers are indistinguishable based on their fluorescence spectrum, it is possible to distinguish them by applying microwaves and observing the fluorescence intensity. Under illuminating light, when an applied microwave field becomes resonant with an NV spin transition energy, the fluorescence intensity is reduced, an effect called optically detected magnetic resonance (ODMR). As a result, ODMR allows spectroscopy at microwave wavelengths with megahertz resolution, much narrower than the fluorescence spectrum of NVs, which extends over 200 nm. In the absence of an external magnetic field, strain in the nanodiamond lattice acts to modify the crystal field splitting and lift the degeneracy of the ±1 ground spin states. This means that individual NV centers have a unique ODMR spectrum depending on strain in the host nanodiamond, which can be used as an identifying fingerprint when no magnetic fields are present.

Importantly, for long-term studies, the same ODMR spectrum is obtained over long periods, and is unaffected by nanodiamond movement within the cells. This allows the optical emission of particular nanodiamonds to be located and tracked without continuous observation. For example, we have demonstrated the ability to relocate specific NV centers in living cells based on their spectral signature after performing confocal scans of several cells in different focal planes over several hours (McGuinness *et al.*, 2011).

The ability to distinguish nanodiamonds by this technique can be estimated by measuring the variability in the ODMR spectrum. Enriching the abundance of ^{13}C in the nanodiamonds to 5% increases the variety of nanodiamond spectra obtained, and we estimate the number of unique nanodiamonds that can be identified by this technique to be over 10^4.

Using microwave rather than optical spectroscopy to spectrally separate fluorophores allows much narrower spectral features to be identified, and thus more channels per given bandwidth. Although the visible spectrum spans 400 nm, spectral overlap of fluorescent emission means that multicolor microscopy is generally limited to 10 colors before crosstalk and bleed-through affect image quality. Each color also requires an additional fluorophore to be added to the specimen, which becomes technically challenging. Linear unmixing can be used to marginally improve spectral separation of fluorophores, but multiple excitation lasers and multiple emission filters are required. Our technique requires only one fluorophore (spectral variation is produced by the addition of a single atom or stress rather than another fluorescent molecule), allows unlimited timescales for tracking (organic fluorophores photobleach) and produces much greater spectral variety with only a single laser excitation wavelength. It should also be noted that

at cryogenic temperatures, resonant optical excitation can also be used to spectrally separate fluorophores.

9.5.2 Nanoparticle orientation tracking

The ability to monitor the orientation of small nanoparticles as they interact with cells is important for measuring drug uptake and efficacy, to better understand membrane nanomechanics, and to observe molecular motion in action. Here, a robust and precise method for orientation tracking of nanodiamonds in the intracellular medium is discussed.

The ODMR spectrum in an external magnetic field depends on both the strength and the orientation of the applied magnetic field. For a field aligned along the NV axis, the $m_s \pm 1$ levels split symmetrically around 2.87 GHz, and their separation gives an accurate measure of the field strength. For a misaligned field, in the weak-field limit ($B \leq 50$ G), the spin levels shift asymmetrically and the contrast is reduced (Epstein *et al.*, 2005). By measuring the ODMR spectrum, this gives a reliable, accurate and relatively easy method to determine the orientation of the nanoparticle with respect to an applied field.

Plate VII shows four-dimensional (spatial and orientation) tracking of a single nanodiamond inside a living cell, with 1° angular resolution in 89 ms. With improvements, the ODMR orientation tracking technique should be able to resolve nanodiamond orientations to within 1° over a 3 ms acquisition interval. Such time resolution is necessary for observing uptake and processing of molecules by cells, and would allow real-time rotation monitoring of trafficking inside cells over long timescales, an important goal in intracellular nanoparticle tracking. This compares well to the sensitivities obtained by reflection and fluorescence polarization microscopy and allows orders-of-magnitude longer tracking time than alternative orientation measurements based on organic molecules.

To further improve the ODMR tracking protocol, *a priori* information about the ODMR shape can be used to monitor fluorescence at the full width half maximum (FWHM) of the ODMR dip. As long as the nanodiamond does not rotate enough to shift the dip by more than the FHWM, the orientation can be measured accurately by relating the monitored fluorescence intensity to a position on the ODMR spectrum. For acquisition rates faster than the rotation rate, large angular changes could be followed by using a servo loop to continuously adjust the microwave frequency near the FWHM.

Finally, we should mention that we have only demonstrated determination of the azimuthal angle with respect to an external magnetic field using this technique. To measure the complete orientation (including the polar angle), more elaborate procedures are required. However, many biological processes are characterized by molecular rotation in a single plane (for example, rotation of the ATP synthase complex and the kinesin motor). Alignment of the external field with this plane should allow the full dynamics to be observed through monitoring only one angle.

Alignment of the NV axis with the plane of rotation, however, is more technically challenging.

9.5.3 Electric sensing

The fluorescence from defects in bulk diamond has also been shown to depend on the presence of electric fields (Dolde *et al.*, 2011; Grotz *et al.*, 2012; Mizuochi *et al.*, 2012), prompting the question as to whether FNDs could be used as effective electric sensors in biology. One route to achieving this would be through charge transfer doping. Chemical solutions with different potential energy have the ability to accept electrons from the diamond lattice, depending on the surface termination. This leads to modification of the NV fluorescence through changes in the charge state, for example $NV^- \rightarrow NV^0$. This effect could be harnessed to use FNDs as chemical sensors, allowing detection of solutions with different chemical potential. Furthermore, the NV quantum state is affected by electric fields, meaning FNDs could be used to detect electric fields in biology. The electric field from a single charge decays less rapidly (as a function of distance) than the magnetic field from a single spin, meaning nanodiamonds could in principle be used to sense electric charges over further distances than is feasible for magnetic sensing.

9.5.4 Nanothermometry

Cellular functions are fundamentally regulated by and dependent on the intracellular temperature. This in turn influences the rate and products of biochemical reactions inside a cell, and temperature distributions can be used as an indicator of cellular activity and energy use (Yang *et al.*, 2011; Okabe *et al.*, 2012). Nanodiamonds containing NV centers can be used as nanothermometers inside living cells, with diffraction-limited resolution and millikelvin sensitivity. Plakhotnik and Gruber (2010) have shown that the fluorescence lifetime of the NV defect varies as a function of temperature, allowing accurate measurements for temperatures between 300 and 700 K. Taking advantage of long coherence in the NV ground state also allows sensitive thermometry to be performed. Acosta *et al.* (2010) have measured the effect of temperature on the coherence of the NV ground state, while Toyli *et al.* (2012, 2013) and Neumann *et al.* (2013) have discussed the implications of this temperature sensitivity for intracellular nanothermometry. Nanodiamond thermometry has been put into practice with one demonstration of temperature measurements with submicron resolution and subkelvin sensitivities in living cells (Kucsko *et al.*, 2013).

9.6 Future trends

Recently two works have demonstrated detection of small (~125 nm^3 volume) nuclear ensembles using shallow NV centers in bulk diamond (Staudacher *et al.*,

2013; Mamin *et al.*, 2013). These works show the possibility of performing NMR on samples approaching the size of a single protein, under ambient conditions. The transferral of these sensitivities into biological environments could feasibly allow detection of single metalloproteins, of the storage and presence of high-spin transition metals in intracellular compartments and of the generation of free radicals. The imaging of single biomolecules in their native state and under physiological conditions is also a driving force behind NV diamond magnetometry.

Magnetic fields and quantum coherence are also thought to play roles in other areas of biology, including olfaction and navigation in birds. Indeed, quantum coherence is thought to play an important role in the energy transport of light-harvesting molecules. A greater understanding of these processes will undoubtedly open up new research areas and improve our understanding of biology at the cellular and molecular levels.

9.7 Sources of further information and advice

Further information on confocal microscopy of living cells can be found in the *Handbook of Biological Confocal Microscopy*, edited by James Pawley, Springer, 2006.

9.8 References

Acosta, V. M., Bauch, E., Ledbetter, M. P., Waxman, A., Bouchard, L. S. and Budker, D. (2010). Temperature dependence of the nitrogen–vacancy magnetic resonance in diamond. *Physical Review Letters*, 104(7), 070801.

Belthangady, C., Bar-Gill, N., Pham, L. M., Arai, K., Le Sage, D. *et al.* (2013). Dressed-state resonant coupling between bright and dark spins in diamond. *Physical Review Letters*, 110(15), 157601.

Bradac, C., Gaebel, T., Naidoo, N., Rabeau, J. R. and Barnard, A. S. (2009). Prediction and measurement of the size-dependent stability of fluorescence in diamond over the entire nanoscale. *Nano Letters*, 9(10), pp. 3555–3564.

Bradac, C., Gaebel, T., Naidoo, N., Sellars, M. J., Twamley, J. *et al.* (2010). Observation and control of blinking nitrogen–vacancy centres in discrete nanodiamonds. *Nature Nanotechnology*, 5(5), pp. 345–349.

Cao, L., Wang, X, Meziani, M. J., Lu, F., Wang, H. *et al.* (2007). Carbon dots for multiphoton bioimaging. *Journal of the American Chemical Society*, 129(37), pp. 11318–11319.

Chang, I. P., Hwang, K. C. and Chiang, C.-S. (2008a). Preparation of fluorescent magnetic nanodiamonds and cellular imaging. *Journal of the American Chemical Society*, 130(46), pp. 15476–15481.

Chang, Y. R., Lee, H. Y., Chen, K., Chang, C. C., Tsai, D. S. *et al.* (2008b). Mass production and dynamic imaging of fluorescent nanodiamonds. *Nature Nanotechnology*, 3(5), pp. 284–288.

Chao, J.-I., Perevedentseva, E., Chung, P. H., Liu, K. K., Cheng, C. Y. *et al.* (2007). Nanometer-sized diamond particle as a probe for biolabeling. *Biophysical Journal*, 93(6), p. 2199.

Chapman, R. and Plakhotnik, T. (2012). Anomalous saturation effects due to optical spin depolarization in nitrogen–vacancy centers in diamond nanocrystals. *Physical Review B*, 86(4), 045204.

Chen, Y.-Y., Shu, H., Kuo, Y., Tzeng, Y.-K. and Chang, H.-C. (2011). Measuring Foerster resonance energy transfer between fluorescent nanodiamonds and near-infrared dyes by acceptor photobleaching. *Diamond and Related Materials*, 20(5–6), pp. 803–807.

Cheng, C. Y., Perevedentseva, E., Tu, J. S., Chung, P. H., Cheng, C. L. *et al.* (2007). Direct and in vitro observation of growth hormone receptor molecules in A549 human lung epithelial cells by nanodiamond labeling. *Applied Physics Letters*, 90(16), p. 3.

Chung, P. H., Perevedentseva, E. and Cheng, C. L. (2007). The particle size-dependent photoluminescence of nanodiamonds. *Surface Science*, 601(18), pp. 3866–3870.

Colpin, Y., Swan, A., Zvyagin, A. V. and Plakhotnik, T. (2006). Imaging and sizing of diamond nanoparticles. *Optics Letters*, 31(5), pp. 625–627.

Dréau, A., Lesik, M., Rondin, L., Spinicelli, P., Arcizet, O. *et al.* (2011). Avoiding power broadening in optically detected magnetic resonance of single NV defects for enhanced dc magnetic field sensitivity. *Physical Review B*, 84(19), 195204.

Epstein, R. J., Mendoza, F. M., Kato, Y. K. and Awschalom, D. D. (2005). Anisotropic interactions of a single spin and dark-spin spectroscopy in diamond. *Nature Physics*, 1(2), pp. 94–98.

Ermakova, A., Pramanik, G., Cai, J., Algara-Siller, G., Kaiser, U. *et al.* (2013). Detection of few metallo-protein molecules using color centers in nanodiamonds. *Nano Letters*, 13(7), pp. 3305–3309.

Faklaris, O., Garrot, D., Joshi, V., Druon, F., Boudou, J.-P. *et al.* (2008). Detection of single photoluminescent diamond nanoparticles in cells and study of the internalization pathway. *Small*, 4(12), pp. 2236–2239.

Faklaris, O., Garrot, D., Joshi, V., Boudou, J.-P., Sauvage, T. *et al.* (2009a). Comparison of the photoluminescence properties of semiconductor quantum dots and non-blinking diamond nanoparticles. Observation of the diffusion of diamond nanoparticles in living cells. *Journal of the European Optical Society*, 4, 09035.

Faklaris, O., Joshi, V., Irinopoulou, T., Tauc, P., Sennour, M. *et al.* (2009b). Photoluminescent diamond nanoparticles for cell labeling: study of the uptake mechanism in mammalian cells. *ACS Nano*, 3(12), pp. 3955–3962.

Faklaris, O., Botsoa, J., Sauvage, T., Roch, J.-F. and Treussart, F. (2010). Photoluminescent nanodiamonds: Comparison of the photoluminescence saturation properties of the NV color center and a cyanine dye at the single emitter level, and study of the color center concentration under different preparation conditions. *Diamond and Related Materials*, 19(7–9), pp. 988–995.

Forkey, J. N., Quinlan, M. E., Alexander, S. M., Corrie, J. E. T. and Goldman, Y. E. (2003). Three-dimensional structural dynamics of myosin V by single-molecule fluorescence polarization. *Nature*, 422(6930), pp. 399–404.

Fu, C. C., Lee, H. Y., Chen, K., Lim, T. S., Wu, H. Y. *et al.* (2007). Characterization and application of single fluorescent nanodiamonds as cellular biomarkers. *Proceedings of the National Academy of Sciences of the United States of America*, 104(3), pp. 727–732.

Funk, R. H., Monsees, T. and Ozkucur, N. (2009). Electromagnetic effects – From cell biology to medicine. *Progress in Histochemistry and Cytochemistry*, 43(4), pp. 177–264.

Gaebel, T., Domhan, M., Wittmann, C., Popa, I., Jelezko, F. *et al.* (2006). Photochromism in single nitrogen–vacancy defect in diamond. *Applied Physics B: Lasers and Optics*, 82(2), pp. 243–246.

Glenn, D. R., Zhang, H., Kasthuri, N., Schalek, R., Lo, P. K. *et al.* (2012). Correlative light and electron microscopy using cathodoluminescence from nanoparticles with distinguishable colours. *Scientific Reports*, 2(865).

Grotz, B., Beck, J., Neumann, P., Naydenov, B., Reuter, R. *et al.* (2011). Sensing external spins with nitrogen–vacancy diamond. *New Journal of Physics*, 13(5), 055004.

Grotz, B., Hauf, M. V., Dankerl, M., Naydenov, B., Pezzagna, S. *et al.* (2012). Charge state manipulation of qubits in diamond. *Nature Communications*, 3, p. 729.

Gruber, A., Drabenstedt, A., Tietz, C., Fleury, L., Wrachtrup, J. and von Borczyskowski, C. (1997). Scanning confocal optical microscopy and magnetic resonance on single defect centers. *Science*, 276(5321), pp. 2012–2014.

Hall, L. T., Hill, C. D., Cole, J. H., Städler, B., Caruso, F. *et al.* (2010). Monitoring ion-channel function in real time through quantum decoherence. *Proceedings of the National Academy of Sciences*, 107(44), pp. 18777–18782.

Hall, L. T., Beart, G. C. G., Thomas, E. A., Simpson, D. A., McGuinness, L. P. *et al.* (2012). High spatial and temporal resolution wide-field imaging of neuron activity using quantum NV-diamond. *Scientific Reports*, 2(401).

Han, K. Y., Willig, K. I., Rittweger, E., Jelezko, F., Eggeling, C. *et al.* (2009). Three-dimensional stimulated emission depletion microscopy of nitrogen–vacancy centers in diamond using continuous-wave light. *Nano Letters*, 9(9), pp. 3323–3329.

Han, K. Y., Kim, S. K., Eggeling, C. and Hell, S. W. (2010). Metastable dark states enable ground state depletion microscopy of nitrogen vacancy centers in diamond with diffraction-unlimited resolution. *Nano Letters*, 10(8), pp. 3199–3203.

Hauf, M. V., Grotz, B., Naydenov, B., Dankerl, M., Pezzagna, S. *et al.* (2011). Chemical control of the charge state of nitrogen–vacancy centers in diamond. *Physical Review B*, 83(8), 081304.

Hui, Y. Y., Zhang, B., Chang, Y.-C., Chang, C.-C., Chang, H.-C. *et al.* (2010). Two-photon fluorescence correlation spectroscopy of lipid-encapsulated fluorescent nanodiamonds in living cells. *Optics Express*, 18(6), pp. 5896–5905.

Jahnke, K., Naydenov, B., Teraji, T., Koizumi, S., Umeda, T. *et al.* (2012). Long coherence time of spin qubits in ^{12}C enriched polycrystalline chemical vapor deposition diamond. *Applied Physics Letters*, 101(1), 012405.

Jiang, W., Kim, B. Y. S., Rutka, J. T. and Chan, W. C. W. (2008). Nanoparticle-mediated cellular response is size-dependent. *Nature Nanotechnology*, 3(3), pp. 145–150.

Kaufmann, S., Simpson, D. A., Hall, L. T., Perunicic, V., Senn, P. *et al.* (2013). Detection of atomic spin labels in a lipid bilayer using a single-spin nanodiamond probe. *Proceedings of the National Academy of Sciences*, 110(27), pp. 10894–10898.

Kirchner, C., Liedl, T., Kudera, S., Pellegrino, T., Muñoz Javier, A. *et al.* (2005). Cytotoxicity of colloidal CdSe and CdSe/ZnS nanoparticles. *Nano Letters*, 5(2), pp. 331–338.

Krueger, A. M. (2008). Diamond nanoparticles: Jewels for chemistry and physics. *Advanced Materials*, 20(12), pp. 2445–2449.

Kucsko, G., Maurer, P. C., Yao, N. Y., Kubo, M., Noh, H. J. *et al.* (2013). Nanometre-scale thermometry in a living cell. *Nature*, 500(7460), pp. 54–58.

Le Sage, D., Arai, K., Glenn, D. R., DeVience, S. J., Pham, L. M., *et al.* (2013). Optical magnetic imaging of living cells. *Nature*, 496(7446), pp. 486–489.

Lien, Z.-Y., Hsu, T.-C., Liu, K.-K., Liao, W.-S., Hwang, K.-C. and Chao, J.-I. (2012). Cancer cell labeling and tracking using fluorescent and magnetic nanodiamond. *Biomaterials*, 33(26), pp. 6172–6185.

Lim, Y. T., Kim, S., Nakayama, A., Stott, N. E., Bawendi, M. G. and Frangioni, J. V. (2003). Selection of quantum dot wavelengths for biomedical assays and imaging. *Molecular Imaging*, 2(1), pp. 50–64.

Liu, K. K., Cheng, C. L., Chang, C. C. and Chao, J. I. (2007). Biocompatible and detectable carboxylated nanodiamond on human cell. *Nanotechnology*, 18(32), p. 325102.

Liu, K. K., Wang, C. C., Cheng, C. L. and Chao, J. I. (2009). Endocytic carboxylated nanodiamond for the labeling and tracking of cell division and differentiation in cancer and stem cells. *Biomaterials*, 30(26), pp. 4249–4259.

London, P., Scheuer, J., Cai, J. M., Schwarz, I., Retzker, A. *et al.* (2013). Detecting and polarizing nuclear spins with double resonance on a single electron spin. *Physical Review Letters*, 111(6), 067601.

Mamin, H. J., Sherwood, M. H. and Rugar, D. (2012). Detecting external electron spins using nitrogen–vacancy centers. *Physical Review B*, 86(19), 195422.

Mamin, H. J., Kim, M., Sherwood, M. H., Rettner, C. T., Ohno, K. *et al.* (2013). Nanoscale nuclear magnetic resonance with a nitrogen–vacancy spin sensor. *Science*, 339(6119), pp. 557–560.

Manus, L. M., Mastarone, D. J., Waters, E. A., Zhang, X.-Q., Schultz-Sikma, E. A. *et al.* (2009). Gd(III)–nanodiamond conjugates for MRI contrast enhancement. *Nano Letters*, 10(2), pp. 484–489.

Maurer, P. C., Maze, J. R., Stanwix, P. L., Jiang, L., Gorshkov, A. V. *et al.* (2010). Far-field optical imaging and manipulation of individual spins with nanoscale resolution. *Nature Physics*, 6(11), pp. 912–918.

McGuinness, L. P., Yan, Y., Stacey, A., Simpson, D. A., Hall, L. T. *et al.* (2011). Quantum measurement and orientation tracking of fluorescent nanodiamonds inside living cells. *Nature Nanotechnology*, 6(6), pp. 358–363.

McGuinness, L. P., Hall, L. T., Stacey, A., Simpson, D. A., Hill, C. D. *et al.* (2013). Ambient nanoscale sensing with single spins using quantum decoherence. *New Journal of Physics*, 15, 073042.

Miyawaki, A. and Llopis, J. (1997). Fluorescent indicators for Ca^{2+} based on green fluorescent proteins and calmodulin. *Nature*, 388(6645), p. 882.

Mkandawire, M., Pohl, A., Gubarevich, T., Lapina, V., Appelhans, D. *et al.* (2009). Selective targeting of green fluorescent nanodiamond conjugates to mitochondria in HeLa cells. *Journal of Biophotonics*, 2(10), pp. 596–606.

Mochalin, V. N. and Gogotsi, Y. (2009). Wet chemistry route to hydrophobic blue fluorescent nanodiamond. *Journal of the American Chemical Society*, 131(13), p. 4594.

Mohan, N., Chen, C.-S., Hsieh, H.-H., Wu, Y.-C. and Chang, H.-C. (2010a). In vivo imaging and toxicity assessments of fluorescent nanodiamonds in *Caenorhabditis elegans*. *Nano Letters*, 10(9), pp. 3692–3699.

Mohan, N., Tzeng, Y.-K., Yang, L., Chen, Y.-Y., Hui, Y. Y. *et al.* (2010b). Sub-20-nm fluorescent nanodiamonds as photostable biolabels and fluorescence resonance energy transfer donors. *Advanced Materials*, 22(7), pp. 843–847.

Neugart, F., Zappe, A., Jelezko, F., Tietz, C., Boudou, J. P. *et al.* (2007). Dynamics of diamond nanoparticles in solution and cells. *Nano Letters*, 7(12), pp. 3588–3591.

Neumann, P., Jakobi, I., Dolde, F., Burk, C., Reuter, R. *et al.* (2013). High precision nano scale temperature sensing using single defects in diamond. *Nano Letters*, 13(6), pp. 2738–2742.

Okabe, K., Inada, N., Gota, C., Harada, Y., Funatsu, T. and Uchiyama, S. (2012). Intracellular temperature mapping with a fluorescent polymeric thermometer and fluorescence lifetime imaging microscopy. *Nature Communications*, 3, p. 705.

Perevedentseva, E., Cheng, C.-Y., Chung, P.-H., Tu, J.-S., Hsieh, Y.-H. and Cheng, C.-L. (2007). The interaction of the protein lysozyme with bacteria *E. coli* observed using nanodiamond labelling. *Nanotechnology*, 18(31), p. 315102.

Perunicic, V. S., Hall, L. T., Simpson, D. A., Hill, C. D. and Hollenberg, L. C. L. (2013). Single molecule NMR detection and spectroscopy using single spins in diamond. Eprint, arXiv:1307.8220.

Peterka, D. S., Takahashi, H. and Yuste, R. (2011). Imaging voltage in neurons. *Neuron*, 69(1), pp. 9–21.

Plakhotnik, T. and Gruber, D. (2010). Luminescence of nitrogen–vacancy centers in nanodiamonds at temperatures between 300 and 700 K: perspectives on nanothermometry. *Physical Chemistry Chemical Physics*, 12(33), pp. 9751–9756.

Rabeau, J. R., Stacey, A., Rabeau, A., Prawer, S., Jelezko, F. *et al.* (2007). Single nitrogen vacancy centers in chemical vapor deposited diamond nanocrystals. *Nano Letters*, 7(11), pp. 3433–3437.

Riley, P. (1994). Free radicals in biology: oxidative stress and the effects of ionizing radiation. *International Journal of Radiation Biology*, 65(1), pp. 27–33.

Rittweger, E., Wildanger, D. and Hell, S. W. (2009a). Far-field fluorescence nanoscopy of diamond color centers by ground state depletion. *Europhysics Letters*, 86(1), p. 14001.

Rittweger, E., Han, K. Y., Irvine, S. E., Eggeling, C. and Hell, S. W. (2009b). STED microscopy reveals crystal colour centres with nanometric resolution. *Nature Photonics*, 3(3), pp. 144–147.

Rojas, S., Gispert, J. D., Martín, R., Abad, S., Menchón, C., *et al.* (2011). Biodistribution of amino-functionalized diamond nanoparticles. *In vivo* studies based on ^{18}F radionuclide emission. *ACS Nano*, 5(7), pp. 5552–5559.

Rondin, L., Dantelle, G., Slablab, A., Grosshans, F., Treussart, F. *et al.* (2010). Surface-induced charge state conversion of nitrogen–vacancy defects in nanodiamonds. *Physical Review B*, 82(11), 115449.

Schrand, A. M., Dai, L., Schlager, J. J., Hussain, S. M. and Osawa, E. (2007a). Differential biocompatibility of carbon nanotubes and nanodiamonds. *Diamond and Related Materials*, 16(12), pp. 2118–2123.

Schrand, A. M., Huang, H. J., Carlson, C., Schlager, J. J., Osawa, E. *et al.* (2007b). Are diamond nanoparticles cytotoxic? *Journal of Physical Chemistry B*, 111(1), pp. 2–7.

Schrand, A. M., Ciftan, S. A. and Shenderova, O. A. (2009). Nanodiamond particles: properties and perspectives for bioapplications. *Critical Reviews in Solid State and Materials Sciences*, 34(1), pp. 18–74.

Schrand, A. M., Lin, J. B., Hens, S. C. and Hussain, S. M. (2011). Temporal and mechanistic tracking of cellular uptake dynamics with novel surface fluorophore-bound nanodiamonds. *Nanoscale*, 3(2), pp. 435–445.

Shin, C., Kim, C., Kolesov, R., Balasubramanian, G., Jelezko, F. *et al.* (2010). Sub-optical resolution of single spins using magnetic resonance imaging at room temperature in diamond. *Journal of Luminescence*, 130(9), pp. 1635–1645.

Sieber, J. J. (2007). Anatomy and dynamics of a supramolecular membrane protein cluster. *Science*, 317, pp. 1072–1076.

Smith, B. R., Niebert, M., Plakhotnik, T. and Zvyagin, A. V. (2007). Transfection and imaging of diamond nanocrystals as scattering optical labels. *Journal of Luminescence*, 127(1), pp. 260–263.

Smith, B. R., Inglis, D. W., Sandnes, B., Rabeau, J. R., Zvyagin, A. V. *et al.* (2009). Five-nanometer diamond with luminescent nitrogen–vacancy defect centers. *Small*, 5(14), pp. 1649–1653.

Staudacher, T., Shi, F., Pezzagna, S., Meijer, J., Du, J. *et al.* (2013). Nuclear magnetic resonance spectroscopy on a (5-nanometer)^3 sample volume. *Science*, 339(6119), pp. 561–563.

Steinert, S., Ziem, F., Hall, L. T., Zappe, A., Schweikert, M. *et al.* (2013). Magnetic spin imaging under ambient conditions with sub-cellular resolution. *Nature Communications*, 4, p. 1607.

Sun, Y. P., Zhou, B., Lin, Y., Wang, W., Fernando, K. A. S. *et al.* (2006). Quantum-sized carbon dots for bright and colorful photoluminescence. *Journal of the American Chemical Society*, 128(24), pp. 7756–7757.

Tisler, J., Balasubramanian, G., Naydenov, B., Kolesov, R., Grotz, B. *et al.* (2009). Fluorescence and spin properties of defects in single digit nanodiamonds. *ACS Nano*, 3(7), pp. 1959–1965.

Tisler, J., Reuter, R., Lämmle, A., Jelezko, F., Balasubramanian, G. *et al.* (2011). Highly efficient FRET from a single nitrogen–vacancy center in nanodiamonds to a single organic molecule. *ACS Nano*, 5(10), pp. 7893–7898.

Toyli, D. M., Christle, D. J., Alkauskas, A., Buckley, B. B., Van de Walle, C. G. *et al.* (2012). Measurement and control of single nitrogen–vacancy center spins above 600 K. *Physical Review X*, 2(3), 031001.

Toyli, D. M., Charles, F., Christle, D. J., Dobrovitski, V. V. and Awschalom, D. D. (2013). Fluorescence thermometry enhanced by the quantum coherence of single spins in diamond. *Proceedings of the National Academy of Sciences*, 110(21), pp. 8417–8421.

Tzeng, Y.-K., Faklaris, O., Chang, B.-M., Kuo, Y., Hsu, J.-H. and Chang, H.-C. (2011). Superresolution imaging of albumin-conjugated fluorescent nanodiamonds in cells by stimulated emission depletion. *Angewandte Chemie International Edition*, 50(10), pp. 2262–2265.

Vaijayanthimala, V., Tzeng, Y.-K., Chang, H.-C. and Li, C.-L. (2009). The biocompatibility of fluorescent nanodiamonds and their mechanism of cellular uptake. *Nanotechnology*, 20(42), p. 425103.

Vlasov, I. I., Barnard, A. S., Ralchenko, V. G., Lebedev, O. I., Kanzyuba, M. V. *et al.* (2009). Nanodiamond photoemitters based on strong narrow-band luminescence from silicon–vacancy defects. *Advanced Materials*, 21(7), pp. 808–812.

Waldermann, F. C., Olivero, P., Nunn, J., Surmacz, K., Wang, Z. Y. *et al.* (2007). Creating diamond color centers for quantum optical applications. *Diamond and Related Materials*, 16(11), pp. 1887–1895.

Waldherr, G., Beck, J., Steiner, M., Neumann, P., Gali, A. *et al.* (2011). Dark states of single nitrogen–vacancy centers in diamond unraveled by single shot NMR. *Physical Review Letters*, 106(15), 157601.

Wee, T. L., Tzeng, Y.-K., Han, C.-C., Chang, H.-C., Fann, W., *et al.* (2007). Two-photon excited fluorescence of nitrogen–vacancy centers in proton-irradiated type Ib diamond. *Journal of Physical Chemistry A*, 111(38), pp. 9379–9386.

Weng, M.-F., Chiang, S.-Y., Wang, N.-S. and Niu, H. (2009). Fluorescent nanodiamonds for specifically targeted bioimaging: Application to the interaction of transferrin with transferrin receptor. *Diamond and Related Materials*, 18(2–3), pp. 587–591.

Yang, J., Yang, H. and Lin, L. (2011). Quantum dot nano thermometers reveal heterogeneous local thermogenesis in living cells. *ACS Nano*, 5(6), pp. 5067–5071.

Yu, S. J., Kang, M. W., Chang, H. C., Chen, K. M. and Yu, Y. C. (2005). Bright fluorescent nanodiamonds: No photobleaching and low cytotoxicity. *Journal of the American Chemical Society*, 127(50), pp. 17604–17605.

Yuan, Y., Chen, Y. W., Lui, J. H., Wang, H. F. and Liu, Y. F. (2009). Biodistribution and fate of nanodiamonds in vivo. *Diamond and Related Materials*, 18(1), pp. 95–100.

Zaitsev, A. M. (2001). *Optical Properties of Diamond: A Data Handbook*. Springer.

Zhang, B., Li, Y., Fang, C.-Y., Chang, C.-C., Chen, C.-S. *et al.* (2009). Receptor-mediated cellular uptake of folate-conjugated fluorescent nanodiamonds: a combined ensemble and single-particle study. *Small*, 5(23), pp. 2716–2721.

Zhao, N., Hu, J.-L., Ho, S.-W., Wan, J. T. K. and Liu, R. B. (2011). Atomic-scale magnetometry of distant nuclear spin clusters via nitrogen–vacancy spin in diamond. *Nature Nanotechnology*, 6(4), pp. 242–246.

Ziem, F. C., Götz, N. S., Zappe, A., Steinert, S. and Wrachtrup, J. (2013). Highly sensitive detection of physiological spins in a microfluidic device. *Nano Letters*, 13(9), pp. 4093–4098.

10

Diamond magnetic sensors

P. MALETINSKY, University of Basel, Switzerland and
V. JACQUES, Université Paris Sud and ENS Cachan, France

DOI: 10.1533/9780857096685.2.240

Abstract: In this chapter, we describe the use of individual nitrogen–vacancy (NV) centers in diamond as nanoscale sensors for magnetic-field detection and imaging. We start by reviewing the original proposals and first proof-of-concept experiments for NV magnetometry and then discuss recent applications of this emerging technology. Special emphasis will be placed on recently achieved imaging of nanomagnetic structures and single electron spins.

Key words: quantum sensing, coherent spin manipulation, nanoscale magnetic imaging, magnetometry, diamond.

10.1 Introduction

In 1996, Sekatskii and Letokhov (1996) published a visionary article in which they proposed the use of single molecules as local probes for nanoscale optical imaging. This was the first time that the use of an isolated, single quantum system was considered for a sensing application, and in this sense they laid the foundation for the diamond-based magnetic-field sensors that will be discussed in this chapter. Almost a decade later, Chernobrod and Berman (2005) proposed a powerful extension to Sekatskii and Letokhov's idea by suggesting the use of individual spins as local probes for magnetic fields. Detecting and imaging weak magnetic fields at the nanoscale has for a long time been a challenging and highly interesting topic owing to its wealth of applications in basic science and technology. Despite the exciting prospects that ensued from these proposals, experimental activity along these lines initially remained sparse, to a great extent because of the lack of a suitable quantum system that could offer sufficient control and stability to be used for these demanding sensing applications.

In recent years, however, it has been realized that the nitrogen–vacancy (NV) center in diamond (Gruber *et al.*, 1997; Jelezko and Wrachtrup, 2006) has exceptional physical properties that render the NV center a nearly ideal candidate to bring the ideas of Chernobrod and Berman to reality. This aspect has been discussed in great detail in work by Taylor *et al.* (2008), who highlighted some performance characteristics and particular magnetic-field sensing modes based on coherent control of NV center spins, and by Degen (2008), who discussed a technique for using diamond nanocrystals in a scanning-probe configuration. These proposals and the many experimental papers that followed their publication

© 2014 Elsevier Ltd

(Balasubramanian *et al.*, 2008; Bouchard *et al.*, 2011; Grinolds *et al.*, 2011; de Lange *et al.*, 2011; Maletinsky *et al.*, 2012; Maze *et al.*, 2008; Rondin *et al.*, 2012) will be discussed in detail in this review.

At least three aspects stand out in the performance of NV centers as magnetic-field sensors: quantum coherence, size and room temperature operation. As will be discussed later (Section 10.2), quantum coherence can be exploited to maximize the sensitivity of the NV center's spin to external magnetic fields. Additionally, the atomic size of the NV center allows high spatial resolution in imaging applications, in principle limited only by the diameter of the electronic wave function of the NV center, which is on the order of angstroms. Importantly, for the NV center, all these properties are preserved even at room temperature, which in principle should allow nanoscale magnetic imaging of biological systems (Hall *et al.*, 2010). A sensor having these properties is most desirable for the exploration of a variety of open scientific questions. The examples where nanoscale detection of weak (magnetic) fields would have a tremendous impact on scientific and technological advancements span a wide range from magnetic imaging of individual nuclear spins in biomolecules (Sidles, 1991), through exotic forms of magnetism in various condensed-matter systems (Mackenzie and Maeno, 2003), to imaging of charge transport in disordered mesoscopic systems (Nowack *et al.*, 2013).

In the following sections, we give an overview of recent theoretical and experimental progress in the context of various NV-based nanoscale magnetometry schemes. We start in Section 10.2 by describing some general features of NV magnetometry, such as the magnetic-field sensitivity and spatial resolution of different approaches to NV-based magnetic sensing. In Section 10.3, we discuss several experimental schemes for scanning NV magnetometry which have been realized thus far. These can be divided into scanning probe techniques using diamond nanocrystals 'glued' onto scanning-probe tips, and scanning probes directly fabricated from bulk diamond. For both implementations, we discuss several nanoscale imaging applications which have been demonstrated in the recent past. We conclude in Section 10.4 with a discussion of the outlook for the emerging field of NV magnetometry in the future.

10.2 Magnetometry with nitrogen–vacancy (NV) centers

10.2.1 General remarks

Magnetic-field imaging technologies are typically benchmarked against two central performance characteristics: magnetic-field sensitivity (the smallest change in magnetic field that can be detected for a given measurement time) and spatial resolution. Figure 10.1(a) shows an overview of the magnetometry techniques that have been experimentally demonstrated in recent years and

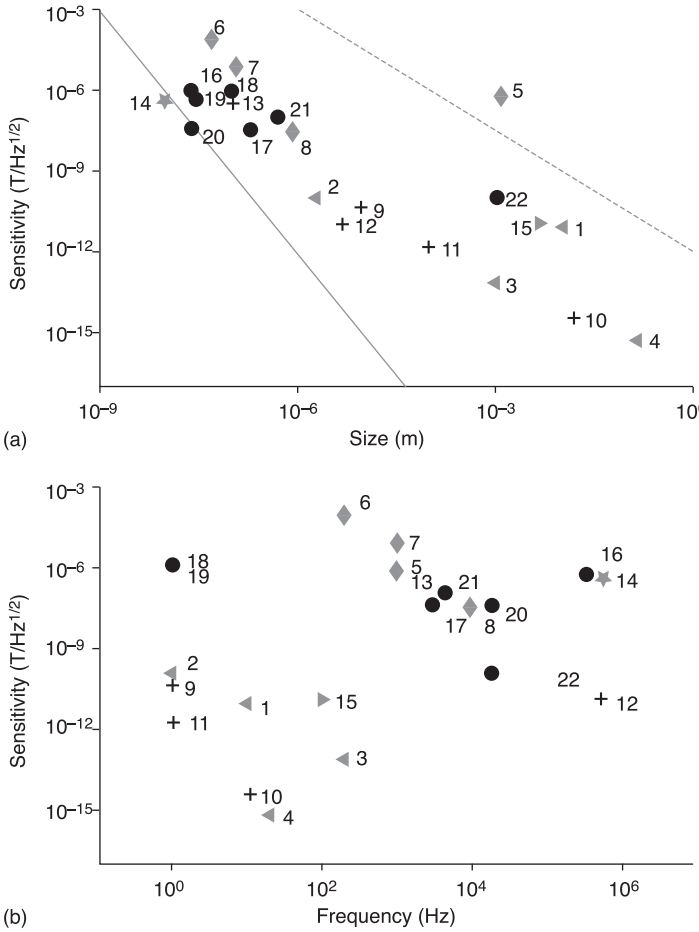

10.1 Overview of the performance of various magnetic imaging and sensing technologies. •, NV-based sensors; ★, MRFM; +, SQUID-based sensors; ◆, Hall bar sensors; ◀, atom-vapor cells; ▶, other sensors. The references in the figure are as follows: 1, Vengalattore *et al.* (2007); 2, Wildermuth *et al.* (2006); 3, Shah *et al.* (2007); 4, Kominis *et al.* (2003); 5, Sandhu *et al.* (2004a); 6, Sandhu *et al.* (2004b); 7, Oral *et al.* (2002); 8, Oral *et al.* (1996); 9, Kirtley *et al.* (1995); 10, Faley *et al.* (2006); 11, Baudenbacher *et al.* (2003); 12, Hatridge *et al.* (2011); 13, Finkler *et al.* (2010); 14, Degen *et al.* (2009); 15, Dong *et al.* (2003); 16, 17, Maze *et al.* (2008); 18, Balasubramanian *et al.* (2008); 19, 20, Maletinsky *et al.* (2012); 21, Pham *et al.* (2011); 22, Le Sage *et al.* (2012). (a) Sensitivity versus sensor size (spatial resolution); the dashed line illustrates the heuristic scaling $1/d^{p/3}$ of the sensitivity as a function of detector size. The solid line indicates the dipolar field of a single electron – only sensors in the vicinity of or below this line have the potential for single-electron spin sensing. (b) The same data as in (a), with sensitivity plotted against detection frequency. We have plotted the demonstrated operating frequencies, but note that most sensors can be operated over a wider range of frequencies.

applied to a variety of imaging and sensing tasks. It is noteworthy that the spatial resolution and magnetic-field sensitivity are each scattered over almost nine orders of magnitude for these vastly different technologies. Nevertheless, a common trend is the trade-off between magnetic-field sensitivity and spatial resolution, caused by the number of 'sensing units' that can be accommodated within a given volume without performance degradation. If N uncorrelated sensors (single atoms, NV centers, Hall bars, . . .) are employed for magnetometry, the sensitivity improves as $\sqrt{N}$ (Budker and Romalis, 2007) over single-sensor operation, while the sensing volume grows with N. For a sensor of typical dimension r, the sensitivity should thus scale roughly as $1/r^{3/2}$ (Romalis, 2008), a behavior illustrated by the dashed line in Fig. 10.1(a). Astonishingly, even sensors based on very different physical principles follow this behavior closely.

If magnetic fields are measured using an ensemble of N quantum systems, a fundamental limit to the magnetic-field sensitivity is given by the spin projection noise (Budker and Romalis, 2007) resulting from the statistical distribution of a quantum mechanical measurement. As we will show, a magnetic measurement with a spin system always involves a measurement of the spin in a basis that is nearly orthogonal to the direction in which the spin was initially prepared. In this case, the distribution of measurement outcomes follows a binomial law whose mean gives the external magnetic field and whose variance is proportional to N (Itano *et al.*, 1993; Wrachtrup and Gruber, 1998). Comparing this random noise with the signal accumulated by the spin through Larmor precession yields the spin-projection-limited magnetic-field sensitivity

$$\eta_{\text{spin-proj.}} \sim \frac{\hbar}{g\mu_B}\frac{1}{\sqrt{NT_2^*}} \qquad [10.1]$$

where T_2* is the spin coherence time, μ_B is the Bohr magneton and $g=2$ is the electron spin's g-factor (Romalis, 2008). In addition to spin-projection noise, other technical noise sources will add in quadrature to the spin-projection noise and thereby further limit the magnetic-field sensitivity. Most notably, if the spin is addressed optically with a readout efficiency $\eta<1$, the magnetic-field sensitivity is further reduced by a factor $1/\sqrt{\eta}$ (Acosta *et al.*, 2009) to $\eta_{\text{photon shot noise}} = \eta_{\text{spin-proj.}}/\sqrt{\eta}$. It is this photon shot-noise-limited sensitivity that up to now has been most relevant for NV-based magnetometers, and it will be the focus of the following discussion.

A third important point for a general characterization of a magnetometer is how fast the device can respond to changes in magnetic field, i.e., the operation frequency of the magnetometer. To assess this additional parameter, Fig. 10.1(b) shows the same sensors as in Fig. 10.1(a) but with the sensitivity plotted against frequency of operation. The frequency range over which a magnetometer can be operated sets important constraints on the possible applications of a given technology. Nanoscale magnetic-field imaging, for instance, requires DC operation in most cases, while nuclear magnetic resonance detection relies on a

detector capable of measuring magnetic fields at frequencies on the order of few megahertz. Figure 10.1(b) contains several data points from NV-based magnetic sensors that have been experimentally demonstrated in the past. In most cases, these sensors were designed to operate in the nanoscale sensing regime, and sensitivities allowing the detection of a single electron spin have been demonstrated (Grinolds *et al.*, 2013). It is an additional striking feature of this novel technology that NV-based magnetometers operate over a huge frequency range, starting with DC operation and extending to AC magnetic-field sensing at frequencies from 1 kHz to a few megahertz (Loretz *et al.*, 2013), with possible further extensions to the gigahertz range (Fuchs *et al.*, 2009).

10.2.2 The NV defect as an atomic-sized magnetic sensor

The negatively charged NV defect in diamond consists of a substitutional nitrogen atom (N) associated with a vacancy (V) in an adjacent lattice site of the diamond matrix (Fig. 10.2(a)). This defect, which behaves as an artificial atom nestled in the diamond matrix, exhibits strong, perfectly photostable photoluminescence (PL) in the red, allowing the detection of individual NV defects using optical confocal microscopy at room temperature (Gruber *et al.*, 1997). Although NV defects occur naturally in diamond, recent progress in ion implantation techniques nowadays allows the controlled creation of single NV defects with a spatial resolution down to a few tens of nanometers, both laterally (Pezzagna *et al.*, 2011) and vertically (Ohno *et al.*, 2012).

An essential feature of NV defects is that their ground level is a spin triplet state with $S=1$, whose sublevels are split in energy by spin–spin interaction into a singlet state of spin projection $m_s=0$ and a doublet $m_s=\pm1$, separated by 2.88 GHz in the absence of a magnetic field (Fig. 10.2(a)). Here, m_s denotes the spin projection along the intrinsic quantization axis of the NV defect, corresponding to the axis joining the nitrogen and the vacancy (the [111] crystal axis). Radiative-transition selection rules associated with the spin state quantum number lead to the fact that a polarization of the NV defect in the ground state spin level $m_s=0$ can be achieved by optical pumping (Manson *et al.*, 2006). Furthermore, the PL intensity of the NV defect is significantly higher when the $m_s=0$ state is predominantly populated. Such a spin-dependent PL enables detection of electron spin resonance (ESR) by purely optical means (Gruber *et al.*, 1997). Indeed, when a single NV defect, initially prepared in the $m_s=0$ state through optical pumping, is driven to the $m_s=\pm1$ spin state by applying a resonant microwave field, a drop in the PL signal is observed, as depicted in Fig. 10.2(b). In recent years, this property has been extensively used in the context of diamond-based quantum information processing, where the NV defect is being explored as a solid-state spin qubit (Dutt *et al.*, 2007; Neumann *et al.*, 2008).

For magnetometry applications, the principle of the measurement is similar to that used in optical magnetometers based on the precession of spin-polarized

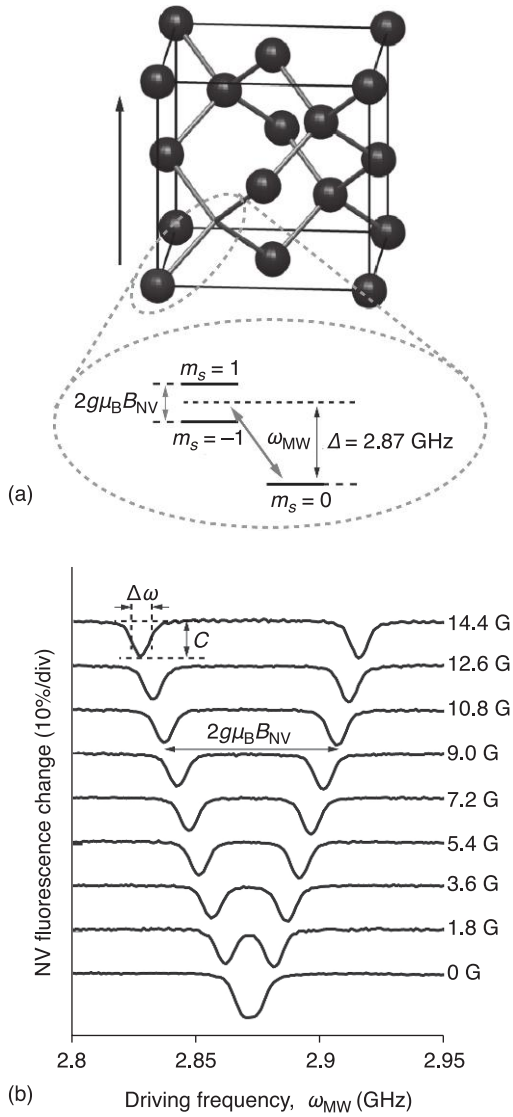

10.2 Basic spin properties of nitrogen–vacancy (NV) centers. (a) Atomic structure and electronic spin structure of the NV center. (b) Optically detected electron spin resonance (ESR) from a single NV center.

atomic gases (Budker and Romalis, 2007). The applied magnetic field is evaluated through the detection of Zeeman shifts of the NV defect electron spin sublevels. When a magnetic field is applied in the vicinity of the NV defect, the degeneracy of the $m_s = \pm 1$ spin sublevels is lifted by the Zeeman effect, leading to the appearance of two resonance lines in the ESR spectrum (Fig. 10.2(b)). In the limit

of weak magnetic fields (<10 mT), the ESR splitting is given by $2g\mu_B B_{NV}$, where B_{NV} is the projection of the magnetic field along the NV axis. A single NV defect therefore behaves as a magnetic sensor with an atomic-sized detection volume.

10.2.3 Magnetic-field sensitivity

The magnetic-field dependence of the ground state electron spin splitting forms the basis of all NV-based magnetic-field-sensing modes. As indicated above, the simplest way to measure an external DC magnetic field is the direct evaluation of the Zeeman splitting in an optically detected ESR spectrum. The magnetic-field sensitivity can be inferred by inspecting the maximum available magnetic-field response and the signal-to-noise ratio associated with an ESR trace, as shown in Fig. 10.2(b). The optimal response of the fluorescence signal to a DC magnetic field is obtained by fixing a driving microwave frequency ω_{MW} to the maximum slope of a given ESR dip, i.e., to a detuning corresponding to the half width at half maximum of the ESR line. Assuming a magnetic-field variation δB, the change in NV fluorescence is then given by $(\partial I_0/\partial B) \times \delta B \times \Delta t$, where I_0 is the NV fluorescence rate and Δt *is* the measurement duration. At the same time, the spin-readout noise for the NV center is dominated by photon shot noise[1] and is therefore equal to $\sqrt{(I_0 \times \Delta t)}$. Comparing these two expressions yields the photon-shot-noise-limited magnetic-field sensitivity, which is defined as the minimum DC magnetic field detectable for a signal-to-noise ratio of one:

$$\eta = \delta B\sqrt{\Delta t} = \frac{\sqrt{I}}{\left(\partial I_0/\partial B\right)} = P \times \frac{\hbar}{g\mu_B}\frac{\Delta\omega}{C\sqrt{I_0}} \qquad [10.2]$$

where $\Delta\omega$ and C are the ESR linewidth and contrast, respectively, and P is a numerical factor, which depends on the exact ESR line shape ($P = 0.7$ for a Gaussian profile and 0.77 for a Lorentzian profile). Since the ESR contrast is fixed by the intrinsic photophysical properties of the NV defect, this parameter is hard to modify.[2] The magnetic-field sensitivity can thus be improved either by decreasing the ESR linewidth $\Delta\omega$ or by increasing the efficiency of collection of the NV defect fluorescence.

The fundamental limit to the ESR linewidth is fixed by the inverse of the inhomogeneous dephasing time of the NV defect electron spin, T_2^*. However, reaching this limit experimentally is not straightforward, since both the readout laser and the driving microwave field induce power broadening of the ESR line (Dréau *et al.*, 2011). The solution to this problem is to separate spin manipulation,

[1] Spin-projection noise can be neglected for the vast majority of NV magnetometry schemes reported to date, owing to the limited photon collection efficiency.

[2] We note that recent magnetometry schemes based on NV defect absorption in the infrared ($\lambda = 1.04\,\mu$m) (Acosta *et al.*, 2010a) might allow one to greatly improve the readout contrast by placing an ensemble of NV defects in a cavity (Dumeige *et al.*, 2013).

spin readout and phase accumulation (magnetic-field measurement) in time. This is most commonly achieved by applying a Ramsey pulse sequence to the NV defect electron spin (Fig. 10.3(a)). A first $\pi/2$ microwave pulse rotates the NV defect electron spin from a prepared state $|0\rangle$ to a coherent superposition $|\Psi\rangle=(1/\sqrt{2})(|0\rangle+|1\rangle)$, which evolves over a time τ. During such a free precession time, the electron spin interacts with the external magnetic field. The $m_S=1$ state therefore acquires a phase $\Phi=\tau g\mu_B B$ with respect to the $m_S=0$ state, corresponding to a precession of the spin in the plane perpendicular to the spin quantization axis, yielding $|\Psi\rangle=(1/\sqrt{2})(|0\rangle+e^{i\Phi}|1\rangle)$. The phase Φ and thus the magnetic field are measured by applying a second $\pi/2$ pulse, which projects the NV electronic spin back onto the quantization axis. The phase is therefore converted into populations, which are finally read out optically though spin-dependent PL of the NV defect.

The magnetic-field sensitivity improves as the free precession time τ is increased, so that the measured signal Φ is maximized. However, magnetic-field noise from the environment of the NV defect randomizes Φ over time with a time constant T_2^*, and leads to a decrease in spin-readout contrast with increasing τ. Comparing the loss in readout contrast with the gain in increased acquired phase, it can be shown (Taylor *et al.*, 2008) that the magnetic-field sensitivity resulting from this procedure is optimized for $\tau\approx T_2^*$. In this pulsed measurement scheme, the rate of detected photons is decreased by the duty cycle of the laser pulses used for spin readout. If the pulse sequence has an optimized duration $\tau\approx T_2^*$, the time-averaged rate of detected photons is given by $I_0 t_L/T_2^*$, where t_L is the duration of the readout laser pulse.[3] Using Eq. 10.2, the optimized magnetic-field sensitivity for a DC magnetic field is therefore given by

$$\eta_{dc} \sim \frac{\hbar}{g\mu_B}\frac{1}{C\sqrt{I_0 t_L}}\times\frac{1}{\sqrt{T_2^*}} \qquad [10.3]$$

The same magnetic-field sensitivity can be achieved by replacing the Ramsey sequence by a single resonant microwave π-pulse with the optimal duration T_2^*, followed by a readout laser pulse (Dréau *et al.*, 2011). Using this simple pulse sequence, ESR spectra with a T_2^*-limited linewidth can be recorded directly by continuously repeating the sequence while sweeping the π-pulse frequency and recording the NV defect PL intensity. While such magnetic-field detection has only a limited dynamic range (essentially given by the ESR linewidth $1/T_2^*$, which typically corresponds to a dynamic range of ~1 G), we note in passing that recently developed frequency-locking schemes (Schoenfeld and Harneit, 2011) can be applied to extend magnetometry operation to almost arbitrary dynamic ranges.

[3] The duration t_L of the readout laser pulse is usually fixed at ~300 ns in order to optimize the contrast of the spin readout.

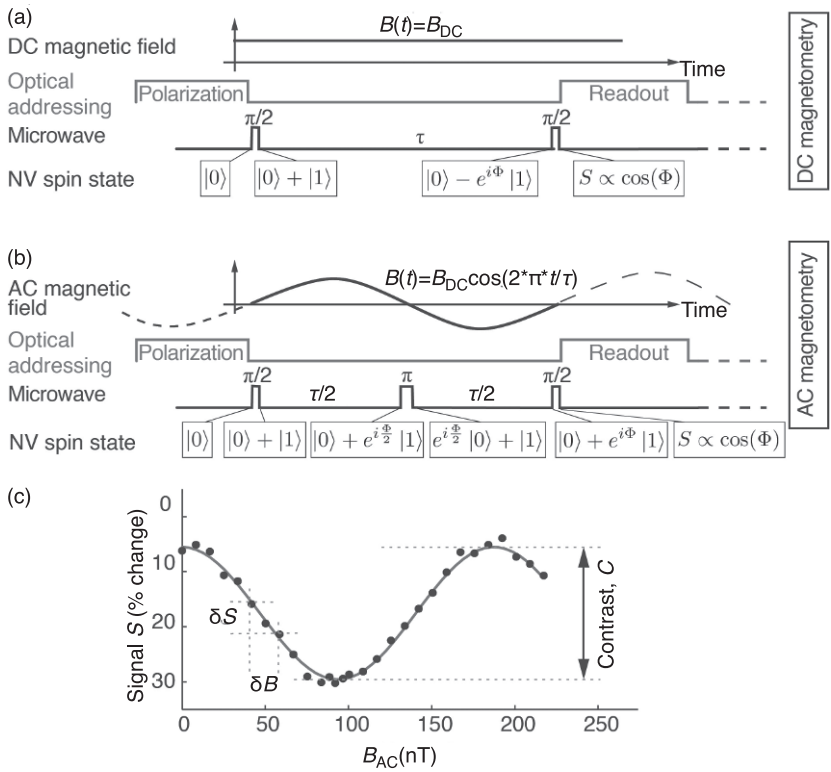

10.3 NV magnetometry sequences. (a) 'DC magnetometry' using a Ramsey pulse sequence on the NV spin. Optical excitation is used to initialize and measure the NV spin. During free evolution, the spin acquires a phase $\Phi = \tau g \mu_B B$, where τ is the total evolution time, μ_B is the Bohr magneton and $g = 2$. (b) 'AC magnetometry' using a Hahn-echo sequence. The phase is accumulated similarly to (a); however, the spin-echo sequence allows a longer $\tau \approx T_2$ before decoherence affects the readout contrast C. (c) Experimental results for AC magnetometry. $\delta B / \delta S$ determines the NV's sensitivity to changes in B_{AC} and is directly proportional to η. Figure adapted from Maze *et al.* (2008).

A further increase in magnetic-field sensitivity can be gained if the magnetic field to be determined occurs not at DC but at a nonzero frequency – a procedure sometimes colloquially referred to as 'quantum lock-in amplification' (Kotler *et al.*, 2011). This improvement in sensitivity is a result of a prolongation of NV spin coherence that can be achieved by periodically flipping the direction of the sensing spin. This key observation was originally made by Hahn (1950), who realized that the T_2^* limit was merely an effect of temporal (or ensemble) averaging in the Ramsey sequence and that the limitations on this inhomogeneous spin-dephasing time were given by slow fluctuations of a given spin's environment. If these fluctuations are slow enough, their effect can be mitigated by adding a

π-pulse after the first half of the free evolution in the Ramsey sequence discussed above, a sequence referred to as 'Hahn echo' (Hahn, 1950) (Fig. 10.3(b)). The result of the π-pulse is to 'swap' the phase acquired by the states $|0\rangle$ and $|1\rangle$, i.e., to perform the operation

$$\frac{1}{\sqrt{2}}\left(|0\rangle + e^{i\Phi/2}|1\rangle\right) \rightarrow \frac{1}{\sqrt{2}}\left(e^{i\Phi/2}|0\rangle + |1\rangle\right)$$

After the second half of the free-evolution time, the $m_S = 1$ state will again acquire a phase due to the magnetic field it experiences. For slow magnetic noise, this phase will be equal to the phase acquired in the first half-period, and no net phase accumulation between $|0\rangle$ and $|1\rangle$ occurs. Therefore, the spin dephasing due to this random noise is reduced and the spin coherence time increased to a value commonly denoted by T_2, following the terminology used in NMR. Using more complex dynamical decoupling schemes, for example 'CPMG'-like pulse sequences (Carr and Purcell, 1954; Meiboom and Gill, 1958), inhomogeneous spin dephasing can be reduced even further. The resulting spin coherence time can exceed T_2^* by several orders of magnitude and therefore dramatically increase the sensitivity of an NV defect to AC magnetic fields:

$$\eta_{ac} = \eta_{dc}\sqrt{\frac{T_2^*}{T_2}} \qquad [10.4]$$

Since the coherence time T_2 can be as long as 2 ms for a single NV defect hosted in an ultrapure diamond sample,[4] the AC magnetic-field sensitivity η_B can reach approximately $10\,\mathrm{nT\,Hz^{-1/2}}$ (Balasubramanian *et al.*, 2009; Maze *et al.*, 2008). Such a high sensitivity recently enabled imaging of the magnetic field from a single electron spin (Grinolds *et al.*, 2013) (see Section 10.3.2), as well as the magnetic detection of small nuclear-spin ensembles (Mamin *et al.*, 2013; Staudacher *et al.*, 2013), using a single-NV magnetometer.

Importantly, the NV center in this sequence is sensitive only to time-varying ('AC') magnetic fields which oscillate at the frequency of the applied pulse sequence (Fig. 10.3(b)). Furthermore, variations on this basic approach using advanced multipulse sensing protocols are applicable to measurements of fluctuating (incoherent) magnetic fields (de Lange *et al.*, 2011).

10.2.4 Effect of the diamond sample

As explained above, the magnetic-field sensitivity is directly linked to the coherence properties of the spin state of the NV defect electrons, which are mainly

[4] In the next section, we give typical values of the coherence time for different types of diamond samples.

limited by magnetic interactions with the bath of paramagnetic impurities in the diamond matrix. The paramagnetic impurities in diamond are, essentially, related to electronic spins bound to nitrogen impurities ($S=1/2$) and ^{13}C nuclei ($I=1/2$). Achieving long coherence times therefore requires us to engineer diamond samples with an extremely low content of impurities, as close as possible to a perfectly spin-free lattice.

For many years, the only diamond crystals available with a low number of impurities were natural ones, grown in the Earth's mantle. In the 1950s, the first synthetic diamond crystals were grown using the high-pressure high-temperature (HPHT) method (Bundy *et al.*, 1955). However, for such crystals the typical content of paramagnetic impurities, mainly nitrogen atoms, is still on the order of hundreds of ppm (parts per million carbon atoms). The coherence times of an NV defect placed in such an electron spin bath are as short as $T_2^* \sim 100\,\text{ns}$ and $T_2 \sim 1\,\mu\text{s}$. For the past few decades, the development of diamond growth using chemical vapor deposition (CVD) processes has allowed much better control of impurities, thus releasing the broad engineering potential of diamond (Markham *et al.*, 2011). In particular, it has become possible to reduce the nitrogen content in single-crystal CVD-grown diamond from a few ppm down to below 1 ppb (part per billion carbon atoms) (Tallaire *et al.*, 2006). In such samples, the electron spin bath can be safely neglected and the decoherence of the NV defect electron spin is dominated by the coupling with a bath of ^{13}C nuclear spins (1.1% natural abundance), leading to $T_2^* \sim 5\,\mu\text{s}$ and $T_2 \sim 300\,\mu\text{s}$. In addition, it was recently shown that diamond crystals can be isotopically purified so as to enrich them in ^{12}C atoms (spinless) during sample growth, thus reducing the content of the ^{13}C isotope below 0.01%. Because the spin is nestled in such a spin-free lattice, the coherence times of the NV defect electron spin are typically given by $T_2^* \sim 100\,\mu\text{s}$ and T_2 2 ms (Balasubramanian *et al.*, 2009; Ishikawa *et al.*, 2012), which are the longest values ever observed in a solid-state system at room temperature. The sample-dependent NV defect coherence times and the corresponding magnetic-field sensitivity are summarized in Table 10.1.

Table 10.1 Typical coherence times of the NV defect electron spin for different types of diamond crystals, with the corresponding magnetic-field sensitivities η_{DC} and η_{AC} for DC and AC magnetic fields, respectively

Diamond sample	T_2^* (μs)	η_{DC} (nT Hz$^{-1/2}$)	T_2 (echo) (μs)	η_{AC} (nT Hz$^{-1/2}$)
HPHT ([N] = 100 ppm)	0.1	1500	1	500
CVD ([N] < 1 ppb)	3	300	300	30
CVD (enriched in ^{12}C)	100	60	2000	10

10.3 Scanning NV magnetometry

The use of NV centers for magnetometry applications has been discussed in essentially two contexts, using either a single NV center as a scanning probe unit or a large ensemble of NV centers for magnetic-field sensing and imaging. The two approaches are distinct in spatial resolution and magnetic-field sensitivity and find applications in different fields of research, ranging from materials science to biology and quantum technologies. If the collective response of a large ensemble of NV defects is used, the collected PL signal is magnified by the number N of the sensing spins and therefore the shot-noise-limited magnetic-field sensitivity is improved by a factor $1/\sqrt{N}$. Although this approach has provided the highest sensitivity to date, the spatial resolution of the magnetic-field imaging is linked to the optical addressing of the ensemble of NV defects and is therefore limited by diffraction (~500 nm). In the following, we focus on scanning NV magnetometry, where a single NV spin is used as an atomic-sized magnetic sensor. The intrinsic spatial resolution of such a magnetometer is fundamentally limited by the size of the NV center's electron spin wave function, which is in the angstrom range.

10.3.1 Implementation

The principle of scanning NV magnetometry is schematically depicted in Fig. 10.4(a). A single NV defect is integrated onto the tip of an atomic force microscope (AFM), and a long-working-distance microscope objective, placed on top of the AFM tip, is used for both exciting and collecting the NV defect spin-dependent PL. By combining nanopositioning instrumentation and microwave excitation, the NV defect electron spin can then be used as a nonperturbing, atomic-sized scanning probe magnetometer under ambient conditions. If the probe spin is brought near a target, it will feel the presence of any local magnetic field emanating from the sample, causing a shift in the associated electron spin resonance, and thus providing a quantitative measurement of the magnetic-field projection along the quantization axis of the NV defect. Although the spatial resolution of scanning NV magnetometry is ultimately given by the atomic-sized detection volume, the effective resolving power is instead limited by the probe-to-sample distance, a common feature of any magnetic microscopy technique.

Engineering the scanning magnetic sensor has been achieved in the recent past by two different approaches. The most straightforward strategy consists in grafting a diamond nanocrystal hosting a single NV defect to the apex of an AFM tip (Balasubramanian *et al.*, 2008; Rondin *et al.*, 2012). Diamond nanocrystals are commercially available, with typical sizes ranging from 10 to 100 nm. Such nanocrystals are produced by milling type Ib HPHT diamond crystals, which contain a high concentration of paramagnetic nitrogen atoms, typically on the order of 200 ppm. Starting from this material, the formation of NV defects is carried out using high-energy electron irradiation followed by annealing at 800 °C under vacuum. The irradiation creates vacancies in the diamond matrix, while the

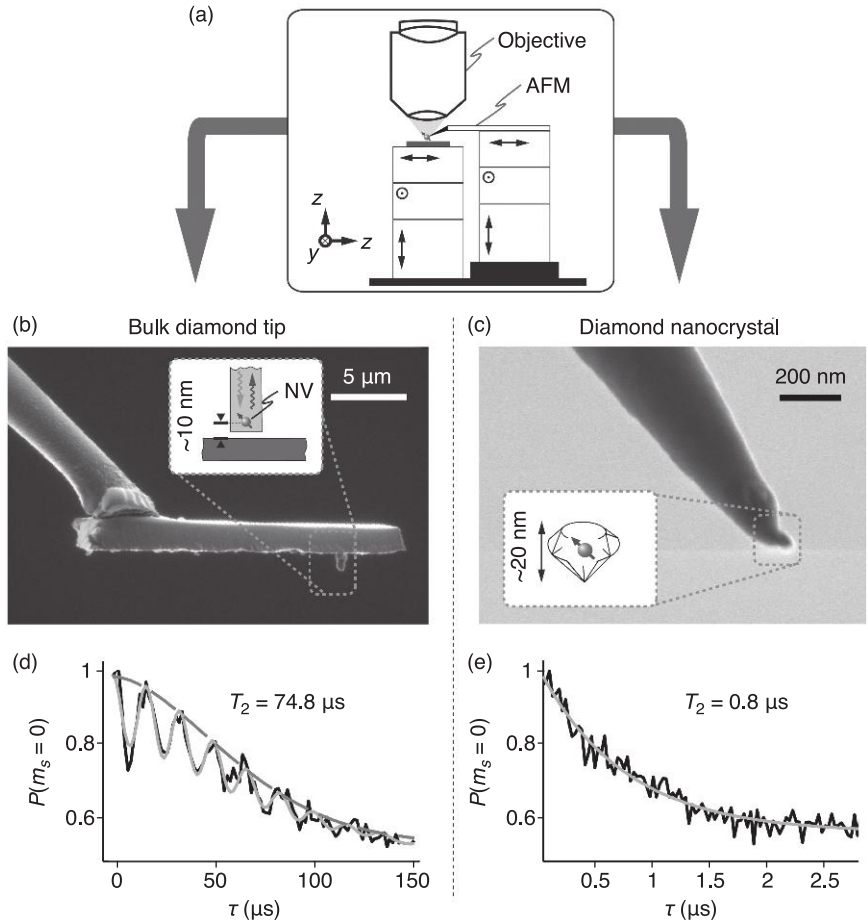

10.4 (a) Schematic illustration of a typical setup for scanning NV magnetometry, including separate positioners for the AFM tip and sample, and optical access through a microscope objective to read out and initialize the scanning NV magnetometer. (b) All-diamond bulk scanning probe for scanning NV magnetometry. (c) Diamond nanocrystal grafted onto a scanning-probe tip. (d) Measurement of the spin coherence time T_2 of an NV center in a device similar to the one shown in (b). (e) Typical measurement of spin coherence time for a diamond nanocrystal.

annealing procedure activates the migration of vacancies to intrinsic nitrogen impurities, leading to bonding of them into NV defects (Mita, 1996). Finally, a nanodiamond hosting a single NV defect can be grafted onto the AFM tip by using either a UV-curable adhesive or a positively charged polymer such as poly-L-lysine (Cuche *et al.*, 2009; Kuhn *et al.*, 2001). However, even though this method is experimentally simple and robust, precise control of the position of the

nanodiamond at the apex of the AFM tip is hard to obtain, thus limiting the minimum achievable distance between the magnetic sensor and the sample of interest. Furthermore, the coherence time of single NV defects in nanodiamonds is typically on the order of $T_2 \sim 1\,\mu$s (Fig. 10.4(e)), since the host material is an HPHT diamond crystal with a high content of paramagnetic impurities (see Table 10.1).

A scanning NV magnetometer that realizes the full potential of NV-based magnetometry should consist of a robust, scannable NV center with long spin coherence times, which can be efficiently read out and scanned in close proximity to an arbitrary sample of interest. Combining these properties is experimentally challenging and is particularly hard using scanning diamond nanocrystals, as discussed above. Recently, a novel approach has been demonstrated that employs all-diamond scanning-probe tips which contain single NV centers and are fabricated from high-purity CVD-grown diamond samples (Maletinsky *et al.*, 2012). More precisely, such a monolithic scanning NV sensor employs a diamond nanopillar as the scanning probe, with an individual NV center artificially created within roughly 10 nm of the pillar tip by ion implantation (Kalish *et al.*, 1997). Figure 10.4(b) shows a typical scanning electron microscope image of such a scanning device. The scanning diamond nanopillars have typical diameters of order 200 nm and lengths of 1 μm and are fabricated on diamond platforms a few microns in size, which are individually attached to AFM tips for scanning. As shown in Fig. 10.4(d), long NV spin coherence times are achieved, as these devices are fabricated from high-purity, single-crystal bulk diamond (Balasubramanian *et al.*, 2009). Furthermore, diamond nanopillars are efficient waveguides for the NV fluorescence (Babinec *et al.*, 2010), which provides a significant improvement in the collection efficiency. These two effects combined lead to a record shot-noise-limited sensitivity $\eta_{AC} \approx 10\,\text{nT}\,\text{Hz}^{-1/2}$ for a scanning NV magnetometer (Grinolds *et al.*, 2013). This promising approach therefore combines high spatial resolution, i.e., close proximity of the NV defect to the sample surface, with high sensitivity.

Although this chapter is focused on NV magnetometry using single NVs in scanning-probe devices, we shall conclude this section with some remarks on ensemble NV magnetometry for the sake of completeness. The appeal of ensemble magnetometry lies in the excellent magnetic-field sensitivity (the currently best reported values are in the range of $100\,\text{pT}\,\text{Hz}^{-1/2}$ (Le Sage *et al.*, 2012)) that this technique can offer. A major drawback of ensemble magnetometry is its spatial resolution, which is limited by the optical readout to ~300 nm. However, approaches to circumvent this limitation are being pursued, either by applying advanced super-resolution optical imaging methods, such as stimulated emission depletion (STED) microscopy (Hell, 2007; Maurer *et al.*, 2010), or by applying strong magnetic-field gradients to the sample (Pham *et al.*, 2011) and using techniques akin to 'conventional' magnetic resonance imaging. Furthermore, in order to achieve a scaling of the magnetic-field sensitivity proportional to $\sqrt{N}$ with

the number N of NV centers, the favorable properties (T_2, charge state, etc.) of the NV centers have to be maintained in ensemble magnetometry. This is particularly challenging in diamonds with high NV densities, which are the most attractive in this context. In most realistic cases, the spin coherence is a strong function of the NV density for diamonds with high NV densities, and in order to maximize the magnetic-field sensitivity, the product $N \cdot T_2^*$ (or $N \cdot T_2$ in the case of AC magnetometry) needs to be maximized (see Eq. 10.1). This materials challenge has been addressed by several groups recently, most notably by Acosta *et al.* (2009), who have demonstrated a density of NV^- centers of 16 ppm with $T_2^* \sim 120\,\text{ns}$, yielding $\eta_{DC} \sim 150\,\text{fT}\,\text{Hz}^{-1/2}$ for a magnetometer volume of $(100\,\mu\text{m})^3$.[5]

10.3.2 Applications

Several applications of nanoscale sensing have been demonstrated using scanning NV magnetometry in the last few years. The key advantages of the approaches used there over alternative methods were the combination of excellent spatial resolution and magnetic-field sensitivity. Furthermore, NV magnetometry is noninvasive and yields quantitative information about stray magnetic fields in samples, which is otherwise a challenging or impossible task. These properties, together with the vectorial nature of the NV magnetic-field measurements, facilitate direct comparisons of measurement outcomes with theoretical predictions. In this section, we describe examples of recent experiments that have capitalized on these properties and have demonstrated novel examples of nanoscale magnetic imaging which would have been hard or impossible to perform with alternative techniques.

The first example of scanning NV magnetometry that we shall present here, using bulk diamond probes (Fig. 10.4(b)), was demonstrated by Maletinsky *et al.* (2012). There, a nanoscale magnetic-field image of magnetic domains was obtained and demonstrated an imaging spatial resolution of a few tens of nanometers; the key data for this experiment are shown in Fig. 10.5. For this measurement, a driving microwave source was modulated between two frequencies $\omega_{MW,1} = 2.766\,\text{GHz}$ and $\omega_{MW,2} = 2.786\,\text{GHz}$, corresponding to a symmetric detuning of $\pm 10\,\text{MHz}$ from the NV spin resonance frequency in the absence of a sample (an external offset magnetic field $B_{NV} \approx 52\,\text{G}$ was applied). NV fluorescence counts ($I_{MW,1}$ and $I_{MW,2}$, respectively) were collected in synchrony with the microwave modulation and then normalized to yield the image shown in Fig. 10.5(a). This measurement thus represents a magnetic-field map of constant projection of the magnetic field $B_{NV} = \pm 3\,\text{G}$ onto the NV axis. A conservative estimate of the spatial resolution in this imaging mode can be extracted from the

[5] We note that the aforementioned results of Le Sage *et al.* (2012) were largely the result of a novel, highly efficient photon detection method, while the work of Acosta *et al.* (2009) presents a detailed study of materials optimization.

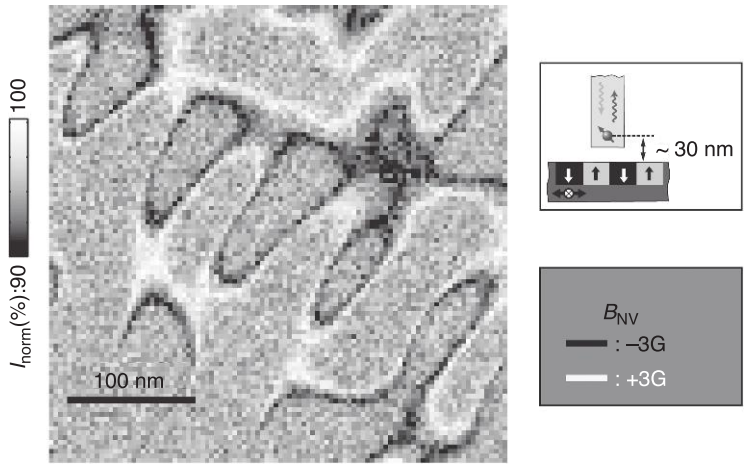

10.5 Example of an application of scanning NV magnetometry: an NV magnetic-field image of tracks on a magnetic hard drive. The image shows normalized data for NV fluorescence recorded at $\omega_{MW,1}$ and $\omega_{MW,2}$ and thereby reveals magnetic field lines corresponding to $B_{NV}=\pm 3\,\mathrm{G}$ (dark and bright contours, respectively). The total image acquisition time was ~11 minutes. The inset to the right illustrates the experimental setting.

smallest observed domain sizes, i.e., approximately 38 nm for the image shown here. Further experiments (Grinolds *et al.*, 2013; Maletinsky *et al.*, 2012) have now reproducibly demonstrated imaging spatial resolutions approaching 10 nm.

The second important ingredient of scanning NV magnetometry is high magnetic-field sensitivity, which allows magnetic imaging to be performed at the single-spin level. This point has recently been demonstrated in an experiment by Grinolds *et al.* (2013), who, using scanning NV magnetometry, performed the first direct magnetic imaging of a single electron spin under ambient conditions. The corresponding experimental setting is illustrated in Fig. 10.6(a): an NV center in a diamond nanopillar (see Section 10.3.1) was scanned in the vicinity of a dilute spin ensemble. This ensemble consisted of individual NV centers in a diamond host crystal. Using NV centers for this experiment was a decisive advantage, since they allowed independent confirmation of single-spin imaging by optical means. To increase magnetic-field sensitivity, the NV magnetometer was operated in an 'AC magnetometry' mode (see Section 10.2.3) by using a 32-pulse XY8 sequence (de Lange *et al.*, 2011) with 40 μs of total evolution time (resulting in $\eta_{ac}=96\,\mathrm{nT\,Hz^{-1/2}}$ for the given photon collection efficiency).

To obtain a time-varying magnetic field from the sample spins, these were periodically inverted, in phase with the AC magnetometry sequence using adiabatic fast passages. Using this sequence, a scanning magnetic image of a single electron spin was obtained, as shown in Fig. 10.6(b). This single-electron-

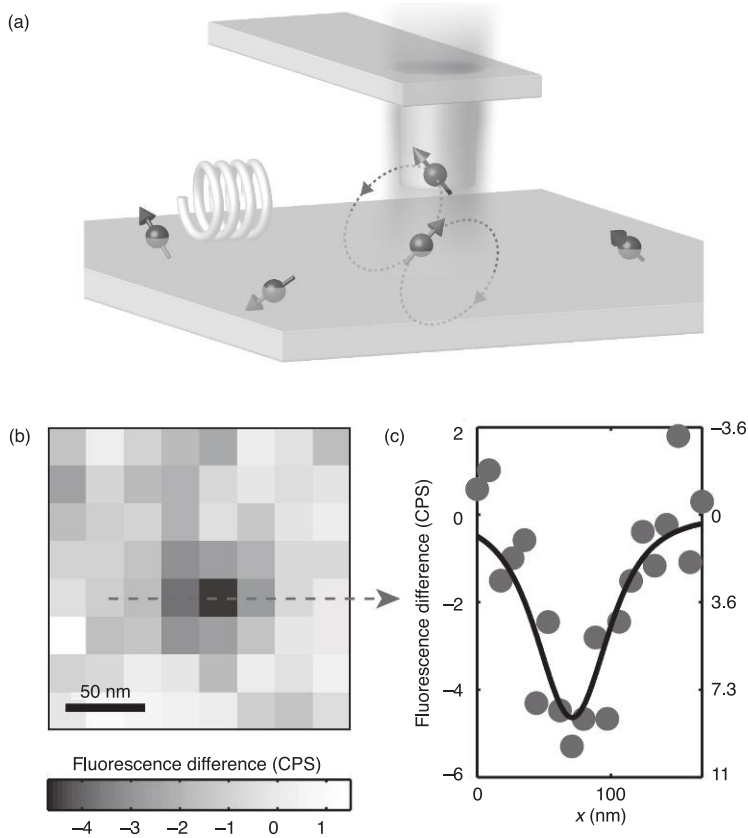

10.6 (a) Schematic illustration of single-spin imaging using a scanning NV magnetometer. Spin addressing is performed optically from above the cantilever using a green laser. Coherent manipulations of the NV spin are performed via a nearby microwave coil. The sensor NV center is scanned over the target spins of interest (here, another diamond crystal with NV centers) to construct magnetic-field images. (b) Magnetic-field image of a target NV spin near the surface of a diamond sample, acquired with the scanning NV magnetometer. While repeatedly running an AC magnetometry pulse sequence (here with a 32-pulse XY8 sequence, with 40 μs of total evolution time), the sensor NV center was scanned laterally over the target, and the magnetometry signal was independently recorded. The signal plotted is a differential spin signal, which depends only on the magnetic interaction of the sensor NV center with the target spin and not on background fluorescence variations (see Grinolds *et al.* (2013) for details). The pronounced drop in fluorescence near the center of the image indicates a detected single-electron spin. (c) An independently recorded magnetometry line scan along the arrow in (b), which has an intensity and width consistent with the recorded image, confirms the single-spin imaging. The measured fluorescence difference was converted to the measured magnetic field using the calibrated field sensitivity and fluorescence rate of the sensor NV center.

spin detection was confirmed by repeating the measurement with a spatial line scan of magnetometry measurements (Fig. 10.6(c)), with a resulting magnetic response that fits well to a vertical separation of ~50 nm between the sensor and target NV centers. The magnetic single-spin measurements presented here were acquired with a total time of 42 min per point, yielding a signal-to-noise ratio of 4.3 – a significant improvement in data acquisition compared with the only single-spin measurement previously achieved (at ultralow temperatures) (Rugar *et al.*, 2004).

We note that, recently, two groups (Mamin *et al.*, 2013; Staudacher *et al.*, 2013) have succeeded in detecting small ensembles of *nuclear* spins external to the diamond host using a single NV magnetometer, albeit in a nonscanning geometry where no imaging was performed. In these experiments, very shallow NV centers (20 and 7 nm, respectively, below the diamond surface) were used for sensing. The nuclei were deposited on the diamond surface in the form of a polymer (PMMA) which could be reversibly applied and removed from the diamond surface to confirm the origin of the signal. Nuclear-spin detection was performed with coherent decoupling sequences very similar to the ones described for electron spin detection ($[XY8]^N$ in the case of Staudacher *et al.* (2013) and an ENDOR-type sequence for Mamin *et al.* (2013)). Given the comparable magnetic-field sensitivity of these experiments (60 nT $Hz^{-1/2}$ in the case of Mamin *et al.* (2013)) to the scanning-probe device described above, it is foreseeable that such detection of a few nuclear spins with NV centers will be extended to (scanning-probe) imaging setups in the near future to achieve the longstanding goal of nano-MRI and molecular-structure resolution using NV magnetometers.

A third notable example of scanning NV magnetometry is the recently achieved nanoscale imaging of magnetic vortex structures (Rondin *et al.*, 2013) (Fig. 10.7). Using scanning NV centers in a diamond nanocrystal, Rondin *et al.* (2013) performed a detailed study of such vortex structures occurring in micron-sized structures of thin permalloy ($Fe_{20}Ni_{80}$) films. The vectorial and quantitative nature of the measurement enabled direct comparisons with theory and micromagnetic simulations and allowed quantitative magnetic studies of the vortices, which would not have been possible otherwise. For example, Rondin *et al.* were able to independently determine the chirality (the direction of the in-plane curling of the magnetization around the vortex) and the polarity (the direction of the vortex magnetization) of their structures. This experiment illustrated that scanning NV magnetometry enables robust comparisons with micromagnetic simulations and therefore offers a powerful tool for fundamental studies in nanomagnetism and, more generally, nanoscience.

10.4 Conclusion and future trends

NV-based magnetometry and, in particular, nanoscale NV magnetometry using single NV centers have seen tremendous progress over the past few years. It is

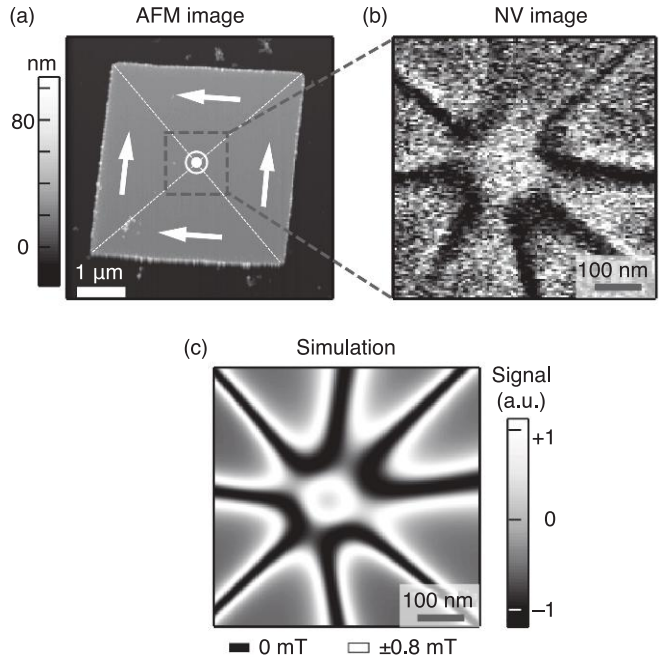

10.7 Example of an application of scanning NV magnetometry: nanoscale image of magnetic vortex structure. (a) AFM image of the magnetic structure investigated: an ~80 nm thick film of permalloy patterned into a square of width 5 μm. After suitable preparation, such structures exhibit magnetic vortices. (b) Scanning NV magnetic image of the core of a magnetic vortex in the device imaged in (a). The magnetometry scheme was similar to the one presented in Fig. 10.5. (c) Nanomagnetic simulation of the experimental situation of (b). The simulation shows excellent agreement with the experimental data and highlights the quantitative nature of NV magnetometry.

remarkable to see how in only five years since the initial discussions of this technique (Balasubramanian *et al.*, 2008; Maze *et al.*, 2008; Taylor *et al.*, 2008), this highly promising, novel sensing technology has evolved from initial proof-of-principle demonstrations to robust implementations of challenging magnetic-imaging tasks. The three examples of nanoscale NV magnetic imaging that we presented in the last section illustrate this impressive progress and the three key performance characteristics of NV magnetometry: nanometric spatial resolution, single-spin sensitivity and quantitative, noninvasive measurements.

Given the ever-growing number of experimental groups working intensively on this topic, it is likely that the next few years will bring further impressive demonstrations of novel nanoscale imaging applications in NV magnetometry. A

grand challenge that is being pursued by many is nanoscale nuclear magnetic resonance imaging, with the ultimate goal of performing structural determination of macromolecules on a single-molecule basis (Sidles, 1991). With the very recently demonstrated magnetic detection of small ensembles of nuclear spins external to the diamond host (Mamin *et al.*, 2013; Staudacher *et al.*, 2013), together with the recent progress in scanning NV magnetometry presented here, this goal appears realistic and could be achieved within the next few years.

Another exciting avenue is the application of scanning NV magnetometry to outstanding problems in solid-state physics, and to the study of exotic states of matter such as topological insulators (Hasan and Moore, 2011) and strongly correlated electron systems (Coleman, 2003). Such experiments would require cryogenic operation of a scanning NV magnetometer, and such extensions thus seem highly attractive. Of course, several technical obstacles (such as promoting 'NV-on-a-tip' approaches to low temperatures and combining high-performance AFM and optical microscopy with cryogenic operation) still need to be addressed, but state-of-the-art experimental technologies make this goal appear within reach.

Further advances can also be expected by exploiting the quantum nature of NV single-spin sensors for even more efficient sensing applications. These include harnessing entanglement or quantum correlations in the time domain for magnetometry beyond the (classical) shot-noise limit. Proof-of-concept demonstrations of such approaches have already been performed (Nusran *et al.*, 2012; Waldherr *et al.*, 2012), but combining these with 'real-life' sensing applications to bring a significant advantage to nanoscale sensing and imaging applications is still outstanding.

Finally, we note that the rich physical properties of the NV center lend themselves to nanoscale sensing applications that go far beyond magnetometry. For example, the NV center is a stable single-photon emitter and a nanoscale light source. With these combined properties, NV centers can be employed for nanoscale optical imaging with a resolution far exceeding the optical diffraction limit and possibly even overcoming the photon shot noise ever present in optical imaging (Michaelis *et al.*, 2000). Furthermore, the NV center has recently been shown to be sensitive to electric fields (Dolde *et al.*, 2011) and temperature (Acosta *et al.*, 2010b) if operated in a suitable regime – two further physical quantities that are hard to detect at the nanoscale and therefore offer unique opportunities for nanoscale imaging and sensing with NV centers.

10.5 References

Acosta, V. M., Bauch, E., Ledbetter, M. P., Santori, C., Fu, K.-M. C., *et al.* (2009) 'Diamonds with a high density of nitrogen–vacancy centers for magnetometry applications'. *Physical Review B* **80**, 115202.

Acosta, V. M., Bauch, E., Jarmola, A., Zipp, L. J., Ledbetter, M. P. and Budker, D. (2010a) 'Broadband magnetometry by infrared-absorption detection of nitrogen–vacancy ensembles in diamond'. *Applied Physics Letters* **97**, 174104.

Acosta, V. M., Bauch, E., Ledbetter, M. P., Waxman, A., Bouchard, L.-S. and Budker, D. (2010b) 'Temperature dependence of the nitrogen–vacancy magnetic resonance in diamond'. *Physical Review Letters* **104**, 070801.

Babinec, T. M., Hausmann, B. J. M., Khan, M., Zhang, Y., Maze, J. R., *et al.* (2010) 'A diamond nanowire single-photon source'. *Nature Nanotechnology* **5**, 195.

Balasubramanian, G., Chan, I., Kolesov, R., Al-Hmoud, M., Tisler, J., *et al.* (2008) 'Nanoscale imaging magnetometry with diamond spins under ambient conditions.' *Nature* **455**, 648.

Balasubramanian, G., Neumann, P., Twitchen, D., Markham, M., Kolesov, R., *et al.* (2009) 'Ultralong spin coherence time in isotopically engineered diamond.' *Nature Materials* **8**, 383.

Baudenbacher, F., Fong, L. E., Holzer, J. R. and Radparvar, M. (2003) 'Monolithic low-transition-temperature superconducting magnetometers for high resolution imaging magnetic fields of room temperature samples'. *Applied Physics Letters* **82**, 3487.

Bouchard, L.-S., Acosta, V. M., Bauch, E. and Budker, D. (2011) 'Detection of the Meissner effect with a diamond magnetometer'. *New Journal of Physics* **13**, 025017.

Budker, D. and Romalis, M. (2007) 'Optical magnetometry'. *Nature Physics* **3**, 227.

Bundy, F. P., Hall, H. T., Strong, H. M. and Wentorf, R. H. (1955) 'Man-made diamond'. *Nature* **176**, 51.

Carr, H. Y. and Purcell, E. M. (1954) 'Effects of diffusion on free precession in nuclear magnetic resonance experiments'. *Physical Review* **94**, 630.

Chernobrod, B. M. and Berman, G. P. (2005) 'Spin microscope based on optically detected magnetic resonance'. *Journal of Applied Physics* **97**, 014903.

Coleman, P. (2003) 'Many body physics: Unfinished revolution'. *Annales Henri Poincare* **4**, 559.

Cuche, A., Drezet, A., Sonnefraud, Y., Faklaris, O., Treussart, F., *et al.* (2009) 'Near-field optical microscopy with a nanodiamond-based single-photon tip'. *Optics Express* **17**, 19969.

de Lange, G., Ristè, D., Dobrovitski, V. V. and Hanson, R. (2011) 'Single-spin magnetometry with multipulse sensing sequences'. *Physical Review Letters* **106**, 080802.

Degen, C. L. (2008) 'Scanning magnetic field microscope with a diamond single-spin sensor'. *Applied Physics Letters* **92**, 243111.

Degen, C. L., Poggio, M., Mamin, H. J., Rettner, C. T. and Rugar, D. (2009) 'Nanoscale magnetic resonance imaging'. *Proceedings of the National Academy of Sciences of the United States of America* **106**, 1313.

Dolde, F., Fedder, H., Doherty, M. W., Nöbauer, T., Rempp, F., *et al.* (2011) 'Electric-field sensing using single diamond spins'. *Nature Physics* **7**, 459.

Dong, S., Li, J.-F. and Viehland, D. (2003) 'Ultrahigh magnetic field sensitivity in laminates of terfenol-d and $PbMg_{1/3}Nb_{2/3}O_3PbTiO_3$ crystals'. *Applied Physics Letters* **83**, 2265.

Dréau, A., Lesik, M., Rondin, L., Spinicelli, P., Arcizet, O., *et al.* (2011) 'Avoiding power broadening in optically detected magnetic resonance of single NV defects for enhanced CD magnetic field sensitivity'. *Physical Review B* **84**, 195204.

Dumeige, Y., Chipaux, M., Jacques, V., Treussart, F., Roch, J.-F., *et al.* (2013) 'Magnetometry with nitrogen–vacancy ensembles in diamond based on infrared absorption in a doubly resonant optical cavity'. *Physical Review B* **87**, 155202.

Dutt, M., Childress, L., Jiang, L., Togan, E., Maze, J., *et al.* (2007) 'Quantum register based on individual electronic and nuclear spin qubits in diamond'. *Science* **316**, 1312.

Faley, M. I., Poppe, U., Urban, K., Paulson, D. N. and Fagaly, R. L. (2006) 'A new generation of the HTS multilayer DC-SQUID magnetometers and gradiometers'. *Journal of Physics: Conference Series* **43**, 1199.

Finkler, A., Segev, Y., Myasoedov, Y., Rappaport, M. L., Ne'eman, L., *et al.* (2010) 'Self-aligned nanoscale SQUID on a tip'. *Nano Letters* **10**, 1046.

Fuchs, G. D., Dobrovitski, V. V., Toyli, D. M., Heremans, F. J. and Awschalom, D. D. (2009) 'Gigahertz dynamics of a strongly driven single quantum spin'. *Science* **326**, 1520.

Grinolds, M. S., Maletinsky, P., Hong, S., Lukin, M. D., Walsworth, R. L. and Yacoby, A. (2011) 'Quantum control of proximal spins using nanoscale magnetic resonance imaging'. *Nature Physics* **7**, 687.

Grinolds, M. S., Hong, S., Maletinsky, P., Luan, L., Lukin, M. D., *et al.* (2013) 'Nanoscale magnetic imaging of a single electron spin under ambient conditions'. *Nature Physics* **9**, 215.

Gruber, A., Drabenstedt, A., Tietz, C., Fleury, L., Wrachtrup, J. and Borczyskowski, C. (1997) 'Scanning confocal optical microscopy and magnetic resonance on single defect centers'. *Science* **276**, 2012.

Hahn, E. (1950) 'Spin echoes'. *Physical Review* **80**, 580.

Hall, L. T., Hill, C. D., Cole, J. H., Städler, B., Caruso, F., *et al.* (2010) 'Monitoring ion-channel function in real time through quantum decoherence'. *Proceedings of the National Academy of Sciences* **107**, 18777.

Hasan, M. Z. and Moore, J. E. (2011) 'Three-dimensional topological insulators'. *Annual Review of Condensed Matter Physics* **2**, 55.

Hatridge, M., Vijay, R., Slichter, D. H., Clarke, J. and Siddiqi, I. (2011) 'Dispersive magnetometry with a quantum limited SQUID parametric amplifier'. *Physical Review B* **83**, 134501.

Hell, S. W. (2007) 'Far field optical nanoscopy'. *Science* **316**, 1153.

Ishikawa, T., Fu, K.-M. C., Santori, C., Acosta, V. M., Beausoleil, R. G., *et al.* (2012) 'Optical and spin coherence properties of nitrogen–vacancy centers placed in a 100 nm thick isotopically purified diamond layer'. *Nano Letters* **12**, 2083.

Itano, W. M., Bergquist, J. C., Bollinger, J. J., Gilligan, J. M., Heinzen, D. J., *et al.* (1993) 'Quantum projection noise: Population fluctuations in two-level systems'. *Physical Review A* **47**, 3554.

Jelezko, F. and Wrachtrup, J. (2006) 'Single defect centres in diamond: A review'. *Physica Status Solidi A* **203**, 3207.

Kalish, R., Uzan-Saguy, C., Philosoph, B., Richter, V., Lagrange, J. P., *et al.* (1997) 'Nitrogen doping of diamond by ion implantation'. *Diamond and Related Materials* **6**, 516.

Kirtley, J. R., Ketchen, M. B., Stawiasz, K. G., Sun, J. Z., Gallagher, W. J., *et al.* (1995) 'High-resolution scanning SQUID microscope'. *Applied Physics Letters* **66**, 1138.

Kominis, I. K., Kornack, T. W., Allred, J. C. and Romalis, M. V. (2003) 'A subfemtotesla multichannel atomic magnetometer'. *Nature* **422**, 596.

Kotler, S., Akerman, N., Glickman, Y., Keselman, A. and Ozeri, R. (2011) 'Single-ion quantum lock-in amplifier'. *Nature* **473**, 61.

Kuhn, S., Hettich, C., Schmitt, C., Poizat, J. and Sandoghdar, V. (2001) 'Diamond colour centres as a nanoscopic light source for scanning near-field optical microscopy'. *Journal of Microscopy* **202**, 2.

Le Sage, D., Pham, L. M., Bar-Gill, N., Belthangady, C., Lukin, M. D., *et al.* (2012) 'Efficient photon detection from color centers in a diamond optical waveguide'. *Physical Review B* **85**, 121202.

Loretz, M., Rosskopf, T. and Degen, C. L. (2013) 'Radio-frequency magnetometry using a single electron spin'. *Physical Review Letters* **110**, 017602.

Mackenzie, A. P. and Maeno, Y. (2003) 'The superconductivity of Sr_2RuO_4 and the physics of spin-triplet pairing'. *Reviews of Modern Physics* **75**, 657.

Maletinsky, P., Hong, S., Grinolds, M., Hausmann, B., Lukin, M. D., *et al.* (2012) 'A robust scanning diamond sensor for nanoscale imaging with single nitrogen vacancy centers'. *Nature Nanotechnology* **7**, 320.

Mamin, H. J., Kim, M., Sherwood, M. H., Rettner, C. T., Ohno, K., *et al.* (2013) 'Nanoscale nuclear magnetic resonance with a nitrogen–vacancy spin sensor'. *Science* **339**, 557.

Manson, N. B., Harrison, J. P. and Sellars, M. J. (2006) 'Nitrogen–vacancy center in diamond: Model of the electronic structure and associated dynamics'. *Physical Review B* **74**, 104303.

Markham, M., Dodson, J., Scarsbrook, G., Twitchen, D., Balasubramanian, G., *et al.* (2011) 'CVD diamond for spintronics'. *Diamond and Related Materials* **20**, 134.

Maurer, P. C., Maze, J. R., Stanwix, P. L., Jiang, L., Gorshkov, A. V., *et al.* (2010) 'Far-field optical imaging and manipulation of individual spins with nanoscale resolution'. *Nature Physics* **6**, 912.

Maze, J. R., Stanwix, P. L., Hodges, J. S., Hong, S., Taylor, J. M., *et al.* (2008) 'Nanoscale magnetic sensing with an individual electronic spin in diamond'. *Nature* **455**, 644.

Meiboom, S. and Gill, D. (1958) 'Modified spin-echo method for measuring nuclear relaxation times'. *Review of Scientific Instruments* **29**, 688.

Michaelis, J., Hettich, C., Mlynek, J. and Sandoghdar, V. (2000) 'Optical microscopy using a single-molecule light source'. *Nature* **405**, 325.

Mita, Y. (1996) 'Change of absorption spectra in type-Ib diamond with heavy neutron irradiation'. *Physical Review B* **53**, 11360.

Neumann, P., Mizuochi, N., Rempp, F., Hemmer, P., Watanabe, H., *et al.* (2008) 'Multipartite entanglement among single spins in diamond'. *Science* **320**, 1326.

Nowack, K. C., Spanton, E. M., Baenninger, M., König, M., Kirtley, J. R., *et al.* (2013) 'Imaging currents in HgTe quantum wells in the quantum spin Hall regime'. *Nature Materials* **12**, 787.

Nusran, N. M., Momeen, M. U. and Dutt, M. V. G. (2012) 'High-dynamic-range magnetometry with a single electronic spin in diamond'. *Nature Nanotechnology* **7**, 109.

Ohno, K., Heremans, F. J., Bassett, L. C., Myers, B. A., Toyli, D. M., *et al.* (2012) 'Engineering shallow spins in diamond with nitrogen delta-doping'. *Applied Physics Letters* **101**, 082413.

Oral, A., Bending, S. J. and Henini, M. (1996) 'Real-time scanning Hall probe microscopy'. *Applied Physics Letters* **69**, 1324.

Oral, A., Kaval, A., Dede, M., Masuda, H., Okamoto, A., *et al.* (2002). 'Room-temperature scanning Hall probe microscope (RT-SHPM) imaging of garnet films using new high-performance InSb sensors'. *IEEE Transactions on Magnetics* **38**, 2438.

Pezzagna, S., Rogalla, D., Wildanger, D., Meijer, J. and Zaitsev, A. (2011) 'Creation and nature of optical centres in diamond for single-photon emission – overview and critical remarks'. *New Journal of Physics* **13**, 035024.

Pham, L. M., Sage, D. L., Stanwix, P. L., Yeung, T. K., Glenn, D., *et al.* (2011) 'Magnetic field imaging with nitrogen–vacancy ensembles'. *New Journal of Physics* **13**, 045021.

Romalis, M. (2008) 'Virtues of diamond defects'. *Nature* **455**, 606.

Rondin, L., Tetienne, J.-P., Spinicelli, P., Savio, C. D., Karrai, K., *et al.* (2012) 'Nanoscale magnetic field mapping with a single spin scanning probe magnetometer'. *Applied Physics Letters* **100**, 153118.

Rondin, L., Tetienne, J.-P., Rohart, S., Thiaville, A., Hingant, T., *et al.* (2013) 'Stray-field imaging of magnetic vortices with a single diamond spin'. *Nature Communications* **4**, 2279.

Rugar, D., Budakian, R., Mamin, H. J. and Chui, B. W. (2004) 'Single spin detection by magnetic resonance force microscopy'. *Nature* **430**, 329.

Sandhu, A., Okamoto, A., Shibasaki, I. and Oral, A. (2004a) 'Nano and micro Hall-effect sensors for room-temperature scanning Hall probe microscopy'. *Microelectronic Engineering* **73**, 524.

Sandhu, A., Sanbonsugi, H., Shibasaki, I., Abe, M. and Handa, H. (2004b) 'High sensitivity InSb ultra-thin film micro-Hall sensors for bioscreening applications'. *Japanese Journal of Applied Physics* **43**, L868.

Schoenfeld, R. S. and Harneit, W. (2011) 'Real time magnetic field sensing and imaging using a single spin in diamond'. *Physical Review Letters* **106**, 030802.

Sekatskii, S. and Letokhov, V. (1996) 'Nanometer-resolution scanning optical microscope with resonance excitation of the fluorescence of the samples from a single-atom excited center'. *JETP Letters* **63**, 319.

Shah, V., Knappe, S., Schwindt, P. D. D. and Kitching, J. (2007) 'Subpicotesla atomic magnetometry with a microfabricated vapour cell'. *Nature Photonics* **1**, 649.

Sidles, J. A. (1991) 'Noninductive detection of single-proton magnetic resonance'. *Applied Physics Letters* **58**, 2854.

Staudacher, T., Shi, F., Pezzagna, S., Meijer, J., Du, J., *et al.* (2013) 'Nuclear magnetic resonance spectroscopy on a (5-nanometer)^3 sample volume'. *Science* **339**, 561.

Tallaire, A., Collins, A. T., Charles, D., Achard, J., Sussmann, R., *et al.* (2006) 'Characterisation of high-quality thick single-crystal diamond grown by CVD with a low nitrogen addition'. *Diamond and Related Materials* **15**, 1700.

Taylor, J., Cappellaro, P., Childress, L., Jiang, L., Budker, D., *et al.* (2008) 'High-sensitivity diamond magnetometer with nanoscale resolution'. *Nature Physics* **4**, 810.

Vengalattore, M., Higbie, J. M., Leslie, S. R., Guzman, J., Sadler, L. E. and Stamper-Kurn, D. M. (2007) 'High-resolution magnetometry with a spinor Bose–Einstein condensate'. *Physical Review Letters* **98**, 200801.

Waldherr, G., Beck, J., Neumann, P., Said, R. S., Nitsche, M., *et al.* (2012) 'High-dynamic-range magnetometry with a single nuclear spin in diamond'. *Nature Nanotechnology* **7**, 105.

Wildermuth, S., Hofferberth, S., Lesanovsky, I., Groth, S., Kruger, P., *et al.* (2006) 'Sensing electric and magnetic fields with Bose–Einstein condensates'. *Applied Physics Letters* **88**, 264103.

Wrachtrup, J. and Gruber, A. (1998) 'Projection noise in the optically detected magnetic resonance signal of a single electron spin'. *Solid State Nuclear Magnetic Resonance* **11**, 59.

11

Hybridization of quantum systems: coupling nitrogen–vacancy (NV) centers in diamond to superconducting circuits

R. AMSÜSS, Technische Universität Wien, Austria and
S. SAITO and W. J. MUNRO, NTT Corporation, Japan

DOI: 10.1533/9780857096685.2.264

Abstract: The negatively charged nitrogen–vacancy (NV^-) center in diamond has gained a lot of attention owing to its unique properties. Applications have been found in the fields of spintronics, quantum metrology, quantum information processing and quantum computation. The development of moderate-scale quantum devices requires stable quantum bits in which we can process, store and transport quantum information. Superconducting circuits are well known for their processing ability, while the electron spins of nitrogen–vacancy centers in diamond are a natural memory resource. Here we discuss strong coupling and coherent exchange of a single quantum of energy between these hybrid systems, and potential quantum memory operations.

Key words: hybrid quantum systems, superconducting circuits, quantum memory.

11.1 Introduction

The discovery of quantum mechanics has been one of the most important developments of the twentieth century, with far-reaching consequences. Quantum mechanics consists of a set of principles that describe physical reality at the atomic level of matter. These principles have been used to develop much of today's advanced technology, including, for example, microprocessors. Furthermore, it proposes radically new ways to process, store, manipulate and transmit information (Feynman, 1982; Nielsen and Chuang, 2000). This new paradigm is known as quantum information processing, a field where intrinsic quantum mechanical features such as the superposition principle, entanglement and indistinguishability of particles play a central role. Over the last decade there has been a huge worldwide effort to 'tame' this quantum world, allowing it to be transformed into quantum technology. Many early proposals pointed out the tremendous advantages of quantum effects for computation (Deutsch and Jozsa, 1992; Shor, 1997), communication (Bennett and Brassard, 1984) and metrology (Kimble *et al.*, 2001), and for simulation (Feynman, 1982) of quantum systems by another programmable quantum mechanical device. This triggered an extremely fast theoretical and experimental development of this field of physics (Ladd *et al.*,

© 2014 Elsevier Ltd

2010) and future technology (Spiller and Munro, 2006) but soon also brought to light clear criteria that quantum systems need to fulfill to outperform their classical counterparts (DiVincenzo, 2000).

Decoherence has, in a sense, become the practical challenge that one needs to overcome. Every quantum object is in contact with an environment of some kind, meaning that the system interacts with a *bath* that is usually not under one's control. The nonunitary evolution of the system into the bath's degrees of freedom constitutes a leakage mechanism. Information is lost from the system into the bath. An interesting observation when looking at different quantum objects is that some naturally possess a higher degree of isolation, whereas others are more easily coupled to external degrees of freedom. By sufficiently isolating a quantum system from its environment, the effects of decoherence tend to be reduced, but with the unfortunate consequence that it becomes more difficult to interact with the target quantum system and control it coherently. This ambivalent nature of decoherence seems to be a major obstacle that must be overcome before future quantum technologies can be developed.

It has become clear that no single system is likely to have all the attributes we require for quantum information processing, that is, excellent processing abilities, long storage times and the ability to communicate over moderate distances. The observations that no single system meets all of DiVincenzo's criteria (DiVincenzo, 2000) have led to the concept of hybrid quantum systems (Kimble, 2008; Xiang *et al.*, 2012). This concept is based on the combination of different quantum systems with complementary properties, where one wishes to exploit the advantageous properties without inheriting (all) the drawbacks of the separated systems. For instance, a desirable combination would bring together systems suitable for long-term storage of quantum information with those that allow good processing capabilities (fast quantum gates). A mediating element would be used to transfer the information from one to the other with low loss and high fidelity. One could also envisage a situation in which either the processor or the memory could be interfaced with an optical link. This would allow distributed processing of quantum information.

In this chapter we are going to consider the first two tasks, of interfacing a quantum processor with a quantum memory. Since there is a wealth of appropriate physical systems for either of the two tasks, it is almost impossible to keep track of all proposals and realizations in this rapidly developing and rather interdisciplinary field. One very promising class of quantum systems is mesoscopic, engineered systems, in contrast to microscopic, natural ones such as atoms, ions, molecules or photons. These solid-state systems typically feature properties that can be chosen on purpose, have better scaling behavior and often rely on fabrication techniques that allow on-chip integration and easy reproduction. Among these artificial qubits, superconducting qubits based on Josephson junctions (Nakamura *et al.*, 1999; Mooij *et al.*, 1999) have been demonstrated to be an extremely robust and powerful technology, possessing all attributes required

for a fast quantum processor (DiCarlo *et al.*, 2009; Neeley *et al.*, 2010). In combination with the generally better coherence properties of electron spins, an all-solid-state hybrid quantum system can be formed. NV^- centers in diamond are one promising candidate here (Marcos *et al.*, 2010; Twamley and Barrett, 2010).

The prototype circuit 'QED' setup employs microwave photons in centimeter-scale, single-mode resonant structures to couple to superconducting qubits. These planar superconducting microwave resonators are exceptionally low-loss devices and confine the electromagnetic field into an extremely small mode volume. The latter leads to greatly enhanced field strengths, which ease the coupling to electric or magnetic degrees of freedom. It was not, however, thought to be enough to be able to couple to single atoms or molecules. The work by Verdu *et al.* (2009), Imamoglu (2009) and Wesenberg *et al.* (2009) illustrated how large ensembles of atoms or electron spins can be coupled with a 'cQED' using magnetic interactions. The cQED couples to a mode of the ensemble where a collective enhancement is seen. For an ensemble of N electron spins, the collective coupling enhancement can be as great as $\sqrt{N}$ times the coupling between a superconducting circuit and a single electron spin. Recent demonstrations have shown how strong coupling and coherent exchange of information have been achieved (Schuster *et al.*, 2010; Kubo *et al.*, 2010; Amsüss *et al.*, 2011; Kubo *et al.*, 2011; Zhu *et al.*, 2011; Kubo *et al.*, 2012; Saito *et al.*, 2013).

In this chapter, we will discuss the coupling of superconducting circuits to ensembles of NV^- centers (Amsüss *et al.*, 2011; Kubo *et al.*, 2011; Zhu *et al.*, 2011). We begin with a brief description of NV^- centers, followed by an introduction to superconducting circuits. Once the individual hybrid-system components have been discussed, we explain the coupling between them and illustrate how the strong-coupling regime can be reached (Marcos *et al.*, 2010; Twamley and Barrett, 2010). We finish with a review of recent work on coherent transfer of information between the two systems, and on the storage of a quantum state of the superconducting circuit in the ensemble and its subsequent retrieval (Kubo *et al.*, 2011; Zhu *et al.*, 2011).

11.2 Spin ensembles

The NV^- center is a point defect in diamond that consists of a substitutional nitrogen atom adjacent to a carbon vacancy (depicted in Fig. 11.1). It has a trigonal symmetry with the threefold axis oriented along $\langle 111 \rangle$. The negatively charged NV^- center is formed by six electrons: five electrons stem from the three dangling bonds due to the vacancy and the two valence electrons from the nitrogen atom, and one extra electron is captured from the crystal. There are two main energy manifolds of interest for quantum information processing. The lowest (the ^3A manifold) is a triplet ground state, which shows a fine structure (zero-field splitting, or ZFS) due to spin–spin interactions (Acosta *et al.*, 2010). The energy levels in this manifold have transition frequencies of a few gigahertz (microwave

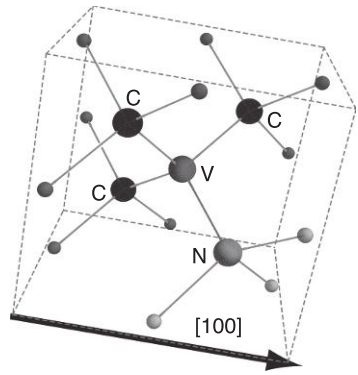

11.1 Schematic illustration showing the structure of an NV^- center in the diamond lattice. The large sphere in the center is the vacancy, and the large sphere at the bottom right is the nitrogen atom. The dark black spheres are the three nearest-neighbor carbon atoms. The NV^- axis can be along four equivalent ⟨111⟩ directions.

frequencies). The second manifold (the ^3E manifold) has quite a complicated energy level structure, but it is important as the transition frequency between this manifold and the lower ^3A manifold is in the optical regime. In fact, there is a zero-phonon line (ZPL) at 637 nm. For the remaining part of this chapter, it is the ^3A manifold that we will focus on.

11.2.1 Preparation of a high-density spin ensemble

In order to take advantage of the collective enhancement of the coupling strength mentioned earlier, high-density spin ensembles are needed. The challenge is to form as many NV^- centers as possible with a minimal amount of substitutional nitrogen atoms and a sufficient number of crystal vacancies. The issue is that any defects that will not convert to NV^- centers introduce new decoherence channels or lead to inhomogeneities in the NV^- center's properties. P1 centers (single substitutional nitrogen atoms) can, for instance, couple via dipole–dipole interactions to the NV^- centers, leading to a dephasing spin bath for the NV^- electron spin. Furthermore, a large number of residual point defects due to vacancies can result in appreciable lattice strain (high local electric fields), so that the strain parameters become large and vary between different NV^- centers, causing inhomogeneous broadening.

Generally, there are two main techniques for creating a dense NV^- spin ensemble in diamond; the first is to implant nitrogen into pure diamond (Kalish *et al.*, 1997), while the second is to create vacancies in nitrogen-rich diamond (Nishida *et al.*, 1989) and then to anneal the sample to bond migrating vacancies to substitutional nitrogen atoms. As we will require a high concentration of NV^- centers, it is this

second approach we will focus on here. Over the years, many different methods and recipes have been reported, aiming at optimizing the conversion from P1 centers to NV^- centers, including electron, neutron, proton and ion irradiation. Here we will briefly describe two techniques that have been used to form samples. Both of these techniques used synthetic high-pressure high-temperature (HPHT) type Ib single-crystal diamonds with a (001) surface orientation and a nominal nitrogen impurity concentration of approximately 100 ppm.

The group at the Institute for Atomic and Subatomic Physics in Vienna (Amsüss *et al.*, 2011) used neutron irradiation from a TRIGA Mark II reactor with a fluence of approximately $5 \times 10^{17}\,\mathrm{cm}^{-2}$. The samples were placed in the reactor for 50 h and then annealed for 4 h at 900 °C in order to support vacancy mobility and heal lattice damage. This led to an NV^- center concentration of roughly 6 ppm ($1.02 \times 10^{18}\,\mathrm{cm}^{-3}$), uniform throughout the crystal. The second approach, used by NTT's basic-research-laboratory group (Zhu *et al.*, 2011), was based on $^{12}C^{2+}$ ion implantation (a dose condition of $3 \times 10^{13}\,\mathrm{cm}^{-2}$) at 700 keV in a high vacuum followed by annealing at 900 °C for 3 h. This generated on the order of 1.1×10^{18} vacancies/cm^3 over a depth of only 0.7 μm.

11.2.2 Hamiltonian ensemble

It is now time to turn our attention to the mathematical description of the ensemble. The ground state of a single NV^- center from the ^3A manifold can be written as (Neumann *et al.*, 2009)

$$H_{\mathrm{NV}} = H_{\mathrm{ZFS}} + H_{\mathrm{Zeeman}} + H_{\mathrm{HF}} + H_{\mathrm{N}}$$

where H_{ZFS} represents the zero-field splitting (ZFS), H_{Zeeman} the Zeeman splitting, H_{HF} the hyperfine interaction between the electron spin **S** of the NV^- center and a nuclear spin species **I**, and H_{N} the quadrupole interaction if required. The NV^- center consists of two unpaired electrons, and therefore spin–spin interactions and strain fields will lift the degeneracy of the ground state. Such an effect is called the zero-field splitting, which we can represent by

$$H_{\mathrm{ZFS}} = h[D(S_z^2 - \tfrac{1}{3}S^2) + E(S_x^2 - S_y^2)]$$

where S_z, S_x, S_y are the usual spin-1 operators and the fine-structure constants are D and E. D is called the zero-field splitting, and E is called the strain splitting. Typically an NV^- center has $D = 2.87$ GHz, with E approximately 10 MHz or less. The zero-field and strain splittings are always present in the NV^- center.

The Zeeman splitting H_{Zeeman} describes the splitting of the ground spin states due to an applied external static magnetic field and can be written as

$$H_{\mathrm{Zeeman}} = h\, g_{\mathrm{e}}\, \mu_{\mathrm{B}}(B_x S_x + B_y S_y + B_z S_z)$$

where $g_{\mathrm{e}}\mu_{\mathrm{B}} \approx 28$ MHz/mT. The Zeeman term splits the $m_s = (-1, 1)$ states by $2g_{\mathrm{e}}\mu_{\mathrm{B}}B_z$, which can be of the order of a few hundred megahertz for a small field of

10 mT. There is also a Zeeman level splitting of the nuclear energy states, which, however, can generally be ignored owing to the much smaller magnetic moment of nuclei.

The Hamiltonian $H_{HF}=hA_{\|}S_zI_z+hA_{\perp}(S_xI_x+S_yI_y)$ represents the hyperfine interaction between a single NV^- center electron spin and an N nuclear spin, where $A_{\|}$ is the axially symmetric parameter and $A_{\perp}$ the nonaxial parameter. As the natural abundance of the nitrogen isotope ^{14}N is 99.6%, we will consider this isotope initially. In this case $A_{\|}=-2.1$ MHz, with $A_{\perp}=-2.7$ MHz. Furthermore, as ^{14}N has a nuclear spin quantum number $I=1$, it will have a quadrupole interaction given by $H_N=hP((a/2)I_z^2-I(I+1))$ with moment $P=-5.04$ MHz.

We can simplify the overall Hamiltonian further once we notice the natural energy level differences between the electron and nuclear spins. Furthermore, as our external magnetic field is along the z-axis, our single NV^- center reduces to

$$H_{NV}=h[DS_Z^2+E(S_x^2-S_y^2)]+hg_e\mu_B B_zS_z+hA_{\|}S_ZI_Z+\tfrac{3}{2}hPI_Z^2$$

As we apply an increasing external magnetic field B_z, the $|\pm1\rangle$ states split (Fig. 11.2), and so the effect of the strain splitting terms becomes negligible.

Next, we cannot measure energy levels directly, but only transitions between them. Whether or not a transition between two levels is allowed is given by the usual selection rules $\Delta m_s=\pm1$ and $\Delta m_I=0$ (for low fields, $\Delta m_s=\pm2$ can be allowed). In the case here with $E=0$, the allowed dipole transitions are $|0\rangle \Leftrightarrow |\pm1\rangle$.

So far, we have considered a single NV^- center, but the extension to an ensemble is straightforward. In such a case we can simply write our ensemble Hamiltonian as

$$H_{ens}=h\Sigma_i DS_{z,i}^2+E_i(S_{x,i}^2-S_{y,i}^2)+g_e\mu_B B_zS_{z,i}+A_{\|}S_{z,i}I_{z,i}$$

We have dropped the nuclear spin terms, as we want to focus our attention primarily on interactions of the electron spin ensemble with superconducting

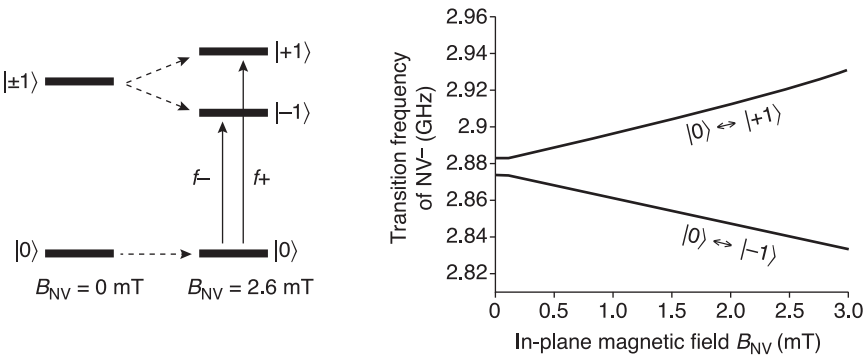

11.2 Transition frequency of an NV^- spin as a function of an in-plane magnetic field B_{NV} [100]

circuits. Furthermore, under an appropriate external magnetic field (such that E can be neglected), and noting that the superconducting circuits are only going to exchange a few excitations with an ensemble containing a large number of centers, we can approximate each transition of the NV^- centers by a harmonic oscillator (Holstein and Primakoff, 1940). In such a case we can write

$$H_{\text{ens}} = h\Sigma_i (D + g_e \mu_B B_z + A_{\parallel} I_{z,i})\, a^{\uparrow}_{+i} a_{+i} + (D - g_e \mu_B B_z - A_{\parallel} I_{z,i})\, a^{\uparrow}_{-i} a_{-i},$$

where $a^{\uparrow}_{+i}$, a_{+i} are the creation and destruction operators for the $|0\rangle \Leftrightarrow |+1\rangle$ transition, and $a^{\uparrow}_{-i}$, a_{-i} are those for the $|0\rangle \Leftrightarrow |-1\rangle$ transition. This simplification allows us to represent our ensemble as a simple sum of harmonic oscillators, one centered at a mean frequency $D + g_e \mu_B B_z$ and the other at $D - g_e \mu_B B_z$. We can also approximate the sum of harmonic oscillators as a single harmonic oscillator in the low-excitation limit such that

$$H_{\text{ens}} = h(D + g_e \mu_B B_z + A_{\parallel} I_z)\, a^{\uparrow}_{+} a_{+} + h\,(D - g_e \mu_B B_z - A_{\parallel} I_z)\, a^{\uparrow}_{-} a_{-}$$

This clearly shows that in the presence of a magnetic field, we would expect to observe two main resonances.

11.2.3 Coherence properties of the spin ensemble

We now need to turn our attention to the coherence properties, as these will be critical to our later investigation of hybridization with superconducting circuits and the potential for them to enter the strong-coupling regime. First let us begin with the longitudinal spin relaxation/thermalization time T_1 of the ensemble, noting that such samples are going to be in a dilution refrigerator operating at 10–50 mK. Jarmola *et al.* (2012) found that the time T_1 of ensembles at low temperature is temperature-independent and mainly determined by cross-relaxation with neighboring spins. For the typical NV^- densities needed in the hybrid devices described, the measured relaxation times T_1 were greater than or equal to 45 s (Amsüss *et al.*, 2011; Jarmola *et al.*, 2012). Next, the dephasing time T_2 (and also T_2^*) is highly dependent on the type of diamond sample used and, especially, depends on impurities in the local environment of the NV^- centers (e.g., P1 centers) (Abragam and Bleaney, 1970). The lower the concentration of these impurities, the better is the phase coherence time.

However, in the preparation of an ensemble in our work, we used synthetic HPHT type Ib single-crystal diamonds with a nominal nitrogen impurity concentration of 100 ppm. Consequently, our NV^- centers were surrounded by a nitrogen-based spin bath. This means that T_2^* is likely to be much shorter than 1 μs. In fact, we know that the inhomogeneous broadening due to random magnetic fields caused by nitrogen (P1) and other centers is likely to be in the region of 1–10 MHz. The strain field E (an exchange-like term between the $|\pm 1\rangle$ levels) also varies from NV^- center to NV^- center but generally has a mean value less than 10 MHz. Under a magnetic field of 2 mT or more, the energy splitting between the

$|\pm 1\rangle$ levels is at least 100 MHz, and so the strain should be operating in a dispersive-like limit and hence have a minimal effect. Next, each NV^- center is coupled with a 2–3 MHz coupling constant to a thermalized nitrogen nuclear spin, which cannot be neglected. Although this is reversible using spin echo techniques, this will have a direct and potentially significant impact on T_2^*. In a series of experiments using crystals with 100 ppm of P1 centers, T_2^* was found to be in the region of 20–50 ns (Kubo *et al.*, 2010; Kubo *et al.*, 2011; Zhu *et al.*, 2011; Saito *et al.*, 2013). If the P1 concentration is decreased to 40 ppm and the magnetic field is aligned along one of the crystal axes of the NV^- centers, T_2^* becomes limited by the hyperfine interaction (Kubo *et al.*, 2011). Let us now move our focus to the second component of our hybrid circuit, the superconducting circuits.

11.3 Superconducting circuits

As has been mentioned in the introduction, superconducting circuits are one of the typical subsystems that have been considered as a component of a composite hybrid system. In terms of superconducting circuits, there are two important types of circuits that are extremely useful, the first being microwave resonators and the second superconducting qubits. We will examine each in turn.

11.3.1 Microwave resonators

In recent years, high-quality-factor superconducting microwave resonators have become an essential part of many quantum optics experiments. These extremely low-loss resonant structures essentially filter out a single mode of the continuous electromagnetic spectrum and hence provide the clean environment needed for experiments on the level of single quanta. From the standpoint of hybrid quantum systems, microwave resonators are appealing for several reasons. Firstly, the possibility of integrating microwave resonators on a small superconducting chip makes these devices especially interesting as a part of an all-solid-state scalable quantum computer architecture. Secondly, their typical resonance frequencies can be easily designed to be between 1 and 20 GHz, which matches the transition frequencies not only of superconducting qubits but also of many paramagnetic spin species such as the NV^- center (~3 GHz).

Over the years, several different microwave resonator geometries have been successfully implemented in cQED. The most common type employed are coplanar waveguide resonators (CPWRs). A CPWR (Fig. 11.3) consists of a coplanar transmission line of definite length L that is capacitively coupled to an input and an output transmission line. For half-wave resonators of length L, the resonance frequency f_0 is determined by (Göppl *et al.*, 2008)

$$f_0 = \frac{c}{\sqrt{\varepsilon_{\text{eff}}}} \frac{1}{2L}$$

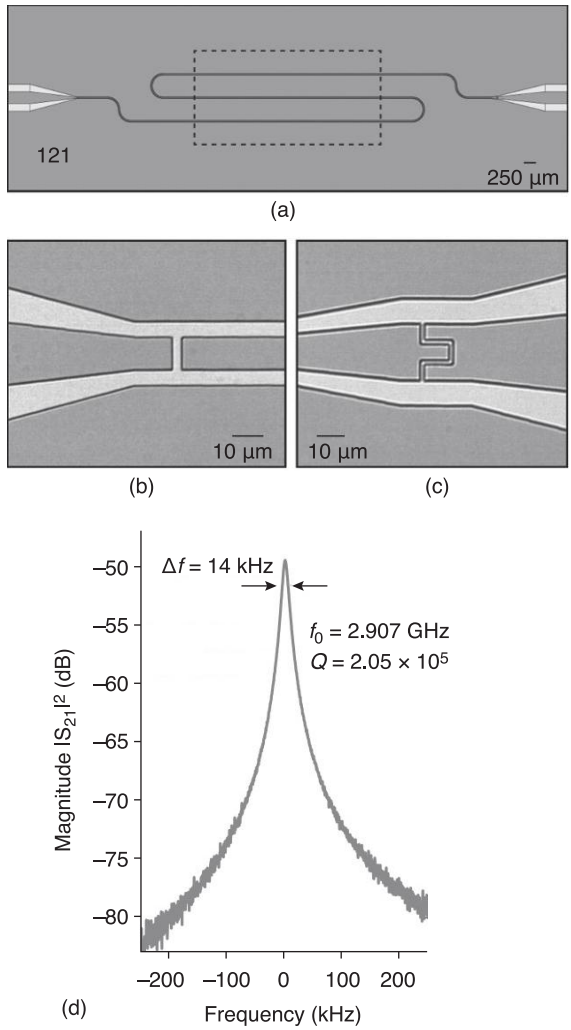

11.3 (a)–(c) Illustration of the design of a CPWR and its input and output coupling structure. Dark areas represent niobium metal, and light shaded areas the sapphire substrate. The black dashed lines indicate the position where the diamond crystal is placed. (d) Magnitude of the complex transmission signal S_{21} of a bare resonator versus frequency.

A center conductor, separated by a few micrometers from ground planes on either side and designed such that the characteristic impedance matches 50 Ω, basically forms the cross section. The planar metal films are fabricated using niobium or aluminum on a low-loss dielectric substrate such as sapphire. Niobium and aluminum are metals that exhibit excellent superconducting properties.

Although CPWRs are restricted to being half a wavelength long, they can have transverse dimensions several orders of magnitude smaller, so that the electromagnetic mode volume is given by $V \sim A\lambda/2$. This should be compared with three-dimensional cavities, where $V \sim (\lambda/2)^3$ generally holds. The reduced mode volume leads to very much enhanced electric and magnetic fields per photon, therefore making it easier to enter the strong-coupling regime even for quantum systems with small dipole moments. Generally, CPWRs support transverse electromagnetic modes of propagation whose transverse fields are not confined to a finite area, and therefore decay quickly with distance from the metal film. For that reason, quantum systems have to be brought close to the metal surface, preferentially at the corners of the CPWR, where the fields are maximum. While this is a particularly easy task when spin systems such as NV^- centers in diamond are considered – the crystal sample needs only to be placed on top of the resonator chip – this becomes challenging if clouds of atoms or molecules are considered (Imamoglu, 2009; Rabl *et al.*, 2006; Verdu *et al.*, 2009; Wesenberg *et al.*, 2009).

Superconducting coplanar waveguide resonators are exceptionally narrow-band filters that behave as a harmonic oscillator described by the Hamiltonian

$$H_{\text{res}} = \hbar\omega_0 \left[b^\dagger b + \frac{1}{2} \right]$$

with the average photon number given by $n = \langle b^\dagger b \rangle$. At typical operating temperatures of about 20 mK, such resonators are effectively cooled to their ground state ($n << 1$). They possess a Lorentzian transmission function S_{21} close to resonance ($f \approx f_0$),

$$S_{21}(f) = \frac{A}{1 + 2iQ\dfrac{f - f_0}{f_0}}$$

where A is the transmission amplitude parameter and Q is the quality factor, which is related to the full width at half maximum by $\Delta_{\text{FWHM}} = f_0/Q$. The total quality factor Q is a figure of merit for the sharpness of the resonance and thus the magnitude of the losses. It is often decomposed into two contributions – the internal losses of the resonator Q_{int}, which need to be minimized, and the losses due to the capacitive coupling to the input/output lines, Q_{ext}. All of these parameters can be extracted from transmission measurements performed using a vector network analyzer. The typical values achieved for Q_{int} are in the range of 10^5–10^6, while Q_{ext} is designed for specific experimental demands. In recent hybrid experiments involving NV^- centers and superconducting microwave resonators (Kubo *et al.*, 2010; Schuster *et al.*, 2010; Chiorescu *et al.*, 2010; Bushev *et al.*, 2011), the measured Q factors of 10^3–10^4 were high enough that photon loss represented only a minor contribution to the total decoherence of the combined hybrid system.

As hybrid quantum systems necessitate complex protocols to transfer quantum information from one part of the circuit to another, frequency-tunable resonators (Palacios-Laloy *et al.*, 2008; Sandberg *et al.*, 2008) are a very well-suited alternative to the simple CPWR design described in Fig. 11.3. These devices allow changes of the resonance frequency on a nanosecond timescale while the loss rate remains extremely small. They are based on the insertion of superconducting quantum interference devices (SQUIDs) into the center conductor, which are flux-biased by fast on-chip current lines (Palacios-Laloy *et al.*, 2008). Since these resonators have the ability to bridge the different timescales of the distinct constituents of hybrid quantum systems, they have played a central role as a quantum bus. Numerous experiments have shown the versatile character of microwave resonators, which can be used to read out and manipulate the quantum state of a superconducting qubit (Wallraff *et al.*, 2004; Wallraff *et al.*, 2005; Mallet *et al.*, 2009), be employed as a quantum bus to transfer quantum information between different qubits (Majer *et al.*, 2007; Sillanpaa *et al.*, 2007) or be employed as an amplifying element with almost quantum-limited performance (Bergeal *et al.*, 2010).

11.3.2 Superconducting qubits

Superconducting qubits are the second type of circuit that is ideal as a component in these hybrid systems. There are quite a number of different types of superconducting qubits that have been developed, with most of them showing controllability, integrability and potential scalability. For our present purpose of coupling to an ensemble of NV^- centers, superconducting flux qubits are particularly noteworthy owing to the potential for direct coupling.

Superconducting flux qubits (Mooij *et al.*, 1999; Orlando *et al.*, 1999) generally consist of three Josephson junctions connected by a low-inductance superconducting loop, where the only tunable parameter is the magnetic flux Φ_ε penetrating the loop. At the degeneracy point, the energy spacing between the ground state and the first excited state reaches its minimum value Δ. At this point the qubit is decoupled from low-frequency flux noise and has the maximum coherence time (Yoshihara *et al.*, 2006; Kakuyanagi *et al.*, 2007). However, there is a significant issue in that the gap Δ is determined only by the Josephson energy and the charge energy of the three Josephson junctions. As such, this gap can only be changed during manufacture and has proved difficult to tune precisely. If we replace the smallest junction of the flux qubit with a DC SQUID, we can change the parameters of the smallest junction by varying the magnetic flux of this DC SQUID and so vary the gap of the flux qubit (Zhu *et al.*, 2010; Paauw *et al.*, 2009; Fedorov *et al.*, 2010). This is a significant advantage when we wish to couple the circuit to other quantum systems, as this gap-tunable flux qubit can be tuned into or out of resonance with other quantum systems while keeping the qubit at its optimal point.

A typical gap-tunable flux qubit is shown in Fig. 11.4 and is composed of four Josephson junctions in two loops. The main loop (gray shading) encloses three junctions: two identical junctions with the same Josephson energy E_J, and one shared with the α control loop (unshaded) with a smaller Josephson energy $\alpha_0 E_J/2$, where $\alpha_0/2$ is the ratio of the Josephson energies of the third and first two junctions. The two junctions in the α control loop are identical and form a DC SQUID. The effective Josephson energy of the DC SQUID, αE_J, can be tuned by the flux Φ_α threading the α control loop, as $\alpha E_J = \alpha_0 E_J |\cos(\pi\Phi_\alpha/\Phi_0)|$. The gap-tunable flux qubit can then be written as an effective two-level system (Mooij *et al.*, 1999) described by

$$H_{qb} = \frac{h}{2}[\varepsilon(\Phi_{qb})\sigma_z + \Delta(\Phi_\alpha)\sigma_x].$$

where $\sigma_{z,x}$ are the usual Pauli spin operators where the eigenstates of σ_z describe clockwise and counterclockwise persistent states of the current I_p in the qubit. The energy imbalance $h\varepsilon = 2I_p\Phi_0(\Phi_{qb}/\Phi_0 - 0.5)$ between the two states can be controlled by $\Phi_{qb} = \Phi_\varepsilon + \Phi_\alpha/2$, where $\Phi_{\varepsilon,\alpha}$ are the magnetic fluxes through the qubit loops. The control lines near the flux qubit mean that the effective magnetic field of the main loop Φ_ε and of the α loop Φ_α can be tuned *in situ* on a nanosecond timescale, meaning that we can control the energy gap $h\Delta$ at the optimal point where it has its best coherence properties. If we want to change the gap of the qubit, we set the shift pulse current of control line 1 to another value and scan the current of control line 2 to sweep the qubit flux $\Phi_{ex} = \Phi_\varepsilon + \Phi_\alpha/2$. This is illustrated in Fig. 11.5, where spectra were taken with different gaps, obtained by adding shift pulses from control lines 1 and 2 with different currents.

Finally, it is worth discussing the coherence properties of these qubits. Generally, the measured T_1 and T_2 are of the order of 1 μs and 400 ns, respectively. This would correspond to natural decay rates of the order of 0.2 and 0.4 MHz.

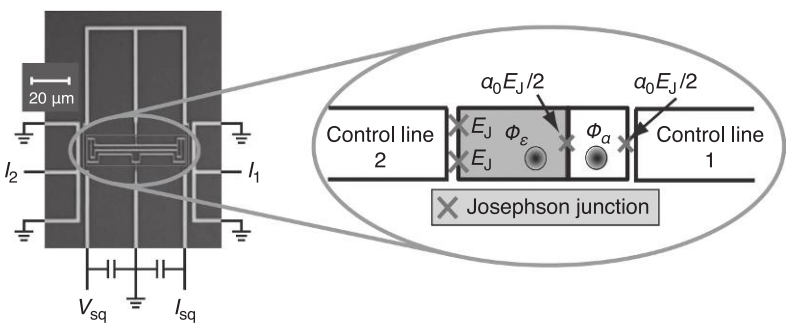

11.4 Illustration of a gap-tunable flux qubit composed of four Josephson junctions in two loops, a main loop (gray shading) and an α loop (not shaded). Two high-bandwidth control lines are placed to tune the flux of each loop.

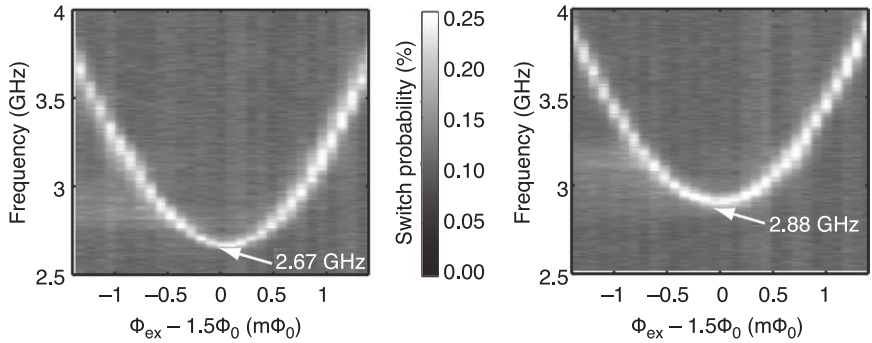

11.5 Spectra of gap-tunable flux qubit with Δ set to 2.67 and 2.88 GHz.

11.4 Collective coupling in the hybrid system

Now that we have described the individual components of our hybrid system, we need to examine how they can be coupled together. Initially, to illustrate this coupling, it is best to consider the resonator and a single NV^- center. The interaction is between the magnetic dipole moment $\boldsymbol{\mu}$ of the NV^- center and the oscillating magnetic field $\boldsymbol{B}$ that is present in both resonators and flux qubits. The Hamiltonian can be written as

$$H_{\text{int}} = -\boldsymbol{\mu} \cdot \boldsymbol{B},$$

where $\boldsymbol{\mu} = h\gamma \boldsymbol{S}$ links the magnetic dipole moment to the NV^- spin $\boldsymbol{S}$, with γ denoting the gyromagnetic ratio.

11.4.1 Collective coupling between resonators and nitrogen–vacancy (NV) ensembles

For the resonator, the oscillating magnetic field $\boldsymbol{B}$ can be expressed as

$$\boldsymbol{B}(r) = B_k \left(f^*(r)\, \boldsymbol{k} \times \boldsymbol{e}_{\boldsymbol{k}}\, b_k + f(r)\, \boldsymbol{k} \times \boldsymbol{e}_{\boldsymbol{k}}^*\, b_k^\dagger\right)$$

where $\boldsymbol{e}_{\boldsymbol{k}}$ denotes a unit polarization vector $\boldsymbol{k} = (k_x, k_y, k_z)$, a discrete wave vector with the property $\boldsymbol{e}_{\boldsymbol{k}} \cdot \boldsymbol{k} = 0$. B_k is the magnitude of the oscillating field along the k direction, $f(r)$ defines the effective magnetic mode volume V and $b_k^\dagger$, b_k are the creation/destruction field operators of the resonator. With a circular polarization of the oscillating magnetic field, we can write this interaction as

$$H_{\text{int}} = hg\left(b\, S^+ + b^\dagger S^-\right)$$

where S^+ and S^- are the appropriate raising and lowering operators for the NV^- center, which obey the appropriate spin selection rules. With a linear polarization for the oscillating field, we can write the field similarly as $H_{\text{int}} = hg(b + b^\dagger)(S^+ + S^-)$,

which in a rotating-wave approximation reduces to $H_{\text{int}}=hg(bS^{+}+b^{\dagger}S^{-})$. The coupling constant g is given by

$$g=-\gamma B_k f^{*}(r) M_k$$

with M_k being the transition element for the circular polarization $\langle 0|S_k|\pm 1\rangle$. We can now express the magnetic field in terms of $B_k=\mu_0 I_{\text{rms}}/\pi d$ (Twamley and Barrett, 2010), where $2d$ is the distance between the ground and central conductors in the resonator and $I_{\text{rms}}=\sqrt{\hbar\omega_r/2L_{\text{r}}}$, with ω_{r} being the angular frequency of the resonator and L_{r} its inductance. In the recent experiments of Kubo *et al.* (2010) and Amsüss *et al.* (2011), the coupling between the resonator and an individual NV^{-} center was on the order of 10 Hz for a spin located 1 μm from the chip surface.

The generalization to an ensemble of N NV^{-} centers is then straightforward:

$$H_{\text{int}}=h\sum_{j=0}^{N} g_j(bS_j^{+}+b^{\dagger}S_j^{-})$$

We can define collective giant spin operators

$$\Xi^{+}=\frac{1}{g_{\text{eff}}}\sum_{j=0}^{N} g_j S_j^{+},\ \Xi^{-}=\frac{1}{g_{\text{eff}}}\sum_{j=0}^{N} g_j S_j^{-}$$

such that H_{int} simplifies to $hg_{\text{eff}}(b\Xi^{+}+b^{\dagger}\Xi^{-})$, where

$$g_{\text{eff}}=\sqrt{\sum_{j=0}^{N}\left|g_j\right|^2}$$

In the presence of a magnetic field that splits the $|\pm\rangle$ states, we can approximate these giant spin operators further as harmonic oscillators and so write (Kubo *et al.*, 2010; Amsüss *et al.*, 2011)

$$H_{\text{int}}=h\frac{g_{\text{eff}}}{\sqrt{2}}(a_{+}^{\dagger}b+a_{+}b^{\dagger})+h\frac{g_{\text{eff}}}{\sqrt{2}}(a_{-}^{\dagger}b+a_{-}b^{\dagger})$$

It is now useful to estimate the magnitude of g_{eff}, which we will do in the following way. First we make the assumption that all the NV^{-} centers have the same $g_j=g$. Then $g_{\text{eff}}=\sqrt{N}g$, where N is the number of centers that couple to the resonator. The number of centers can be estimated using simple geometric considerations (the dimensions of the resonator) and the concentration of the NV^{-} ensemble. In the experiment done by Amsüss *et al.*, the number of NV^{-} centers was approximately the product of the coupling area of the resonator, the length ($\lambda/2$) and the concentration ($20\,\mu\text{m}\times 8.3\,\mu\text{m}\times 2.15\,\text{cm}\times 5\times 10^{17}\,\text{cm}^{-3}$), which is approximately $2\times 10^{12}/\text{cm}^3$. This implies $g_{\text{eff}}\sim 14$ MHz. With the energy damping rate of the resonator ($\kappa_{\text{res}}\sim 0.8$ MHz) and the coherence of the ensemble ($\gamma_{\text{ens}}\sim 8$ MHz) mentioned above, we can estimate the cooperativity parameter **C** as (Amsüss *et al.*, 2011)

$$\mathbf{C} = \frac{(g_{\text{eff}}/\sqrt{2})^2}{\kappa_{\text{res}}\gamma_{\text{ens}}} \sim 14 - 26$$

Similar estimates for the cooperativity parameter were obtained by Kubo *et al.* (2010). Hence, both the simple CPWR and the tunable CPWR coupled to an ensemble should be operating in the strong-coupling regime.

Spectroscopic measurements of a coplanar waveguide resonator coupled to the NV^- ensemble used by the Vienna group were performed for a varying external magnetic field. As the coplanar waveguide resonator had a fixed frequency (2.701 GHz), an external magnetic field was used to split the $|\pm 1\rangle$ states, so bringing the $|0\rangle \Leftrightarrow |-1\rangle$ transition into resonance with the resonator. Only one transition should be observable at a time. The spectroscopy measurements are shown in Fig. 11.6 and an avoided crossing is seen. This clearly shows that coupling has been achieved between the two components of the hybrid system. Furthermore, the appearance of two peaks, shown at $B = 8.6$ mT, demonstrates definite hybridization and hence confirms that the strong-coupling regime has been reached.

The pioneering experiment at Saclay used a tunable coplanar waveguide resonator coupled to an NV^- ensemble and so, by varying the flux bias, the group could in principle observe resonances for both of the $|0\rangle \Leftrightarrow |\pm 1\rangle$ transitions (Kubo *et al.*, 2010). This is shown in Fig. 11.7, where strong coupling is clearly observed.

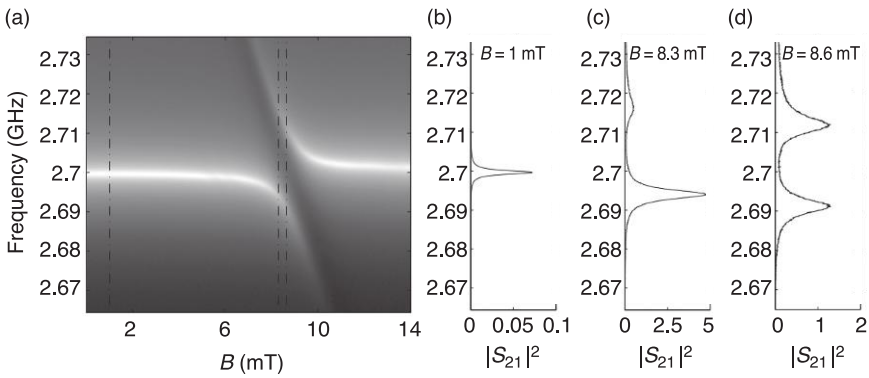

11.6 Spectroscopic measurement of the transmission function of a CPWR versus applied external magnetic field (Amsüss, 2011). A clear avoided-crossing structure is observed for an external magnetic field of 8 mT. In (b)–(d), the transmission function S_{21} is plotted versus frequency for fields of 1, 8.3 and 8.6 mT. Characteristic features of the strong-coupling regime can be clearly identified.

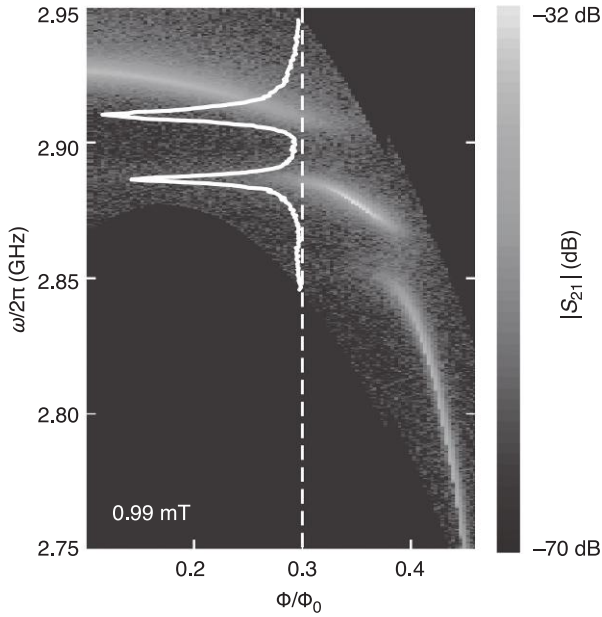

11.7 Spectroscopic measurement of the transmission function of a tunable CPWR versus flux bias (Kubo *et al.*, 2010). Clear avoided-crossing structures are observed. (Courtesy Patrice Bertet, Quantronics Group, Saclay).

11.4.2 Collective coupling between flux qubit and NV ensemble

Let us now turn our attention to the coupling between a flux qubit and an NV^- ensemble, which can be handled in a similar way as it is also based on a magnetic dipole. The anti-aligned magnetic fields created by the circular persistent current of the flux qubit are in the z direction. Considering the flux qubit and a single NV^- center, we can write their coupling interaction as (Marcos *et al.*, 2010)

$$H_{\text{int}} = h\, g_e\, \mu_B\, \sigma_z\, \boldsymbol{B}.\boldsymbol{S}$$

where $g_e = 2$ is the NV^- Landé factor, $\mu_B = 14\,\text{MHz/mT}$ is the Bohr magneton and $\mathbf{B}$ is the magnetic field associated with the flux qubit. We can generally express this as $\mathbf{B}.\mathbf{S} = B_x S_x + B_y S_y + B_z S_z$. The $B_z S_z$ term can generally be neglected, as we will make a rotating-wave approximation. Furthermore, as our flux qubit magnetic field B_{qb} is associated with left and right circularly rotating currents, we can rewrite H_{int} as

$$H_{\text{int}} = h\, g_e\, \mu_B\, (B_{qb}\, \sigma^- S^+ + B^*_{qb}\, \sigma^+ S^-) = h\, (g\, \sigma^- S^+ + g^*\, \sigma^+ S^-)$$

which looks quite similar to the expression we saw in the resonator case. In this case we need to determine the magnitude of B_{qb}, which can be estimated using the Biot–Savart law. To first order, $B_{qb}=\mu_0 I_p/2R$, where $\mu_0=4\pi\times10^{-7}$ N A^{-2}, I_p is the persistent current in the qubit and R is the distance between the flux qubit and a single NV$^-$ center. The coupling strength g between the flux qubit and a single NV$^-$ center can then be estimated as

$$g=g_e\,\mu_B\,\mu_0\,I_p/2\,R.$$

Using typical parameters for the persistent current in the flux qubit $I_p\sim300$ nA and $R\sim1.2$ μm, the coupling strength g is of order 4.4 kHz. This is about 1000 times larger than in the resonator case.

As in the resonator case, the generalization to a flux qubit coupled to an ensemble containing N NV$^-$ centers is straightforward:

$$H_{int}=h\sum_{j=0}^{N}g_j(\sigma^-S_j^+ + \sigma^+S_j^-)$$

We can then define collective giant spin operators

$$\Xi^+=\frac{1}{g_{eff}}\sum_{j=0}^{N}g_jS_j^+,\Xi^-=\frac{1}{g_{eff}}\sum_{j=0}^{N}g_jS_j^-$$

such that H_{int} simplifies to $hg_{eff}(\sigma^-\Xi^+ + \sigma^+\Xi^-)$, where

$$g_{eff}=\sqrt{\sum_{j=0}^{N}\left|g_j\right|^2}$$

Furthermore, when have a magnetic field splitting the $|\pm1\rangle$ states, we can approximate these giant spin operators as harmonic oscillators and so write (Kubo *et al.*, 2010; Amsüss *et al.*, 2011)

$$H_{int}=h\frac{g_{eff}}{\sqrt{2}}(a_+^\dagger\sigma^- + a_+\sigma^+)+h\frac{g_{eff}}{\sqrt{2}}(a_-^\dagger\sigma^- + a_-\sigma^+)$$

We need to estimate the magnitude of g_{eff}, which we will do in the following way. First we make the assumption that all the NV$^-$ centers have the same $g_j=g$. Then $g_{eff}=\sqrt{N}g$, where N is the number of centers that couple to the resonator. The flux qubits used in these experiments had an area of ~40 μm^2, while the depth of the NV$^-$ centers in the ensemble was ~0.7 μm. With an NV$^-$ concentration of ~4.7×10^5/μm^3 (or 4.7×10^{17}/cm^3), we can estimate $N\sim30\times0.7\times10^6=10^7$, implying

$$g_{eff}\sim 14\,\text{MHz}$$

With the coherence parameters for the flux qubit mentioned above, we can estimate the cooperativity parameter **C** as (Saito *et al.*, 2013)

$$\mathbf{C}=\frac{(g_{eff}/\sqrt{2})^2}{\kappa_{qubit}\gamma_{ens}}\sim8$$

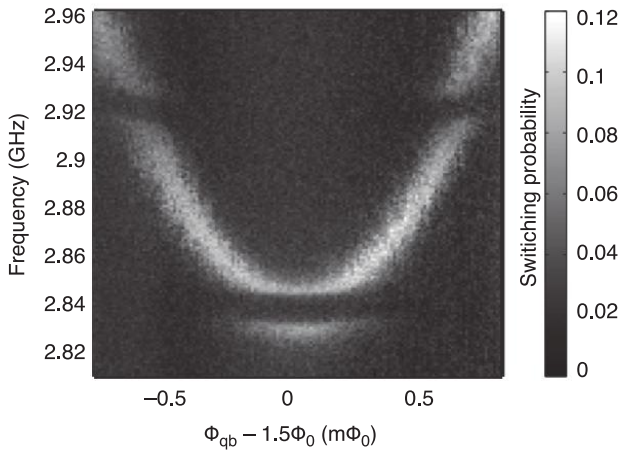

11.8 Energy spectrum of a flux qubit coupled to an NV^- spin ensemble in an external field of magnitude 2.6 mT.

where κ_{qubit} is larger than normal owing to the reduced coherence time associated with placing the diamond sample on top of the qubit. In principle, this allows the strong-coupling regime to be examined, and so we should observe a signature of it in spectroscopy measurements of the flux qubit. In Fig. 11.8, we show the energy spectrum of the flux qubit coupled to the spin ensemble in an external field of magnitude 2.6 mT along the crystallographic [100] direction. Two clear anticrossings are observed symmetrically near 2.878 GHz, which represent when the flux qubit is in resonance with the NV^- $|0\rangle \Rightarrow |1\rangle$ (upper anticrossing at 2.92 GHz) and $|0\rangle \Rightarrow |-1\rangle$ (lower anticrossing at 2.84 GHz) transitions. The vacuum Rabi splitting is 8.9 MHz (effectively $g_{\text{eff}}/\sqrt{2}$).

11.4.3 Moving to the time domain

All the results presented so far were obtained by performing spectroscopic measurements in the frequency domain. An alternative approach is to work in the time domain, where similar information can be gained about the state of the hybrid system. Again we start with the resonator situation, and we examine a cavity ring-down approach using homodyne measurements. In this case, a microwave signal is split into two, a signal part and a local oscillator part. The signal part is sent through the resonator and then recombined with the local oscillator in an IQ mixer to perform a homodyne measurement. The phase of the local oscillator can be varied, enabling both $X(t)$ and $P(t)$ quadrature measurements to be performed. The amplitude and phase of the transmission function of the resonator cavity can be obtained from the results of these quadrature measurements using

$$A(t) = \sqrt{X(t)^2 + P(t)^2} \text{ and } \phi(\text{t}) = \tan^{-1}[X(t)/P(t)]$$

In Fig. 11.9, we display $A(t)$ for both an empty resonator (far detuned from the ensemble) and the situation where the resonator is interacting with the diamond ensemble.

The situation in Fig. 11.9, where the ensemble is far detuned from the resonator, shows the expected exponential decay of the amplitude when the microwave field is in resonance with the resonator. When the ensemble is brought into resonance with the resonator, the amplitude shows the characteristic Rabi oscillations

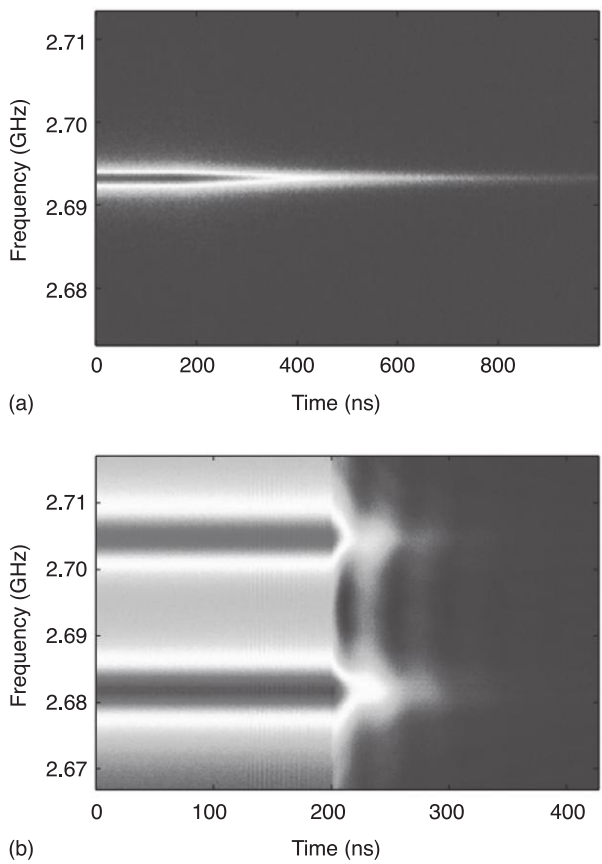

11.9 Cavity ring-down: calculated amplitude versus detuning and time. After the input signal is switched off at $t \approx 175$ ns, the steady-state field amplitude decays exponentially. (a) A situation where the spin ensemble is far detuned and so is not coupled to the resonator. (b) The case where the ensemble is in resonance with the resonator.

expected for a strongly coupled system. From these curves (Fig 11.9(b)), we can determine the coherence properties of the hybrid system.

The dynamics of the flux-qubit–ensemble hybrid system in the time domain can be investigated using a measurement cycle similar to that used for qubit–LC-resonator coupled systems. This works by first moving the flux qubit far off resonance with the diamond ensemble and then exciting the flux qubit to $|1\rangle_{qb}$. The qubit is then brought into resonance with the NV^- ensemble, where exchange of a single energy quantum between the flux qubit and the NV^- ensemble at resonance is manifested as vacuum Rabi oscillations

$$|1\rangle_{qb}|0\rangle_{ens} \Leftrightarrow |0\rangle_{qb}|1\rangle_{ens}$$

More specifically, the system oscillates from $|1\rangle_{qb}|0\rangle_{ens}$ through $|1\rangle_{qb}|0\rangle_{ens} + i|0\rangle_{qb}|1\rangle_{ens}$ to $|0\rangle_{qb}|1\rangle_{ens}$ and then back through $|1\rangle_{qb}|0\rangle_{ens} - i|0\rangle_{qb}|1\rangle_{ens}$ to $|1\rangle_{qb}|0\rangle_{ens}$, where $|0\rangle_{ens}$ is the ground state of the ensemble and $|1\rangle_{ens}$ the first collective excited state. After a certain period of time τ, the flux qubit is then measured in its computational basis to determine whether it was in the excited state or not. Figure 11.10 shows vacuum Rabi oscillations between the flux qubit and the ensemble of electronic spins at the 2.878 GHz resonance; however, the decay time of the oscillations is quite short (70–80 ns). The oscillations in these results indicate that the process is coherent – an excitation is being coherently transferred between the two

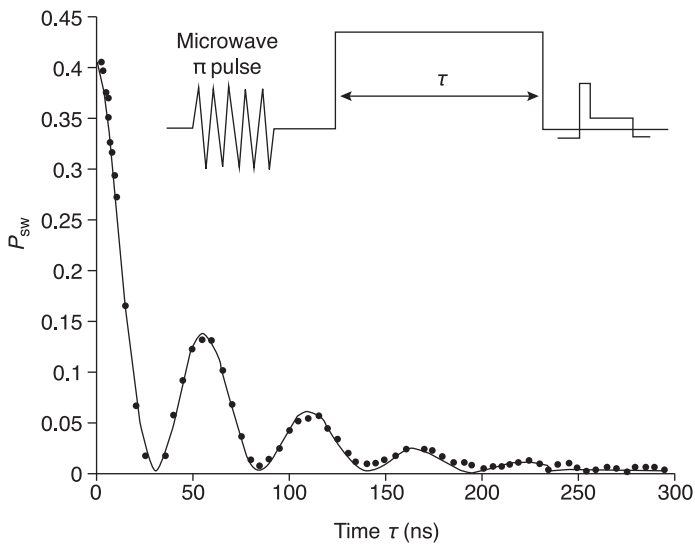

11.10 Plot of the qubit switching probability versus time τ for a vacuum Rabi measurement at the optimum point. The dots are the experimentally measured data points, and the curve gives the values predicted by a theoretical model.

components of the hybrid system. At certain times, the population of the flux qubit is effectively zero, indicating that the qubit is in its ground state and some proportion of the excitation is in the ensemble. At other times, the flux qubit has a significant population. This is a clear signature of strong coupling. Furthermore, this coherent exchange provides an excellent basis for being considered for storage of quantum states in the ensemble.

11.5 Towards quantum memory operations

The demonstration of Rabi oscillations was a significant step along the path to realizing quantum memory operations. At certain points in the vacuum Rabi oscillations shown in Fig. 11.10, the flux qubit is in its ground state and the quantum state has been transferred to the ensemble. This is the basis for memory operations, which is schematically depicted in Fig. 11.11 for a single excitation. To realize such a memory operation, we first excite the qubit while it is far detuned from the NV^- spin transition. This allows us to prepare a well-known state in the flux qubit without any coupling to the ensemble. We then rapidly tune it into resonance with the spin transition for a time corresponding to half a Rabi oscillation period. This performs an iSWAP gate. The flux qubit is then rapidly detuned away from the transition again to decouple it from the ensemble. At this

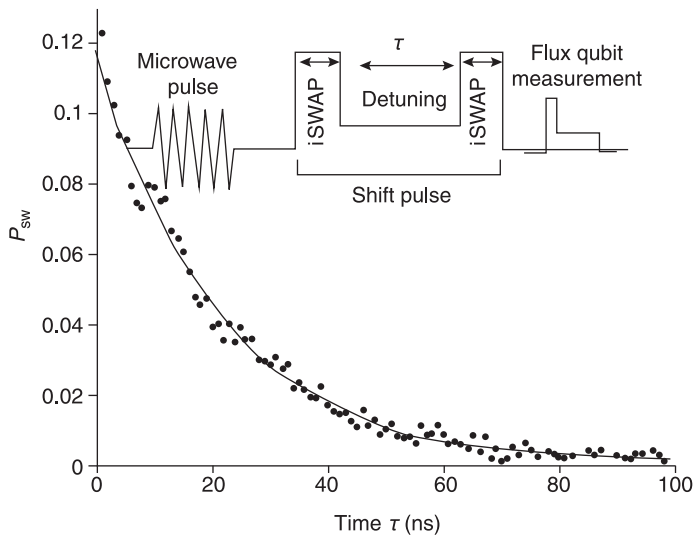

11.11 Schematic diagram showing the transfer of an excitation from a flux qubit to an ensemble, where it is stored for a time τ (the flux qubit is far detuned from the ensemble) and then retrieved. The dots are the experimentally measured data points, and the curve gives the values predicted by a theoretical model (Saito *et al.*, 2013).

stage, the excitation is stored in the ensemble. After a storage time τ, the qubit is brought into resonance with the ensemble again and an iSWAP gate performed. This transfers the stored quantum state in the ensemble back to the qubit, where it can be measured.

Such an experiment was performed, and in Fig. 11.11, we plot the measured population of the flux qubit after the excitation has been stored in the ensemble for a time τ. An exponential decay curve is seen as expected; however, the decay time is quite short (20–30 ns). This needs to be compared with the relaxation time of an individual NV^- center, which is $T_1 \sim 45$ s (Amsüss *et al.*, 2011; Jarmola *et al.*, 2012). It is thus natural to wonder what is happening here, as the difference is at least nine orders of magnitude. The explanation, however, is quite straightforward when we consider how this excitation is stored in the ensemble. The first excited state $|1\rangle_{\text{ens}}$ is a collective state with a single excitation present in it. We can write such a state as

$$|1\rangle_{\text{ens}} = \frac{1}{g_{\text{eff}}} \sum_{j=1}^{N} g_i S_j^+ \, |0\rangle_{\text{NV1}} \, |0\rangle_{\text{NV2}} \ldots |0\rangle_{\text{NV}N}$$

where the S_j^+ are appropriate raising operators for the jth NV^- center. As we are working with a magnetic field to split the $|\pm 1\rangle$ states and our flux qubit is only ever resonant with $|0\rangle \Leftrightarrow |+1\rangle$, we can write

$$|1\rangle_{\text{ens}} = \frac{1}{g_{\text{eff}}} \left(g_1 \, |+1\rangle_{\text{NV1}} \, |0\rangle_{\text{NV2}} \ldots |0\rangle_{\text{NV}N} + g_2 \, |0\rangle_{\text{NV1}} \, |+1\rangle_{\text{NV2}} \ldots |0\rangle_{\text{NV}N} + \ldots \right)$$

that is, our collective excited state is a superposition of a single excitation distributed over the entire ensemble. Spontaneous emission from each of the individual NV^- centers will occur on the timescale of 40 s. However, inhomogeneous broadening etc. will cause dephasing (T_2^*) between the individual components of this superposition, resulting in a new single excitation state that is unable to collectively couple to the flux qubit. In such a case, the excitation stored in the ensemble will not be able to transfer back to the flux qubit during the iSWAP gate. The flux qubit will interpret this as the excitation being lost, and hence the time will appear to be proportional to T_2^*. As the dephasing arises from inhomogeneous broadening caused primarily by the P1 centers, the natural solution is to reduce the P1 center concentration. The transition from storing a single excitation to an arbitrary quantum state is straightforward and the memory protocol described above does not need to change. Only a different state needs to be created with the flux qubit.

In recent work by Kubo *et al.* (2011), a transmon–resonator–ensemble coupled hybrid system was employed. These authors used a diamond crystal with significantly fewer P1 centers (~40 ppm rather than 100 ppm) and found a significantly longer coherence time in this memory (Fig. 11.12). In fact, the coherence time became limited by the hyperfine interaction rather with 14 N nuclear spin than the P1 centers.

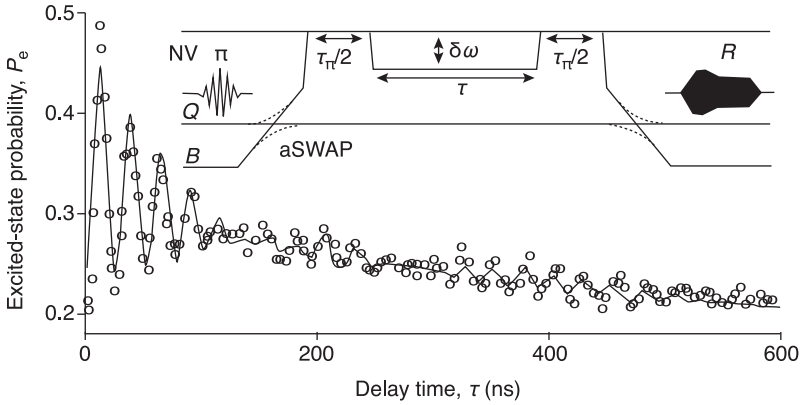

11.12 Schematic diagram showing a Ramsey-like experiment on a spin ensemble at the single-photon level where an excitation is stored for a time τ and then retrieved. The dots are the experimentally measured data points, and the curve gives the values predicted by a theoretical model. (Courtesy Patrice Bertet, Quantronics Group, Saclay).

11.6 Conclusions and future trends

Despite the initial success, there is a long road ahead until a full-fledged quantum processor in a hybrid architecture becomes a useful device. The main obstacles so far have been the surprisingly short coherence times of the spin ensemble. Although long dephasing times in very clean diamond have been demonstrated, the high spin densities needed for reaching strong coupling are accompanied by a new loss mechanism: inhomogeneous broadening. Another source of line broadening is due to dipolar hyperfine coupling to ^{13}C nuclear spins. Samples with the natural abundance of 1.1% ^{13}C typically show T_2^* times of about 1 μs ($T_2 \sim 300$ μs) (Dutt *et al.*, 2007). These numbers can be improved only by using isotopically purified diamond samples (Balasubramanian *et al.*, 2009). Therefore, even if decreasing the initial nitrogen content reduces the inhomogeneous broadening caused by the P1 centers, below ~1 ppm the line width will still be limited by ^{13}C hyperfine coupling. These considerations suggest that isotope engineering together with increased N-to-NV$^-$ conversion efficiencies are necessary in order to make NV$^-$ center spin ensembles a useful quantum memory resource. Another way out would be to use refocusing techniques as used in other fields of quantum information (Lvovsky *et al.*, 2009), by which an increase in memory times by two orders of magnitude would be possible (Kubo *et al.*, 2011; Kurucz *et al.*, 2011; Malissa *et al.*, 2013). Polarization of the ^{13}C and ^{14}N nuclear spins is also possible.

An alternative approach would be to increase the coupling strengths between the superconducting circuits and centers in the ensemble. The advantage here

would be that one could reduce the required spin densities and one could also benefit from energy gap (cavity) protection (Diniz *et al.*, 2011; Kurucz *et al.*, 2011). It is thus useful to reexamine the coupling between a single NV^- center and, say, a flux qubit, which is given by

$$g = g_e \mu_B \mu_0 I_p / 2R.$$

When the persistent current I_p is increased from 300 nA to 3 μA and the centers are brought to approximately 10 nm from the flux qubit, the coupling constant increases by a factor of 1000 – hence going from $g \sim 5$ kHz to $g \sim 5$ MHz. In principle, this implies that strong coupling between a flux qubit and a single center would be possible. Furthermore, isotope-engineered diamond with low impurities (N and ^{13}C) would mean removing the broadening effects seen in the ensemble systems, and polarization of the ^{14}N nuclear spin into its $|m_s = 0\rangle_{nuc}$ state would decouple the electron and nuclear spins, giving us quite a pure hybrid system.

The use of NV^- centers in these hybrid circuits also opens up another important possibility aside from potentially providing long-lived quantum memories. As NV^- centers have an optical transition, we should in principle be able to move information from a superconducting circuit to a single NV^- center (or ensemble) and from there to optical photons. This would provide a natural interface between the optical and microwave worlds and, in principle, allow distributed quantum information processing where photons are used as the communication bus and the microwave regime for efficient local gates.

11.7 References

Abragam, A. and B. Bleaney (1970), *Electron Paramagnetic Resonance of Transition Ions*, Oxford: Clarendon.

Acosta, V. M., E. Bauch, M. P. Ledbetter, A. Waxman, L.-S. Bouchard and D. Budker (2010), 'Temperature dependence of the nitrogen–vacancy magnetic resonance in diamond', *Physical Review Letters* 104, 1–4.

Amsüss, R., C. Koller, T. Nöbauer, S. Putz, S. Rotter, K., *et al.* (2011), 'Cavity QED with magnetically coupled collective spin states', *Physical Review Letters* 107, 1–5.

Balasubramanian, G., P. Neumann, D. Twitchen, M. Markham, R. Kolesov, *et al.* (2009), 'Ultralong spin coherence time in isotopically engineered diamond', *Nature Materials* 8, 383–387.

Bennett, C. H. and G. Brassard (1984), 'Quantum cryptography: Public-key distribution and coin tossing', in *Proceedings of IEEE International Conference on Computers, Systems, and Signal Processing*, pp. 175–179, IEEE Press.

Bergeal, N., F. Schackert, M. Metcalfe, R. Vijay, V. E. Manucharyan, *et al.* (2010), 'Phase-preserving amplification near the quantum limit with a Josephson ring modulator', *Nature* 465, 64–68.

Bushev, P., A. K. Feofanov, H. Rotzinger, I. Protopopov, J. H. Cole, *et al.* (2011), 'Ultralow power spectroscopy of a rare-earth spin ensemble using a superconducting resonator', *Physical Review B* 84, 060501.

Chiorescu, I., N. Groll, S. Bertaina, T. Mori and S. Miyashita (2010), 'Magnetic strong coupling in a spin–photon system and transition to classical regime', *Physical Review B* 82, 1–7.

Deutsch, D. and R. Jozsa (1992), 'Rapid solutions of problems by quantum computation', *Proceedings of the Royal Society of London A* 439, 553.

DiCarlo, L., J. M. Chow, J. M. Gambetta, L. S. Bishop, B. R. Johnson, *et al.* (2009), 'Demonstration of two-qubit algorithms with a super-conducting quantum processor', *Nature* 460, 240–244.

Diniz, I., S. Portolan, R. Ferreira and P. Bertet (2011), 'Strongly coupling a cavity to inhomogeneous ensembles of emitters: Potential for long-lived solid-state quantum memories', *Physical Review A* 84, 063810.

DiVincenzo, D. P. (2000), 'The physical implementation of quantum computation', *Fortschritte der Physik* 48, 9–11.

Dutt, G. M. V., L. Childress, L. Jiang, E. Togan, J. Maze, *et al.* (2007), 'Quantum register based on individual electronic and nuclear spin qubits in diamond', *Science* 316, 1312–1316.

Fedorov, A., A. K. Feofanov, P. Macha, P. Forn-Díaz, C. J. P. M. Harmans and J. E. Mooij (2010), 'Strong coupling of a quantum oscillator to a flux qubit at its symmetry point', *Physical Review Letters* 105, 060503.

Feynman, R. P. (1982), 'Simulating physics with computers', *International Journal of Theoretical Physics* 21, 467–488.

Göppl, M., A. Fragner, M. Baur, R. A. Bianchetti, S. Filipp, *et al.* (2008), 'Coplanar waveguide resonators for circuit quantum electrodynamics', *Journal of Applied Physics* 104, 11.

Holstein, T. and H. Primakoff (1940), 'Field dependence of the intrinsic domain magnetization of a ferromagnet', *Physical Review* 58, 1098–1113.

Imamoglu, A. (2009), 'Cavity QED based on collective magnetic dipole coupling: Spin ensembles as hybrid two-level systems', *Physical Review Letters* 102, 083602.

Jarmola, A., V. M. Acosta, K. Jensen, S. Chemerisov and D. Budker (2012), 'Temperature and magnetic field dependent longitudinal spin relaxation in nitrogen–vacancy ensembles in diamond', *Physical Review Letters* 108, 197601.

Kalish, R., C. Uzan-Saguy, B. Philosoph, V. Richter, J. P. Lagrange, *et al.* (1997), 'Nitrogen doping of diamond by ion implantation', *Diamond and Related Materials* 6, 516.

Kakuyanagi, K., T. Meno, S. Saito, H. Nakano, K., Semba, H., *et al.* (2007), 'Dephasing of a superconducting flux qubit', *Physical Review Letters* 98, 047004.

Kimble, H. J. (2008), 'The quantum internet', *Nature* 453, 1023–1030.

Kimble, H., Y. Levin, A. Matsko, K. Thorne and S. Vyatchanin (2001), 'Conversion of conventional gravitational-wave interferometers into quantum non-demolition interferometers by modifying their input and/or output optics', *Physical Review D* 65, 022002.

Kubo, Y., F. R. Ong, P. Bertet, D. Vion, V. Jacques, *et al.* (2010), 'Strong coupling of a spin ensemble to a superconducting resonator', *Physical Review Letters* 105, 140502.

Kubo, Y., C. Grezes, A. Dewes, T. Umeda, J. Isoya, *et al.* (2011), 'Hybrid quantum circuit with a superconducting qubit coupled to a spin ensemble', *Physical Review Letters* 107, 220501.

Kubo, Y., I. Diniz, A. Dewes, V. Jacques, A. Dréau, *et al.* (2012), 'Storage and retrieval of a microwave field in a spin ensemble', *Physical Review A* 85, 012333.

Kurucz, Z., J. H. Wesenberg and K. Molmer (2011), 'Spectroscopic properties of inhomogeneously broadened spin ensembles in a cavity', *Physical Review A* 83, 053852.

Ladd, T. D., F. Jelezko, R. Laflamme, Y. Nakamura, C. Monroe and J. L. O'Brien (2010), 'Quantum computers', *Nature* 464, 45–53.

Lvovsky, A. I., B. C. Sanders and W. Tittel (2009), 'Optical quantum memory', *Nature Photonics* 3, 706–714.

Majer, J., J. M. Chow, J. M. Gambetta, J. Koch, B. R. Johnson, *et al.* (2007), 'Coupling super-conducting qubits via a cavity bus', *Nature* 449, 443–447.

Malissa, H., D. I. Schuster, A. M. Tyryshkin, A. A. Houck and S. A. Lyon (2013), 'Superconducting coplanar waveguide resonators for low temperature pulsed electron spin resonance spectroscopy', *Review of Scientific Instruments* 84, 025116.

Mallet, F., F. R. Ong, A. Palacios-Laloy, F. Nguyen, P. Bertet, *et al.* (2009), 'Single-shot qubit readout in circuit quantum electrodynamics', *Nature Physics* 5, 791–795.

Marcos, D., M. Wubs, J. M. Taylor, R. Aguado, M.D. Lukin and A. S Sørensen (2010), 'Coupling nitrogen–vacancy centers in diamond to superconducting flux qubits', *Physical Review Letters* 105, 210501.

Mooij, J. E., T. Orlando, L. Levitov, L. Tian, C. H. van der Wal and S. Lloyd (1999), 'Josephson persistent-current qubit', *Science* 285, 1036–1039.

Nakamura, Y., Y. A. Pashkin and J. S. Tsai (1999), 'Coherent control of macroscopic quantum states in a single-Cooper-pair box', *Nature* 398, 786–788.

Neeley, M., R. C. Bialczak, M. Lenander, E. Lucero, M. Mariantoni, *et al.* (2010), 'Generation of three-qubit entangled states using superconducting phase qubits', *Nature* 467, 570–573.

Neumann, P., R. Kolesov, V. Jacques, J. Beck, J. Tisler, *et al.* (2009), 'Excited-state spectroscopy of single NV defects in diamond using optically detected magnetic resonance', *New Journal of Physics* 11, 013017.

Nielsen, M. A. and I. L. Chuang (2000), *Quantum Computation and Quantum Information*, Cambridge University Press.

Nishida, Y., Y. Mita, K. Mori, S. Okuda, S. Sato, *et al.* (1989), 'Color centers in annealing of neutron-irradiated type Ib and Ia diamonds', *Materials Science Forum* 38–41.

Orlando, T. P., J. E. Mooij, I. Tian, C. H. van der Wal, L. S. Levitov, *et al.* (1999), 'Superconducting persistent-current qubit', *Physical Review B* 60, 15398–15413.

Paauw, F. G., A. Fedorov, C. J. P. M Harmans and J. E. Mooij (2009), 'Tuning the gap of a superconducting flux qubit', *Physical Review Letters* 102, 090501.

Palacios-Laloy, A., F. Nguyen, F. Mallet, P. Bertet, D. Vion and D. Esteve (2008), 'Tunable resonators for quantum circuits', *Journal of Low Temperature Physics* 151, 1034–1042.

Rabl, P., D. DeMille, J. M. Doyle, M. D. Lukin, R. J. Schoelkopf and P. Zoller (2006), 'Hybrid quantum processors: Molecular ensembles as quantum memory for solid state circuits', *Physical Review Letters* 97, 3.

Saito, S., X. Zhu, R. Amsüss, Y. Matsuzaki, K. Kakuyanagi, *et al.* (2013), 'Towards realizing a quantum memory for a superconducting qubit: Storage and retrieval of quantum states', *Physical Review Letters* 111, 107008.

Sandberg, M., C. M. Wilson, F. Persson, T. Bauch, G. Johansson, *et al.* (2008), 'Tuning the field in a microwave resonator faster than the photon lifetime', *Applied Physics Letters* 92, 203501.

Schuster, D. I., A. Sears, E. Ginossar, L. DiCarlo, L. Frunzio, *et al.* (2010), 'High-cooperativity coupling of electron-spin ensembles to superconducting cavities', *Physical Review Letters* 105, 140501.

Shor, P. W. (1997), 'Polynomial-time algorithms for prime factorization and discrete logarithms on a quantum computer', *SIAM Journal on Computing* 26, 1484–1509.

Spiller, T. P. and W. J. Munro (2006), 'Towards a quantum information technology industry', *Journal of Physics: Condensed Matter* 18, V1–V10.

Sillanpaa, M. A., J. I. Park and R. W. Simmonds (2007), 'Coherent quantum state storage and transfer between two phase qubits via a resonant cavity', *Nature* 449, 438–442.

Twamley, J. and S. D. Barrett (2010), 'Superconducting cavity bus for single nitrogen–vacancy defect centers in diamond', *Physical Review B* 81, 241202R.

Verdu, J., H. Zoubi, C. Koller, J. Majer, H. Ritsch and J. Schmiedmayer (2009), 'Strong magnetic coupling of an ultracold gas to a superconducting waveguide cavity', *Physical Review Letters* 103, 043603.

Wallraff, A., D. I. Schuster, A. Blais, L. Frunzio, R. S. Huang, *et al.* (2004), 'Strong coupling of a single photon to a superconducting qubit using circuit quantum electrodynamics', *Nature* 431, 162–167.

Wallraff,A., D. I. Schuster, A. Blais, L. Frunzio, J. Majer, *et al.* (2005), 'Approaching unit visibility for control of a superconducting qubit with dispersive readout', *Physical Review Letters* 95, 060501.

Wesenberg, J. H., A. Ardavan, G. A. D. Briggs, J. J. L. Morton, R. J. Schoelkopf, *et al.* (2009), 'Quantum computing with an electron spin ensemble', *Physical Review Letters* 103, 070502.

Xiang, Z.-L., S. Ashhab, J. Q. You and F. Nori (2012), 'Hybrid quantum circuits: Superconducting circuits interacting with other quantum systems', arXiv preprint 1204.2137v3.

Yoshihara, F., K. Harrabi, A. O. Niskanen, Y. Nakamura and J. S. Tsai (2006), 'Decoherence of flux qubits due to 1/*f* flux noise', *Physical Review Letters* 97, 167001.

Zhu, X., A. Kemp, S. Saito and K. Semba (2010), 'Coherent operation of a gap-tunable flux qubit', *Applied Physics Letters* 97, 102503.

Zhu, X., S. Saito, A. Kemp, K. Kakuyanagi, S. Karimoto, *et al.* (2011), 'Coherent coupling of a superconducting flux qubit to an electron spin ensemble in diamond', *Nature* 478, 221–224.

12

Neural circuits and *in vivo* monitoring using diamond

K. FOX and S. PRAWER, University of Melbourne, Australia

DOI: 10.1533/9780857096685.2.291

Abstract: This chapter discusses the growing trend towards using diamond for biosensing, electrical stimulation and biological interfacing. Diamond has been proven to be an excellent material at the cell–material interface owing to its excellent chemical and biological stability. The chapter reviews the different applications of diamond depending on its surface chemistry, termination preferences and electrical conductivity. In particular, this chapter focuses on biosensing, preferential neural-network development, and the neural-stimulation and recording applications of diamond.

Key words: neural, interface, diamond, network, biosensing.

12.1 Introduction

Presently, one of the biggest obstacles facing brain–computer interface, brain-on-chip, biomarking and neural-interfacing research is the basic mechanics of the biomaterial–cell interface itself. Considerable interest has thus been placed in determining the biomaterials capable of interfacing directly with neural tissue and cell bodies at the molecular scale. Accordingly, significant research has been undertaken in the past two decades in order to unlock the details of the interface between neural networks and functional biomaterials for cell control and connectivity. Direct interfaces with the peripheral and cortical neural systems have had moderate success with successful interfacing. One of the pioneering techniques to understand neural activity was the use of extracted lamprey brains to externally control robots using basic light stimulation techniques.[1] More recently, Alpert Bozkurt's group has reported that basic electronic circuitry can be interfaced with insects to 'remote control' their movement by sending external signals into their antennae.[2–4] To this end, he was able to control the movement of both a cockroach and a moth through a maze via a remote controller. Direct cortical stimulation has recently had the most success for limb control in macaque monkeys. Using direct connection with the brain, the monkeys have been successfully able to move a robotic limb.[5, 6] However, the transition of this to human subjects has been somewhat mixed, particularly in relation to interfacing directly with the brain, with long-term limb control mostly limited to the peripheral neural interface.[5, 7–9]

Although the research into interfacing and neural control appears very exciting, there are many complexities that have restricted progress. One of the major issues

© 2014 Elsevier Ltd

stifling progression has been interfacial incompatibilities with the biomaterials used. To this end, the substrate must facilitate good cell–substrate interactions whilst constantly providing a healthy microenvironment by stimulating the interfacing cells using substrate-bound chemical, biological, electrical or mechanical signals. Silicon and metals such as platinum and titanium, although successful, suffer from long-term implantation restrictions, and thus the standard electrodes as currently used have both fabrication and biocompatibility limitations on direct interfacing with neuronal populations. Diamond has shown good evidence of being a candidate for cellular interfacing. Diamond is a material capable of both *in vivo* simulation and recording of extracellular and intracellular signals,[10, 11] and accordingly, is fast becoming a material used for electrical cellular-interfacing applications. Diamond itself is a chemically, mechanically and biologically robust biomaterial, and thus it provides the optimal direct interfacing material for sensing, stimulation, recording and network design applications. More importantly for biological applications, diamond is one of the allotropic forms of carbon, a primary component of biological tissue.

12.2 The diamond–cell interface

Inherently nanocrystalline diamond is well established as a biocompatible material for neural cells.[12–21] In fact, a study by Jakubowski *et al.* suggests that nanocrystalline diamond is a superior biomaterial to traditional medical metals owing to its resistance to bacterial colonisation.[17, 22] Furthermore, the nanocrystalline topography is reported to resemble the natural architecture of the extracellular matrix.[20] Terminated diamond, usually terminated with hydrogen, has been shown to induce and regulate neural stem cell differentiation,[12, 13] as well as to provide a DNA immobilisation tool.[16, 23–25] Chen *et al.* showed that hydrogen-terminated ultrananocrystalline films increased the capabilities of neurons to differentiate from neural stem cells.[12, 13] Accordingly, it is presumed that the increased capability of the nanocrystalline material stems from the nanoscale relationship of the diamond to the cell media due to the surface chemistry of the material.[13, 26] More specifically to ultrananocrystalline diamond, the promotion of cellular activity and proliferation may be due to the high density of wide grain boundaries in the nanostructure, characterised by a mixture of sp^2 and sp^3 carbon bonds.[27]

The chemical and physical properties of the substrate (surface energy, topography, electrostatic charge and hydrophilicity) are critical for regulating the biological activities of cells, for example proliferation, differentiation and migration.[12] The tunability of the surface termination of diamond is also a mechanism that has been reported to influence the cell interface.[12, 13, 20, 26] Plate X (see colour section between pages 218 and 219) and Fig. 12.1 show the differentiation of stem cells on diamond surfaces with different surface terminations, illustrating the dependence of stem cells on the material properties. The relatively highly hydrophilic nature of oxygen-terminated diamond is reported to form weak cell interfaces.[20] Accordingly, as the

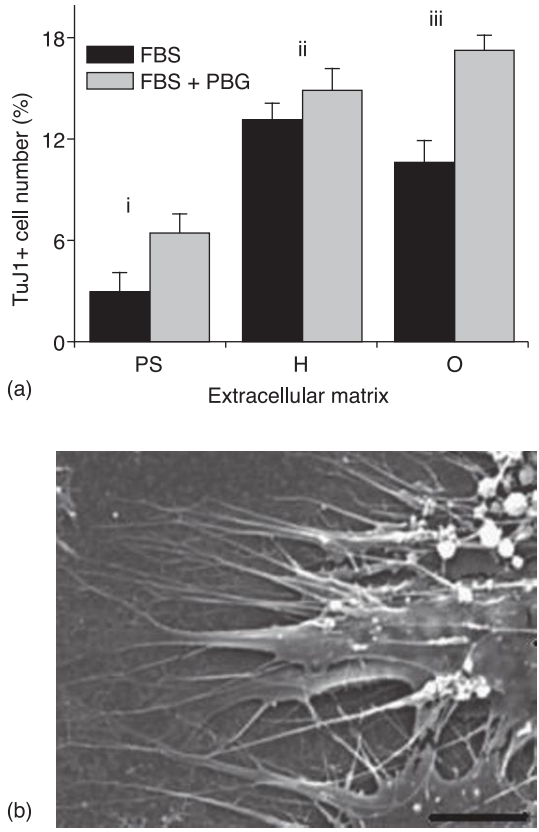

12.1 The differentiation of stem cells on diamond surfaces. (a) Numbers of cells on the substrates pictured in Plate X. (b) Mesenchymal stem cells cultured for 1 day on H-terminated ultrasmooth nanostructured diamond showing that the after one day, the cells are beginning to spread across the diamond surface. The scale bar represents 5 μm. (a) is reproduced with permission from Chen *et al.*[12] and (b) is reproduced with permission from Clem *et al.*[26]

surface becomes more hydrophilic, cell molecules may detach from the biomaterial surface over time. Alternatively, hydrogen-terminated nanocrystalline diamond, which is less hydrophilic than oxygen-terminated diamond, reportedly encourages cellular activity on the diamond surface.[20, 26, 28] In order to compensate for cell delamination on oxygen-terminated diamond, adhesion layers (e.g. poly-D-lysine and laminin) are widely used. Reports have clearly indicated that oxygen-terminated diamond surfaces with an adhesion layer have a surviving cell population above that of tissue culture plastic.[21] The influence of the hydrophobicity was assessed further by Marcon *et al.*,[29] who patterned a series of boron-doped diamond

nanowires. Here, it was reported that HeLa cells were able to grow on a nanowire patterned using silanisation (using C_{18} alkyl chains), whereby HeLa cells in FCS-supplemented media preferentially seeded on the super-hydrophobic nanowire surfaces.

The impact of diamond on cells at the interface was closely assessed by Sommer *et al.* to determine whether diamond provides a better cell scaffold than traditional materials such as polystyrene.[15] Presently, the industry standard for cell culture is polystyrene or glass, with polystyrene favoured owing to its cost. In this research, Sommer *et al.* found that a nanocrystalline diamond dish presented a better cell culture biomaterial than polystyrene, which had previously been considered the optimal material as it was unaffected by biological solutions.[15, 30, 31] This is due to two premier qualities in diamond, hardness and a lack of inherent interfacial water layers, qualities which both fail polystyrene, which reportedly softens over the cell-culturing period and forms reactive ion species, both of which are undesirable for cellular activity and longevity at the nanoscale.[15] It is well established that the cell–material interface is mediated by weak chemical bonds (polar, hydrogen and electrostatic) between cell membrane receptors and the surface chemistry of the biomaterial. Synthetic diamond, particularly that grown by chemical vapour deposition, thus has two advantages in its inherent material properties. First, its surface chemistry enables it to have an oxygen termination, where oxygen binds to dangling bonds left remaining by its surface grain boundaries, and second, its high ratio of sp^2 bonds gives the surface a negatively charged chemistry.[20, 21, 27] Both qualities are preferential for cellular adhesion.[32] The properties of hardness and mechanical, physical and chemical stability cannot be underestimated in a biological environment in which the biomaterial must remain in constant contact with physiological fluid.

12.3 Diamond biosensors

Diamond biosensors are rapidly attracting more researchers to investigate their use, owing to the exceptional electrochemical properties of diamond versus other more traditional materials. Diamond has a wide electrochemical water window. This is a very important feature for an interfacing material, as materials selected for electrical activity must remain stable without exceeding voltage limits which would harm the surrounding tissue. Accordingly, the wider the window of 'safe operation', the more flexibility there is in the material when under electrical stress and the less chance there is of material degradation, as the stimulation is less likely to be near the edge of the safe window.[33–38] More importantly, diamond has the advantage of being able to be tuned to control the material conductivity. By tuning the level of dopants such as nitrogen and boron, the diamond itself can be controlled to be highly doped (conductive and equivalent to a metal) or intrinsic (non-conductive).[16, 36]

In sensing applications, a biomaterial must be specifically tailored to the application it is required for. Here, the diamond must resist the non-specific

binding of proteins whilst providing an affinity for the specific biomolecule it is sensing. To this end, diamond provides an excellent biomaterial owing to the flexibility of diamond surfaces towards electrical and chemical modification and tailoring.[24] Most importantly, diamond appears to be stable during long-term biological exposure and to be resistant to biofouling.[39, 40] Biofouling is the most limiting problem for a sensing biomaterial, since the interface with the material is so important. In a biological microenvironment in which there is a complex matrix of proteins, boron-doped diamond has been reported to resist fouling better than glassy carbon, a material commonly used for biosensing.[40, 41] Diamond has therefore been used as a sensor for a variety of bioanalytes and particularly neurotransmitters, such as adenosine,[42] dopamine[39, 43, 44] and serotonin.[41, 45] In particular, diamond electrodes have been able to detect neurotransmitters at very low doses. Furthermore, treated electrodes have proved to be highly stable.[39, 43] This is proposed to be due to its inherently low baseline current.[38] Boron-doped diamond, owing to its conductivity has predominantly been used as a sensor;[46] however, nitrogen-doped diamond has also been reported as a successful sensor.[44] Owing to its electrochemical properties, boron-doped diamond has been used to detect neurotransmitters, as they are electrochemically active. This enables real-time detection of neurotransmitters such as dopamine and adenosine using fast-scan cyclic voltammetry, an electrochemical technique established for other carbon-based microelectrodes.[42, 44, 47] To this end, using fast-scan cyclic voltammetry or chronoamperometry, adenosine and serotonin release has been detected in real time in neonatal rat models using boron-doped microelectrodes,[42, 48] and, using nitrogen-doped diamond microelectrodes in similar models, dopamine was detected at limits (27–50 nM) similar to those for the current gold standard, carbon fibre microelectrodes.[39, 44] Dopamine sensing is difficult owing to its cohabitation with ascorbic acid within the brain. Since ascorbic acid has an oxygen potential very similar to that of dopamine, selective detection is somewhat challenging. Figure 12.2 demonstrates a possible experimental set-up for the detection of serotonin using an implanted boron-doped diamond electrode as the sensing electrode.

12.4 Neural networks using diamond

The development of biomaterials capable of promotion of specific cells is a long-existing challenge. Many biomaterials selected for such applications have, however, failed at the interface, whereby either specificity was achieved but the material failed over time in the harsh biological environment or the cell promotion/specificity was uncontrolled over time. One of the main objectives of achieving such cell specificity is to provide neural networks. Accordingly, the transition from a neural-compatible material to a biomaterial capable of network development is a challenging prospect. To this end, to create a functional neuronal network *in vitro*, an ordered arrangement of neuronal cells is required. This involves placing

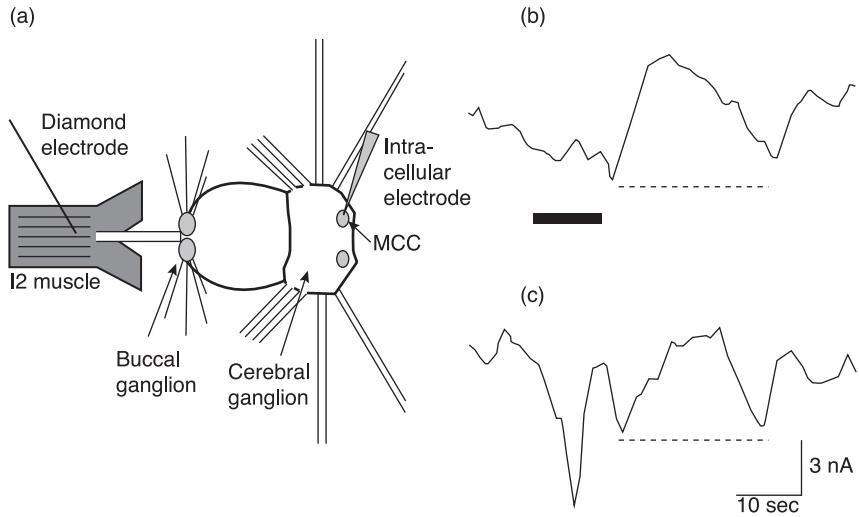

12.2 In vitro detection of serotonin in the I2 muscle of the mollusc *Aplysia californica*. (a) Experimental set-up using a boron-doped diamond electrode. An electrode is placed inside a metacerebral cell (MCC) and the diamond electrode in the I2 muscle. (b) Stimulation of the metacerebral cell. The black bar shows the stimulus, providing 36 action potentials (current vs time recorded at 0.667 V vs Ag/AgCl). (c) The control wherein 10 mL of 10 nM serotonin was added to the both and the stimulation conditions of (b) repeated. Reproduced with permission from Halpern *et al.*[48]

cells in specific locations to create organised structures. Current methods to achieve this involve patterning techniques to selectively control neural seeding and network development or orientation. More specifically, substrates are typically not inherently capable of promoting neuronal growth. Thus, secondary coatings using adhesion molecules or promoters such as polyornithine, poly-D-lysine and laminin have been used to control the geometry of neuronal networks, guide neurite outgrowth, and act as an attraction and retention mechanism for neuronal cell populations.[21, 49]

Many studies have attempted to develop neural networks on diamond. Using single-crystal diamond, Specht *et al.*[50] developed a neural population from cortical neurons from mouse embryos. In this research, oxygen-terminated (hydrophilic) and hydrogen-terminated (hydrophobic) single-crystal diamond was stamped with secondary proteins such as laminin to form patterned cell-attractive scaffolds. The primary neuron attachment appeared to be directly dependent on the laminin pattern, and neurons were undetected on uncoated diamond (Fig. 12.3). Neurite patterns were detected after 48 h, with neurite formation detectable within the first day. In later work, Thalhammer *et al.*[51] showed that the nanotopography of diamond may be a key to successful network formation. Here it was reported that

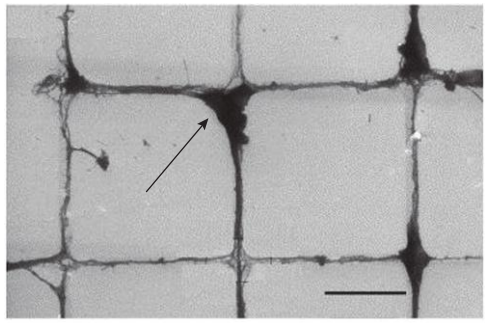

12.3 Example of a successfully patterned neural network on diamond. A network of neurons cultured on laminin-coated hydrophilic diamond. The scale bar represents 25 μm. The arrow shows the neurons cutting the corner of the pattern. This is likely to be due to inconsistencies in the stamping of the pattern rather than material affinity. Modified from Specht *et al.*[50]

using a nanodiamond coating on a variety of biomaterials (glass, nanocrystalline diamond, polycrystalline diamond and silicon) was sufficient for neuronal-network formation, eliminating the need for adhesion promoters (Plate XI). This follows the literature reports for other materials. Silicon, for example, has been used a cell culture material, where patterned cell growth of nigral cells (nerve cells from the subthalamus) was elicited by forming a grid of nanoroughened silicon (R_a 25 nm) on polished silicon (3 nm).[52] After seeding, it was reported that on day 5, the cells had migrated and adhered to the rougher elements of the grid. Combining the results of Specht *et al.*[50] and Thalhammer *et al.*,[51] May *et al.*[21] recently sought to produce a neural network using laser-patterned oxygen-terminated boron-doped microcrystalline diamond. Although they were able to grow a patterned neural network using a combination of poly-D-lysine and laser patterning, it could not be proven that the differentiation on the microcrystalline diamond was due to the material, the adhesion promoters, the unfriendly underlying silicon or the remnant by-products of laser etching (Plate IX).

12.5 Neural stimulation and recording using diamond

As discussed previously, the capacity for the development of conducting diamond using dopants such as nitrogen and boron provides an exceptional opportunity for diamond to be used in neural stimulation and recording applications. The use of diamond microelectrodes for passive recording applications extends back to the early 2000s, when research was undertaken to test the capabilities of boron-doped diamond as a neural recorder by hooking a diamond microelectrode to the buccal nerve of a marine mollusc, *Aplysia californica*, a commonly used animal model for neurodynamic studies.[46, 48] Similarly, nitrogen-doped nanocrystalline diamond

films (originally developed by Argonne Laboratories) have also proven to be a successful candidate for neural stimulation.[14, 36, 53]

Further interest in diamond for neural applications has been generated by the development of high-density microelectrode arrays for neural recording. Microelectrode arrays are one means to stimulate cells and record extracellular electrical activity from electrically active neural networks. However, a major impediment to using the current metallic-based electrodes is that high-density arrays require a large number of wires to address each electrode. Diamond, on the other hand, can be used to make large-density microelectrode arrays using the microfabrication techniques established in the electronics industry.[54–56] Here, using lithography, a monolithic diamond material can be converted into an array by selective doping. The high surface area of the conductive diamond material ($\approx$ 5 nm crystals) reportedly provides a charge injection of 15 to 170 $\mu C\,cm^{-2}$, placing it as an equivalent biomaterial to platinum for neural-stimulation applications (Table 12.1).[36]

Owing to the aforementioned high charge injection of doped ultrananocrystalline diamond[10, 36] and its recognised value as a medical coating material,[16, 19, 53, 57–59] significant interest has occurred recently in its use as an implantable neural electrode. In particular, diamond has formed the primary interface material in three versions of artificial retina devices. Argonne Laboratories has investigated the use of undoped ultrananocrystalline diamond as a bioinert coating material for silicon microchip encapsulation.[53] Meanwhile, the Dreams project[28, 55, 56] headed by Philippe Bergonzo has investigated the development of a biocompatible artificial nanocrystalline diamond device for retinal stimulation, in which the planned multielectrode array uses diamond as its semiconductor material to form 64 electrodes capable of interfacing with neurons in the retina. In 2011, Bergonzo *et al.*[55] reported the fabrication of a 3D retinal multielectrode device (Fig. 12.4(a)). That paper reported the fabrication of a flexible 3D device comprising 64 isolated electrodes fabricated using the standard nanotechnology processes of seeding, patterning and growth using sacrificial substrates. No stimulation data was

Table 12.1 The reported charge injection of various biomaterials used in neural stimulation

Electrode material	Charge injection capacity ($\mu C\,cm^{-2}$)
N-UNCD	15.4–37.4
Activated N-UNCD	49–300
Pt and PtIr alloys	50–150
Titanium nitride	1000
Iridium oxide	1000–5000

UNCD, ultrananocrystalline diamond

Sources: UNCD values taken from Garrett *et al.*[36] and Hadjinicolaou *et al.*[14]; Pt, Ti and IrO_x values taken from Cogan.[33]

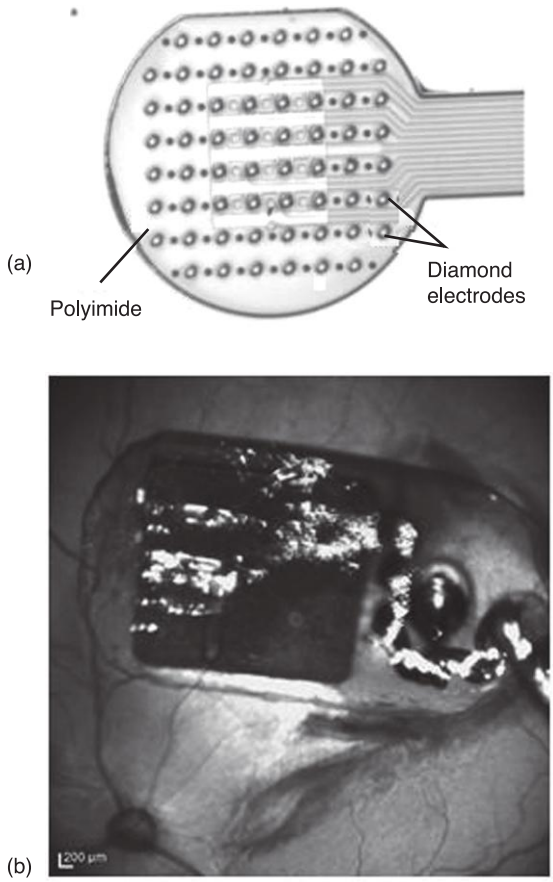

12.4 Current retinal implants comprising diamond. (a) The diamond implant developed by the Dreams project (modified from Bergonzo *et al.*[55]). (b) Image of an implanted Bionic Eye Project device. Both devices use diamond as the stimulating electrode.

reported, so it can be presumed that the device was inactive, but histology suggests that when it is implanted sub-retinally (underneath the retina), no biocompatibility issues occur. No further data has been published on this research project.

Work on the most advanced retinal implant comprising diamond electrodes has recently commenced as part of the Bionic Eye Project, an Australian research project formed to develop next-generation retinal implant devices.[36, 54, 60] The retinal prosthesis includes a multielectrode array comprising a series of independent and electrically isolated nitrogen-doped ultrananocrystalline diamond electrodes within an insulating polycrystalline diamond sheet (Fig. 12.4(b)). Although pre-clinical data is yet to be reported, *in vitro* results indicate that ultrananocrystalline diamond can effectively stimulate explanted wholemount

retina from pigmented Long Evans rats.[14] By directly stimulating the retinal ganglion cells in the wholemount retina, electrical stimulation of the somas could be achieved using the conducting ultrananocrystalline electrodes. The electrodes achieved this at 200 $\mu C\,cm^{-2}$, well within the anticipated charge injection limit of 250 $\mu C\,cm^{-2}$.

12.6 Future trends

Diamond-based microelectrode arrays have a long future in neural applications. In particular, the capacity of diamond to be fabricated to build high-resolution, small, tightly packed electrode arrays using wet chemistry, lithography and other standard microfabrication techniques enables it to be easily integrated with microcircuitry. Diamond devices have the capacity to be developed using top-down and bottom-up processes. This provides significant material flexibility. However, one of the greatest advantages of the material is the capacity for 3D structures to be formed without the need for wires, using instead the conductivity introduced by doping to provide conductive channels that interface directly with electronic circuitry. For a high-electrode device, this is paramount. Microelectrodes themselves are a technology driven by need. In particular, in neurophysiology, diamond-based electrodes have the requisite high sensitivity, temporal resolution and small size to be able to be directly inserted into neural networks and synaptic spaces.[61] Given the recognised high affinity for neural cells at the interface between the biology and the biomaterial, diamond is ideally poised to take a leading role in long-term neural stimulation and recording applications.

One of the leading advantages of diamond microelectrode or even nanoelectrode arrays is the ability to develop three-dimensional array systems. Given that diamond deposition commonly occurs using sacrificial scaffolds in a chemical vapour deposition chamber, 3D structures are easily fabricated (see for example Ganesan *et al.*[54]). What this may achieve in the future as the resolution of devices becomes higher is that direct neural stimulation and recording may be possible within the cell matrix as neurons envelop the biomaterial. This is essential when one considers that the human brain is reported to have an estimated 85 billion neurons.[62] Diamond itself is well equipped to answer many questions about neural interfacing. By producing multielectrode arrays from diamond, one can provide the signal transduction required to ensure that both the environment and the material remain stable over time, a property crucial for direct neural or cell interfacing.

12.7 References

1. K. F. B. Reger, V. Sanguineti, S. S. Alford and F. Mussa-Ivaldi, ‘Connecting brains to robots: an artificial body for studying computational properties of neural tissues’, *Artificial Life*, vol. 6, pp. 307–324, 2000.

2. T. Latif and A. Bozkurt, 'Line following terrestrial insect biobots', *34th International Conference of the IEEE Engineering in Medicine and Biology Society*, pp. 972–975, 2012.
3. A. Bozkurt, R. F. Gilmour, A. Sinha, D. Stern and A. Lal, 'Insect–machine interface based neurocybernetics', *IEEE Transactions on Biomedical Engineering*, vol. 56, pp. 1727–1733, 2009.
4. A. Bozkurt, R. F. Gilmour and A. Lal, 'Balloon-assisted flight of radio-controlled insect biobots', *IEEE Transactions on Biomedical Engineering*, vol. 56, pp. 2304–2307, 2009.
5. S. Perel, A. B. Schwartz, M. C. Spalding, M. Velliste and A. S. Whitford, 'Cortical control of a prosthetic arm for self-feeding', *Nature*, vol. 453, pp. 1098–1101, 2008.
6. D. D. M. Nicolelis, J. Carmena, R. Crist, G. Lehew, J. Kralik and S. Wise, 'Chronic, multisite, multielectrode recordings in macaque monkeys', *Proceedings of the National Academy of Sciences of the USA*, vol. 100, pp. 11041–11046, 2003.
7. L. R. Hochberg, M. D. Serruya, G. M. Friehs, J. A. Mukand, M. Saleh, *et al.*, 'Neuronal ensemble control of prosthetic devices by a human with tetraplegia', *Nature*, vol. 442, pp. 164–171, 2006.
8. E. E. Fetz, C. T. Moritz and S. I. Perlmutter, 'Direct control of paralysed muscles by cortical neurons', *Nature*, vol. 456, pp. 639–643, 2008.
9. K. Warwick and V. Ruiz, 'On linking human and machine brains', *Neurocomputing*, vol. 71, pp. 2619–2624, 2008.
10. R. B. Jackman, 'Diamond electronics', *Semiconductor Science and Technology*, vol. 18, pp. S86–S95, 2003.
11. D. J. Garrett, K. Ganesan, A. Stacey, K. Fox, H. Meffin and S. Prawer, 'Ultra-nanocrystalline diamond electrodes: optimization towards neural stimulation applications', *Journal of Neural Engineering*, vol. 9, p. 10, 2012.
12. Y.-C. Chen, D.-C. Lee, C.-Y. Hsiao, Y.-F. Chung, H.-C. Chen, *et al.*, 'The effect of ultrananocrystalline diamond films on the proliferation and differentiation of neural stem cells', *Biomaterials*, vol. 30, pp. 3428–3435, 2009.
13. Y.-C. Chen, D.-C. Lee, T.-Y. Tsai, C.-Y. Hsiao, J.-W. Liu, *et al.*, 'Induction and regulation of differentiation in neural stem cells on ultrananocrystalline diamond films', *Biomaterials*, vol. 31, pp. 5575–5587, 2010.
14. A. E. Hadjinicolaou, R. T. Leung, D. J. Garrett, K. Ganesan, K. Fox, *et al.*, 'Electrical stimulation of retinal ganglion cells with diamond and the development of an all diamond retinal prosthesis', *Biomaterials*, vol. 33, pp. 5812–5820, 2012.
15. A. P. Sommer, M. Haddad and H.-J. Fecht, 'It is time for a change: Petri dishes weaken cells', *Journal of Bionic Engineering*, vol. 9, pp. 353–357, 2012.
16. C. E. Nebel, D. Shin, B. Rezek, N. Tokuda, H. Uetsuka and H. Watanabe, 'Diamond and biology,' *Journal of the Royal Society Interface*, vol. 4, pp. 439–461, 2007.
17. W. Jakubowski, G. Bartosz, P. Niedzielski, W. Szymanski and B. Walkowiak, 'Nanocrystalline diamond surface is resistant to bacterial colonisation', *Diamond and Related Materials*, vol. 13, pp. 1761–1763, 2004.
18. M. Amaral, P. S. Gomes, M. A. Lopes, J. D. Santos, R. F. Silva and M. H. Fernandes, 'Cytotoxicity evaluation of nanocrystalline diamond coatings by fibroblast cells', *Acta Biomaterialia*, vol. 5, pp. 755–763, 2009.
19. K. Fox, R. Judge, J. Palamara and A. D. Greentree, 'Diamond as a scaffold for bone growth', *Journal of Materials Science: Materials in Medicine*, vol. 24, pp. 849–861, 2012.

20. L. Grausova, L. Bacakova, A. Kromka, M. Vanecek, B. Rekek and V. Lisa, 'Molecular markers of adhesion, maturation and immune activation of human osteoblast-like MG 63 cells on nanocrystalline diamond films', *Diamond and Related Materials*, vol. 18, pp. 258–263, 2009.
21. P. W. May, E. M. Regan, A. Taylor, J. Uney, A. D. Dick and J. McGeehan, 'Spatially controlling neuronal adhesion on CVD diamond', *Diamond and Related Materials*, vol. 23, pp. 100–104, 2012.
22. K. Mitura, P. Niedzielski, G. Bartosz, J. Moll, B. Walkowiak and Z. Pawlowska, 'Interactions between carbon coatings and tissue', *Surface and Coatings Technology*, vol. 201, pp. 2117–2123, 2006.
23. N. Bijnens, V. Vermeeran, M. Daenan, L. Grieten, K. Haenen and S. Wenmackers, 'Synthetic diamond films as a platform material for label-free protein sensors', *Physica Status Solidi A: Applied Materials*, vol. 206, pp. 520–526, 2009.
24. R. J. Hamers, J. E. Butler, T. Lasseter, B. M. Nichols, J. N. Russell, *et al.*, 'Molecular and biomolecular monolayers on diamond as an interface to biology', *Diamond and Related Materials*, vol. 14, pp. 661–668, 2005.
25. K. Takahashi, M. Tanga, O. Takai and H. Okamura, 'DNA preservation using diamond chips', *Diamond and Related Materials*, vol. 12, pp. 572–576, 2003.
26. W. C. Clem, S. Chowdhury, S. Cateledge, J. Weimer, F. Shaikh, *et al.*, 'Mesenchymal stem cell interaction with ultra-smooth nanostructured diamond for wear-resistant orthopaedic implants', *Biomaterials*, vol. 29, pp. 3461–3468, 2008.
27. B. Shi, Q. Jin, L. Chen and O. Auciello, 'Fundamentals of ultrananocrystalline diamond (UNCD) thin films as biomaterials for developmental biology: Embryonic fibroblasts growth on the surface of (UNCD) films', *Diamond and Related Materials*, vol. 18, pp. 596–600, 2009.
28. M. Kopecek, L. Bacakova, J. Vacik, F. Fendrych, V. Vorlicek, *et al.*, 'Transparent diamond-on-glass micro-electrode arrays for ex-vivo neuronal study', *Physica Status Solidi A: Applied Materials*, vol. 205, p. 2146, 2008.
29. L. Marcon, A. Addad, Y. Coffinier and R. Boukherroub, 'Cell micropatterning on superhydrophobic diamond nanowires', *Acta Biomaterialia*, vol. 9, pp. 4585–4591, 2013.
30. A. P. Sommer, D. Zhu, T. Scharnweber and H.-J. Fecht, 'Body building on diamond', *Journal of Bionic Engineering*, vol. 6, pp. 14–17, 2009.
31. A. P. Sommer, D. Zhu, M. Wiora and H.-J. Fecht, 'Top of the biomimetic triangle', *Journal of Bionic Engineering*, vol. 5, pp. 91–94, 2008.
32. J. E. Davies, 'The importance and measurement of surface charge species in cell behaviour at the biomaterial interface', in *Surface Characterization of Biomaterials*, ed. B. D. Ratner, Amsterdam: Elsevier Science, 1988, pp. 219–234.
33. S. F. Cogan, 'Neural stimulation and recording electrodes', *Annual Review of Biomedical Engineering*, vol. 10, pp. 275–309, 2008.
34. S. B. Brummer and M. J. Turner, 'Electrochemical considerations for safe electrical stimulation of the nervous system with platinum electrodes', *IEEE Transactions on Biomedical Engineering*, vol. 24, pp. 59–63, 1977.
35. S. B. Brummer, L. S. Robblee and F. T. Hambrecht, 'Criteria for selecting electrodes for electrical-stimulation – theoretical and practical considerations', *Annals of the New York Academy of Sciences*, vol. 405, pp. 159–171, 1983.
36. E. M. Hudak, J. T. Mortimer and H. B. Martin, 'Platinum for neural stimulation: voltammetry considerations', *Journal of Neural Engineering*, vol. 7, p. 026005, 2010.
37. H. B. Martin, A. Argoitia, A. Anderson, U. Landau and J. C. Angus, 'Hydrogen and oxygen evolution on boron doped diamond electrodes', *Journal of the. Electrochemical Society*, vol. 143, pp. L133–L136, 1996.

38. A. Fujishima, T. N. Rao, E. Popa, B. V. Sarada, I. Yagi and D. A. Tryk, 'Electroanalysis of dopamine and NADH at conductive diamond electrodes', *Journal of Electroanalytical Chemistry*, vol. 473, pp. 179–185, 1999.
39. R. Trouillon and D. O'Hare, 'Comparison of glassy carbon and boron doped diamond electrodes: Resistance to biofouling', *Electrochimica Acta*, vol. 55, pp. 6586–6595, 2010.
40. A. Fagan-Murphy, F. Watt, K. A. Morgan and B. A. Patel, 'Influence of different biological environments on the stability of serotonin detection on carbon-based electrodes', *Journal of Electroanalytical Chemistry*, vol. 684, pp. 1–5, 2012.
41. S. Xie, G. Shafer, C. G. Wilson and H. B. Martin, '*In vitro* adenosine detection with a diamond-based sensor', *Diamond and Related Materials*, vol. 15, pp. 225–228, 2006.
42. D. A. Tryk, H. Tachibana, H. Inoue and A. Fujishima, 'Boron-doped diamond electrodes: The role of surface termination in the oxidation of dopamine and ascorbic acid', *Diamond and Related Materials*, vol. 16, pp. 881–887, 2007.
43. P. U. Arumugam, H. Zeng, S. Siddiqui, D. P. Covey, J. A. Carlisle and P. A. Garris, 'Characterization of ultrananocrystalline diamond microsensors for *in vivo* dopamine detection', *Applied Physics Letters*, vol. 102, 253107, 2013.
44. H. Zhao, X. Bian, J. J. Galligan and G. M. Swain, 'Electrochemical measurements of serotonin (5-HT) release from the guinea pig mucosa using continuous amperometry with a boron-doped diamond microelectrode', *Diamond and Related Materials*, vol. 19, pp. 182–185, 2010.
45. J. M. Halpern, M. J. Cullins., H. J. Chiel and H. B. Martin, 'Chronic *in vivo* nerve electrical recordings of *Aplysia californica* using a boron-doped polycrystalline diamond electrode', *Diamond and Related Materials*, vol. 19, pp. 178–181, 2010.
46. K. A. El-Nour and A. Brajter-Toth, 'Sensitivity of electrochemically nanostructured carbon fiber ultramicroelectrodes in the determination of adenosine', *Electroanalysis*, vol. 12, pp. 805–810, 2000.
47. J. M. Halpern, S. Xie, G. P. Sutton, B. T. Higashikubo, C. A. Chestek, *et al.*, 'Diamond electrodes for neurodynamic studies in *Aplysia californica*', *Diamond and Related Materials*, vol. 15, pp. 183–187, 2006.
48. S. Kelly, E. Regan, J. Uney, A. Dick, J. McGeehan, *et al.*, 'Patterned growth of neuronal cells on modified diamond-like carbon substrates', *Biomaterials*, vol. 29, pp. 2573–2580, 2008.
49. C. Specht, O. Williams, R. B. Jackman and R. Schoepfer, 'Ordered growth of neurons on diamond', *Biomaterials*, vol. 25, pp. 4073–4078, 2004.
50. A. Thalhammer, R. J. Edgington, L. A. Cingolani, R. Schoepfer and R. B. Jackman, 'Nanodiamond monolayer coating promotes formation of functional neuronal networks', *Biomaterials*, vol. 31, pp. 2097–2104, 2010.
51. Y. W. Fan, F. Z. Cui, S. P. Hou, Q. Y. Xu, L. N. Chen and I.-S. Lee, 'Culture of neural cells on silicon wafers with nano-scale surface topography', *Journal of Neuroscience Methods*, vol. 120, pp. 17–23, 2002.
52. O. Auciello and A. V. Sumant, 'Status review of the science and technology of ultrananocrystalline diamond (UNCD™) films and application to multifunctional devices', *Diamond and Related Materials*, vol. 19, pp. 699–718, 2010.
53. K. Ganesan, A. Stacey, H. Meffin, S. Lichter, U. Greferath, *et al.*, 'Diamond penetrating electrode array for epi-retinal prosthesis', presented at the Annual International Conference of the IEEE Engineering in Medicine and Biology Society, 2010.
54. P. Bergonzo, A. Bongrain, E. Scorsone, A. Bendali, L. Rousseau, *et al.*, '3D shaped mechanically flexible diamond microelectrode arrays for eye implant applications: The MEDINAS project', *IRBM*, vol. 32, pp. 91–94, 2011.

55. M. Bonnauron, S. R. L. Saada, G. Lissorgues, C. Mer and P. Bergonzo, 'High aspect ratio diamond microelectrode array for neuronal activity measurements', *Diamond and Related Materials*, vol. 17, pp. 1399–1404, 2008.
56. M. J. Papo, S. A. Catledge and Y. K. Vohra, 'Mechanical wear behavior of nanocrystalline and multilayered diamond coatings on temporomandibular joint implants', *Journal of Materials Science: Materials in Medicine*, vol. 15, p. 773, 2004.
57. L. Booth, S. Catledge, D. Nolen, R. Thompson and Y. Vohra, 'Synthesis and characterization of multilayered diamond coatings for biomedical implants', *Materials*, vol. 4, pp. 857–868, 2011.
58. K. L. Soh, W. P. Kang, J. L. Davidson, Y. M. Wong, D. E. Cliffel and G. M. Swain, 'Diamond-derived ultramicroelectrodes designed for electrochemical analysis and bioanalyte sensing', *Diamond and Related Materials*, vol. 17, pp. 900–905, 2008.
59. F. Azevedo, L. Carvalho, L. Grinberg, J. Farfel, R. Ferretti, *et al.*, 'Equal numbers of neuronal and non-neuronal cells make the human brain an isometrically scaled-up primate brain', *Journal of Computational Neuroscience*, vol. 513, pp. 532–541, 2009.

Part III

The future

This page intentionally left blank

13

Promising directions in diamond technologies for quantum information processing (QIP) and sensing

I. AHARONOVICH, University of Technology Sydney, Australia and S. PRAWER, University of Melbourne, Australia

DOI: 10.1533/9780857096685.3.307

Abstract: This final chapter summarizes some of the emerging topics in the usage of diamond for quantum information processing. Practical applications include biosensing and bioimaging using colour centres in diamond, as well as pathways towards integrated quantum photonics using diamond as a platform. On the other hand, challenges will be discussed, including surface terminations and engineering new, superior optically active defects. Finally, we discuss the outlook for the field of quantum information processing (QIP) with diamond.

Key words: diamond nanophotonics, sensing, emitter stability near surface, ultrabright defects, optomechanics.

13.1 Introduction

In this final chapter, we would like to highlight several directions in which diamond, particularly quantum emitters in diamond, will play a central role. There are three main themes that will keep scientists, engineers and entrepreneurs very occupied:

- Practical applications, predominantly in sensing, that have huge commercial opportunities and prospects in the life science field.
- Fundamental science, mainly the understanding of light–matter interactions at the nanoscale and exploration of novel phenomena in diamond, for example optomechanics, Raman lasing and strong coupling.
- Challenges in diamond that have to be solved to achieve superior sensing performance, higher-quality single emitters, control of the diamond surface and much more.

13.2 Nanodiamonds for high-resolution sensors

Nanodiamonds containing single NV centres are becoming the platform of choice for a variety of quantum sensing applications. Some of these have been highlighted in other chapters of this book. Here we like to draw the reader's attention to four more promising directions (to date) where nanodiamonds can be enviable building blocks for high-resolution sensors, particularly in biological systems.

© 2014 Elsevier Ltd

Quantum sensing in biological systems is possible using optical readout of the electron spin state of the NV centre, which can be accomplished under ambient conditions. By understanding the spin Hamiltonian, one can see that several sensing avenues are easy to demonstrate.[1] The first and most straightforward sensing application is ambient magnetic fields. Since the first magnetometer was demonstrated in 2008, magnetic sensing employing nanodiamonds has sparked considerable interest.[2–7] As was described in Chapter 12, nanodiamonds hosting single NV centres can be incubated within living cells and used as nanoscale magnetic probes. Imaging fluctuating magnetic fields due to diffusing calcium or other ions in biological ion channels and lipid bilayers is becoming a reality.[8, 9] Moreover, nanodiamonds have been used as non-invasive biomedical probes to image *in vivo* – within scattering tissues.[10] Finally, research into nanoscale magnetometers has recently enabled a ground-breaking realization of nanoscale nuclear magnetic resonance (NMR).[11, 12] The NMR spectrum was recorded from a $(5\,\text{nm})^3$ volume voxel of various fluids, located on top of a bulk diamond surface. The atomic magnetic sensor was a single NV centre pre-positioned within 7 nm of the diamond surface. The incredible development of nanoscale magnetometry with single NV centres will certainly continue, and nanoscale MRI employing diamond platforms will be a hot topic in the coming decade.

In addition, however, since we are dealing with an isolated quantum system, fluctuations in the electric field, strain and temperature also alter the system, and therefore can be detected.[13] As expected, single NV centres have been employed to demonstrate electric-field sensing, temperature sensing and even pressure sensing. The initial experiments were performed with bulk diamond crystals; however, for biological purposes, there is strong incentive to translate these measurements to the nanodiamond platform. Recently, several groups have independently demonstrated temperature sensing using nanodiamonds, with the impressive achievement of temperature measurement within a biological medium (a living cell)[14–16] (Plate XII; see colour plate section between pages 218 and 219). These temperature measurements are possible owing to the temperature dependence of the spin Hamiltonian of a single NV centre. Therefore, using certain coherent pulse sequences, one can isolate the temperature contribution and determine the temperature with a resolution of several mK $\text{Hz}^{-1/2;}$.

The versatile sensing platform enabled by nanodiamonds paves the way for fascinating opportunities in nanoscale biological applications, for instance monitoring and controlling temperature-dependent chemical processes within living cells, tumour activity identification, and localized thermoablative therapy. In addition, the combination of magnetic- and electric-field sensing employing the same probe – a nanodiamond – will allow the identification and mapping of complex systems in three dimensions, including neuron mapping, and hopefully assist us in understanding the most complex system of all – our brain.

However, before this occurs, several challenges must be addressed, including the optimization of coherence times in smaller crystals, the elimination of

surrounding paramagnetic defects and the optimization of the production of NV centres with nanoscale resolution. We will discuss this in more detail in Section 13.3.

13.3 Exploiting fundamental properties: optomechanics and other areas of advanced research

In this section, we will highlight possible directions that leverage the fundamental properties of quantum emitters and the diamond platform. The coupling between optical, electrical and mechanical degrees of freedom allows advanced investigation of topics such as light–matter interactions and optomechanics.

13.3.1 Optomechanics

The field of optomechanics is fascinating because it gives direct evidence of coupling between mechanical and optical degrees of freedom. Ground-breaking work employing silicon nanoresonators has demonstrated intriguing physical phenomena such as the cooling of resonators to their ground state, and radiation pressure forces.[17, 18] Diamond offers yet another advantage, as it can host single optically active defects that can be coupled to the mechanical modes of a resonator.[19]. In addition, mechanical control of the electron spin in a single NV centre offers yet another degree of quantum computation and sensing. Indeed, several recent reports have demonstrated coherent quantum control of a single spin driven by the motion of a mechanical resonator[20, 21] (see Plate XIII(a) for a schematic illustration). By monitoring the spin state of the NV centre, one can sense the motion of the resonator. Since the NV centre is effectively an atomically localized spin sensor, the sensitivity of the hybrid system is ~50 pm/(Hz)$^{1/2}$, which is comparable with that of optical interferometry techniques. By integrating NC systems that exhibit T_2 values of a few milliseconds and by enhancement of the collection efficiency, displacement amplitude sensitivities below 30 fm/(Hz)$^{1/2}$ can potentially be achieved.

Diamond exhibits the highest Young's modulus of all materials and can potentially operate at higher frequencies. In parallel with developing spin–mechanical interfaces, several groups have fabricated very high-Q diamond mechanical resonators with quality factors exceeding one million at low temperatures and approaching half a million at room temperature.[22, 23] Combining the spin interface with extremely high-quality mechanical resonators is paving the way to a new era of nanoscale sensing.

13.3.2 Quantum photonics

The realization of many quantum photonic architectures requires optical coupling of several components, including waveguides, resonators, optical cavities and others. Before diamond photonic networks become a reality, routine fabrication of individual

components will need to be available. Indeed, tremendous progress in the realization of photonic resonators and optical cavities has been achieved in recent years. In these two hybrid approaches, polycrystalline materials and single-crystal diamond have been subjected to dedicated nanofabrication processes that eventually resulted in high-quality devices.[19, 24–30] However, it is well acknowledged that we are still way behind silicon and GaAs in terms of device quality factors, scalability and performance.

The fabrication and design of various devices were highlighted in Chapter 5. That chapter also included a rather revolutionary method for the fabrication of devices out of single-crystal diamond using an angled reactive-ion-etching technique. Interestingly, the construction of the first diamond photonic-crystal cavity out of polycrystalline material was demonstrated almost a decade ago.[31] However, it took several years to realize a working device made entirely out of single-crystal diamond. This emphasizes the main difficulty in diamond photonics – the availability of high-quality thin diamond membranes (a few hundred nanometres thick) made from very high-quality material.[32] Recent research has demonstrated several approaches to addressing this hurdle. In one approach, damaged diamond membranes are employed to grow a new, pristine, single-crystal diamond layer that can subsequently be used for devices. This 'bottom-up' version of a method to generate photonic resonators also enables the fabrication of three-dimensional structures that are fundamentally not available with top-down etching.[33, 34] A different approach to tackling the same problem, perhaps inspired by the field of graphene, involves the generation of vertical membranes by patterning 'lines' in single-crystal diamond.[35] The resulted diamond 'nanowalls' are then exfoliated and positioned on top of a new substrate.

Although a large-scale integrated photonic network in diamond is yet to be shown, entanglement between two remote NV centres has been demonstrated.[36, 37] Surprisingly, this rather complicated and conceptually challenging task required only the addition of diamond solid immersion lenses, which are relatively easy to fabricate. In principle, every component required to demonstrate entanglement among multiple NV centres exists, and it will be only a matter of time until such an experiment is done. From there onwards, the route to quantum computation and quantum information processing, and particularly quantum simulation, is widely anticipated.

Looking forward towards a fully integrated photonic network, or at least a coupled photonic-crystal cavity connected via a waveguide, an immediately emerging issue is control over the position of the emitters within the network. In systems such as GaAs, a quantum dot can be grown epitaxially and, hence, deterministically positioned in the middle of a photonic crystal. In diamond, the emitters are engineered via ion implantation or incorporation via growth. These two techniques are yet to show nanometre resolution. Moreover, the constant issue of the proximity of the emitter to the surface, which results in spectral broadening, spectral diffusion and blinking, is an unsolved problem, which will be discussed below. We envision that a significant proportion of research will be dedicated to addressing these issues.

13.3.3 Electrically activated single-photon sources

Another paramount direction in diamond quantum information science is the electrical excitation of single-photon sources. Electrically activated devices are important for several reasons:

- They allow efficient packaging and device integration. Electrical excitation of optical components such as light-emitting diodes (LEDs) and lasers enables the final device to be to miniaturized further.
- They provide scalability. Electrical excitation will immediately result in arrays of emitters that can be excited in parallel.
- They will provide better understanding of the photophysics of emitters. Optical excitation of diamond emitters due to sub-band-gap excitation (i.e. 532 nm light) often occurs. However, electrical excitation of single emitters will give us a better understanding of the relaxation paths and charge transfer within the diamond band gap.
- Finally, hybrid devices will become possible and become easier to fabricate, for instance by the generation of hybrid GaN–diamond, AlN–diamond or ZnO–diamond devices, where charge transfer occurs at the interface between the two semiconductors.

Nevertheless, despite the promising opportunities, research into the electrical excitation of quantum emitters in diamond is sparse. The focal challenge remains the efficient generation of n-type material and low-threshold emitter excitation. It is important to mention that the initial interest in the electronic–optical domain in diamond started with the discovery of silicon–vacancy emitters via cathodoluminescence. The group led by A. Gorokhovsky demonstrated electrically excited Xe centres; however, that work was based on ensemble measurements.[38] Electrical excitation of quantum emitters was achieved only recently, by two independent, though closely related approaches[39,40] (see Plate XIII(b) for a schematic illustration). Here, vertical and horizontal pin junctions in diamond were fabricated with single NV centres located in the 'i' part of the diode. Despite the working device, most of the fluorescence was associated with a neutral NV centre, rather than the desired negative one. This is due to the level structure of these centres within the large conduction band of diamond. Subsequent work by Kato *et al.*[41] showed, in fact, that applying a negative bias to the LED resulted in a shift from NV^0 to NV^-. However, electrically driven single NV centres are yet to be shown.

13.4 Challenges in diamond materials science

13.4.1 Drive for stable emitters very near surfaces

As has recently been stated in a review by Wrachtrup *et al.*,[42] the fabrication of NV centres with properties such as a long decoherence time very close (<10 nm) to the surface is highly desirable for applications in magnetometry and for the coupling of

NV centres to photonic structures. For many applications, it is also highly desirable to be able to deterministically place an NV centre with a lateral precision of within a nanometre. However, the diamond surface can play havoc with the properties of NV centres. Surface termination, surface defects and surface functionalization can all affect the charge stability of NV centres. Recently, there has been a growing awareness that the damage due to polishing may be a limiting factor and that there is a need to develop techniques for the production of ultrasmooth, defect-free surfaces. One intermediate step is to reduce the effect of the surface by the overgrowth of a 30 nm thick epitaxial layer of diamond on a surface which has been irradiated with low-energy (2.5 keV) N ions.[43] This technique was found to increase the T_2 time by an order of magnitude. Of course, the overgrowth increases the distance between the NV centre and the surface. An alternative approach is to grow a delta-doped layer of N-doped diamond sandwiched between two layers of undoped diamond.[44] That study showed that proximity to the surface remained a source of decoherence, with T_2 increasing from 100 μs when the cap layer was 5 nm thick to 600 μs when the cap layer thickness was greater than 50 nm.

These studies point to the need to both understand and control the diamond surface better, if possible at the nanoscale. Common surface termination techniques such as exposure to H or O plasmas can result in etching or pitting of the surface. Techniques such as NEXAFS[45] can provide much insight into properties of the very near-surface region, but lack nanometre-scale lateral resolution. Nanometre-resolution STM/AFM studies of diamond surfaces are relatively sparse in the literature, but when reported[46] often reveal that even carefully prepared surfaces are often defective and spatially inhomogeneous on the nanometre scale.

In the absence of chemical/mechanical polishing techniques such as those used to produce atomically flat silicon surfaces, alternative termination schemes for diamond surfaces need to be investigated. Investigations of fluorine,[47] lithium,[48] nitrogen and silicon termination are in their infancy, but may hold the key to the production of atomically flat and defect-free surfaces. Interestingly, defect-free diamond surfaces might have implications beyond the production of stable NV centres very close to the surface. For example, Cai *et al.*[49] have recently proposed a large-scale quantum simulator based on fluorinated diamond surfaces. The realization of such a simulator would require levels of perfection of diamond surfaces that are beyond our current capabilities. Although nanometre-scale patterning of diamond surfaces has been used to create structures such as single-hole transistors,[50] the control of the diamond surface is very far from that achieved for the atomic-scale doping of silicon,[51] and hence it may be some time before we can create structures such as those suggested by Cai *et al.*

13.4.2 New ultrabright emitters, new spin defects

Especially for biological applications, there is a desire to produce very bright emission in very small nanodiamonds. For example, nanodiamonds smaller than

10 nm in diameter are sought after because such particles are expected to be able to cross the blood–brain barrier and therefore be effective probes for neuroscience applications. Very recently, a number of novel approaches to the production of ultrasmall, ultrabright nanodiamonds have been reported. One of these approaches has been to crush diamond produced by high-pressure/high-temperature (HPHT) processes.[52] This HPHT diamond, containing a high N content, is irradiated with an MeV electron beam and annealed using standard techniques. After jet milling, bead milling and purification, 10 nm nanodiamonds can be isolated, about 30% of which are luminescent. Given that the original estimate of the N content in the starting material is 140 ppm, and assuming that about 10% of the N transform into active NV centres, the estimate of the maximum NV concentration is of the order of 10 ppm, which implies that a 10 nm crystal will contain, on average about one NV centre. If the brightness of these very small nanodiamonds is to be increased significantly, much higher concentrations of NV centres are required. In this regard, a recent study by Baranov *et al.*[53] is of particular interest. These authors reported the results of investigations of NV emission from nanodiamonds sintered under HPHT conditions (800 °C, 6 GPa). They claimed that this material contained up to 10 000 ppm of NV centres, or 1 NV/nm^3. Clearly, if such material is crushed and purified using techniques similar to those reported above, each 10 nm-sized nanodiamond might be expected to contain hundreds of NV centres (provided that the surfaces can be appropriately terminated). If the emission from such ultrasmall nanodiamonds preserves the well-known features of NV centres such as brightness and long-term stability, then such nanodiamonds would most likely become highly sought-after materials for biolabelling. Super-resolution imaging using nanodiamonds has already been demonstrated using a variety of imaging modalities (e.g. stimulated emission depletion microscopy[54] and the recently coined term 'deterministic emitter switch microscopy'[55]), and the availability of superbright, sub-10 nm nanodiamonds may well lead to nanoscale imaging becoming almost routine in biological systems. There is therefore a need to explore further the possibilities arising from sintered nanodiamonds and to confirm the remarkable findings reported by Baranov *et al*.

The search for ultrabright emitters is also driven by their potential application as sources for quantum communications. In this regard, there have been reports on unknown ultrabright emitters, as well as a detailed study of chromium-related emitters in diamond – both of these exhibited emission rates of millions of counts per second.[56, 57] Intriguingly, one of the most studied defects in diamond, the SiV, has recently attracted a lot of attention. As demonstrated by the work of Neu and colleagues, if the defect is grown on an iridium substrate, emission at several megahertz can be observed.[58, 59]

Another interesting trend is the long-standing search for defects other than the NV centre that display similarly attractive quantum properties at room temperature, such as optical spin readout. Despite many reports of very bright emitters suitable as single-photon sources, reports of optically active defects in diamond that

display ODMR (optically detected magnetic resonance) signatures are very rare. Very recently, the Stuttgart group[60] reported a new defect, labelled ST1, which emits at 550 nm (zero-phonon line, ZPL) with an exceptionally high optical spin signal contrast of up to 45% (Plate XIV). This newly discovered centre was used to control a single nuclear spin of a nearby ^{13}C atom spin centre. Because this new centre is believed to possess a spin-free ground state, it is expected to be a promising candidate for increasing the storage time of quantum information. However, the origin of this very promising ST1 centre is as yet unknown. These centres were observed in ultrapure HPHT samples after the fabrication of nanowires by reactive ion etching. The authors of that study conjecture that oxygen may be a constituent of the defect, since the etching of the nanowires took place in an oxygen ambient. However, this is by no means certain, and it may well be that the defect does not incorporate any impurity at all. Given the reports of the properties of the ST1 defect, it would seem that efforts to identify its origins will be most worthwhile.

In the search for the origins of defects in diamond, recent studies suggest that perhaps the role of hydrogen has been underestimated. Hydrogen is the only impurity to show unambiguous evidence of diffusion in diamond. One recent study points to the potential of hydrogen to quench NV luminescence up to 100 μm below the surface following exposure to a hydrogen plasma[61] (Plate XIV(c)). Other studies have shown that single Ni-related defects can have narrowband emission lines,[62] while in another study,[63] it has been demonstrated that very bright centres displaying a sharp ZPL in the range of 750–780 nm can be induced in diamond via annealing in forming gas. In that study, annealing in pure argon or oxygen did not result in the formation of these new centres. Indeed, it was found that annealing in forming gas was an essential step for their formation, with neither ion implantation of impurities nor the introduction of vacancies increasing their occurrence. These results are only the first step towards a complete map of single defects in diamond.

13.5 Conclusion

Since the discovery of single NV centres and the ability to coherently control and read out the electron spin, the field of quantum information processing with diamond has accelerated. The tremendous progress in experimental and theoretical work is remarkable, and it took just over a decade from the first antibunching curve to be recorded from a single NV centre to a demonstration of entanglement between remote defects. From this point onwards, it is up to the scientists and engineers to decide which direction the field will move in.

Drawing some analogies from silicon and III–V semiconductors, the commercialization of basic device prototypes is vital. Commercialization is often self-feeding, and it promotes the science as it gives a clear motivation, a financial boost and interest from the technology side. This was evident in the rapid growth

of GaN LEDs, SiC devices and many other devices. Via the pathways of commercialization, understanding of the practical challenges will become easier and scientists can focus more on the real obstacles. This is particularly important in the case of diamond, because the cost, the lack of large-area single-crystal substrates and the relative difficulty of processing mean that its use will be justified only for those special applications where other material systems are manifestly inadequate.

There is little doubt that the fast pace of research and development will continue for many more years, as we are only at the beginning of unravelling all the fascinating opportunities in quantum diamond.

13.6 References

1. M. W. Doherty, F. Dolde, H. Fedder, F. Jelezko, J. Wrachtrup, *et al.*, *Physical Review B* **85**, 205203 (2012).
2. J. R. Maze, P. L. Stanwix, J. S. Hodges, S. Hong, J. M. Taylor, *et al.*, *Nature* **455**, 644 (2008).
3. G. Balasubramanian, I. Y. Chan, R. Kolesov, M. Al-Hmoud, J. Tisler, *et al.*, *Nature* **455**, 648 (2008).
4. C. L. Degen, *Applied Physics Letters* **92**, 243111 (2008).
5. D. Le Sage, K. Arai, D. R. Glenn, S. J. DeVience, L. M. Pham, *et al.*, *Nature* **496**, 486 (2013).
6. K. Fang, V. M. Acosta, C. Santori, Z. Huang, K. M. Itoh, *et al.*, *Physical Review Letters* **110**, 130802 (2013).
7. V. M. Acosta, E. Bauch, M. P. Ledbetter, C. Santori, K. M. C. Fu, *et al.*, *Physical Review B* **80**, 115202 (2009).
8. L. T. Hall, C. T. Hill, J. H. Cole, B. Stadler, F. Caruso, *et al.*, *Proceedings of the National Academy of Sciences of the United States of America* **107**, 18777 (2010).
9. L. T. Hall, J. H. Cole, C. D. Hill and L. C. L. Hollenberg, *Physical Review Letters* **103**, 4 (2009).
10. A. Hegyi and E. Yablonovitch, *Nano Letters* **13**, 1173 (2013).
11. T. Staudacher, F. Shi, S. Pezzagna, J. Meijer, J. Du, *et al.*, *Science* **339**, 561 (2013).
12. H. J. Mamin, M. Kim, M. H. Sherwood, C. T. Rettner, K. Ohno, *et al.*, *Science* **339**, 557 (2013).
13. F. Dolde, H. Fedder, M. W. Doherty, T. Nobauer, F. Rempp, *et al.*, *Nature Physics* **7**, 459 (2011).
14. P. Neumann, I. Jakobi, F. Dolde, C. Burk, R. Reuter, *et al.*, *Nano Letters* **13**, 2738 (2013).
15. D. M. Toyli, C. F. de las Casas, D. J. Christle, V. V. Dobrovitski and D. D. Awschalom, *Proceedings of the National Academy of Sciences* **110**, 8417 (2013).
16. G. Kucsko, P. C. Maurer, N. Y. Yao, M. Kubo, H. J. Noh, *et al.*, *Nature* **500**, 54 (2013).
17. M. Eichenfield, J. Chan, R. M. Camacho, K. J. Vahala and O. Painter, *Nature* **462**, 78 (2009).
18. T. J. Kippenberg and K. J. Vahala, *Science* **321**, 1172 (2008).
19. P. Rath, S. Khasminskaya, C. Nebel, C. Wild and W. H. P. Pernice, *Nature Communications* **4**, 1690 (2013).
20. S. Kolkowitz, A. C. B. Jayich, Q. P. Unterreithmeier, S. D. Bennett, P. Rabl, *et al.*, *Science* **335**, 1603 (2012).

21. S. K. Hong, M. S. Grinolds, P. Maletinsky, R. L. Walsworth, M. D. Lukin and A. Yacoby, *Nano Letters* **12**, 3920 (2012).
22. Y. Tao and C. Degen, *Advanced Materials* **25**, 3962 (2013).
23. P. Ovartchaiyapong, L. M. A. Pascal, B. A. Myers, P. Lauria and A. C. B. Jayich, *Applied Physics Letters* **101**, 163505 (2012).
24. P. Rath, N. Gruhler, S. Khasminskaya, C. Nebel, C. Wild and W. H. P. Pernice, *Optics Express* **21**, 11031 (2013).
25. F. Andrei, S. Charles, H. Zhihong, C. F. Kai-Mei, M. A. Victor, *et al.*, *New Journal of Physics* **15**, 025010 (2013).
26. B. J. M. Hausmann, I. B. Bulu, P. B. Deotare, M. McCutcheon, V. Venkataraman, *et al.*, *Nano Letters* **13**(5), 1898–1902 (2013).
27. Y. Kubo, C. Grezes, A. Dewes, T. Umeda, J. Isoya, *et al.*, *Physical Review Letters* **107**, 220501 (2011).
28. O. Benson, Nature **480**, 193 (2011).
29. C. Santori, P. E. Barclay, K. M. C. Fu, R. G. Beausoleil, S. Spillane and M. Fisch, *Nanotechnology* **21**, 274008 (2010).
30. M. Barth, S. Schietinger, S. Fischer, J. Becker, N. Nusse, *et al.*, *Nano Letters* **10**, 891 (2010).
31. C. F. Wang, R. Hanson, D. D. Awschalom, E. L. Hu, T. Feygelson, *et al.*, *Applied Physics Letters* **91**, 201112 (2007).
32. A. Magyar, J. C. Lee, A. M. Limarga, I. Aharonovich, F. Rol, *et al.*, *Applied Physics Letters* **99**, 081913 (2011).
33. I. Aharonovich, J. C. Lee, A. P. Magyar, B. B. Buckley, C. G. Yale, *et al.*, *Advanced Materials* **24**, OP54 (2012).
34. I. Aharonovich, J. C. Lee, A. P. Magyar, D. O. Bracher and E. L. Hu, *Laser and Photonics Reviews* **7**, L61 (2013).
35. O. Gaathon, J. S. Hodges, E. H. Chen, L. Li, S. Bakhru, *et al.*, *Optical Materials* **35**, 361 (2013).
36. H. Bernien, B. Hensen, W. Pfaff, G. Koolstra, M. S. Blok, *et al.*, *Nature* **497**, 86 (2013).
37. E. Togan, Y. Chu, A. S. Trifonov, L. Jiang, J. Maze, *et al.*, *Nature* 466, 730 (2010).
38. A. M. Zaitsev, A. A. Bergman, A. A. Gorokhovsky and M. B. Huang, *Physica Status Solidi Applied Research* **203**, 638 (2006).
39. N. Mizuochi, T. Makino, H. Kato, D. Takeuchi, M. Ogura, *et al.*, *Nature Photonics* **6,** 299 (2012).
40. A. Lohrmann, S. Pezzagna, I. Dobrinets, P. Spinicelli, V. Jacques, *et al.*, *Applied Physics Letters* **99**, 251106 (2011).
41. H. Kato, M. Wolfer, C. Schreyvogel, M. Kunzer, W. Muller-Sebert, *et al.*, *Applied Physics Letters* **102**, 151101 (2013).
42. J. Wrachtrup, F. Jelezko, B. Grotz and L. P. McGuinness, *MRS Bulletin* **38**, 149 (2013).
43. T. Staudacher, F. Ziem, L. Haussler, R. Stohr, S. Steinert, *et al.*, *Applied Physics Letters* **101**, 212401 (2012).
44. K. Ohno, F. J. Heremans, L. C. Bassett, B. A. Myers, D. M. Toyli, *et al.*, *Applied Physics Letters* **101**, 082413 (2012).
45. A. Stacey, B. C. C. Cowie, J. Orwa, S. Prawer and A. Hoffman, *Physical Review B* **82**, 125427 (2010).
46. H. Kawarada, M. Nagao, N. Kobayashi, Y. Takano, T. Sasaki and T. Nishizaki, *International Journal of Modern Physics B* **27**, 1362014 (2013).
47. K. J. Rietwyk, S. L. Wong, L. Cao, K. M. O'Donnell, L. Ley, *et al.*, *Applied Physics Letters* **102**, 091604 (2013).

48. K. M. O'Donnell, M. T. Edmonds, J. Ristein, A. Tadich, L. Thomsen, *et al.*, *Advanced Functional Materials* 23, 5608–5614 (2013).
49. J. Cai, A. Retzker, F. Jelezko and M. B. Plenio, *Nature Physics* **9**, 168 (2013).
50. M. Tachiki, H. Seo, T. Banno, Y. Sumikawa, H. Umezawa and H. Kawarada, *Applied Physics Letters* **81**, 2854 (2002).
51. M. Fuechsle, J. A. Miwa, S. Mahapatra, H. Ryu, S. Lee, *et al.*, *Nature Nanotechnology* **7**, 242 (2012).
52. J.-P. Boudou, J. Tisler, R. Reuter, A. Thorel, P. A. Curmi, *et al.*, *Diamond and Related Materials* **37**, 80 (2013).
53. P. G. Baranov, A. A. Soltamova, D. O. Tolmachev, N. G. Romanov, R. A. Babunts, *et al.*, *Small* **7**, 1533 (2011).
54. E. Rittweger, K. Y. Han, S. E. Irvine, C. Eggeling and S. W. Hell, *Nature Photonics* **3**, 144 (2009).
55. E. H. Chen, O. Gaathon, M. E. Trusheim and D. Englund, *Nano Letters* **13**, 2073 (2013).
56. S. Pezzagna, D. Rogalla, D. Wildanger, J. Meijer and A. Zaitsev, *New Journal of Physics* **13**, 035024 (2011).
57. I. Aharonovich, S. Castelletto, D. A. Simpson, C. H. Su, A. D. Greentree and S. Prawer, *Reports on Progress in Physics* **74**, 076501 (2011).
58. E. Neu, R. Albrecht, M. Fischer, S. Gsell, M. Schreck and C. Becher, *Physical Review B* **85**, 245207 (2012).
59. E. Neu, D. Steinmetz, J. Riedrich-Moeller, S. Gsell, M. Fischer, *et al.*, *New Journal of Physics* **13**, 025012 (2011).
60. S.-Y. Lee, M. Widmann, T. Rendler, M. W. Doherty, T. M. Babinec, *et al.*, *Nature Nanotechnology* **8**, 487 (2013).
61. A. Stacey, D. A. Simpson, T. J. Karle, B. C. Gibson, V. M. Acosta, *et al.*, *Advanced Materials* **24**, 3333 (2012).
62. S. Castelletto, A. Edmonds, T. Gaebel and J. Rabeau, *IEEE Journal of Selected Topics in Quantum Electronics* **18**, 1792 (2012).
63. D. Lau, T. J. Karle, B. C. Johnson, B. Gibson, S. Tomljenovic-Hanic, *et al.*, *Applied Physics Letters Materials* (2013).

Index

A system, 11–12
ab initio approach, 58
ab initio calculation, 85
AC magnetometry mode, 255
Advanced Encryption Standard (AES), 32
air annealing, 73
air humidity, 169
angled-ion-etching technique, 310
antibunching, 86–7, 133, 146–7, 161
Aplysia californica, 297–8
atomic force microscope (AFM), 169, 251
atomic magnetic sensor, 308
atomic-sized magnetic sensor
  NV defect, 244–6
    basic spin properties of NV centres, 245
attenuated laser pulses, 150–1
attenuated light pulses
  quantum key distribution (QKD) principles, 21–33
    BB84 protocol, 22–4
    fibre-based QKD, 27–9
    free-space QKD, 29–31
    future trends, 32–3
    implementing QKD, 26–7
    protocol extensions and alterations, 24–5
Aunt Martha, 26

back-scattered Rayleigh light, 225
band gap, 135–6
BB84 protocol, 22–4, 152
  QKD principles, 22–4
    illustration, 223
Bell's inequality, 205
biofouling, 294–5
bioimaging, 220–4
biolabel size, 220–2
  TEM image of fluorescent ultrananocrystalline diamond film and fluorescence spectra, 221–2
biomagnetometry, 227–8
Bionic Eye Project, 299–300
Biot–Savart law, 280
Bohr magnetron, 243
Born-Oppenheimer approximation, 200–1
Bragg mirrors, 162
bulk diamond, 143–4, 188
  probes, 254–5

carbon chemistry, 222
cathodoluminescence, 225, 311
cavity-dipole coupling rate, 7–8
cavity photon, 12
charge state stability, 148–9
chemical doping, 51
chemical vapour deposition (CVD), 7, 39–40, 72, 106–7, 137, 164, 250, 294
chip-scale integrated nanophotonics, 113–15
chromium-related centres, 54, 141–2
chronoamperometry, 294–5
circuit-based schemes, 94
coherence properties, 270–1
cold implantation rapid annealing (CIRA), 50
cold-lens microscopes, 78
collection efficiency, 134, 142–4
  single dipole radiating at 770 nm using collection optics with numerical aperture 0.8, 144
collective coupling
  flux qubit and NV ensemble, 279–81
    energy spectrum in external field of magnitude 2.6mT, 281

hybrid system, 276–84
moving to time domain, 281–4
cavity ring-down illustration, 282
plot of qubit switching probability vs time for vacuum Rabi measurement at optimum point, 283
resonators and nitrogen-vacancy (NV) ensembles, 276–9
transmission function of CPWR vs external magnetic field, 278
transmission function of CPWR vs flux bias, 279
collective giant spin operators, 277
collision cascade, 41
colour centres
specific properties, 142–50
collection efficiency, 142–4
photostability and charge state stability, 148–9
polarisation of emitted photons, 149–50
quantum efficiency and shelving states, 144–8
suitability in diamond as single-photon sources, 135–7
emission range and band gap, 135–6
phonons, 136
refractive index, 137
types investigated as single emitters, 137–42
chromium-related centres, 141–2
nickel-related centres, 140–1
nitrogen-based colour centres, 137–40
other colour centres, 142
photoluminescence spectra of NV vs SiV vs near-infrared-emitting centre, 139
silicon centres, 140
summary of colour centres demonstrated as single-photon emitters, 138
computer simulations, 44
damage in diamond, 57–64
diamond-graphite interface, 61–4
solids and general considerations, 57–8
diamond and graphite, 58–61
computation of displacement energy, 59–60
critical defect density for diamond-to-graphite conversion, 60–1
confocal microscopy, 70–1
confocal Raman mapping, 225
continuous-wave (CW) signals, 91
conventional microscopy, 224–6
coplanar waveguide resonator (CPWR), 271
critical damage density
graphitisation of diamond, 44–7
resistance of damaged diamond as function of fluence for 100 keV C and 320 KeV ions, 46
SIMS depth profiles of boron and lithium-implanted diamond, 47
critical defect density
simulations for diamond-to-graphite conversion, 60–1
evolution of structure of heavily damage region, 61

damage-annealing schemes, 49–50
Debye-Waller effects, 202
Debye-Waller factor, 136, 171
decoy protocols, 25
defect centres
nanodiamonds as single-plasmon sources, 174–7
coupling of NV centres to plasmonic structures, 175–6
properties in nanodiamonds, 164–8
fluorescence spectrum of single NV centre and measured spectral jump rate, 168
optical properties studied at single-centre level, 165
saturation measurements of stable, bright NV centre, 166
SEM image of CVD diamond nanocrystals and magnified images, 165
usage in diamonds to build photonic and quantum optical devices, 160–89
applications of engineered single-photon sources based on nanodiamonds, 180–7
architectures for single-photon collection and single-photon interaction, 161–3
fundamental photonic and plasmonic elements assembled from nanodiamonds, 171–9
future trends, 187–9
method for controlled assembly of fundamental photonic elements, 168–70
photonic elements made from nanodiamonds in laser-written structures, 177–9

dephasing rates, 91–2
deterministic approaches, 169
deterministic emission depletion microscopy, 313
detonation-chamber growth, 164
diamond
  challenges in materials science, 311–14
    drive for stable emitters very near surfaces, 311–12
    new ultrabright emitters and new spin defects, 312–14
  defect centres usage to build photonic and quantum optical devices, 160–89
    applications of engineered single-photon sources based on nanodiamonds, 180–7
    architectures for single-photon collection and single-photon interaction, 161–3
    fundamental photonic and plasmonic elements assembled from nanodiamonds, 171–9
    future trends, 187–9
    method for controlled assembly of fundamental photonic elements, 168–70
    photonic elements made from nanodiamonds in laser-written structures, 177–9
    properties in nanodiamonds, 164–8
  effect of sample, 249–50
    typical coherence times of NV defect electron spin for different diamond crystals, 250
  heterostructures, 10
  impurities, 3–4
  ion implantation for quantum information processing (QIP) doping and damaging, 36–65
    applications of graphitisation, 54–7
    computer simulations, 57–64
    controlled formation of implant-defect centres, 50–4
    doping diamond, 38–40, 41–50
  nanocrystals, 187–8
  nanowires, 106–9
    nanowire fluorescence below saturation and normalised coincidence counts, 108
  neural circuits and *in vivo* monitoring, 291–300
    diamond biosensors, 294–5
    diamond-cell interface, 292–4
    future trends, 300
  neural networks, 295–7
    example of successfully patterned neural network, 297
    in vitro detection of serotonin in 12 muscle of *Aplysia californica*, 296
  neural stimulation and recording, 297–300
    current retinal implants comprising diamond, 299
    reported charge injection of various biomaterials, 298
  quantum information processing (QIP) principles, 3–17
    key properties of nitrogen-vacancy (NV) centres, 6–8
    NV centres and diamond photonic networks, 10–17
    role of diamond impurities, 3–4
    techniques for creating NV centres, 8–10
    types of diamond colour centre, 4–6
  quantum systems hybridisation and coupling NV centres to superconducting circuits, 264–87
    collective coupling in hybrid system, 276–84
    future trends, 286–7
    spin ensembles, 266–71
    superconducting circuits, 271–6
    towards quantum memory operations, 284–6
  single defects characterisation in quantum devices development, 68–95
    fluorescence microscopy of single colour centres, 70–81
    future trends, 95
    optical spectroscopy of single defects, 81–6
    photon statistics, 86–90
    spin resonance, 90–5
  spin-photon entanglement for quantum optical networks, 195–216
    future trends, 213–16
    generation, 202–10
    Hong-Ou-Mandel interference between identical photons from NV centres, 210–12
    measurements results in entanglement, 196–200

optical properties of nitrogen-vacancy (NV) centre for generation, 200–2
single-shot projective readout of NV centres, 213
diamond-based single-photon sources
application in quantum key distribution, 127–53
characterisation and key parameters of single-photon source, 130–5
colour centres and specific properties, 142–50
colour centres and types of colour centres investigated as single emitters, 137–42
future trends, 153
nitrogen-vacancy (NV) and silicon-vacancy (SiV) centres, 150–2
single-photon emission principles, 129–30
single-photon sources, 128–9
suitability of colour centres, 135–7
diamond biosensors, 294–5
diamond-cell interface, 292–4
differentiation of stem cells on diamond surfaces, 293
diamond colour centre, 4–6
diamond defect centres, 224
diamond-graphite interface simulation, 61–4
heavily damaged region in diamond following different implantation schemes, 63
NV complex formation, 62–4
diamond graphitisation
applications by highly damaging implantations, 54–7
formation of free-standing diamond membranes, 54–5
ion-beam-induced graphitisation for realisation of nanosized features, 56–7
photonic crystals in diamond by ion beams, 55–6
diamond magnetic sensors, 240–59
future trends, 257–9
magnetometry with nitrogen-vacancy (NV) centres, 241–50
scanning NV magnetometry, 251–7
diamond on insulator (DOI), 113–15
diamond photonic networks, 10–17
cartoon of photonic-network QIP device, 11
experimental progress and challenges, 16–17
requirements, 14–16
cavity-enhanced photon generation from spin qubit with optical transition, 15
scheme for measurement-based entanglement between two spin qubits, 13
transfer of quantum state between two distant qubits, 12
diamond-silver hybrid resonators, 109–13
illustration of diamond-plasmonic system and simulated spontaneous-emission, 110
normalised fluorescence decays and background-subtracted photoluminescence spectra, 112
performance plot of saturation intensity and SEM image of diamond nanopost, 113
SEM image of array of diamond posts and confocal microscope scan of array, 111
diamond technologies
promising directions for quantum information processing (QIP) and sensing, 307–15
challenges in diamond materials science, 311–14
exploiting fundamental properties of optomechanics and other areas of research, 309–11
nanodiamonds for high-resolution sensors, 307–9
dielectric structures, 162
Diffie-Hellman codes, 32
dipolar coupling, 229
displacement energy, 44
DNA immobilisation tool, 292
dopant atoms, 38
dopant centres, 40
doping diamond, 38–40
chemical vapour deposition (CVD) growth, 39–40
electrically active defect complexes, 40
high-pressure high-temperature (HPHT) growth, 38
ion implantation, 41–50
collision cascade following penetration into diamond, 42

damage-annealing schemes for efficient ion implantation doping, 49–50
general considerations, 41–3
SRIM damage and ion profiles for 100 keV C and 320 keV Xe ions, 43
ion implantation-related damage, 44–9
critical damage density for graphitisation, 44–7
displacement energy, 44
electrical effects of native defects in diamond, 48
properties of partially damaged diamond, 48–9

electric sensing, 232
electrical excitation, 311
electrically activated single-photon sources, 311
electrically active defect complexes, 40
electron beam lithography (EBL), 101–2
electron irradiation, 9, 51
electron microscopy, 225
electron spin detection, 257
electron spin resonance (ESR), 244
emission lifetime, 130–1
emission range, 135–6
emitted photons polarisation, 149–50
single SiV centre recorded using linear polarisation analyser, 150
European Space Agency, 30
excitation-emission cycle, 129
excited-state population, 131–2
experimental methods, 70–81
explosive detonation, 73

Fabry-Pérot cavity, 162
Fabry-Pérot etalon, 83
Faraday cage, 103
Faraday mirror, 28–9
fast scan cyclic voltammetry, 294–5
Fermi level, 48
Fermi's golden rule, 162
fibre-based quantum key distribution, 27–9
finite-difference time-domain (FDTD) simulations, 106–7
fluorescence intermittence, 148–9, 223–4
fluorescence microscopy, 225
basic equipment, 70–2
photoluminescence of vibronic defects, 71
experimental methods of single colour centres in diamonds, 70–81
light collection issues and strategies, 73–5
low-temperature systems, 78
sample requirements, 72–3
scanning confocal imaging, 75, 77
super-resolution imaging, 78–81
fluorescent nanodiamonds, 220
flux-qubit-ensemble hybrid system, 283
flying qubit, 11
Fock state, 133–4, 180–1
focused ion beam (FIB), 55
milling, 101
Förster resonant energy transfer (FRET), 225
Fourier transform, 91
Franck-Condon coupling, 7–8
Franck-Condon effects, 202
Franck-Condon principle, 70, 82
free-space quantum key distribution, 29–31
schematic illustration, 31
Fresnel reflection, 137
full width half maximum (FWHM), 231
fundamental photonic elements, 168–70

gap-tunable qubit, 275
Gaussian profile, 246
glass fibre systems, 27–8
graphitisation-liftoff procedure, 55–6
graphitisation limit, 45
green laser excitation, 138–9
Greenberg-Horne-Zeilinger (GHZ), 94

Hadamard gate, 198
Hahn echo, 91–2, 248–9
Hamiltonian ensemble, 268–70
Hamiltonian interaction, 203
Hanbury Brown and Twiss (HBT), 107
interferometer, 132–3
measurements, 86–7
set-up, 161
harmonic oscillators, 277
Heisenberg's uncertainty, 23
high-density microelectrode arrays, 298
high-density spin ensemble, 267–8
high impurity content, 227
high-numerical-aperture optics, 149
high-pressure high-temperature (HPHT) diamond, 106–7, 137
high-pressure high-temperature (HPHT) growth, 38, 164

high-pressure high-temperature (HPHT) method, 250, 267–8, 312–13
high-resolution optical near-field microscopy, 129
high-resolution sensors, 307–9
hollow-core photonic-crystal fibre (HCPCF), 184–5
Hong-Ou-Mandel (HOM) interference, 197
  identical photons from NV centres, 210–12
    schematic illustration of apparatus, 211
    single-emitter second-order autocorrelation functions and demonstration, 212
Huang-Rhys
  effects, 202
  factor, 82, 136
hybrid diamond-metal device, 109–10
hydrogen annealing, 73

implant-defect centres
  controlled formation, 50–4
    nitrogen-vacancy (NV) complexes in diamond by ion implantation, 51–3
    optically active complexes in diamond by ion implantation, 53–4
impurity-defect complexes, 51
in vivo monitoring
  neural circuits using diamond, 291–300
    diamond biosensors, 294–5
    diamond-cell interface, 292–4
    future trends, 300
    neural networks, 295–7
    neural stimulation and recording, 297–300
incoherent optical initialisation, 7
incoherent single-photon conversion, 184–7
  experimental implementation, 185–7
    count rates from conversion to near infrared using HCPCF, 187
  general concept, 184–5
    schematic of HCPCF and CCD fluorescence image of photoluminescence, 185
    two complementary approaches to on-demand single-photon generation, 184
inductively coupled plasma (ICP), 102–3
infinitesimal time resolution, 203
inhomogeneous broadening, 81–2
insulating polycrystalline diamond, 299–300
integrated ring resonators, 113–15
  confocal image and second-order cross-correlation and spectrum collected at gratings, 115
  SEM image of waveguide-coupled diamond ring resonator and transmission spectrum, 114
intensity autocorrelation function, 131
interferometer, 28–9
ion-beam-induced graphitisation, 56–7
ion implantation, 9–10
  diamond for quantum information processing (QIP) doping and damaging, 36–65
    applications of graphitisation by highly damaging implantations, 54–7
    computer simulations, 57–64
    controlled formation of implant-defect centres, 50–4
    doping diamond, 38–40, 41–50
  -related damage, 44–9
    critical damage density for graphitisation of diamond, 44–7
    displacement energy, 44
    electrical effects of native defects in diamond, 48
    properties of partially damaged diamond, 48–9
ion slicing, 101
irradiation, 10
iSWAP gate, 284–5

Jahn-Teller effect, 83, 202
Josephson energy, 275

large-scale integrated photonic network, 310
Larmor frequency, 229
Larmor precession yields, 243
laser clean-up filter, 72
laser-written structures, 177–9
light collection issues
  strategies, 73–5
    fluorescence collection efficiency as function of numerical aperture, 74
    spherical aberrations resulting from focusing through planar diamond surface, 76
light-emitting diodes (LEDs), 311
linear polarisation analyser, 149–50

lithography, 298
living cells, 226–8
local quantum probes, 189
local spin interactions, 93–5
local strain effects, 84–6
Lorentzian profile, 246
Lorentzian transmission function, 273
low-temperature systems, 78
  scanning confocal microscopy of single colour centres, 79

magnetic-field fluctuations, 7
magnetic-field sensitivity, 241–3, 246–9, 255
  NV magnetometry sequences, 248
magnetic resonance imaging, 253–4
magnetic vortex structures, 257
magnetometry, 226–9, 243–4
  nanobiomagnetometry, 228–9
    high-density two-dimensional layer usage allow wide areas of neurons to be imaged, 229
  nitrogen-vacancy (NV) centres, 241–50
    defect as an atomic-sized magnetic sensor, 244–6
    effect of diamond sample, 249–50
    general remarks, 241–4
    magnetic-field sensitivity, 246–9
    performance of various magnetic imaging and sensing technologies, 242
  quantum measurements in living cells, 226–8
Maxwell's equation, 180–1
measurement-based entanglement, 12–13
measurement-based schemes, 94
microfabrication techniques, 298
microphotonic system, 179
microwave-frequency nanoparticle identification, 230–1
microwave resonators, 271–4
Mie resonances, 143
molecular dynamics simulations, 44
Monte Carlo calculations, 59
Monte Carlo computer programs, 41
multipulse sensing protocols, 249

nanobiomagnetometry, 228–9
nanocrystalline diamond, 292
nanocrystalline topography, 292
nanodiamond, 73, 164–8, 171–9
  applications of engineered single-photon sources, 180–7
    fundamental experiment to measure quantum nature of light, 180–3
    incoherent single-photon conversion, 184–7
    schematic illustration and photograph of single-photon source, 180
  chemistry, 222–3
  high-resolution sensors, 307–9
  properties for bioimaging, 220–4
    optical properties, 223–4
    quantum properties, 224
    size, 220–2
  quantum microscopy, 219–33
    conventional microscopy, 224–6
    future trends, 232–3
    magnetometry, 226–9
    rotational tracking, electrometry and thermometry, 230–2
nanoelectrode arrays, 300
nanofabrication
  photonic devices from single-crystal diamond for quantum information processing (QIP), 98–119
    fabrication approaches for nanostructures, 101–6
    single-photon sources in nanostructured diamond, 106–13, 113–17
nanoparticle orientation tracking, 231–2
nanophotonics, 188
nanoscale magnetic-field imaging, 243–4
nanoscale magnetometers, 308
nanotechnology, 298–9
nanothermometry, 232
nanotopography, 296–7
near-infrared-emitting centre, 141
near-infrared-emitting dyes, 223
near infrared photon, 186
neural circuits
  in vivo monitoring using diamond, 291–300
    diamond biosensors, 294–5
    diamond-cell interface, 292–4
    future trends, 300
    neural networks, 295–7
    neural stimulation and recording, 297–300
neural networks, 295–7
neural recording, 297–300
neural stimulation, 297–300
neurite patterns, 296–7
neutron irradiation, 268
NEXAFS technique, 312
Ni-nitrogen (NE8) complex, 54

nickel-related centres, 140–1
nitrogen-based colour centres, 137–40
nitrogen impurity, 9
nitrogen-vacancy (NV) centre, 133–4, 150–2, 164, 241–4
  Hong-Ou-Mandel interference between identical photons, 210–12
  key properties, 6–8
    electronic structure, 6
  optical properties spin-photon entanglement for generation, 200–2
    hierarchy of interactions for ground and excited state triplets, 201
  quantum systems hybridisation in diamond to superconducting circuits, 264–87
    collective coupling in hybrid system, 276–84
    future trends, 286–7
    spin ensembles, 266–71
    superconducting circuits, 271–6
    towards quantum memory operations, 284–6
  single-shot projective readout, 213
  techniques for creation, 8–10
    diamond heterostructures, 10
    ion implantation, 9–10
    irradiation, 10
nitrogen-vacancy (NV) complex, 50–1
  diamond by ion implantation, 51–3
    experimental set-up for single-ion implantation, 52
    histogram summarising evolution of NV photoluminescence intensity, 53
normal temperature and pressure (NTP), 38
nuclear magnetic resonance (NMR), 308

off-resonant excitation, 167
off-resonant pumping, 131–2
oil immersion lenses, 78
on-chip electrodes, 17
optical confocal microscopy, 244
optical excitation, 129–30
optical filters, 72
optical imaging, 229
optical microcavities
  single-photon harvesting, 171–4
    positioning of nanodiamond in photonic-crystal S1 cavity using pick and place, 173
    positioning of nanodiamond in photonic-crystal S1 cavity using SEM manipulator, 172
optical properties, 223–4
optical spectroscopy, 230–1
  single defects, 81–6
    local strain effects, 84–6
    photoluminescence excitation (PLE) spectroscopy, 82–4
    photoluminescence (PL) spectroscopy, 82
optical transitions, 8
optically active complexes, 53–4
optically active defect centres, 164–5
optically active impurity-vacancy complexes, 44
optically detected magnetic resonance (ODMR), 90–3, 230, 313–14
optomechanics, 309
oxygen-based plasma etching, 103
oxygen plasma, 73

p-i-n diode, 153
p-n junctions, 39
Pauli spin operators, 275
pentaerythritol tetraacrylate (PETTA), 177
2D percolation model, 45
phonon sidebands (PSBs), 202
phonons, 136
photochromism *see* green laser excitation
photoluminescence centre, 54
photoluminescence excitation (PLE) spectroscopy, 82–4
  data from three different single NV defects, 84
photoluminescence excitation spectrum, 205–8
photoluminescence (PL), 70, 244
  spectroscopy, 81, 82
photon antibunching, 131
photon statistics, 86–90
  Hanbury Brown and Twiss (HBT) measurements, 86–7
  rate equation analysis, 87–90
    second-order autocorrelation function measured using Hanbury Brown and Twiss methods, 88
photonic-crystal cavities, 115–17, 310
  SEM images of arrays of 1D diamond suspended photonic crystal nanobeams, 116
photonic-crystal membrane, 172–3
photonic crystals, 55–6

realisations by diamond by ion beams, 55–6
illustration of fabrication of thin diamond membrane by graphitisation-etching-liftoff procedure, 56
photonic devices
defect centres usage in diamonds to build quantum optical devices, 160–89
applications of engineered single-photon sources based on nanodiamonds, 180–7
architectures for single-photon collection and single-photon interaction, 161–3
fundamental photonic and plasmonic elements assembled from nanodiamonds, 171–7
future trends, 187–9
method for controlled assembly of fundamental photonic elements, 168–70
photonic elements made from nanodiamonds in laser-written structures, 177–9
properties in nanodiamonds, 164–8
nanofabrication from single-crystal diamond for quantum information processing (QIP), 98–119
fabrication approaches for nanostructures, 101–6
single-photon sources in nanostructured diamond, 106–13, 113–17
photonic elements
made from nanodiamonds in laser-written structures, 177–9
integrated microoptical assembly, 179
two-photon direct laser-writing in diamond photoresist, 178
photostability, 148–9
pick and place technique, 170
planar photonic structures, 103–4
plug & play system, 29
point spread function (PSF), 75
Poissonian light statistics, 150–1
Poissonian photon number distribution, 161
Poissonian statistics, 9–10, 133–4
polarisation anisotropy, 149
polarisation-filtered photons, 153
positron emission tomography, 223
positron irradiation, 9
privacy amplification, 24
pulsed microwave signals, 91
Purcell, 14–15
Purcell enhancement, 111–12, 162
Purcell factor, 171

quantum bit error ratio (QBER), 24
quantum bit (qubit), 54–5
quantum bits, 128
quantum candela, 128–9
quantum channels, 27
quantum coherence, 233
quantum control, 93–5
quantum cryptography, 128
quantum devices development
single defects characterisation in diamond, 68–95
experimental methods for fluorescence microscopy of single colour centres, 70–81
future trends, 95
optical spectroscopy of single defects, 81–6
photon statistics, 86–90
spin resonance, 90–5
quantum dots (QDs), 220
quantum efficiency, 134, 144–8
excitation and de-excitation processes for single colour centre in diamond, 145
pulsed photon correlation and continuous-excitation measurements of SiV centre, 147
quantum eraser effect, 204
quantum information processing (QIP)
diamond technologies promising directions for sensing, 307–15
challenges in diamond materials science, 311–14
fundamental properties of optomechanics and other areas of research, 309–11
nanodiamonds for high-resolution sensors, 307–9
ion implantation in diamond doping and damaging, 36–65
applications of graphitisation by highly damaging implantations, 54–7
computer simulations, 57–64
controlled formation of implant-defect centres, 50–4
doping diamond, 38–40, 41–50

nanofabrication of photonic devices from single-crystal diamond, 98–119
fabrication approaches for nanostructures, 101–6
single-photon sources in nanostructured diamond, 106–13, 113–17
principles and diamond usage, 3–17
key properties of nitrogen-vacancy (NV) centres, 6–8
NV centres and diamond photonic networks, 10–17
role of diamond impurities, 3–4
techniques for creating NV centres, 8–10
types of diamond colour centre, 4–6
quantum information protocols, 128
quantum key distribution (QKD)
diamond-based single-photon sources and application, 127–53
characterisation and key parameters of single-photon source, 130–5
colour centres and specific properties, 142–50
colour centres and types of colour centres investigated as single emitters, 137–42
future trends, 153
suitability of colour centres, 135–7
implementation, 26–7
setup for first quantum cryptography demonstration, 26
nitrogen-vacancy (NV) and silicon-vacancy (SiV) centres, 150–2
simulation and experimental data for number of exchanged secure bits vs attenuation, 151
principles using attenuated light pulses, 21–33
BB84 protocol, 22–4
fibre-based QKD, 27–9
free-space QKD, 29–31
future trends, 32–3
protocol extensions and alterations, 24–5
quantum light nature
experimental implementation, 181–3
measurement of g2 function in single-detector configuration, 183
tools illustration, 182
fundamental experiment for measurement, 180–3
general concept, 180–1
HBT correlator and configuration for photon correlation, 181
interpretation, 183
quantum lock-in amplification, 248
quantum measurements, 226–8
quantum memory operations, 284–6
diagram of Ramsey-like experiment on spin ensemble at single-photon level, 286
schematic of transfer of an excitation from flux qubit to an ensemble, 284
quantum microscopy
nanodiamonds, 219–33
conventional microscopy, 224–6
future trends, 232–3
magnetometry, 226–9
properties for bioimaging, 220–4
rotational tracking, electrometry and thermometry, 230–2
quantum optical devices
defect centres usage in diamonds to build photonic devices, 160–89
applications of engineered single-photon sources based on nanodiamonds, 180–7
architectures for single-photon collection and single-photon interaction, 161–3
fundamental photonic and plasmonic elements assembled from nanodiamonds, 171–9
future trends, 187–9
method for controlled assembly of fundamental photonic elements, 168–70
photonic elements made from nanodiamonds in laser-written structures, 177–9
properties in nanodiamonds, 164–8
quantum optical networks
spin-photon entanglement in diamond, 195–216
future trends, 213–16
generation, 202–10
Hong-Ou-Mandel interference between identical photons from NV centres, 210–12
measurements results in entanglement, 196–200
optical properties of nitrogen-vacancy (NV) centre for generation, 200–2

single-shot projective readout of NV centres, 213
quantum photonics, 309–10
quantum sensing
diamond technologies for quantum information processing (QIP), 307–15
challenges in diamond materials science, 311–14
fundamental properties of optomechanics and other areas of research, 309–11
nanodiamonds for high-resolution sensors, 307–9
quantum systems hybridisation
coupling nitrogen-vacancy (NV) centres in diamond to superconducting circuits, 264–87
collective coupling in hybrid system, 276–84
future trends, 286–7
spin ensembles, 266–71
superconducting circuits, 271–6
towards quantum memory operations, 284–6
quarter-wave plate (QWP), 205–8

Rabi oscillations, 89, 129–30, 282–3
radial distribution function (RDF), 58
radiation damage, 41
Raman scattering, 72
Raman spectroscopy, 45–7
Ramsey interference, 91–2
Ramsey pulse, 246–7
random techniques, 168–9
rapid thermal annealing, 116–17
rate equation analysis, 87–90
reactive-ion etching, 101–2
readout laser pulse, 247
red diode laser, 186
refractive index, 73–4, 137, 142–3
remote spin qubits, 196–7
repetition rate, 130–1
3D retinal multielectrode device, 298–9
retinal prosthesis, 299–300

scanning confocal imaging, 75, 77
schematic optical set-up, 77
scanning diamond nanopillars, 253
scanning electron microscope, 169, 253
scanning magnetic sensor, 251–3
scanning NV magnetometry, 251–7
applications, 254–7
example of NV magnetic-field image tracks on magnetic hard drive, 255
illustration of single-spin imaging and magnetic-field image and recorded line scan, 256
nanoscale image of magnetic vortex structure, 258
implementation, 251–4
illustration of set-up and all-diamond bulk scanning probe and nanocrystals, 252
scanning probe technique
fundamental photonic and plasmonic elements assembled from nanodiamonds, 171–7
defect centres as single-plasmon sources, 174–7
optical microcavities for single-photon harvesting, 171–4
method for controlled assembly of fundamental photonic elements, 168–70
pick and place technique, 170
scanning tunnelling microscope (STM), 51
scattered Raman-shifted light, 225
Schrödinger equation, 203
secondary ion mass spectrometry, 45
SECOQC demonstration network, 32–3
selective nitrogen doping, 9
SeQureNet, 29
shelving states, 144–8
sifted key, 23–4
signal-to-noise ratio, 226, 246
silicon centres, 140
silicon microchip encapsulation, 298
silicon-vacancy (SiV) centre, 140, 150–2, 164
single colour centres, 70–81
single-crystal diamond
fabrication approaches for nanostructures, 101–6
illustration of triangular-prism and conical faraday cage and directions of ions, 104
SEM images of nanobeams and cavities, 105
sequence for diamond nanowire and SEM images of arrays of 2 μm tall nanowires, 102
thinning of thick single-crystal membrane and waveguide-coupled ring resonator, 106

nanofabrication of photonic devices for quantum information processing (QIP), 98–119
single-photon sources in nanostructured diamond, 106–13, 113–17
single defects, 81–6
single defects characterisation
diamond in quantum devices development, 68–95
experimental methods for fluorescence microscopy of single colour centres, 70–81
future trends, 95
optical spectroscopy of single defects, 81–6
photon statistics, 86–90
spin resonance, 90–5
single molecule spectroscopy, 223
single-photon collection
architectures for single-photon interaction, 161–3
different approaches to increasing single-photon emission into specific modes, 163
illustration of HBT set-up and measurement of normalised second-order coherence, 162
single-photon detector, 27, 70
single-photon emission
principles, 129–30
schematic illustration using non-resonant optical excitation, 129
single-photon harvesting, 171–4
single-photon interaction, 161–3
single-photon purity, 131–4
single-photon sensitive detector, 132–3
single-photon sources, 128–9
characterisation and key parameters, 130–5
collection efficiency, 134
emission lifetime and repetition rate, 130–1
indistinguishable photons, 135
quantum efficiency, 134
single-photon purity and statistics, 131–4
spectral properties and polarisation, 134–5
nanostructured diamond, 106–13, 113–17
diamond nanowires, 106–9
diamond-silver hybrid resonators, 109–13
integrated ring resonators, 113–15
photonic-crystal cavities, 115–17
single-plasmon sources, 174–7
single-shot projective readout, 213
nitrogen-vacancy (NV) centre, 213
SEM image of solid immersion lens and fluorescence time trace of NVA, 214
shorter measurement windows the readout becomes nondestructive, 215
singlet polarisation state, 199
solid immersion lenses (SILs), 143–4
solid-state quantum emitters, 15–16
solid-state quantum systems, 164–5
spatial resolution, 81, 241–3
spectral filtering aids, 134–5
spectral properties, 134–5
spin-coating, 176
spin defects, 312–14
spin ensembles, 266–71
coherence properties, 270–1
Hamiltonian ensemble, 268–70
transition frequency of an NV spin as function of in-plane magnetic field, 269
high-density spin ensemble preparation, 267–8
schematic illustration of structure of NV centre in diamond lattice, 267
spin Hamiltonian, 308
spin-photon entanglement
diamond for quantum optical networks, 195–216
future trends, 213–16
Hong-Ou-Mandel interference between identical photons from NV centres, 210–12
optical properties of nitrogen-vacancy (NV) centre for generation, 200–2
single-shot projective readout of NV centres, 213
experimental realisation, 205–10
photoluminescence excitation spectrum of single NV centre, 207
schematic illustration for generation and verification, 206
verification of polarisation selection rules for entanglement transition, 207
generation, 202–10

theoretical analysis of scheme, 203–5
measurements results in entanglement, 196–200
action of beam splitter on photon spatial modes and level structure for generation, 198
remote entanglement generation between two solid-state spin qubits, 197
spin-photon state transfer process, 15–16
spin-readout noise, 246
spin resonance, 90–5
optically detected magnetic resonance (ODMR) of NV centres, 90–3
hyperfine splitting due to coupling between NV electron spin and nuclear spin, 92
optical and microwave pulse sequences for pulsed spin resonance measurements, 93
quantum control via local spin interactions, 93–5
spin-spin coupling, 91
SRIM code, 41
Stark effect, 210
Stark-shift, 17
steady-state population, 132
stimulated emission depletion (STED), 225
stimulated emission depletion (STED) microscopy, 78–80, 253–4, 313
stimulated Raman adiabatic passage (STIRAP), 14–15
technique, 129–30
strain splitting, 268
sub-Poissonian, 86–7
subsequent angled etching, 103
subwavelength diamond waveguide, 109
super-resolution imaging, 78–81, 221–2, 312–13
schematic illustration of principle of spatial-resolution enhancement using STED, 80
superconducting circuits, 271–6
microwave resonators, 271–4
illustration of design of CPWR and input and output coupling structure, 272
quantum systems hybridisation and coupling nitrogen-vacancy (NV) centres in diamond, 264–87
collective coupling in hybrid system, 276–84
future trends, 286–7
spin ensembles, 266–71
superconducting circuits, 271–6
towards quantum memory operations, 284–6
superconducting qubits, 274–6
illustration of gap-tunable flux qubit composed of four Josephson junctions, 275
spectra of gap-tunable qubit, 276
superconducting quantum interference devices (SQUIDs), 274
superconducting qubits, 274–6
superconducting single-photon detector (SSPD), 181–2
superposition state, 22–3, 209
surface plasmon polaritons (SPPs), 163

Tersoff potential, 58, 60
thermal spike, 41
thermodynamic process, 38
three-dimensional array system, 300
three-node Darpa Quantum Network, 32–3
time-bon coding, 28
top-down etching, 103, 310
top-down nanofabrication procedure, 106–7
transmon-resonator-ensemble coupled hybrid system, 285
TRIGA Mark II, 268
triplet polarisation state, 199
two-photon fluorescence correlation spectroscopy, 225–6
two-photon microscopy, 225–6

ultrabright emitters, 312–14
new spin defects, 312–14
ultrahigh-Q cavities, 55
ultrananocrystalline diamond, 298
electrodes, 299–300

weak coherent pulses (WCPs), 150–1
Wigner-Weisskopf theory, 203

Young's modulus, 309

Zeeman effect, 6–7, 91
Zeeman splitting, 268
Zen shifts, 244–6
zero-field splitting (ZFS), 266–7
zero-phonon line (ZPL), 6, 83, 136, 167, 202, 266–7, 313–14

This page intentionally left blank

This page intentionally left blank